Springer Series in Solid-State Sciences 179

Peter Sigmund

Particle Penetration and Radiation Effects Volume 2

Penetration of Atomic and Molecular Ions

Springer

Springer Series in Solid-State Sciences

Volume 179

For further volumes:
http://www.springer.com/series/682

The Springer Series in Solid-State Sciences consists of fundamental scientific books prepared by leading researchers in the field. They strive to communicate, in a systematic and comprehensive way, the basic principles as well as new developments in theoretical and experimental solid-state physics.

Peter Sigmund

Particle Penetration and Radiation Effects Volume 2

Penetration of Atomic and Molecular Ions

With a Contribution by Jens Ulrik Andersen

Springer

Peter Sigmund
Department of Physics, Chemistry
and Pharmacy
University of Southern Denmark
Odense M
Denmark

ISSN 0171-1873 ISSN 2197-4179 (electronic)
ISBN 978-3-319-05563-3 ISBN 978-3-319-05564-0 (eBook)
DOI 10.1007/978-3-319-05564-0
Springer Cham Heidelberg New York Dordrecht London

Library of Congress Control Number: 2006922238

With a contribution by Jens Ulrik Andersen
Reprinted and slightly updated from Mat. Fys. Medd. Dan. Vid. Selsk. 52 no. 2, 655–698 (2006)

Typesetting by the author

Printed on acid-free paper

Springer is part of Springer Science+Business Media (www.springer.com)

To my students and coworkers

Preface

This book represents the second part of a planned three-volume monograph on Particle Penetration and Radiation Effects. The aim of the series is to introduce students, researchers, engineers and radiologists working with accelerators and their applications in research and technology to theoretical tools and to some important predictions and results.

Volume 1, which appeared in 2006[1] has the additional goal to introduce students of physics and related fields to general aspects of particle penetration. About half the chapters of Volume 1, based on lectures delivered at the University of Copenhagen and later at the University of Southern Denmark, served that purpose. Also the present volume contains introductory material of general interest, but here this division refers to individual chapters, and no attempt has been made to define a precise border line.

Originally, in the late 1970s, the book was intended to be an introduction to the theory of particle stopping. Progress on the project was slow at that time because of the author's involvement in numerous parts of an active field of research. This, in turn, implied the wish to cover a broader research area, hence the expansion into a three-volume series.

Throughout this process it has been my ambition that a reader working within accelerator-oriented physics, trying to find an answer to a specific question, should get help here, either in the form of a reader-friendly formula or computer program, perhaps an outline of a theory, reference to pertinent literature, and if nothing else, a note that information is missing to the author's knowledge. It is up to the reader to judge the degree to which this ambition has been fulfilled. I am of course aware of gaps. Most notably, readers in high-energy physics and high-energy accelerators may ask numerous questions which this book does not answer. Conversely, my ambition had the consequence that numerous research programs were initiated and completed on the way, with the result that finishing the first volume took several decades and the present volume took about seven years.

[1] P. Sigmund, Particle Penetration and Radiation Effects. General Aspects and Stopping of Swift Point Charges, Springer 2006; paperback edition, Springer 2007.

Volume 1 introduced general concepts of the theory of particle penetration, and specific applications dealt with swift point charges, i.e., protons, antiprotons and alpha particles. This restriction has been given up in the present volume, which addresses the penetration of heavier ions as well as molecules and clusters. Also the restriction to swift ions has been relaxed. Moreover, the reader will find theoretical descriptions of phenomena which were discussed only briefly in Volume 1, such as multiple scattering and nuclear stopping. Special attention has been given to the charge states of penetrating ions, a topic of central importance in electronic stopping of partially-stripped ions.

I do not expect the average reader to read this book from one end to the other. The chosen structure should allow you to pick a chapter and read it from the beginning to the end. However, in view of numerous references to Volume 1, my recommendation is to have easy access to that book.

Theoretical tools available in the field of particle penetration and radiation effects have been developed over about a century. Like in all fields of research, and almost all aspects of modern life, computers have come to play an ever increasing role. It is useful here to distinguish between computation and simulation. Theory and simulation usually start at some basic equations, but the difference lies in the use of mathematics, which is replaced by numerics in simulation. My personal experience with simulation is that of an interested spectator. Although I have written a couple of small simulation codes, I doubt whether I would be able to write a code of the type that occupies a large machine for hours, days or months, and convince myself that it produces acceptable results. Therefore, simulation codes, when mentioned at all, are characterized by the physics that enters, rather than computational techniques.

As indicated above, this book is a direct continuation of Volume 1. Only in rare cases did I repeat calculations and/or arguments from there. As in Volume 1, I have marked some parts with a star, indicating that those parts can be left out in a first reading. There are few of the kind, since I expect mostly readers with a clear definition of their interests and needs.

There are problems in the end of each chapter, but they are fewer in number than in Volume 1, and mostly of the type where a calculation sketched in the main text should be carried through explicitly.

A notorious problem in a field of research with roots a century ago is the list of literature references. The BibTeX database which I collected for use in this series of monographs has now come up to over 7000 items. Even though not all of those are relevant to the present volume, a tough selection had to be made to generate a meaningful bibliography. In general, the number of references has been kept low in topics that are treated in extenso, while those treated in a cursory manner are represented more generously in the bibliography. Other selection criteria are clarity and simplicity of the arguments. Although there are numerous references to papers with my name in the by-line, I like to emphasize that also those titles represent a selection. I mention this to make sure that if you find that a relevant paper of mine is not referred to, you should not automatically deduce that it is obsolete.

Unquestionably, numerous worthwhile contributions had to be left out. However, I tried to catch papers that initiated major developments. With this, modern biblio-

graphic tools should enable the interested reader to complete the list of references for most of the topics discussed here.

The table of contents of this volume shows all those items that I mentioned in the preface of Volume 1. However, when arriving at the chapter on Channeling, it occurred to me that my colleague Jens Ulrik Andersen at Aarhus University had contributed a chapter to my collection on 'Ion Beam Science, Solved and Unsolved Problems'[2], which deserves to be more widely known and, coming from first-hand experience, is much more well-disposed and formulated than I would be able to do it. Even though that chapter has been written with a slightly different target group in mind, I am glad to include it in the present book with the kind permission of the author and the publisher.

Odense, January 2014 *Peter Sigmund*

[2] J. U. Andersen, Mat. Fys. Medd. Dan. Vid. Selsk. 52, 655-698 (2006)

Acknowledgements

Although first drafts of some parts date back to many years ago, most of this book has been written after I retired from my professorship at the University of Southern Denmark. I am grateful to the Dean, professor Henrik Pedersen, as well as to four department heads, P. Morgen, M. Goodsite, I. Johannsen and F. Lauritsen, for providing emeritus status and access to all necessary facilities including office space on Campus. Financial support has been received from the Danish Natural Science Research Council (FNU), the Carlsberg Foundation, the Collstrop Foundation and the Ib Henriksen Foundation.

Much of my own research, as far as it is referred to in this book, has been performed jointly or discussed with colleagues and students in Denmark and abroad. In connection with the present volume I want to mention the late H.H. Andersen, the late D.S. Gemmell, the late Jens Lindhard and the late J.E. Westmoreland, as well as J.U. Andersen, N.R. Arista, A. Belkacem, F. Besenbacher, R. Bimbot, A. Fettouhi, H. Geissel, L.G. Glazov, P.L. Grande, J. Heinemeier, P. Hvelplund, J. Jensen, E.P. Kanter, H. Knudsen, V. Kuzmin, A.D. Marwick, H.H. Mikkelsen, A. Närmann, O. Osmani, H. Paul, R.H. Ritchie, G. Schiwietz, A. Schinner, A.H. Sørensen, C. Vockenhuber, H.J. Whitlow and K.B. Winterbon.

Special thanks are due to Lev Glazov, Erik Horsdal, Andreas Schinner and Bruce Winterbon for careful reading of and providing invaluable feedback to large parts of the manuscript, and to the publishers, especially project coordinator Adelheid Duhm, for active support in the final production.

Numerous figures have been reprinted with the kind permission of the American Physical Society, Argonne National Laboratory, EDP Sciences, Elsevier, IOP Sciences, NRC Research Press, the Royal Danish Academy of Sciences and Letters, Springer, and the authors. Chapter 11 has been reprinted with the kind permission of Jens Ulrik Andersen and the Royal Danish Academy of Sciences and Letters.

Contents

Part III Scattering

General Notations

- Sections marked by a star ($\star$) can be jumped over in a first reading.
- Problems marked by a star ($\star$) are considerably more difficult and/or time-consuming than average.
- Notations $< \cdots >$ or $\overline{\cdots}$ are utilized synonymously to indicate averages, dependent on readability.
- The symbol $(T, \mathrm{d}T)$ indicates the interval limited by T and $T + \mathrm{d}T$. Similarly, $(\boldsymbol{\Omega}, \mathrm{d}^2\boldsymbol{\Omega})$ indicates a solid angle $\mathrm{d}^2\boldsymbol{\Omega}$ around the unit vector $\boldsymbol{\Omega}$, and $(\boldsymbol{r}, \mathrm{d}^3\boldsymbol{r})$ indicates a volume element $\mathrm{d}^3\boldsymbol{r} = \mathrm{d}x\,\mathrm{d}y\,\mathrm{d}z$ located at a vector distance $\boldsymbol{r}$ from the origin.

$\boldsymbol{A}$	Vector potential
A_1, A_2	Mass number of projectile and target atom
A_n	Coefficient in pathlength
A_ℓ^n	Coefficient in vector range
a	Screening radius
a_0	Bohr radius, 0.529177 Å
a_{ad}	Adiabatic radius, v/ω
a_{TF}	Thomas-Fermi radius, $0.8853 a_0 Z^{-1/3}$
B	Bethe parameter, $2mv^2/\hbar\omega$
$B_\gamma(a, b)$	Incomplete beta function
b	Collision diameter $2e_1e_2/m_0v^2$
C, C_{12}, C_{22}	Coefficient in power cross section
c	Speed of light, $2.99792 \cdot 10^8$ m/s
c_j, c_ℓ, c_J	Expansion coefficient
$\mathrm{d}^3\boldsymbol{k}$	Volume element in Fourier space
$\mathrm{d}R$	Pathlength element
$\mathrm{d}^3\boldsymbol{r}$	Volume element
$\mathrm{d}\sigma, \mathrm{d}\sigma_{12}, \mathrm{d}\sigma_{22}$	Differential cross section
$d_{\mu\nu}$	Internuclear distance in molecule or solid

$\boldsymbol{E}$	Electric field
E	Energy
$E_\perp$	Transverse energy
$\boldsymbol{e}$	Unit vector on the impact plane
$\mathcal{E}$	Total energy
e	Elementary charge, $1.602176 \cdot 10^{-19}$ Coulomb
eV	Electron volt, $1.602176 \cdot 10^{-19}$ J
$\boldsymbol{F}, F$	Force
$F_R(\boldsymbol{v}, \boldsymbol{r})$	Range profile
$\mathbf{F}(x) = \|\|F_{IJ}(x)\|\|$	Transition matrix
$F(\Delta E, x), \mathbf{F}(\Delta E, x), F_{IJ}(\Delta E, x)$	Energy-loss spectrum
$F(E, R)$	Pathlength distribution
$F_e(\boldsymbol{v}, \boldsymbol{r})$	Spatial distribution of deposited electronic energy
$F_n(\boldsymbol{v}, \boldsymbol{r})$	Spatial distribution of deposited nuclear energy
F_J	Charge fraction
$F(\alpha, t), F(\alpha, x)$	Angular multiple-scattering profile
$F(\boldsymbol{k}, x)$	Fourier transform of multiple-scattering profile
$F(\boldsymbol{\alpha}, \boldsymbol{\rho}, x)$	Angular-lateral multiple-scattering distribution
f_n, $f_{n\ell}$, $f(\omega)\mathrm{d}\omega$	Oscillator strength
$G(\rho, x)$	Lateral multiple-scattering distribution
$g(\xi)$	Screening function
$\mathcal{H}, H$	Hamiltonian
$H_n(\xi)$	Hermite polynomial
$He_n(\xi)$	Modified Hermite polynomial
h	Planck's constant, $6.62607 \cdot 10^{-34}$ Js
$\hbar$	$h/2\pi$, $6.58212 \cdot 10^{-16}$ eV s
I	Mean logarithmic excitation energy (I-value)
i	Imaginary unit
J_0	Bessel function
K_0, K_1	Modified Bessel functions
$K(\phi)$	$\mathrm{d}\sigma(\boldsymbol{\phi})/\mathrm{d}^2\boldsymbol{\phi}$
k	Electronic-stopping constant, (9.39)
keV	10^3 eV
$\boldsymbol{k}, k$	Wave vector, wave number
k_F	Fermi wave number
L	Stopping number
L	Cube length in periodicity volume
ln	Natural logarithm

ℓ	Angular-momentum quantum number
M_1	Mass of projectile ion
M_2	Mass of target atom
$M^{(n)}(E)$	Moment over pathlength distribution
M_ℓ^n	Moment in Legendre polynomial expansion
MeV	10^6 eV
m	Electron mass, $9.10938{\cdot}10^{-31}$ kg
m	Exponent in power cross section
N	Number of atoms per volume
N_1	Number of electrons bound to an atom $= Z_1 - q_1$
N_A	Avogadro's number, $6.02214{\cdot}10^{23}$/mol
N_i	Mean number of ion pairs in cascade
n	Number of electrons per volume, NZ_2
n	Principal quantum number
nm	Nanometer, 10^{-9} m
P	Probability
$\boldsymbol{P}, P$	Momentum
P_ℓ	Legendre polynomial
P_n	Poisson distribution
$\boldsymbol{p}, p$	Impact parameter
$P_\perp$	Transverse momentum
$\mathbf{Q} = \|\|Q_{IJ}\|\|$	$\sigma_{IJ} - \delta_{IJ}\sum_L \sigma_{IL}$
Q	Inelastic energy loss
q_1	Projectile charge number
$q_1 e$	Projectile charge
$\langle q_1 \rangle$	Mean ionic charge number
$\boldsymbol{q}, q$	Wave vector, wave number
$\boldsymbol{R}(t)$	Projectile trajectory
R	Internuclear distance
$R(E)$	Range, pathlength
$R(E, E_1)$	Pathlength for slowing-down from E to E_1
R_p	Projected range
$R_\perp$	Lateral range
$\boldsymbol{r}, r$	Vectorial, scalar distance from origin
$\boldsymbol{r}, \boldsymbol{r}_v$	Position operator for electron(s)
r_s	Wigner-Seitz radius, $(3/4\pi n a_0^3)^{1/3}$
r, r_0	Internuclear distance in dicluster

S	Stopping cross section
S_{e}	Electronic stopping cross section
S_{n}	Nuclear stopping cross section
$S^{(1)}$	Transport stopping cross section
$\mathcal{S}$	Eikonal
S_J, S_{JK}	State-separated stopping cross section
s	Variable in Laplace space
s, s_n, s_e	Stopping cross section in Lindhard-Scharff units
T	Energy transfer
T_e	Electronic energy loss
T_n	Nuclear energy loss
$T_{\max}$	Maximum energy transfer in collision
t	Time
$U(\boldsymbol{r})$	Axial potential
U	Ionization or binding energy
u	Atomic mass unit, $1.660538{\cdot}10^{-27}$ kg
$u(\boldsymbol{r})$	Time-independent wave function
$\boldsymbol{u}, u$	Relative velocity in c.m.s. frame
u	ω/kv_F
$\mathcal{V}, V, V_1, V_2$	Potential (=potential energy)
$\mathcal{V}_3$	Three-body potential
v_0	Bohr speed, $e^2/\hbar = c/137.0360$
$\boldsymbol{v}, \boldsymbol{v}_i, v, v_i$	Velocity, speed
$\boldsymbol{v}_e$	Orbital electron velocity
v_{F}	Fermi speed
v_{TF}	Thomas-Fermi speed
W	Straggling parameter $\int T^2 \,\mathrm{d}\sigma(T)$
W	Mean energy to create an ion pair
$\boldsymbol{W} = \|\|W_{IJ}\|\|$	Straggling parameter, state-separated
$\boldsymbol{w}$	Velocity in centre-of-mass frame
w_n	Dimensionless nuclear-straggling parameter
w	Wave function
x	x-coordinate
x	Penetration depth
$Y_{\ell\mu}$	Spherical harmonics
y	y-coordinate
Z	Atomic number
Z_1	Atomic number of projectile nucleus
$\mathcal{Z}_1$	Effective nuclear-charge number

Z_2	Atomic number of target nucleus
z	z-coordinate
z	$k/2k_F$
$\boldsymbol{\alpha}, \alpha$	Multiple-scattering angle
α	Fine-structure constant, 1/137.0360
$\tilde{\alpha}$	Multiple-scattering angle in Thomas-Fermi units
$\hat{\alpha}$	Multiple-scattering angle in Born units
β_0	$0.2118/Z_1^{2/3}$ in Thomas-Fermi-Dirac theory
$\boldsymbol{\beta}, \beta$	$\boldsymbol{\rho}/x$, ρ/x, chord angle in multiple scattering
β	v/c
Γ	Scale factor between angular and lateral multiple-scattering distribution
γ^2	Effective-charge ratio
γ	$4M_1M_2/(M_1+M_2)^2$
γ	Lorentz factor $1/\sqrt{1-v^2/c^2}$
ΔE	Energy loss
δ_ℓ	Phase shift
$\delta\boldsymbol{r}, \delta\boldsymbol{R}$	Infinitesimal path element
$\varepsilon(k,\omega)$	Longitudinal dielectric function
ϵ	Ion energy in Lindhard-Scharff scaling, (6.38)
ϵ	Transverse energy
ϵ_j	Excitation energy
η	$\epsilon \sin^2(\Theta/2)$
η	$2mv_F a/\hbar$
$\eta(\epsilon)$	Energy deposited in electronic motion in Lindhard-Scharff scaling
ζ	R/a
Θ	Centre-of-mass scattering angle
θ	Polar angle
κ	$2Z_1v_0/v$
κ	Wave number
κ_k	$2.871e^2a_0$ in Thomas-Fermi theory
κ_a	$0.739e^2$ in Thomas-Fermi-Dirac theory
λ	de Broglie wavelength, h/mv
λ	Mean free path
$\lambda\!\!\!^{-}$	$\lambda/2\pi$, $\hbar/mv$

μm	Micro meter, 10^{-6} m
μ	Reduced mass $M_1 M_2/(M_1 + M_2)$
$\boldsymbol{\nabla}$	nabla operator, $(\partial/\partial x, \partial/\partial y, \partial/\partial z)$
$\nu(\epsilon)$	Energy deposited in nuclear motion in Lindhard-Scharff scaling
ν	Sommerfeld parameter $Z_1 e^2/\hbar v$
ρ	Electron density
ρ_e	Charge density, charge/volume
σ	Cross section
σ_0	$0.09553(me/\hbar)^{3/2}$ in Thomas-Fermi theory
σ_c	Capture cross section
$\sigma^{(1)}$	Transport cross section
$\sigma(k)$	Transport cross section in multiple scattering
σ_{IJ}	Cross section for transition from state I to J
τ	Time integral
τ	Time constant in Coulomb explosion
τ	Thickness in Thomas-Fermi units, multiple scattering
τ_0	$\sqrt{e/2\pi^2 a_0}$ in Thomas-Fermi-Dirac theory
Φ	Electric potential
Φ_{ind}	Induced potential
$\tilde{\phi}$	Single-scattering angle in Thomas-Fermi units, multiple scattering
$\hat{\phi}$	Single-scattering angle in Born units, multiple scattering
ϕ_0	$mv^2/2e$ in Thomas-Fermi theory
$\boldsymbol{\phi}, \phi, \boldsymbol{\phi}', \phi'$	Scattering angle in laboratory frame
ϕ	Angle defining orientation of dicluster
χ^2	$e^2/\pi\hbar v_F$
χ	Azimuthal angle
$\chi(\boldsymbol{r}, t)$	Wave function
χ_{min}	Minimum yield
$\psi(\boldsymbol{r}, t)$	Wave function
ψ_1, ψ_c	Lindhard angle
ξ	Dimensionless impact parameter p/a
ξ	Dimensionless length unit $N\pi a^2 \gamma x$

$\boldsymbol{\Omega}$	Solid angle
Ω^2	Straggling (variance)
Ω_R^2	Range straggling
ω	Angular frequency
ω_{P}	Plasma frequency, $\sqrt{4\pi\rho e^2/m}$
ω_{j0}	Transition frequency
ω_k	$\hbar k^2/2m$

Part I
Charge States of Swift Ions

Chapter 1
Charge Equilibrium

Abstract The mean equililibrium charge of a penetrating ion can be estimated on the basis of Bohr's velocity criterion or Lamb's energy criterion. Qualitative and quantitative results are derived on the basis of the Thomas-Fermi model of the atom, which is discussed explicitly. This includes a brief introduction to the Thomas-Fermi-Dirac model. Special attention is paid to trial function approaches by Lenz and Jensen as well as Brandt and Kitagawa. The chapter also offers a preliminary discussion of the role of the stopping medium, gas-solid differences, and a survey of data compilations.

1.1 Introductory Comments

Volume 1 was dedicated to the stopping and scattering of point charges. This provided an opportunity to illustrate fundamental theoretical concepts and procedures. In practice the theory applies to light particles such as electrons and positrons, protons and antiprotons, and heavier ions above a limiting energy which increases rapidly with increasing atomic number.

The restriction to penetrating point charges has been dropped in the present volume. Already about a century ago, Flamm and Schumann (1916) suggested that an alpha particle may capture an electron from the penetrated medium. Henderson (1923) and Rutherford (1924) demonstrated experimentally the presence of singly-charged helium ions in an emerging beam. It was clear that electron capture must be possible for all ions including protons. Conversely, neutral atoms may lose electrons by collisions with the atoms of the penetrated medium.

As a result of a sequence of electron capture and loss events one may expect a penetrating ion to approach a state of dynamical equilibrium around a charge state for which the number of capture events equals the number of loss events per unit time or pathlength in the average. Whether such a state is actually achieved does not only depend on the thickness of the penetrated layer but also on the rate of energy loss, since cross sections for electron capture and loss depend on beam energy.

P. Sigmund, *Particle Penetration and Radiation Effects Volume 2*,
Springer Series in Solid-State Sciences 179, DOI: 10.1007/978-3-319-05564-0_1,

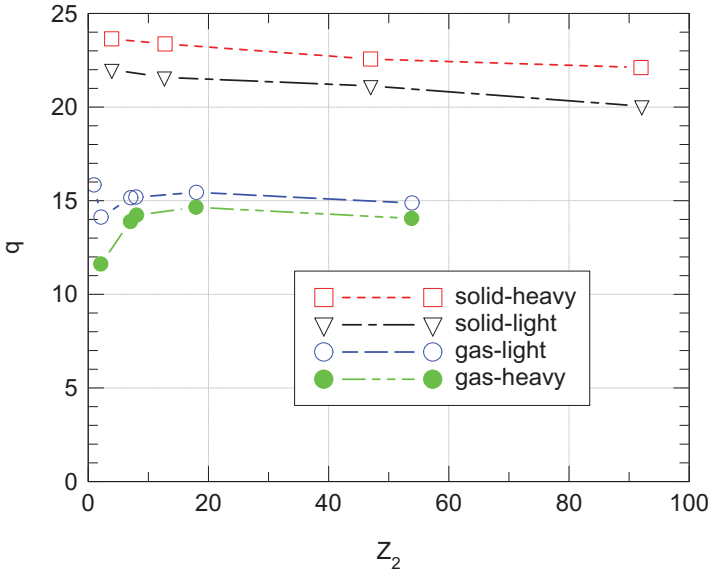

Fig. 1.1 Mean charges of fission fragments penetrating through gaseous targets and emerging from solid targets vs. atomic number Z_2 of the material, according to Lassen (1951b). Separate data are shown for light and heavy fragments

Mean equilibrium charges of alpha particles are close to 2 at energies in the MeV range. Therefore, penetration studies involving composite particles only became urgent with the discovery of nuclear fission (Hahn and Strassmann, 1939, Meitner and Frisch, 1939), where medium-mass heavy ions at MeV energies are involved. Measurements of track lengths of such fission fragments in cloud chambers were performed almost instantaneously by Brostrøm et al. (1940), and a number of now classical papers appeared which addressed the charge and energy loss of those particles (Bohr, 1940, 1941, Lamb, 1940, Knipp and Teller, 1941, Brunings et al., 1941). This early development was summarized by Bohr (1948).

Systematic experimental studies of the charges of fission fragments were initiated by Lassen (1951b,a), who reported a striking difference between solid and gaseous stopping media: Figure 1.1 shows that these ions had mean charges ranging from $\sim$ 11 to 24, which were higher for ions emerging from a solid than for ions penetrating through a gas. This 'density effect' became the subject of much lively discussion for almost half a century, starting with early theoretical studies by Bell (1953), Bohr and Lindhard (1954), Neufeld (1954), Gluckstern (1955) and others.

A particularly distressing feature of this density effect, indicated already in Lassen's early studies but clearly confirmed in later measurements on tandem accelerators by Pierce and Blann (1968), was the near absence of a corresponding density effect in the energy loss. This seeming inconsistency intensified the discussion.

In this monograph the complex of charge-state distributions and charge-dependent stopping has been divided up into three problem areas which will be treated in five

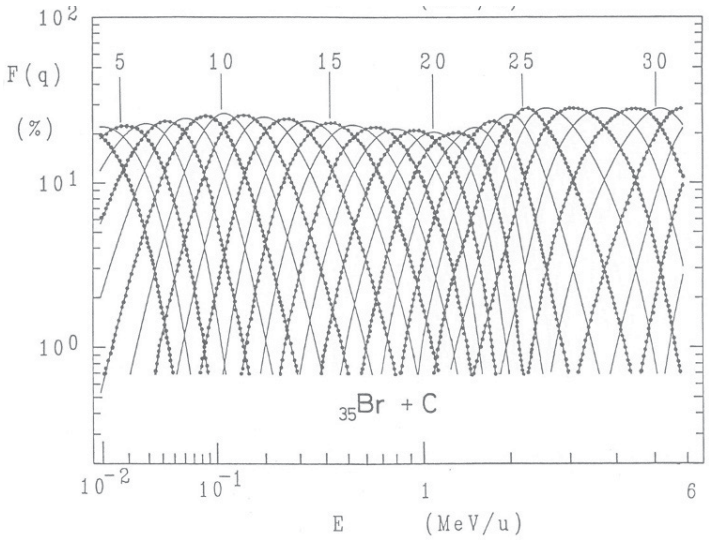

Fig. 1.2 Equilibrium charge fractions for bromine ions in carbon. Numbers above the curves represent the charge number. See text. From Shima et al. (1992)

successive chapters. The present chapter addresses equilibrium charge states without explicit reference to charge-exchange cross sections. Chapter 2 deals with cross sections for electron capture and loss, and Chap. 3 with the associated statistics and energetics. Chapters 4 and 5 deal with the mean energy loss and straggling of swift heavy ions, respectively.

1.2 Qualitative Orientation

Increasing the charge of an ion requires energy. Therefore, as a rough guideline we may assume that the cross section for electron loss decreases with increasing ion charge. Conversely, with decreasing ion charge the capture cross section will decrease and will rapidly approach zero for negative ion charges. Therefore, the probability of a projectile to be in a certain charge state, the *charge fraction*, will have a maximum near some equilibrium charge state and decrease monotonically in both directions.

If the incident charge is higher than the equilibrium charge, capture typically dominates over loss, and vice versa in the opposite case. Remind, however, that charge exchange is a stochastic process: For an individual trajectory, charge fractions can take any value that is compatible with conservation laws.

Figure 1.2 illustrates the situation on the example of Br in C. That figure is based on interpolation and scaling of experimental data by Shima et al. (1992). Numbers above the graphs denote the charge state q. As an example, take $q = 20$, which is

the most abundant one at $E \simeq 1\,\mathrm{MeV/u}$. Neighbouring charge states 19 and 21 are slightly less abundant, while charge fractions for states 15+ and 25+ are about a factor of 30 lower at that energy.

We may conclude that the distribution in charge-states in equilibrium at a given beam energy may be rather narrow, so that it makes sense to neglect the difference between the average and the peak value and, as a first estimate, to characterize the equilibrium charge state by one number, which in principle depends on the atomic numbers Z_1 and Z_2 of the projectile and the target, respectively, and the beam energy as well as on the physical state of the medium.

1.3 Stripping Criteria

Strictly speaking, the mean equilibrium charge is defined as an average over charge distributions such as those shown in Fig. 1.2. This need not be an integer number. The definition mentioned above requires the average number of capture events per unit time or pathlength to equal the number of loss events. This is already an approximation, since capture and loss cross sections for atoms with a non-integer number of electrons do not make sense. Moreover, databases over cross sections are necessarily incomplete, in particular for condensed stopping media. Therefore, simpler models that do not require quantitative information about cross sections are highly desirable. Let us have a look at options proposed in the literature.

1.3.1 Velocity Criterion

Consider a projectile moving with a velocity $\boldsymbol{v}$ and carrying a number of electrons with orbital speeds v_e. Viewed in a moving reference frame, the projectile is exposed to a beam of target electrons and nuclei. Bohr (1940) divided the projectile electrons into two groups according to whether their orbital speed is greater or smaller than v. Those with orbital speeds significantly smaller than the projectile speed v are relatively weakly bound and will, consequently, have a relatively high ionization cross section and hence be stripped efficiently. Conversely, those with orbital velocities significantly greater than v will tend to respond adiabatically to the disturbance and have only a small chance to be stripped off. The physical content of the adiabaticity criterion has been discussed in Problem 2.19, Vol. 1.

Moreover, you will see in Chap. 2 that electron capture is inefficient when the projectile speed exceeds the orbital speed.

With this we have arrived at the Bohr stripping criterion: In the equilibrium charge state, electrons with orbital velocities $v_e < v$ are stripped off or, in other words: If the projectile carries more electrons initially than predicted by the Bohr stripping criterion, ionization will dominate until the outermost electrons have the orbital speed v.

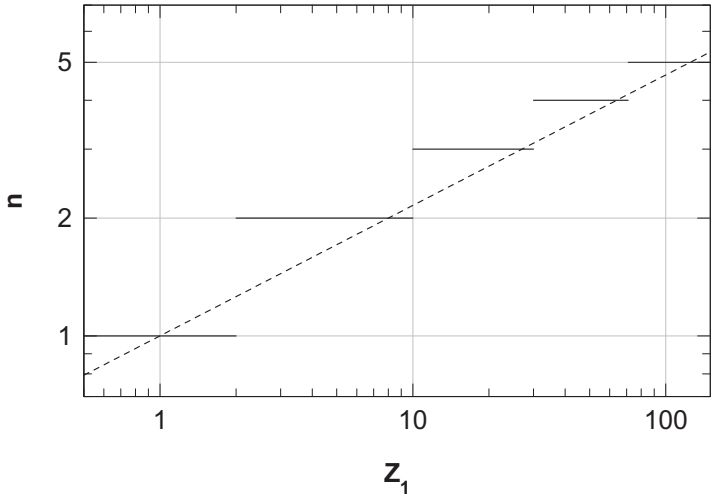

Fig. 1.3 Principal quantum number and shell filling. See text

If the projectile carries fewer electrons than predicted by the Bohr stripping criterion, the outermost electrons will have large orbital velocities. This implies that there are empty states into which electrons can be captured. Hence, capture cross sections will be sizable, while ionization is inefficient.

Equilibrium charge states resulting from the Bohr stripping criterion depend on the adopted atom model. Bohr (1948) argued as follows: Consider an electron in the outermost shell of an ion with the charge $q_1 e$. Within a hydrogenic model, its orbital velocity may be written as

$$v_e \simeq \frac{q_1}{n} v_0, \tag{1.1}$$

where n is the principal quantum number of that shell and $v_0 = c/137$ the Bohr speed.

Figure 1.3 illustrates the filling of shells according to the periodic table. The step-like curve shows the principal quantum number of the outermost occupied shell vs. atomic number Z_1. Also shown is the curve

$$n = Z_1^{1/3}\,, \tag{1.2}$$

which approximately connects the upper ends of the steps. With this approximation the Bohr stripping criterion implies

$$v \simeq \frac{q_1}{Z_1^{1/3}} v_0 \tag{1.3}$$

or (Bohr, 1948)

$$q_1 \simeq Z_1^{1/3} \frac{v}{v_0}, \tag{1.4}$$

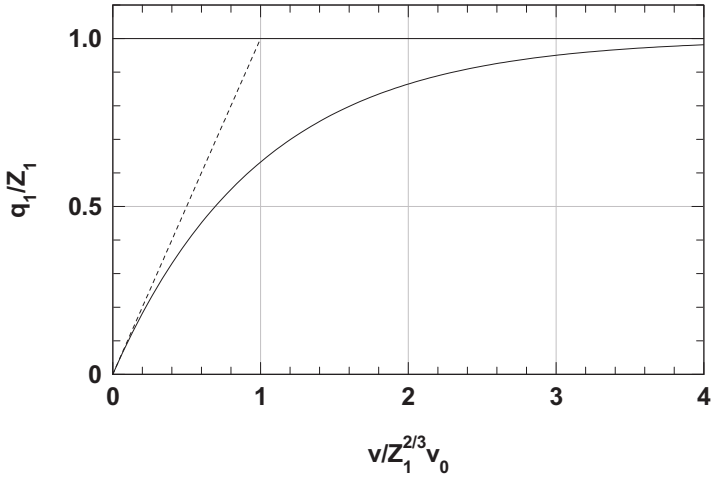

Fig. 1.4 Equilibrium charge fraction vs. projectile speed according to (1.4) and (1.6)

where q_1 denotes the equilibrium charge. However, q_1 cannot increase indefinitely. A plausible way to extend the range of validity of this estimate is to write (1.4) in the form

$$\frac{q_1}{Z_1} \simeq \frac{v}{Z_1^{2/3} v_0}. \tag{1.5}$$

Since q_1/Z_1 cannot exceed unity, we may try a simple extrapolation of (1.4) to arrive at

$$q_1 \simeq Z_1 \left(1 - \mathrm{e}^{-v/Z_1^{2/3} v_0}\right), \tag{1.6}$$

as proposed by Pierce and Blann (1968) and shown in Fig. 1.4. You may already have noticed the Thomas-Fermi speed

$$v_{\mathrm{TF}} = Z_1^{2/3} v_0, \tag{1.7}$$

which was mentioned in Sect. 7.2.1, Vol. 1.

While the derivation of these expressions is clearly qualitative, (1.4) and (1.6) compare favourably in general with measured equilibrium charges for a wide variety of projectile-target combinations. Numerous modifications based on empirical data have been made (Betz, 1972), but the Bohr stripping criterion as formulated above is still a useful tool in the field of heavy-ion penetration.

Figure 1.5 shows a more quantitative evaluation of the Bohr criterion. Here, the quantity $\langle v_e^2 \rangle$ has been evaluated for individual shells via tabulated Hartree-Fock wave functions from Clementi and Roetti (1974). For Fluorine and Chlorine you may see 3 and 5 steps, respectively, reflecting subshells of the neutral atom. In bromine and iodine, s and p electrons have been combined for each shell.

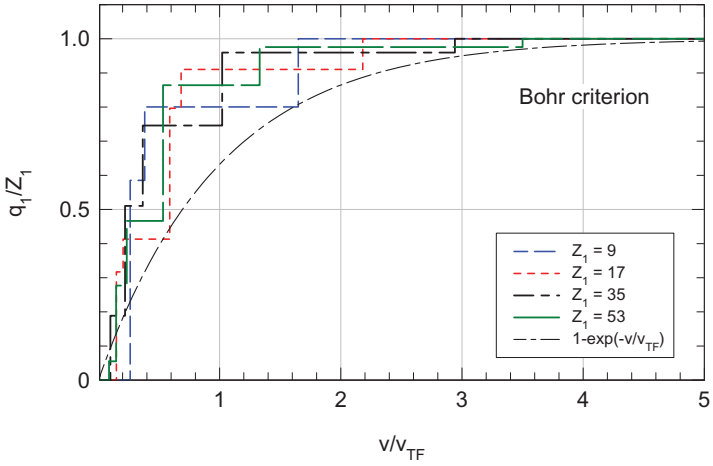

Fig. 1.5 Equilibrium charge fraction vs. projectile speed for halogen ions evaluated from the requirement that $\langle v_e^2 \rangle > v^2$. From Schinner and Sigmund (2014)

1.3.2 Energy Criterion

A different criterion was first introduced by Lamb (1940) who, like Bohr, assumed that loosely-bound electrons are stripped off rapidly. This process is assumed to continue until the most loosely bound electron has a binding energy exceeding $mv^2/2$, the kinetic energy of a free target electron in a reference frame moving with the ion. For a hydrogenic atom, the binding energy of the outermost electron is $= mv_e^2/2$. In that case Lamb's stripping criterion is equivalent with Bohr's.

This criterion may be formulated more quantitatively. Consider a given ion with N_1 electrons. Let its ground-state energy be $E(N_1)$. If the ion moves with a speed v, its total energy will be given as

$$\mathcal{E}(N_1) = E(N_1) + \frac{1}{2}(M_1 + N_1 m)v^2, \tag{1.8}$$

where $M_1 v^2/2$, the kinetic energy of the nucleus, is taken as a constant in the present context.

Now let N_1 vary: If N_1 is small, the ion will be highly charged and hence have a high energy $E(N_1)$, while $N_1 m v^2/2$ is small. If N_1 is large, the ion is nearly neutral, so $E(N_1)$ is low but $N_1 m v^2/2$ is large. Hence, $\mathcal{E}(N_1)$ must be expected to have a minimum at N_{eq}, so that

$$\mathcal{E}(N_{\mathrm{eq}} \pm 1) > \mathcal{E}(N_{\mathrm{eq}}). \tag{1.9}$$

Insertion of (1.8) into (1.9) leads to

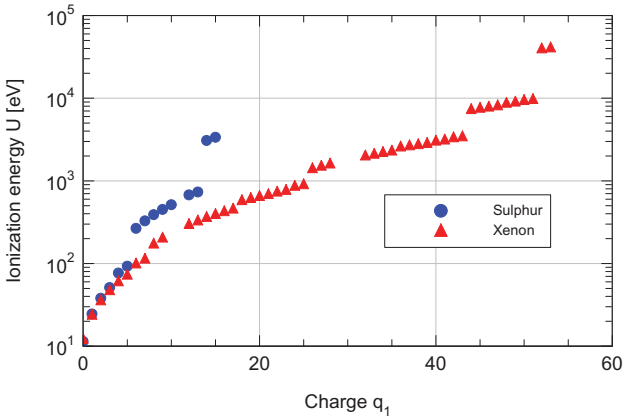

Fig. 1.6 Computed binding energies for all charge states of sulphur and xenon ions according to Carlson et al. (1970). From Schinner and Sigmund (2014)

$$E(N_{\rm eq}) - E(N_{\rm eq}+1) < \frac{1}{2}mv^2 < E(N_{\rm eq}-1) - E(N_{\rm eq}). \tag{1.10}$$

This means that v vs. $N_{\rm eq}$, and hence q_1 vs. v, has a step-like structure in this model.

The energy criterion assumes that if the ion moves in a medium, collisions with the nuclei and electrons of the target allow the charge of the ion to equilibrate, i.e., to let the ion attain the lowest energy state by losing or capturing electrons. According to (1.8) this state is independent of the properties of the medium, although the time it takes to approach equilibrium must depend on the type of interactions taking place.

For ions with many electrons we may approximate (1.9) by

$$\frac{{\rm d}\mathcal{E}(N_1)}{{\rm d}N_1} = \frac{{\rm d}E(N_1)}{{\rm d}N_1} + \frac{1}{2}mv^2 = 0 \tag{1.11}$$

for $N_1 = N_{\rm eq}$. As it stands, both (1.9) and (1.11) involve the assumption that $E(N_{\rm eq})$ represents the ground state energy of the ion, whatever it is isolated or embedded into a medium. This may be a limitation on the validity of the model, as will be discussed in Sect. 1.5.

Setting $dE(N_1)/dN_1 \simeq U(N_1)$, where $U(N_1)$ is an effective ionization energy of an ion with N_1 electrons, the energy criterion (1.11) reduces to

$$U(N_1) \simeq mv^2/2. \tag{1.12}$$

This is the criterion proposed by Lamb (1940).

Figure 1.6 shows binding energies for all charge states of sulphur and bromine computed by Carlson et al. (1970).

Figure 1.7 shows equilibrium charge states of halogen ions calculated from data like those shown in Fig. 1.7 and (1.12). Steps of the type shown in Fig. 1.3 are still present, although less pronounced.

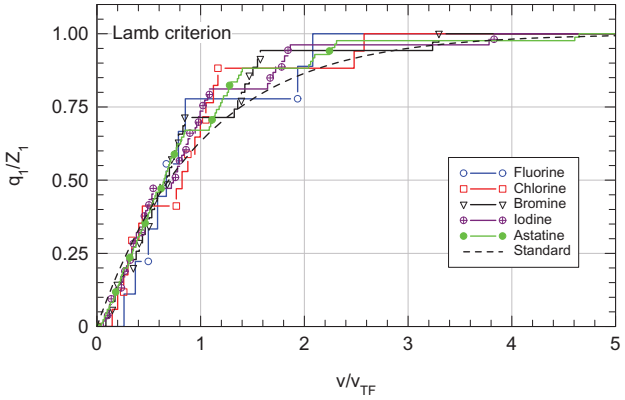

Fig. 1.7 Mean equilibrium charge fractions for halogen ions according to (1.12). The simple formula (1.6) has been included for reference. From Schinner and Sigmund (2014)

1.4 Thomas-Fermi Theory

The energy criterion allows a quantitative evaluation on the basis of the Thomas-Fermi model of the atom, which was briefly introduced in Sects. 7.2.1–7.2.3, Vol. 1, mainly in order to establish scaling relations for stopping parameters. Use will be made more frequently of the model in the present volume dealing with heavier ions, since the accuracy of Thomas-Fermi theory increases with atomic number. Some essential features of the theory will be outlined here, following by and large the presentation of Gombas (1949, 1956).

1.4.1 Thomas-Fermi Equation for an Atomic Ion

The Thomas-Fermi model treats an atom, molecule or even an extended medium as an ensemble of Fermi gases of infinitesimal size of varying density, often called a 'local density approximation'. The energy of an ion with atomic number Z_1 and N_1 electrons $E(N_1)$ can be expressed as

$$E(N_1) = E^{\mathrm{kin}}(N_1) + E^{\mathrm{Coul}}(N_1) + E^{\mathrm{excor}}(N_1) \tag{1.13}$$

where

$$E^{\mathrm{kin}}(N_1) = \int \mathrm{d}^3\boldsymbol{r}\ \rho(\boldsymbol{r})\,\frac{3}{5}\frac{\hbar^2 k_F^2}{2m} \tag{1.14}$$

is the kinetic energy in accordance with (7.3), Vol. 1 and k_F the Fermi wave number. Making use of the relation $\rho = k_F^3/3\pi^2$, see (5.146), Vol. 1, we may write this in the form

$$E^{\mathrm{kin}}(N_1) = \kappa_k \int \mathrm{d}^3\boldsymbol{r}\, \rho(\boldsymbol{r})^{5/3}, \tag{1.15}$$

where

$$\kappa_k = \frac{3}{5}\frac{\hbar^2}{2m}(3\pi^2)^{2/3} = 2.871 e^2 a_0. \tag{1.16}$$

The electrostatic energy reads

$$E^{\mathrm{Coul}}(N_1) = -Z_1 e^2 \int \mathrm{d}^3\boldsymbol{r}\, \frac{\rho(\boldsymbol{r})}{r} + \frac{e^2}{2}\int \mathrm{d}^3\boldsymbol{r} \int \mathrm{d}^3\boldsymbol{r}'\, \frac{\rho(\boldsymbol{r})\rho(\boldsymbol{r}')}{|\boldsymbol{r}-\boldsymbol{r}'|}. \tag{1.17}$$

One distinguishes between the straight Thomas-Fermi model (Thomas, 1926, Fermi, 1927, 1928) where the exchange-correlation term $E^{\mathrm{excor}}(N_1)$ in (1.13) is ignored, and the Thomas-Fermi-Dirac model (Dirac, 1930) where $E^{\mathrm{excor}}(N_1)$ is determined on the basis of the exchange energy of the Fermi gas.

Explicit calculations will be shown mainly for the straight Thomas-Fermi model ignoring both exchange and correlation. Additional features introduced by exchange will be mentioned briefly. Correlation terms, stemming from higher-order perturbation theory in terms of the Coulomb interaction between electrons affect quantitative details (Gombas, 1943) but will not be considered here. For an estimate of the correlation term being based on many-body electron theory you might consult Hedin and Lundqvist (1969).

In the straight Thomas-Fermi model we have

$$\mathcal{E}(N_1) = \kappa_k \int \mathrm{d}^3\boldsymbol{r}\, \rho(\boldsymbol{r})^{5/3} - Z_1 e^2 \int \mathrm{d}^3\boldsymbol{r}\, \frac{\rho(\boldsymbol{r})}{r} + \frac{e^2}{2}\int \mathrm{d}^3\boldsymbol{r} \int \mathrm{d}^3\boldsymbol{r}'\, \frac{\rho(\boldsymbol{r})\rho(\boldsymbol{r}')}{|\boldsymbol{r}-\boldsymbol{r}'|} + \frac{1}{2}(M_1 + N_1 m)v^2. \tag{1.18}$$

We wish to find an electron density $\rho(r)$ which minimizes $\mathcal{E}(N_1)$. Once that function has been determined we may find the number of electrons by integration,

$$N_1 = \int \mathrm{d}^3\boldsymbol{r}\, \rho(r). \tag{1.19}$$

This differs from the standard presentations of Thomas-Fermi theory (Gombas, 1949, 1956), where the ion charge is given, so that (1.19) represents a boundary condition which enters into the scheme via a Lagrange parameter.

For an infinitesimal variation $\delta\rho(\boldsymbol{r})$ we find the change in energy $\delta\mathcal{E}(N_1)$,

$$\delta\mathcal{E}(N_1) = \int \mathrm{d}^3\boldsymbol{r}\, \delta\rho(\boldsymbol{r}) \left(\frac{5}{3}\kappa_k \rho(\boldsymbol{r})^{2/3} - \frac{Z_1 e^2}{r} + e^2 \int \mathrm{d}^3\boldsymbol{r}'\, \frac{\rho(\boldsymbol{r}')}{|\boldsymbol{r}-\boldsymbol{r}'|} + \frac{1}{2}mv^2\right), \tag{1.20}$$

and hence, from $\delta\mathcal{E}(N_1) = 0$,

$$\frac{5}{3}\kappa_k \rho(\boldsymbol{r})^{2/3} - \frac{Z_1 e^2}{r} + e^2 \int \mathrm{d}^3\boldsymbol{r}' \, \frac{\rho(\boldsymbol{r}')}{|\boldsymbol{r} - \boldsymbol{r}'|} + \frac{1}{2} m v^2 = 0. \tag{1.21}$$

Now, the quantity

$$\phi(r) = \frac{Z_1 e}{r} - e \int \mathrm{d}^3\boldsymbol{r}' \, \frac{\rho(\boldsymbol{r}')}{|\boldsymbol{r} - \boldsymbol{r}'|} \tag{1.22}$$

represents the potential seen by a test charge. With this, (1.21) may be written in the form

$$\rho(r) = \left(\frac{3}{5\kappa_k}\right)^{3/2} \left[e\phi(r) - \frac{1}{2} m v^2\right]^{3/2}. \tag{1.23}$$

Expressing $\rho(r)$ by Poisson's equation $\nabla^2 \phi(r) = 4\pi e \rho(r)$ you finally arrive at

$$\nabla^2 \big[\phi(r) - \phi_0\big] = 4\pi e \sigma_0 \big[\phi(r) - \phi_0\big]^{3/2}, \tag{1.24}$$

where

$$\phi_0 = \frac{m v^2}{2e} \tag{1.25}$$

and

$$\sigma_0 = \left(\frac{3e}{5\kappa_k}\right)^{3/2} = 0.09553 \left(\frac{me}{\hbar}\right)^{3/2}. \tag{1.26}$$

Equation (1.24) is the well-known Thomas-Fermi equation introduced in Sect. 7.2.3, Vol. 1. This includes the quantity ϕ_0 which, in the standard case of N_1 being predetermined, represents a Lagrange parameter. In the present context, ϕ_0 is predetermined via the projectile speed according to (1.25).

1.4.2 Solution

Following Gombas (1949) again you may write the potential in the form

$$\phi(r) - \phi_0 = \frac{Z_1 e}{r} g(\xi), \tag{1.27}$$

where $\xi = r/a$. Here a is a screening radius which may be chosen such as to incorporate all dependence on atomic number. If so, $g(\xi)$ will be a universal screening function.

Noting that

$$\nabla^2 = \frac{1}{r} \frac{\mathrm{d}^2}{\mathrm{d}r^2} r \tag{1.28}$$

for a spherically symmetric function, you may rewrite (1.24) in the form (cf. Problem 1.1)

$$\frac{\mathrm{d}^2 g(\xi)}{\mathrm{d}\xi^2} = \frac{C_1}{\xi^{1/2}} g(\xi)^{3/2} \tag{1.29}$$

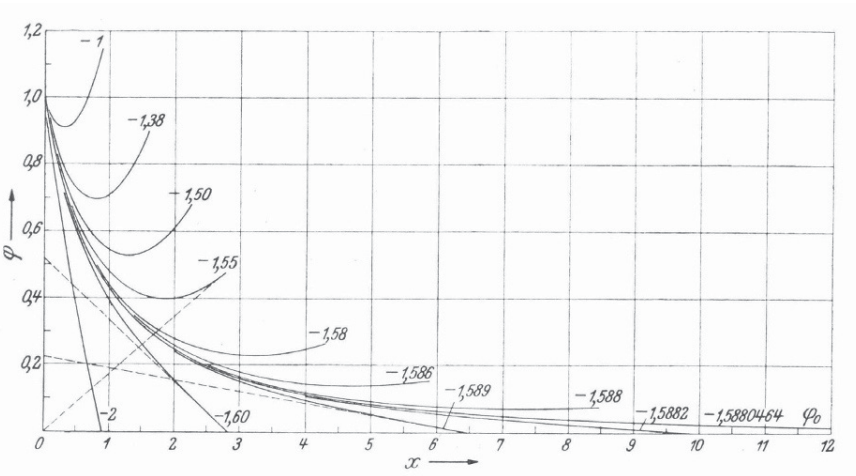

Fig. 1.8 Solutions of the Thomas-Fermi equation (1.31) for $g(0) = 1$. Numbers at the curves indicate the values of $dg(\xi)/\mathrm{d}\xi|_{\xi=0}$. From Gombas (1949)

with

$$C_1 = \left[2\left(\frac{4}{3\pi}\right)^{2/3} \frac{aZ_1^{1/3}}{a_0}\right]^{3/2}, \tag{1.30}$$

where $a_0 = \hbar^2/me^2$ is the Bohr radius and use has been made of (1.16) and (1.26).

We may define the screening radius a such that $C_1 = 1$. With this the Thomas-Fermi equation reduces to

$$\frac{\mathrm{d}^2 g(\xi)}{\mathrm{d}\xi^2} = \frac{g(\xi)^{3/2}}{\xi^{1/2}} \tag{1.31}$$

and

$$a = a_{\mathrm{TF}} = 0.8853\, a_0\, Z_1^{-1/3}, \tag{1.32}$$

which defines the numerical constant quoted in (7.15), Vol. 1.

Equation (1.31) can be solved if two constants are given. Since $\phi(r)$ must approach the Coulomb potential close to the nucleus we have

$$g(0) = 1. \tag{1.33}$$

Figure 1.8 shows solutions for various values of $g'(0) = dg(\xi)/\mathrm{d}\xi|_{\xi=0}$. You may notice that the shape of the solutions is quite sensitive to the value of $g'(0)$. As $-g'(0)$ increases, the integral under the curves decreases. Remembering (1.19), you may expect this quantity to be uniquely related to the number of electrons surrounding the nucleus.

Inspection of (1.23) indicates that there is a point r_0 for which

$$e\phi(r_0) = \frac{1}{2}mv^2 \tag{1.34}$$

and hence $\rho(r_0) = 0$, so that $\rho(r) = 0$ for $r > r_0$, assuming that $\phi(r)$ falls off monotonically. Outside r_0 we must have a Coulomb potential with the ion charge q_1,

$$\phi(r) = \frac{(Z_1 - N_1)e}{r} \quad \text{for } r \geq r_0 \tag{1.35}$$

and, at $r = r_0$,

$$\phi(r_0) = \frac{(Z_1 - N_1)e}{r_0} = \phi_0, \tag{1.36}$$

where the last identity follows from (1.27). Thus, the charge number q_1 is given by

$$q_1 = Z_1 - N_1 = \frac{r_0\phi_0}{e} = \frac{r_0 m v^2}{2e^2} \tag{1.37}$$

In Thomas-Fermi units this reads

$$\frac{q_1}{Z_1} = \frac{0.8853}{2}\xi_0 \frac{v^2}{v_{\mathrm{TF}}^2}, \tag{1.38}$$

where $v_{\mathrm{TF}} = v_0 Z_1^{2/3}$ is the Thomas-Fermi speed.

Equation (1.38) provides the connection between the ion charge and the beam velocity, once the Thomas-Fermi equation has been solved for a given value of $g'(0)$. The connection between $g'(\xi_0)$ and q_1 or N_1 is found from

$$N_1 = \int_{0<r\leq r_0} \mathrm{d}^3\boldsymbol{r}\ \rho(r) = \frac{1}{4\pi e}\int_{0<r\leq r_0} \mathrm{d}^3\boldsymbol{r}\ \nabla^2\phi(r). \tag{1.39}$$

After inserting (1.27) and $r = a\xi$ this reads

$$N_1 = Z_1 \int_{0+}^{\xi_0} \mathrm{d}\xi\, \xi g''(\xi) = Z_1\Big(\xi g'(\xi) - g(\xi)\Big)_0^{\xi_0}, \tag{1.40}$$

where $\xi_0 = r_0/a$. With $g(0) = 1$ and $g(\xi_0) = 0$ this reduces to

$$\xi_0 g'(\xi_0) = -\frac{q_1}{Z_1}. \tag{1.41}$$

Equations (1.36) and (1.41) also follow from the standard treatment, where N_1 is predetermined and the atom at rest (Gombas, 1949, 1956). This implies that the relation between the charge distribution $\rho(r)$ and the number of electrons N_1 is independent of the projectile speed. In other words, in the present description, the ion charge depends on the projectile speed, while the electron density reflects the ground-state configuration of the ion for the given ion charge, whatever the projectile speed.

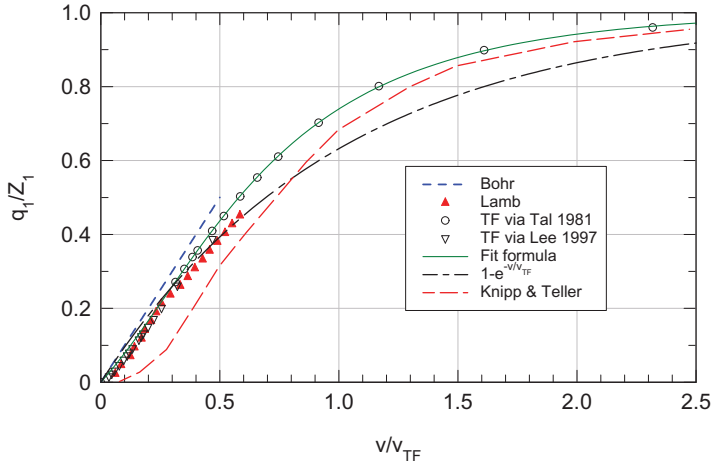

Fig. 1.9 Equilibrium charge fraction q_1/Z_1 of a free Thomas-Fermi ion vs. velocity. Dots: Evaluated from numerical tabulations (Tal and Levy, 1981, Lee and Wu, 1997) of Thomas-Fermi functions for different charge states; also included is Bohr's estimate (1.5), the results given by Lamb (1940) and by Knipp and Teller (1941) as well as (1.42) and (1.6)

Accurate tabulations of the Thomas-Fermi function for varying charge numbers are available. Dots in Fig. 1.9 were found from tables by Tal and Levy (1981) and by Lee and Wu (1997). This result is equivalent with that of Yarlagadda et al. (1978). It is seen to be well represented by a fitting formula

$$\frac{q_1}{Z_1} = \frac{1 - \mathrm{e}^{-1.43v/Z_1^{2/3}v_0}}{1 + \mathrm{e}^{-3.56v/Z_1^{2/3}v_0}}. \tag{1.42}$$

Small deviations from the result of Lamb (1940) are presumably due to inaccuracies of the Thomas-Fermi functions available at the time. The behaviour at low speed ($v \ll v_{\mathrm{TF}}$) is represented by Bohr's expression, $q_1 = Z_1^{1/3}v/v_0$, multiplied by 0.725. Deviations from the frequently-used exponential curve (1.6) are, however, noticeable. The result of Knipp and Teller (1941), based on the velocity criterion, differs significantly, in particular at low speed.

1.4.3 Trial Function Approach

Variational principles are frequently explored by means of trial functions. In Thomas-Fermi theory, the first ansatz goes back to Lenz (1932) and Jensen (1932). Before reporting specific results, let us first look at a rather general formulation, setting

$$\rho(\boldsymbol{r}) = \frac{N_1}{a^3} f(\xi), \tag{1.43}$$

where $\xi = r/a$ and

$$\int 4\pi\xi^2 \,\mathrm{d}\xi \; f(\xi) = 1. \tag{1.44}$$

The Thomas-Fermi-Dirac energy, (1.18), reads

$$\mathcal{E} = A_1 \frac{N_1^{5/3}}{a^2} - A_2 \frac{Z_1 N_1}{a} + A_3 \frac{N_1^2}{a} - A_4 \frac{N_1^{4/3}}{a} + N_1 \frac{mv^2}{2}, \tag{1.45}$$

where

$$A_1 = \kappa_k \int_0^\infty 4\pi\xi^2 \,\mathrm{d}\xi \; f(\xi)^{5/3}, \tag{1.46}$$

$$A_2 = e^2 \int_0^\infty 4\pi\xi \,\mathrm{d}\xi \; f(\xi), \tag{1.47}$$

$$A_3 = e^2 \int_0^\infty 4\pi\xi \,\mathrm{d}\xi f(\xi) \int_0^\xi 4\pi\xi'^2 \,\mathrm{d}\xi' f(\xi'), \tag{1.48}$$

$$A_4 = \kappa_a \int_0^\infty 4\pi\xi^2 \,\mathrm{d}\xi \; f(\xi)^{4/3}. \tag{1.49}$$

In the Ritz procedure, the function $f(\xi)$ is not varied freely but will be given some form which is expected to be more or less realistic. It may contain variational parameters. N_1 and a are independent variational parameters.

If $f(\xi)$ does not contain additional parameters, minimization of (1.45) with respect to N_1 and a yields

$$\frac{\partial \mathcal{E}}{\partial N_1} = \frac{5A_1}{3} \frac{N_1^{2/3}}{a^2} - A_2 \frac{Z_1}{a} + 2A_3 \frac{N_1}{a} - \frac{4A_4}{3} \frac{N_1^{1/3}}{a} + \frac{mv^2}{2} = 0 \tag{1.50}$$

$$\frac{\partial \mathcal{E}}{\partial a} = -2A_1 \frac{N_1^{5/3}}{a^3} + A_2 \frac{Z_1 N_1}{a^2} - A_3 \frac{N_1^2}{a^2} + A_4 \frac{N_1^{4/3}}{a^2} = 0. \tag{1.51}$$

Here, (1.51) provides a connection between the screening radius and the number of electrons which is independent of v, as was found in the previous section in case of the exact solution. Equation (1.50) specifies the connection between N_1 and the speed v.

Let us have a look at limiting cases. For a bare ion, $N_1 = 0$, you readily verify from (1.51) that $a = 0$ and, consequently, $v = \infty$ according to (1.50). For a neutral ion, $N_1 = Z_1$, you may expect $v = 0$, but this is not generally the case. In the Thomas-Fermi case where $A_4 = 0$ you find

$$a = \frac{2A_1}{(A_2 - A_3) Z_1^{1/3}} \tag{1.52}$$

$$\frac{mv^2}{2} = \frac{(A_2 - A_3)(A_2 - 7A_3) Z_1^{4/3}}{12A_1}. \tag{1.53}$$

Table 1.1 Parameters entering Ritz variational procedure. See text

	$f(\xi)$	$mA_1/\hbar^2$	A_2/e^2	A_3/e^2	A_4/e^2	$(A_2-7A_3)/e^2$
Lenz-Jensen	$\exp(-\xi^{1/2})/16\pi\xi^{3/2}$	0.06324	0.5	0.0625	0.05629	0.0625
Yukawa	$\exp(-\xi)/4\pi\xi$	0.24000	1.0	0.2500	0.17756	-0.7500
Exponential	$\exp(-\xi)/8\pi$	0.03614	0.5	0.2969	0.10638	-1.5781

If we assume that a neutral ion is the most stable configuration at low speed we must have

$$A_2 \geq 7A_3, \tag{1.54}$$

and if we want $q_1(v=0) = Z_1$ we must have

$$A_2 = 7A_3. \tag{1.55}$$

Inspection of (1.47) and (1.48) shows that this condition only involves the function $f(\xi)$, independent of N_1 and a.

Equation (1.55) is a fairly strong requirement. In the Thomas-Fermi-Dirac model, where A_4 is taken into account you find, for $N_1 = Z_1$,

$$a = \frac{2A_1}{(A_2 - A_3 + A_4 Z_1^{-2/3})Z_1^{1/3}}, \tag{1.56}$$

$$\frac{mv^2}{2} = \frac{(A_2 - A_3 + A_4 Z_1^{-2/3})(A_2 - 7A_3 + 3A_4 Z_1^{-2/3})Z_1^{4/3}}{12A_1}, \tag{1.57}$$

i.e.,

$$A_2 = 7A_3 - 3A_4/Z_1^{2/3}. \tag{1.58}$$

This may give a hint on how to incorporate an explicit Z_1 dependence into a trial function for the Thomas-Fermi-Dirac case.

1.4.4 Examples of Trial Functions

A successful variational procedure involving trial functions was developed by Lenz (1932) and Jensen (1932). In the present notation their charge density may be expressed through (1.43) with

$$f(\xi) = \text{const}\,\frac{\exp(-\xi^{1/2})}{\xi^{3/2}}\left(\sum_{j=0}^{n} c_j \xi^{j/2}\right), \tag{1.59}$$

where $c_0 = 1$ and c_j for $j = 1 \ldots n$ are additional variational parameters. In practice n was set to either zero or 1.

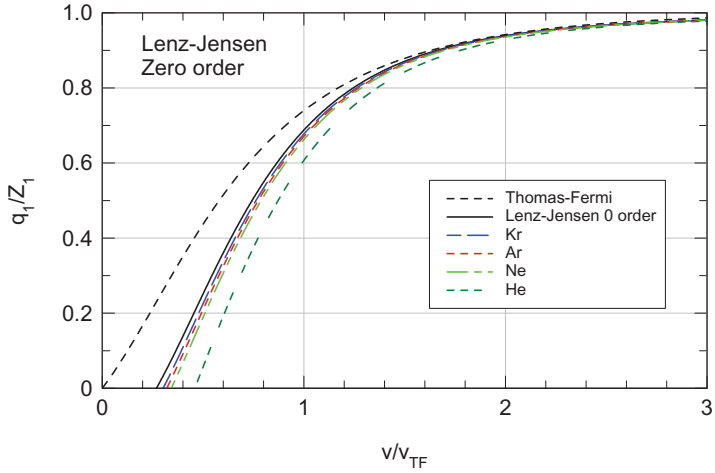

Fig. 1.10 Mean equilibrium charge fraction q_1/Z_1 in statistical theory. The dot-dashed line is the Thomas-Fermi curve shown in Fig. 1.9. The solid line results from the zero-order Lenz-Jensen model ($c_j = 0$ for $j \geq 1$). The four lines in colour are based on the same model but include the exchange term in accordance with the Thomas-Fermi-Dirac model. The dashed curve ('LJ corrected') neglects exchange but was constructed by multiplying A_3 by a factor $8/7$

Results for the case of $n = 0$ are compared in Table 1.1 together with two other examples,

- a Yukawa function (Brandt and Kitagawa, 1982),

$$\rho(r) = \frac{N_1}{4\pi a^2 r} \mathrm{e}^{-r/a}, \tag{1.60}$$

and

- a simple exponential

$$\rho(r) = \frac{N_1}{8\pi a^3} \mathrm{e}^{-r/a}. \tag{1.61}$$

In addition to the coefficients A_j, $j = 1, \ldots 4$, also the expression $A_2 - 7A_3$ has been included in Table 1.1. This quantity is positive but small for Lenz-Jensen interaction, indicating that N_1 does not drop completely to zero as v approaches zero. This reflects the fact that for an atom or ion at rest, the c_1 term cannot be neglected (Gombas, 1949).

Conversely, for the two other trial functions, $A_2 - 7A_3$ is negative and substantial. Although adding the A_4-term provides a correction in the desired direction, it is far from large enough to generate a physically acceptable picture. This discourages any attempt to determine equilibrium charges with one of these trial functions on the basis of the Lamb criterion.

Figure 1.10 shows results for the Lenz-Jensen model. All curves are found to lie below the Thomas-Fermi result shown in Fig. 1.9. The straight zero-order Lenz-Jensen result shows q_1 to drop below zero at $v \simeq v_{\mathrm{TF}}/3$. The dashed curve ('LJ

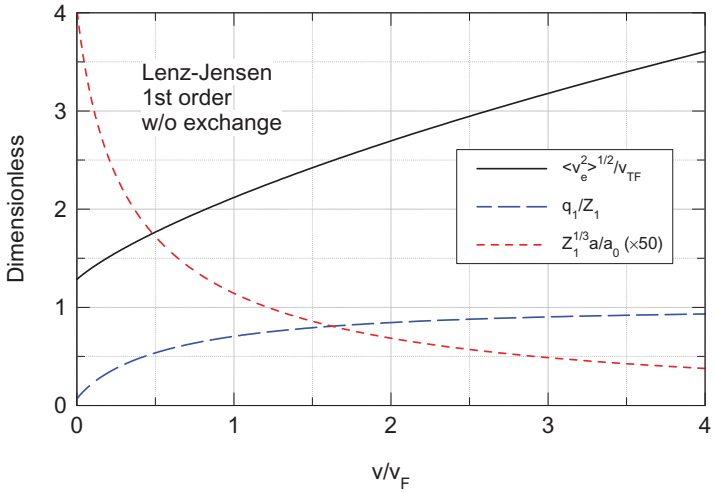

Fig. 1.11 First-order Lenz-Jensen approximation. Solid curve: Rms orbital velocity vs. beam speed according to Schinner and Sigmund (2014). Dashed curve: Charge fraction. Dotted curve: Screening radius. All in Thomas-Fermi units

corrected') was found by multiplying A_3 by $8/7$, thus forcing q_1 to approach zero at $v = 0$. This is just to indicate that the behaviour of these curves at low charge states/beam velocities is quite sensitive to minor modifications of the input.

Also included in the graph are four curves including exchange. As noticed already, the exchange correction is quite small except for helium, but it moves the curves away from the origin rather than towards it.

Finally, let us have a look at the first-order Lenz-Jensen approximation. For $c_1 \neq 0$, c_1 is treated as an additional variational parameter, which adds a third equation to (1.50) and (1.51). You find some hints in Problem 1.6.

Figure 1.11, which is based on this approximation, shows a significantly more reasonable behaviour of the charge fraction at low projectile speed, as compared to the zero-order result from Fig. 1.10. Also shown is the rms orbital speed vs. projectile speed according to Schinner and Sigmund (2014). While this is not the speed that is entering the Bohr stripping criterion, the two speeds are evidently not unrelated.

1.4.5 Brandt-Kitagawa Theory

It is evident from Table 1.1 that the Yukawa potential is not a suitable trial function in connection with the straight Thomas-Fermi model. Nevertheless, Brandt and Kitagawa (1982) proposed a description, based on this trial function, which has been utilized with considerable success. How is this possible? Well, the problem

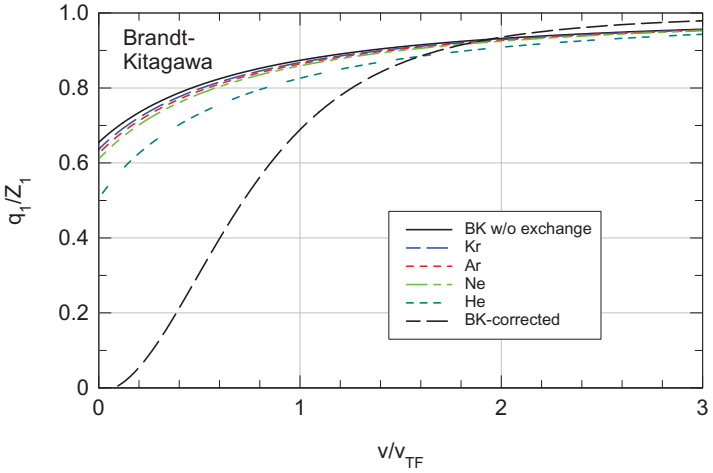

Fig. 1.12 Same as Fig. 1.10 for Yukawa trial function. Solid curve ('BK w/o exchange'): Full Coulomb interaction without exchange and correlation. Dashed curve ('BK corrected'): Coulomb interaction reduced by factor 4/7. Dashed coloured lines: Including exchange for Kr, Ar, Ne, He (top to bottom)

lies in the quantity $A_2 - 7A_3$ which, according to Table 1.1, is nonvanishing, so the projectile is not neutral for $v = 0$, see Fig. 1.12.

Brandt and Kitagawa (1982) proposed to force the quantity $A_2 - 7A_3$ to vanish by reducing the Coulomb energy of the electron gas by a factor of 4/7. They argued that the exchange-correlation energy lowers the Coulomb interaction and that, in the average, this could be accounted for by a constant factor. The result is shown as the dashed curve in Fig. 1.12. It was also demonstrated, by comparison with the Lenz-Jensen function, that energy and screening versus charge state showed a reasonable behaviour.

Despite this success, there are obvious objections:

1. If $A_1 - 7A_2$ differs significantly from zero, this indicates a weak point in the trial function, not in the expression for the energy.
2. The exchange-correlation energy of the Fermi gas is here treated as output rather than as input, as it should in a variational calculation where the electron density is the variable.
3. According to Table 1.1 as well as Fig. 1.12 the relative magnitude of the exchange term is much smaller than the necessary correction, and the correlation term is even smaller.

A critical discussion of the model of Brandt and Kitagawa was presented by Mathar and Posselt (1995), where also possible modifications by taking into account the orbital motion of the target electrons were analyzed.

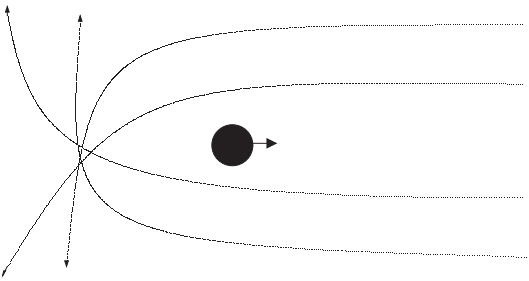

Fig. 1.13 Pile-up of electron trajectories behind a moving ion. See text

1.5 Effect of the Stopping Medium

Up to this point the charge state of a moving ion has been considered as independent of the medium. However, as mentioned in Sect. 1.1, a significant gas-solid difference in the equilibrium charge of fission fragments was observed long ago by Lassen (1951b,a). One may assume that differences of this kind are more general, and that dependencies on other physical and chemical properties of the target might exist.

We shall see in Chap. 3 that cross sections for electron capture and loss play a central role in the theoretical interpretation of the gas-solid effect observed for fission fragments and other swift heavy ions. However, even within the present picture, where we look at the minimum-energy state of a moving ion, the stopping medium has an influence by modifying the Coulomb potential of the projectile and thus the energy levels of bound electrons.

An early hint on such an influence is due to Neufeld and Snyder (1957). Figure 1.13 shows the situation in the rest frame of the projectile. Here the projectile is exposed to a homogeneous current of target electrons which experience its attractive force and hence are deflected toward the ion trajectory. As a consequence there will be collected an excess negative charge behind the ion.

Neufeld and Snyder (1957) asserted that the repulsive potential determined by this negative charge will give rise to expulsion of projectile electrons and, hence, to an increased ion charge state. The magnitude of this effect must increase with increasing density of the stopping material.

1.5.1 Linear Theory

One way of studying this effect is by use of the polarization potential discussed in Chap. 5, Vol. 1,

$$\Phi_{\mathrm{ind}}(\boldsymbol{r},t) = \frac{Z_1 e}{2\pi^2}\int \frac{\mathrm{d}^3\boldsymbol{k}}{k^2}\mathrm{e}^{i\boldsymbol{k}\cdot(\boldsymbol{r}-\boldsymbol{v}t)}\left(\frac{1}{\varepsilon(k,\omega)}-1\right) \tag{1.62}$$

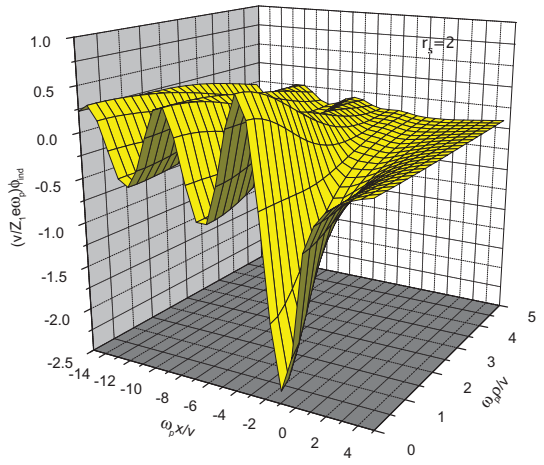

Fig. 1.14 Induced potential for Fermi gas at $B = 2mv^2/\hbar\omega_P = 10$ and $r_s = 2$. From Schinner and Sigmund (2012)

according to Lindhard (1954), where $\varepsilon(k, \omega)$ is the dielectric function which is most often taken to be the one for a Fermi gas of density ρ.

The polarization (or *wake*) potential has been discussed extensively in connection with the penetration of molecules and clusters. Therefore, a detailed discussion will be found in Chap. 10. Only some selected results will be shown here.

The potential (1.62) has cylindrical symmetry. Therefore, introducing cylindrical coordinates $(x, \boldsymbol{\rho})$ and viewing the situation from a reference frame moving with the projectile velocity $\boldsymbol{v}$, we may write the induced potential in the form introduced by Neufeld and Ritchie (1955),

$$\Phi_{\mathrm{ind}}(x,\rho) = \frac{Z_1 e}{\pi}\int_0^\infty k\,\mathrm{d}k\,J_0(k\rho)\int_{-\infty}^{\infty}\frac{\mathrm{e}^{i\kappa x}\,\mathrm{d}\kappa}{k^2+\kappa^2} \times\left(\frac{1}{\varepsilon\left(\sqrt{k^2+\kappa^2},\kappa v\right)}-1\right), \quad (1.63)$$

where J_0 indicates a Bessel function in standard notation (Abramowitz and Stegun, 1964).

Numerous graphs from the literature show wake potentials calculated from this or related models (Echenique et al., 1990). Figure 1.14 shows a three-dimensional picture of the induced potential of a point charge moving at $B = 2mv^2/\hbar\omega_p = 10$ through a Fermi gas with an electron density ρ characterized by a Wigner-Seitz radius $r_s = 2$, where

$$\frac{4\pi}{3}(r_s a_0)^3\rho = 1. \quad (1.64)$$

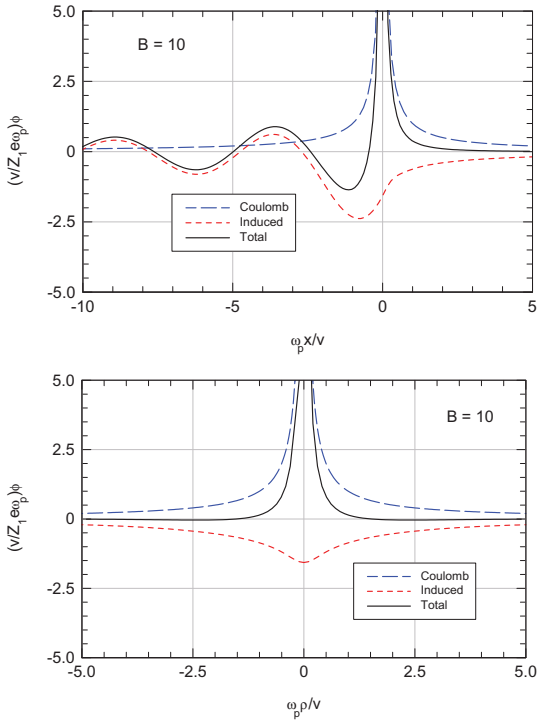

Fig. 1.15 The induced potential shown in Fig. 1.14 in the plane $\rho = 0$ (top) and $x = 0$ (bottom), together with the bare Coulomb potential and the total potential. From Schinner and Sigmund (2012)

The Fermi gas has been described by the dielectric function of Lindhard (1954), (5.154)–(5.156), Vol. 1.

Figure 1.15 shows the induced potential, the Coulomb potential and the sum of the two, the potential seen by a test charge. Two prominent features are evident in the total potential. Near the projectile the Coulomb potential is screened asymmetrically. Further away, at some distance behind the projectile, the potential is dominated by the induced potential.

Consider first the behaviour of the potential in the vicinity of the projectile near $x = \rho = 0$. Here the induced potential tends to screen the Coulomb potential. Figure 1.15 shows that screening is lacking forward-backward symmetry and, moreover, varies from the longitudinal to the transverse plane. Comparison with Fig. 1.16 indicates that the variation with projectile speed is negligible in the transverse and the forward direction — when visualized in the proper scaled variable $\omega_p \rho/v$ — while the variation in the backward direction is noticeable.

We may draw the qualitative conclusion that screening of the Coulomb potential must reduce the number of bound states. Therefore, in the absence of other effects, the induced potential must tend to decrease the number of bound electrons.

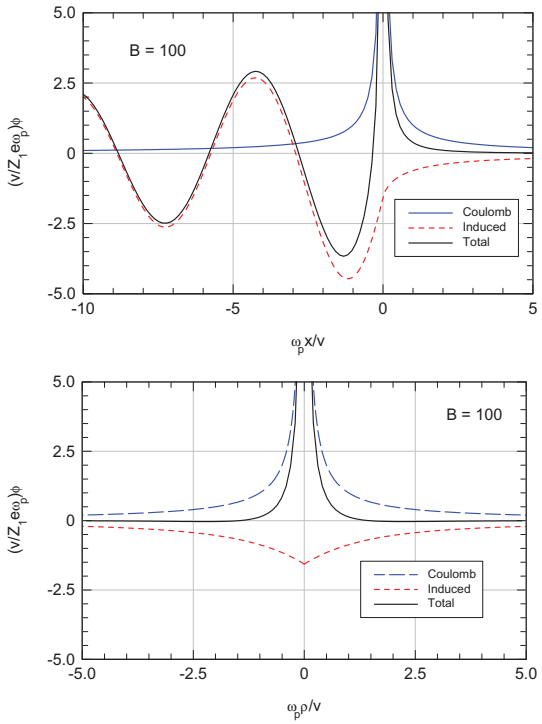

Fig. 1.16 Same as Fig. 1.15 for $B = 2mv^2/\hbar\omega_p = 100$. From Schinner and Sigmund (2012)

1.5.2 Application to Light Ions

Quantitative estimates in the literature have focused on protons, following pioneering work by Neelavathi et al. (1974). Key questions have been:

1. Under which conditions can a proton moving through an electron gas bind an electron, and
2. Under which conditions can a proton bind two electrons.

An illuminating review of this aspect has been provided by Arista (2006). With a focus on projectile speeds well below the Fermi velocity, theoretical tools employed in those studies were taken from condensed-matter physics, going far beyond the simple linear theory sketched in the previous section.

In addition to a careful review of the literature, where there are mutually conflicting results, Arista (2006) presented simple estimates based on a nonlinear theory of the Fermi gas which is to be discussed in Chap 8. This theory involves the Friedel sum rule, which is discussed in Appendix 8.10.2 and operates with three trial functions for the potential of a proton embedded in the electron gas.

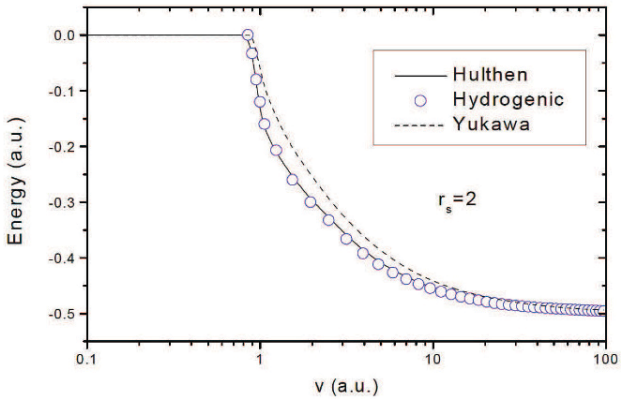

Fig. 1.17 Binding energy of an electron state around a proton moving in a Fermi gas ($r_s = 2$) at a speed v. Atomic units v_0 and e^2/a_0. From Arista (2006)

The main result of such an estimate — which is supported by experimental evidence — is shown in Fig. 1.17, indicating that a bound state exists only for $v \gtrsim v_0$, and that the binding energy of neutral hydrogen in vacuum is reached at v/v_0 above 10. Results based on the three trial functions for the potential, each of which being characterized by one variational parameter, the screening radius, are in close agreement with each other.

Arista (2006) concludes that 'slow protons in metals behave as free particles dressed by a screening cloud of conduction electrons', while bound states appear at higher velocities.

1.5.3 Wake-Riding Electrons

The oscillatory structure behind the ion which you have seen in Figs. 1.14–1.16 has given rise to lively discussions in the literature. One interesting aspect is the question of whether electrons could be trapped in bound states in the first or higher potential maxima (Neelavathi et al., 1974) — i.e., in the minima of the potential energy of electrons — where the potential has a quasi-paraboloidal shape. Such a 'wake-riding' electron would be expected to leave the target about simultaneously with the projectile ion, and since it cannot any longer be expected to be bound, it would be recordable as a free electron with the velocity of the emerging ion and with a direction close to that of the ion beam.

However, energy spectra of electrons emitted by swift ions emerging from a solid target show signatures of a wide variety of processes, which will be the subject of a chapter in Volume 3. In the present context, *cusp* or *convoy* electrons are of interest. The term 'cusp' refers to the narrow distribution in both energy and direction of

these electrons. The term 'convoy' refers to an original prediction (Neelavathi et al., 1974) of wake-riding electrons.

Cusp electrons have been observed in numerous experiments in both solids and gases, and relevant processes include both electron capture and electron loss into the continuum (Macek, 1970). Experimental evidence (Laubert et al., 1978, Meckbach et al., 1977, Breinig et al., 1982, Kroneberger et al., 1996) appears to favour the latter processes rather than wake-riding. However, regardless of the specific interpretation, the very fact that electrons are emitted with a velocity close to that of the projectile indicates proximity in space. While such electrons contribute to the screening of the ionic potential, their number is usually considerably less than one electron per ion.

Calculated electronic binding energies in such states depend on the material and the projectile speed (Neelavathi et al., 1974, Flores and Echenique, 1991). For 2.5 MeV protons, Neelavathi et al. (1974) quote 4.08 eV in aluminium. For $v = 0.8v_0$, Salin et al. (1999) quote 136 eV in an electron gas with $r_s = 2.07$. Considering either Bohr's or Lamb's stripping criteria, the lifetime of wake-riding electrons must be quite short.

1.5.4 Effect of Screening

Now, consider the effect of projectile screening on the charge state of a heavier ion. Following Schinner and Sigmund (2014) we ignore forward-backward asymmetry of the screening radius and set the potential to

$$\phi(r) \simeq \frac{Z_1 e}{r} e^{-\omega r/v}, \tag{1.65}$$

as was done by Lindhard (1976) in a different context. Since we are concerned about the potential in the vicinity of the nucleus, we may approximate

$$\phi(r) \simeq \frac{Z_1 e}{r}\left(1 - \frac{\omega r}{v}\right), \tag{1.66}$$

assuming the projectile speed to be high enough so that v/ω is large compared to the effective projectile radius. Here, ω is an effective plasma frequency of the medium.

This implies that a term

$$\int d^3\boldsymbol{r}\, \rho_e(\boldsymbol{r}) \left(\frac{-Z_1 e\omega}{v}\right) = -Z_1 N_1 e^2 \frac{\omega}{v} \tag{1.67}$$

has to be added to the energy $\mathcal{E}(N_1)$ in (1.18). This leaves (1.51) unchanged but adds an additional term to (1.50). Since (1.65) represents an expansion up to first order in ω/v, it is appropriate also to solve the resulting cubic equation for N_1/Z_1,

$$\frac{v^2}{v_{TF}^2} = \xi^2 - \eta\frac{v_{TF}}{v} \tag{1.68}$$

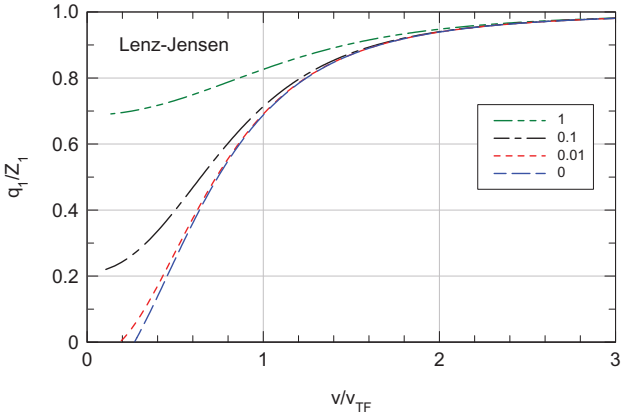

Fig. 1.18 Influence of the stopping medium on the equilibrium charge according to the Lamb criterion applied to a Lenz-Jensen trial function. Evaluated from (1.15). Labels of the curves indicate the value of η, (1.70). From Schinner and Sigmund (2014)

with

$$\xi^2 = \frac{(A_2 - 7A_3N_1/Z_1)(A_2 - A_3N_1/Z_1)}{6A_1(N_1/Z_1)^{2/3}mv_0^2} \tag{1.69}$$

and

$$\eta = \frac{2\hbar\omega}{Z_1 m v_0^2} \tag{1.70}$$

by expansion up to the first order in ω/v. Then,

$$\frac{v^2}{v_{TF}^2} \simeq \xi^2 - \frac{\eta}{\xi}. \tag{1.71}$$

Figure 1.18 illustrates the case of Lenz-Jensen interaction. You may note that even for rather small values of η there is a noticeable positive solid-gas difference.

1.6 Data

Numerous measurements have been performed aiming at equilibrium charges of ions penetrating through gaseous and solid materials. Experimental techniques have been described in classical reviews by Allison (1958) and Betz (1972) who focused on light and heavy ions, respectively. For a more recent review focusing on experimental methods, the reader is referred to Geissel et al. (2002).

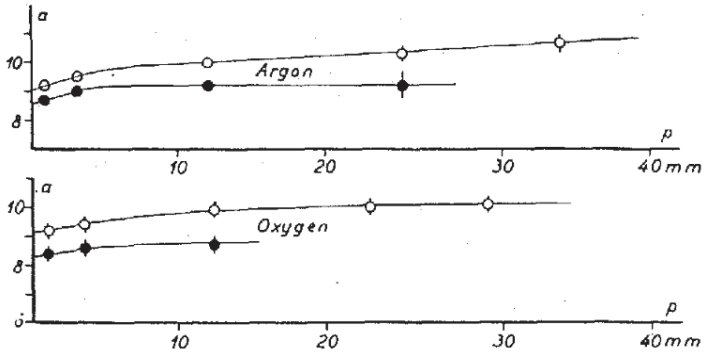

Fig. 1.19 Mean charges of light and heavy fission fragments penetrating through argon and oxygen vs. gas pressure, from Lassen (1951b)

1.6.1 Gas-Solid Difference

Pioneering measurements, performed by Lassen (1951b) by means of fission fragments, were mentioned in Sect. 1.1. In view of the limited range of accessible atomic numbers and beam energies, the most obvious variation to study appeared to be the influence of the medium. Measurements were performed on solids and gases, the latter as a function of gas pressure. Results were shown in Fig. 1.1.

Figure 1.19 shows equilibrium charges in gases vs. pressure, likewise from Lassen (1951b). A clear increase with gas pressure is seen. Here, as in Fig. 1.1, the charge increases with the electron density of the medium, pointing at a common origin. This will be discussed in Sect. 3.3.3.

1.6.2 Compilations

In view of the large number of projectile-target combinations of potential interest, much attention has been paid to scaling properties of the mean equilibrium charge $\langle q_1 \rangle$ in three-dimensional parameter space (Z_1, Z_2, v). Guided by theoretical estimates of the type of (1.6), where properties of the target material do not enter at all, special efforts have been made to identify an adequate scaling variable of the type of $v/Z_1^{2/3}v_0$, while Z_2-dependencies were most often treated as perturbations, except for gas-solid differences mentioned above.

Figure 1.20 shows average charge fractions for ions with Z_1 ranging from 16 to 92 for ions emerging from carbon foils (upper graph) and from gas targets (lower graph). Adopted scaling variables are $v/Z_1^{0.45}v_0$ according to Nikolaev and Dmitriev (1968) in the upper graph and $v/Z_1^{0.55}v_0$ in the lower graph (Betz, 1972). Noticeably higher values are observed in the upper graph over the entire velocity range covered, confirming the existence of a distinct gas-solid difference.

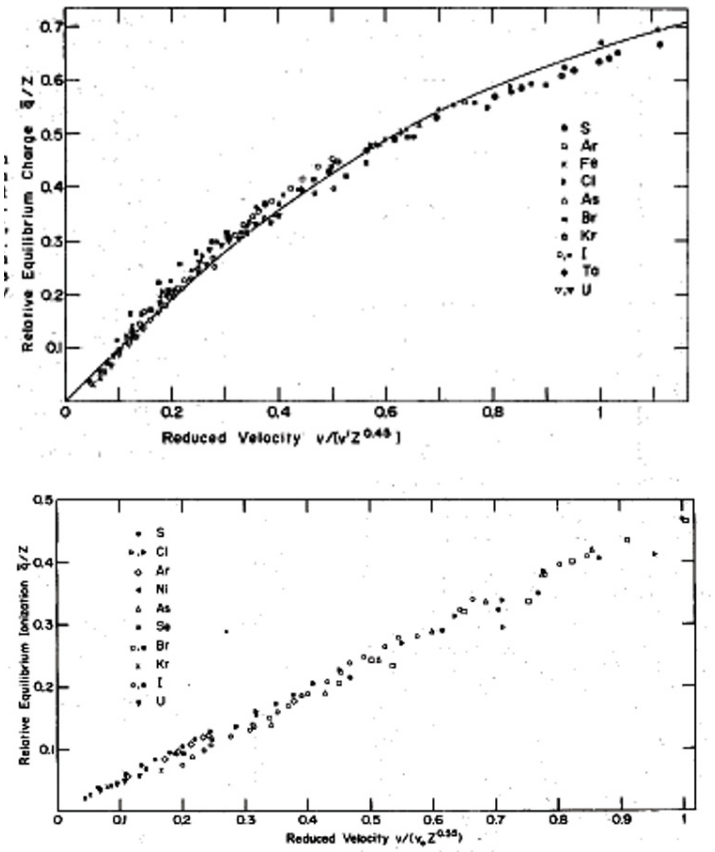

Fig. 1.20 Average charge fraction of sulphur to uranium ions vs. scaled velocity. Upper graph: Carbon foil. Velocity variable $v/Z_1^{0.45}v'$ with $v' = v_0/0.608$. Lower graph: Gas targets of N_2, O_2 and air. Velocity variable $v/Z_1^{0.55}v_0$. From Betz (1972)

An extensive analysis of measured equilibrium charge fractions in carbon (Shima et al., 1982) has led to an empirical formula which has frequently been utilized in estimates also on other solid targets,

$$\frac{\langle q_1 \rangle}{Z_1} = 1 - \mathrm{e}^{-1.25X+0.32X^2-0.11X^3}; \quad X = 0.608v/Z_1^{0.45}v_0. \tag{1.72}$$

Comparison with (1.6) indicates a somewhat steeper slope in the low-velocity limit as well as a difference in the Z_1-dependence.

More recently, Schiwietz and Grande (2001) proposed

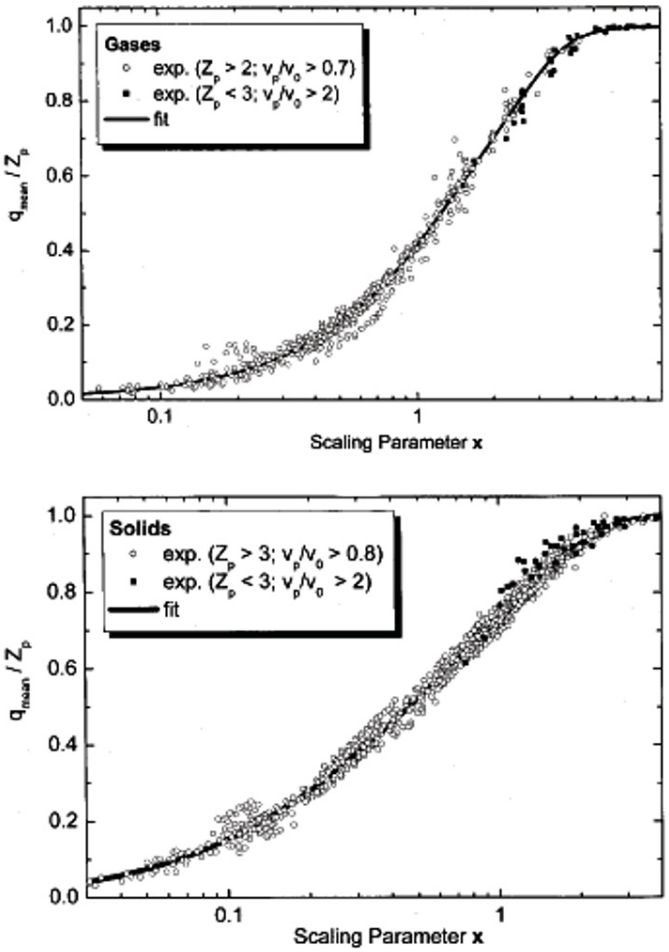

Fig. 1.21 Average charge fraction in gases (upper graph) and solids (lower graph) and empirical fits, (1.73) and (1.74) vs. scaled velocity. Z_p and v_p stand for Z_1 and v, respectively. From Schiwietz and Grande (2001)

$$\frac{\langle q_1 \rangle}{Z_1} = \frac{x^6 + 376x}{x^6 + 690x - 1206x^{0.5} + 1428}$$
$$x = \left(\frac{\eta}{Z_2^{0.017\eta - 0.03}} \right)^{1+0.4/Z_1} \tag{1.73}$$

for gas targets and

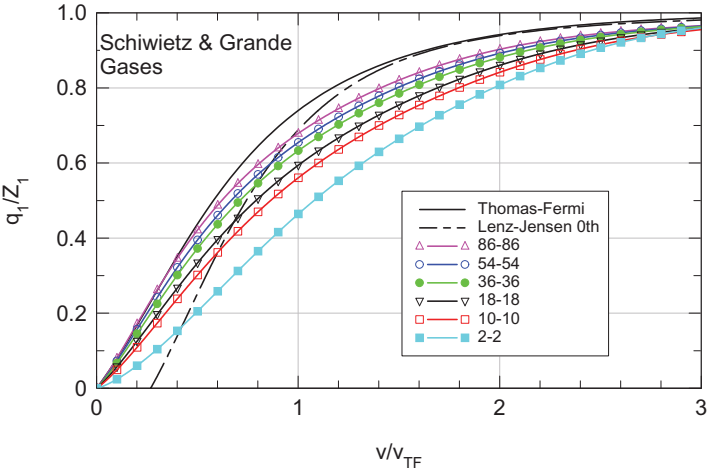

Fig. 1.22 Average charge fraction vs. speed according to Schiwietz and Grande (2001) for gases, plotted in Thomas-Fermi units. $Z_1 = Z_2$. Also included is the Thomas-Fermi curve from Fig. 1.9 and the zero-order Lenz-Jensen curve from Fig. 1.10.

$$\frac{\langle q_1 \rangle}{Z_1} = \frac{x^4 + 12x}{x^4 + 10.37x + 0.3x^{0.5} + 6 + 0.07/x}$$
$$x = \left(\frac{\eta}{1.68 Z_2^{0.019\eta}} \right)^{1+1.8/Z_1} \tag{1.74}$$

for solids with

$$\eta = \frac{v}{Z_1^{0.52} v_0}. \tag{1.75}$$

Here, the approach to complete ionization is asserted to be power-like rather than exponential. At low velocities, $\langle q_1 \rangle$ is asserted to be $\propto v^{1+0.4/Z_1}$ for gases and $\propto v^{2+3.6/Z_1}$ for solids.

Figure 1.21 gives an impression both of the quality of the scaling and the accuracy of the fit. Clearly, these fitting formulae are entirely empirical, and deviations from adopted scaling properties may well be systematic. On the other hand, rough estimates of equilibrium charge states are possible for systems where measurements are unavailable.

Figure 1.22 shows the curve from Fig. 1.21 plotted in Thomas-Fermi units. It is seen that the curve denoted 'Thomas-Fermi', taken from Fig. 1.9, lies consistently above the empirical interpolation, although the difference gets less pronounced with increasing atomic number. The Lenz-Jensen curve from Fig. 1.10 represents a reasonable average behaviour at low speed but approaches the TF curve at high speed.

Finally, Fig. 1.23 shows plots of (1.74) and (1.73) in Thomas-Fermi units. The gas-solid difference clearly emerges from these graphs, as well as the near-independence of the mean equilibrium charge on the atomic number of the stopping

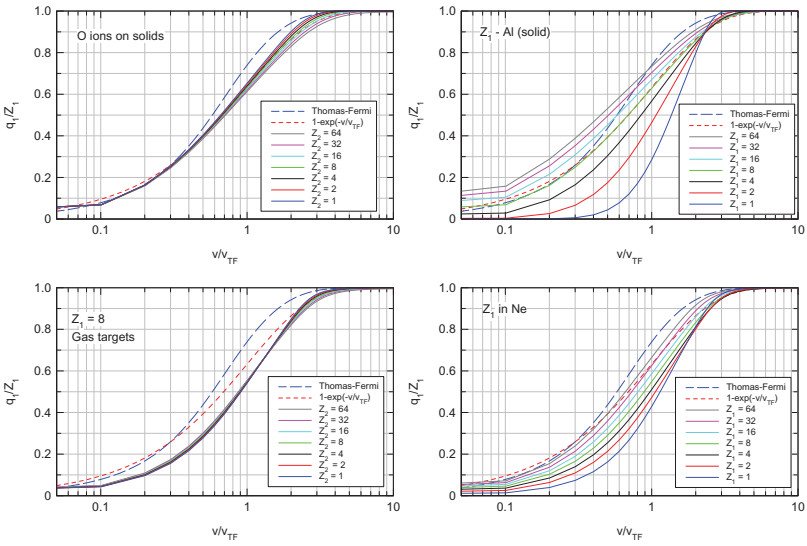

Fig. 1.23 Equilibrium charges according to Schiwietz and Grande (2001) plotted in Thomas-Fermi units

material. Conversely, deviations from v/v_{TF} scaling are pronounced, albeit mostly so for small Z_2, where the Thomas-Fermi model cannot expected to be valid.

You may have noticed that none of the scaling relations mentioned so far takes into account shell effects such as the plateaus seen in Figs. 1.3 and 1.7.

1.7 Discussion and Outlook

The prime message of this chapter is that ions in charge equilibrium experience considerable screening for $v \lesssim v_{\mathrm{TF}}$ or

$$E \lesssim 0.025 Z_1^{4/3}\,\mathrm{MeV/u}, \tag{1.76}$$

and that the K shell can only be expected to be stripped for $v \gtrsim Z_1 v_0$ or

$$E \gtrsim 0.025 Z_1^2\,\mathrm{MeV/u}. \tag{1.77}$$

Theoretical estimates presented in this chapter refer mostly to penetration through gas targets. The energy criterion has been dominating, mostly because it can be formulated quantitatively. Its main weakness is the lack of a statement on the time or pathlength required to reach charge equilibrium. Moreover, it does not say anything about the width of the charge-state spectrum. Thomas-Fermi estimates tend to predict higher equilibrium charges than measured.

Determining equilibration distances and charge-state populations requires explicit knowledge of the kinetics of charge exchange, as expressed by cross sections or transition amplitudes and appropriate statistical tools. This will be the subject of the following two chapters.

The observation of the gas-solid difference in the charge state and the ongoing controversy about its origin has, until a few years ago, been a considerable challenge to theoreticians. We shall come back to this repeatedly.

Both the very definition of the charge state of an atom moving in a medium and the validity of procedures to estimate transition probabilities or amplitudes have been the subject of lively discussion. I shall not go into details here but mainly mention a few points of interest and supply pertinent references.

From an experimental point of view, there are two obvious ways to approach the problem, observation of processes accompanying the emerging ion, and in situ analysis of the penetrating ion. The first option is related primarily to electron emission, the second to X-ray emission.

The first aspect has been discussed in Sect. 1.5.3. Bound states of swift protons moving through a solid material have been a subject of lively discussion. For a recent review you are referred to Arista (2006). Several theoretical predictions were based on the Fermi gas model described in Chap. 5, Vol. 1, but even within that framework, predictions varied from 0 to 2 permitted charge states (Brandt, 1975, Cross, 1977, Peñalba et al., 1992). Arista's conclusion appears to be close to the view of Cross (1977) who considered the coupling between the ion and the electron gas to be weak and, consequently, considered the charge-state evolution as a sequence of capture and loss processes much like in a gas.

As to the second aspect, in situ observation of charge states in solids is possible by X-ray spectrometry. Energies of inner-shell electrons are shifted according to the charge state. This *satellite* structure may be observed in precision measurements and thus may provide information about charge fractions of penetrating ions (Knudson et al., 1974). These experiments are difficult both because of the smallness of the shifts and the interference with the Doppler effect.

Measurements of this type appear most promising for heavy ions at very high velocities, where ions are highly charged and K X-ray levels shifted considerably. Results obtained with 11.4 MeV Ca ions by Rosmej et al. (2005) indicate a reasonable agreement between charge states deduced from x-ray spectra and those measured by magnetic deflection of ions after emergence from the foil.

1.8 Appendix

1.8.1 Exchange Energy in the Thomas-Fermi Equation

This appendix presents a brief derivation of the exchange term, (1.90).

Consider first a 2-electron system, where, in an individual-particle description, two stationary states 1 and 2 are occupied. Write the wave function $\Psi(x_1, x_2)$ in the form

$$\Psi(x_1, x_2) = \frac{1}{\sqrt{2}} \left[u_1(x_1) u_2(x_2) - u_2(x_1) u_1(x_2) \right], \tag{1.78}$$

where x stands for both space and spin variables. The Coulomb interaction energy is given by

$$E_{\text{Coulomb}} = \iint \mathrm{d}x_1 \mathrm{d}x_2 \Psi(x_1, x_2)^\star \frac{e^2}{|\boldsymbol{r}_1 - \boldsymbol{r}_2|} \Psi(x_1, x_2). \tag{1.79}$$

Since e^2/r_{12} does not depend on the spin, E_{Coulomb} is nonvanishing only when the two states 1 and 2 have identical spin. We can, therefore, replace x by $\boldsymbol{r}$ and write

$$E_{\text{Coulomb}} = e^2 \iint \mathrm{d}^3\boldsymbol{r}_1 \mathrm{d}^3\boldsymbol{r}_2 \frac{\rho(\boldsymbol{r}_1)\rho(\boldsymbol{r}_2)}{|\boldsymbol{r}_1 - \boldsymbol{r}_2|} + E_{\text{exch}}, \tag{1.80}$$

where

$$E_{\text{exch}} = - \iint \mathrm{d}^3\boldsymbol{r}_1 \mathrm{d}^3\boldsymbol{r}_2 \frac{u_1^\star(\boldsymbol{r}_1) u_2^\star(\boldsymbol{r}_2) u_2(\boldsymbol{r}_1) u_1(\boldsymbol{r}_2)}{|\boldsymbol{r}_1 - \boldsymbol{r}_2|}, \tag{1.81}$$

where the first term represents the classical Coulomb interaction energy. We evaluate the exchange term $E^{\text{exch}}_{\text{Coulomb}}$ for free electrons with

$$u_j(\boldsymbol{r}) = \frac{1}{\sqrt{\Omega}} \mathrm{e}^{\mathrm{i}\boldsymbol{k}_j \cdot \boldsymbol{r}}, \tag{1.82}$$

where Ω represents the volume of a large box. With this, the Coulomb potential has the expansion

$$\frac{e^2}{r} = \sum_{\boldsymbol{q}} \frac{4\pi e^2}{\Omega q^2} \mathrm{e}^{\mathrm{i}\boldsymbol{q}\cdot\boldsymbol{r}}. \tag{1.83}$$

Carrying out the above integral you will find

$$E^{\text{exch}}_{\text{Coulomb}} = - \frac{4\pi e^2}{\Omega(\boldsymbol{k}_1 - \boldsymbol{k}_2)^2}. \tag{1.84}$$

Now, consider a Fermi gas characterized by a density ρ or a Fermi wave number k_F. The total exchange energy is then given by the integral

$$\mathcal{E}_{\text{exch}} = - \left(\frac{\Omega}{(2\pi)^3} \right)^2 \iint \mathrm{d}^3\boldsymbol{k}_1 \mathrm{d}^3\boldsymbol{k}_2 \frac{4\pi e^2}{\Omega(\boldsymbol{k}_1 - \boldsymbol{k}_2)^2}. \tag{1.85}$$

If you are willing to solve Problem 1.4, you will find that

$$\mathcal{E}_{\text{exch}} = \frac{e^2 \Omega k_F^4}{4\pi^3}. \tag{1.86}$$

With

$$k_F^3 = 3\pi^2\rho \tag{1.87}$$

you find the energy density

$$\frac{\mathcal{E}}{\Omega} = \kappa_a \rho^{4/3} \tag{1.88}$$

with

$$\kappa_a = \frac{3}{4}\left(\frac{3}{\pi}\right)^{1/3} e^2 \tag{1.89}$$

in the notation of Gombas (1949).

1.8.2 Thomas-Fermi-Dirac Theory

Following Gombas (1949), we take into account the exchange contribution (Dirac, 1930), which adds a term

$$E^{\text{exch}} = -\kappa_a \int \mathrm{d}^3\boldsymbol{r}\, \rho(\boldsymbol{r})^{4/3} \tag{1.90}$$

with

$$\kappa_a = \frac{3^{4/3}}{4\pi^{1/3}} e^2 \tag{1.91}$$

to (1.13).

Carrying out the argument described in Sects. 1.4.1 and 1.4.2, you will obtain an additional term $-4(\kappa_a/3)\rho(\boldsymbol{r})^{1/3}$ to (1.21) which leads to

$$\rho(\boldsymbol{r}) = \sigma_0 \left(\tau_0 + \sqrt{\tau_0^2 + \phi(\boldsymbol{r}) - \phi_0}\right)^3 \tag{1.92}$$

with

$$\tau_0 = \sqrt{\frac{e}{2\pi^2 a_0}}. \tag{1.93}$$

Applying Poisson's formula you arrive at the Thomas-Fermi-Dirac equation

$$\nabla^2\left(\phi(\boldsymbol{r}) - \phi_0 + \tau_0^2\right) = 4\pi\sigma_0 e \left(\tau_0 + \sqrt{\tau_0^2 + \phi(\boldsymbol{r}) - \phi_0}\right)^3 \tag{1.94}$$

or, in Thomas-Fermi units,

$$g''(\xi) = \xi\left[\sqrt{\frac{g(\xi)}{\xi}} + \beta_0\right]^3 \tag{1.95}$$

with

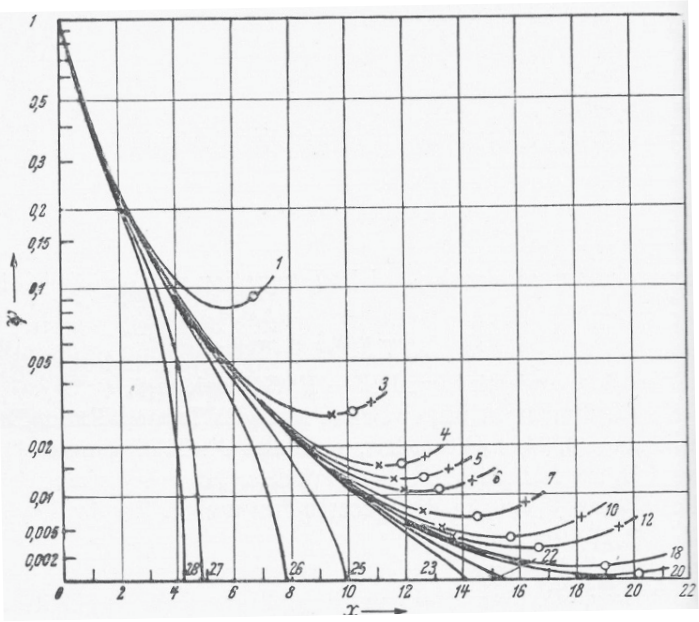

Fig. 1.24 Same as Fig. 1.8 for solutions of the Thomas-Fermi-Dirac equation. $Z_1 = 54$. From Gombas (1949)

$$\beta_0 = \tau_0 \sqrt{a/Z_1 e} = \frac{0.2118}{Z_1^{2/3}}, \tag{1.96}$$

$\xi = r/a$, and

$$\phi(r) + \tau_0^2 - \phi_0 = \frac{Z_1 e}{r} g(\xi). \tag{1.97}$$

So far, this derivation follows Gombas (1949), except again that the constant $\phi_0 = mv^2/2e$ is predefined, while the number N_1 of electrons on the projectile is free and follows from the charge density $\rho(\boldsymbol{r})$.

However, from (1.92) and Fig. 1.24 you may note that the charge density does not approach zero. Since the number of electrons must be finite, there must be a certain radius r_0 where $\rho(\boldsymbol{r})$ is truncated. Determining this radius is part of the minimizing procedure, as recognized by Jensen (1934, 1935). The present evaluation is slightly different, since there are no boundary conditions, but the result is identical with Jensen's.

Writing the total energy as

$$\mathcal{E}(N_1) = \frac{1}{2} M_1 v^2 + \kappa_k \int \mathrm{d}^3\boldsymbol{r}\, \rho(\boldsymbol{r})^{5/3} - \kappa_a \int \mathrm{d}^3\boldsymbol{r}\, \rho(r)^{1/3} - Z_1 e^2 \int \mathrm{d}^3\boldsymbol{r}\, \frac{\rho(\boldsymbol{r})}{r} + \frac{e^2}{2} \int \mathrm{d}^3\boldsymbol{r}\, \mathrm{d}^3\boldsymbol{r}'\, \frac{\rho(\boldsymbol{r})\rho(\boldsymbol{r}')}{|\boldsymbol{r} - \boldsymbol{r}'|} + \frac{1}{2} m v^2 \int \mathrm{d}^3\boldsymbol{r}\, \rho(r), \tag{1.98}$$

we minimize the energy with respect to r_0,

$$\frac{dE}{dr_0} = 4\pi r_0^2 \left(\kappa_k \rho(r_0)^{5/3} - \kappa_a \rho(r_0)^{4/3} - \frac{Z_1 e^2}{r} \rho(r_0) + \rho(r_0) e^2 \int_{r'<r_0} \mathrm{d}^3 \boldsymbol{r}' \, \frac{\rho(r')}{|\boldsymbol{r} - \boldsymbol{r}'|} \bigg|_{r=r_0} + \frac{m v^2}{2} \rho(r_0) \right) = 0. \quad (1.99)$$

Noting that the third, fourth and fifth term in the brackets may be written as $-e\rho(r_0)[\phi(r_0) - \phi_0]$, and inserting $\phi(r_0) - \phi_0$ from (1.92) you end up with

$$\frac{dE}{dr_0} = 4\pi r_0^2 \rho(r_0) \left[\kappa_k \rho(r_0)^{2/3} - \kappa_a \rho(r_0)^{1/3} + 2e\tau_0 \left(\frac{\rho(r_0)}{\sigma_0} \right)^{1/3} - e \left(\frac{\rho(r_0)}{\sigma_0} \right)^{2/3} \right] \quad (1.100)$$

or

$$\frac{dE}{dr_0} = 4\pi r_0^2 \rho(r_0) \left[-\frac{2}{3} \kappa_k \rho(r_0)^{2/3} + \frac{1}{3} \kappa_a \rho(r_0)^{1/3} \right]. \quad (1.101)$$

Setting $dE/dr_0 = 0$ leads to

$$\rho(r_0) = \left(\frac{\kappa_a}{2\kappa_k} \right)^3 = \frac{0.002127}{a_0^3}. \quad (1.102)$$

This result is identical with the one quoted by Gombas (1949), although the derivation is simpler: For a fixed number N_1 of electrons, $\rho(r)$ and r_0 cannot be varied independently. Therefore, in the derivation of Gombas (1949) also a derivative $\mathrm{d}\rho(r)/\mathrm{d}r_0$ needs to be considered.

For the standard Thomas-Fermi model, where κ_a is ignored, we find $\rho(r_0) = 0$, in agreement with (1.34) in Sect. 1.4.2. For the Thomas-Fermi-Dirac model, on the other hand, the electron density at the edge has a fixed nonvanishing value, (1.102), independent of atomic number and charge state.

The number N_1 of electrons on the projectile is found from

$$N_1 = \int \mathrm{d}^3 \boldsymbol{r} \, \rho(r) = Z_1 \int_0^{\xi_0} \mathrm{d}\xi \, \xi g''(\xi) = Z_1 \left[\xi_0 g'(\xi_0) - g(\xi_0) + 1 \right] \quad (1.103)$$

or

$$q_1 = Z_1 - N_1 = Z_1 \left[g(\xi_0) - \xi_0 g'(\xi_0) \right]. \quad (1.104)$$

A major benefit of the straight Thomas-Fermi model is the universal dependence of the charge density on r/a_{TF}. This feature is no longer present in the Thomas-Fermi-Dirac model, where an explicit dependence on Z_1 enters via the term β_0 in (1.95). This, in addition to the abrupt fall-off to zero at r_0, may well generate some doubt

as to whether including electron exchange in the theory is an overall improvement of the scheme. I shall touch this aspect once more in the next section.

Problems

1.1. Derive (1.29) and (1.30) from (1.18), (1.27) and (1.28).

1.2. Show that (1.31) approaches the solution

$$g(\xi) \sim 144/\xi^3 \tag{1.105}$$

for large ξ.

1.3. Compare the behaviour of $\rho(r)$ at small r for the exact solution of the Thomas-Fermi equation with the behaviour of the ansatz by Lenz and Jensen.

1.4. Derive (1.86) from (1.85). Hint: The straightforward but a bit cumbersome way is by introducing spherical coordinates and carrying out the angular integrations first. A more elegant procedure is making use of the Fourier transform of the Coulomb potential.

1.5. Show that, if (1.50) and (1.51) are valid, the equilibrium charge behaves as $\propto v^2$ at low projectile speed.

1.6. Try to reproduce the curves shown in Fig. 1.10.

1.7. Make an estimate of the expected difference between charge ratios for light and heavy fission fragments shown in Fig. 1.1 on the basis of (1.6).

1.8. Look up an element representative for heavy fission fragments and its representative energy, and find the gas-solid difference from (1.73) and (1.74). Compare this with Fig. 1.1.

References

Abramowitz M. and Stegun I.A. (1964): *Handbook of mathematical functions*. Dover, New York

Allison S.K. (1958): Experimental results on charge-changing collisions of hydrogen and helium atoms and ions at kinetic energies above 0.2 keV. Rev Mod Phys **30**, 1137–1168

Arista N.R. (2006): Charge states and energy loss of ions in solids. Mat Fys Medd Dan Vid Selsk **52**, 595–623

Bell G.I. (1953): The capture and loss of electrons by fission fragments. Phys Rev **90**, 548–557

Betz H.D. (1972): Charge states and charge-changing cross sections of fast heavy ions penetrating through gaseous and solid media. Rev Mod Phys **44**, 465–539

Bohr N. (1940): Scattering and stopping of fission fragments. Phys Rev **58**, 654–655

Bohr N. (1941): Velocity-range relation for fission fragments. Phys Rev **59**, 270–275

Bohr N. (1948): The penetration of atomic particles through matter. Mat Fys Medd Dan Vid Selsk **18 no. 8**, 1–144

Bohr N. and Lindhard J. (1954): Electron capture and loss by heavy ions penetrating through matter. Mat Fys Medd Dan Vid Selsk **28 no. 7**, 1–31

Brandt W. (1975): Ion screening in solids. In S. Datz, B.R. Appleton and C.D. Moak, editors, *Atomic Collisions in Solids*, 261–288. Plenum Press, New York

Brandt W. and Kitagawa M. (1982): Effective stopping-power charges of swift ions in condensed matter. Phys Rev B **25**, 5631–5637

Breinig M., Elston S.B., Huldt S., Liljeby L., Vane C.R., Berry S.D., Glass G.A., Schauer M., Sellin I.A., Alton G.D. et al. (1982): Experiments concerning electron capture and loss to the continuum and convoy electron production by highly ionized projectiles in the 0.7–8.5-MeV/u range transversing the rare gases, polycrystalline solids, and axial channels in gold. Phys Rev A **25**, 3015–3048

Brostrøm K.J., Bøggild J.K. and Lauritsen T. (1940): Cloud-chamber studies of fission fragment tracks. Phys Rev **58**, 651–653

Brunings J.H.M., Knipp J.K. and Teller E. (1941): On the momentum loss of heavy ions. Phys Rev **60**, 657

Carlson T.A., Nestor C.W., Wasserman N. and McDowell J.D. (1970): Calculated ionization potentials for multiply charged ions. Atomic Data **2**, 63–99

Clementi E. and Roetti C. (1974): Roothaan-Hartree-Fock atomic wave functions. Atomic Data & Nucl Data Tables **14**, 177

Cross M.C. (1977): Charge states of fast protons in solids. Phys Rev B **15**, 602–607

Dirac P.A.M. (1930): Note on exchange phenomena in the Thomas atom. Proc Cambridge Phil Soc **26**, 376–385

Echenique P.M., Flores F. and Ritchie R.H. (1990): Dynamic screening of ions in condensed matter. Sol State Phys **43**, 229–318

Fermi E. (1927): Un metodo statistico per la determinazione di alcune proprietá dell' atomo. Rend Acad Lincei **6**, 602

Fermi E. (1928): Eine statistische Methode zur Bestimmung einiger Eigenschaften des Atoms und ihre Anwendungen auf die Theorie des periodischen Systems der Elemente. Z Physik **48**, 73

Flamm L. and Schumann R. (1916): Die Geschwindigkeitsabnahme der α-Strahlen in Materie. Ann Physik **50**, 655

Flores F. and Echenique P. (1991): Dynamic screening, charge states and energy loss of ions in solids. Nucl Instrum Methods B **56/57**, 358–360

Geissel H., Weick H., Scheidenberger C., Bimbot R. and Gardès D. (2002): Experimental studies of heavy-ion slowing down in matter. Nucl Instrum Methods B **195**, 3–54

Gluckstern R.L. (1955): Electron capture and loss by ions in gases. Phys Rev **98**, 1817–1821

Gombas P. (1943): Erweiterung der Statistischen Theorie des Atoms. Z Physik **121**, 523–542

Gombas P. (1949): *Die Statistische Theorie des Atoms*. Springer, Vienna

Gombas P. (1956): Statistische Behandlung des Atoms. In S. Flügge, editor, *Handbuch der Physik*, vol. 36, 109–231. Springer, Berlin

Hahn O. and Strassmann F. (1939): Über den Nachweis und das Verhalten der bei der Bestrahlung des Urans mittels Neutronen entstehenden Erdalkalimetalle. Nat Wiss **27**, 11–15

Hedin L. and Lundqvist S. (1969): *Effects of electron-electron and electron-phonon interactions on the one-electron states of solids*, vol. 23 of *Solid State Physics*, 1–181. Academic Press, New York

Henderson G.H. (1923): Changes in the charge of an alpha-particle passing through matter. Proc Roy Soc A **102**, 496–U14

Jensen H. (1932): Die Ladungsverteilung in Ionen und die Gitterkonstante des Rubidiumbromids nach der statistischen Methode. Z Physik **77**, 722

Jensen H. (1934): Über Den Austausch im Thomas-Fermi-Atom. Z Physik **89**, 713–719

Jensen H. (1935): Erg"anzung Zur Arbeit: Über Den Austausch im Thomas-Fermi-Atom. Z Physik **93**, 232–235

Knipp J. and Teller E. (1941): On the energy loss of heavy ions. Phys Rev **59**, 659–669

Knudson A.R., Burghalter P.G. and Nagel D.J. (1974): Vacancy configurations of argon projectile ions in solids. Phys Rev A **10**, 2118–2122

Kroneberger K., Sigaud G.M., Kuzel M., Maier R., Schosnig M., Schlosser D., Groeneveld K.O., Focke P., Suarez S. and Meckbach W. (1996): Beam-foil convoy electrons emerging from uncleaned and cleaned surfaces in coincidence with charge-analysed projectiles including neutrals. J Phys B **29**, 3727–3740

Lamb W.E. (1940): Passage of uranium fission fragments through matter. Phys Rev **58**, 696–702

Lassen N.O. (1951a): Total charges of fission fragments as functions of the pressure in the stopping gas. Mat Fys Medd Dan Vid Selsk **26 no. 12**, 1–19

Lassen N.O. (1951b): The total charges of fission fragments in gaseous and solid stopping media. Mat Fys Medd Dan Vid Selsk **26 no. 5**, 1–28

Laubert R., Sellin I.A., Vane C.R., Suter M., Elston S.T., Alton G.D. and Thoe R.S. (1978): Z, velocity and target material dependence of convoy electrons from solids. Phys Rev Lett **41**, 712

Lee P.S. and Wu T.Y. (1997): Statistical potential of atomic ions. Chin J Physics **35**, 6–11

Lenz W. (1932): Über die Anwendbarkeit der statistischen Methode auf Ionengitter. Z Physik **77**, 713

Lindhard J. (1954): On the properties of a gas of charged particles. Mat Fys Medd Dan Vid Selsk **28 no. 8**, 1–57

Lindhard J. (1976): The Barkas effect – or Z_1^3, Z_1^4-corrections to stopping of swift charged particles. Nucl Instrum Methods **132**, 1–5

Macek J. (1970): Theory of the forward peak in the angular distribution of electrons ejecteed by fast protons. Phys Rev A **1**, 235–241

Mathar R.J. and Posselt M. (1995): Effective-charge theory of the electronic stopping of heavy ions in solids: Stripping criteria and target-electron models. Phys Rev B **51**, 107–116

Meckbach W., Chiu K.C.R., Brongersma H.H. and McGowan J.W. (1977): Do present charge-transfer to continuum theories correctly describe production of $v_i = v_e$ electrons in ion beam-foil collisions? J Phys B **10**, 3255–3270

Meitner L. and Frisch O.R. (1939): Physical evidence for the division of heavy nuclei under neutron bombardment. Nature **143**, 276

Neelavathi V.N., Ritchie R.H. and Brandt W. (1974): Bound electron states in the wake of swift ions in solids. Phys Rev Lett **33**, 302–305

Neufeld J. (1954): Electron capture and loss by moving ions in dense media. Phys Rev **96**, 1470–1478

Neufeld J. and Ritchie R.H. (1955): Passage of charged particles through plasma. Phys Rev **98**, 1632–1642

Neufeld J. and Snyder W.S. (1957): Dependence of the average charge of an ion on the density of the surrounding medium. Phys Rev **107**, 96–102

Nikolaev V.S. and Dmitriev I.S. (1968): On the equilibrium charge distributions of heavy elemental ion beams. Phys Lett A **28**, 277–278

Peñalba M., Arnau A., Echenique P.M., Flores F. and Ritchie R.H. (1992): Stopping power for protons in aluminum. Europhys Lett **19**, 45

Pierce T.E. and Blann M. (1968): Stopping powers and ranges of 5-90-MeV S^{32}, Cl^{35},Br^{79}, and I^{127} ions in H_2, He, N_2, and Kr: A semiempirical stopping power theory for heavy ions in gases and solids. Phys Rev **173**, 390–405

Rosmej O.N., Blazevic A., Korostiy S., Bock R., Hoffmann D.H.H., Pikuz S.A., Efremov V.P., Fortov V.E., Fertman A., Mutin T. et al. (2005): Charge state and stopping dynamics of fast heavy ions in dense matter. Phys Rev A **72**, 052901

Rutherford E. (1924): The capture and loss of electrons by alpha particles. Philos Mag **47**, 277

Salin A., Arnau A., Echenique P.M. and Zaremba E. (1999): Dynamic nonlinear screening of slow ions in an electron gas. Phys Rev B **59**, 2537–2548

Schinner A. and Sigmund P. (2012): Polarization wake of penetrating ions: Oscillator model. Europ Phys J D **66**, 56

Schinner A. and Sigmund P. (2014): Unpublished

Schiwietz G. and Grande P.L. (2001): Improved charge-state formulas. Nucl Instrum Methods B **175-177**, 125–131

Shima K., Ishihara T. and Mikumo T. (1982): Empirical formula for the average charge-state of heavy ions behind various foils. Nucl Instrum Methods **200**, 605–608

Shima K., Kuno N., Yamanouchi M. and Tawara H. (1992): Equilibrium charge fractions of ions of $Z = 4 - 92$ emerging from a carbon foil. At Data Nucl Data Tab **51**, 173–241

Tal Y. and Levy M. (1981): Expectation Values of Atoms and Ions: The Thomas-Fermi Limit. Phys Rev A **23**, 408–415

Thomas L.H. (1926): The calculation of atomic fields. Proc Cambr Philos Soc **23**, 542–547

Yarlagadda B.S., Robinson J.E. and Brandt W. (1978): Effective-charge theory and the electronic stopping power of solids. Phys Rev B **17**, 3473–3483

Chapter 2
Charge Exchange: Atomistics

Abstract This chapter addresses primarily the process of charge exchange and cross sections for electron capture. The theory of electron loss, which is similar to the theory of target ionization, is indicated only briefly in this chapter. The treatment of charge exchange includes classical and quantal theory of the Thomas process as well as other classical models by Bohr and others. Essential steps are described in the development of the quantum theory of charge exchange for light ions, in particular problems encountered with the Brinkman-Kramers theory and the significance of first- vs. second-order perturbation theory in charge exchange. Brief accounts are given of the distorted-wave and eikonal approximations to charge exchange as well as the process of radiative electron capture. The chapter concludes with a list of data sources.

2.1 Introductory Comments

An ion penetrating through a gaseous or condensed material can experience a change in its charge by losing or capturing one or more electrons in collisions with the constituents of the medium. Such events affect the stopping and scattering of the penetrating particle and, therefore, more or less directly, the induced radiation effects.

Electron loss in a collision may be viewed as an ionization event, where the roles of the projectile and the target are interchanged. This implies that much of the theory described in other chapters of Volumes 1 and 2 of this monograph can be applied to electron loss. However, the particle that loses electrons is typically positively charged now rather than neutral. Conversely, the particle that gives rise to electron loss is a target atom which, in the context of this monograph, is most often electrically neutral.

There is no analog to electron capture in what we have looked at so far. However, the jump of an electron from one atom or ion to another one is one of the central

P. Sigmund, *Particle Penetration and Radiation Effects Volume 2*,
Springer Series in Solid-State Sciences 179, DOI: 10.1007/978-3-319-05564-0_2,

problems in many areas of science, especially in chemistry and biochemistry, plasma physics, biophysics and astrophysics.

From an atomic-collision physics point of view, a charge-exchange process between two atomic particles may be viewed from any frame of reference. In other words, the theory of the process

$$A^+ + B^0 \rightarrow A^0 + B^+ \tag{2.1}$$

is independent of whether A^+ or B^0 is viewed as the target. Therefore, in atomic-collision physics the term 'charge exchange' denotes what is called 'electron capture' in particle penetration. In particle penetration, on the other hand, 'charge exchange' denotes the exchange of an electron between the projectile and the medium, and hence the interplay of capture *and* loss of electrons by the projectile.

The phenomenon of electron capture was predicted by Flamm and Schumann (1916) and discovered experimentally by Henderson (1923) who identified the presence of He^+ ions in a beam of alpha particles penetrating through a gas. A first attempt of a theoretical explanation was made by Thomas (1927) on the basis of classical collision theory, and the quantal approach was pioneered by Oppenheimer (1928) and Brinkman and Kramers (1930).

Renewed interest in charge-changing processes in connection with particle penetration arose with the discovery of nuclear fission. Fragments from a fission reaction are fairly heavy, highly-charged ions with atomic numbers around 40 and 50, respectively, with initial velocities $v/v_0 \lesssim 10$. The importance of charge-exchange processes in the slowing down of such fragments was recognized by Bohr (1940, 1941) immediately after the discovery of fission. This was followed up in extensive measurements by Lassen (1951a,b) which were mentioned in the previous chapter.

When particle accelerators became available for atomic-physics experiments, measurements on charge exchange became a favoured subject, as is evidenced in early reviews by Allison (1958), Nikolaev (1965) and Betz (1972) that are still worthwhile reading. In the meantime the literature has exploded, but the present survey will focus on topics that are of importance in particle penetration. Amongst central theoretical references I like to mention classic papers by Thomas (1927), Brinkman and Kramers (1930), Bell (1953) and Bohr and Lindhard (1954), and more recent comprehensive reviews by Bransden and McDowell (1992), Dewangan and Eichler (1994) and Tolstikhina and Shevelko (2013).

While the theory of charge exchange is one of the most challenging areas in atomic-collision physics, a reader interested mostly in applications may jump over this chapter on first reading and return to specific sections as the need arises.

2.2 Charge-Changing Events

Let us first consider the simple case of a stripped ion, e.g., a swift proton meeting a free electron. Can the electron be captured by the proton? Well, if no other particle

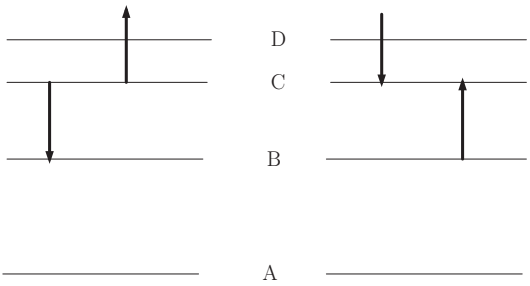

Fig. 2.1 Left: Electron emission by Auger process; right: Electron capture by inverse Auger recombination. Symbols A–D indicate energy levels

is involved, the process is forbidden by the conservation laws of energy and momentum: If it were allowed, the reverse process would likewise be allowed, where a hydrogen atom spontaneously emits its electron without any external action.

To be more precise, consider the process in the rest frame of the ion: A free electron approaching the nucleus has a positive energy, and hence will be scattered rather than captured. Hence, in order to be captured, the electron must have a way to get rid of its energy.

Let us see what happens if a third particle is involved. This could be a photon. Indeed, if the collision is accompanied by the emission of a photon, excess energy can be carried away so that the electron can end up in a bound state. This is called radiative recombination (Oppenheimer, 1928) or 'radiative electron capture' (REC). While the cross section for such a process is negligible at velocities $v \ll c$, radiative electron capture is an important process in the relativistic regime.

Restrictions imposed by conservation laws can also be overcome if the ion carries electrons to start with. The kinetic energy of the captured electron may be transmitted to one or more electrons which get excited. You may view this as an inverse Auger process. Figure 2.1(left) illustrates an Auger process, where an electron jumps from a level C to a lower level B, thereby giving its energy to another electron that can jump from level C to the continuum. The inverse process, i.e., inverse Auger recombination, is illustrated on the right diagram in Fig. 2.1.

More important in the context of particle penetration is the charge exchange between two or more atomic particles. In that case, energy and momentum conservation are taken care of primarily by the motion of the recoiling nuclei which, as a first approximation, is independent of the behaviour of the electrons. These nuclei provide a time-dependent potential that governs the motion of the electrons, somewhat similar to what happens in a molecule. In close collisions, electron orbits may even temporarily resemble those in a 'united atom', i.e., an atom with atomic number $Z_1 + Z_2$. An electron bound to one atom before a collision has a statistical chance to be bound to the other one at the time of separation. This process has high probability if it can proceed without a major change in orbital speed. Therefore, the cross section for the process decreases rapidly when the projectile speed does not match

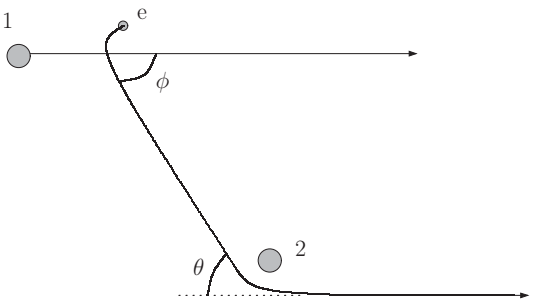

Fig. 2.2 Double-scattering process leading to electron capture according to Thomas (1927)

an orbital speed. A proper description of this type of resonant process invokes the laws of quantum mechanics.

At high relative velocities, multiple collisions between an electron and the colliding nuclei may end up with an electron bound to the projectile. This process will be discussed in the following section.

Special considerations may be necessary for particles penetrating through condensed matter, where the question of whether or not an electron is bound to a projectile may not have a unique answer. This is not only of theoretical interest: Swift ions emerging from a foil are accompanied by electrons. As mentioned in Sect. 1.5.3, the energy spectrum of these emitted 'secondary electrons' frequently shows a 'convoy peak' in the beam direction at an energy $\sim mv^2/2$, where v is the velocity of the emerging ion beam. Such convoy or 'cusp' electrons, which may reflect 'capture into continuum' or 'loss into the continuum' may have travelled in the vicinity of the ion for a certain pathlength.

In this connection an operational definition of the charge of an ion travelling through a material is needed. This may be achieved with X-ray spectroscopic methods: Since the energy of an X-ray emission line depends on the charge of the emitting atom, X-rays emitted from penetrating ions will be split into a family of satellite lines reflecting the charge states involved (Knudson et al., 1974, Horvat et al., 1995).

2.3 Early Estimates

2.3.1 Double Scattering: The Thomas Process

A simple process leading to electron capture was proposed by Thomas (1927), see Fig. 2.2. A projectile **1** moves with a speed v toward a target atom **2** and hits a target electron **e** which is kicked off with a recoil speed v_e. If the electron can be considered initially at rest, the relation between the recoil angle ϕ and the electron energy reads

$$\frac{1}{2}mv_e^2 = 2mv^2\cos^2\phi\,. \tag{2.2}$$

according to (3.7) and (3.8), Vol. 1. Hence, for $\phi = 60°$ we have

$$v_e = v\,. \tag{2.3}$$

This is a necessary condition for the electron to be captured by the projectile, but not a sufficient one, since the direction of motion does not match that of the projectile. However, if the spatial configuration allows a subsequent collision with the target nucleus, the electron may scatter another 60° with negligible energy loss. If this happens in the same scattering plane, and if the kinetic energy $mu^2/2$ in a reference frame moving with the projectile is lower than the binding energy, the electron can be considered as being captured.

Up to this point the argument rests on conservation laws of energy and momentum and is, therefore, independent of whether a classical or quantal description is adopted. When it comes to the evaluation of the cross section, there is, however, a difference. Thomas (1927) evaluated a cross section for this process on the basis of classical collision theory. His derivation hinges heavily on the relation between impact parameter and scattering angle for the two consecutive collisions. The neglect of the orbital motion implies that the theory can only be valid for $v \gg v_0$. In that velocity range a classical description of electron motion becomes questionable according to Sect. 2.3.6, Vol. 1. The predicted capture cross section, which will not be derived here, reads

$$\sigma_c = \frac{64\sqrt{2}}{3}\pi a_0^2 Z_1^2 Z_2^{7/2} \left(\frac{a_0}{b_1}\right)^{7/2} \left(\frac{v_0}{v}\right)^{11} \tag{2.4}$$

for alpha particles in hydrogen, where $b_1 = 2Z_1e^2/mu_{\max}$ and $u_{\max}$ is the maximum allowed relative speed where the electron still is bound to the projectile.

Equation (2.4), when taken literally as *the* theory of charge exchange at high velocity, was found to predict cross sections several orders of magnitude smaller than measured. This, however, does not imply that the process does not exist:

1. The predicted velocity dependence $\propto v^{-11}$ of the capture cross section was subsequently found to describe the behaviour of the total capture cross section in the limit of high but nonrelativistic projectile speed (Drisko, 1955).
2. Despite a low *total* capture cross section the process leaves a signature in the *differential* cross section, i.e., the cross section at a given scattering angle of the projectile. Indeed, since the electron carries away a lateral momentum $mv\sin\phi$, the Thomas process should be observable at an angle

$$\theta \simeq \frac{m}{M_1}\sin\phi = \frac{\sqrt{3}}{2}\frac{m}{M_1} \tag{2.5}$$

from the incident-beam direction. This peak was found in experiments by Horsdal-Pedersen et al. (1983) on H^+-He and H^+-H_2 and by Vogt et al. (1986) on H^+-H, as is illustrated in Fig. 2.3.

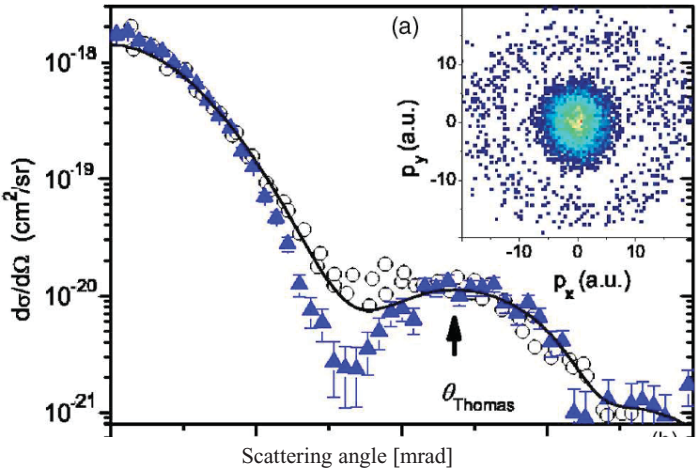

Fig. 2.3 Differential cross section for single-electron capture in 7.5 MeV H^+-He collision. Empty symbols: Measurements of Horsdal-Pedersen et al. (1983). Solid symbols: Measurements of Fischer et al. (2006). Solid line: Measurements of Fischer et al. (2006) convoluted with experimental resolution of Horsdal-Pedersen et al. (1983). From Fischer et al. (2006)

3. Double scattering processes may be treated in second-order quantal perturbation theory. Such calculations have been performed and will be discussed in Sect. 2.4.5.1.
4. Spruch (1978) demonstrated that the classical treatment of the Thomas process is valid when applied to the charge exchange between highly excited, high-angular-momentum quantum states.

2.3.2 Bohr's Model

A characteristic feature of the Thomas model is the fact that the orbital motion of the target electron in its initial state is left out of consideration in the kinematics of the capture process. Instead, the electron speed is adjusted to that of the projectile by the first of two collision events. This feature also enters into an early estimate by Bohr (1948) which, like the Thomas model, addressed electron capture by swift alpha particles. Bohr notes that the cross section for acceleration to $\sim v$ is given by

$$\sigma_v \sim \pi b^2 \tag{2.6}$$

with $b = 2Z_1 e^2/mv^2$ (cf. Problem 3.7, Vol. 1). The criterion for capture, however, is quantal and requires the electron to be confined to a sphere with a radius $a' \sim \hbar/mv$ around the projectile nucleus. The probability P for this to happen is given by the ratio $(a'/a)^3$, where $a = a_0/Z_1$ is the orbital radius in the projectile ground state, i.e.,

$$P \sim \left(\frac{Z_1 v_0}{v}\right)^3 . \tag{2.7}$$

On the basis of a simple atomic model, Bohr argued that the number of target electrons that could be captured by this process was given by

$$n \sim Z_2^{1/3} \frac{v}{v_0} . \tag{2.8}$$

Collecting these factors, Bohr obtained a capture cross section

$$\sigma_c \sim 4\pi a_0^2 Z_1^5 Z_2^{1/3} \left(\frac{v_0}{v}\right)^6 . \tag{2.9}$$

While Bohr reported reasonable agreement with early measurements on alpha-particle ranges by Rutherford (1924), we need to keep in mind that direct measurements of capture cross sections did not exist at the time of writing[1].

2.4 Quantum Theory of One-Electron Capture ⋆

2.4.1 A Qualitative Estimate

An essential feature of both the Thomas and the Bohr model is the need to *accelerate* the electron in the capture process. However, regardless of the magnitude of the projectile speed v, there is a probability for an electron in an atom to have an orbital speed v_e of the order of or even exceeding v, although this probability decreases rapidly as v exceeds the mean velocity of the tightest-bound electrons. Therefore, quantum theory allows charge exchange by a process where the electron velocity in the target frame matches an orbital velocity in the projectile.

Figure 2.4 illustrates this process in classical terms: An electron with an orbital speed v_e, bound to a target nucleus 2, has a velocity $\boldsymbol{v}_e - \boldsymbol{v}$ relative to a penetrating projectile 1. Let us assume the two nuclei to be identical, e.g. hydrogen. Then, if

$$|\boldsymbol{v}_e - \boldsymbol{v}| = v_e , \tag{2.10}$$

the electron may orbit around the projectile nucleus 1 after the collision without having to get rid of (or gain) kinetic energy.

From (2.10) you easily derive

$$\boldsymbol{v} \cdot \boldsymbol{v}_e = v^2/2 . \tag{2.11}$$

This condition can only be fulfilled if

$$v_e \geq v/2 . \tag{2.12}$$

[1] Bohr's paper, although printed in 1948, had been essentially finished about a decade earlier.

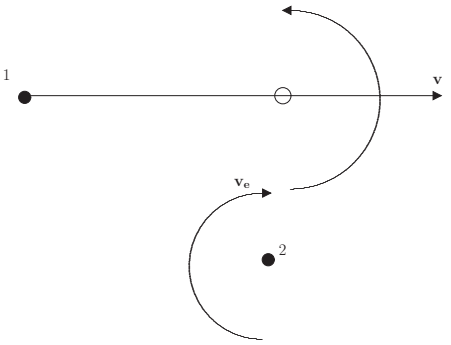

Fig. 2.4 Classical illustration of resonant electron capture. See text

Now, in classical mechanics, orbital radius and speed are uniquely related by Kepler's third law. Therefore this process is only possible for a distinct configuration in space (impact parameter) and time. In quantum mechanics the uncertainty principle allows these conditions to relax. We may then estimate a capture cross section

$$\sigma_c \propto \pi r_0^2 P_1(v/2) P_2(v/2), \,, \tag{2.13}$$

where

$$P_2(v/2) = \int_{v_e > v/2} \mathrm{d}^3 \boldsymbol{v}_e f_2(\boldsymbol{v}_e) \,, \tag{2.14}$$

is the probability for a target electron to have an orbital speed exceeding $v/2$. Here $f_2(\boldsymbol{v}_e)$ is the velocity distribution in the initial state, $P_1(v/2)$ is the analog of $P_2(v/2)$ for the projectile, and

$$r_0(v) \sim \frac{2\hbar}{v} \tag{2.15}$$

is a representative radius defining the area in which capture is possible.

For $Z_1 = Z_2$ and hydrogenic $1s$ wave functions with a screening radius a you may like to estimate the probability $P_2(v/2)$ in Problem 2.4. For $v \gg v_0/Z$ you find

$$P_2(v/2) = \frac{4}{5\pi} \left(\frac{a_0 v_0}{a v} \right)^5 \,. \tag{2.16}$$

With this, (2.13) reduces to

$$\sigma_c \sim \frac{2^{22}}{25\pi} a_0^2 Z^{10} \left(\frac{v_0}{v} \right)^{12} \,. \tag{2.17}$$

Apart from a numerical factor, this is identical with the result of the rigorous quantal calculation by Brinkman and Kramers (1930) which will be sketched below.

Note distinctly different dependencies on the projectile speed v in (2.4), (2.9) and (2.17), providing stringent experimental tests on existing theories.

2.4.2 General Considerations

We shall now have a look at charge exchange from a similar starting point as in Sect. 4.3, Vol. 1, where the Bethe theory of excitation and energy loss was presented on the basis of quantal perturbation theory. Charge exchange is more complex, since the initial and final wave functions belong to different basis sets generated by different hamiltonians, dependent on whether it is the target or the projectile that binds an electron.

Unlike the Bethe theory which, in its original form, is still today a quantitative tool in the description of stopping for a considerable fraction of the pertinent parameter space in particle penetration, the original theory of charge exchange, initiated by Oppenheimer (1928) and Brinkman and Kramers (1930), encountered unexpected problems, the solution of which turned out to be a longlasting, somewhat painful but also illuminating process. You may find a clear and encyclopedic description of this development, summarizing contributions from over 400 references to the pertinent literature, in a review by Dewangan and Eichler (1994). The discussion in the following two sections relies heavily on this work, but I shall shortcut the historical development and try to arrive at the simplest conclusions more or less directly, still following Dewangan and Eichler (1994) in numerous details.

The notation in this chapter will be more similar to the one adopted in Volume 1 than to the standard notation that has developed in the literature on charge exchange over the years.

2.4.3 Semiclassical Theory

We shall consider a three-particle system consisting of a target nucleus with atomic number Z_2 located in the origin, a projectile nucleus with atomic number Z_1 in uniform motion,

$$\boldsymbol{R}(t) = \boldsymbol{p} + \boldsymbol{v}t\,, \tag{2.18}$$

and an electron bound initially to the target nucleus. Eqeation (2.18) implies that we operate in the semiclassical (or impact-parameter) picture. You may recall from Sects. 4.3 and 4.4, Vol. 1 that apart from terms of the order of m/M_1 and m/M_2, the semiclassical picture delivers the same excitation cross sections as a fully quantal description involving an incident plane wave. The same can be shown to be true in charge exchange (Crothers and Holt, 1966, Dewangan and Eichler, 1994) but will not be detailed here.

2.4.3.1 The Hamiltonian

The hamiltonian of the system may be written in the form

$$\mathcal{H} = \frac{p^2}{2m} + V_2(r) + V_1(|\boldsymbol{r} - \boldsymbol{R}|) + V_{12}(R)\,, \tag{2.19}$$

where

$$V_2(r) = -\frac{Z_2 e^2}{r}; \quad V_1(|\boldsymbol{r} - \boldsymbol{R}|) = -\frac{Z_1 e^2}{|\boldsymbol{r} - \boldsymbol{R}|}; \quad V_{12}(R) = \frac{Z_1 Z_2 e^2}{R}\,. \tag{2.20}$$

The interaction potential $V_{12}(R)$ between the nuclei does not produce a force on the electron, but it has been included nevertheless because it depends on time through $R(t)$. The kinetic energy of the projectile nucleus, on the other hand, is taken constant here and can, therefore, safely be neglected.

In the absence of the projectile, electron motion is governed by the hamiltonian

$$H = \frac{p^2}{2m} + V_2(r) \tag{2.21}$$

with eigenstates $u_j(\boldsymbol{r})$ and energies ϵ_j.

We now split the hamiltonian $\mathcal{H}$ according to

$$\mathcal{H} = \mathcal{H}_2 + \mathcal{V}_1\,, \tag{2.22}$$

where

$$\mathcal{H}_2 = H + V_{12}(R) + V_1(R) \tag{2.23}$$

and

$$\mathcal{V}_1 = V_1(|\boldsymbol{r} - \boldsymbol{R}|) - V_1(R)\,. \tag{2.24}$$

Here, a term $V_1(R)$ has been added to the unperturbed hamiltonian and subtracted from the perturbation. This innocently-looking step was first proposed by Bates (1958), but it was Cheshire (1964) who recognized its central significance. Since it causes the perturbation $\mathcal{V}_1$ to decrease as R^{-2} for large R, it removes undesired consequences of the long range of the Coulomb force of the type encountered in Sect. 3.5.1, Vol. 1.

2.4.3.2 Unperturbed Wave Functions

Let us first determine the unperturbed eigenstates of

$$\mathcal{H}_2 = H + f(t) \tag{2.25}$$

with

$$f(t) = V_{12}(R) + V_1(R) = \frac{Z_1(Z_2 - 1)e^2}{R}\,. \tag{2.26}$$

Since $f(t)$ does not contain the electron coordinate $\boldsymbol{r}$, it will make itself noticed as a phase factor $\mathrm{e}^{-\mathrm{i}\alpha(t)}$ in the wave function with

$$\alpha(t) = \frac{1}{\hbar}\int^t \mathrm{d}t'\, f(t') = \frac{1}{\hbar}\int^t \mathrm{d}t'\, \frac{Z_1(Z_2-1)e^2}{\sqrt{p^2+(vt')^2}} \tag{2.27}$$

or

$$\alpha(t) = -\nu_1 \ln\frac{R-vt}{p} + \alpha_0\,, \tag{2.28}$$

where

$$\nu_1 = \frac{Z_1(Z_2-1)e^2}{\hbar v}\,, \tag{2.29}$$

and α_0 is an arbitrary constant which can be set equal to zero.

With this, eigenstates to $\mathcal{H}_2$ may be written as

$$\psi_j(\boldsymbol{r},t) = \mathrm{e}^{\mathrm{i}\nu_1 \ln[(R-vt)/p]}\mathrm{e}^{-\mathrm{i}\epsilon_j t/\hbar} u_j(\boldsymbol{r})\,. \tag{2.30}$$

Although we are now ready in principle to perform a perturbation expansion in terms of $\mathcal{V}_1$, we need a valid description of the end configuration, where the electron is bound to the projectile. To this end we split the hamiltonian according to

$$\mathcal{H} = \mathcal{H}_1 + \mathcal{V}_2\,, \tag{2.31}$$

where

$$\mathcal{H}_1 = \frac{p^2}{2m} + V_1(|\boldsymbol{r}-\boldsymbol{R}|) + V_{12}(R) + V_2(R) \tag{2.32}$$

and

$$\mathcal{V}_2 = V_2(r) - V_2(R)\,, \tag{2.33}$$

in strict analogy to (2.22)–(2.24).

Denoting eigenstates and energies of an electron in a projectile atom at rest as $v_\ell(\boldsymbol{r})$ and η_ℓ, respectively, an alternative basis set for the entire three-body system, making reference to bound projectile states, reads

$$\chi_\ell(\boldsymbol{r},t) = \mathrm{e}^{\mathrm{i}\nu_2 \ln[(R-vt)/p]}\mathrm{e}^{-\mathrm{i}\eta_\ell t/\hbar} v_\ell(\boldsymbol{r}-\boldsymbol{R})\,\mathrm{e}^{\mathrm{i}(\boldsymbol{k}\cdot\boldsymbol{r}-\omega t)}\,, \tag{2.34}$$

where

$$\nu_2 = \frac{Z_2(Z_1-1)e^2}{\hbar v}\,. \tag{2.35}$$

The last factor in (2.34) accounts for the uniform motion of the projectile. You may verify in problem 2.1 that

$$\hbar\boldsymbol{k} = m\boldsymbol{v}; \quad \hbar\omega = mv^2/2\,. \tag{2.36}$$

2.4.3.3 Transition Amplitude

Since the $\chi_\ell(\boldsymbol{r},t)$ form a complete basis set for the hamiltonian $\mathcal{H}$, they can serve as a basis for expansion of the exact wave function $\psi(\boldsymbol{r},t)$ of the system,

$$\psi(\boldsymbol{r},t) = \sum_{\ell} c_\ell(t)\, \chi_\ell(\boldsymbol{r},t) \tag{2.37}$$

with coefficients

$$c_\ell(t) = \int \mathrm{d}^3\boldsymbol{r}\; \chi_\ell^*(\boldsymbol{r},t)\, \psi(\boldsymbol{r},t) \tag{2.38}$$

which, in addition to time, depend on velocity $\boldsymbol{v}$ and impact parameter $\boldsymbol{p}$. The probability for the electron to be bound to the projectile into a state ℓ after the collision is given by

$$P_\ell(\boldsymbol{p},\boldsymbol{v}) = |c_\ell(\infty)|^2 \ . \tag{2.39}$$

We may write the transition amplitude in the form

$$c_\ell(\infty) = \int_{-\infty}^{+\infty} \mathrm{d}t\, \frac{\mathrm{d}}{\mathrm{d}t} \int \mathrm{d}^3\boldsymbol{r}\; \chi_\ell^*(\boldsymbol{r},t)\psi(\boldsymbol{r},t)\,, \tag{2.40}$$

since the overlap integral between the unperturbed initial target state and the unperturbed final projectile state, both taken at $t = -\infty$, vanishes.

You may rewrite the time derivative making use of the Schrödinger equation, noting that $\psi(\boldsymbol{r},t)$ is governed by $\mathcal{H}$ and $\chi_\ell(\boldsymbol{r},t)$ by $\mathcal{H}_1$,

$$\begin{aligned} c_\ell(\infty) &= \frac{1}{\mathrm{i}\hbar} \int_{-\infty}^{+\infty} \mathrm{d}t \int \mathrm{d}^3\boldsymbol{r}\; \chi_\ell^*(\boldsymbol{r},t)(\mathcal{H}-\mathcal{H}_1)\psi(\boldsymbol{r},t) \\ &= \frac{1}{\mathrm{i}\hbar} \int_{-\infty}^{+\infty} \mathrm{d}t \int \mathrm{d}^3\boldsymbol{r}\; \chi_\ell^*(\boldsymbol{r},t)\mathcal{V}_2\psi(\boldsymbol{r},t). \end{aligned} \tag{2.41}$$

If you miss some details in this derivation, go to Problem 2.2.

2.4.3.4 Perturbation Expansion

Equation (2.41) is an exact relationship. In order to determine $c_\ell(\infty)$ we need to find the function $\psi(\boldsymbol{r},t)$, which is a solution to the Schrödinger equation for the three-particle system. An impressive arsenal of theoretical/computational methods has become available for this purpose (Bransden and McDowell, 1992, Dewangan and Eichler, 1994). Here we apply a perturbation expansion in powers of $\mathcal{V}_1$ which, according to (4.36)–(4.38), Vol. 1 can be written in the form

$$\psi(\boldsymbol{r},t) = \psi_0(\boldsymbol{r},t) + \sum_j d_j^{(1)}(t)\psi_j(\boldsymbol{r},t) + \ldots \tag{2.42}$$

with

$$d_j^{(1)}(t) = \frac{1}{\mathrm{i}\hbar} \int_{-\infty}^{t} \mathrm{d}t' \int \mathrm{d}^3\boldsymbol{r}\; \psi_j^*(\boldsymbol{r},t')\mathcal{V}_1(\boldsymbol{r},t')\psi_0(\boldsymbol{r},t')\,. \tag{2.43}$$

With this we find

$$c_\ell(\infty) = c_\ell^{(1)}(\infty) + c_\ell^{(2)}(\infty)\ldots\,, \tag{2.44}$$

where

$$c_\ell^{(1)}(\infty) = \frac{1}{\mathrm{i}\hbar}\int_{-\infty}^{+\infty} \mathrm{d}t \int \mathrm{d}^3\boldsymbol{r}\; \chi_\ell^*(\boldsymbol{r},t)\mathcal{V}_2\psi_0(\boldsymbol{r},t) \tag{2.45}$$

and

$$c_\ell^{(2)}(\infty) = -\frac{1}{\hbar^2}\sum_j \int_{-\infty}^{\infty} \mathrm{d}t \int \mathrm{d}^3\boldsymbol{r}\; \chi_\ell^*(\boldsymbol{r},t)\mathcal{V}_2(\boldsymbol{r},t)\psi_j(\boldsymbol{r},t) \int_{-\infty}^{t} \mathrm{d}t' \int \mathrm{d}^3\boldsymbol{r}'\, \psi_j^*(\boldsymbol{r}',t')\mathcal{V}_1(\boldsymbol{r}',t')\psi_0(\boldsymbol{r}',t'). \tag{2.46}$$

While evaluating the leading term $c_\ell^{(1)}(\infty)$ is by no means trivial, the form of the second term indicates that the analytical complexity will increase rapidly with increasing order.

2.4.4 First-Order Perturbation

Ignoring the second-order term for a while let us focus on the first-order term

$$\psi(\boldsymbol{r},t) \simeq \psi_0(\boldsymbol{r},t)\,, \tag{2.47}$$

where $n = 0$ denotes the initial state, so that

$$c_\ell(\infty) = \frac{1}{\mathrm{i}\hbar}\int_{-\infty}^{+\infty} \mathrm{d}t \int \mathrm{d}^3\boldsymbol{r}\; \chi_\ell^*(\boldsymbol{r},t)\left(\frac{Z_2e^2}{R(t)} - \frac{Z_2e^2}{r}\right)\psi_0(\boldsymbol{r},t)\,. \tag{2.48}$$

This result, reflecting the B1B or 'boundary-corrected first Born approximation', was demonstrated by Dewangan and Eichler (1986) to produce results in good agreement with measurements of charge-exchange cross sections. The fact that valid predictions may emerge already from the first Born approximation was in contrast to the accepted view for many years.

You may wonder why it is the potential $\mathcal{V}_2$ that appears in the transition amplitude equation (2.41) rather than the perturbing potential $\mathcal{V}_1$. Well, the projection of ψ on χ_ℓ with ψ_j as the initial state is the same as the projection of ψ on ψ_j if χ_ℓ is the final state. If you adopt the latter description, you end up with (2.41), but with $\mathcal{V}_2$ replaced by $\mathcal{V}_1$, as you may verify by working on Problem 2.2.

Dual descriptions of scattering processes play a key role in the literature. This has given rise to a special nomenclature which, however, will not be followed here, because we are not going deeply enough into this subject matter to justify the effort.

2.4.4.1 Resonance Charge Exchange

Evaluation of the multiple integral equation (2.48) is complicated in general, but suitable tools have been developed for fully analytical evaluation in special cases, and accurate numerical evaluation in others. As an example we shall have a look at a relatively simple case, so-called resonance charge exchange, where $Z_1 = Z_2 = Z$ and charge exchange is considered between equivalent levels $0 \rightarrow 0$. Then, by insertion of (2.34), (2.48) reduces to

$$c_0(\infty) = \frac{1}{\mathrm{i}\hbar} \int_{-\infty}^{\infty} \mathrm{d}t \int \mathrm{d}^3\boldsymbol{r}\, \mathrm{e}^{-\mathrm{i}(\boldsymbol{k}\cdot\boldsymbol{r}-\omega t)} u_0^*(\boldsymbol{r}-\boldsymbol{R}) \left(\frac{Ze^2}{R} - \frac{Ze^2}{r}\right) u_0(\boldsymbol{r})\,, \quad (2.49)$$

where the t-dependent phase factors $\alpha(t)$ have dropped out. Now, since

$$\left(-\frac{\hbar^2}{2m}\nabla^2 - \frac{Z_2 e^2}{r}\right) u_0(\boldsymbol{r}) = \epsilon_0 u_0(\boldsymbol{r})\,, \quad (2.50)$$

where ϵ_0 is the energy of the initial (and final) state we may replace

$$\left(\frac{Ze^2}{R} - \frac{Ze^2}{r}\right) u_0(\boldsymbol{r}) = \left(\frac{Ze^2}{R} + \epsilon_0 + \frac{\hbar^2}{2m}\nabla^2\right) u_0(\boldsymbol{r})\,. \quad (2.51)$$

After introduction of the Fourier transform

$$u_0(\boldsymbol{r}) = \frac{1}{(2\pi)^{3/2}} \int \mathrm{d}^3\boldsymbol{q}\, u_0(\boldsymbol{q}) \mathrm{e}^{\mathrm{i}\boldsymbol{q}\cdot\boldsymbol{r}} \quad (2.52)$$

you find

$$c_0(\infty) = \frac{1}{(2\pi)^3 \mathrm{i}\hbar} \int_{-\infty}^{\infty} \mathrm{d}t \int \mathrm{d}^3\boldsymbol{r} \int \mathrm{d}^3\boldsymbol{q} \int \mathrm{d}^3\boldsymbol{q}' \mathrm{e}^{-\mathrm{i}(\boldsymbol{k}\cdot\boldsymbol{r}-\omega t)} \times \mathrm{e}^{-\mathrm{i}\boldsymbol{q}'\cdot(\boldsymbol{r}-\boldsymbol{R})} u_0^*(\boldsymbol{q}') \left(\frac{Ze^2}{R} + \epsilon_0 + \frac{\hbar^2}{2m}\nabla^2\right) u_0(\boldsymbol{q}) \mathrm{e}^{\mathrm{i}\boldsymbol{q}\cdot\boldsymbol{r}}. \quad (2.53)$$

Here you may carry out the ∇^2-operation and integrate over $\boldsymbol{r}$. As a result you will identify a Dirac function $\delta(-\boldsymbol{k} - \boldsymbol{q}' + \boldsymbol{q})$. After integration over $\boldsymbol{q}'$ you then arrive at

$$c_0(\infty) = \frac{1}{\mathrm{i}\hbar} \int_{-\infty}^{\infty} \mathrm{d}t\, \mathrm{e}^{\mathrm{i}\omega t} \int \mathrm{d}^3\boldsymbol{q} \times \mathrm{e}^{\mathrm{i}(\boldsymbol{q}-\boldsymbol{k})\cdot\boldsymbol{R}}\, u_0^*(\boldsymbol{q}-\boldsymbol{k}) \left(\frac{Ze^2}{R} + \epsilon_0 - \frac{\hbar^2 q^2}{2m}\right) u_0(\boldsymbol{q}). \quad (2.54)$$

2.4.4.2 Brinkman-Kramers Approximation

Recalling that R depends on time, cf. (2.18), you will find it reasonable to split (2.54) into two,

$$c_0(\infty) = c_0^{\mathrm{BK}}(\infty) + \Delta c_0(\infty)\,, \tag{2.55}$$

where $c_0^{\mathrm{BK}}(\infty)$ originates in the term $\epsilon_0 - \hbar^2 q^2/2m$ and $\Delta c_0(\infty)$ in Ze^2/R. The superscript 'BK' stands for Brinkman-Kramers[2]. Considering the former term we may integrate over time and obtain

$$c_0^{\mathrm{BK}}(\infty) = \int \mathrm{d}^3\boldsymbol{q}\; \mathrm{e}^{\mathrm{i}(\boldsymbol{q}-\boldsymbol{k})\cdot\boldsymbol{p}}\; \delta(\boldsymbol{q}\cdot\boldsymbol{v} - \boldsymbol{k}\cdot\boldsymbol{v} + \omega)\; f_0(\boldsymbol{q}) \tag{2.56}$$

with

$$f_0(\boldsymbol{q}) = \frac{2\pi}{\mathrm{i}\hbar}\, u_o^*(\boldsymbol{q}-\boldsymbol{k}) \left(\epsilon_0 - \frac{\hbar^2 q^2}{2m}\right) u_0(\boldsymbol{q}). \tag{2.57}$$

In the original work of Oppenheimer (1928) and Brinkman and Kramers (1930), the term $\Delta c_0(\infty)$ was absent. If we ignore it for a moment we may go over to the cross section

$$\sigma_0^{\mathrm{BK}} = \int \mathrm{d}^2\boldsymbol{p}\; \left|c_0^{\mathrm{BK}}(\infty)\right|^2 \tag{2.58}$$

or, after insertion of (2.56) and integration over $\boldsymbol{p}$,

$$\sigma_0 = \frac{(2\pi)^2}{v} \int \mathrm{d}^3\boldsymbol{q}\; \delta(\boldsymbol{q}\cdot\boldsymbol{v} - \boldsymbol{k}\cdot\boldsymbol{v} + \omega)\, |f_0(\boldsymbol{q})|^2 \tag{2.59}$$

according to a procedure which was used in Sect. 4.3.4, Vol. 1.

Noting first that $\omega - \boldsymbol{k}\cdot\boldsymbol{v} = -\hbar k^2/2m$ we recognize that the Dirac function under the integral implies that $\boldsymbol{q}\cdot\boldsymbol{k} = k^2/2$ and thus,

$$(\boldsymbol{q}-\boldsymbol{k})^2 = q^2. \tag{2.60}$$

Since $\hbar\boldsymbol{q}$ is the initial momentum of the target electron and $\hbar(\boldsymbol{q}-\boldsymbol{k})$ the final momentum of the captured electron seen from the laboratory frame, we learn from (2.60) that charge exchange in this model is only possible in case of exact velocity-matching. This is a quantification of the process sketched in Sect. 2.4.1, in particular Fig. 2.4. Note the equivalence of (2.60) with (2.10).

Equation (2.60) also tells us that for s-states, all angular dependence is contained in the Dirac function. Integration over the angular variable then leads to

[2] In the literature, the term OBK, which stands for Oppenheimer-Brinkman-Kramers, occurs frequently instead of BK. Both schemes, Oppenheimer (1928) and Brinkman and Kramers (1930) operate in the first Born approximation without the term Ze^2/R in the brackets, and in both schemes, (2.49) plays a central role, although Oppenheimer (1928) derived it from the plane-wave Born approximation, while Brinkman and Kramers (1930) started from the semiclassical impact-parameter description. However, while the explicit evaluation by Brinkman and Kramers (1930) involves exact integrations as described below, the evaluation by Oppenheimer (1928) invokes approximations which lead to drastic discrepancies.

$$\sigma_0^{\mathrm{BK}} = \frac{(2\pi)^5}{\hbar^2 v^2} \int_{k/2}^{\infty} q \, \mathrm{d}q \, |u_0(q)|^4 \left(\epsilon_0 - \frac{\hbar^2 q^2}{2m} \right)^2 . \tag{2.61}$$

For the $1s$ state of a hydrogen-like atom with

$$u_0(\boldsymbol{r}) = \frac{1}{\sqrt{\pi a^3}} e^{-r/a} \tag{2.62}$$

you may derive (Problem 2.3) the particularly simple result

$$\sigma_0^{\mathrm{BK}} = \pi a_0^2 2^8 \frac{v_0^2}{v^2} \int_{q=k/2}^{\infty} \frac{\mathrm{d}(qa)^2}{(1+q^2a^2)^6} \tag{2.63}$$

or, after integration,

$$\sigma_0^{\mathrm{BK}} = \pi a_0^2 \frac{2^{18} Z^{10} v_0^{12}}{5v^2(v^2+4Z^2v_0^2)^5} . \tag{2.64}$$

For $v \gg 2Z_2 v_0$ this result differs from the qualitative estimate (2.17) by a factor of $5\pi^2/16 = 3.1$. As we shall learn shortly, (2.64) predicts a too large value, and (2.17) comes closer to the correct result.

From a physical point of view, the steep decrease of the capture cross section with increasing projectile speed reflects the fact that the process involves exclusively the far tails of the velocity distribution of the electron in the target and projectile state.

This calculation can be generalized to capture into an excited state with the principal quantum number $n > 1$. For a one-electron system with arbitrary Z_1, Z_2 one finds (McDowell and Coleman, 1970)

$$\sigma_n^{\mathrm{BK}} = \pi a_0^2 \frac{2^{18}(Z_1Z_2)^5 v^8 v_0^{12}}{5n^3 \left[v^4 + 2(Z_2^2 + Z_1^2/n^2)v^2v_0^2 + (Z_2^2 - Z_1^2/n^2)^2 v_0^4 \right]^5} . \tag{2.65}$$

Setting $Z_1 = Z_2$ you may recognize that the cross section for capture into excited states falls off approximately as n^{-3}.

2.4.4.3 Relativity

Equation (2.64) experiences a major change at beam velocities approaching the velocity of light (Mittleman, 1964, Shakeshaft, 1979, Moiseiwitsch, 1980, Bransden and McDowell, 1992). Calculations on the basis of the Dirac equation show a difference between charge exchange with and without spinflip, which increases with increasing energy up to a factor of ~ 4 in the extreme relativistic regime. Available analytic estimates are based on approximations valid in the moderately relativistic range and differ from author to author. Moiseiwitsch (1980) reports capture cross sections which can be written in the form

$$\sigma_{c,\mathrm{direct}} = \frac{2^7\pi}{5} a_0^2 \frac{\alpha^{12}}{\gamma - 1} \left(\frac{\gamma + 1}{\gamma - 1 + 2\alpha^2} \right)^5 \tag{2.66}$$

for capture without spinflip and

$$\sigma_{c,\text{spinflip}} = \frac{2^3\pi}{5} a_0^2 \alpha^{12} \frac{(\gamma+1)^3}{(\gamma-1+2\alpha^2)^4} \tag{2.67}$$

for capture with spinflip. Here, $\alpha = v_0/c = 1/137$ is the fine structure constant and $\gamma = 1/\sqrt{1-v^2/c^2}$.

Both expressions are seen to go as $\sim 1/\gamma$ with increasing projectile energy, i.e., inversely proportional to the beam energy, in contrast to the steep decrease in the nonrelativistic limit.

While (2.66) approaches (2.64) for $v/c \ll 1$, (2.67) reads

$$\sigma_{c,\text{spinflip}} \overset{v/c\ll 1}{=} \frac{2^{10}\pi}{5} a_0^2 \alpha^4 \left(\frac{v_0^2}{v^2+4v_0^2}\right)^4 . \tag{2.68}$$

The factor α^4 makes this a very small quantity.

2.4.4.4 B1B Approximation

You may recall that (2.64) stems from ignoring the term Ze^2/R in (2.54) or (2.49). The term $\Delta c_0(\infty)$ in (2.55) has been evaluated by Jackson and Schiff (1953) and by Bates and Dalgarno (1952). Instead of going through a rather cumbersome integration procedure I shall try to demonstrate how it happens that incorporation of this term reduces the cross section (2.64) substantially in case of the H-H system.

For clarity, change the spatial variable in (2.49) according to $\boldsymbol{r} \to \boldsymbol{r} + \boldsymbol{R}/2$, so that

$$c_0(\infty) = \frac{1}{\mathrm{i}\hbar} \int_{-\infty}^{\infty} \mathrm{d}t\, \mathrm{e}^{-\mathrm{i}(\boldsymbol{k}\cdot\boldsymbol{R}/2+\omega t)} \int \mathrm{d}^3\boldsymbol{r}\, \mathrm{e}^{-\mathrm{i}\boldsymbol{k}\cdot\boldsymbol{r}} \\ u_0^*(\boldsymbol{r}-\boldsymbol{R}/2)\left(\frac{Ze^2}{R} - \frac{Ze^2}{|\boldsymbol{r}+\boldsymbol{R}/2|}\right) u_0(\boldsymbol{r}+\boldsymbol{R}/2), \tag{2.69}$$

Figure 2.5 shows plots of the function $u_0^*(\boldsymbol{r}-\boldsymbol{R}/2)u_0(\boldsymbol{r}+\boldsymbol{R}/2)$ for the ground state of hydrogen for $R/a = 2$ and 1/2. You may identify a horizontal ridge along the connection line between the two nuclei and otherwise a strong decrease. Taylor expansion of the factor $Ze^2/R - Ze^2/|\boldsymbol{r}+\boldsymbol{R}/2|$ around the midpoint between the nuclei, which is $\boldsymbol{r} = 0$ in (2.69), leads to

$$\frac{Ze^2}{R} - \frac{Ze^2}{|\boldsymbol{r}+\boldsymbol{R}/2|} \simeq \frac{Ze^2}{R} - \frac{2Ze^2}{R}\left(1 - 2\frac{\boldsymbol{R}\cdot\boldsymbol{r}}{R^2}\ldots\right) . \tag{2.70}$$

Here, the leading term for large R is $-1/R$. If we had failed to include the first term in (2.70), the result would have been $-2/R$ instead. Since the cross section is governed by the square of the transition amplitude, we may expect a substantial correction.

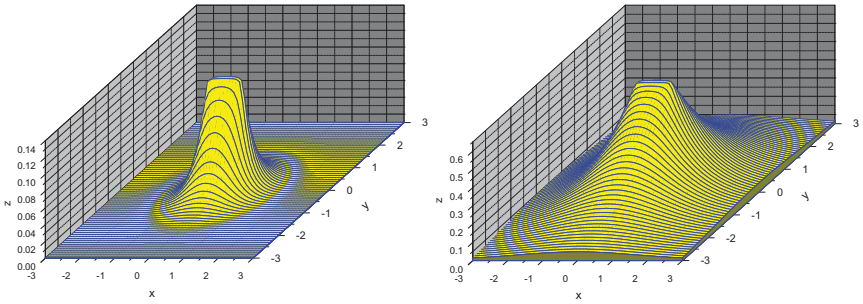

Fig. 2.5 Plots of the function $u_0^*(\boldsymbol{r} - \boldsymbol{R}/2)u_0(\boldsymbol{r} + \boldsymbol{R}/2)$ for the $1s$ state of a hydrogen-like atom. Left: $a/R = 1/2$; right: $a/R = 2$. x denotes the component of $\boldsymbol{r}$ in the direction of $\boldsymbol{R}$ in units of a. y denotes a component perpendicular to $\boldsymbol{R}$ in units of a

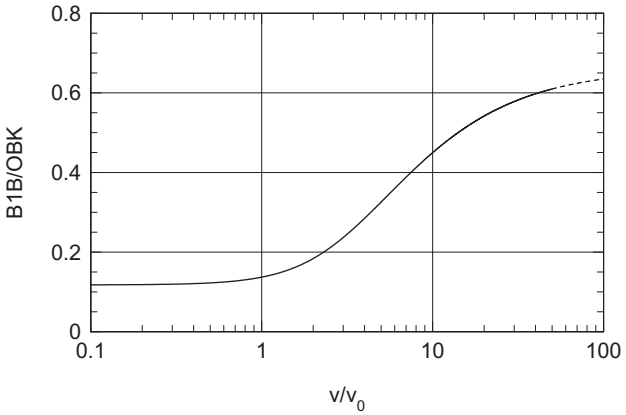

Fig. 2.6 The ratio $\sigma^{\mathrm{B1B}}/\sigma^{\mathrm{BK}}$ according to Jackson and Schiff (1953) for the H^+-H system, cf. (2.71). The dashed line indicates the regime where relativistic corrections need to be considered

According to Jackson and Schiff (1953), the ratio between the complete B1B cross section and the BK result reads

$$\frac{\sigma^{B1B}}{\sigma^{BK}} = \frac{1}{192}\left(127 + 56\frac{v_0^2}{v^2} + 32\frac{v_0^4}{v^4}\right) - \frac{1}{48}\frac{v_0}{v}\arctan\frac{v}{2v_0}\left(83 + 60\frac{v_0^2}{v^2} + 32\frac{v_0^4}{v^4}\right) + \frac{1}{24}\frac{v_0^2}{v^2}\arctan^2\frac{v}{2v_0}\left(31 + 32\frac{v_0^2}{v^2} + 16\frac{v_0^4}{v^4}\right) \quad (2.71)$$

for the H^+-H system. This function is shown in Fig. 2.6. Evidently, the B1B correction causes a decrease by up to an order of magnitude below the BK result in the pertinent velocity range $v \sim v_0$.

Relativistic calculations have been performed by Eichler (1987). For the H^+-H system, corrections to Figure 2.6 amount to a few per cent in the upper end of the graph but become very substantial for heavy ions.

2.4.4.5 Problems with the Brinkman-Kramers Approximation

For a full description of the historical development the reader is referred to the article by Dewangan and Eichler (1994). In brief, measurements on charge exchange in H^+-H collisions by Keene (1949) and Ribe (1951) demonstrated that the predictions of Brinkman and Kramers (1930) overestimated the capture cross section by about a factor of four at beam energies ranging from a few keV to over 100 keV. Almost simultaneously, Bates and Dalgarno (1952) and Jackson and Schiff (1953) pointed out that this discrepancy could be removed by adding a term e^2/R to the perturbing potential $-e^2/|\boldsymbol{r}-\boldsymbol{R}|$. The justification of this term was the fact that the hamiltonian equation (2.19) of the three-body system contains the internuclear interaction $Z_1 Z_2 e^2/R$. While it was unclear why the internuclear interaction should have such a drastic influence on the electronic transition probability, the agreement with experiment was very convincing over an energy range from $\sim$ 30 to 150 keV. It seemed plausible that poor agreement at lower velocities was due to insufficiencies of the Born approximation.

As a test of the validity of this model it was applied to heavier ions, in casu C^{6+}, N^{7+} and F^{9+} on Ar by Halpern and Law (1975). Here, cross sections calculated in the modified BK approach overestimated existing experimental values by two to three orders of magnitude. From the above derivation you may recognize that this was caused by incorporation of a term $Z_1 Z_2 e^2/R$ instead of $Z_2 e^2/R$ in the perturbation. Therefore, this extension of the Brinkman-Kramers scheme could not be taken as an acceptable solution of the charge-exchange problem.

In Sect. 2.3.1 we have seen that the Thomas capture mechanism invokes two scattering events by the electron. It seemed reasonable, therefore, to assume that a quantal description of charge exchange would warrant a treatment up to the second order in the perturbation expansion (Drisko, 1955). A wealth of clever theory has been developed based on this assumption over almost half a century, cf. the review by Dewangan and Eichler (1994). And indeed, second-order terms in the BK expansion may well be dominating over those of first order. However, once second-order terms become comparable in magnitude with first-order terms the question becomes relevant whether third- and higher-order terms ever become negligible. Indeed, even the convergence of the Born expansion itself has been questioned many years ago (Aaron et al., 1961).

It was Cheshire (1964) who identified the long range of the Coulomb interaction as the cause of the problem and who showed how to eliminate it by rearranging the hamiltonian, adding and subtracting the term $Z_2 e^2/R$. However, only H^+-H was addressed, wherewith the results of Bates and Dalgarno (1952) and Jackson and Schiff (1953) were reproduced. As a consequence, the true scope of this was only slowly recognized in the subsequent development (Belkić et al., 1979). The

breakthrough came with a paper by Dewangan and Eichler (1986) that produced a fairly reasonable description of charge exchange in the H^+-Ar system already in the first Born approximation.

2.4.4.6 Heteronuclear Systems

Electrons may be captured into a variety of final projectile states, particularly in heteronuclear collision systems, i.e., for $Z_1 \neq Z_2$, where the resonance condition $\epsilon_j = \eta_\ell$ is normally not fulfilled. Exact analytical calculations, asymptotic expansions and accurate numerical evaluations may be found in the literature, and again Bransden and McDowell (1992) and Dewangan and Eichler (1994) are very valuable sources for a literature search. Several comparisons with experimental data are shown there, which demonstrate good agreement between theory and experiment for charge exchange between bare Z_1-ions ($Z_1 > 1$) and hydrogen as well as between protons and the K-shell of an atom ($Z_2 > 1$).

Here I like to briefly discuss features that deserve attention in this context, in particular the role of the phase factor $\alpha(t)$.

Keeping within first-order perturbation theory, we may go back to (2.48) which, after insertion of (2.30) and (2.34) reads

$$c_\ell(\infty) = \frac{1}{\mathrm{i}\hbar}\int_{-\infty}^{+\infty} \mathrm{d}t \int \mathrm{d}^3\boldsymbol{r}\, \mathrm{e}^{\mathrm{i}\nu \ln[(R-vt)/p]}\, \mathrm{e}^{\mathrm{i}(\eta_\ell-\epsilon_0)t/\hbar} \times v_\ell^*(\boldsymbol{r}-\boldsymbol{R})\, \mathrm{e}^{-\mathrm{i}(\boldsymbol{k}\cdot\boldsymbol{r}-\omega t)} \left(\frac{Z_2 e^2}{R(t)} - \frac{Z_2 e^2}{r}\right) u_0(\boldsymbol{r}), \quad (2.72)$$

where

$$\nu = \nu_1 - \nu_2 = \frac{(Z_2 - Z_1)e^2}{\hbar v}. \quad (2.73)$$

You may note that the terms going as $Z_1 Z_2$, expressing the interaction $V_{12}(R)$ between the target nuclei and which enter ν_1 and ν_2, have dropped out in the difference ν. While this was to be expected, it appears gratifying nevertheless. However, a phase factor $\exp(i\,\nu \ln[|\boldsymbol{R} - \boldsymbol{v}t|/p]$ has to be dealt with for heterogeneous systems ($Z_1 \neq Z_2$). To this adds a phase factor $\exp(i\,[\eta_\ell - \epsilon_0]t/\hbar)$.

Note also that the p-dependence in (2.72) gives rise to a phase factor $\mathrm{e}^{-\mathrm{i}\nu \ln p}$. This complicates calculations on differential cross sections for charge exchange. This phase factor drops out when the capture probability $|c_\ell(\infty)|^2$ is determined, which leads to the total cross section for charge exchange.

It is of interest to study the role of the phase factor $\exp(i\,\nu \ln[(R - vt)/p])$. Figure 2.7 shows the function

$$\ln \frac{R - vt}{p} = \ln\left(\sqrt{1 + (vt/p)^2} - vt/p\right) \quad (2.74)$$

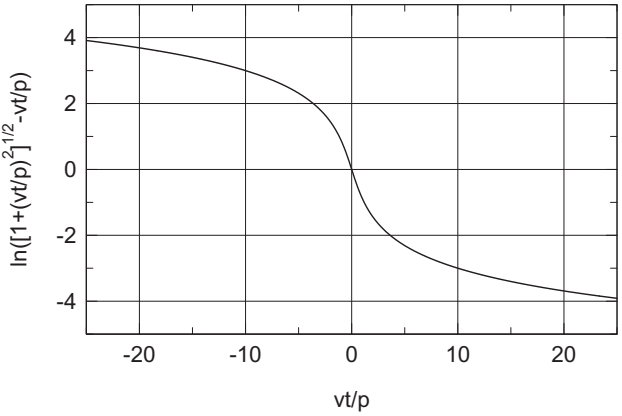

Fig. 2.7 The function $\ln(\sqrt{1+(vt/p)^2} - vt/p)$ governing the phase factor $\exp(i\nu \ln[(R - vt)/p])$ in (2.72)

versus vt/p. You may note that except in the vicinity of $t = 0$, this phase factor gives rise to rapid oscillations of the integrand, indicating that the time interval in which capture is likely, narrows in as Z_1 increases with Z_2 kept constant[3].

Figure 2.8 shows the real and imaginary part of the phase factor for $\nu = 1/2$ and 2, respectively. The theory as presented above is a high-speed theory. Hence, small values of ν appear most representative. Evidently, rapid oscillations in this case complicate the evaluation and require reliable computational methods.

2.4.5 Beyond First-Order Perturbation Theory

In addition to straight second-order perturbation theory, an impressive number of attempts has been made to explain and repair the discrepancies between calculated and measured cross sections for charge exchange. Dewangan and Eichler (1994) list and discuss twenty-one theoretical schemes. Many of them exist in a 'boundary-corrected' version, where the electron wave function carries a phase factor of the type of $\alpha(t)$, (2.28) with an arbitrary constant α_0, and an uncorrected version, where such a factor is missing. In view of the central importance of the Coulomb boundary correction, uncorrected versions may be considered inadequate, except for

[3] In the literature you will most often find a slightly different form of this phase factor, which is found by replacing p in the denominator by another constant, in casu the de Broglie wavelength $\lambda\!\!\!^{-} = \hbar/mv$, so that

$$\ln \frac{R - vt}{p} \to \ln \frac{mv(R - vt)}{\hbar}\,, \tag{2.75}$$

which is the form proposed by Cheshire (1964). This replacement reflects a different choice of the constant α_0 mentioned in (2.28) and does not affect the final result, unless an approximation is made that spoils this invariance.

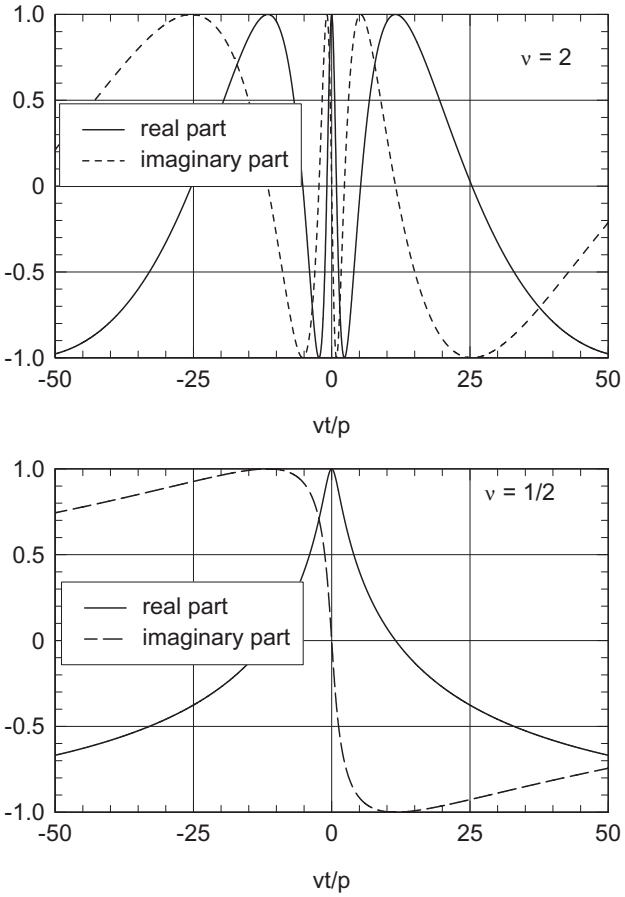

Fig. 2.8 Real and imaginary part of the phase factor $\exp(i\nu \ln[(R - vt)/p])$ entering the transition amplitude for heterogeneous collision systems, $Z_1 \neq Z_2$. Upper graph: $\nu = 2$; Lower graph: $\nu = 1/2$

$Z_1 = Z_2$, where the phase factors cancel out. Amongst eight schemes for which a boundary-corrected version exists, I wish to give preference to the CDW (continuum distorted wave) picture and the eikonal approximation.

2.4.5.1 Second-order Perturbation Theory

Contributions from second-order perturbation theory to charge exchange were discussed qualitatively right from the beginning, but interest in these contributions increased dramatically as the deficiencies of the Brinkman and Kramers (1930) approach discussed in Sect. 2.4.4.5 became evident. You may have noticed in Chaps. 3

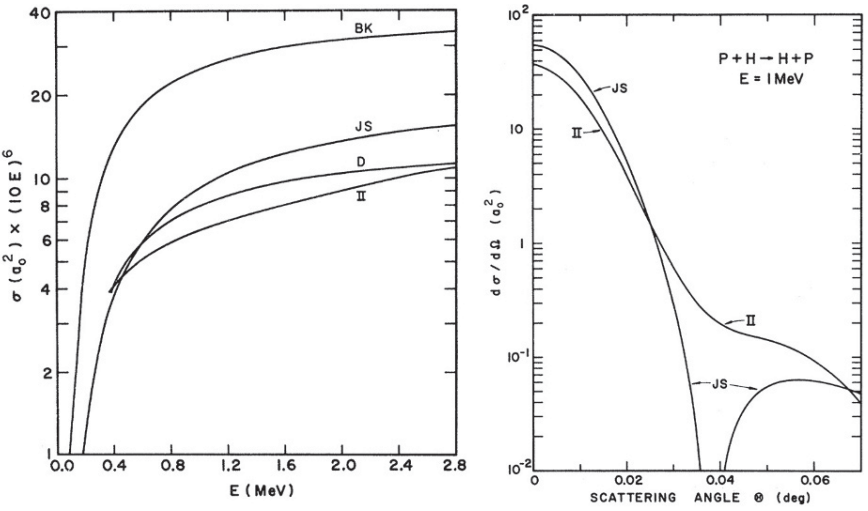

Fig. 2.9 Total (left) and differential (right) cross section for charge exchange in the H^+-H system. BK: Brinkman and Kramers (1930); JS: Jackson and Schiff (1953); D: Drisko (1955); II: Second Born approximation (Kramer, 1972); From Kramer (1972)

and 6, Vol. 1, and again in Sect. 2.4.3.4, that perturbation theory for collision processes gets considerably more complex when you go from the first to higher orders. But in hindside, the major obstacle in front of a successful theory was the lacking recognition of the Coulomb boundary condition and the importance of the rearrangement of the hamiltonian expressed by (2.22).

Early second-order theories starting with Drisko (1955), Dettmann (1971) and Kramer (1972) were straight extensions of the Brinkman-Kramers approach. Most importantly, it was found that asymptotically the contribution to the capture cross section from the second Born approximation behaved as v^{-11}, in agreement with the classical estimate of capture by double scattering (Thomas, 1927). Although the practical significance of this result is limited because relativistic corrections were neglected, it meant that first-order perturbation theory could not provide a quantitative description.

The scheme did not lead to better agreement with experimental results than the BK calculation. This led to an impressive theoretical effort by several research groups, which resulted in a variety of theoretical schemes. In addition to the distorted-wave and eikonal approximations to be sketched below, I like to mention schemes which take into account higher-order contributions in terms of either Z_1 or Z_2, whichever is bigger. Such approaches seemed appropriate for strongly asymmetric collision partners (Briggs, 1977, Macek and Shakeshaft, 1980, Macek and Taulbjerg, 1981). If you are interested in a comprehensive discussion of the pros and cons of such approaches, I refer again to Bransden and McDowell (1992) and Dewangan and Eichler (1994).

We have seen in Sect. 2.4.4.4 that the scheme of Jackson and Schiff (1953) yields results compatible with those of the B1B approximation when applied to H^+-H. From (2.46) you may extract that this feature also pertains in the second order. Therefore, an early numerical evaluation by Kramer (1972) may be expected to provide valid results. Figure 2.9 shows comparisons between first- and second-order results for both the total charge-exchange cross section and the cross section differential in scattering angle, which reflects the dependence of the charge-exchange probability on impact parameter.

In the total cross section (Fig. 2.9left) you see that a major improvement is the step from the Brinkman-Kramers to the Jackson-Schiff result, while the second Born approximation provides a further, but only minor decrease. The differential cross section drops down to zero at some intermediate angle. This reflects a change in sign of the transition amplitude. According to Horsdal-Pedersen (1981) this dip is a general phenomenon related to the way how the nucleus-nucleus interaction is taken into account in the hamiltonian.

Calculations for other systems with $Z_1 = Z_2$ were performed by Belkić et al. (1987), and for $Z_1 \neq Z_2$ by Decker and Eichler (1989). Note here that the number of integrations invoked in (2.46) is prohibitively large for numerical evaluation in general. While it is tempting, as a first step, to carry out the summation over j, this is not straightforward since a simple closure relation

$$\sum_j \psi_j(\boldsymbol{r},t)\psi_j(\boldsymbol{r}',t) = \delta(\boldsymbol{r}-\boldsymbol{r}') \tag{2.76}$$

holds only for $t = t'$. Therefore, an approximation has frequently been used where the intermediate states are approximated by free-particle wave functions,

$$u_j(\boldsymbol{r},t) = \frac{1}{(2\pi)^{3/2}} \mathrm{e}^{\mathrm{i}[\boldsymbol{k}\cdot\boldsymbol{r}-(\hbar k^2/2m)t]}. \tag{2.77}$$

With this, the sum over j reduces to an integration over $\boldsymbol{k}$,

$$\sum_j \psi_j(\boldsymbol{r},t)\psi^*(\boldsymbol{r},t') = \frac{1}{(2\pi)^3} f(t,t') \int \mathrm{d}^3\boldsymbol{k}\, \mathrm{e}^{\mathrm{i}\boldsymbol{k}\cdot(\boldsymbol{r}-\boldsymbol{r}')} \mathrm{e}^{-\mathrm{i}(\hbar k^2/2m)(t-t')} \tag{2.78}$$

with

$$f(t,t') = \exp\left(\mathrm{i}\nu_1 \ln\frac{R-vt}{R-vt'}\right). \tag{2.79}$$

This integral can be evaluated in closed form (Problem 2.5), so that

$$\sum_j \psi_j(\boldsymbol{r},t)\psi^*(\boldsymbol{r},t') = \mathrm{e}^{-3\mathrm{i}\pi/4}\left(\frac{m}{2\pi\hbar(t-t')}\right)^{3/2} f(t,t') \exp\left[\mathrm{i}\frac{m(\boldsymbol{r}-\boldsymbol{r}')^2}{2\hbar(t-t')}\right] \tag{2.80}$$

2.4.5.2 Distorted-Wave Picture

Distorted-wave scattering theories are perturbation expansions in which part of the perturbation has been incorporated into the zero-order wave function. In other words, an interaction potential $\mathcal{V}_{\mathrm{DW}}(r,t)$ is adopted which allows for an analytic or at least accurate nonperturbational determination of zero-order wave functions. The subsequent perturbation expansion operates on the basis of an effective interaction $\mathcal{U}(r,t) = \mathcal{V}(r,t) - \mathcal{V}_{\mathrm{DW}}(r,t)$ which is weaker than the actual interaction $\mathcal{V}(r,t)$ and therefore leads to a more rapidly converging perturbation series.

Thus, perturbation theory as outlined in Sect. 2.4.3 is a distorted-wave theory with the special choice of $\mathcal{U}_{\mathrm{DW}}(r,t) = V_1(r) - V_1(R(t))$. We have seen that this rearrangement of the interaction implies the phase factor $\mathrm{e}^{-\mathrm{i}\alpha(t)/\hbar}$. However, in the literature on charge exchange these features do not always appear together: There are distorted-wave theories which do not incorporate a phase factor, or allow for a phase factor only in either the incoming or the outgoing wave.

The success of a distorted-wave theory hinges on a suitable model interaction which approximates the real interaction and, at the same time, allows to find appropriate wave functions in zero order, preferrably exact ones. Since deviations from free undisturbed motion are expected to be most pronounced at maximum interaction, distorted-wave potentials have typically a short range.

Calculations on charge exchange with DW models have been performed by many authors starting from Cheshire (1964). For analytical convenience, DW potentials frequently depend on the time variable only. A popular choice is

$$\mathcal{V}_{\mathrm{DW}}(t) = \int \mathrm{d}^3\boldsymbol{r}\; \psi_0^*(\boldsymbol{r},t)\, \mathcal{V}(\boldsymbol{r},t)\, \psi_0(\boldsymbol{r},t) \tag{2.81}$$

which, for a hydrogen-like target and an interaction of the form of (2.24), leads to

$$\mathcal{V}_{\mathrm{DW}}(t) = Z_1 e^2 \left(\frac{1}{R(t)} + \frac{1}{a}\right) \mathrm{e}^{-2R(t)/a}\,, \tag{2.82}$$

as you may find by solving Problem 2.6. Selected results will be shown below.

2.4.5.3 Eikonal Approximation

Consider the function

$$\psi_{\mathrm{eik}}(\boldsymbol{r},t) = \mathrm{e}^{-\mathrm{i}\mathcal{S}(\boldsymbol{r},t)/\hbar}\, \psi_0(\boldsymbol{r},t)\,, \tag{2.83}$$

where

$$\mathcal{S}(\boldsymbol{r},t) = \int^t \mathrm{d}t'\, \mathcal{V}(\boldsymbol{r},t) \tag{2.84}$$

and $\psi_0(\boldsymbol{r},t)$ is an eigenfunction to $\mathcal{H}_0$. $\psi_{\mathrm{eik}}(\boldsymbol{r},t)$ is not an exact solution to the Schrödinger equation, $[\mathcal{H}_0 + \mathcal{V}(\boldsymbol{r},t)]\psi(\boldsymbol{r},t) = \mathrm{i}\hbar\partial\psi(\boldsymbol{r},t)/\partial t$, but you may easily

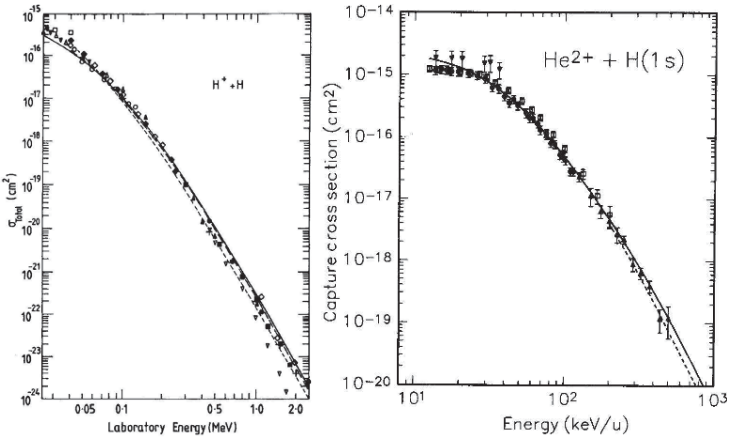

Fig. 2.10 Left: Total capture cross section for H^+-H. Solid line: B1B approximation (Belkić et al., 1987); dotted line: CDW approximation (Belkić et al., 1979); dashed line: Eikonal approximation (Dewangan and Eichler, 1994). Right: Same for He^{++}-H. Solid line: B1B approximation (Belkić et al., 1987); dotted line: CDW approximation (Belkić and Janev, 1973, Belkić et al., 1992). Experimental data refer to atomic hydrogen quoted by Dewangan and Eichler (1994). From Dewangan and Eichler (1994)

verify that

$$\mathrm{i}\hbar\frac{\partial\psi_{\mathrm{eik}}(\boldsymbol{r},t)}{\partial t} = [\epsilon_0 + \mathcal{V}(\boldsymbol{r},t)]\,\psi_{\mathrm{eik}}(\boldsymbol{r},t)\,. \tag{2.85}$$

Therefore, $\psi_{\mathrm{eik}}(\boldsymbol{r},t)$ will normally be a better approximation to the exact wave function than the zero-order approximation $\psi_0(\boldsymbol{r},t)$, where $\mathcal{V}(\boldsymbol{r},t)$ would be missing on the right-hand side of (2.85).

The quantity $\mathcal{S}(t)$ as defined by (2.84) is called the eikonal. A similar quantity in optics is called the optical path. The eikonal approximation (2.83) is a standard scheme in quantum mechanics (Schiff, 1981), which was introduced into scattering theory by Molière (1947).

In the context of (2.24), the eikonal reads

$$\begin{aligned}\mathcal{S}(\boldsymbol{r},t) &= \int^t \mathrm{d}t'\left[V_1(|\boldsymbol{r}-\boldsymbol{R}(t)|) - V_1\left(R(t)\right)\right] \\ &= \frac{Z_1 e^2}{v}\ln\frac{v|\boldsymbol{r}-\boldsymbol{R}| + \boldsymbol{v}\cdot(\boldsymbol{r}-\boldsymbol{R})}{vR - \boldsymbol{v}\cdot\boldsymbol{R}}.\end{aligned} \tag{2.86}$$

You may note that $\mathcal{S} = 0$ for $t = \pm\infty$. This implies that the full phase factor $\exp(-i\alpha(t)/\hbar$ has to be added to the eikonal wave function in order that it satisfies the Coulomb boundary condition. This condition is fulfilled if $\psi_0(\boldsymbol{r},t)$ is taken in the boundary-corrected form, (2.30).

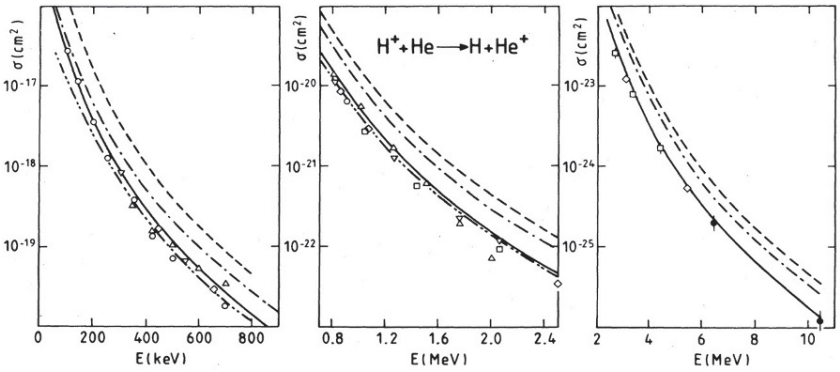

Fig. 2.11 Total capture cross sections for H^+-He for three energy intervals (left to right). Solid lines: B1B; dot-dashed lines: DWBA; dashed lines: OBK; double-dot-dashed lines: eikonal (Kobayashi et al., 1985). Experimental data quoted by Toshima et al. (1987). From Toshima et al. (1987)

2.4.5.4 Comparison with Experiment

The unperturbed wave function ψ_0, the CDW wave function ψ_{CDW} or the eikonal wave function ψ_{eik} can all serve as first-order approximations in a perturbation theory of charge exchange. Either approximation can be improved by going to the next order or by applying other approaches such as variational procedures.

Figure 2.10 shows results for protons in hydrogen. Calculations refer to atomic hydrogen as a target. Five sets of experimental data were likewise found with atomic hydrogen, while the remaining six data sets refer to molecular hydrogen. The agreement with experimental results appears very good, and differences between three theoretical results are comparable with the scatter of experimental data. Note that the cross section varies over almost nine orders of magnitude for an energy variation over only two orders of magnitude.

Figure 2.11 shows comparisons between several calculational schemes and measurements for H^+-He. It appears that the best agreement with experiment is achieved with the B1B and the eikonal method. However, calculations refer to $1s - 1s$ processes only, and the calculated cross sections were multiplied by a constant factor of 1.2 to account for the fact that measured cross sections do not differentiate between final states.

Figure 2.12 shows the measured differential cross section for charge exchange in H^+-He by Fischer et al. (2006) which was already shown in Fig. 2.3, but now compared with two theoretical results. Although the Thomas peak is clearly identified in both measurement and theory, quantitative agreement with experimental data does not appear better than about a factor of two. It is important here to note the angular scale: Considering the necessary angular resolution, it is a remarkable achievement by the experimentalists (Horsdal-Pedersen et al., 1983, Fischer et al., 2006) that the peak has been identified at all.

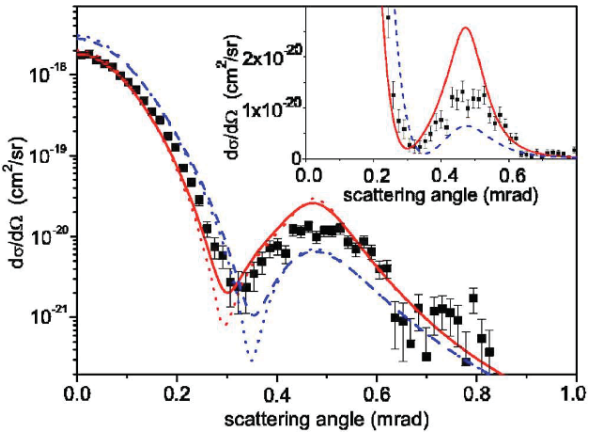

Fig. 2.12 Differential cross section for single-electron capture in 7.5 MeV H^+-He collision. Solid symbols: Measurements of Fischer et al. (2006). Solid line: CDW calculation (Abufager et al., 2005); dashed line: multiple-scattering (Faddeev) calculation (Adivi and Bolorizadeh, 2004). Theoretical calculations convoluted with the experimental resolution of the apparatus. Dotted lines: Theory before convolution. From Fischer et al. (2006)

2.5 Multiple-Electron Systems

2.5.1 Classical Models

A number of models for electron capture in a single event have been developed on the basis of classical collision theory. It is instructive to confront these models with quantal estimates to be discussed in the following section.

2.5.1.1 Bell Model

The estimate of Bell (1953) addressed electron capture from light gas atoms by fission fragments with a high projectile charge $q_1 e$. Even in a distant interaction, the force exerted by the projectile on a target electron can exceed its binding force. From the instant when this happens, the electron is considered only to interact with the projectile, and the effect of the target is ignored. The electron is considered as captured if its speed in the rest frame of the projectile is below the escape velocity.

Quantitative estimates on the basis of this model involve standard relations of classical Kepler motion. Trends of the capture cross sections were mentioned by Bell, but quantitative conclusions were only reported on equilibrium charges, which also invoke a model for electron loss.

Extensive calculations on the basis of a modified Bell model were performed by Gluckstern (1955).

2.5.1.2 Bohr-Lindhard Model

The model of Bohr and Lindhard (1954) likewise addresses capture and loss by fission fragments. Similar to Bell, they introduce a critical distance r_0 at which the Coulomb force due to the projectile balances the centrifugal force of the electron in its Kepler motion around the target nucleus. While the projectile approaches the target even further, the electron is assumed to gradually adjust its velocity toward the projectile speed, so that at some time its energy in the rest frame (kinetic plus potential) becomes zero. If this happens while the distance between the two nuclei is still less than r_0, the electron is considered as captured, so that the capture cross section is $\sigma_c = \pi r_0^2$.

On the basis of a simple atomic model, Bohr and Lindhard (1954) find

$$\sigma_c = \pi a_0^2 q_1^2 Z_2^{1/3} \left(\frac{v_0}{v}\right)^3 . \tag{2.87}$$

While this formula differs from Bohr's earlier expression, (2.9), you may recall that (2.87) is geared toward fission fragments, while (2.9) was developed with application to alpha particles in mind.

Bohr and Lindhard also note that the considered process favours electrons moving at a speed close to $v/2$, where only a minor adjustment in velocity is required for the electron to bind to the projectile, cf. Fig. 2.4 above. This condition may be difficult to fulfill for very light target atoms, with the consequence of electron capture becoming a rare process. By relaxing the criterion for capture, an alternative expression was found, valid specifically for weakly-bound target electrons, where

$$\sigma_c = \pi a_0^2 q_1^2 \left(\frac{v_0}{v}\right)^2 \frac{q_2^2}{n'^3} . \tag{2.88}$$

Here $q_2 e$ represents a screened charge of the target nucleus and n' an effective quantum number.

Knudsen et al. (1981b) applied the Bohr-Lindhard model in conjunction with a simple atomic model to establish an approximate scaling relationship for capture cross sections for a wide range of collision systems. Figure 2.13 shows a comparison of their formula with a large number of experimental data. While the scaling is by no means perfect, the formula may well provide a reliable order-of-magnitude estimate of a capture cross section in situations where experimental data are unavailable.

2.5.1.3 Straight Simulation

Computer simulation, i.e., straight numerical solution of the pertinent equations of motion has become increasingly successful with the development of powerful computers. In the context of charge exchange, pertinent equations of motion are Newton's second law as well as the Schrödinger and the Dirac equation.

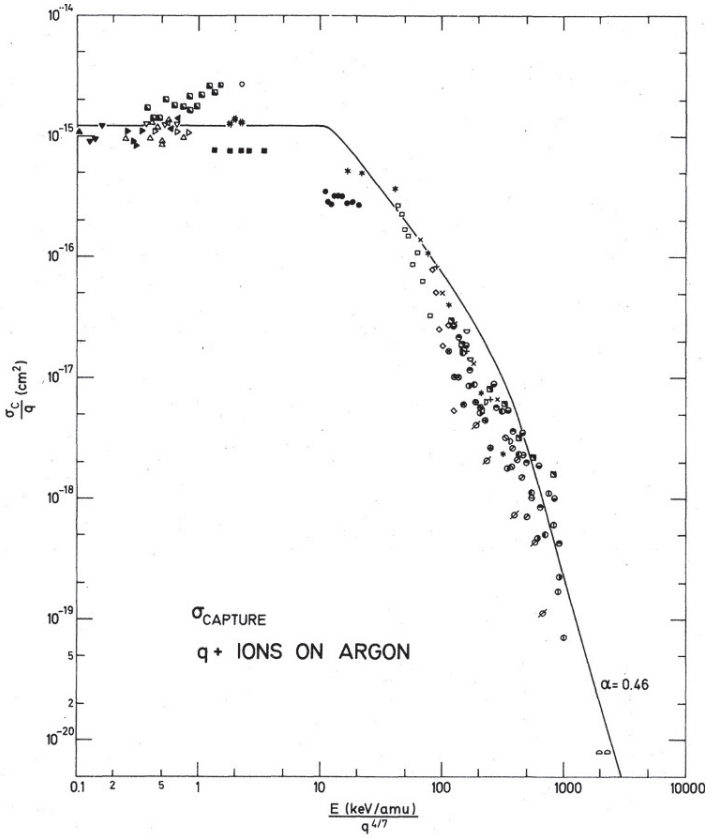

Fig. 2.13 Capture cross section for positive ions in argon. Experimental data for N, O, F, Ne, Ar, Br, Kr, I, Xe and W ions with charges q varying from 4 to 17 from a large number of sources quoted by Knudsen et al. (1981a) and compared with an empirical scaling relation. From Knudsen et al. (1981a)

We have seen that a classical description may well be appropriate if certain conditions are fulfilled. However, proper incorporation of the orbital motion of target and projectile electrons makes even the simplest collision systems untractable by conventional mathematical methods. This stimulated Abrines and Percival (1966a) to establish a straight numerical approach, which now goes under the label CTMC, or classical-trajectory Monte Carlo Calculation.

CTMC invokes three steps,

- the preparation of a statistical sample,
- simulating the dynamics of each configuration, and
- a statistical analysis of the outcome.

Quantum mechanics enters implicitly via input parameters such as binding energies and velocity distributions of the electrons. Obtaining accurate results requires good

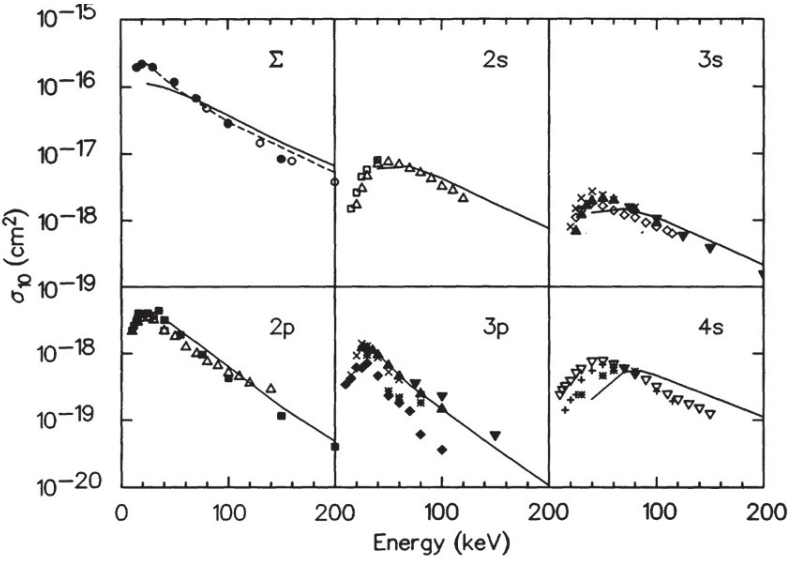

Fig. 2.14 State-separated cross sections for charge exchange in H^+-He collisions calculated by the CTMC method compared with experimental results. From Schultz et al. (1992)

statistics and, hence, extensive computation time. On the other hand, one and the same output obtained by this method can be used to extract a variety of quantities of physical interest, e.g., excitation and ionization cross sections.

Abrines and Percival (1966b) applied the scheme to charge exchange in H^+-H with good success. The range of applicability of the method has been greatly expanded by the work of Olson and Salop (1977), whose code has become a standard tool in atomic-collision theory, in particular when highly-charged ions and high-Z_2 targets are involved. Figure 2.14 shows an example.

Numerical solutions of the Schrödinger equation have become common in atomic-collision physics. Such calculations can be performed by the 'coupled-channel' method, where the wave function is expanded in terms of some basis such as (2.37), but instead of solving the resulting set of linear equations by perturbation expansion, a complete numerical solution is found by defining a subset of a finite number of states that are supposed to govern the process considered.

The number of states involved in charge-exchange and ionization processes increases with increasing projectile velocity. Therefore, the applicability of this method is limited by computational power to not too high projectile speeds. Differential cross sections are less CPU-intensive than total cross sections which may require reliable results for a wide range of impact parameters.

An example is the the END (Electron Nuclear Dynamics) code, which was designed with a view to the kinetics of chemical reactions (Deumens et al., 1994). In this code the nuclear motion is described by quantal wave packets of width zero. The adopted formalism is a quantal version of the Lagrange formalism known from

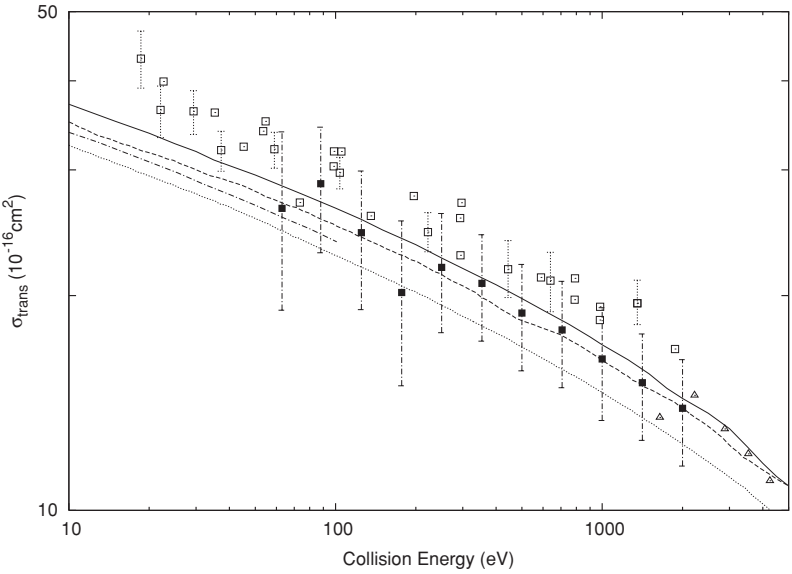

Fig. 2.15 Total capture cross section for H^+-H. Solid curve: END (Killian et al., 2004); Experimental data and other theoretical curves quoted by Killian et al. (2004). From Killian et al. (2004)

classical mechanics. The forward and backward coupling between electronic and nuclear motion is taken into account, as well as electron-electron interaction. In that sense, the code is suitable for application in systems containing many electrons, but the main limitations is available computational power. An example is shown in Fig. 2.15.

2.5.2 Data

An extensive compilation of calculated and measured capture cross sections may be found in three articles by Janev et al. (1983), Gallagher et al. (1983) and Janev and Gallagher (1983).

On the basis of empirical scaling relations found by Alonso and Gould (1982), Knudsen et al. (1981a), Ryufuku (1982) and Janev et al. (1980), Schlachter et al. (1983) proposed the empirical scaling relation

$$\sigma_c = \frac{\sqrt{q_1}}{Z_2^{1.8}} \frac{1.1 \times 10^{-8}}{\tilde{E}^{4.8}} \left(1 - \mathrm{e}^{-0.037\tilde{E}^{2.2}}\right) \left(1 - \mathrm{e}^{-2.44\times10^{-5}\tilde{E}^{2.6}}\right) , \qquad (2.89)$$

where

$$\tilde{E} = \frac{E}{Z_2^{1.25} q_1^{0.7}} , \qquad (2.90)$$

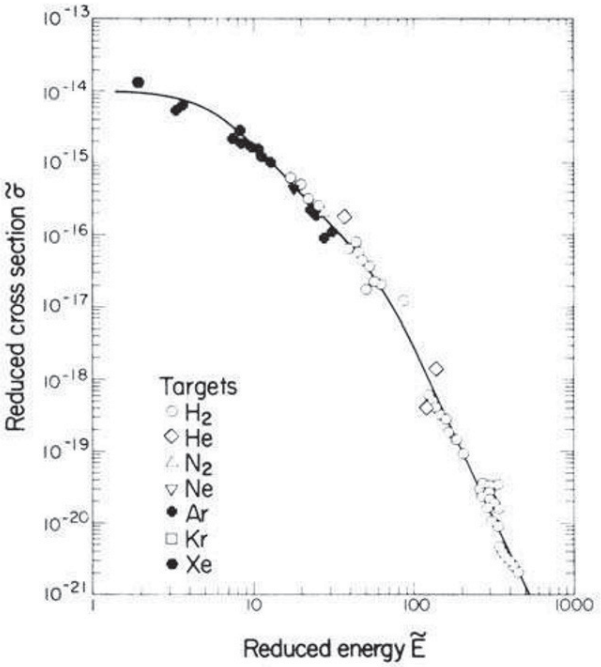

Fig. 2.16 Scaling of electron capture cross sections according to Schlachter et al. (1983). Solid line: (2.89). Points: Measured. From Schlachter et al. (1983)

with σ_c in cm^2 and E in keV/u. Here, the $\tilde{E}^{-4.8}$ dependence determines the high-energy behaviour for $\tilde{E} \gtrsim 100$. The second factor causes a bend-over in the interval $10 \lesssim \tilde{E} \lesssim 100$, and the last factor causes a further bend-over so that the function approaches a constant for $\tilde{E} < 10$. An example is shown in Fig. 2.16.

Comparisons with measurements on a number of systems were performed by Shevelko et al. (2010). Two examples, referring to measurements with Ge^{31+} on Ne (Stöhlker et al., 1992) and Xe^{18+} on N_2 (Olson et al., 2002), are shown in Fig. 2.17. The agreement achieved with (2.89) and theoretical estimates, CTMC and eikonal approximation (Stöhlker et al., 1992) as well as CDW and the CAPTURE code (Shevelko et al., 2004) illustrates the statement by Tolstikhina and Shevelko (2013) that 'getting an accuracy within a factor of 2 is a rather tedious task'.

2.6 Radiative Electron Capture ⋆

It has been mentioned in Sect. 2.2 that an ion may capture a free electron if the process is accompanied by the emission of a photon. This process, illustrated schemati-

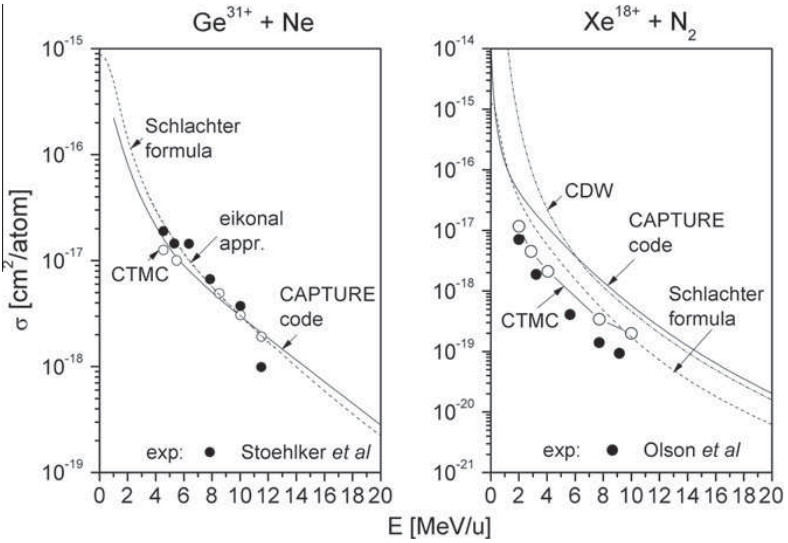

Fig. 2.17 Comparison of measured single-electron capture cross sections with semi-empirical formula and theoretical estimates. See text. From Shevelko et al. (2010)

cally in the left part of Fig. 2.18, is called *radiative recombination*. The right part of the figure indicates that radiative recombination is the inverse of the wellknown photoemission (or photoelectric emission) process. Radiative recombination can also take place with an electron that is initially bound to another atom or molecule. Then we talk about 'radiative electron capture'.

The existence of this effect was deduced by Raisbeck and Yiou (1971) from measurements of equilibrium charge states of high-energy (40–600 MeV) protons penetrating thin metal foils.

Subsequently, Schnopper et al. (1972) found X-ray emission in experiments with S, Cl and Br ions with energies up to 140 MeV. Ions in that energy range are highly charged, so that the emission of characteristic X-rays is greatly reduced. Measured continuous X-ray spectra were ascribed to radiative electron capture.

Kienle et al. (1973) made similar experiments with N, Ne and Ar beams at energies up to 288 MeV and, in addition to demonstrating convincing comparisons with theory, identified that also Bremsstrahlung was active.

From the experimental conditions specified here you may get an impression of radiative electron capture being a high-velocity phenomenon. Let us see how we can get at an estimate without diving too much into relativistic collision theory.

Fig. 2.18 Radiative recombination (left) and photoemission (right)

2.6.1 Detailed Balance

Figure 2.18 suggests a relation between photoemission and radiative recombination. One condition that must be common to both phenomena is energy conservation,

$$\hbar\omega = U + E_\mathrm{e}\,, \tag{2.91}$$

where $\hbar\omega$ is the photon energy, E_e the kinetic energy of the free electron and U the binding energy of the electron in the atom.

However, also the cross sections are related. To appreciate this, consider first an elastic collision between two particles 1 and 2. In Chap. 3, Vol. 1 we have considered the differential cross section both classically and quantally and have moved freely between the laboratory and the centre-of-mass frame of reference. We also made use of a reference frame in which the projectile was at rest. The differential cross section was expressed in various variables, but its magnitude was independent of the frame of reference, at least in the nonrelativistic limit. Indeed, in classical nonrelativistic collision theory the differential cross section is equal to an area $2\pi p\,dp$, the magnitude of which is the same, whether viewed from the laboratory, the projectile or any other reference frame.

The process shown in Fig. 2.18 is not an elastic collision, hence the above argument does not apply here. However, the *transition probability* must be independent of the arrow of the time, as long as energy conservation is fulfilled. This is called the *principle of detailed balance*. You may convince yourself of this by looking into Problem 2.7. In order to convert it into a relation between cross sections we employ the definition emerging from (2.1), Vol. 1, where the cross section for an event was found to be given by the ratio of the mean number of events per unit time and the incident current density.

Following Landau and Lifshitz (1960) we consider a reaction between two particles which results in a change of their identity, so that 1 and 2 represent the state of the system before and after the interaction. If the initial state is specified, the final state will represent a variety of configurations, such that the probability for transition to a given state j_2 is given by some function $P(j_1, j_2)$. In the reverse process, on the other hand, it is the state j_2 that is specified, while j_1 comprises a variety of configurations. The time reversal implied by the Schrödinger equation, on the other hand, specifies both the initial and the final state.

It is convenient to consider a finite normalization volume L^3 here, as has been done in Sect. 5.7.1, Vol. 1, so that a free particle is characterized by a wave function

$$\psi_{\boldsymbol{k}}(\boldsymbol{r}) = \frac{1}{L^{3/2}} \mathrm{e}^{\mathrm{i}\boldsymbol{k}\cdot\boldsymbol{r}} \tag{2.92}$$

with $\boldsymbol{k} = (\nu_x, \nu_y, \nu_z)2\pi/L$.

The total number of quantum states in an element $\mathrm{d}^3\boldsymbol{k}$ in momentum space (disregarding spin) is then given by

$$\left(\frac{L}{2\pi}\right)^3 \mathrm{d}^3\boldsymbol{k}\,. \tag{2.93}$$

We may then express the transition probability by a probability density w_{12},

$$P(j_1, j_2) \to w_{12} \left(\frac{L}{2\pi}\right)^3 \mathrm{d}^3\boldsymbol{k}_2\,. \tag{2.94}$$

where both the incident and the final configuration represent single quantum states. Hence the quantity w_{12} so defined must satisfy detailed balance,

$$w_{12} = w_{21}\,. \tag{2.95}$$

We may write the cross section $\mathrm{d}\sigma_{12}$ in the form

$$\mathrm{d}\sigma_{12} = \mathrm{d}K_{12}\delta(E_1 - E_2)\mathrm{d}E_2\,, \tag{2.96}$$

where the Dirac function represents energy conservation, cf. (2.91), while $\mathrm{d}K_{12}$ contains all other dependencies.

The transition probability is given by the product of the cross section, and the incident current density, so that

$$w_{12} = \left(\frac{2\pi}{L}\right)^3 v_1 N_1 \mathrm{d}K_{12}\delta(E_1 - E_2)\frac{\mathrm{d}E_2}{\mathrm{d}^3\boldsymbol{k}}\,, \tag{2.97}$$

where N_1 and v_1 represent the number of incident particles per volume and their speed, respectively.

The same relation holds for the inverse process with subscripts 1 and 2 interchanged. With this, (2.95) reduces to

$$v_1\,\mathrm{d}K_{12}\,\frac{\mathrm{d}E_2}{k_2^2\mathrm{d}k_2\mathrm{d}^2\Omega_2} = v_2\,\mathrm{d}K_{21}\,\frac{\mathrm{d}E_1}{k_1^2\mathrm{d}k_1\mathrm{d}^2\Omega_1}\,, \tag{2.98}$$

where we have set $N_1 = N_2 = 1/L^3$, i.e., one incident particle in either process.

Now, let state 1 represent a photon and 2 an electron, so that $\mathrm{d}K_{12}$ is the cross section for photoemission and $\mathrm{d}K_{21}$ the cross section for radiative recombination. Then,

$$E_1 = \hbar k_1 c; \quad v_1 = c \tag{2.99}$$

and

$$E_2 = \hbar^2 k_2^2/2m; \quad v_2 = \hbar k_2/m\,, \tag{2.100}$$

so that (2.98) reduces to

$$k_1^2 \frac{\mathrm{d}K_{12}}{\mathrm{d}^2\Omega_2} = k_2^2 \frac{\mathrm{d}K_{21}}{\mathrm{d}^2\Omega_1} \tag{2.101}$$

or

$$\frac{\mathrm{d}\sigma_{\mathrm{RR}}}{\mathrm{d}\Omega} = \left(\frac{\hbar\omega}{mvc}\right)^2 \frac{\mathrm{d}\sigma_{\mathrm{ph}}}{\mathrm{d}\Omega} \tag{2.102}$$

With this, the problem has been reduced to finding a cross section for photoemission, a classic topic from the early days of quantum theory.

2.6.2 Photoemission

In order to find the latter we have to go back to the problem of excitation of an atom by an electromagnetic wave which has been considered in Sect. A.5.2, Vol. 1. That treatment was based on the dipole approximation, i.e., long wavelength or low photon energy. This assumption does not necessarily apply when we want to consider radiative electron capture by swift ions. Here, the mismatch between the orbital speed and the ion speed is typically so large that photon energies will lie in the x ray or even gamma regime.

Quantal calculations of the cross section for photoemission were initiated by Wentzel (1926) and followed up by Sommerfeld and Schur (1930) and Stobbe (1930).

The interaction of an electron with an electromagnetic field can be described by a hamiltonian

$$H = \frac{1}{2m}\left(\boldsymbol{P} + \frac{e}{c}\boldsymbol{A}\right)^2 - e\Phi\,, \tag{2.103}$$

where $\boldsymbol{A}$ and Φ denote the vector and scalar potential, respectively[4] and $\boldsymbol{P}$ the momentum.

We may describe a monochromatic electromagnetic wave by

$$\boldsymbol{A} = \boldsymbol{A}_0 \cos(\boldsymbol{k}\cdot\boldsymbol{r} - \omega t); \qquad \boldsymbol{k}\cdot\boldsymbol{A}_0 = 0; \qquad \Phi = 0\,. \tag{2.104}$$

This is equivalent with an electric field

$$\boldsymbol{E} = \boldsymbol{E}_0 \sin(\boldsymbol{k}\cdot\boldsymbol{r} - \omega t) \tag{2.105}$$

for $\boldsymbol{A}_0 = c\boldsymbol{E}_0/\omega$. With this, the interaction of the wave with a Z-electron atom may be described by a hamiltonian

[4] As everywhere else in this monograph we operate in gaussian units here. For translation to SI units refer to Sect. A.1.1, Vol. 1 or to Jackson (1975).

$$\mathcal{H} = H + \mathcal{V}\,, \tag{2.106}$$

where H is the hamiltonian of the free atom and

$$\mathcal{V} = \frac{e}{mc}\sum_{\nu=1}^{Z} \boldsymbol{A}(\boldsymbol{r}_\nu, t)\cdot\boldsymbol{P}_\nu\,. \tag{2.107}$$

We have dropped the quadratic term in $\boldsymbol{A}$ since we are only going up to the first order in a perturbation expansion.

Assume the field to be switched on at $t = 0$ and to be switched off at $t = t_1$. Then, the transition amplitude from the initial state $|0\rangle$ to a state $|j\rangle$ is given by

$$c_j(t_1) = \frac{1}{\mathrm{i}\hbar}\int_0^{t_1} \mathrm{d}t\, \mathrm{e}^{\mathrm{i}\omega_{j0}t}\,\langle j|\mathcal{V}|0\rangle \tag{2.108}$$

according to (4.37), Vol. 1, or

$$c_j(t_1) = -\frac{e}{2\hbar mc}\left(\left\langle j\left|\sum_\nu \mathrm{e}^{\mathrm{i}\boldsymbol{k}\cdot\boldsymbol{r}_\nu}\boldsymbol{A}_0\cdot\boldsymbol{P}_\nu\right|0\right\rangle \frac{\mathrm{e}^{\mathrm{i}(\omega_{j0}-\omega)t}-1}{\omega_{j0}-\omega} + \left\langle j\left|\sum_\nu \mathrm{e}^{-\mathrm{i}\boldsymbol{k}\cdot\boldsymbol{r}_\nu}\boldsymbol{A}_0\cdot\boldsymbol{P}_\nu\right|0\right\rangle \frac{\mathrm{e}^{\mathrm{i}(\omega_{j0}+\omega)t}-1}{\omega_{j0}+\omega}\right). \tag{2.109}$$

Here,

$$\hbar\omega_{j0} = E_j - E_0 \tag{2.110}$$

represents the excitation energy. The denominator in the first term in the brackets of (2.109) indicates that this term is going to be large when the photon energy $\hbar\omega$ comes close to $\hbar\omega_{j0}$. By the same argument we may deduce that the second term, with $\omega + \omega_j$ in the denominator, is small by comparison in the present context and will be neglected.

The transition probability per unit time is then given by

$$w = \frac{1}{t_1}\sum_j |c_j(t_1)|^2 = \frac{e^2}{\hbar^2 m^2 c^2 t_1} \times \sum_j \left|\left\langle j\left|\sum_\nu \mathrm{e}^{\mathrm{i}\boldsymbol{k}\cdot\boldsymbol{r}_\nu}\boldsymbol{A}_0\cdot\boldsymbol{P}_\nu\right|0\right\rangle\right|^2 \left(\frac{\sin\frac{(\omega_{j0}-\omega)t_1}{2}}{\omega_{j0}-\omega}\right)^2, \tag{2.111}$$

as long as $w \ll 1$, where the sum over j goes over all states that are compatible with energy conservation, $\omega_{j0} = \omega$.

Before evaluating the sum, let us consider the matrix element in (2.111). Since we deal with electrons ejected at fairly high energies we may approximate the final state as a free-electron state,

$$|j\rangle = \frac{1}{L^{3/2}} \mathrm{e}^{\mathrm{i}\boldsymbol{k}_j \cdot \boldsymbol{r}} \,. \tag{2.112}$$

Then, in an independent-particle model of the atom we may write

$$\left\langle j \left| \sum_\nu \mathrm{e}^{\mathrm{i}\boldsymbol{k}\cdot\boldsymbol{r}_\nu} \boldsymbol{A}_0 \cdot \boldsymbol{P}_\nu \right| 0 \right\rangle = \frac{1}{L^{3/2}} \sum_\nu \int \mathrm{d}^3\boldsymbol{r}\, \mathrm{e}^{-\mathrm{i}\boldsymbol{k}_j\cdot\boldsymbol{r}} \mathrm{e}^{\mathrm{i}\boldsymbol{k}\cdot\boldsymbol{r}} \boldsymbol{P} u_\nu(\boldsymbol{r}) \,, \tag{2.113}$$

where $\boldsymbol{P} = -\mathrm{i}\hbar\nabla$ and $u_\nu(\boldsymbol{r})$ is the wave function describing the νth initially occupied single-electron state. By partial integration this reduces to

$$\left\langle j \left| \sum_\nu \mathrm{e}^{\mathrm{i}\boldsymbol{k}\cdot\boldsymbol{r}_\nu} \boldsymbol{A}_0 \cdot \boldsymbol{P}_\nu \right| 0 \right\rangle = \frac{\hbar}{L^{3/2}} \sum_\nu \left(\boldsymbol{A}_0 \cdot \boldsymbol{k}_j\right) \int \mathrm{d}^3\boldsymbol{r}\, \mathrm{e}^{\mathrm{i}(\boldsymbol{k}-\boldsymbol{k}_j)\cdot\boldsymbol{r}} u_\nu(\boldsymbol{r}) \,, \tag{2.114}$$

Going back to (2.111) we need to evaluate the sum over j. The condition $\omega_{j0} = \omega$ implies that only states in a thin shell with radius $\sqrt{2m(\hbar\omega - U)}$ in $\boldsymbol{k}$-space can be excited. Following (2.93) we may introduce a density of states $\varrho(E)$ in energy space by means of the relation

$$\varrho(E_j)\mathrm{d}E_j = \left(\frac{L}{2\pi}\right)^3 \int \mathrm{d}^3\boldsymbol{k} \,, \tag{2.115}$$

where the integration goes over all states with a specified energy. The sum over j is the replaced by an integration over E_j, which is conveniently performed by making the replacement

$$x = (\omega_{j0} - \omega)t_1/2 \tag{2.116}$$

and yields

$$w_{12} = \frac{e^2 k_j \mathrm{d}^2\Omega_j}{(4\pi)^2\hbar m c^2} \left(\boldsymbol{A}_0 \cdot \boldsymbol{k}_j\right)^2 \left| \sum_\nu \int \mathrm{d}^3\boldsymbol{r}\, \mathrm{e}^{\mathrm{i}(\boldsymbol{k}-\boldsymbol{k}_j)\cdot\boldsymbol{r}} u_\nu(\boldsymbol{r}) \right|^2 . \tag{2.117}$$

With a photon current density

$$\frac{cE_0^2}{8\pi\hbar\omega} = \frac{\omega A_0^2}{8\pi\hbar c} \tag{2.118}$$

we then find the differential cross section for photoemission

$$\mathrm{d}\sigma = \frac{e^2 k_j k_{jz}^2}{2\pi m c\omega} \mathrm{d}^2\Omega_j \left| \int \mathrm{d}^3\boldsymbol{r}\, \mathrm{e}^{\mathrm{i}(k_x - \boldsymbol{k}_j\cdot\boldsymbol{r})} u_\nu(\boldsymbol{r}) \right|^2 , \tag{2.119}$$

where the x-axis denotes the direction of propagation and the z-axis the polarization of the incident wave. This result, as well as the essence of the derivation, follows Schiff (1981).

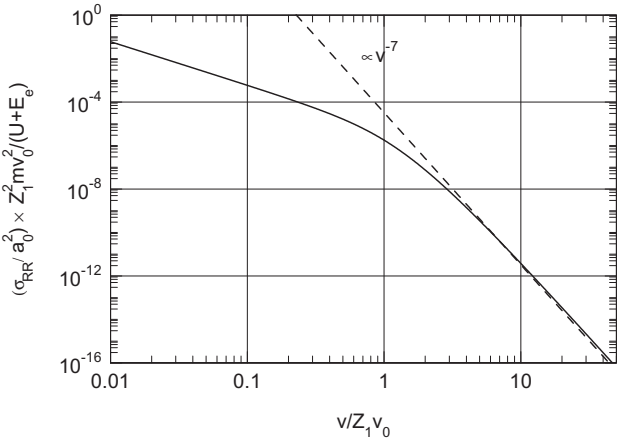

Fig. 2.19 Cross section σ_{RR} for radiative recombination according to the Stobbe formula (2.122)

2.6.3 Examples

For capture into the K shell, Stobbe (1930) finds the total cross section for radiative recombination, in the notation of Eichler and Meyerhof (1995),

$$\sigma_{\mathrm{ph}} = \frac{2^8\pi^2}{3}\frac{e^2}{mc\omega}\left(\frac{\nu^2}{1+\nu^2}\right)^3 \frac{\exp\left(-4\nu\arctan(1/\nu)\right)}{1-\exp(-2\pi\nu)}, \tag{2.120}$$

where ν is the Sommerfeld parameter

$$\nu = \frac{Z_1 e^2}{\hbar v}. \tag{2.121}$$

With this, and (2.102), the cross section for radiative recombination reads, in the nonrelativistic limit,

$$\sigma_{\mathrm{RR}} = \frac{2^8\pi^2}{3}\frac{\hbar\omega}{mv^2}a_0^2\alpha^3\left(\frac{\nu^2}{1+\nu^2}\right)^3 \frac{\exp\left(-4\nu\arctan(1/\nu)\right)}{1-\exp(-2\pi\nu)}, \tag{2.122}$$

where $\alpha = 1/137$ is the fine structure constant.

Figure 2.19 shows a universal plot of (2.122). It is seen that, due to the factor α^3, the absolute value of the capture cross section is small when taken in atomic units. However, with increasing projectile speed a $\propto v^{-7}$ dependence is approached which is much slower than that for nonradiative capture, going as $\propto v^{-11}$ or $\propto v^{-12}$.

An extensive discussion of the relativistic case has been given by Eichler and Meyerhof (1995), based on pioneering work by Sauter (1931a,b).

While (2.119) together with (2.98) shows essential features of radiative electron capture, such as the dependence on the frequency ω of the emitted X-ray as well as

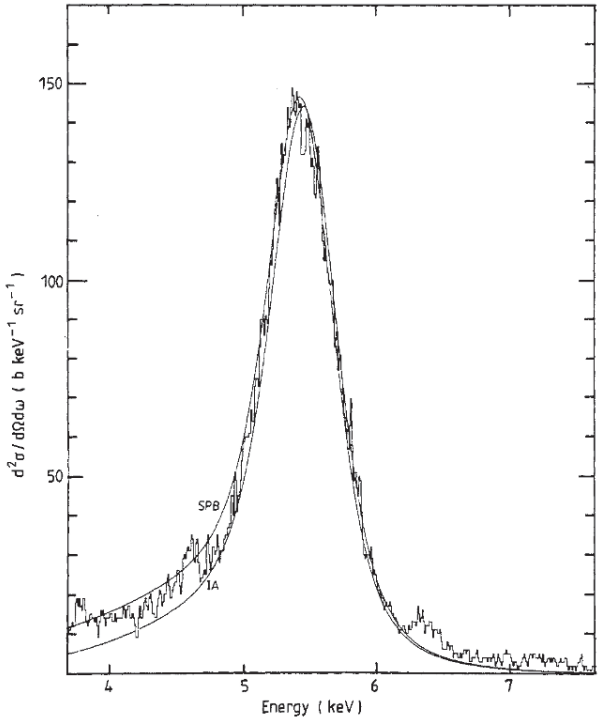

Fig. 2.20 Calculated and measured differential cross section for radiative electron capture to 125 MeV S^{16+} in carbon. Smooth curves represent strong-potential Born approximation (SPB) and impulse approximation (IA). From Jakubassa-Amundsen et al. (1984)

the order of magnitude of the effect, detailed theory is more complex (Kleber and Jakubassa, 1975, Eichler and Stöhlker, 2007).

Figure 2.20 shows an example of capture from carbon into the K shell of a fully-stripped sulphur ion. You may note first that the triply-differential cross section (solid angle and X-ray energy) is of the order of 100 b = 10^{-22} cm^2. The peak located between $\hbar\omega \simeq 5$ and 6 is made up primarily by the kinetic energy of a target electron in the rest frame of the ion, i.e., $mv^2/2$=2.1 keV and the K shell binding energy of 3.5 keV.

2.7 Electron Loss

From a theoretical point of view, electron loss is an ionization process seen from a reference frame moving with the projectile. For passage through a gaseous medium, the particle at rest in the moving reference frame is charged, while the one in motion

is neutral. For passage through a conducting medium it may be necessary also to consider ionization by free target electrons.

Both Volume 1 and the present volume in this monograph address primarily the first and the second moment over the energy-loss spectrum. The ionization cross section is related to the zero'th moment and, as such, is more sensitive to the behaviour near threshold. Since ionization phenomena are central to the topic of radiation effects, the treatment of ionization cross sections and ionization thresholds will be reserved to Volume 3. Therefore, the treatment of loss cross sections presented here is rather superficial.

2.7.1 Single and Multiple Loss

A look at stopping cross sections for heavy ions will tell you that ionization cross sections can be quite large, so that the probability for single, double and higher ionizations may become significant. This implies that we have to distinguish between single and multiple loss events.

Consider, for simplicity, ionization of a given shell containing n electrons in an atom at rest. In an independent-particle model, let $Q(\boldsymbol{p})$ be the probability per electron to be liberated after passage of a projectile at a vectorial impact parameter $\boldsymbol{p}$. Then, the probability for emission of exactly one electron is

$$P_1(\boldsymbol{p}) = nQ(\boldsymbol{p})\,[1 - Q(\boldsymbol{p})]^{n-1} \ . \tag{2.123}$$

Similarly, the probability for emission of two electrons is given by

$$P_2(w\,\boldsymbol{p}) = \frac{n(n-1)}{2}\,[Q(\boldsymbol{p})]^2\,[1 - Q(\boldsymbol{p})]^{n-2} \ . \tag{2.124}$$

In other words, the cross section for loss of ν electrons is given by

$$\sigma_\nu = \binom{n}{\nu} \int \mathrm{d}^2\boldsymbol{p}\ [Q(\boldsymbol{p})]^\nu\,[1 - Q(\boldsymbol{p})]^{n-\nu} \ . \tag{2.125}$$

For not too large values of $Q(\boldsymbol{p})$ we may approximate the cross section for single ionization by

$$\sigma_1 \simeq n \int \mathrm{d}^2\boldsymbol{p}\ Q(\boldsymbol{p}) - n(n-1) \int \mathrm{d}^2\boldsymbol{p}\ [Q(\boldsymbol{p})]^2 \tag{2.126}$$

and the cross section for double ionization by

$$\sigma_2 \simeq \frac{n(n-1)}{2} \int \mathrm{d}^2\boldsymbol{p}\ [Q(\boldsymbol{p})]^2 \ , \tag{2.127}$$

so that

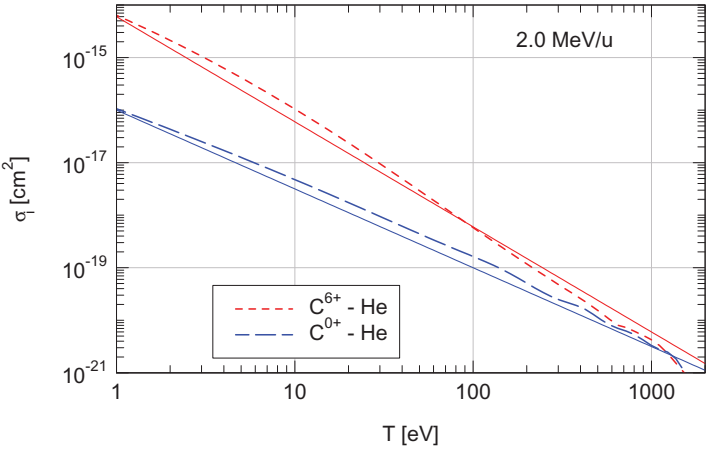

Fig. 2.21 Differential energy loss cross section for C-He collision according to PASS code (Weng et al., 2006) (dashed lines). Energy transferred to He atom. Neutral and fully-stripped carbon projectile. Solid lines: $\propto T^{-3/2}$ and $\propto T^{-2}$, respectively

$$\sigma_1 \simeq \sigma_I - 2\sigma_2 \,, \tag{2.128}$$

where

$$\sigma_I = n \int \mathrm{d}^2 \boldsymbol{p}\, Q(\boldsymbol{p}) \tag{2.129}$$

is the total ionization cross section.

These considerations can be formulated such as to invoke electrons from different shells (McGuire and Weaver, 1977). Rigourous definitions would have to involve transition amplitudes between many-body wave functions.

2.7.2 Theoretical Schemes

In principle, any theoretical scheme to treat ionization processes should be applicable to treat electron loss. This also includes theoretical schemes designed for stopping, such as the Bethe theory, binary theory or CasP.

Since ionization cross sections are determined primarily by energy transfers close to threshold, soft collisions provide the dominating contribution at least at high projectile speeds. In the present case, where the 'projectile' is a neutral atom, the screening of the Coulomb interaction implies that this dominance is weakened.

Figure 2.21 shows a comparison between differential energy-loss cross sections for neutral and fully-stripped carbon ions on helium, calculated by a version of the PASS code that generates differential energy-loss cross sections (Weng et al., 2006). This graph includes shell and Barkas-Andersen corrections. While the spectrum for fully-stripped C ions shows only a minor deviation from the T^{-2}-dependence for

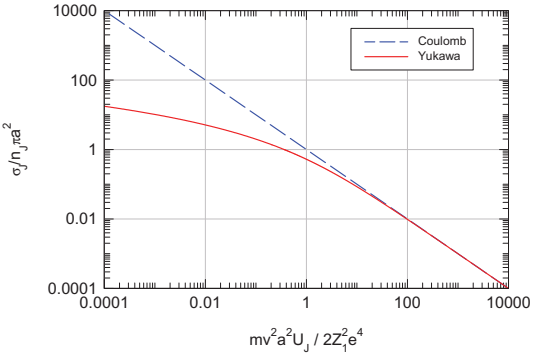

Fig. 2.22 Simple estimate of single-loss cross section σ_J. See text

free-Coulomb scattering, the spectrum for neutral carbon is very close to a $T^{-3/2}$ dependence.

The standard scheme for calculating ionization cross sections is the Born approximation (Inokuti, 1971). This scheme involves quite complex calculations, once the upper integration limit becomes essential.

It is useful here to recall the scaling properties of corrections to the straight Bethe theory of stopping:

- The shell correction is characterized by $\langle v_e^2 \rangle / v^2 \propto Z_2^{4/3} v_0^2 / v^2$,
- The Barkas-Andersen correction is characterized by the inverse of the parameter entering the Bohr stopping formula, $Z_1 e^2 \omega / m v^3 \propto Z_1 Z_2 v_0^3 / v^3$,
- The screening correction is characterized by $v_{TF}^2 / v^2 \propto Z_1^{4/3} v_0^2 / v^2$.

Thus, calculations on the basis of the Born approximation will be appropriate for light ions, provided that shell corrections are taken into account. Conversely, whatever scheme is employed for heavy ions, projectile screening need to be considered. The role to be assigned to the Barkas-Andersen correction depends on the desired accuracy.

Like the Born approximation, the classical-trajectory-Monte-Carlo (CTMC) simulation method (Olson et al., 1989) differentiates between single and multiple ionization events.

In the regime of dominating single ionization, classical binary scattering is most convenient. Assume the interaction between a neutral atom and a projectile electron to be given by

$$V(r) = \frac{-Z_1 e^2}{r} \phi(r/a)\,, \tag{2.130}$$

with a given screening function and radius, ϕ and a, respectively. Then, from (3.76) and (3.8), Vol. 1 you will be able to derive a relation for the energy loss

$$T = T(v, p) \tag{2.131}$$

to a projectile electron, where v is the projectile speed and p the impact parameter between a projectile electron and a target nucleus. The loss cross section for a given shell J is then given by

$$\sigma_J = n_J \pi p_J^2 \,, \tag{2.132}$$

where p_J is defined by

$$T(v, p_J) = U_J \,, \tag{2.133}$$

U_J being the ionization energy of the Jth shell. Such a calculation includes screening but ignores Barkas-Andersen and shell corrections.

Figure 2.22 shows an example for $\phi(r/a) = \exp(-r/a)$, where the scattering integral can be evaluated analytically (cf. Problem 2.8). Also included is the estimate for straight Coulomb interaction,

$$\sigma_J = \frac{2\pi n_J Z_1^2 e^4}{m v^2 U_J} \,. \tag{2.134}$$

Even though the accuracy of the Yukawa prediction deteriorates at low energies, you will note that the difference to the Coulomb cross section becomes substantial.

2.7.3 Data

Numerous available experimental data for both capture and loss cross sections may be found in compilations. Lo and Fite (1969) offer data for both gaseous and metallic ions in gas targets over en energy range covering the keV and lower MeV region. Dehmel et al. (1973) cover a similar energy range with many more data and include a bibliography ordered by ion-target combination. Tables by Tawara et al. (1985) and Janev et al. (1988), focusing on nuclear fusion, offer extensive data for charge exchange in atomic and molecular hydrogen as well as helium. Dmitriev et al. (2010) provide a summary of their own data, taken over half a century and covering a broad spectrum of ion-target combinations in the keV/u energy range.

Calculated capture and loss cross sections at higher energies can be extracted from output of the ETACHA code (Rozet et al., 1996) for $Z_1 \leq 36$. The LOSS code by Shevelko et al. (2001) delivers calculated electron loss cross sections for heavier ions at high energies.

2.8 Discussion and Outlook

Although the process of electron capture in atomic collisions was studied originally in connection with particle penetration, the subject has developed its own dynamics both from an experimental and a theoretical point of view. If you find that this chapter overemphasizes charge exchange in simple hydrogen-like collision systems,

you are unquestionably right, when comparing with monographs on related subjects such as Kumakhov and Komarov (1981) or Nastasi et al. (1996). On the other hand, this is only a rudimentary account of the effort spent in the field and reported by Bransden and McDowell (1992) or Dewangan and Eichler (1994).

Just as in other areas of ion-beam physics, there is a striking contrast between the degree of sophistication of both theory and experiment on the one hand, and the degree of agreement between theoretical predictions and experimental results on the other. Clearly there is space for improvement.

To the extent that charge exchange can be characterized by cross sections, the statistical theory aiming at equilibrium charges, fluctuations and approach to equilibrium can be developed without reference to specific ion-target combinations. This is the topic of the following chapter.

Problems

2.1. Show that (2.34) satisfies the Schrödinger equation

$$\mathcal{H}_1 \chi_\ell(\boldsymbol{r},t) = i\hbar \frac{\partial \chi_\ell(\boldsymbol{r},t)}{\partial t} \tag{2.135}$$

and demonstrate that the electron density is centered around the projectile position $\boldsymbol{R}(t)$.

2.2. Go through the derivation of (2.41) from (2.38). You need to write down the Schrödinger equation for the two pertinent hamiltonians. You will also need the relation

$$\int d^3\boldsymbol{r}\ \psi_1^*(\boldsymbol{r}) \boldsymbol{O} \psi_2(\boldsymbol{r}) = \int d^3\boldsymbol{r}\ [\boldsymbol{O}\psi_1(\boldsymbol{r})]^* \psi_2(\boldsymbol{r}) \tag{2.136}$$

for hermitian operators (Schiff, 1981).

2.3. Derive (2.63) from (2.61) for the H^+-H system using (2.62).

2.4. Find the velocity distribution $f(v_e)$ for the wave function (2.62) and determine the probability $P(v/2) = \int_{v/2}^{\infty} f(v_e) 4\pi v_e^2 dv_e$ for an electron to have a velocity $v_e > v/2$.

2.5. Derive (2.80) from (2.78) and demonstrate that (2.80) approaches a Dirac function $\delta(\boldsymbol{r} - \boldsymbol{r}')$ for $t \to t'$. [Hint: Show first that the integral over $\boldsymbol{r}'$ yields $f(t,t')$ for arbitrary t and t'. Then study the behaviour of the function for $t \to t'$].

2.6. Derive (2.82)

2.7. Demonstrate that, for an arbitrary collision event, the transition probability P_{12} from a state 1 to a state 2 of the particles involved, is identical with the probability for the inverse process P_{21}. Hint: Write $\psi_2 = S\psi_1$ and look at the properties of the operator S. If needed, consult Landau and Lifshitz (1960).

2.8. Try to reproduce Fig. 2.22 from the information given in the text.

References

Aaron R., Amado R.D. and Lee B.W. (1961): Divergence of the Green's function series for rearrangement collisions. Phys Rev **121**, 319–323

Abrines R. and Percival I.C. (1966a): Classical theory of charge transfer and ionization of hydrogen by protons. Proc Phys Soc **88**, 861–872

Abrines R. and Percival I.C. (1966b): A generalized correspondence principle and proton-hydrogen collisions. Proc Phys Soc **88**, 873–883

Abufager P.N., Fainstein P.D., Martinez A.E. and Rivarola R.D. (2005): Single electron capture differential cross section in He^+ + He collisions at intermediate and high collision energies. J Phys B **38**, 11–22

Adivi E.G. and Bolorizadeh M.A. (2004): Faddeev treatment of single-electron capture by protons in collision with many-electron atoms. J Phys B **37**, 3321–3338

Allison S.K. (1958): Experimental results on charge-changing collisions of hydrogen and helium atoms and ions at kinetic energies above 0.2 keV. Rev Mod Phys **30**, 1137–1168

Alonso J. and Gould H. (1982): Charge-changing cross-sections for Pb and Xe ions at velocities up to 4 x 109 cm/sec. Phys Rev A **26**, 1134–1137

Bates D.R. (1958): Electron capture in fast collisions. Proc Roy Soc A **247**, 294–301

Bates D.R. and Dalgarno A. (1952): Electron capture I: Resonance capture from hydrogen atoms by fast protons. Proc Phys Soc **A65**, 919–925

Belkić D., Gayet R. and Salin A. (1979): Electron-capture in high-energy ion-atom collisions. Phys Rep **56**, 279–369

Belkić D., Gayet R. and Salin A. (1992): Cross-sections for electron-capture from atomic-hydrogen by fully stripped ions. At Data Nucl Data Tab **56**, 59–150

Belkić D. and Janev R.K. (1973): Electron capture from atomic hydrogen and helium atoms by fast alpha particles. J Phys B **6**, 1020–1027

Belkić D., Saini S. and Taylor H.S. (1987): Critical test of first-order theories for electron transfer in collisions between multicharged ions and hydrogen: The boundary condition problem. Phys Rev A **36**, 1601–1617

Bell G.I. (1953): The capture and loss of electrons by fission fragments. Phys Rev **90**, 548–557

Betz H.D. (1972): Charge states and charge-changing cross sections of fast heavy ions penetrating through gaseous and solid media. Rev Mod Phys **44**, 465–539

Bohr N. (1940): Scattering and stopping of fission fragments. Phys Rev **58**, 654–655

Bohr N. (1941): Velocity-range relation for fission fragments. Phys Rev **59**, 270–275

Bohr N. (1948): The penetration of atomic particles through matter. Mat Fys Medd Dan Vid Selsk **18 no. 8**, 1–144

Bohr N. and Lindhard J. (1954): Electron capture and loss by heavy ions penetrating through matter. Mat Fys Medd Dan Vid Selsk **28 no. 7**, 1–31

Bransden B.H. and McDowell M.R.C. (1992): *Charge exchange and the theory of ion-atom collisions*. Clarendon Press, Oxford

Briggs J.S. (1977): Impact-parameter formulation of the impulse approximation for charge exchange. J Phys B **10**, 3075–3089

Brinkman H.C. and Kramers H.A. (1930): Zur Theorie der Einfangung von Elektronen durch Alpha-Teilchen. Proc Roy Acad Amsterdam **33**, 973–984

Cheshire I.M. (1964): Continuum distorted wave approximation; resonant charge transfer by fast protons in atomic hydrogen. Proc Phys Soc **84**, 89–98

Crothers D.F.S. and Holt A.R. (1966): The first Born approximation for collisions between heavy particles. Proc Phys Soc **88**, 75–81

Decker F. and Eichler J. (1989): Exact second-order Born calculations for charge exchange with Coulomb boundary conditions. J Phys B **22**, L95–L100

Dehmel R.C., Chau H.K. and Fleischmann H.H. (1973): Experimental stripping cross sections for atoms and ions in gases 1950-1970. Atomic Data **5**, 231–289

Dettmann K. (1971): Wave packet theory of Coulomb scattering. Z Physik **244**, 86

Deumens E., Diz A., Longo R. and Öhrn Y. (1994): Time-dependent theoretical treatments of the dynamics of electrons and nuclei in molecular systems. Rev Mod Phys **66**, 917–983

Dewangan D.P. and Eichler J. (1986): A first-order Born approximation for charge exchange with Coulomb boundary conditions. J Phys B **19**, 2939–2944

Dewangan D.P. and Eichler J. (1994): Charge exchange in energetic ion-atom collisions. Phys Rep **247**, 59–219

Dmitriev I.S., Teplova Y.A., Belkova Y.A., Novikov N.V. and Fainberg Y.A. (2010): Experimental electron loss and capture cross sections in ion-atom collisions. Atomic Data Nucl Data Tab **96**, 85–121

Drisko R.M. (1955): The theories of positronium and of rearrangement collisions. Ph.D. thesis, Carnegie-Mellon University

Eichler J. (1987): Theory of relativistic charge exchange with Coulomb boundary conditions. Phys Rev A **35**, 3248–3255

Eichler J. and Meyerhof W.E. (1995): *Relativistic atomic collisions*. Academic Press, San Diego

Eichler J. and Stöhlker T. (2007): Radiative electron capture in relativistic ion-atom collisions and the photoelectric effect in hydrogen-like high-Z systems. Physics Rep **439**, 1–99

Fischer D., Støchkel K., Cederquist H., Zettergren H., Reinhed P., Schuch R., Källberg A., Simonsson A. and Schmidt H.T. (2006): Experimental separation of the Thomas charge-transfer process in high-velocity p-He collisions. Phys Rev A **73**, 052713

Flamm L. and Schumann R. (1916): Die Geschwindigkeitsabnahme der α-Strahlen in Materie. Ann Physik **50**, 655

Gallagher J.W., Bransden B.H. and Janev R.K. (1983): Evaluated theoretical cross section data for charge exchange of multiply charged ions with atoms. II. Hydrogen atom-partially stripped ion systems. J Phys Chem Ref Data **12**, 873–890

Gluckstern R.L. (1955): Electron capture and loss by ions in gases. Phys Rev **98**, 1817–1821

Halpern A.M. and Law J. (1975): Full first Born approximation for inner-shell pickup in heavy-ion collisions. Phys Rev A **12**, 1776–1780

Henderson G.H. (1923): Changes in the charge of an alpha-particle passing through matter. Proc Roy Soc A **102**, 496–U14

Horsdal-Pedersen E. (1981): On the two-state approximation for capture. J Phys B **14**, L249–L253

Horsdal-Pedersen E., Cocke C.L. and Stockli M. (1983): Experimental observation of the Thomas peak in high-velocity electron capture by protons from He. Phys Rev Lett **50**, 1910–1913

Horvat V., Watson R.L. and Parameswaran R. (1995): Spectra of l-x-rays from fast highly-charged xe ions traveling in solids. Phys Rev A **51**, 363–373

Inokuti M. (1971): Inelastic collisions of fast charged particles with atoms and molecules – the Bethe theory revisited. Rev Mod Phys **43**, 297–347

Jackson J.D. (1975): *Classical electrodynamics*. John Wiley & Sons, New York

Jackson J.D. and Schiff H. (1953): Electron capture by protons passing through hydrogen. Phys Rev **89**, 359–365

Jakubassa-Amundsen D.H., Höppler R. and Betz H.D. (1984): Radiative electron capture in fast ion-atom collisions. J Phys B **17**, 3943–3949

Janev R.K., Bransden B.H. and Gallagher J.W. (1983): Evaluated theoretical cross section data for charge exchange of multiply charged ions with atoms. I. Hydrogen atom-fully stripped ion systems. J Phys Chem Ref Data **12**, 829–872

Janev R.K. and Gallagher J.W. (1983): Evaluated theoretical cross section data for charge exchange of multiply charged ions with atoms. III. Nonhydrogenic target atoms. J Phys Chem Ref Data **13**, 1199–1249

Janev R.K., Phaneuf R.A. and Hunter H.T. (1988): Recommended cross sections for electron capture and ionization in collisions of C^{q+} and O^{q+} ions with H, He and H_2. Atomic Data Nucl Data Tab **40**, 249–281

Janev R.K., Presnyakov L.P. and Shevelko V.P. (1980): One-electron capture from the inner shells in atom-multicharged ion collisions. Phys Lett A **76**, 121–124

Keene J.P. (1949): Ionization and charge exchange by fast ions of hydrogen and helium. Phil Mag **40**, 369–385

Kienle P., Kleber M., Povh B., Diamond R.M. and Stephens F.S. (1973): Radiative capture and bremsstrahlung of bound electrons induced by heavy ions. Phys Rev Lett **31**, 1099–1102

Killian B.J., Cabrera-Trujillo R., Deumen E. and Öhrn Y. (2004): Resonant charge transfer between H^+ and H from 1 to 5000 eV. J Phys B **37**, 4733–4747

Kleber M. and Jakubassa D.H. (1975): Radiative electron capture in heavy-ion collisions. Nucl Phys A **252**, 152–162

Knudsen H., Haugen H.K. and Hvelplund P. (1981a): Single-electron-capture cross section for medium- and high-velocity, highly charged ions colliding with atoms. Phys Rev A **23**, 597–610

Knudsen H., Haugen H.K. and Hvelplund P. (1981b): Single-electron capture cross section ofr medium- and high-velocity, highly charged ions colliding with atoms. Phys Rev A **23**, 597–610

Knudson A.R., Burghalter P.G. and Nagel D.J. (1974): Vacancy configurations of argon projectile ions in solids. Phys Rev A **10**, 2118–2122

Kobayashi K., Toshima N. and Ishihara T. (1985): Eikonal approximation for proton-helium electron capture processes. Phys Rev A **32**, 1363–1368

Kramer P.J. (1972): Exact calculation of the second-order Born terms for proton-hydrogen electron-transfer collisions. Phys Rev A **6**, 2125–2130

Kumakhov M.A. and Komarov F.F. (1981): *Energy loss and ion ranges in solids*. Gordon and Breach, New York

Landau L.D. and Lifshitz E.M. (1960): *Quantum mechanics. Non-relativistic theory*, vol. 3 of *Course of theoretical physics*. Pergamon Press, Oxford

Lassen N.O. (1951a): Total charges of fission fragments as functions of the pressure in the stopping gas. Mat Fys Medd Dan Vid Selsk **26 no. 12**, 1–19

Lassen N.O. (1951b): The total charges of fission fragments in gaseous and solid stopping media. Mat Fys Medd Dan Vid Selsk **26 no. 5**, 1–28

Lo H.H. and Fite W.L. (1969): Electron-capture and loss cross sections for fast heavy particles passing through gases. Atomic Data **1**, 305–328

Macek J. and Taulbjerg K. (1981): Correction to Z_p/Z_t expansions for electron-capture. Phys Rev Lett **46**, 170–174

Macek J.H. and Shakeshaft R. (1980): Second Born approximation with the Coulomb Green's function: Electron capture from a hydrogenlike ion by a bare ion. Phys Rev A **22**, 1441–1446

McDowell M.R.C. and Coleman J.P. (1970): *Introduction to the theory of ion-atom collisions*. North Holland Publ. Co., Amsterdam

McGuire J.H. and Weaver L. (1977): Independent electron approximation for atomic scattering by heavy particles. Phys Rev A **16**, 41–47

Mittleman M.H. (1964): Relativistic effects in charge transfer. Proc Phys Soc **84**, 453–454

Moiseiwitsch B.L. (1980): Relativistic effects in atomic collisions theory. Adv At Mol Phys **16**, 281–318

Molière G. (1947): Theorie der Streuung schneller geladener Teilchen I. Einzelstreuung am abgeschirmten Coulomb-Feld. Z Naturforsch **2a**, 133–145

Nastasi M., Hirvonen J.K. and Mayer J.W. (1996): *Ion-solid interactions: Fundamentals and applications*. Cambridge University Press, Cambridge

Nikolaev V.S. (1965): Electron capture and loss by fast ions in atomic collisions. Usp Fiz Nauk **85**, 679 – 720. [Engl. Transl. Sov. Phys. Uspekhi 8, 269 - 294 (1965)]

Olson R., Ullrich J. and Schmidt-Boecking H. (1989): Multiple-ionization collision dynamics. Phys Rev A **39**, 5572

Olson R.E. and Salop A. (1977): Charge-transfer and impact-ionization cross sections for fully and partially stripped positive ions colliding with atomic hydrogen. Phys Rev A **17**, 531–541

Olson R.E., Watson R.L., Horvat V. and Zaharakis K.E. (2002): Projectile and target ionization in MeV u(-1) collisions of Xe ions with N-2. J Phys B **35**, 1893–1907

Oppenheimer J.R. (1928): On the quantum theory of the capture of electrons. Phys Rev **31**, 349–356

Raisbeck G. and Yiou F. (1971): Electron capture by 40-, 155-, and 600-MeV protons in thin foils of mylar, Al, Ni, and Ta. Phys Rev A **4**, 1858–1868

Ribe F.L. (1951): Electron-capture cross sections for protons passing through hydrogen gas. Phys Rev **83**, 1217–1225

Rozet J.P., Stephan C. and Vernhet D. (1996): ETACHA: a program for calculating charge states at GANIL energies. Nucl Instrum Methods B **107**, 67–70

Rutherford E. (1924): The capture and loss of electrons by alpha particles. Philos Mag **47**, 277

Ryufuku H. (1982): Ionization, excitation, and charge-transfer for impacts of H^+, Li^{3+}, B^{5+}, C^{6+}, and Si^{14+} ions on atomic-hydrogen. Phys Rev A **25**, 720–736

Sauter F. (1931a): Über den atomaren Photoeffekt bei grosser Härte der anregenden Strahlung. Ann Physik **401**, 217–248

Sauter F. (1931b): Über den atomaren Photoeffekt in der K-Schale nach der relativistischen Wellenmechanik Diracs. Ann Physik **403**, 454–488

Schiff L.I. (1981): *Quantum mechanics*. McGraw-Hill, Auckland

Schlachter A.S., Stearns J.W., Graham W.G., Berkner K.H., Poyle R.V. and Tanis J.A. (1983): Electron capture for fast highly charged ions in gas targets: An empirical scaling rule. Phys Rev A **27**, 3372–3374

Schnopper H.W., Betz H.D., Delvaille J.P., Kalata K. and Sohval A.R. (1972): Evidence fo radiative electron capture by fast, highly stripped heavy ions. Phys Rev Lett **29**, 898–901

Schultz D.R., Reinhold C.O., Olson R.E. and Seely D.G. (1992): Differential cross sections for state-selective electron capture in 25-100-keV proton-helium collisions. Phys Rev A **46**, 275–383

Shakeshaft R. (1979): Relativistic effects in electron capture from a hydrogenlike atom by a fast-moving bare ion. Phys Rev A **20**, 779–786

Shevelko V.P., Rosmej O., Tawara H. and Tolstikhina I.Y. (2004): The target-density effect in electron-capture processes. J Phys B **37**, 201–213

Shevelko V.P., Stohlker T., Tawara H., Tolstikhina I.Y. and Weber G. (2010): Electron capture in intermediate-to-fast heavy ion collisions with neutral atoms. Nucl Instrum Methods B **268**, 2611–2616

Shevelko V.P., Tolstikhina I.Y. and Stöhlker T. (2001): Stripping of fast heavy low-charged ions in gaseous targets. Nucl Instrum Methods B **184**, 295–308

Sommerfeld A. and Schur G. (1930): Über den Photoeffekt in der K-Schale der Atome, insbesondere über die Voreilung der Photoelektronen. Ann Physik **396**, 409–432

Spruch L. (1978): High-impact-velocity forward charge transfer from high-Rydberg states as a classical process. Phys Rev A **18**, 2016–2021

Stobbe M. (1930): Zur Quantenmechanik photoelektrischer Prozesse. Ann Physik **7**, 661–715

Stöhlker T., Kozhuharov C., Mokler P.H., Olson R.E., Stachura Z. and Warczak A. (1992): Single and double electron-capture in collisions of highly ionized decelerated Ge ions with Ne. J Phys B **25**, 4527–4532

Tawara H., Kato T. and Nakai Y. (1985): Cross sections for electron capture and loss for positive ions in collisions with atomic and molecular hydrogen. At Data Nucl Data Tab **32**, 235–303

Thomas L.H. (1927): On the capture of electrons by swiftly moving electrified particles. Proc Roy Soc **114**, 561

Tolstikhina I.Y. and Shevelko V.P. (2013): Collision processes involving heavy many-electron ions interacting with neutral atoms. Physics-Uspekhi **56**, 213–242

Toshima N., Ishihara T. and Eichler J. (1987): Distorted-wave theories for electron capture and the associated high-energy behavior of cross sections. Phys Rev A **36**, 2659–2666

Vogt H., Schuch R., Justitiano E., Schulz M. and Schwab W. (1986): Experimental test of higher-order electron-capture processes in collisions of fast protons with atomic hydrogen. Phys Rev Lett **57**, 2256–2259

Weng M.S., Schinner A., Sharma A. and Sigmund P. (2006): Primary electron spectra from swift heavy-ion impact: Scaling relations and estimates from modified Bohr theory. Europ Phys J D **39**, 209–221

Wentzel G. (1926): Zur Theorie des photoelektrischen Effekts. Z Physik **11**, 574–589

Chapter 3
Charge Exchange: Statistics and Energetics

Abstract This chapter deals with three interrelated topics. In the first part, stochastic theory of charge-state distributions is developed with cross sections for electron capture and loss as well as excitation cross sections and lifetimes as input. This yields general expressions for equilibrium charge fractions as well as transients. The second part addresses the energetics of charge-changing collisions, taking into account electronic binding energies and the momentum of recoiling nuclei. The third part addresses general expressions for mean energy loss and straggling in the presence of charge exchange.

3.1 Introductory Comments

Charge exchange has an influence on energy loss. Firstly, energy is spent in a charge-changing event. This contributes to electronic stopping but is neither explicitly nor implicitly contained in those estimates that have been considered in various chapters of Volume 1. Secondly, the stopping cross section depends on the ion charge. Therefore the energy loss per pathlength will oscillate irregularly around some equilibrium value. This effect may to some degree average out in the mean energy loss, but it definitely contributes to energy-loss straggling. The significance of the effect was pointed out by Bohr (1948), while quantitative predictions and experiments came much later, starting with Vollmer (1974), Efken et al. (1975) and Winterbon (1977).

A special complication which has frequently been left out of theoretical treatments is the influence of excited projectile states on the equilibrium charge state: A projectile may undergo excitation without electron capture or loss. This will, as a first approximation, give rise to a higher cross section for electron loss than that of a projectile in its ground state. Ignoring this feature may result in an incorrect prediction of the equilibrium charge.

P. Sigmund, *Particle Penetration and Radiation Effects Volume 2*,
Springer Series in Solid-State Sciences 179, DOI: 10.1007/978-3-319-05564-0_3,

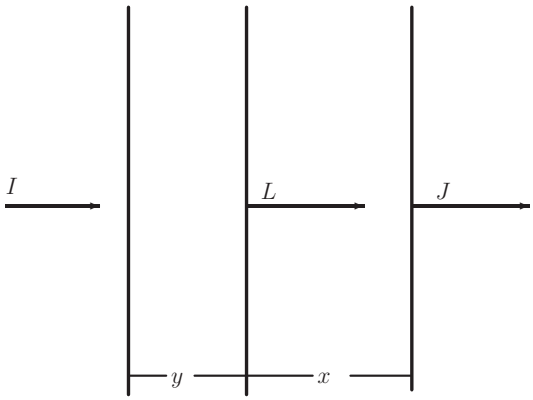

Fig. 3.1 Charge exchange in sandwich target. See text

In the present chapter we shall look first into the statistics of charge-changing events, thereafter energy loss in charge-changing events and, finally, the statistics of energy loss in the presence of charge exchange.

3.2 Statistics of Charge and Excitation States

In this section we shall have a look at statistical relations that govern the evolution of the charge state as an ion travels through a stopping medium. The focus will be on two approaches that are physically equivalent but make use of different mathematical tools. Fundamental equations will invoke occupation probabilities for 'projectile states', but when misunderstanding is unlikely we may also call them 'charge fractions'.

3.2.1 Transition Matrix

Let us start by considering an ion incident on a layer of some homogeneous target material (Fig. 3.1) of thickness $x + y$. This thickness is assumed small enough so that energy loss and angular deflection can be ignored. Let us specify the electronic states of the ion by capital letters $I = 1, 2 \ldots$ which are thought to run over all charge and excitation states. Let $F_{IJ}(x)$ be the probability that a projectile initially in state I be in a state J after penetrating through a layer x.

Assuming statistical independence of events in the two layers shown in Fig. 3.1 we must have

$$F_{IJ}(x + y) = \sum_L F_{IL}(y) F_{LJ}(x). \tag{3.1}$$

This follows from the fundamental laws of multiplication and addition of probabilities.

Equation (3.1) is seen to be a matrix equation. Indeed, if we define a matrix

$$\|F_{IJ}(x)\| = \mathbf{F}(x), \tag{3.2}$$

(3.1) reads

$$\mathbf{F}(x+y) = \mathbf{F}(y)\mathbf{F}(x). \tag{3.3}$$

This equation has the general solution

$$\mathbf{F}(x) = \mathrm{e}^{Nx\mathbf{Q}}, \tag{3.4}$$

where $\mathbf{Q}$ is an arbitrary square matrix with as many rows and columns as there are states contributing to $\mathbf{F}(x)$. The exponential of a matrix is defined in straight analogy to the exponential of a scalar quantity,

$$\mathrm{e}^{Nx\mathbf{Q}} = \sum_{\nu=0}^{\infty} \frac{(Nx\mathbf{Q})^{\nu}}{\nu!}. \tag{3.5}$$

The density N, the number of atoms per volume, has been factorized out since we know already that the proper measure of the layer thickness is the number of atoms per area, Nx.

The explicit form of the matrix $\mathbf{Q}$ is governed by the physics of the process involved. Consider a very thin target so that

$$\mathbf{F}(x) = \mathbf{1} + Nx\mathbf{Q}\ldots \tag{3.6}$$

Truncating the series at the term linear in Nx indicates restriction to the single-collision limit. Now, in that case we can easily write down $F_{IJ}(x)$, which will be given by

$$F_{IJ}(x) = \delta_{IJ}\left(1 - \sum_{L} Nx\sigma_{IL}\right) + Nx\sigma_{IJ}, \tag{3.7}$$

where σ_{IJ} is the cross section for transition from state I to state J in a single collision. The transition $I \rightarrow J$ may represent a capture, loss or excitation of one or more electrons. The first term on the right-hand side in (3.7) represents the probability for penetration through x without any such transition.

Remembering that the unit matrix is given by $\mathbf{1} = ||\delta_{IJ}||$ we deduce

$$Q_{IJ} = \sigma_{IJ} - \delta_{IJ}\sum_{L}\sigma_{IL} \tag{3.8}$$

from (3.6) and (3.7). From this follows

$$\sum_{J} Q_{IJ} = 0 \tag{3.9}$$

for arbitrary I, a relation that will become useful in the following.

This description was proposed by the author (Sigmund, 1992). Apart from the assumptions of negligible energy loss and angular deflection—which could be abandoned if necessary—another, more serious assumption enters the above derivation, the separability of individual collision events. This is not expected to be a problem if the medium is a dilute gas. Whether or not the assumption is problematic for condensed matter can be judged by inspecting pertinent cross sections. If this inspection indicates mean free paths for charge exchange of the order of the interatomic distance, the use of transition probabilities becomes questionable, so that quantal transition amplitudes may have to be considered instead.

The notation introduced in this chapter applies to a number of discrete states, as it would be the case if we only considered charge states. The notation also allows for a finite number of discrete states belonging to one and the same charge state. In practice, the number of such states will be kept small.

3.2.2 Rate Equations

You may recognize that the above derivation and Fig. 3.1 are analogous to the exposition of the Bothe-Landau formula for the energy-loss spectrum in Sect. 9.2.1, Vol. 1. You may also recall that an alternative derivation of the Bothe-Landau formula goes over transport equations, of which there exist forward and backward versions, discussed in Sect. 9.5.2, Vol. 1. You are invited to derive equivalent equations for the charge fractions in Problem 3.1, following a procedure described in Sect. 9.5.1, Vol. 1. Here we shall follow a more direct approach.

Differentiation of (3.4) with respect to x yields

$$\frac{\mathrm{d}\mathbf{F}(x)}{\mathrm{d}x} = N\mathbf{F}(x)\mathbf{Q} = N\mathbf{Q}\mathbf{F}(x). \tag{3.10}$$

When written in components the first identity reads

$$\frac{\mathrm{d}F_{IJ}}{\mathrm{d}x} = N\sum_L \big(F_{IL}\sigma_{LJ} - F_{IJ}\sigma_{JL}\big). \tag{3.11}$$

This represents a set of *rate equations* which are frequently encountered in the literature (Bohr and Lindhard, 1954, Allison, 1958, Betz, 1972). The first term on the right-hand side represents the increase per travelled pathlength in the charge fraction J by transitions from all L to J, whereas the second term reflects the loss from J to all L. You will encounter this type of rate equation wherever you deal with stochastic processes.

The second identity reads

$$\frac{\mathrm{d}F_{IJ}}{\mathrm{d}x} = N\sum_L \sigma_{IL}\big(F_{LJ} - F_{IJ}\big). \tag{3.12}$$

This is the backward form of the rate equation which has only rarely been mentioned in the present context (Sigmund, 1991). Operationally, the forward form (3.11) is most suitable for performing averages over incident states, while averages over final states are conveniently evaluated via the backward equation (3.12).

A major advantage of an approach via rate equations is the option to include an explicit dependence of the cross sections for charge exchange on the beam energy (Burenkov et al., 1992).

3.2.3 Spontaneous Processes

Transitions in the electron structure of the projectile are not necessarily collision-induced: An excited projectile may relax into a lower level by a radiative transition. Moreover, the projectile may undergo charge exchange by an Auger process. While such processes are stochastic, the pertinent variable is real time t rather than path-length $x = vt$.

Spontaneous processes may be included in the statistic description by means of the replacement

$$N x \sigma_{IJ} \rightarrow N v t \sigma_{IJ} + t \Lambda_{IJ} \tag{3.13}$$

and using either t or vt as the independent variable, where Λ_{IJ} denotes a transition probability per unit time.

Equation (3.13) tells you that the relative significance of collision-induced and spontaneous processes depends on the quantity $N v \sigma_{IJ} / \Lambda_{IJ}$. At low density and/or low projectile speed there is time enough between collisions for spontaneous processes to proceed. Thus there will be a good chance that after a collision the projectile will be able to relax into its ground state before the subsequent encounter.

3.2.4 Examples

It has been most common to determine the charge evolution either by numerical solution of the rate equations (3.11) or by Monte Carlo simulation. Direct evaluation of the transition matrix has not been customary except for the two-state case discussed below, even though this method is certainly competitive and perhaps superior, especially with regard to accuracy, necessary programming effort and computing power, as documented by Osmani and Sigmund (2011).

3.2.4.1 The Two-State Case

As a start, consider a system with only two states, $I, J = 1, 2$. Then the matrix $\mathbf{Q}$ reads

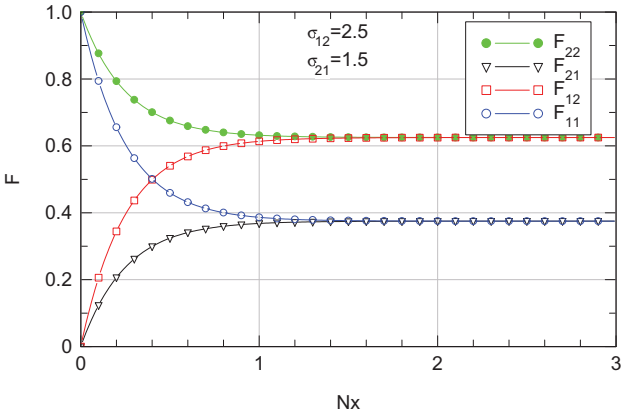

Fig. 3.2 Development of charge fraction F_{IJ} with penetration depth x for two-state system. Arbitrary units, except that the unit of Nx must be the inverse of the unit of the cross section σ_{IJ}. Numerical values of cross sections do not refer to a specific system

$$\mathbf{Q} = \begin{Vmatrix} -\sigma_{12} & \sigma_{12} \\ \sigma_{21} & -\sigma_{21} \end{Vmatrix}. \tag{3.14}$$

Note that diagonal elements σ_{11} and σ_{22}—which are undefined and meaningless—do not enter.

From (3.14) follows

$$\mathbf{Q}^2 = -\sigma\mathbf{Q} \tag{3.15}$$

and, hence,

$$\mathbf{Q}^n = (-\sigma)^{n-1}\mathbf{Q}, \tag{3.16}$$

where

$$\sigma = \sigma_{12} + \sigma_{21}. \tag{3.17}$$

With this the exponential series (3.4) reduces to

$$\mathrm{e}^{Nx\mathbf{Q}} = \mathbf{1} + \frac{\mathbf{Q}}{\sigma}\left(\mathbf{1} - \mathrm{e}^{-Nx\sigma}\right) \tag{3.18}$$

or

$$\|F_{IJ}(x)\| = \frac{1}{\sigma}\begin{Vmatrix} \sigma_{21} & \sigma_{12} \\ \sigma_{21} & \sigma_{12} \end{Vmatrix} + \frac{1}{\sigma}\begin{Vmatrix} \sigma_{12} & -\sigma_{12} \\ -\sigma_{21} & \sigma_{21} \end{Vmatrix}\mathrm{e}^{-Nx\sigma}. \tag{3.19}$$

Here the first term is independent of x and, hence, represents the equilibrium charge fractions

$$F_1 = \frac{\sigma_{21}}{\sigma}; \quad F_2 = \frac{\sigma_{12}}{\sigma}. \tag{3.20}$$

The second term represents the transient behaviour: For $x = 0$ it ensures that $F_{IJ}(0) = \delta_{IJ}$ as it must be. More important, the $1/e$ depth for approaching equilibrium is

$$\Lambda = \frac{1}{N\sigma}. \tag{3.21}$$

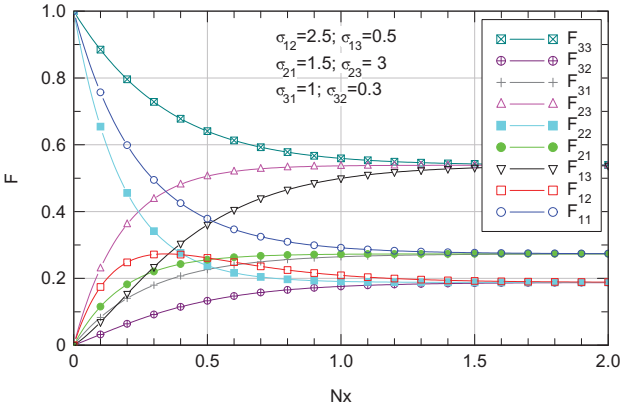

Fig. 3.3 Development of charge fractions F_{IJ} with penetration depth x for three-state system. Arbitrary units, except that the unit of Nx must be the inverse of the unit of the cross section σ_{IJ}. Numerical values of cross sections do not refer to a specific system

Figure 3.2 shows an example. Diagonal elements start at unity for $x = 0$, while off-diagonal elements start at zero. Asymptotic charge fractions are independent of the initial state.

3.2.4.2 More than Two States

Also the three-state system has an algebraic solution. It was derived by Allison (1958) from the rate equation and by the author (Sigmund, 1992) via the matrix method. However, with six free parameters in the general case, that solution is difficult to bring into an illuminating form. Instead we shall have a look at examples.

The matrix $\mathbf{Q}$ reads

$$\mathbf{Q} = \begin{Vmatrix} -\sigma_1 & \sigma_{12} & \sigma_{13} \\ \sigma_{21} & -\sigma_2 & \sigma_{23} \\ \sigma_{31} & \sigma_{32} & -\sigma_3 \end{Vmatrix}, \tag{3.22}$$

where

$$\sigma_1 = \sigma_{12} + \sigma_{13}; \quad \sigma_2 = \sigma_{21} + \sigma_{23}; \quad \sigma_3 = \sigma_{31} + \sigma_{32} \tag{3.23}$$

are the total cross sections for transitions from levels 1, 2 and 3, respectively. Charge fractions have been determined by straight numerical summation of the series (3.4).

Figure 3.3 shows an example. If, for a moment, you only consider $F_{11}(x)$, $F_{13}(x)$, $F_{31}(x)$ and $F_{33}(x)$, you will see essentially Fig. 3.2 apart from quantitative details. However, the intermediate state brings about a new feature: F_{12} develops a maximum as a function of penetration depth. The rapid initial increase is due to the relatively large cross section σ_{12} in conjunction with a small value of σ_{13}, while the subsequent decrease is due to the relatively large value of σ_{23}.

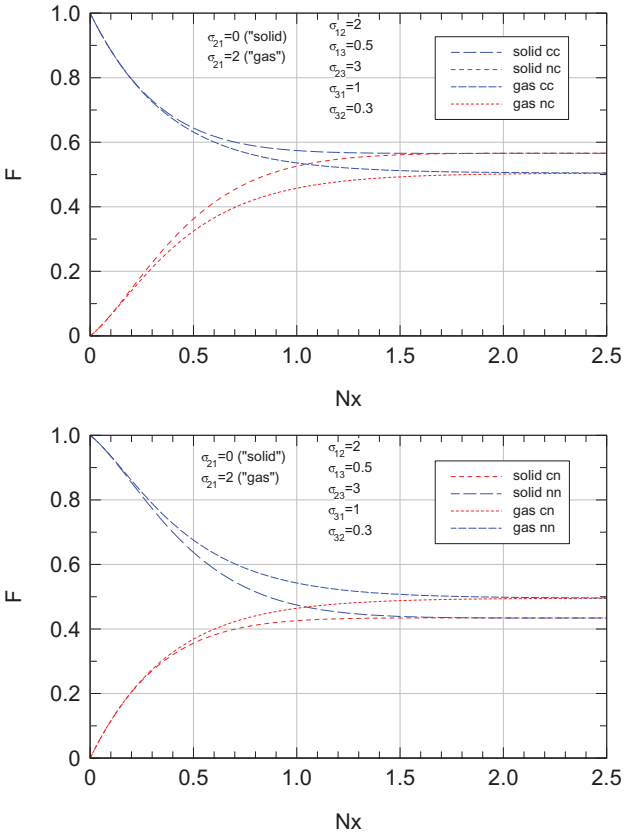

Fig. 3.4 Approach to charge equilibrium in three-state system with two states for the neutral atom. Upper graph: charged component; lower graph: neutral component. See text

Figure 3.4 also shows a three-state system. Explicit numbers do not refer to a specified system, but we may consider 1 to denote the ground state and 2 an excited state of a neutral projectile, while 3 denotes a state where an electron has been lost. The upper graph shows the neutral fractions $nn = F_{11} + F_{12}$ and $cn = F_{31} + F_{32}$ for an initially neutral or charged projectile, respectively, while the lower graph shows the charged fractions $nc = F_{13}$ and $cc = F_{33}$ for an initially neutral or charged particle, respectively. Each of the two graphs shows two sets of input, differing only in one quantity, namely the cross section σ_{21} for decay from the excited state 2 to the neutral ground state 1. The case where this quantity is set to zero (thick lines) is referred to as 'solid', with reference to the model by Bohr and Lindhard (1954) to be discussed below. The case where it is nonvanishing (thin lines) is referred to as 'gas'. At present we just note that the presence of an intermediate state affects both the transient behaviour and the equilibrium charge. It is seen that the equilibrium charge increases when deexcitation of the excited state is forbidden.

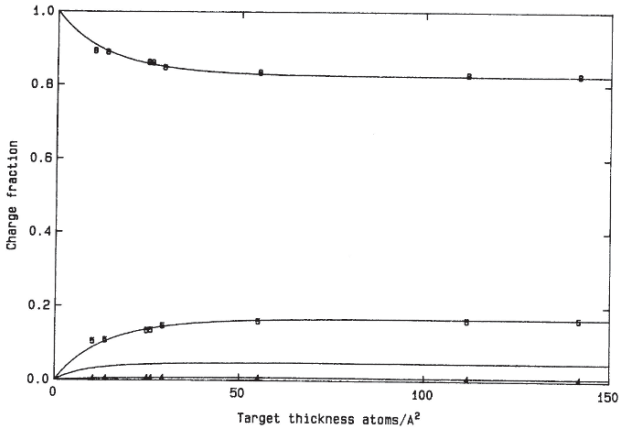

Fig. 3.5 Measured charge fractions C^{6+}, C^{5+} and C^{4+} (top to bottom) versus target thickness for incident C^{6+} ions at 3.0 MeV/u. The solid line without data point shows the fraction of C^{5+} ions in an excited state. From Read (1984)

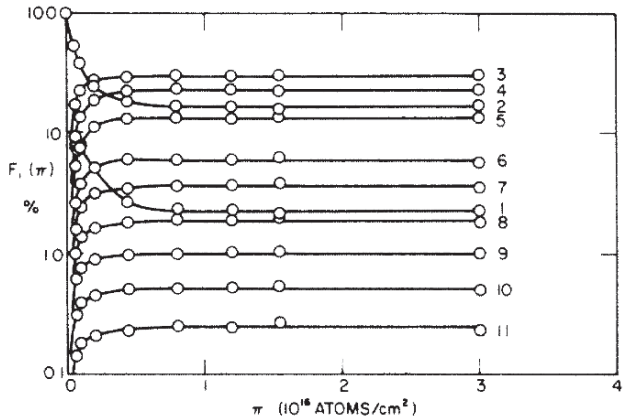

Fig. 3.6 Measured charge fractions for 6.0 MeV I^{2+} ions in argon. The abscissa variable is $\pi = Nx$. From Ryding et al. (1969)

Figure 3.5 shows the development of charge states for incident C^{6+} ions. The theoretical analysis is based on four states. While the fraction of C^{4+} is found to be negligible, the fraction of excited C^{5+} ions is found to be significant.

Figure 3.6 shows an example of measured charge fractions as a function of penetrated pathlength for 11 charge states of iodine ions in argon. The incident charge is $q = 2$. Consequently, F_2 decreases monotonically, while F_1 goes through a maximum but decreases even more rapidly thereafter. Neutrals are not recorded, while even F_{11} accounts for ~ 2 pct. in equilibrium.

3.2.5 Eigenvalue Expansion ★

According to elementary calculus, solutions of linear differential equations with constant coefficients can be expressed in terms of exponentials. In the present context this implies that the matrix (3.4) can be written as

$$\mathbf{F}(x) = \sum_{\nu} \mathbf{F}^{(\nu)} \mathrm{e}^{Nxq^{(\nu)}}, \tag{3.24}$$

where $q^{(\nu)}$ is an eigenvalue to $\mathbf{Q}$,

$$\mathbf{Q}\Phi^{(\nu)} = q^{(\nu)}\Phi^{(\nu)}. \tag{3.25}$$

The number of terms in the sum (3.24) is equal to the number of states. One can prove (Sigmund, 1992) that one of the eigenvalues $q^{(\nu)}$, say $q^{(0)}$ is vanishing, while the others are negative. Thus, the matrix $\mathbf{F}^{(0)}$ contains the equilibrium charge fractions, while the others determine the approach to equilibrium.

Equation (3.24) assumes all eigenvalues to be different, i.e., no degeneracy. In case of degeneracy, exponentials get multiplied by polynomials of first or higher order, dependent on the degree of degeneracy.

The Laplace transform $\mathbf{f}(s)$ of $\mathbf{F}(x)$ reads

$$\mathbf{f}(s) = \int_0^\infty \mathrm{d}x\, \mathrm{e}^{-sx}\, \mathbf{F}(x) = \sum_{\nu} \frac{\mathbf{F}^{(\nu)}}{s - Nq^{(\nu)}} \tag{3.26}$$

according to (3.24), or

$$\mathbf{f}(s) = \frac{1}{s\mathbf{1} - N\mathbf{Q}} \tag{3.27}$$

according to (3.4). Thus, charge fractions may be determined from the residues of the poles of the matrix (3.27).

For many applications the very existence of the above expansion is helpful even when none or not all of the coefficients $\mathbf{F}^{(\nu)}$ are evaluated explicitly (Sigmund, 1992, 1994).

Equation (3.19) represents an example of (3.24).

3.3 Charge Equilibrium

Both the two-state and the three-state case show that with increasing depth x, average charge fractions approach an asymptotic value, the *equilibrium charge fraction* which is independent of the initial charge state. This is a much more general result. Abbreviating $F_{IJ}(\infty) = F_J$ we may write (3.11) in the limit of large x,

$$\frac{\mathrm{d}F_J}{\mathrm{d}x} = N \sum_L \left(F_L \sigma_{LJ} - F_J \sigma_{JL}\right) = 0. \tag{3.28}$$

In other words, in an equilibrated beam, the number of ions per time or pathlength being fed into a state J is equal to the number of those lost from that state,

$$\sum_L F_L \sigma_{LJ} = F_J \sum_L \sigma_{JL}. \tag{3.29}$$

The sum over all states is important here. Except in special cases, e.g. for a two-state system, detailed balancing does not hold,

$$F_L \sigma_{LJ} \neq F_J \sigma_{JL}, \tag{3.30}$$

as you may prove in Problem 3.2.

3.3.1 Continuum Approximation ⋆

Bohr and Lindhard (1954) found an elegant procedure to determine charge distributions for heavy ions by assuming the number of charge states involved to be large enough so that a continuum description may be justified. Only one state is involved for each ion charge q, called $F_q(x)$ in the following, so that

$$\sum_q F_q(x) = 1. \tag{3.31}$$

We also need the average charge

$$F^{(1)}(x) = \sum_q q F_q(x) \tag{3.32}$$

and the square average

$$F^{(2)}(x) = \sum_q q^2 F_q(x). \tag{3.33}$$

Cross sections for charge exchange are denoted as

$$\sigma_{\Delta q}(q). \tag{3.34}$$

For $\Delta q < 0$ we deal with a capture cross section, while loss cross sections refer to $\Delta q > 0$. Evidently, this notation allows for multiple loss and capture events.

We may derive a rate equation for $F_q(x)$ from (3.11) by dropping the index I and substituting $J \to q$,

$$\frac{\mathrm{d}F_q}{\mathrm{d}x} = N \sum_{\Delta q} \left[F_{q-\Delta q}\sigma_{\Delta q}(q-\Delta q) - F_q \sigma_{\Delta q}(q) \right]. \tag{3.35}$$

Multiplying by q and summing over q then yields

$$\frac{\mathrm{d}F^{(1)}}{\mathrm{d}x} = N \sum_{q,\Delta q} \Delta q F_q \sigma_{\Delta q}(q). \tag{3.36}$$

Now, assume cross sections to vary slowly with the ion charge, so that

$$\sigma_{\Delta q} \simeq \sigma_{\Delta q}(q_{\mathrm{equ}}) + (q - q_{\mathrm{equ}})\sigma'_{\Delta q}(q_{\mathrm{equ}}), \tag{3.37}$$

where q_{equ} is the mean equilibrium charge at the beam velocity under consideration. With this, (3.36) reduces to

$$\frac{\mathrm{d}F^{(1)}}{\mathrm{d}x} = N(F^{(1)} - q_{\mathrm{equ}}) \sum_{\Delta q} \Delta q \sigma'_{\Delta q}(q_{\mathrm{equ}}) + N \sum_{\Delta q} \Delta q \sigma_{\Delta q}(q_{\mathrm{equ}}). \tag{3.38}$$

Now, in charge equilibrium we have $F^{(1)}(x) \equiv q_{\mathrm{equ}}$, so that both the term on the left-hand side and the first term on the right-hand side must vanish. This implies that also the second term on the right-hand side must vanish,

$$\sum_{\Delta q} \Delta q \sigma_{\Delta q}(q_{\mathrm{equ}}) = 0. \tag{3.39}$$

This relation determines the equilibrium charge. In the special case when only single-electron processes are allowed, equilibrium is defined by the cross-over of the cross sections for capture and loss. Using (3.39) we may write (3.38) in the form

$$\frac{\mathrm{d}}{\mathrm{d}x}(F^{(1)} - q_{\mathrm{equ}}) = -\frac{1}{\lambda}(F^{(1)} - q_{\mathrm{equ}}), \tag{3.40}$$

where

$$\frac{1}{\lambda} = -N \sum_{\Delta q} \Delta q \sigma'_{\Delta q}(q_{\mathrm{equ}}) \tag{3.41}$$

defines the approach to equilibrium. Then,

$$F^{(1)}(x) = q_{\mathrm{equ}} + \left[F^{(1)}(0) - q_{\mathrm{equ}} \right] \mathrm{e}^{-x/\lambda}. \tag{3.42}$$

Going back to (3.35), multiplying by q^2 and summing over q we find an equivalent relation for $F^{(2)}(x)$,

$$\frac{\mathrm{d}F^{(2)}}{\mathrm{d}x} = N \sum_{q,\Delta q} F_q \sigma_{\Delta q}(q) \left[2q\Delta q + \Delta q^2 \right]. \tag{3.43}$$

After approximating the cross sections by (3.37), you will arrive at a relation which, on the right-hand side, contains terms with both $F^{(2)}$, $F^{(1)}$ and $F_0 = 1$. This relation becomes more compact after going over to the variance

$$M_2(x) = F^{(2)}(x) - \left[F^{(1)}(x)\right]^2, \tag{3.44}$$

where it reduces to

$$\frac{\mathrm{d}M_2}{\mathrm{d}x} = -\frac{2}{\lambda}M_2 + N\left[F^{(1)} - q_{\mathrm{equ}}\right]\sum_{\Delta q}\Delta q^2\sigma'_{\Delta q}(q_{\mathrm{equ}}) + N\sum_{\Delta q}\Delta q^2\sigma_{\Delta q}(q_{\mathrm{equ}})\,. \tag{3.45}$$

Now, in charge equilibrium the term on the left-hand side as well as the second term on the right-hand side must vanish, so that

$$M_{2,\mathrm{equ}} = \frac{N\lambda}{2}\sum_{\Delta q}\Delta q^2\sigma_{\Delta q}(q_{\mathrm{equ}}). \tag{3.46}$$

This defines the width of the charge-state distribution in equilibrium.

3.3.2 Gaussian Apparoximation

From the mean charge and its variance one may construct a gaussian charge distribution. Numerous measurements have confirmed the approximately gaussian shape of equilibrium charge distributions Nikolaev (1965), Betz (1972). From an extensive discussion in Chap. 9, Vol. 1, you may recall that Bothe-Landau-type profiles approach gaussians with increasing pathlength.

However, exceptions have been found. Figure 3.7 shows equilibrium charge distributions for bromine ions in carbon at two different energies. An almost perfectly gaussian profile is found at 100 MeV, while a significantly steeper decrease at the high-charge end is observed for 140 MeV. The explanation offered by the authors is based on the fact that a major drop is found from charge state 25 to 26. Since $Z_1 = 35$ for bromine, this implies that a Br^{25+} ion has a filled L shell, while for $q = 26$ a hole in the L shell must be created which has a much higher binding energy than M electrons and, hence, a lower loss cross section. Clearly, a proper description of this feature goes beyond the continuum model: The assumption of a linear dependence of capture and loss cross section on the ion charge is incompatible with a sudden drop of the loss cross section.

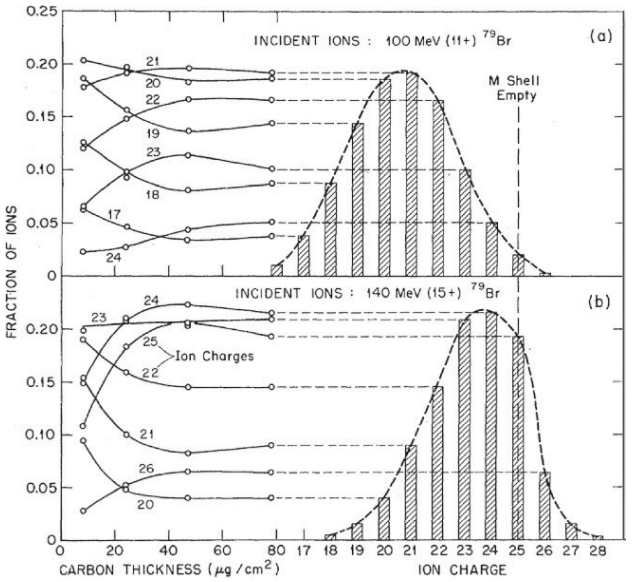

Fig. 3.7 Charge fractions of 100 MeV (upper graph) and 140 MeV (lower graph) bromine ions in carbon as a function of travelled pathlength and profiles (left) and equilibrium distributions (right). Incident charge states were 11 and 15, respectively. From Moak et al. (1967)

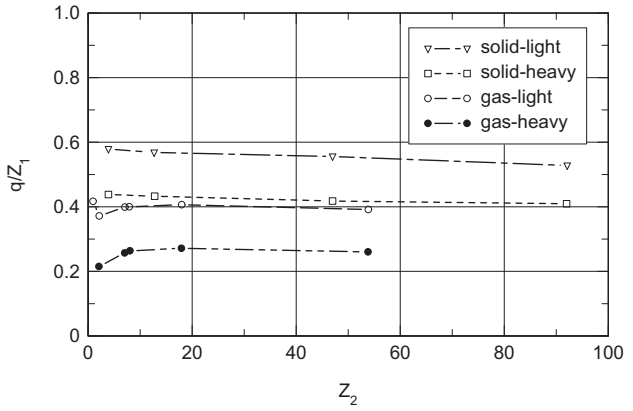

Fig. 3.8 Mean charge fractions of fission fragments penetrating through gaseous targets and emerging from solid targets vs. atomic number Z_2. Data from Lassen (1951b)

3.3.3 Gas-Solid Difference

3.3.3.1 Lassen's Measurements

Even though the two graphs in Fig. 1.21 do not refer to the same abscissa scale, it is evident that mean charge fractions are higher in the lower graph than in the upper

one. This is in accordance with observations by Lassen (1951b) shown in Figs. 1.1 and 1.19.

Lassen also noted that the sign of the gas-solid difference is inverted from the light to the heavy fragment. However, from the scaling rules discussed in Chap. 1 we know that comparison with theory ought to go via charge fractions rather than absolute charges. Thus, when the same data are plotted as charge fractions (Fig. 3.8), the sign of the gas-solid difference is the same for the light and the heavy fragment.

While differences between light and heavy fragments may be ascribed to different velocities (Problem 1.7), the gas-solid difference is clearly outside the scatter which you may expect according to Fig. 1.21.

The increase of the mean equilibrium charge in gases with increasing pressure shown in Fig. 1.19 is much weaker than the gas-solid effect and, with the exception of measurements on hydrogen gas, barely outside experimental accuracy. Nevertheless the effect was considered real and, as you will see below, its existence was confirmed in subsequent studies.

3.3.3.2 Analysis by Bohr & Lindhard

While there is a number of potential reasons for observing a gas-solid difference, the observation of a pressure dependence in experiments on gas targets, referred to in Fig. 1.19 appears to point at a density effect as the prime candidate for an explanation.

A thorough analysis by Bohr and Lindhard (1954), based on their solution of rate equations discussed in Sect. 3.3.1 as well as simple estimates of capture and loss cross sections, showed reasonable absolute agreement with measured equilibrium charge states of fission fragments in gases by Lassen (1951b,a). Their version of the rate equations, which considers only one projectile state for each ion charge, assumes that at a given velocity, cross sections for capture and loss only depend on the ion charge and not on the detailed electron structure. In other words, if an ion has undergone a collision ending up in an excited state, it will have time enough to relax into its ground state by a radiative transition before the next collision. The degree to which this condition is satisfied will typically depend on the density of the target medium.

Bohr & Lindhard argued that with increasing gas pressure, an increasing fraction of the penetrating ions will not have time to decay into their ground states between collisions and hence be in an excited state. This will cause an increase in the effective cross section for electron loss and thus a shift of the equilibrium between capture and loss processes toward higher charge states. This explanation appeared particularly plausible because the effect was more pronounced in hydrogen than in helium and argon gas: Excited states in hydrogen lie relatively close to the continuum, while excited states in heavier atoms are distributed more uniformly.

Bohr & Lindhard asserted that similar considerations apply to the gas-solid difference reported by Lassen (1951b), although they emphasized the complexity of the phenomenon. In particular, they pointed out that highly excited ions emerging

from a solid may emit electrons and thus end up in a higher charge state before hitting the detecting device.

3.3.3.3 Further Development

The gas-solid difference in charge state received increased interest when monoenergetic, mass- and charge-separated heavy-ion beams became available at tandem accelerators (cf. Sect. 1.3.1, Vol. 1). Particular interest was paid to a seeming paradox: From the fact that the stopping cross section for a point charge $Z_1 e$ is proportional to Z_1^2, one expected an approximate q_1^2 dependence of the stopping cross section for a heavy ion on its charge $q_1 e$. Thus, a noticeable gas-solid difference in the equilibrium ion charge would result in an even more pronounced gas-solid difference in equilibrium stopping. Such a difference was not found in a thorough and extensive experimental study by Pierce and Blann (1968). We shall come back to this aspect in Chap. 4. At this point, let us just look at a few more measurements on charge states.

Figure 3.9 shows charge fractions measured by Ryding et al. (1970) as a function of target thickness for chlorine ions in hydrogen. Pertinent cross sections for electron capture and loss were determined by fitting the low-thickness portion of the measured charge fractions to the rate equations (3.11). The obtained fit was found only to describe the measured dependence over a limited thickness interval.

The analysis was then repeated with density-dependent cross sections by dividing up the interval covered by measurements into six overlapping regimes, each assuming density-independent cross sections. These regimes are indicated in the graph. The resulting effective cross sections are shown in the lower graph. A weak increase of the effective ionization cross section is found, in agreement with the expectation of Bohr and Lindhard (1954), but a more pronounced decrease of the capture cross section.

While one could possibly argue for a decreased capture cross section for ions penetrating solids, Betz and Grodzins (1970) asserted that electron emission after emergence from the target, mentioned by Bohr and Lindhard (1954) as an additional process, was actually the dominating one. This was a plausible way to explain the seeming absence of a gas-solid difference in stopping cross section mentioned above. Since electron emission by highly excited ions proceeds via Auger electrons, this explanation implies that a number of Auger electrons equivalent with the gas-solid difference in charge state would have to be detectable near the exit point. In an experiment with 125 Br ions in carbon, Schramm and Betz (1992) found less than one Auger electron per incident ion. This is much less than required to confirm the assertion of Betz and Grodzins (1970).

The question of whether the loss or the capture cross section has the dominating influence on the density effect and/or the gas-solid effect is unresolved and still a matter of discussion. Figure 3.10 shows experimental results from measurements with singly-charged or bare Ni ions at very high beam velocities. Notice in particular that measurements were performed on both solid and gaseous methane. No evidence

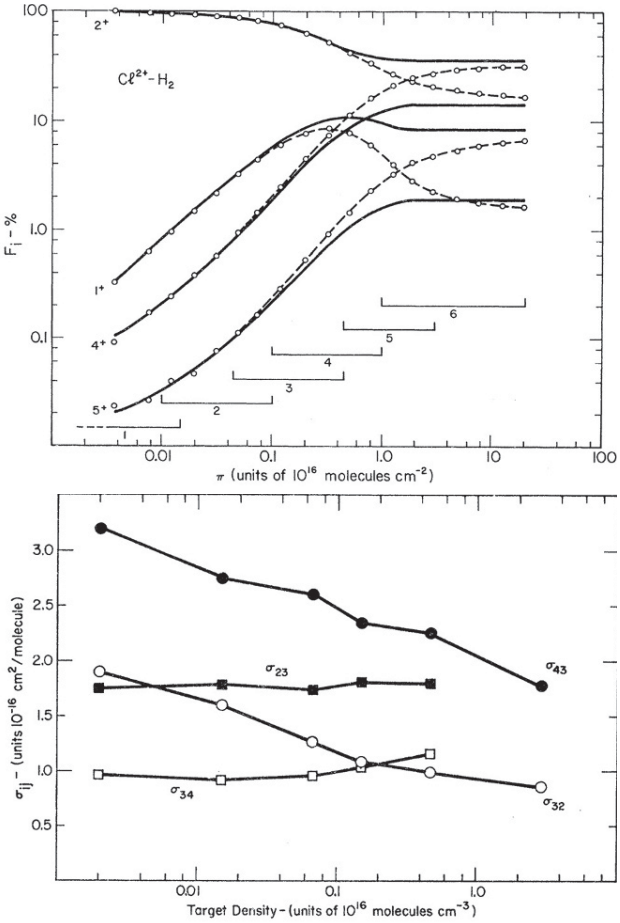

Fig. 3.9 Upper graph: Charge fractions of 4 MeV incident Cl^{2+} ions in hydrogen as a function of target thickness. Circles: Measurements. Solid lines: Based on rate equations and measurements at low thicknesses assuming cross sections independent of target density. The measured mean equilibrium charge is 3.24. Lower graph: Extracted capture cross sections σ_{32}, σ_{43} and loss cross sections σ_{23}, σ_{34}. From Ryding et al. (1970)

was found for a gas-solid difference in the capture cross sections, while a $\sim$ 40 pct. difference was found for the loss cross section.

3.3.3.4 Limits of Classical Statistics

An aspect to be mentioned here is the question to what extent the rate equations derived in Sect. 3.2.2 can provide a valid statistical description of the evolution of charge states. The Chapman-Kolmogorov relation (3.1) rests on the assumption that

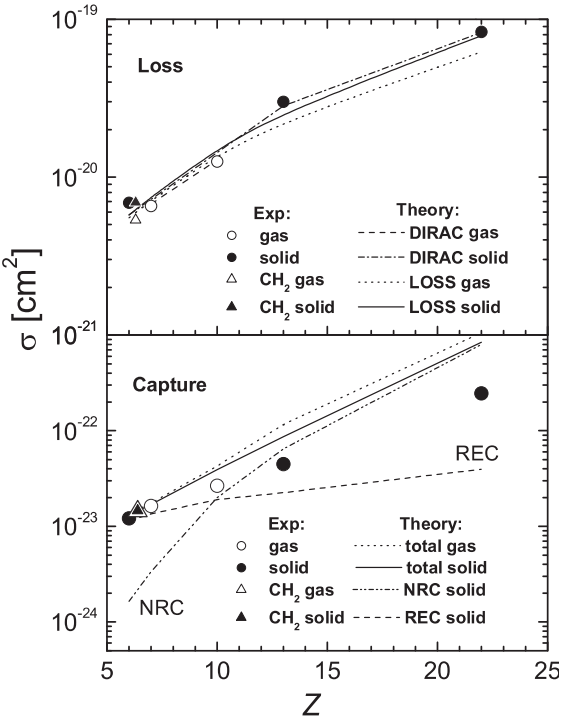

Fig. 3.10 Effective loss and capture cross sections of gases and solids for 200 MeV/u Ni^{27+} and Ni^{28+} ions, respectively. Points: Measured under single-collision conditions by Ogawa et al. (2007). Lines: Calculated for loss (Surzhykov et al., 2005, Shevelko et al., 2001) and capture (Surzhykov et al., 2005, Shevelko et al., 2004). From Ogawa et al. (2007)

events in the two layers depicted in Fig. 3.1 are separable and independent of each other. This is not necessarily true when the layer thickness approaches atomic dimensions. The point becomes even clearer when you look at the derivation of the rate equations, (3.11) and (3.12), where it is explicitly assumed that transitions from one state to another can be separated into distinct (typically atomic) interactions.

A proper quantal description considers the superposition of transition *amplitudes* instead of probabilities or cross sections. As a rough guidance we may expect a description in terms of cross sections to be valid whenever the pertinent events are well separated in space, i.e., if the mean free path for charge-changing events,

$$\lambda_{\text{chex}} = \frac{1}{N \sum_J \sigma_{IJ}} \tag{3.47}$$

is large compared to the interatomic distance D of the medium.

Methods of treating the problem when a quantal description appears indicated have been explored in the literature. Arbó et al. (1999) and Reinhold et al. (2000) considered transitions in swift one-electron atoms without charge exchange by a quantal Langevin equation for relativistic protons and for 13.6 MeV/u Ar^{17+} ions, respectively. The latter calculations refer to measurements of the excitation state of emitted emerging ions.

3.4 Energetics of Charge Exchange ⋆

In addition to cross sections for electron capture and loss we shall also be interested in the energy balance of these events. After all, if an electron is captured in a collision between a swift ion and a stationary target atom, the electron will, in addition to its orbital motion, be superimposed a translational motion along with the ion. Conversely, in case of electron loss, the binding energy will have to be provided. The pertinent source of energy is, by and large, the kinetic energy of the projectile.

You may be tempted to estimate the energy loss in a capture event as

$$T = \frac{1}{2}mv^2 + U_2 - U_1, \tag{3.48}$$

where the first term denotes the energy necessary to accelerate a target electron to the beam velocity, the second term denotes the energy necessary to remove the electron from the target, while the third term denotes the energy released upon capture. However, electron capture is not necessarily an isolated event and may have to be considered along with the recoiling energy of the nucleus as well as simultaneous excitation processes in the target and/or projectile atom.

You may also try to write down an intuitive relation for energy loss in an electron-loss event, but I like to issue a warning already now, because it may quite well happen that you end up with a wrong result.

In the following we therefore shall consider the energetics from first principles. You may wish to glance over this section in your first reading, but I don't encourage you to skip it completely.

3.4.1 Definitions

If the projectile carries electrons, it has internal energy and centre-of-mass energy. If it is exposed to an external electric or magnetic field, also considerations regarding potential energy may become of interest. Leaving out the latter possibility, we still need to define what we mean by *energy loss*. As we shall see now, the proper definition depends on the quantity measured.

The situation is straightforward in an atomic-collision experiment in a dilute gas target, where single collisions prevail. Assuming the collision partners to be in their ground states initially, the difference between the translational energies before and after the collision—which is independent of the chosen reference frame—will be denoted inelastic energy loss Q in the absence of electron loss.

Numerous phenomena in radiation physics are related to the energy deposited in the stopping medium. In that case, a fundamental quantity is potential and kinetic energy transferred to the constituents of the target.

The signal in a stopping measurement is most often provided by the projectile, although exceptions exist, such as thermometric measurements of the type discussed

in Sect. 7.4.2 of volume 1. Now, the energy of an ion depends on the number of electrons carried by the projectile and their excitation states. This quantity will vary stochastically both upward and downward. It is, therefore, not a suitable parameter to characterize stopping, where energy *loss* is expected to dominate over energy gain.

Instead, the *change in projectile velocity* will be utilized to characterize energy loss (Sigmund and Glazov, 1998, 2003). This does not prevent us from using conventional energy units. After all, the energy loss per atomic mass unit—the key parameter in most tabulations—is a measure of velocity degradation. In practice we shall operate with the quantity $M_1\Delta(v^2/2)$, where M_1 is the *initial mass of the projectile ion*, i.e., the mass of the nucleus and all electrons.

In other words, except for relativistic corrections, energy loss in a single collision event will be defined as

$$T = \frac{M_1}{2}\left(v_1^2 - {v_1'}^2\right), \tag{3.49}$$

where v_1 and v_1' are the initial and final projectile speeds, respectively, even in case of charge exchange, where the final projectile mass will differ from M_1.

3.4.2 Electron Capture: One Dimension

Consider a rather simple case first. For resonance charge transfer between like atoms, $Z_1 = Z_2$ and $M_1 = M_2$, the internal energy does not change. Let us restrict ourselves for a moment to one dimension. Then, conservation laws read

$$M_1 v_1 = (M_1 + m)v_1' + (M_2 - m)v_2' \tag{3.50}$$

$$\frac{1}{2}M_1 v_1^2 = \frac{1}{2}(M_1 + m){v_1'}^2 + \frac{1}{2}(M_2 - m){v_2'}^2, \tag{3.51}$$

where v_1 and v_1' denote the projectile velocity before and after the collision, respectively, and $v_2 = 0$ and v_2' those of the recoiling target atom. You may remember from Sect. 2.2 that the target atom plays a central role in the energy-momentum balance.

In Problem 3.3 you are invited to derive the following solutions of (3.50) and (3.51), still for $M_2 = M_1$,

$$v_1' = \frac{v_1}{1 + m/2M_1} \tag{3.52}$$

or, for $m \ll M_1$,

$$M_1(v_1 - v_1') = \frac{mv_1}{2}. \tag{3.53}$$

From this you find

$$T = \frac{M_1}{2}\left(v_1^2 - {v_1'}^2\right) = \frac{m}{2}v_1^2. \tag{3.54}$$

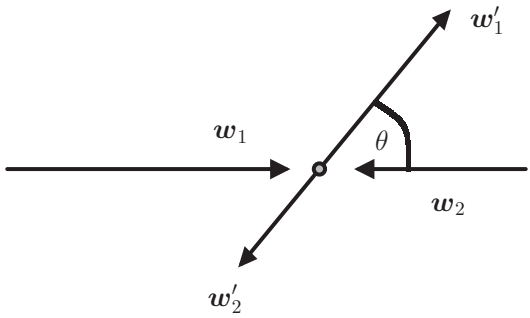

Fig. 3.11 Inelastic collision viewed in the centre-of-mass frame of reference

Consider now the case of nonresonant charge exchange. While the momentum equation (3.50) does not change, energy conservation now requires

$$\frac{1}{2}M_1 v_1^2 - U_2 = \frac{1}{2}(M_1 + m)v_1'^2 - U_1 + \frac{1}{2}(M_2 - m)v_2'^2, \tag{3.55}$$

where U_2 and U_1 are the binding energies of the captured electron in its initial and final state, respectively.

By solving Problem 3.4 you will derive that now

$$T = \frac{1}{2}\left(v_1^2 - v_1'^2\right) = \frac{1}{2}mv_1^2 + U_2 - U_1 \tag{3.56}$$

for $m \ll M_1, M_2$, in agreement with (3.48).

3.4.3 Planar Collision: Excitation only

As a preliminary exercise for a three-dimensional inelastic collision, consider the interaction between two heavy particles leading to electronic excitation of either or both collision partners but without charge exchange or electron loss. Defining velocities $\boldsymbol{w}_1, \boldsymbol{w}_2$ in the centre-of mass system (Fig. 3.11) by

$$\boldsymbol{w}_1 = \boldsymbol{v}_1 - \boldsymbol{V}; \quad \boldsymbol{w}_2 = -\boldsymbol{V} \tag{3.57}$$

with $\boldsymbol{V} = M_1\boldsymbol{v}_1/(M_1 + M_2)$, we may write conservation laws in the form

$$M_1\boldsymbol{w}_1 + M_2\boldsymbol{w}_2 = M_1\boldsymbol{w}_1' + M_2\boldsymbol{w}_2' = 0 \tag{3.58}$$

and

$$\frac{1}{2}M_1 w_1^2 + \frac{1}{2}M_2 w_2^2 = \frac{1}{2}M_1 w_1'^2 + \frac{1}{2}M_2 w_2'^2 + Q \tag{3.59}$$

where $\boldsymbol{w}_1'$ and $\boldsymbol{w}_2'$ are velocities after the collision and Q is the sum of the excitation energies of target and projectile. Eliminating $\boldsymbol{w}_2$ and $\boldsymbol{w}_2'$ you find

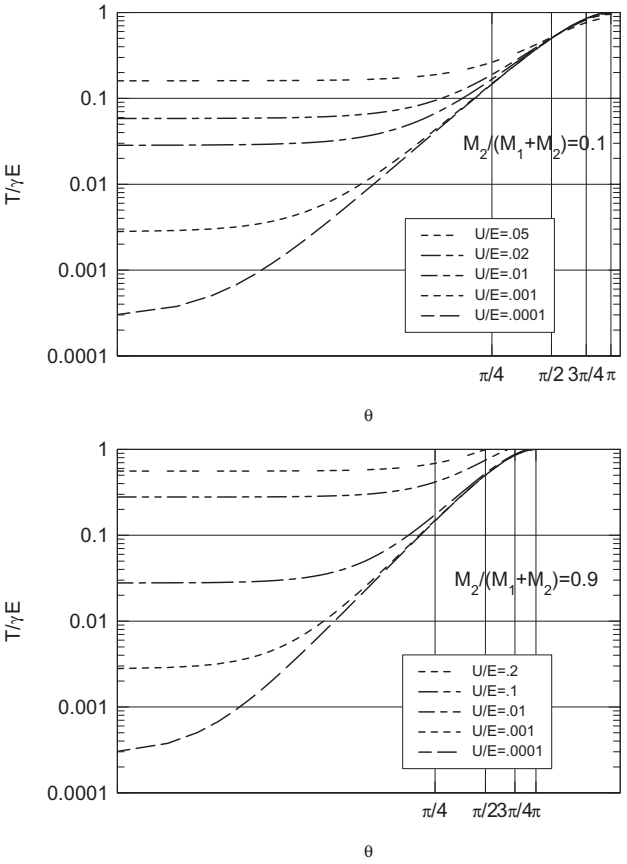

Fig. 3.12 Energy transfer T in inelastic collision without ionization of either target or projectile. See text

$$w_1'^{\,2} = w_1^2 - \frac{2M_2 Q}{M_1(M_1 + M_2)}. \tag{3.60}$$

Setting

$$\boldsymbol{w}_1' = \left(w_1' \cos\theta, w_1' \sin\theta\right) \tag{3.61}$$

you find

$$\begin{aligned} T &= \frac{M_1}{2}\left(v_1^2 - v_1'^{\,2}\right) \\ &= \frac{1}{2}\gamma E\left(1 - \cos\theta\sqrt{1 - \left(1 + \frac{M_1}{M_2}\right)\frac{Q}{E}}\right) + \frac{M_2 Q}{M_1 + M_2}, \end{aligned} \tag{3.62}$$

where

$$E = \frac{M_1}{2} v_1^2 \tag{3.63}$$

and

$$\gamma = \frac{4 M_1 M_2}{(M_1 + M_2)^2}. \tag{3.64}$$

Examples are shown in Fig. 3.12.

For swift ions we may expand the square root to first order in Q. Then,

$$T = \gamma E \sin^2 \frac{\theta}{2} + \left(1 - \frac{2M_1}{M_1 + M_2} \sin^2 \frac{\theta}{2}\right) Q. \tag{3.65}$$

In the limit of soft collisions, where θ is small, T reduces to the excitation energy Q. Keep in mind, however, that Q is not a constant but is correlated with θ via the impact parameter.

3.4.4 Planar Collision: Electron Capture

Consider now electron capture in two dimensions. In the centre-of-mass frame of reference, conservation laws now read

$$M_1 \boldsymbol{w}_1 + M_2 \boldsymbol{w}_2 = (M_1 + m)\boldsymbol{w}_1' + (M_2 - m)\boldsymbol{w}_2' = 0 \tag{3.66}$$

and

$$\frac{1}{2} M_1 w_1^2 + \frac{1}{2} M_2 w_2^2 - U_2 = \frac{1}{2}(M_1 + m) w_1'^2 + \frac{1}{2}(M_2 - m) w_2'^2 - U_1 + Q. \tag{3.67}$$

It is assumed here that only one electron is captured, but additional excitation in the target and/or projectile is accounted for via an excitation energy Q.

Going through the same procedure as above, expanding up to the first power in m/M, U_i/E and Q/E you arrive at

$$T = \gamma E \sin^2 \frac{\theta}{2} + \left(1 - \frac{2M_1}{M_1 + M_2} \sin^2 \frac{\theta}{2}\right) \left(\frac{1}{2} m v_1^2 + U_2 - U_1 + Q\right). \tag{3.68}$$

This relation is similar to (3.65). Note in particular that (3.56) from the linear model is reproduced in the limit of $\theta = 0$, apart from the excitation energy Q which was neglected there. Multielectron capture processes could be treated similarly.

3.4.5 Three-dimensional Collision: Electron Loss

Before discussing the above results, let us also look at the case of electron loss from the projectile (Fig. 3.13). Here, conservation laws read

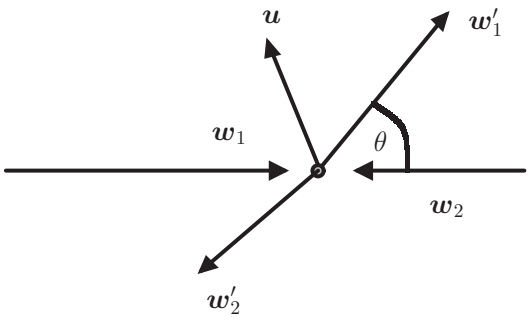

Fig. 3.13 Electron-loss collision viewed in the centre-of-mass frame of reference

$$M_1\boldsymbol{w}_1 + M_2\boldsymbol{w}_2 = (M_1 - m)\boldsymbol{w}_1' + M_2\boldsymbol{w}_2' + m\boldsymbol{u} = 0 \tag{3.69}$$

and

$$\frac{1}{2}M_1 w_1^2 + \frac{1}{2}M_2 w_2^2 = \frac{1}{2}(M_1 - m){w_1'}^2 + \frac{1}{2}M_2 {w_2'}^2 + \frac{1}{2}mu^2 + U_1, \tag{3.70}$$

where $\boldsymbol{u}$ is the velocity of a liberated electron in the centre-of-mass frame of reference and U_1 its binding energy.

After eliminating $\boldsymbol{w}_2$ and $\boldsymbol{w}_2'$ and omitting terms of higher than first order in m/M and U/E, you arrive at an equation equivalent with (3.59) but with Q replaced by

$$Q \to U_1 + \frac{m}{2}\left(\boldsymbol{u} + \frac{M_1}{M_2}\boldsymbol{w}_1\right)^2 - \frac{m}{2}\left(1 + \frac{M_1}{M_2}\right)^2 w_1^2 \tag{3.71}$$

or

$$Q \to U_1 + \frac{m}{2}(\boldsymbol{u} + \boldsymbol{V})^2 - \frac{m}{2}v_1^2. \tag{3.72}$$

Introducing the velocity $\boldsymbol{v}_\mathrm{e}$ of the liberated electron in the laboratory frame of reference,

$$\boldsymbol{v}_\mathrm{e} = \boldsymbol{u} + \boldsymbol{V}, \tag{3.73}$$

we finally obtain

$$T = \gamma E \sin^2\frac{\theta}{2} + \left(1 - \frac{2M_1}{M_1 + M_2}\sin^2\frac{\theta}{2}\right)\left(U_1 + \frac{m}{2}v_\mathrm{e}^2 - \frac{m}{2}v_1^2\right) \tag{3.74}$$

in agreement with a result derived by Sigmund and Glazov (2003).

3.4.6 Elastic and Inelastic Energy Loss

The expressions (3.65), (3.68) and (3.74) all contain a term $\gamma E \sin^2\frac{\theta}{2}$, which is the energy loss in an elastic collision according to (3.8), Vol. 1. In Problem 3.6 you will

have an opportunity to demonstrate that this term represents the energy of the recoiling atom including the number of electrons attached to it after the interaction even for inelastic collisions. Therefore, at least within the present linear approximation in Q/E, we may continue to identify this term as 'nuclear energy loss' T_n.

With this, we may write T in the form

$$T = T_\mathrm{e} + T_\mathrm{n} + \Delta T, \tag{3.75}$$

where

$$T_\mathrm{e} = \begin{array}{ll} Q & \text{for excitation,} \\ \frac{1}{2}mv_1^2 + U_2 - U_1 + Q & \text{for single-electron capture,} \\ U_1 + \frac{1}{2}m(v_\mathrm{e}^2 - v_1^2) & \text{for single-electron loss} \end{array} \tag{3.76}$$

and

$$\Delta T = -\frac{2M_1}{M_1 + M_2} T_\mathrm{e} \sin^2 \frac{\theta}{2} \tag{3.77}$$

represents a coupling term between electronic and nuclear energy loss.

We are presently engaged in an energy regime where electronic energy loss dominates. Nevertheless, there is always a small range of scattering angles (or impact parameters) where nuclear energy loss exceeds electronic energy loss. Disregarding this angular range we restrict our attention to scattering angles for which $T_\mathrm{n} \ll T_\mathrm{e}$. In that angular regime, the coupling term is seen to be $\propto (m/M_2)^2$ and hence negligible. We shall get to the complementary case when addressing stopping of low-energy ions in Chap. 8.

Excitation and capture are not mutually excluding processes, nor are excitation and loss. These phenomena may be quantified by suitable differential cross sections taking into account both charge exchange and energy loss, as we shall do in the following chapter. At this point let me just mention the energy transfer in a complete (one-electron) capture-loss cycle,

$$T_\mathrm{e} = \frac{1}{2}mv_\mathrm{e}^2 + U_2 + Q, \tag{3.78}$$

where Q now stands for the sum of all excitation energies except from the respective ground states U_1 and U_2. This is a central quantity in the analysis of experimental data.

The importance of the energy spent in charge-changing events was mentioned already by Bohr (1948). However, quantitative estimates of the energy spent in capture and loss processes are rarely found in the literature. In calculations of stopping cross sections the effect is normally ignored, and the same is true in numerous estimates of straggling where this may not be justified, as will be seen below.

Cowern et al. (1984a) have extracted a value of $T_\mathrm{e} = 2.30\,\mathrm{keV}$ from stopping measurements involving 3 MeV/u C^{5+} and C^{6+} in carbon. Ogawa et al. (1991a) mention (3.76). The fact that electron loss cannot be treated as if it were a simple projectile excitation was recognized by Sigmund and Glazov (2003). The importance of charge exchange in light-ion stopping was demonstrated by Schiwietz (1990) and Grande and Schiwietz (1991).

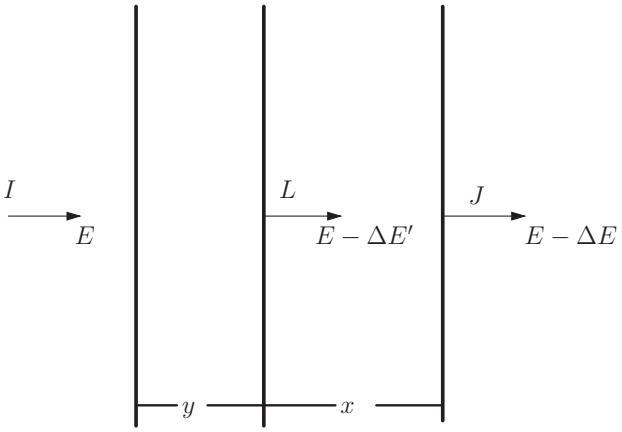

Fig. 3.14 Energy loss and charge exchange in two layers. See text

3.4.7 Radiative Electron Capture

In radiative electron capture the excess energy of a captured electron is carried away by a photon. At nonrelativistic projectile speeds, the momentum of the electron, on the other hand, is taken up by the projectile since the momentum of the emitted photon goes as $1/c$. Therefore, we may write

$$T = \Delta\left(\frac{P^2}{2M_1}\right) = \frac{P}{M_1}\Delta P = mv^2 \tag{3.79}$$

as an adequate approximation in the nonrelativistic regime, where the cross section for radiative capture is small.

3.4.8 Spontaneous Processes

We have considered spontaneous transitions in Sect. 3.2.3. The direct effect of radiative transitions on projectile energy loss is small, since the momentum carried away by the photon is proportional to $1/c$, as noted in the foregoing section.

The situation is different for Auger processes, where an electron carries away a momentum $m\boldsymbol{u}$, where $mu^2/2$ is an Auger energy. With this we obtain an energy change

$$T = \Delta\left(\frac{P^2}{2M_1}\right) = mvu\cos\phi, \tag{3.80}$$

where ϕ is the emission angle.

We may assume Auger emission to be isotropic as a first approximation. This implies that Auger emission does not contribute to the mean energy loss but may become significant in straggling.

3.5 Statistics of Energy Loss and Charge Exchange

In this section we shall look at the coupling between energy loss and charge exchange. This will involve the statistics of charge exchange as presented in Sect. 3.2 and of energy loss presented in Chap. 9, Vol. 1, taking into account the correlation between the two processes. Much of the presentation is an elaboration of two of the author's papers (Sigmund, 1991, 1992).

3.5.1 Generalized Bothe-Landau Formula

Consider an ion in state I with an energy E in $x = 0$. Let us define

$$F_{IJ}(\Delta E, x)\,\mathrm{d}(\Delta E) \tag{3.81}$$

as the probability for the ion to be in state J and to have suffered an energy loss $(\Delta E, \mathrm{d}(\Delta E))$ after having penetrated a pathlength x.

We may find a relation to be satisfied by $F_{IJ}(\Delta E, x)$ from Fig. 3.14, which is identical with Fig. 3.1, except that energy loss ΔE has been added as a statistical variable. Then, in complete analogy to (3.1) above as well as (9.4), Vol. 1, we find the following relation for a double layer,

$$F_{IJ}(\Delta E, x + y) = \sum_L \int \mathrm{d}(\Delta E')\, F_{IL}(\Delta E', y) F_{LJ}(\Delta E - \Delta E', x), \tag{3.82}$$

assuming statistical independence of the events in the second from those in the first layer. Moreover, the argument is only valid for energy losses $\Delta E \ll E$, since the independence of pertinent cross sections of the beam energy is essential for the argument.

Following the procedure outlined in Sect. 9.2.1, of Vol. 1, we go into Fourier space,

$$F_{IJ}(k, x) = \int_{-\infty}^{\infty} \mathrm{d}(\Delta E)\, \mathrm{e}^{-ik\Delta E}\, F_{IJ}(\Delta E, x), \tag{3.83}$$

where (3.82) reads

$$F_{IJ}(k, x + y) = \sum_L F_{IL}(k, y) F_{LJ}(k, x) \tag{3.84}$$

or, in matrix notation,

$$\mathbf{F}(k, x + y) = \mathbf{F}(k, y) \cdot \mathbf{F}(k, x), \tag{3.85}$$

where $\mathbf{F}(k, x) = \|F_{IJ}(k, x)\|$. Equation (3.85) has the general solution

$$\mathbf{F}(k, x) = \mathrm{e}^{Nx\mathbf{C}(k)}, \tag{3.86}$$

where $\mathbf{C}(k)$ is a matrix to be determined from the physics, in casu the single-collision limit, where

$$\mathbf{F}(k, x) = 1 + Nx\mathbf{C}(k) \ldots . \tag{3.87}$$

Considering explicitly what may happen during penetration through a thin layer we find

$$F_{IJ}(\Delta E, x) = \left[1 - Nx \sum_L \int \mathrm{d}T \; K_{IL}(T)\right] \delta_{IJ}\delta(\Delta E) + NxK_{IJ}(\Delta E) \ldots , \tag{3.88}$$

where $K_{IJ}(T) = \mathrm{d}\sigma_{IJ}/\mathrm{d}T$ is the differential cross section per target atom or molecule for energy loss T *and* transition from state I to state J. Also,

$$\int dT \; K_{IJ}(T) = \sigma_{IJ} \tag{3.89}$$

is the cross section for transition from state I to state J regardless of energy loss, as it was introduced in Sect. 3.2.1. Note, however, that unlike in Sect. 3.2, the case of $J = I$ has a well-defined meaning, once energy loss is involved: It is the differential cross section for energy loss in a charge-conserving collision.

In Fourier space, (3.88) reduces to

$$F_{IJ}(k, x) = \left[1 - Nx \sum_L \sigma_{IL}\right] \delta_{IJ} + Nx \int \mathrm{d}T \; K_{IJ}(T)\mathrm{e}^{-ikT} + \ldots \tag{3.90}$$

After adding and subtracting a term $Nx\sigma_{IJ}$, this reads

$$F_{IJ}(k, x) = \delta_{IJ} + NxQ_{IJ} - Nx\sigma_{IJ}(k), \tag{3.91}$$

where Q_{IJ} is defined in (3.8) and

$$\sigma_{IJ}(k) = \int \mathrm{d}T \; K_{IJ}(T) \left(1 - \mathrm{e}^{-ikT}\right) \tag{3.92}$$

is a generalized transport cross section of the type introduced in (9.15), of Vol. 1. With this, (3.91) may be written in matrix form

$$\mathbf{F}(k, x) = \mathbf{1} + Nx\mathbf{Q} - Nx\boldsymbol{\sigma} \ldots . \tag{3.93}$$

Comparing this to (3.87) we find that

$$\mathbf{C}(k) = \mathbf{Q} - \boldsymbol{\sigma}(k), \tag{3.94}$$

and hence, after inverse Fourier transform,

$$F_{IJ}(\Delta E, x) = \frac{1}{2\pi} \int \mathrm{d}k \, \mathrm{e}^{\mathrm{i}k\Delta E} \left(\mathrm{e}^{Nx[\mathbf{Q}-\boldsymbol{\sigma}(k)]}\right)_{IJ} . \tag{3.95}$$

This expression (Sigmund, 1992) is a straight generalization of the Bothe-Landau formula for the energy-loss spectrum discussed in Chap. 9, Vol. 1. If there is only one state, we have $\mathbf{Q} = 0$, and (3.95) reduces to the standard form. In Problem 3.7 you may verify that integration over ΔE leads back to the charge-state distribution (3.4).

3.5.2 Transport Equations

As in the separate energy-loss and charge-state distributions, also the joint spectrum can be derived from transport equations. In Problem 3.8 you will be asked to derive the following relationships, valid for a thin target with negligible energy loss,

$$-\frac{\partial}{\partial x} F_{IJ}(\Delta E, x) = N \sum_L \int \mathrm{d}T \left[F_{IJ}(\Delta E, x) K_{JL}(T) - F_{IL}(\Delta E - T, x) K_{LJ}(T)\right] \tag{3.96}$$

$$-\frac{\partial}{\partial x} F_{IJ}(\Delta E, x) = N \sum_L \int \mathrm{d}T \, K_{IL}(T) \big[F_{IJ}(\Delta E, x) - F_{LJ}(\Delta E - T, x)\big], \tag{3.97}$$

where the upper equation is of the forward and the lower of the backward type.

If you integrate either of these relations over ΔE and observe that

$$\int \mathrm{d}(\Delta E) \, F_{IJ}(\Delta E, x) = F_{IJ}(x), \tag{3.98}$$

you arrive back at the rate equations introduced in Sect. 3.2.2.

3.5.3 Mean Energy Loss

A procedure to derive mean energy loss and straggling from the Bothe-Landau formula has been described in Sect. 9.2.3, Vol. 1. The same procedure will now be applied to (3.95) in order to determine state-specific mean energy loss and straggling from $F_{IJ}(\Delta E, x)$. As a first step we determine moments

$$F_{IJ}^{(1)}(x) = \int \mathrm{d}(\Delta E) \, \Delta E F_{IJ}(\Delta E, x) = i \, \frac{\partial}{\partial k} \left(\mathrm{e}^{Nx\mathbf{C}(k)}\right)_{IJ} \Big|_{k=0} \tag{3.99}$$

and

$$F_{IJ}^{(2)}(x) = \int \mathrm{d}(\Delta E)\, \Delta E^2 F_{IJ}(\Delta E, x) = -\frac{\partial^2}{\partial k^2} \left(\mathrm{e}^{Nx\mathbf{C}(k)}\right)_{IJ}\Big|_{k=0}. \quad (3.100)$$

in straight analogy with the scalar case.

Since $\exp(Nx\mathbf{C})$ is defined by an exponential series of the type of (3.5), differentiation can conveniently proceed over that series, so that

$$\frac{\partial}{\partial k}\mathrm{e}^{Nx\mathbf{C}(k)} = \sum_{n=1}^{\infty} \frac{(Nx)^n}{n!} \left(\mathbf{C}'\mathbf{C}^{n-1} + \mathbf{C}\mathbf{C}'\mathbf{C}^{n-2} + \cdots + \mathbf{C}^{n-1}\mathbf{C}'\right). \quad (3.101)$$

Now, according to (3.94) we have

$$\mathbf{C}(k=0) = \mathbf{Q} \quad (3.102)$$

and

$$\mathbf{C}'(k=0) = \frac{\mathrm{d}\mathbf{C}(k)}{\mathrm{d}k}\Big|_{k=0} = -i\mathbf{S} \quad (3.103)$$

with $\mathbf{S} = \|S_{IJ}\|$ and

$$S_{IJ} = \int \mathrm{d}T\, T K_{IJ}(T). \quad (3.104)$$

With this we find

$$F_{IJ}^{(1)}(x) = \sum_{n=1}^{\infty} \frac{(Nx)^n}{n!} \left(\mathbf{S}\mathbf{Q}^{n-1} + \mathbf{Q}\mathbf{S}\mathbf{Q}^{n-2} + \cdots + \mathbf{Q}^{n-1}\mathbf{S}\right)_{IJ}. \quad (3.105)$$

3.5.3.1 Summing over Projectile States

Equation (3.105) can be greatly simplified for two limiting cases which are of particular interest.

If we are only interested in the total stopping of the beam, we may sum over all exit charge states J. Now, because of the sum rule (3.9), this implies that all those terms in (3.105) which end with $\mathbf{Q}$ will drop out, so that

$$F_I^{(1)}(x) = \sum_J F_{IJ}^{(1)}(x) = \sum_J \sum_{n=1}^{\infty} \frac{(Nx)^n}{n!} \left(\mathbf{Q}^{n-1}\mathbf{S}\right)_{IJ}. \quad (3.106)$$

The sum can be rewritten as an integral over x, whereafter it can be summed with the result

$$F_I^{(1)}(x) = N \sum_J \int_0^x \mathrm{d}x' \left(\mathrm{e}^{Nx'\mathbf{Q}}\mathbf{S}\right)_{IJ} = N \sum_{JK} \int_0^x \mathrm{d}x'\, F_{IJ}(x') S_{JK}, \quad (3.107)$$

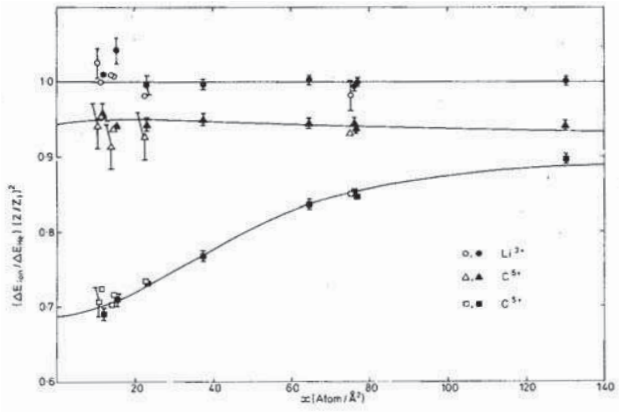

Fig. 3.15 Relative energy loss versus pathlength of 3 MeV/u Li^{3+}, C^{6+} and C^{5+} ions incident on carbon, divided by $(Z_1/2)^2$ times the measured energy loss of helium ions. From Cowern et al. (1984b)

where $F_{IJ}(x)$ is the charge fraction (3.4), which we have learned to calculate by a simple algebraic procedure.

Differentiation of (3.107) with respect to x leads to the specific energy loss at depth x,

$$\frac{\mathrm{d}F_I^{(1)}}{\mathrm{d}x} = N \sum_J F_{IJ}(x) S_J . \tag{3.108}$$

Here,

$$S_J = \sum_K S_{JK} \tag{3.109}$$

represents the stopping cross section of an ion in state J, and $F_{IJ}(x)$ the probability for the projectile to be in state J at depth x. While we could have written down this relation without going over a complex matrix formalism, that same formalism also allows to derive relations that would have been hard to arrive at by mere intuition.

Note that S_J contains contributions both from collisions which affect the projectile state ($J \neq I$) and those which do not ($J = I$).

3.5.3.2 Example: The Two-State Case

As an instructive example, consider the two-state case, for which we already know the charge fractions from Sect. 3.2.4.1. Here, (3.107) reads

$$(\Delta E)_1 = Nx \left(\frac{\sigma_{21}}{\sigma} S_1 + \frac{\sigma_{12}}{\sigma} S_2 \right) + \frac{\sigma_{12}}{\sigma^2} (S_1 - S_2) \left(1 - \mathrm{e}^{-Nx\sigma} \right) . \tag{3.110}$$

The corresponding equation for $(\Delta E)_2$ is found by interchanging indices 1 and 2.

The first term in (3.110) represents the energy lost by an equilibrated beam, while the second term leads to an intercept $\delta(\Delta E) = \sigma_{12}(S_1 - S_2)/\sigma^2$, if the asymptotic straight line is extrapolated toward zero pathlength. The actual behaviour of $(\Delta E)_1$ at small pathlengths reads

$$(\Delta E)_1 \simeq N x S_1 - \frac{1}{2} N^2 x^2 \sigma_{12} (S_1 - S_2) . \tag{3.111}$$

An interesting quantity is the difference

$$(\Delta E)_1 - (\Delta E)_2 = \frac{1}{\sigma} (S_1 - S_2) \left(1 - \mathrm{e}^{-N x \sigma}\right), \tag{3.112}$$

which allows to determine the difference $S_1 - S_2$. Evidently, measurements of the energy loss at low thickness for the two charge states, of equilibrium stopping, of charge fractions and of the above difference leave little uncertainty about input parameters σ_{12}, σ_{21}, S_1 and S_2. Note, however, that measurements of the mean energy loss alone do not differentiate between diagonal elements S_{11} and S_{22} and off-diagonal elements S_{12} and S_{21} without some theoretical input.

Figure 3.15 shows data of Cowern et al. (1984b), plotted as relative energy losses with the equilibrium energy loss of helium ions as a reference. While the graph illustrates qualitative features, quantitative analysis is obscured by the mixing up with helium data, stimulated by the effective-charge concept which is to be discussed in Chap. 4. A more direct way employing relative data goes as follows: Consider a two-state system with O^{6+} as state 1 and O^{5+} as state 2 and normalize energy losses to $N x S_1$, i.e., the energy loss of a bare oxygen ion that does not undergo charge exchange. You are invited to carry out such an analysis in Problem 3.9.

3.5.3.3 Equilibrated Beam

Another limiting case is to consider an ion beam that is already *equilibrated* from the start. This can be described by a distribution

$$F_J(\Delta E, x) = \sum_I F_I F_{IJ}(\Delta E, x), \tag{3.113}$$

i.e., a straight superposition. With this we may determine the mean energy loss of an equilibrated beam from (3.105). In carrying out the sum it is then useful to recognize that

$$\sum_I F_I Q_{IK} = 0, \tag{3.114}$$

as you may verify by inserting the definition (3.8) and observing (3.29). This implies that terms in (3.105) which have a factor $\mathbf{Q}$ on the left, will not contribute to the sum. As a result we find

$$\sum_I F_I F^{(1)}_{IJ}(x) = \sum_{n=1}^{\infty} \frac{(Nx)^n}{n!} \sum_I F_I \left(\mathbf{S}\mathbf{Q}^{n-1}\right)_{IJ}$$
$$= N \int_0^x \mathrm{d}x' \sum_I F_I S_{IK} F_{KJ}(x'). \quad (3.115)$$

Finally, we may consider the mean energy loss of an equilibrated beam, in which case terms with **Q** on either end may be dropped. This leads to

$$\langle \Delta E \rangle = \sum_{IJ} F_I \langle \Delta E \rangle_{IJ} = Nx \sum_{IJ} F_I S_{IJ}, \quad (3.116)$$

which is consistent with (3.108).

It is useful to keep in mind that even though we have looked at an equilibrated beam, the mean energy loss depends on the exit charge state. As an illustration, consider a situation where you decide to measure the energy loss of a beam with a mean charge $\langle q \rangle = Z_1/2$, but where you direct your detector at ions emerging in the very rare charge state $q = Z_1$. Clearly, an ion that has travelled for a certain pathlength in this high charge state will have suffered more than average stopping.

3.5.4 State-Specific Mean Energy Loss ⋆

Let us now go back to the state-specific mean energy loss as given by (3.105). Evaluating the matrix sums is straightforward numerically if proper input is available. However, for understanding what goes on it is useful again to consider the two-state case which can be evaluated in closed form.

3.5.4.1 Two-State Case

The sums over n in (3.105) can readily be evaluated if you make use of (3.16). You will then obtain

$$F^{(1)}_{IJ}(x) = \int_0^x \mathrm{d}x' \left[N\mathbf{S} + \frac{N}{\sigma}\left(1 - \mathrm{e}^{-Nx'\sigma}\right)(\mathbf{SQ} + \mathbf{QS}) \right.$$
$$\left. + \frac{N}{\sigma^2}\left(1 - \mathrm{e}^{-Nx'\sigma} - Nx'\sigma \mathrm{e}^{-Nx'\sigma}\right)\mathbf{QSQ} \right]_{IJ}, \quad (3.117)$$

which may be rearranged into

$$F_{IJ}^{(1)}(x) = \int_0^x \mathrm{d}x' \left(N\mathbf{R}\boldsymbol{S}\mathbf{R}\left[1 - \mathrm{e}^{-Nx'\sigma}\right] + N\mathrm{e}^{-Nx'\sigma}\left[\boldsymbol{S} - \frac{Nx'}{\sigma}\mathbf{Q}\boldsymbol{S}\mathbf{Q}\right]\right)_{IJ}. \quad (3.118)$$

or, after integration,

$$F_{IJ}^{(1)}(x) = Nx\mathbf{R}\mathbf{S}\mathbf{R} - \frac{1}{\sigma}\left(1 - \mathrm{e}^{-Nx\sigma}\right)\left[\mathbf{R}\frac{\mathbf{Q}}{\sigma} + \frac{\mathbf{Q}}{\sigma}\mathbf{R}\right] + Nx\mathrm{e}^{-Nx\sigma}\frac{\mathbf{Q}}{\sigma}\mathbf{R}\frac{\mathbf{Q}}{\sigma}, \quad (3.119)$$

where

$$\frac{1}{\sigma}\mathbf{Q} = \begin{Vmatrix} -F_2 & F_2 \\ F_1 & -F_1 \end{Vmatrix}; \qquad \mathbf{R} = \left(\mathbf{1} + \frac{\mathbf{Q}}{\sigma}\right) = \begin{Vmatrix} F_1 & F_2 \\ F_1 & F_2 \end{Vmatrix} \quad (3.120)$$

according to (3.14).

For $Nx\sigma \gg 1$, (3.118) leads to

$$\langle \Delta E \rangle_{IJ} = \frac{F_{IJ}^{(1)}(x)}{F_{IJ}(x)} \to Nx\,(F_1 S_1 + F_2 S_2) + (\Delta E_0)_{IJ}, \quad (3.121)$$

where $(\Delta E_0)_{IJ}$ is an intercept which you are invited to evaluate in Problem 3.10.

We may set

$$S_{12} = \sigma_{12}\epsilon_{12} \equiv \sigma F_2 \epsilon_{12} \quad (3.122)$$

$$S_{21} = \sigma_{21}\epsilon_{21} \equiv \sigma F_1 \epsilon_{21}, \quad (3.123)$$

where ϵ_{12} and ϵ_{21} are mean energies spent in the respective charge exchange processes.

Figure 3.16 shows calculated curves for a system studied experimentally by Ogawa et al. (1991b,a, 1992). Numerical input has been adopted from Ogawa et al. (1991b,a). Bare helium ions are dominating in equilibrium by about five orders of magnitude while neutral ions are below the detection limit. At an energy of 32 MeV, the energy loss ϵ_{21} in a capture event is so large that the spectrum $F_{11}(\Delta E, x)$ splits up into two clearly identifiable peaks with increasing target thickness. Peak energy losses for the first and second peak have been included in Fig. 3.16. Note, however, that at the target thicknesses covered in the graph, peak energy losses are smaller than mean energy losses. This may well be the reason for a minor discrepancy between the calculated and measured data for the case 11.

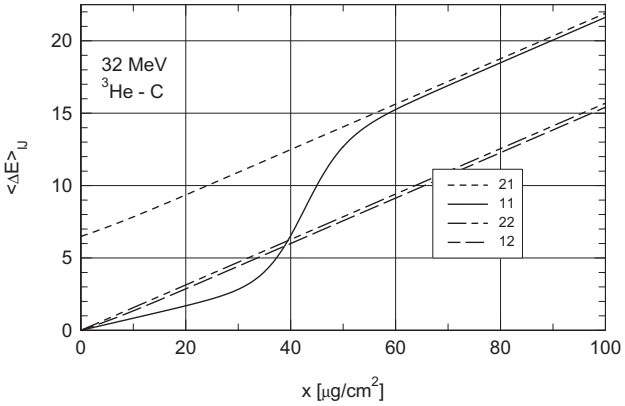

Fig. 3.16 Mean energy loss of 32 MeV ^{3}He ions in carbon as a function of thickness. Only singly (1) and doubly (2) charged ions are considered. Experimental points from Ogawa et al. (1991a). See text

3.5.4.2 More than Two States

While (3.119) could in principle be written down explicitly in terms of the cross sections involved, it appears difficult to get it into an illuminating form, except in limiting cases of large or small pathlength. This type of complexity increases rapidly as the number of involved states increases. On the other hand, if numerical values of all pertinent cross sections are available, evaluating state-specific mean energy losses is straightforward. In addition to (3.105), suitable tools are the two transport equations

$$-\frac{\partial}{\partial x}F_{IJ}^{(1)}(x) = N\sum_L\left[F_{IJ}^{(1)}(x)\sigma_{JL} - F_{IL}^{(1)}(x)\sigma_{LJ} - F_{IL}(x)S_{LJ}\right]$$
$$-\frac{\partial}{\partial x}F_{IJ}^{(1)}(x) = N\sum_L\left[\sigma_{IL}F_{IJ}^{(1)}(x) - \sigma_{IL}F_{LJ}^{(1)}(x) - S_{IL}F_{LJ}(x)\right], \tag{3.124}$$

where the charge fractions $F_{IJ}(x)$ enter as input.

Another tool is the Monte Carlo method which, in this context, has been employed by Blazevic et al. (2000). Figure 3.17 shows a summary of output from such a code[1]. Out of 1 million incident ions, 183,302 did not undergo charge exchange and ended up in the initial charge state 10+. This accounts for 45.1% of all ions with final charge state 10+. Amongst the rest, 161,056 ions (or 39.6%) capture an electron but lose it again, while another 32,957 (or 8.1%) end up in charge state 10+

[1] The published figure contains minor errors in the percentages. Figure 3.17 is a corrected version kindly provided by Dr. Blazevic.

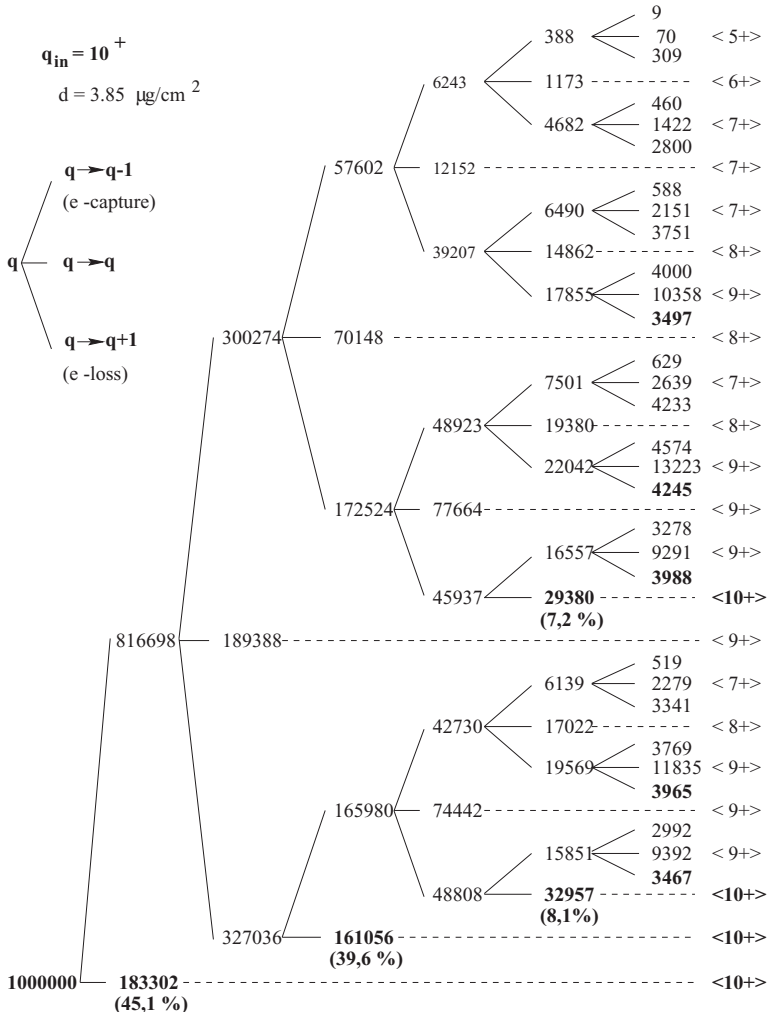

Fig. 3.17 Charge-changing events during passage of 2 MeV/u Ne ions with an initial charge $+10$ through a 3.8 µg/cm^2 carbon foil. See text. From Blazevic et al. (2000)

after two loss-capture cycles. Finally, 29,380 ions (or 7.2%) end up in charge state $10+$ after two capture events in sequence and two subsequent loss events.

A table of this kind allows to tabulate mean energy losses, if frozen-charge stopping cross sections S_{II} and energy losses ϵ_{IJ} in charge-changing events are known.

These Monte Carlo calculations were triggered by extensive measurements performed by the same authors (Blazevic et al., 2000). The data analysis resulted in a set of frozen-charge stopping cross sections S_{II}, which we will get back to in Sect. 4.8.3.

Measurements by Frey et al. (1995) with 1 MeV/u Ni ions on carbon foils revealed a large number of charge states involved. Again, we shall come to these data in Sect. 4.8.3.

3.5.5 Straggling

We are now ready to determine the second moment $\langle \Delta E^2 \rangle$ starting from (3.100) and following Sigmund (1992) and Närmann and Sigmund (1994). As in Sect. 3.5.3.1 we consider the total outgoing beam, i.e., we sum over outgoing projectile states. Then, in taking the derivative of (3.101) we only need to take into account terms that do not end with **Q**, i.e.,

$$\sum_J F^{(2)}_{IJ}(x) = \sum_J \left\{ \sum_{n=1}^{\infty} \frac{(Nx)^n}{n!} \mathbf{Q}^{n-1}\mathbf{W} + 2\sum_{n=2}^{\infty} \frac{(Nx)^n}{n!} \left(\mathbf{S}\mathbf{Q}^{n-2}\mathbf{S} + \mathbf{Q}\mathbf{S}\mathbf{Q}^{n-3}\mathbf{S} + \cdots + \mathbf{Q}^{n-2}\mathbf{S}^2\right) \right\}_{IJ}, \quad (3.125)$$

where

$$W_{IJ} = \int \mathrm{d}T\, T^2 K_{IJ}(T). \quad (3.126)$$

This may be rearranged into

$$\sum_J F^{(2)}_{IJ}(x) = \sum_J \left(\int_0^x N\,\mathrm{d}x' \mathrm{e}^{Nx'\mathbf{Q}}\mathbf{W} + 2\int_0^x N\,\mathrm{d}x' \int_0^{x'} N\,\mathrm{d}x'' \mathrm{e}^{N(x-x')\mathbf{Q}}\mathbf{S}\mathrm{e}^{Nx''\mathbf{Q}}\mathbf{S} \right)_{IJ}. \quad (3.127)$$

To prove this, expand the exponentials in (3.127) and perform the integrals (see also Problem 3.11).

In terms of charge fractions this reads

$$\sum_J F^{(2)}_{IJ}(x) = \sum_K \int_0^x N\,\mathrm{d}x'\, F_{IK}(x')W_K + 2\sum_{KLM} \int_0^x N\,\mathrm{d}x' \int_0^{x'} N\,\mathrm{d}x''\, F_{IK}(x-x')S_{KL}F_{LM}(x'')S_M, \quad (3.128)$$

where

$$W_I = \sum_J W_{IJ}. \quad (3.129)$$

Since we have summed over all charge states, we have

$$\sum_J F_{IJ}^{(2)}(x) = \langle \Delta E^2 \rangle_I . \tag{3.130}$$

In order to get the variance we need to subtract $\langle \Delta E \rangle_I^2 = \left[F_I^{(1)}(x) \right]^2$ from (3.107). Taking the derivative with respect to x we obtain the differential straggling at depth x,

$$\left(\frac{\mathrm{d}\Omega^2(x)}{N\,\mathrm{d}x} \right)_I = \left(\frac{\mathrm{d}\Omega^2(x)}{N\,\mathrm{d}x} \right)_{I,\mathrm{coll}} + \left(\frac{\mathrm{d}\Omega^2(x)}{N\,\mathrm{d}x} \right)_{I,\mathrm{chex}} \tag{3.131}$$

where

$$\left(\frac{\mathrm{d}\Omega^2(x)}{N\,\mathrm{d}x} \right)_{I,\mathrm{coll}} = \sum_J F_{IJ}(x) W_J \tag{3.132}$$

is conventionally called *collisional straggling*, and

$$\left(\frac{\mathrm{d}\Omega^2(x)}{N\,\mathrm{d}x} \right)_{I,\mathrm{chex}} = 2 \sum_{JL} N \int_0^x \mathrm{d}x' \left[\sum_K F_{IJ}(x - x') S_{JK} F_{KL}(x') - F_{IJ}(x') S_J F_{IL}(x) \right] S_L \tag{3.133}$$

is called *charge-exchange straggling*[2].

The term $\sum_J F_{IJ}(x) W_J$ is analogous to (3.108) and does not need special consideration at this point. The charge-exchange contribution can be rewritten as

$$\left(\frac{\mathrm{d}\Omega^2(x)}{N\,\mathrm{d}x} \right)_{I,\mathrm{chex}} = 2 \sum_{JKL} N \int_0^x \mathrm{d}x'\, F_{IJ}(x - x') S_{JK} \times \left(F_{KL}(x') - F_{IL}(x) \right) S_L , \tag{3.134}$$

which makes it clear that the integral receives contributions mainly from small values of x'.

Now, let us consider this quantity for large values of x, where

$$F_{KL}(x') - F_{IL}(x) \to F_{KL}(x') - F_L , \tag{3.135}$$

which differs from zero only for x' smaller than some depth comparable to the equilibration distance. If x is large compared to this quantity, we have

$$F_{IJ}(x - x') \to F_J , \tag{3.136}$$

[2] Strictly speaking, nondiagonal terms W_{IJ} for $I \neq J$ belong to charge-exchange straggling. The present, slightly imprecise notation is compatible with the literature, where energy loss due to charge exchange has most often been neglected.

and hence,

$$\left(\frac{\mathrm{d}\Omega^2}{N\,\mathrm{d}x}\right)_{\mathrm{chex}} = 2N \sum_{JKL} F_J S_{JK} \int_0^\infty \mathrm{d}x\ (F_{KL}(x) - F_L)\, S_L. \tag{3.137}$$

3.5.5.1 The Two-state Case

It is instructive again to consider the two-state case. After insertion of (3.19) you may evaluate the integrals and obtain

$$\left(\frac{\mathrm{d}\Omega^2}{N\,\mathrm{d}x}\right)_{\mathrm{chex}} = \frac{2}{\sigma}\,(S_1 - S_2) \sum_{J=1}^{2} F_J\,(F_2 S_{J1} - F_1 S_{J2})\,. \tag{3.138}$$

Charge-exchange straggling for the two-state case was first analysed by Vollmer (1974), who neglected all energy loss in charge-changing events. With this, (3.138) reduces to

$$\left(\frac{\mathrm{d}\Omega^2}{N\,\mathrm{d}x}\right)_{\mathrm{chex}} = \frac{2}{\sigma} F_1 F_2\,(S_{11} - S_{22})^2 = \frac{2\sigma_{12}\sigma_{21}}{\sigma^3}\,(S_{11} - S_{22})^2\,. \tag{3.139}$$

This relation was first derived by Efken et al. (1975), while the complete expression (3.138) was found by the author (Sigmund, 1992).

You are kindly invited to analyse the physical content of (3.138) in Problems 3.12 and 3.13.

3.5.5.2 Continuum Approximation ⋆

Equation (3.137) is ready to be evaluated if $F_{IJ}(X)$ and S_{IJ} are available for all significant states. Nevertheless, let us try to reduce the expression to an even handier form. Following Sigmund et al. (2011) and Fig. 3.18 assume that the charge-dependent stopping cross section S_I varies approximately linearly around the equilibrium value S, in analogy to an approximation described in Sect. 3.3.1,

$$S_I \simeq S + (q_I - q)\Delta S, \tag{3.140}$$

where q_I is the charge number, q the equilibrium charge and $\Delta S = dS_I/dq_I$ at q. With this you find

$$\sum_L (F_{KL}(x) - F_L)\, S_L$$
$$= S \sum_L (F_{KL}(x) - F_L) + \Delta S \sum_L (F_{KL}(x) - F_L)\,(q_L - q)\,. \tag{3.141}$$

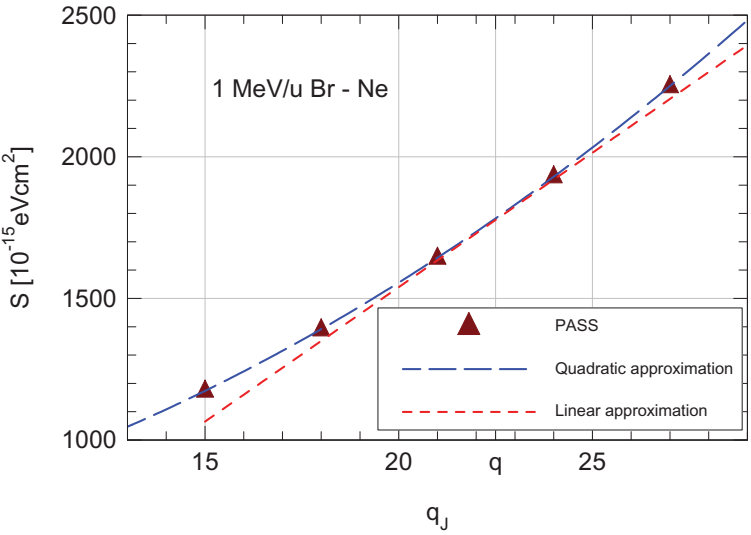

Fig. 3.18 Stopping cross section for 1 MeV Br^{q_J+} ions in Ne calculated by the PASS code. Target excitation/ionization only. Also included are a linear and a quadratic approximation. $q = 22.5$ is the mean equilibrium charge at 1 MeV/u according to ETACHA Rozet et al. (1996). From Sigmund et al. (2011)

Here, the first term vanishes since $\sum_L F_{KL}(x) = 1$ for all K. The second term reduces to

$$\Delta S\,(q(K,x) - q)\,, \tag{3.142}$$

where

$$q(K,x) = \sum_L F_{KL}(x) q_L \tag{3.143}$$

is the mean charge at depth x, if the particle was in state K at $x = 0$.

Then,

$$\left(\frac{\mathrm{d}\Omega^2}{N\,\mathrm{d}x}\right)_{\mathrm{chex}} = 2N\Delta S \sum_{JK} F_J S_{JK} Q_K, \tag{3.144}$$

where

$$Q_K = \int_0^\infty \mathrm{d}x\ (q(K,x) - q)\,. \tag{3.145}$$

You may verify that in the two-state case this actually delivers the exact result (Problem 3.14).

Going back to (3.144), let us separate diagonal from off-diagonal terms in S_{JK}. Consider first the diagonal terms and set

$$S_{JJ} \simeq S_0 + (q_J - q)\Delta S_0, \tag{3.146}$$

which then differs from (3.140) in that S_0 and ΔS_0 refer to the diagonal terms of the stopping cross section, while S and ΔS include capture and loss.

With this,

$$\left(\frac{\mathrm{d}\Omega^2}{N\,\mathrm{d}x}\right)_{\text{chex,diag}} = 2NS_0\Delta S\sum_J F_J Q_J + 2N\Delta S\Delta S_0\sum_J F_J\,(q_J - q)\,Q_J\,. \quad (3.147)$$

After going back to the definition (3.145), it is seen that the first term vanishes in view of

$$\sum_J F_J F_{JL}(x) = F_L\,, \quad (3.148)$$

since the equilibrium distribution does not change as a function of pathlength. Hence,

$$\left(\frac{\mathrm{d}\Omega^2}{N\,\mathrm{d}x}\right)_{\text{chex,diag}} = 2N\Delta S\Delta S_0\sum_J F_J\,(q_J - q)\,Q_J\,. \quad (3.149)$$

Next, consider the off-diagonal terms which are connected to charge exchange.

$$\left(\frac{\mathrm{d}\Omega^2}{N\,\mathrm{d}x}\right)_{\text{chex,offdiag}} = 2N\Delta S\sum_{J\neq K} F_J S_{JK} Q_K \quad (3.150)$$

As a first approximation, assume that only one-electron capture and loss are significant, so that

$$\left(\frac{\mathrm{d}\Omega^2}{N\,\mathrm{d}x}\right)_{\text{chex,offdiag}} = 2N\Delta S\sum_J F_J\,(S_{J,J+1}Q_{J+1} + S_{J,J-1}Q_{J-1})\,. \quad (3.151)$$

After redefining indices this can also be written as

$$\left(\frac{\mathrm{d}\Omega^2}{N\,\mathrm{d}x}\right)_{\text{chex,offdiag}} = 2N\Delta S\sum_J (F_{J-1}S_{J-1,J} + F_{J+1}S_{J+1,J})\,Q_J\,. \quad (3.152)$$

Here the quantity in the parentheses depends on J, and we may again assume that near equilibrium it depends linearly on the charge, so that

$$F_{J-1}S_{J-1,J} + F_{J+1}S_{J+1,J} \simeq F_J\,(S_{\text{chex}} + (q_J - q)\Delta S_{\text{chex}})\,. \quad (3.153)$$

This *defines* S_{chex} and ΔS_{chex}.

After insertion into (3.152), the term going as S_{chex} drops out just as above, so that

$$\left(\frac{\mathrm{d}\Omega^2}{N\,\mathrm{d}x}\right)_{\text{chex,offdiag}} = 2N\Delta S\Delta S_{\text{chex}}\sum_J F_J(q_J - q)Q_J\,, \quad (3.154)$$

which looks similar to (3.149). Summing up the two contributions we find

$$\left(\frac{\mathrm{d}\Omega^2}{N\,\mathrm{d}x}\right)_{\mathrm{chex}} = 2N\Delta S\,(\Delta S_0 + \Delta S_{\mathrm{chex}}) \sum_J F_J(q_J - q)Q_J, \tag{3.155}$$

In Problem 3.15 you are welcome to demonstrate that charge-exchange straggling in the present approximation reduces to the *exact* result in the two-state case.

The factor in front of the sum in (3.155) shows that charge-exchange straggling is essentially proportional to the square of the *variation* of the stopping cross section with the ion charge. The sum over J, on the other hand, contains only charge fractions including transients. We have learned early in this chapter how to evaluate the latter. In the following chapter we shall see how to determine charge-dependent stopping cross sections.

3.5.6 Energy-Loss Profiles

In Chap. 9, Vol. 1, qualitative features of energy-loss spectra have been discussed. Following Bohr (1948), three domains have been identified according to the travelled path length,

I A thin-target regime, where the spectrum is characterized by a peak position significantly below the mean energy loss and a Coulomb-like tail up to the maximum energy transfer T_{max},
II A moderately-thick-target regime where the spectrum is a slightly-skewed gaussian, and
III A very-thick-target regime, where the energy loss is a substantial fraction of the initial energy.

Regime III does not present any major challenges beyond those already considered: Energy-loss profiles are determined by mean energy loss, straggling and perhaps skewness, and charge exchange, if significant, may be taken into account in accordance with the results of the previous two sections.

The situation is different with regard to regimes I and II. According to the Bohr criterion (Bohr, 1948) the two regimes are separated by the parameter

$$\varkappa = \frac{\Omega^2}{T_{\mathrm{max}}^2}, \tag{3.156}$$

where $\varkappa < 1$ specifies the thin-target regime and $\varkappa > 1$ the moderately-thick-target regime. Moreover, for $\varkappa \ll 1$ the spectrum approaches the Landau form (Landau, 1944), while for $\varkappa \gg 1$ the spectrum is gaussian-like. The intermediate regime between the latter two extremes may be wide and requires special attention.

We have seen in Fig. 3.16 that energy-loss spectra may split up into contributions from different numbers of capture-loss cycles. Let us see under what conditions such separation is possible.

Consider swift ions with

$$T_{\max} \simeq 2mv^2; \qquad \epsilon \simeq \frac{1}{2}mv^2, \tag{3.157}$$

where ϵ, the mean energy loss in a capture-loss cycle, is governed primarily by the contribution from capture. Now, in regime II, where $\Omega > T_{\max}$, the width of the profile is greater than four times the separation between individual peaks. Therefore, individual peaks will not be visible and deconvolution will be difficult if not impossible. Thus, pronounced individual peaks can only be expected in regime I, and only at target thicknesses significantly below the Bohr limit. To actually see more than one peak one also has to satisfy experimental requirements on energy resolution and peak-to-background ratio of the detecting device.

The first calculations of energy-loss spectra including charge exchange were reported by Winterbon (1977) on the basis of transport equations and the moment method. In brief, moments up to 4th order were taken over (3.97), and the resulting equations were solved recursively with input available at the time, i.e., capture and loss cross sections for 15 MeV iodine ions in oxygen, tabulated by Betz (1972) and a simple Coulomb-like model for collisional energy loss. Energy loss in charge exchange was ignored, i.e. the possibility of multiple peaks was eliminated from start.

A striking feature of Winterbon's results is the observation that both relative straggling, relative skewness and relative kurtosis increase strongly with *decreasing* ion charge. This can be traced to the assumption of q^2 dependence of the differential cross section on the ion charge q. We shall see in the following chapter that higher moments become less and less sensitive to q. Hence, caution is indicated regarding the *quantitative* results of Winterbon's calculations.

More recently, a number of studies of the problem were reported by Glazov in cooperation with the author ((Glazov, 1998, 2002, Glazov et al., 2002) and references quoted there). The emphasis in this work is on the development of accurate calculational methods to describe energy-loss spectra over a wide range of target thicknesses. Systems analysed include He, Li and O ions on carbon, where experimental data are available (see Ogawa et al. (1996) and references quoted there). Measurements as well as calculations refer to two significant charge states. Except for Glazov et al. (2002), authors employed empirical data for stopping and charge-exchange cross sections.

Two calculational methods were employed, both of which are extensions to multistate systems of calculational tools described in Vol. 1: For low thicknesses a generalization of Landau's scheme is utilized which has been described in Sect. 9.3.4, Vol. 1, while for larger thicknesses an extension of the steepest-descent method (Sigmund and Winterbon, 1985) as described in Sect. 9.4.2, Vol. 1 was employed. Comparison to straight numerical results showed that the ranges of validity of the two methods overlap.

In the following I shall restrict myself to line out Glazov's description for thin targets and the way how multiple-peak structure shows up, and quote a number of

results for the two-state case which illustrate the general behaviour. For much of the mathematics I have to refer to the original papers.

In accordance with Glazov (2002) let us define a matrix $\mathbf{F}^{(p)}(\Delta E, x)$ such that $F_{IJ}^{(p)}(\Delta E, x)d(\Delta E)$ is the probability for an ion in an initial charge state I to end up in charge state J after pathlength x with an energy loss $(\Delta E, \mathrm{d}(\Delta E))$ and p charge-changing events.

We may find a recursion formula for $F_{IJ}^{(p+1)}(\Delta E, x)$,

$$F_{IJ}^{(p+1)}(\Delta E, x) = \sum_{K \neq L} \int_0^x N \,\mathrm{d}x' \int \mathrm{d}(\Delta E') \int \mathrm{d}T \\ F_{IK}^{(0)}(\Delta E', x') K_{KL}(T) F_{LJ}^{(p)}(\Delta E - \Delta E' - T, x - x'), \quad (3.158)$$

which expresses the probability for the projectile to travel a pathlength x' without charge exchange, to switch from state K to L in $(x', \mathrm{d}x')$ and to undergo p charge-changing events before ending up at x with an energy loss ΔE. By definition we have

$$F_{IJ}^{(0)}(\Delta E, x) = \delta_{IJ} \mathrm{e}^{-N x \sigma_I} F_I(\Delta E, x), \quad (3.159)$$

where

$$\sigma_I = \sum_J \sigma_{IJ}, \quad (3.160)$$

$F_I(\Delta E, x)$ is the energy-loss distribution for a frozen charge,

$$F_I(\Delta E, x) = \frac{1}{2\pi} \int \mathrm{d}k \, \mathrm{e}^{\mathrm{i}k\Delta E - N x \sigma_{II}(k)}, \quad (3.161)$$

and

$$\sigma_{II}(k) = \int dT \, K_{II}(T) \left(1 - \mathrm{e}^{-\mathrm{i}kT}\right). \quad (3.162)$$

With this, $F_{IJ}^{(p)}(\Delta E, x)$ can be calculated for arbitrary p, although values of $p > 4$ have neither been calculated nor resolved in measurements.

Figure 3.19 shows results for 32 MeV He ions in carbon, reflecting experimental conditions of the work of Ogawa et al. (1991b) and later work. Terms in the above expansion were evaluated numerically with realistic input for the energy-loss spectrum and charge-exchange cross sections. An extension of the Landau spectrum allowing for charge exchange was developed at the same time and gave results very close to those shown in Fig. 3.19.

The equilibrium charge state of 32 MeV He ions is close to 2+. Therefore, integrated charge fractions for (+in,+out) (right graph) are five orders of magnitude smaller than for (++in,++out) (left graph). Similarly, for (++in,++out), the vast majority of particles detected have not undergone charge exchange, while the number of particles having undergoing 1 or 2 charge-exchange cycles, denoted by (2) or (4), respectively, is 3–4 and 7 orders of magnitude smaller. Conversely, at the foil

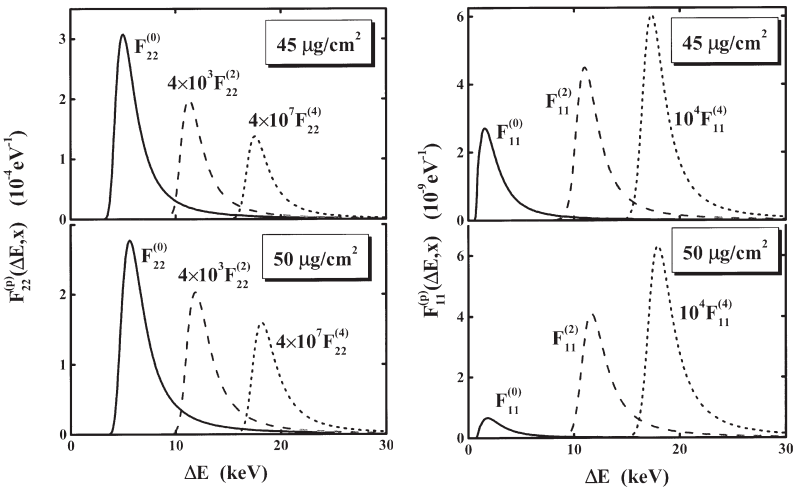

Fig. 3.19 Calculated energy-loss spectra for 32 MeV He ions in carbon foils, separated into contributions from 0, 2 and 4 charge-changing collisions. Left: Incident and exit charge state 2+. Right: Incident and exit charge state 1+

thicknesses depicted in the graphs, almost all ions detected with (+in,+out) have undergone at least one charge-changing event.

3.6 Discussion and Outlook

You have probably realized that major portions of the present chapter report fairly recent and, in part, ongoing work including work in which the author of this monograph is heavily involved. Similar observations will be appropriate when you read the following two chapters.

I have given much attention to the matrix method in the stochastic theory of charge exchange, even though I am not sure whether it will be competitive in the long run with the Monte Carlo method or numerical solution of rate equations, but because it leads to compact expressions especially for energy loss and straggling and, hence, increased insight into energy-loss processes. I admit that the results arrived at as final results may not yet be explicit enough for a representative user. For this reason, work in this area has not yet stopped but is going on, as you may note from recent papers (Osmani and Sigmund, 2011, Sigmund et al., 2011, Vockenhuber et al., 2013).

Energetics of charge exchange is usually dealt with in a rather cursory manner. The results of the treatment offered here, taking account binding energies as well as momentum of recoiling nuclei, are not necessarily dramatic from a numerical

point of view, but they indicate that it is important to establish a unique relationship between quantities measured and those calculated.

Problems

3.1. Derive forward and backward transport equations for charge fractions from (3.1) by assuming either x or y to be small enough so that the probability for more than one collision becomes negligible.

3.2. Find a physical or a mathematical argument to support the statement on detailed balancing made in (3.30). One possible way is to study a three-state system.

3.3. Derive (3.54) from (3.50) and (3.51) and find an argument why transverse momentum transfer can be neglected.

3.4. Derive (3.56) from (3.50) and (3.55).

3.5. Derive the three relations (3.65), (3.68) and (3.74).

3.6. Write down the law of energy conservation for the three types of collision event discussed in Sect. 3.4 in the laboratory frame of reference, and demonstrate that the relation

$$\frac{1}{2}M_1 v_2'^{\,2} = \gamma E \sin^2 \frac{\theta}{2}, \tag{3.163}$$

which you know for elastic collisions with a target atom initially at rest, also holds for these three types of inelastic collisions, at least up to first order in m/M_2, Q/E and U_i/E.

3.7. Show that (3.95) satisfies the following relation,

$$\int_{-\infty}^{\infty} \mathrm{d}(\Delta E) F_{IJ}(\Delta E, x) = F_{IJ}(x)\,. \tag{3.164}$$

3.8. Derive (3.97) by the method described in Sect. 9.5.1 of Volume 1 and Sect. 3.2.2 in the present chapter.

3.9. Carry out an analysis of Figs. 3.5 and 3.15 by the method sketched in the last paragraph of Sect. 3.5.3.2.

3.10. Derive analytical expressions for the intercepts $(\Delta E_0)_{11}$ and $(\Delta E_0)_{21}$ and evaluate numbers with input given by Ogawa et al. (1991a,b):

$$\sigma_{12} = 5.23 \cdot 10^{-18}\ \mathrm{cm}^2;\ \sigma_{21} = 8.12 \cdot 10^{-23}\ \mathrm{cm}^2 \tag{3.165}$$

$$S_{11} = 83.8\ \mathrm{eVcm}^2/\mu\mathrm{g};\ S_{22} = 156.9\mathrm{eVcm}^2/\mu\mathrm{g}; \tag{3.166}$$

$$\epsilon_{12} + \epsilon_{21} = 6.49\ \mathrm{keV}\,. \tag{3.167}$$

3.11. Verify the step form (3.125) to (3.127). You will need the integral

$$\int_0^1 \mathrm{d}t\, t^m (1-t)^n = m!n!/(m+n+1)! \tag{3.168}$$

3.12. Consider straggling in the two-state case and split it into three contributions,

- one where S_{12} and S_{21} as well as W_{12} and W_{21} are neglected,
- one where S_{11} and S_{22} W_{11} and W_{22} are neglected and
- what remains.

Try to appreciate the origin of the respective fluctuations and try to make rough estimates of the significance of various terms dependent on beam velocity, based on what you have learned in Sect. 3.4 on the energetics of charge exchange.

3.13. Evaluate the three contributions to straggling for the two-state system in Sect. 3.5.5.1 with the numbers specified in Problem 3.10. Set $W_{12} = \sigma_{12}\epsilon_{12}^2$ and similarly for W_{21}. Verify that the dominating correction to Bohr straggling is NxW_{21}, and show that charge-exchange straggling is insignificant for this system at the specified energy.

3.14. Show that (3.144) reduces to the exact result, (3.138), for the two-state case. Evaluate the Q_{IJ} on the basis of (3.19).

3.15. Demonstrate that (3.154) reduces to the exact result, (3.138), in the two-state case. Hint: There is a common factor in (3.149) and (3.154),

$$\sum_J F_J(q_J - q)Q_J = \frac{\sigma_{12}\sigma_{21}}{N\sigma^3}(q_1 - q_2)^2, \tag{3.169}$$

so that

$$\left(\frac{d\Omega^2}{Ndx}\right)_{\text{chex}} = 2\Delta S\,(\Delta S_0 + \Delta S_{\text{chex}})\,\frac{\sigma_{12}\sigma_{21}}{\sigma^3}(q_1 - q_2)^2\,. \tag{3.170}$$

This comes already close to the exact result. Use (3.153) to derive two linear equations determining S_{chex} and ΔS_{chex}, and insert the solutions into (3.170).

3.16. Evaluate (3.128) for the case of three projectile states. You may get help from Sigmund (1992).

References

Allison S.K. (1958): Experimental results on charge-changing collisions of hydrogen and helium atoms and ions at kinetic energies above 0.2 keV. Rev Mod Phys **30**, 1137–1168

Arbó D.G., Reinhold C.O., Kürpick P., Yoshida S. and Burgdörfer J. (1999): Quantum transport theory for atomic states through solids. Phys Rev A **60**, 1091–1102

Betz H.D. (1972): Charge states and charge-changing cross sections of fast heavy ions penetrating through gaseous and solid media. Rev Mod Phys **44**, 465–539

Betz H.D. and Grodzins L. (1970): Charge states and excitation of fast heavy ions passing through solids: a new model for the density effect. Phys Rev Lett **25**, 211–214

Blazevic A., Bohlen H.G. and von Oertzen W. (2000): Charge-state changing processes for Ne ions passing through thin carbon foils. Phys Rev A **61**, 032901

Bohr N. (1948): The penetration of atomic particles through matter. Mat Fys Medd Dan Vid Selsk **18 no. 8**, 1–144

Bohr N. and Lindhard J. (1954): Electron capture and loss by heavy ions penetrating through matter. Mat Fys Medd Dan Vid Selsk **28 no. 7**, 1–31

Burenkov A.F., Komarov F.F. and Fedotov S.A. (1992): The ion charge fluctuation effect on impurity depth distributions for high-energy ion implantation — the backward transport equation-based simulation. phys stat sol B **169**, 33–49

Cowern N.E.B., Read P.M., Sofield C.J., Bridwell L.B., Huxtable G. and Miller M. (1984a): Charge state dependence of dE/dx for ions in very thin targets. Nucl Instrum Methods B **2**, 112–115

Cowern N.E.B., Read P.M., Sofield C.J., Bridwell L.B. and Lucas M.W. (1984b): Charge-changing energy loss, higher-order Z_1 dependence, and pre-equilibrium behavior in the stopping power for energetic ions in solids. Phys Rev A **30**, 1682–1691

Efken B., Hahn D., Hilscher D. and Wüstefeld G. (1975): Energy loss and energy loss straggling of N, Ne, and Ar ions in thin targets. Nucl Instrum Methods **129**, 219–225

Frey C.M., Dollinger G., Bergmaier A., Faestermann T. and Maier-Komor P. (1995): Charge state dependence of the stopping power of 1 MeV/A ^{58}Ni-ions in thin carbon foils. Nucl Instrum Methods B **99**, 205–209

Glazov L. (1998): Energy-loss spectrum of swift ions in charge-state equilibrium. Phys Rev A **57**, 2746–2757

Glazov L.G. (2002): Multiple-peak structures in energy-loss spectra of swift ions. Nucl Instrum Methods B **193**, 56–65

Glazov L.G., Sigmund P. and Schinner A. (2002): Statistics of heavy-ion stopping. Nucl Instrum Methods B **195**, 183–187

Grande P.L. and Schiwietz G. (1991): Impact-parameter dependence of electronic energy loss and straggling of incident bare ions on H and He atoms by using the coupled-channel method. Phys Rev A **44**, 2984–2992

Landau L. (1944): On the energy loss of fast particles by ionization. J Phys USSR **8**, 201–205

Lassen N.O. (1951a): Total charges of fission fragments as functions of the pressure in the stopping gas. Mat Fys Medd Dan Vid Selsk **26 no. 12**, 1–19

Lassen N.O. (1951b): The total charges of fission fragments in gaseous and solid stopping media. Mat Fys Medd Dan Vid Selsk **26 no. 5**, 1–28

Moak C.D., Lutz H.O., Bridwell L.B., Northcliffe L.C. and Datz S. (1967): Evidence of shell effects and the approach to equlibrium in the charge-state distributions for 15-160 MeV ^{79}Br and ^{127}I ions in carbon. Phys Rev Lett **18**, 41–43

Närmann A. and Sigmund P. (1994): Statistics of energy-loss and charge-exchange of penetrating particles. Higher moments and transients. Phys Rev A **49**, 4709–4715

Nikolaev V.S. (1965): Electron capture and loss by fast ions in atomic collisions. Usp Fiz Nauk **85**, 679 – 720. [Engl. Transl. Sov. Phys. Uspekhi 8, 269 - 294 (1965)]

Ogawa H., Geissel H., Fettouhi A., Fritzsche S., Portillo M., Scheidenberger C., Shevelko V.P., Surzhykov A., Weick H., Becker F. et al. (2007): Gas-solid difference in charge-changing cross sections for bare and H-like nickel ions at 200 MeV/u. Phys Rev A **75**, 020703

Ogawa H., Katayama I., Haruyama Y., Fukuzawa F., Yoshida K., Aoki A., Tosaki M., Sugai I. and Ikegami H. (1991a): Charge-changing contribution to energy loss of 32 MeV ^{3}He^{+} in the charge state non-equilibrium region. Phys Lett A **160**, 77

Ogawa H., Katayama I., Ikegami H., Haruyama Y., Aoki A., Tosaki M., Fukuzawa F., Yoshida K., Sugai I. and Kaneko T. (1991b): Direct Measurement of fixed-charge stopping power for 32-MeV He^{3+} in a charge-state nonequilibrium region. Phys Rev B **43**, 11370–11376

Ogawa H., Katayama I., Sugai I., Haruyama Y., Aoki A., Tosaki M., Fukuzawa F., Yoshida K. and Ikegami H. (1992): Charge state dependent energy loss of light ions. Nucl Instrum Methods B **69**, 108–112

Ogawa H., Katayama I., Sugai I., Haruyama Y., Saito M., Yoshida K. and Tosaki M. (1996): Energy loss of high velocity ^{6}Li^{2+} ions in carbon foils in charge state non-equilibrium region. Nucl Instrum Methods B **115**, 66–69

Osmani O. and Sigmund P. (2011): Charge-state evolution of swift heavy-ion beams explored by matrix method. Nucl Instrum Methods B **269**, 813–816

Pierce T.E. and Blann M. (1968): Stopping powers and ranges of 5-90-MeV S^{32}, Cl^{35},Br^{79}, and I^{127} ions in H_2, He, N_2, and Kr: A semiempirical stopping power theory for heavy ions in gases and solids. Phys Rev **173**, 390–405

Read P.M. (1984): Projectile charge dependence of heavy ion stopping. Ph.D. thesis, University of Salford. Harwell Report AERE - R 11418

Reinhold C.O., Arbó D.G., Burgdörfer J., Gervais B., Lamour E., Vernhet D. and Rozet J.P. (2000): Enhanced population of high-ℓ states due to the interplay between multiple scattering and dynamical screening in ion-solid collisions. J Phys B **33**, L111–L117

Rozet J.P., Stephan C. and Vernhet D. (1996): ETACHA: a program for calculating charge states at GANIL energies. Nucl Instrum Methods B **107**, 67–70

Ryding G., Betz H.D. and Wittkower A. (1970): Influence of ionic excitation in heavy-ion charge-exchange cross sections. Phys Rev Lett **24**, 123–125

Ryding G., Wittkower A.B. and Rose P.H. (1969): Equilibrium charge-state distributions for iodine in gases (1-12 MeV). Phys Rev **185**, 129–134

Schiwietz G. (1990): Coupled-channel calculation of stopping powers for intermediate-energy light ions penetrating atomic H and He targets. Phys Rev A **42**, 296–306

Schramm R. and Betz H.D. (1992): Problems concerning the effective charge of swift heavy ions traversing gaseous and solid targets. Nucl Instrum Methods B **69**, 123–126

Shevelko V.P., Rosmej O., Tawara H. and Tolstikhina I.Y. (2004): The target-density effect in electron-capture processes. J Phys B **37**, 201–213

Shevelko V.P., Tolstikhina I.Y. and Stöhlker T. (2001): Stripping of fast heavy low-charged ions in gaseous targets. Nucl Instrum Methods B **184**, 295–308

Sigmund P. (1991): Statistics of charged-particle penetration. In A. Gras-Marti, H.M. Urbassek, N. Arista and F. Flores, editors, *Interaction of charged particles with solids and surfaces*, vol. 271 of *NATO ASI Series*, 73–144. Plenum Press, New York

Sigmund P. (1992): Statistical theory of charged-particle stopping and straggling in the presence of charge exchange. Nucl Instrum Methods B **69**, 113–122

Sigmund P. (1994): Analysis of charge-dependent stopping of swift ions. Phys Rev A **50**, 3197–3201

Sigmund P. and Glazov L. (1998): Energy loss and charge exchange: statistics and atomistics. Nucl Instrum Methods B **136-38**, 47–54

Sigmund P. and Glazov L.G. (2003): Interplay of charge exchange and projectile excitation in the stopping of swift heavy ions. Europ Phys J D **23**, 211–215

Sigmund P., Osmani O. and Schinner A. (2011): Charge-exchange straggling in equilibrium. Nucl Instrum Methods B **269**, 804–809

Sigmund P. and Winterbon K.B. (1985): Energy loss spectrum of swift charged particles penetrating a layer of material. Nucl Instrum Methods B **12**, 1–16

Surzhykov A., Koval P. and Fritzsche S. (2005): Algebraic tools for dealing with the atomic shell model. 1. Wavefunctions and integrals for hydrogen-like ions. Comp Phys Commun **165**, 139–156

Vockenhuber C., Jensen J., Julin J., Kettunen H., Laitinen M., Rossi M., Sajavaara T., Osmani O., Schinner A., Sigmund P. et al. (2013): Energy-loss straggling of 2-10 MeV/u Kr ions in gases. Europ Phys J D **67**, 145

Vollmer O. (1974): Der Einfluss der Ladungsfluktuationen auf die Energieverlustverteilung geladener Teilchen. Nucl Instrum Methods **121**, 373–377

Winterbon K.B. (1977): Electronic energy loss and charge-state fluctuations of swift ions. Nucl Instrum Methods **144**, 311–315

Part II
Energy Loss of Swift Ions

Chapter 4
Stopping

Abstract This chapter reports theoretical tools to determine stopping cross sections for heavy ions. The focus is on binary stopping theory (PASS code) and PCA/UCA theory (CasP code), but also convergent kinetic energy and approaches via transport cross sections are characterized. Problems with the effective-charge scheme are discussed, and extensive comparisons with measured stopping cross sections are presented. Applications include charge-dependent stopping, stopping in compound materials as well as impact-parameter-dependent energy loss.

4.1 Introductory Comments

Until the late 1930s, measurements on stopping of charged particles were performed mainly with α and β particles. Heavier ions were employed in gas discharges, but little was known about their penetration properties, since experimental techniques to measure ranges or energy losses at accessible energies—which were in the eV and lower keV range at the time—were not available. This situation changed with the discovery of nuclear fission, as a result of which heavy ions with energies of the order of 100 MeV and hence velocities in excess of the Bohr velocity became available. Tracks of these particles could be observed in a cloud chamber, and their ranges were studied in some detail in a series of measurements by Brostrøm et al. (1940).

These measurements were analysed by Bohr (1940, 1941), who pointed out several features which distinguished heavy from light ions with regard to their stopping behaviour:

- Stopping by elastic nuclear collisions plays a far greater role, in particular toward the end of the track,
- Heavy ions are not necessarily point charges but must be expected to carry bound electrons, the number of which may fluctuate during slowing down, so that the effective ion charge will be smaller than the nuclear charge,

P. Sigmund, *Particle Penetration and Radiation Effects Volume 2*,
Springer Series in Solid-State Sciences 179, DOI: 10.1007/978-3-319-05564-0_4,

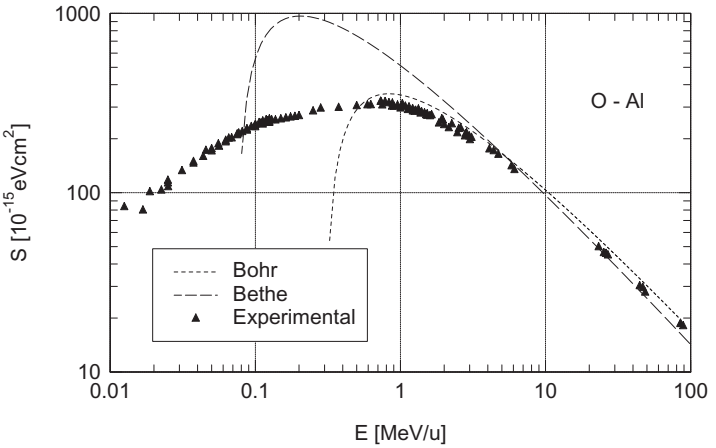

Fig. 4.1 Measured stopping cross sections for oxygen ions in aluminium, compared with Bohr and Bethe formula. Experimental data from several sources compiled by Paul (2013)

- Application of the Bethe theory to heavy-ion stopping becomes questionable because of the breakdown of the Born approximation for ions of high atomic number Z_1.

You may see an illustration of the last point in Fig. 4.1, which shows more recently measured stopping cross sections for oxygen ions in polycrystalline aluminium. Also included are stopping cross sections calculated from the standard formula

$$S = \frac{4\pi Z_1^2 Z_2 \mathrm{e}^4}{mv^2} L\,, \tag{4.1}$$

where

$$L = \begin{cases} \ln(2mv^2/\hbar\omega_0) & \text{(Bethe)} \\ \\ \ln(C\,mv^3/Z_1 e^2 \omega_0) & \text{(Bohr)} \end{cases}. \tag{4.2}$$

according to (4.93) and (4.118), Vol. 1, with $C = 1.1229$ and $\hbar\omega_0 = 166\,\mathrm{eV}$.

According to (2.80), Vol. 1, classical scattering theory should be valid for $\kappa = 2Z_1 v_0/v \gg 1$ or

$$E \ll Z_1^2 \cdot 0.1\ \mathrm{MeV/u}\,, \tag{4.3}$$

i.e., $E \ll 6.4\,\mathrm{MeV/u}$ for the system under consideration. Figure 4.1 shows that the two theoretical curves cross each other at that energy and that the Bohr formula comes closer to the experimental data below the crossing, while the opposite is found above the crossing. This is in full agreement with the expectation from the Bohr criterion: The Born approximation takes over above the limit of validity of classical stopping theory.

Figure 4.1 also demonstrates that the two theoretical expressions break down at low velocities, but initially both expressions overestimate the stopping cross section. This may be ascribed to the neglect of screening due to electrons bound to

the projectile. The fact that both expressions turn negative at some lower velocity is in part a consequence of the mathematical approximations applied, as discussed in Chap. 4, Vol. 1, but also due to the neglect of several physical phenomena that become exceedingly important at lower beam energies and which will be discussed in this chapter.

We shall see in Sect. 4.3 that for a rather long period of time, stopping measurements involving heavy ions were analysed in terms of the Bethe theory also at velocities below the limit of validity of the Born approximation. This implied that for the system shown in Fig. 4.1, projectile screening had to be taken to be the origin of an overestimate by up to a factor of 3 of the Bethe stopping cross section. Bethe himself was not involved in this development, and Bohr had died in 1963. However, Lindhard repeatedly emphasized the importance of the Bohr criterion in this context, implying that something was seriously wrong with the physics here.

About two decades ago the author of this monograph was asked by the International Commission of Radiation Units and Measurements (ICRU) to chair a committee collecting available knowledge on stopping of heavy ions and to issue a table of recommended values of stopping cross sections for materials of interest. At that time the field was dominated by empirical interpolation schemes with little if any underlying theoretical foundation. A notable exception was the work by Brandt and Kitagawa (1982) which will be commented below.

As a result I devoted several years of research to the development of a theoretical scheme to calculate stopping cross sections for ions heavier than helium, with Bohr stopping theory as the most feasible available starting point. This research has resulted in a report (ICRU, 2005), a monograph (Sigmund, 2004), a summary (Sigmund, 2006) and a rather large number of research papers. I shall try here to sum up this development, which also stimulated other research groups to work in the area, in some detail. Therefore I shall to some extent deviate from the general strategy in this monograph and devote a comparatively large fraction of space to the presentation of my own and my coworkers' contributions.

4.2 Experiments

Until the mid 1960s, measurements were performed with fission fragments which have a relatively narrow range of initial energies. Information on stopping gained from ion ranges measured at a fixed energy is rather limited. Accurate stopping measurements have became possible with the use of tandem accelerators in the late 1960s. This made it possible to specify not only the initial energy but also the mass and charge of the beam particles (Moak and Brown, 1963, 1966).

We have seen in Chap. 3 that the presence of various charge states in the beam varies along the trajectory but tends toward a dynamic equilibrium. Tabulated stopping cross sections are generally supposed to represent stopping in charge equilibrium. This implies the more or less tacit assumption that charge equilibrium is

established over a path length that is small compared to the foil thickness in a given measurement.

Measurements on thin foils with varying thickness allow to follow the approach to charge equilibrium and the influence of the ion charge on the energy loss (Cowern et al., 1984). In rare cases measurements have been performed of energy-loss spectra for a specific entrance and exit charge state (Ogawa et al., 1991, Blazevic et al., 2002). From a theoretical point of view such measurements are particularly interesting in those cases where it is possible to distinguish between particles that have undergone charge exchange and those that have not (Datz et al., 1972).

A particularly intriguing feature has been the gas-solid difference in charge state mentioned in Chap. 3. The discussion about the physical origin of the difference in mean charge has already been mentioned in Sect. 3.3.3, but even more intriguing was the subsequent discovery that this difference apparently did not affect the stopping cross section (Pierce and Blann, 1968). As a consequence, Betz and Grodzins (1970) proposed that there was no gas-solid difference in equilibrium charge state, and that the increased charge of ions emerging from solid targets was caused by Auger decay on the way from the foil to the detector. As we shall see, it took many years to resolve this question.

It was mentioned above that nuclear stopping is not necessarily negligible in measurements with heavy ions. It actually becomes dominating at low energy. Nuclear energy losses also imply angular deflection. This may complicate the analysis of stopping measurements with heavy ions, in particular at low beam energy. This aspect will be discussed in Chap. 7.

An interesting feature is the oscillatory dependence of electronic stopping cross sections at a fixed beam velocity v on the atomic number Z_1 of the ion, so-called Z_1 oscillations (Ormrod and Duckworth, 1963, Ormrod et al., 1965, Fastrup et al., 1966), which will be discussed in Chap. 8.

Figure 4.2 shows a survey of ion-target (Z_1, Z_2) combinations for which equilibrium stopping cross sections were available by october of 2009[1]. Some holes have been filled since then, but the general picture remains unchanged: There are large islands that are not covered by data at all, and for most other ion-target combinations only 1–4 data sets are available. Note that an accelerator typically covers about one order of magnitude variation in beam energy, while the range of beam energies of potential interest goes over more than six orders of magnitude.

In other words, theory is indispensable in this field and will remain so for many years.

4.3 Effective Charge and its Problems

Consider for a moment the stopping of fission fragments. With a mass of $\sim 100\,\mathrm{u}$ and an energy of $\sim 100\,\mathrm{MeV}$ the energy lies in the range of $\sim 1\,\mathrm{MeV/u}$ and, hence,

[1] The author is grateful to Prof. H. Paul for producing this graph.

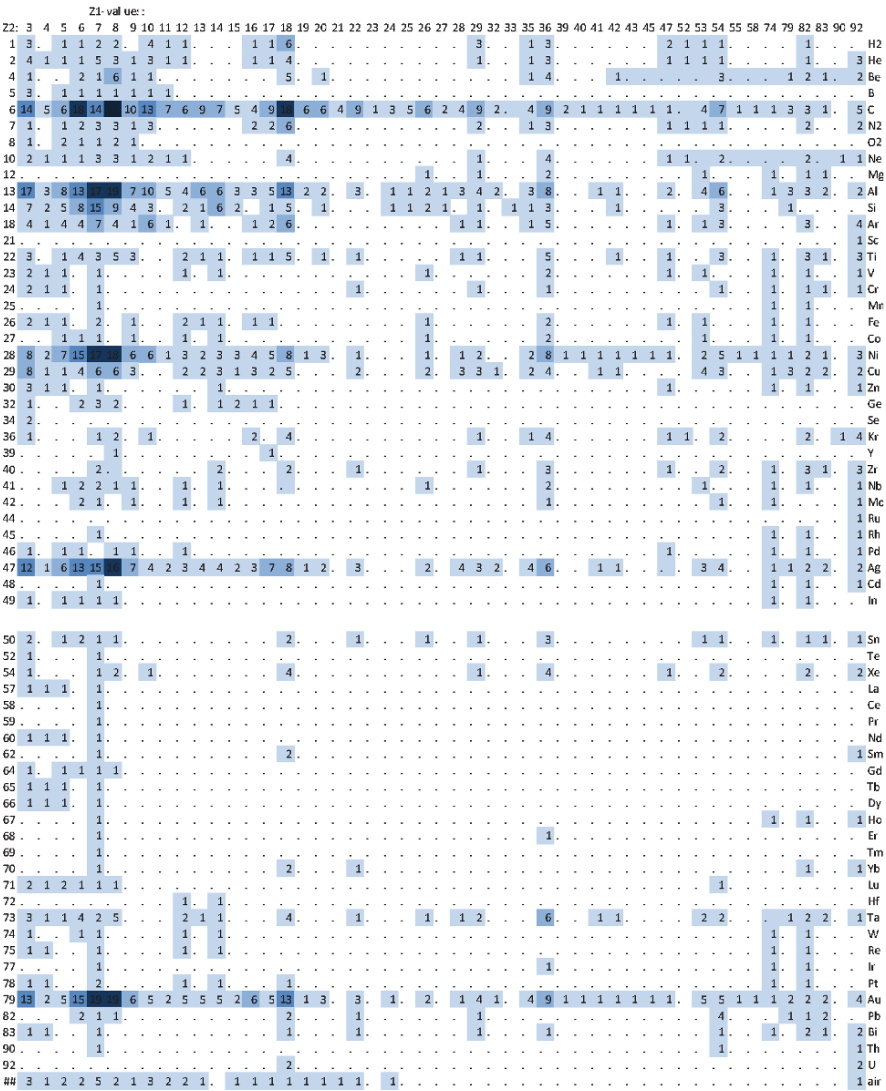

Fig. 4.2 Ion-target combinations covered by stopping data by october 2009. Graph updated from ICRU (2005). Numbers denote the number of available literature references. Compiled by H. Paul

a velocity of $v \sim 6v_0$. The mean charge fraction is given roughly by

$$\frac{q_1}{Z_1} \sim \frac{v}{Z_1^{2/3} v_0} \sim 0.5\,. \tag{4.4}$$

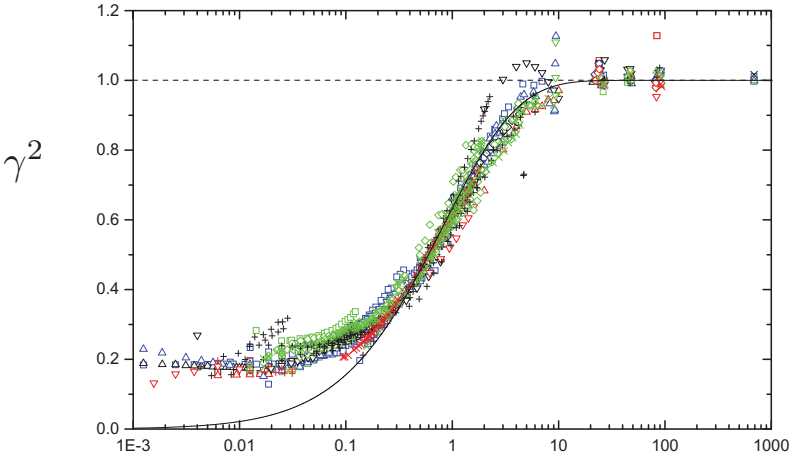

Fig. 4.3 Effective-charge ratio γ^2 for oxygen in numerous target materials, determined from (4.6). From Paul (2013). Also included is the square of the Thomas-Fermi charge fraction (thin solid line)

Both Bohr and Bethe stopping theory were developed for bare projectiles, i.e., point charges. The question arises, therefore, how to accommodate the above reduction in the effective ion charge into stopping theory. Bohr (1940, 1941) recognized that $\kappa = 2Z_1 v_0/v > 1$ for fission fragments and replaced Z_1 by q_1 in the Bohr formula in order to obtain a rough estimate of the penetration depth.

This idea was taken up by Northcliffe (1960), but with the important difference that Bohr stopping theory was replaced by Bethe theory. Unlike in Bohr theory, the charge enters only as a factor here. Northcliffe proposed to define an effective-charge ratio by reference to the stopping cross section for protons,

$$\gamma^2 = \frac{1}{Z_1^2} \frac{S(Z_1, Z_2, v)}{S(1, Z_2, v)} \tag{4.5}$$

or to α particles,

$$\gamma^2 = \left(\frac{2}{Z_1}\right)^2 \frac{S(Z_1, Z_2, v)}{S(2, Z_2, v)}\,, \tag{4.6}$$

where $S(Z_1, Z_2, v)$ is the stopping cross section of an atom Z_2 for an ion Z_1 *in charge equilibrium*. In either case, γ^2 was suggested to depend on Z_1 and v but not on Z_2. The effective-charge ratio γ^2 could then be determined empirically for those ions and velocities where data were available, and the rest could be handled by interpolation, making use of analytical fitting formulae. An example is given in Fig. 4.3. Once $\gamma(Z_1, v)$ has been determined, $S(Z_1, Z_2, v)$ can be found for any material for which a proton or α stopping cross section is available.

While this scheme, or a slight modification thereof, was employed in numerous tabulations and codes providing stopping cross sections for heavy ions (Steward, 1968, Northcliffe and Schilling, 1970, Hubert et al., 1980, Ziegler et al., 1985, Hu-

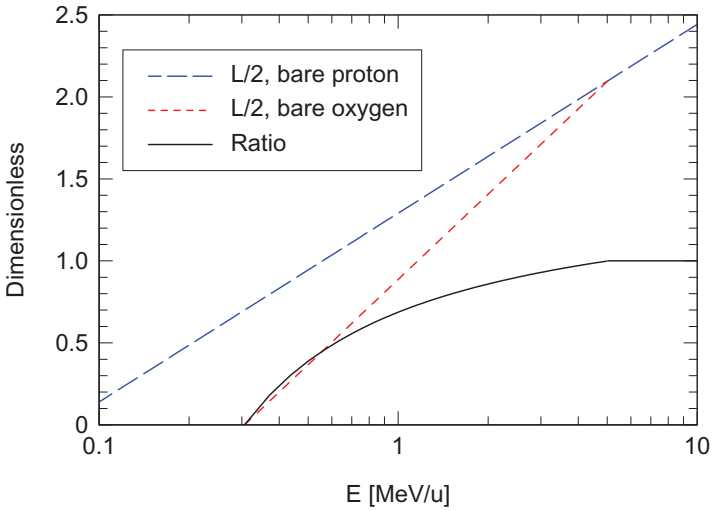

Fig. 4.4 Solid line: 'Effective-charge ratio' calculated for bare ions (schematic). Straight lines represent Bohr (dotted) and Bethe (dashed) stopping numbers. See text

bert et al., 1990, Paul and Schinner, 2001), several problems are either obvious or have shown up gradually:

- The effective-charge ratio γ^2 extracted from (4.5) or (4.6) deviates significantly from the corresponding quantity extracted from the measured charge population.
- This has been found to be the case both for the absolute magnitude and the dependence on v and Z_1. An example is seen in Fig. 4.3, where the function $\left[1-\exp(-v/Z_1^{2/3}v_0)\right]^2$, which represents the square of the simple Thomas-Fermi charge fraction, has been included.
- Evidently, γ^2 is not independent of Z_2.
- On the theoretical side, the application of a formula derived for point charges to screened ions, i.e., the replacement of the nuclear charge by the ion charge, was questionable from the beginning,
- The role of the Barkas-Andersen (or Z_1^3) effect in heavy-ion stopping was not clear,
- For heavy ions in the classical regime the atomic number does not only enter as a factor but also under the logarithm and, most important,
- Since screening is important for $v \lesssim v_0 Z_1^{2/3}$ and the Born regime is confined to projectile speeds $v \gtrsim v_0 Z_1$, the scheme can be expected to be valid for

$$v_0 Z_1 \lesssim v \lesssim v_0 Z_1^{2/3}\,, \tag{4.7}$$

a condition that is not fulfilled for any ion with $Z_1 > 1$.

The next-to-last point is illustrated in Fig. 4.4, which shows stopping numbers for bare protons and bare oxygen according to the simple Bohr and Bethe formu-

lae, (4.2). The two curves coincide above 6 MeV/u. Also shown is the ratio between the two curves, which is $= 1$ above 6 MeV/u, but at lower energies looks suspiciously like an effective-charge ratio γ^2, except that it turns negative at the apparent threshold defined by the Bohr formula. While this curve exhibits the qualitative behaviour seen in the empirical data in Fig. 4.3, it is completely unrelated to projectile screening.

Brandt and Kitagawa (1982) have made an attempt to establish a theoretical basis for the effective-charge concept. This work had a profound effect on the theory of heavy-ion stopping, even though the effective-charge concept has now been largely abandoned.

4.4 Bohr Theory Extended

The Bohr criterion (4.3) for validity of a classical-orbit theory of ion-electron scattering, $E \ll Z_1^2\, 0.1\,\text{MeV/u}$, comprises a rather wide energy range for $Z_1 \gg 1$. Therefore I shall try to use Bohr stopping theory as described in Sect. 4.2, Vol. 1, as a starting point to develop a theory of heavy-ion stopping. This will require incorporation of a number of effects which were unknown when Bohr (1913) proposed his theory (Sigmund, 2005) and which did not enter the discussion in Volume 1.

4.4.1 Low-Speed Limit

According to Fig. 4.1, both the simple Bethe formula and the simple Bohr formula predict negative stopping cross sections below some threshold. Since the derivation of those formulae does not involve negative energy losses, this feature must be an artifact introduced by mathematical approximations. Figure 4.3 in Sect. 4.5.1, Vol. 1, shows that if you avoid asymptotic expansions of Bessel functions, the resulting Bohr stopping cross section approaches zero stopping at zero energy smoothly (Sigmund, 1996).

4.4.2 Screening

As a preliminary exercise let us consider Bohr stopping theory with the Coulomb interaction $\Phi(\boldsymbol{r}, t)$ in (4.13), Vol. 1 replaced by a screened potential

$$\Phi(\boldsymbol{r}, t) = \frac{e_1}{|\boldsymbol{r} - \boldsymbol{R}(t)|} g\left(|\boldsymbol{r} - \boldsymbol{R}(t)|\right), \tag{4.8}$$

where $g(r)$ is some screening function. A simple example is

$$g_0(r) = \mathrm{e}^{-r/a} \tag{4.9}$$

with a screening radius a left open for now. while a more realistic representation could be achieved by a sum of exponentials such as

$$g(r) = \sum_n \alpha_n \mathrm{e}^{-r/a_n}; \qquad \sum_n \alpha_n = 1\,. \tag{4.10}$$

Note first that

$$\frac{1}{r}\mathrm{e}^{-r/a} = \frac{1}{2\pi^2}\int \frac{\mathrm{d}^3\boldsymbol{q}}{q^2 + 1/a^2}\,\mathrm{e}^{\mathrm{i}\boldsymbol{q}\cdot\boldsymbol{r}}\,. \tag{4.11}$$

If you are unfamiliar with this relation you are invited to verify it by going to Problem 4.1. Comparing (4.11) with (4.15), Vol. 1, you will see that the denominator q^2 has been expanded to $q^2 + 1/a^2$. As noted by Johnson (1982), you may include this modification in the calculation presented in detail in Sect. 4.2.2, Vol. 1, and end up with the following expression for the Fourier transform of the electric field at the position of the target electron,

$$\boldsymbol{E}(\omega) = -\frac{e_1\omega}{\pi v^2}\left(iK_0\left(\sqrt{\zeta^2 + p^2/a^2}\right), K_1\left(\sqrt{\zeta^2 + p^2/a^2}\right), 0\right), \tag{4.12}$$

where

$$\zeta = \frac{\omega p}{v}\,. \tag{4.13}$$

Now, remind that according to (4.11), Vol. 1, the quantity

$$T = \frac{1}{2m}\left|\int_{-\infty}^{\infty}\mathrm{d}t\ (-e\boldsymbol{E}(t))\,\mathrm{e}^{\mathrm{i}\omega_0 t}\right|^2 \tag{4.14}$$

represents the energy transfer in a single distant collision to an electron bound harmonically with a resonance frequency ω_0. Then, (4.12) tells us that in Bohr's calculation we need to replace

$$\frac{\omega^2}{v^2} \to \frac{\omega^2}{v^2} + \frac{1}{a^2}\,. \tag{4.15}$$

Here $v/\omega = a_{\mathrm{ad}}$ is the adiabatic radius which represents the effective screening due to harmonic binding of the target electron, whereas a represents screening in the ion-electron potential. Thus, while the two types of screening have different physical origins, they nevertheless enter in a completely equivalent manner into (4.15).

You may turn this argument around: Instead of incorporating binding of the target electron as a separate harmonic potential in the equation of motion, we could instead include it in an exponentially-screened ion-electron potential (4.9) with a screening radius specified in (4.15).

To complete this argument, let us go back to unscreened Coulomb interaction by setting $a = \infty$. Then we may replace the harmonic potential in the Bohr model by an exponentially-screened Coulomb potential with the adiabatic radius as the

screening radius. This is exactly what has been found already in Sect. 6.4.5, Vol. 1 when binary stopping theory was discussed.

4.4.3 Charge Dependence

Equation (4.8) or (4.9) could approximately represent a neutral atom. Characterizing an ion with a charge $q_1 e$ requires an extension such as

$$\mathcal{V}(r) = -\frac{q_1 e^2}{r} - \frac{(Z_1 - q_1)e^2}{r}\, g(r)\,, \tag{4.16}$$

where $Z_1 - q_1$ denotes the number of electrons bound to the projectile (Brandt and Kitagawa, 1982).

Let us keep to an exponential dependence, $g = g_0(r)$ in accordance with (4.9). Then, making use of (4.12) you will find

$$T = \frac{2Z_1^2 \mathrm{e}^4}{mv^2 p^2} f(p) \tag{4.17}$$

with

$$f(p) = \left[\frac{q_1}{Z_1}\zeta K_1(\zeta) + \left(1 - \frac{q_1}{Z_1}\right)\sqrt{\zeta^2 + p^2/a^2}\, K_1\left(\sqrt{\zeta^2 + p^2/a^2}\right)\right]^2 + \left[\frac{q_1}{Z_1}\zeta K_0(\zeta) + \left(1 - \frac{q_1}{Z_1}\right)\zeta K_0\left(\sqrt{\zeta^2 + p^2/a^2}\right)\right]^2. \tag{4.18}$$

This relation reduces to Bohr's formula, (4.23), Vol. 1, for $q_1 = Z_1$ and $a = \infty$. It has been utilized in the calculation of stopping cross sections within the general framework of the Bohr theory (Sigmund, 1997). However, an important ingredient is missing here: The Barkas-Andersen correction which accounts for deviations from the Z_1^2 law could become substantial for $Z_1 \gg 1$.

4.5 Binary Stopping Theory and PASS Code

Binary stopping theory has been documented in a number of papers by A. Schinner and the author, primarily Sigmund and Schinner (2000, 2002) and ICRU (2005).

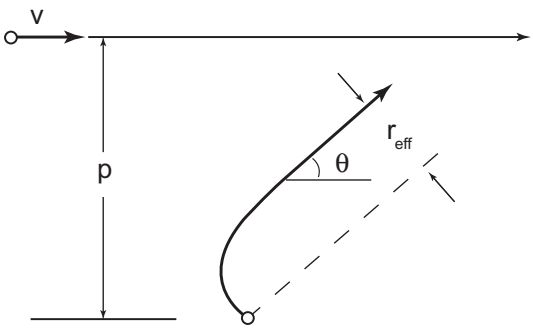

Fig. 4.5 Definition of r_{eff}. See text

4.5.1 The Kernel

The essential point in binary theory, described in Sect. 6.4.5, Vol. 1, is the representation of binding by screening of the interaction potential. We have seen that this is achieved by the replacement (4.15). Thus, the effective ion-electron interaction potential for a screened ion emerges from (4.16) by this replacement,

$$\mathcal{V}(r) = -\frac{q_1 e^2}{r}\,\mathrm{e}^{-\omega r/v} - \frac{(Z_1 - q_1)e^2}{r}\,\mathrm{e}^{-\sqrt{\omega^2/v^2+1/a^2}\,r}\,, \tag{4.19}$$

if we adopt exponential screening. More complex screening function such as (4.10) can be handled correspondingly.

The energy transfer to a free target electron,

$$T = 2mv^2 \sin^2 \Theta/2\,, \tag{4.20}$$

where Θ is the centre-of-mass scattering angle, can be evaluated from (3.76), Vol. 1 for a distant collision,

$$\Theta = -\frac{2}{mv^2 p}\int_p^\infty \frac{\mathrm{d}r}{\sqrt{1-p^2/r^2}}\,\frac{\mathrm{d}}{\mathrm{d}r}\,[r\mathcal{V}(r)] \tag{4.21}$$

to the leading power in V. Insertion of (4.19) and integration then reproduces (4.17) with f given by the first term in (4.18) to the leading term in Z_1 (cf. Problem 4.2).

The missing second term in (4.18) was shown in Sect. 6.4.5, Vol. 1 to originate in the transfer of potential energy to a harmonically bound electron. While there is no transfer of potential energy to a free electron, the equivalent of this contribution could nevertheless be determined via the transfer of angular momentum, which does occur also in a free binary collision. The argument goes as follows:

The angular momentum J achieved by a target electron, with reference to its initial position in the laboratory frame of reference, may be written as

$$J = r_{\text{eff}} P\,. \tag{4.22}$$

Here, P is the transferred momentum and r_{eff} the distance of the asymptotic (straight line) trajectory from the point of departure (Fig. 4.5). r_{eff} can be expressed by the time integral τ (cf. Sect. 3.3.4, Vol. 1) and reduces to

$$r_{\text{eff}} \to 2\tau - p\Theta \tag{4.23}$$

for distant collisions, while P reduces to

$$P \to mv\Theta \tag{4.24}$$

in that limit.

The transfer of potential energy is then given by

$$E_{\text{pot}} = \frac{1}{2} m\omega^2 r_{\text{eff}}^2 . \tag{4.25}$$

We therefore need to evaluate the time integral for the potential (4.19). This can be achieved by the relation

$$\tau = -\frac{1}{mv^2} \int_p^\infty \frac{\mathrm{d}r}{\sqrt{r^2 - p^2}} \frac{\mathrm{d}}{\mathrm{d}r} \left[r^2 \mathcal{V}(r) \right] \tag{4.26}$$

which yields[2]

$$r_{\text{eff}} = \frac{2Z_1 e^2}{mv^2} \left[\beta K_0(\zeta) + (1-\beta) K_0 \left(\sqrt{\zeta^2 + p^2/a^2} \right) \right] . \tag{4.27}$$

Inserting this into (4.25) you obtain the missing second term in (4.18).

With this, an exact mapping has been achieved of the extended Bohr model discussed in Sect. 4.4.3 for screened ions on a binary scattering model for *distant collisions*. It was shown by Sigmund and Schinner (2000) that the validity of this approach also extends to the next order in Z_1. However, unlike the leading order, the equivalence in the second order is not algebraically exact.

Binary stopping theory does not make use of a perturbation expansion. Instead, the scattering problem defined by the interaction potential (4.19) is solved by numerical integration of the scattering integrals (3.34) and (3.61) derived in Volume 1. The energy transfer $T(v, p)$ is then determined as a function of projectile speed and impact parameter from (4.20) and (4.25). Integration over the impact parameter delivers the stopping cross section $S(v) = \int 2\pi p \, \mathrm{d}p \, T(v, p)$, as well as the straggling parameter $W(v) = \int 2\pi p \, \mathrm{d}p \, T(v, p)^2$ if desired.

As described up till now, binary stopping theory delivers a stopping cross section for a one-electron atom interacting with a partially-stripped ion. Since no perturbation expansion has been made, the Barkas-Andersen effect is inherent in the scheme. The incorporation of higher-order terms is not exact, but its numerical accuracy was

[2] There is a misleading misprint in (A.33), Vol. 1, p. 399: The contents of the square brackets should read $K_0(p/a) - (p/a)K_1(p/a)$. Moreover, '$\mathrm{d}r$' is missing in the integral (A.132).

tested by Sigmund and Schinner (2000) against an explicit evaluation of the Z_1^3 term for screened heavy ions (Schinner and Sigmund, 2000).

In order to allow prediction of stopping cross sections, further extensions of the Bohr theory are necessary:

- We need to allow for more than one electron in a target atom,
- The orbital motion of the target electrons needs to be incorporated,
- A smooth transition to the Bethe regime needs to be ensured,
- Projectile excitation and electron capture and loss need to be allowed for,
- Relativistic corrections need to be incorporated.

These features have to be accounted for in any theory of heavy-ion stopping. They can be dealt with in a variety of ways. Before looking into how they enter into binary stopping theory, let us try to find some qualitative criteria for their respective significance.

According to Sect. 6.6, Vol. 1, the shell correction produces a leading correction term to the stopping number of the order of v_e^2/v^2 at large ion speeds. Within the Thomas-Fermi model of the atom (cf. Sect. 7.2.2, Vol. 1), we have $v_e \simeq v_0 Z_2^{2/3}$. Thus, the shell correction goes as

$$\Delta L_{\text{shellcor}} \propto Z_2^{4/3} \frac{v_0^2}{v^2} \,. \tag{4.28}$$

We have already seen that the Barkas-Andersen correction produces a correction term of the order of $Z_1 e^2 \omega / m v^3$. With the Thomas-Fermi expression for the I-value, $\hbar\omega \propto Z_2 m v_0^2$ this leads to a correction

$$\Delta L_{\text{Barkas}} \propto Z_1 Z_2 \frac{v_0^3}{v^3} \,. \tag{4.29}$$

Screening due to electrons accompanying the projectile becomes significant when the ratio $v/Z_1^{2/3} v_0$ is not $\gg 1$.

Finally, the Bloch correction is governed by the Bohr parameter $2Z_1 v_0/v$. All these corrections may be taken as small at high projectile speeds, and with decreasing speed their relative importance depends on Z_1 and Z_2. For $Z_1 > Z_2$, the Bloch correction is most important, followed by screening, Barkas-Andersen and shell correction. Conversely, for $Z_1 < Z_2$, the shell correction is leading, followed by the Bloch and Barkas-Andersen terms, and screening becomes noticeable at even lower projectile speeds.

4.5.2 Multiple-Electron Atoms

Binary stopping theory assumes independent target electrons. This implies that a neutral atom is characterized by Z_2 resonance frequencies. Some of those may be identical. In practice we need a set of resonance frequencies ω_n or $\omega_{n\ell}$ for the nth

principal shell or the $n\ell$th subshell and the number of electrons $Z_2 f_n$ or $Z_2 f_{n\ell}$ in the respective shell or subshell, where f_n and $f_{n\ell}$ are taken as dipole oscillator strengths introduced in Sect. 4.5.3, Vol. 1.

Several procedures have been proposed for deriving appropriate sets of (f_n, ω_n) pairs for individual atoms. A convenient option, proposed by Sternheimer (1952) is as follows,

- $Z_2 f_{n\ell}$ is taken as identical with the nominal number of electrons in the $n\ell$th subshell according to the periodic table,
- $\hbar\omega_{n\ell}$ is taken as proportional to the respective subshell binding energy $U_{n\ell}$,
- The common proportionality constant α is chosen such that

$$\ln I = \sum_{n\ell} f_n \ln(\alpha U_{n\ell}) \,, \tag{4.30}$$

where I is the logarithmic mean excitation energy, the 'I-value' of the material.

Since binding energies $U_{n\ell}$ are well documented for all materials (Carlson et al., 1970), this is a very convenient procedure. The proportionality between ω and U appears well justified as a function of Z_2 for specific shells, cf. Fig. 7.13, Vol. 1. However, the assumption of a common proportionality factor between different shells of one and the same atom is not corroborated by comparisons of more reliable data, as you may see in Table 7.1, Vol. 1. Moreover, the procedure assumes the I-value to be wellknown and thus implicitly involves fitting of stopping data.

This procedure has been adopted in the CasP code to be discussed below (Grande and Schiwietz, 2010). In the PASS code, an implementation of binary stopping theory, it has been incorporated as an option for determining $(f_{n\ell}, \omega_{n\ell})$ when more reliable data are unavailable.

The standard procedure adopted in the PASS code makes reference to continuous oscillator-strength spectra $f(\omega)$ found from optical and X-ray data, cf. Sect. 7.6.2, Vol. 1. Here,

$$Z_2 f_{n\ell} = \int_{n\ell} \mathrm{d}\omega f(\omega) \tag{4.31}$$

and

$$Z_2 f_{n\ell} \ln \omega_{n\ell} = \int_{n\ell} \mathrm{d}\omega f(\omega) \ln(\omega) \,, \tag{4.32}$$

where $\int_{n\ell}$ indicates an integral over a frequency range which can be assigned to the $n\ell$th subshell. The delimitation of the principal shells is suggested by absorption edges in the spectra for the innermost shells. Separation of subshells may be less clear, but because of the logarithmic averaging expressed in (4.31) this delimitation does not have a critical influence on the final outcome. The same statement applies to outer shells, where an assignment to shells and subshells on the basis of measured spectra is usually ambiguous.

Oscillator-strength spectra may also be calculated. A major effort was taken in the 1970s to compute moments and logarithmic mean values over such spectra for elements up to krypton (Dehmer et al., 1975, Inokuti et al., 1981). These calcula-

tions reproduced relative variations found in stopping and other measurements as a function of Z_2, but the calculated absolute values were not accurate enough for computing stopping parameters. Recent efforts along this line combine computational methods and experimental data (Smith et al., 2006).

4.5.3 Projectile Excitation and Ionization

According to (3.108), the mean energy loss per path length, summed over all charge states, is given by

$$\left(-\frac{\mathrm{d}E}{\mathrm{d}x}\right)_I = N \sum_{JK} F_{IJ}(x) S_{JK} \,, \tag{4.33}$$

where $F_{IJ}(x)$ is the probability for an ion to occupy state J at depth x if it was in state I at $x = 0$ and $S_{IJ} = \int T \mathrm{d}\sigma_{IJ}(T)$ is a partial stopping cross section.

When the stationary state is reached, this reads

$$-\frac{\mathrm{d}E}{\mathrm{d}x} = N \sum_{J} F_J S_J \,, \tag{4.34}$$

where

$$S_J = \sum_K S_{JK} \tag{4.35}$$

and $F_J = F_{IJ}(\infty)$. A rigorous evaluation of (4.34) does not only require knowledge of F_J for all significant charge and excitation states of the projectile, it also requires knowledge of the cross sections for charge exchange and the associated energy transfers *from all those states*, in addition to the energy-loss cross sections for target excitation in a 'frozen' charge state. In order to get a tractable expression we need to make some simplifications.

We shall see below that most often, target excitation is the dominant energy-loss process. This process depends on the *charge state* of the ion but is less sensitive to its *excitation state*. Therefore, with regard to target excitation we may restrict the sum over J to go over the significant charge states.

In Sect. 3.5.5.2 the stopping cross section was approximated as a linear function of the charge state. This implies that instead of averaging over the stopping cross section we can try to average over the charge state. Then, (4.34) reduces to

$$-\frac{\mathrm{d}E}{\mathrm{d}x} \simeq N S(\overline{q}) \,, \tag{4.36}$$

where $\overline{q}$ is the equilibrium charge. The quality of this approximation and its limitations will be discussed in Sect. 4.8.3.

In the PASS code the approximation (4.36) has been applied to all processes undergone by a projectile in the equilibrium charge state, not only to target excitation. This appears acceptable as long as other processes are not dominant.

Consider now energy loss by charge exchange. We may assume that single-electron processes dominate. With this, the stopping cross section in (4.36) reduces to

$$S(\overline{q}) = S_{\text{frozen}}(\overline{q}) + S_{\text{capt}}(\overline{q}) + S_{\text{loss}}(\overline{q})\,. \tag{4.37}$$

Now, in charge equilibrium, the mean number of electrons captured per path length is equal to the mean number of electrons lost per pathlength. When only single-electron capture and loss events are allowed, also the mean number of capture events per pathlength must equal the mean number of loss events per pathlength. And if the distribution of charge fractions does not have a narrow peak around the maximum, we may even assume that the cross sections for capture and loss are approximately equal in charge equilibrium

$$\sigma_{\text{capt}} \simeq \sigma_{\text{loss}} = \sigma_{\text{chex}}\,, \tag{4.38}$$

despite the cautionary remark in connection with (3.29).

If we allow this approximation, we may write

$$S(\overline{q}) \simeq S_{\text{frozen}}(\overline{q}) + \sigma_{\text{chex}} T_{\text{cl}}\,, \tag{4.39}$$

where T_{cl} is the mean energy loss per capture-loss cycle from (3.78).

The quantity S_{frozen}, the stopping cross section for an ion which does not change its charge, consists of two contributions, one related to target excitation/ionization which has been discussed earlier in this section, and another one related to projectile excitation.

Projectile excitation is treated parallel to target excitation as much as possible. This is most easily visualized by viewing the collision from a reference frame moving with the projectile. Then

- The roles of target and projectile are switched, but the relative speed is the same,
- Now it is the 'projectile' that is neutral, while the 'target' particle is partially stripped, and
- Only energy transfers $0 \le T \le U$ are considered (Sigmund and Glazov, 2003), where U is the binding energy of the 'target' taken from (Carlson et al., 1970).

It was asserted above that the excitation state of the true projectile has only a minor influence on the stopping cross section for target excitation. This statement is not necessarily true when it comes to projectile excitation, since that stopping cross section increases with decreasing shell binding energy if the projectile is in an excited state.

This feature has been handled in the PASS code by allowing one of two options,

- The projectile is in its ground state at the given charge, or
- Individual shells are only partially occupied. They are assumed to be filled to a fraction q_1/Z_1 from the bottom up.

A more realistic description may be expected to be intermediate between the two extremes. This allows to estimate the uncertainty introduced by this feature.

Any dependence of $U_{n\ell}$ and $\omega_{n\ell}$ on the charge state has been ignored in the PASS code until the time of writing.

4.5.4 Extension into the Bethe Regime

In Sect. 6.3.3, Vol. 1 an inverse-Bloch correction was mentioned which, when added to the Bohr stopping formula, produces the Bethe stopping formula. This correction—which does not depend on the material, has been incorporated as an option into the PASS code. In this way, stopping cross sections predicted by PASS approach the Bethe form at high projectile speeds.

However, the inverse-Bloch correction makes reference to bare ions. Therefore we need to pay attention to the possibility that it needs to be modified for partially-screened projectile ions.

Remember that the transition point between the Bohr and the Bethe regime lies at $v \propto 2Z_1 v_0$, while the mean charge is given by (1.6) approximately. This implies that the average charge fraction at the transition point is given by

$$\frac{q_{\text{crit}}}{Z_1} \simeq 1 - \mathrm{e}^{-2Z_1^{1/3}} . \tag{4.40}$$

This is 0.86 for protons, 0.94 for lithium and even closer to 1 for heavier ions. Moreover, the ratio approaches 1 rapidly with increasing speed. In other words, unless you need high-precision data it appears well justified, in the determination of stopping cross sections in charge equilibrium, to apply the inverse-Bloch correction for bare ions.

4.5.5 Shell Correction

The shell correction takes into account the orbital motion of the target electrons. The Bohr theory, operating with a classical model of the atom, ignores this feature. Although the shell correction is fully incorporated in the Bethe theory of stopping, the simple Bethe logarithm $\ln 2mv^2/\hbar\omega$ is based on an asymptotic expression, where terms of order $\langle v_e^2/v^2\rangle$ are neglected. Also the Bloch correction, (6.20), Vol. 1, follows this pattern. Therefore, a shell correction has to be incorporated over the entire velocity range, except at projectile speeds much larger than the highest orbital speed.

The topic has been discussed extensively in Sect. 6.6, Vol. 1. A convenient way of incorporating the shell correction is kinetic theory, presented in Sect. 6.6.4, Vol. 1. This scheme is particularly well suited for use in binary collisions, where it is exact, as far as the kinetic-energy transfer (4.20) is concerned. Moreover, Sigmund and Schinner (2006) demonstrated that what is commonly denoted as shell corrections can fully be accounted for by

- avoiding asymptotic expansions in powers of $1/v$ and
- accounting for orbital velocities v_e in accordance with kinetic theory (Sigmund, 1982).

In the PASS code the same formalism has been applied to the potential-energy transfer (4.25). This is not justified on theoretical grounds, but since potential-energy transfer is generally small compared to the kinetic term, the error made is asserted to be tolerable.

4.5.6 Relativistic Effects

Stopping at relativistic projectile speeds has been discussed in Sect. 6.7, Vol. 1. When dealing with very heavy ions we have to address the fact that relativistic velocities do not lie automatically in the Bethe regime. Indeed, the Sommerfeld parameter $Z_1 v_0/v$ may come close to 1 at $v \simeq c$ for the heaviest ions. Since the relativistic corrections in Bohr and Bethe theory differ from each other, there might be a reason for concern.

This problem was addressed in a comprehensive manner by Lindhard and Sørensen (1996), who developed their theory on the basis of relativistic quantum theory of scattering and wrote the main result in the form of a correction to the relativistic Bethe stopping formula, cf. (6.121), Vol. 1. This theory ignores screening by projectile electrons as well as shell corrections. It has been implemented by A.H. Sørensen in a FORTRAN code which, by courtesy of A.H. Sørensen, has been incorporated in the PASS code.

In precision measurements of stopping of very heavy ions, screening by projectile K electrons may not be negligible. This aspect has been treated by Sørensen (2007), but it is not part of the PASS code.

4.6 PCA/UCA Approximation and CasP Code

Grande and Schiwietz (1998) proposed a scheme to determine stopping cross sections for light and heavy ions as well as straggling parameters and impact-parameter dependencies. The scheme has, after further development, resulted in the CasP code which is available on the internet (Grande and Schiwietz, 2010). Although the original derivation starts from the Bethe theory, the essential features can as well be characterized within the Bohr theory.

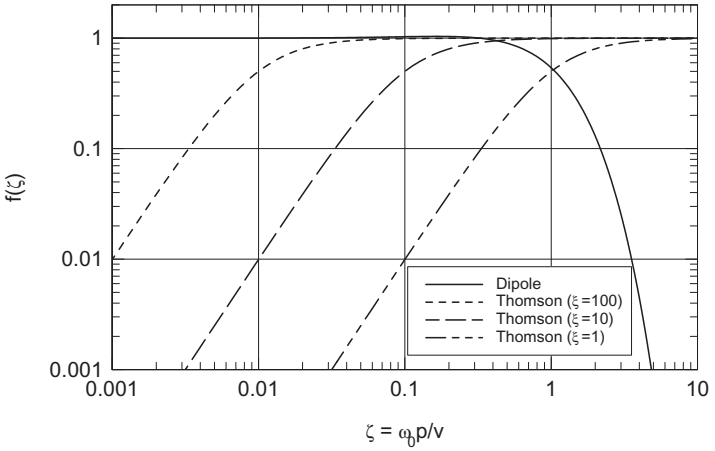

Fig. 4.6 Replot of Fig. 4.2, Vol. 1: Plotted is the function $f(v, p)$ in (4.41) as a function of $\zeta = \omega_0 p/v$. Solid line: Dipole approximation. Broken lines: Thomson formula for three values of $\xi = mv^3/Z_1 e^2 \omega_0$

4.6.1 The Kernel

Let us consider a one-electron atom with a resonance frequency ω_0. Then, according to (4.22), Vol. 1, the energy loss $T(p)$ at an impact parameter p is given by

$$T_0(p) = \frac{2Z_1^2 \mathrm{e}^4}{mv^2 p^2} f(p, v)\,, \tag{4.41}$$

where $f(v, p)$ is a dimensionless function which, in the Bohr theory, was determined separately for close and distant collisions.

Grande and Schiwietz (1998) considered three impact-parameter regimes. For large p the dipole approximation

$$f(v, p) = \zeta^2 \left[(K_0(\zeta))^2 + (K_1(\zeta))^2 \right]; \qquad \zeta = \omega_0 p/v \tag{4.42}$$

is employed according to (4.23), Vol. 1. Figure 4.6 shows $f(\zeta)$, which is close to 1 up to the adiabatic radius and drops rapidly toward zero as the impact parameter increases. The figure is equivalent to Fig. 4.2, Vol. 1, but the logarithmic scale is more illustrative for the present purpose.

In the opposite end, the expression $T_0(p) = 2Z_1^2 \mathrm{e}^4/mv^2 p^2$ diverges at small impact parameters. In the Bohr theory this divergence is removed by employing the Thomson formula, which is equivalent with (4.84), Vol. 1,

$$f(p) = \frac{1}{1 + (b/2p)^2} \equiv \frac{\zeta^2}{\zeta^2 + 1/\xi^2}\,, \tag{4.43}$$

where $b = 2Z_1e^2/mv^2$ is the collision diameter and $\xi = mv^3/Z_1e^2\omega_0$. Three representative cases, corresponding to different projectile speeds, have been included in Fig. 4.6.

It is seen that there is an intermediate range of impact parameters where both functions are close to 1, dependent on speed. This allows to join the two regimes in the Bohr theory, cf. Sect. 4.5.1, Vol. 1. You may go to Problem 4.3 and try to derive the above result starting from the Born approximation (Grande and Schiwietz, 1998).

Grande and Schiwietz (1998) added two features to this scheme, both of which are quantum features that are absent in the Bohr theory. Firstly, if we define p as the impact parameter to the *nucleus*, we need to convolute $T_0(p)$ with the spatial distribution function $g_e(r_e)$ of the electrons,

$$T(p) = \int \mathrm{d}^3\boldsymbol{r}_e g_e(r_e) T_0\left(|\boldsymbol{p} - \boldsymbol{\rho}_e|\right) , \tag{4.44}$$

where $\boldsymbol{\rho}_e$ is the component of $\boldsymbol{r}_e$ in the impact plane perpendicular to the projectile velocity. This modification has been applied both in the low-p and the intermediate regime.

As a second modification, the orbital velocity distribution $f_e(v_e)$ was taken into account in the close-collision regime. The resultant expression, which was likewise derived from the Born approximation, does not contain Planck's constant except through $f_e(v_e)$, i.e., it must be equivalent with what can be derived by the methods presented in Sect. 6.5.1, Vol. 1.

Evidently the scheme does not predict a Barkas-Andersen effect. You may also worry about the validity of treating the spatial distribution $g_e(r_e)$ and the velocity distribution $f_e(v_e)$ as uncorrelated. However, that approximation does not affect the stopping cross section, which is found by integration over the impact parameter.

4.6.2 Extensions

Starting from this kernel of the theory, called perturbative convolution approximation (PCA), extensions are necessary of the same type as those listed on page 161 for the binary theory:

- The extension to multielectron atoms follows by summing up contributions from individual subshells. $(f_{n\ell}, \omega_{n\ell})$ pairs are determined by the procedure of Sternheimer (1952) described above.
- Screening by electrons bound to the projectile has been allowed for (Azevedo et al., 2000), following the scheme outlined by Sigmund (1997).
- A smooth transition to the classical regime has been achieved by an impact-parameter-dependent Bloch correction (Schiwietz and Grande, 1999). While this is problematic from a conceptual point of view, it was determined in practice by inserting a scaling factor into the Thomson formula (4.43), which made the

stopping cross section to agree with Bloch's result, (6.4), Vol. 1. The resultant scheme is called unitary convolution approximation (UCA).
- Projectile excitation/ionization has been allowed for by interchanging the roles of projectile and target.
- Electron capture has not been included.
- Relativity corrections have been included in accordance with the Bethe theory. The Lindhard-Sørensen correction has not been included.
- A Barkas-Andersen correction has been incorporated by means of a multiplicative factor, so that the ratio between the corrected and the uncorrected stopping cross section is taken over from binary stopping theory.

A detailed summary of the scheme was presented by Grande and Schiwietz (2002).

4.7 Transport Cross Section

According to (3.118) the stopping cross section is closely related to the transport cross section

$$\sigma^{(1)} = \int \mathrm{d}\sigma(\Theta)\,(1-\cos\Theta)\ . \tag{4.45}$$

For a heavy particle interacting with free electrons, the relation reads

$$S = mv^2\sigma^{(1)}\ . \tag{4.46}$$

This relation allows to employ methods of classical or quantal scattering theory, in particular those described in Chap. 3, Vol. 1, to be employed in the calculation of stopping cross sections.

Calculations of the transport cross section frequently make use of the partial-wave expansion. As a result, the transport cross section can be expressed by phase shifts,

$$\sigma^{(1)} = \frac{4\pi}{k^2}\sum_{\ell}(\ell+1)\sin^2(\delta_\ell-\delta_{\ell+1}) \tag{4.47}$$

according to (3.119), Vol. 1.

In the context of stopping theory this relation was first used in a thesis on low-velocity stopping by Finnemann (1968). This, as well as a large number of followup papers will be discussed in Chap. 8. In the present chapter we shall have a look at studies of high-velocity stopping on the basis of this scheme.

One of those studies has already been discussed in Sects. 6.3.2 and 6.7.2, Vol. 1, where the Bloch correction was determined via the difference between the transport cross section for free-Coulomb scattering and its perturbation limit.

4.7.1 A General Remark

Unlike Lindhard and Sørensen (1996), who studied *differences* in transport cross sections, theoretical schemes discussed in the present section employ the transport cross section approach to determine *absolute* stopping cross sections. Therefore the question arises to what extent (4.46), which is exact for free target electrons, is valid for bound electrons.

Let us start with the Bohr theory. In Sect. 6.4.5, Vol. 1, we found that the transfer of kinetic energy to a target electron is given by

$$T(p) = 2mv^2 \sin^2 \frac{\Theta(p)}{2} = \frac{2Z_1^2 \mathrm{e}^4 \omega_0^2}{mv^4} \left[K_1 \left(\frac{\omega_0 p}{v} \right) \right]^2 \tag{4.48}$$

in a free ion-electron collision governed by a Yukawa potential with a screening radius v/ω_0. Equation (4.48) represents the leading term in an expansion in powers of Z_1. It coincides with the first term emerging from the Bohr theory. However, the second term,

$$\Delta T(p) = \frac{2Z_1^2 \mathrm{e}^4 \omega_0^2}{mv^4} \left[K_0 \left(\frac{\omega_0 p}{v} \right) \right]^2 , \tag{4.49}$$

is ignored here. Now, in Problem 4.4 you may find that

$$\int_0^\infty 2\pi p \, \mathrm{d}p \, \Delta T = \frac{4\pi Z_1^2 \mathrm{e}^4}{mv^2} \frac{1}{2} . \tag{4.50}$$

Thus, at least in this case the transport equation approach misses a term 1/2 in the stopping number L.

A similar result emerges from the Born approximation, as was observed by Arista (2002): From the differential cross section for a Yukawa potential, (3.94), Vol. 1, you may determine the transport cross section and, by setting the screening radius equal to v/ω_0, arrive at a stopping cross section

$$S = \int T \, \mathrm{d}\sigma = \frac{4\pi Z_1^2 \mathrm{e}^4}{mv^2} \left[\frac{1}{2} \ln \left(1 + B^2 \right) - \frac{1}{2} \frac{B^2}{1 + B^2} \right] \tag{4.51}$$

with $B = 2mv^2/\hbar\omega_0$. Evidently, for $B \gg 1$ a factor 1/2 is missing in the stopping number.

Figure 4.7 shows a comparison between the stopping number L following from (4.51) and the exact result from the Born approximation for a harmonic oscillator (Sigmund and Haagerup, 1986). Also included is the simple Bethe logarithm. The difference between the exact (Born) result and the Bethe logarithm reflects the shell correction. It is seen that the difference between the transport cross section and the Bethe logarithm is almost constant down to about $B = 3$. At this low energy, omitting the term 1/2 underestimates the stopping cross section by almost a factor of two. Even at $B = 100$ the error is about 10%.

Evidently, this aspect has to be dealt with in any stopping theory based on (4.46).

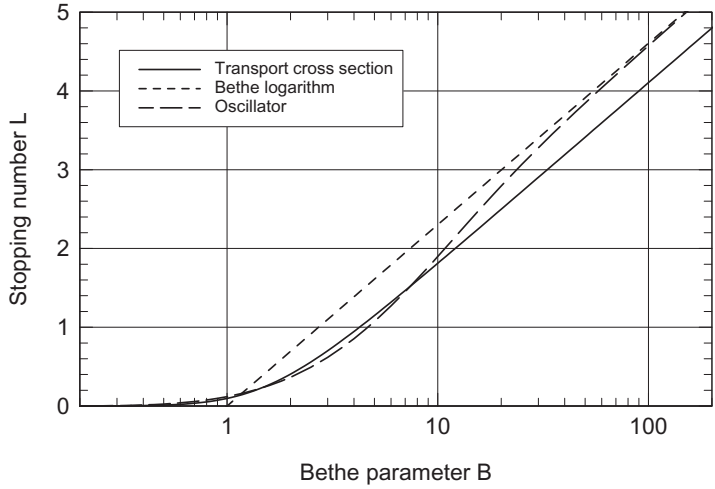

Fig. 4.7 Stopping number $L = Smv^2/4\pi Z_1^2 e^4$ for a harmonic oscillator in the Born approximation. Solid line: Found from transport cross section, (4.51). Dashed line: Exact result (Sigmund and Haagerup, 1986). Dotted line: Bethe logarithm

4.7.2 Generalized Friedel Sum Rule

The transport-equation approach is particularly suited to study deviations from the Born approximation. Indeed, exact evaluation of the scattering theory for a Yukawa potential or other screened-Coulomb potentials will generally deliver a Barkas-Andersen effect as well as a Bloch-type correction. The significance of these effects tends to increase with decreasing projectile speed. The choice of the screening radius is crucial here. While the choice of $a = v/\omega_0$ appears to represent reality well at high projectile speed, this does not necessarily remain true down to low speed.

In the present section we shall have a look at a procedure in which the screening radius is determined by requiring a sum rule to be fulfilled. The starting point is the Friedel sum rule (Friedel, 1952) which ensures neutrality of a free electron gas in the presence of a charged impurity, discussed in Appendix 8.10.2. The approach was first proposed by Cherubini and Ventura (1985) and used in low-velocity stopping (Calera-Rubio et al., 1994).

Subsequently, Nagy and Bergara (1996) extended the approach to higher beam velocities. It was assumed that the electron distribution is in equilibrium, so that a neutrality requirement can be imposed. It was also assumed that the dynamically-screened potential is spherical. Within these assumptions, the argument leading to the Friedel sum rule—which involves phase shifts of a spherical potential—can be generalized to a Fermi sphere displaced in velocity space by an amount corresponding to the beam velocity.

One useful result of this work is an expression of the effective screening radius a as a function of the beam velocity,

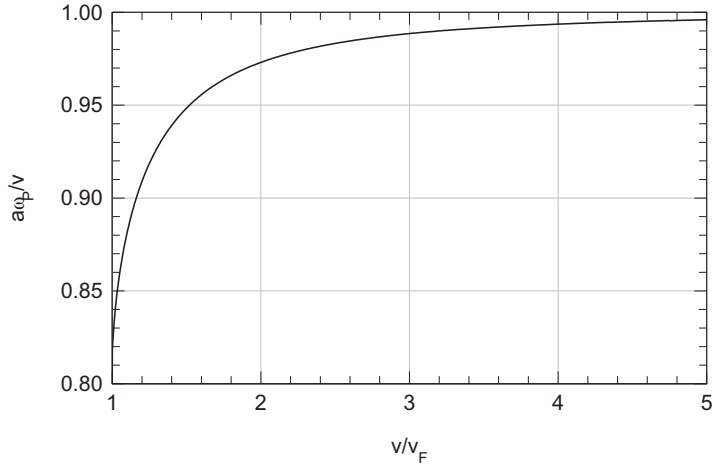

Fig. 4.8 Screening radius in Yukawa potential to describe velocity-dependent stopping according to (4.52)

$$a^2 = \frac{v_F^2}{3\omega_P^2}\left\{\frac{1}{2} + \frac{v_F^2 - v^2}{4vv_F}\ln\left|\frac{v+v_F}{v-v_F}\right|\right\}^{-1} . \tag{4.52}$$

As you may see in Fig. 4.8, a is very close to the adiabatic radius v/ω_P down to $v \sim 2v_F$.

The approach was developed and systematized further by Lifschitz and Arista (1998), who applied it to an analysis of proton-antiproton differences in stopping (Arista and Lifschitz, 1999). Arista (2002) applied the model to heavy-ion stopping by allowing for static screening in the potential. A more detailed summary has been presented subsequently (Arista and Lifschitz, 2004). Arista and Sigmund (2007) pointed out that phase shifts computed by numerical solution of the Schrödinger equation can be replaced by semi-classical (WKB) phase shifts without significant loss of accuracy.

The method has been successful in the analysis of experimental data—as will be seen below—but in view of unsolved problems I refrain from going into details:

- The assumption of an electron distribution in equilibrium around a swift projectile is a mere postulate which has been noted as such by Nagy and Bergara (1996). It has not been proven, and no attempt has been published to the author's knowledge to even make it plausible.
- As was shown in Sect. 4.7.1, the transport-equation approach fails to reproduce the potential-energy transfer. This problem was avoided in binary stopping theory by invoking angular-momentum transfer. A way to overcome this obstacle has not been found in the present approach.
- The approach is geared toward the free electron gas, and inner shells have usually been treated by conventional methods. This may be adequate in low-velocity stopping but imposes further questions at high projectile speed.

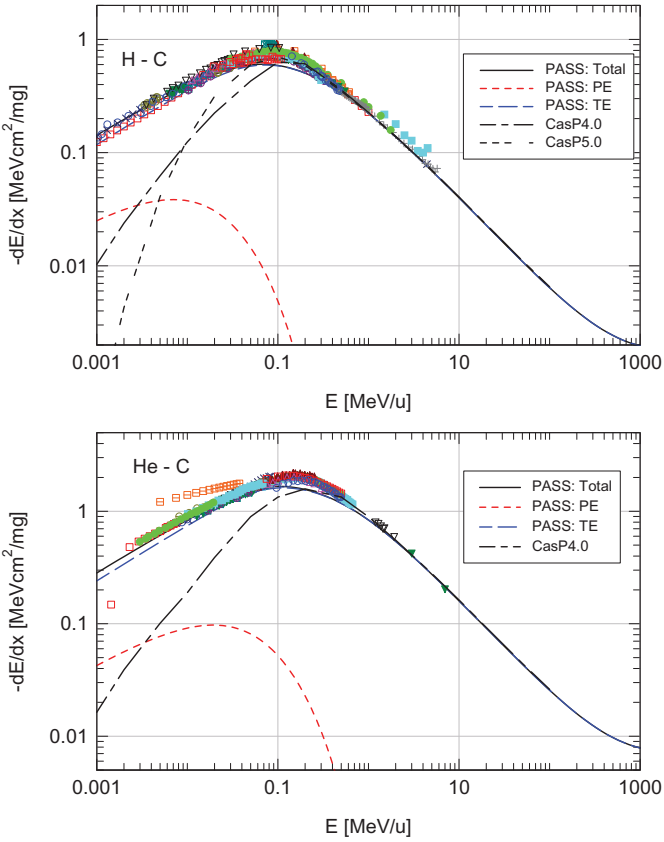

Fig. 4.9 Predicted stopping force for H and He in carbon. Standard version of PASS (ICRU, 2005) and Grande and Schiwietz (2008, 2011). Experimental data from Paul (2013). TE: Target excitation/ionization only; PE: Projectile excitation/ionization only

4.7.3 Convergent Kinetic Theory (CKT)

In Sect. 1.8.6, Vol. 1, you have got acquainted with a method to circumvent the problem that the transport-equation approach does not produce the entire stopping cross section but only the kinetic part. In essence, the approach of Lindhard and Sørensen (1996) boils down to setting

$$S = S_0 + \Delta S\,, \tag{4.53}$$

where S is the exact stopping cross section, S_0 a convenient zero-order approximation, and

$$\Delta S = S - S_0 \tag{4.54}$$

the rest, which can be approximated such as to account for a correction considered to be important. Lindhard and Sørensen (1996) discussed the Bloch correction, which

originates in close collisions. Therefore, S_0 was chosen such that distant collisions were covered adequately, with the Bethe expression being the proper choice. The difference ΔS could then be determined from two transport cross sections. This simplified the problem because electron binding is of minor importance for close collisions and therefore could be ignored.

Maynard et al. (2001) generalized this approach in two ways. Firstly, S_0 was not necessarily identified as the Bethe expression. Secondly, more than one iteration was allowed for, such as

$$S = S_0 + (S_1 - S_0) + (S - S_1)\,, \tag{4.55}$$

where the two differences on the right-hand side account for different effects.

Such an approach delivers insight into the relative importance of corrections. The two expressions of which a difference is formed have to be determined by identical procedures except for the specific effect that is analysed.

The starting point of the work of Maynard et al. (2001) is the kinetic theory of high-temperature plasmas, and the main goal is the slowing-down of highly-charged ions in such plasmas. A number of scenarios have been analysed, with either the Bethe or the Bohr expression as the zero-order approximation S_0. Corrections accounted for are projectile screening, Bloch correction and Barkas-Andersen effect as well as shell correction.

4.8 Applications

4.8.1 Equilibrium Stopping Forces from PASS and CasP

Figures 4.9–4.11 show stopping forces in carbon calculated by the PASS and CasP code compared with experimental data. The latter are quoted from an extensive compilation by Paul (2013), which has been updated at regular intervals starting from 2000, and where also all original references may be found. The selected ions reflect the availability of experimental data covering a significant energy range, cf. Fig. 4.2.

Calculations with CasP have mainly been based on the 4.0 version from 2008, where both shell and Barkas-Andersen correction are included. For comparison, data computed by the 5.0 version from 2011 have been included for H-C and Xe-C. Charge-dependent stopping cross sections are averaged over equilibrium charge fractions. Calculations have been stopped at 100 MeV/u, because not all relativistic corrections are applied in the code.

Calculations with PASS have been performed with input from ICRU (2005). The charge dependence has been handled by evaluating stopping cross sections at the mean equilibrium charge, for which the Thomas-Fermi expression (1.6) has been adopted for all ions. Barkas-Andersen and shell correction are included as well as projectile excitation, capture and loss.

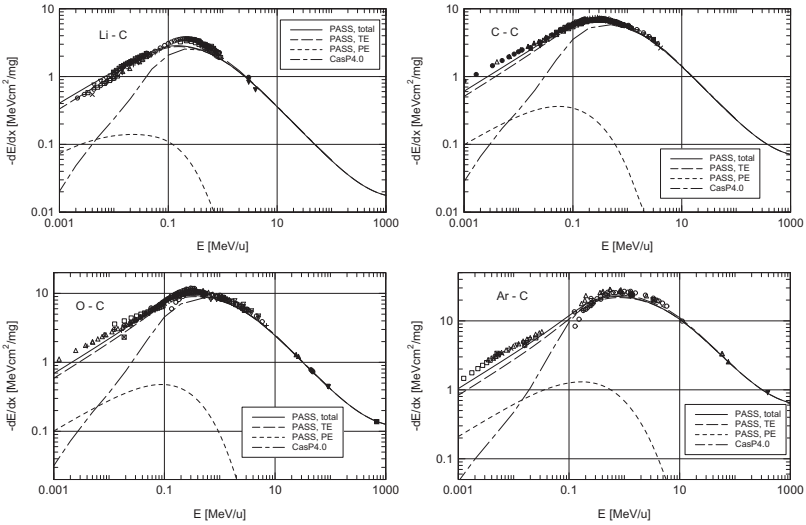

Fig. 4.10 Same as Fig. 4.9 for Li, C, O and Ar ions

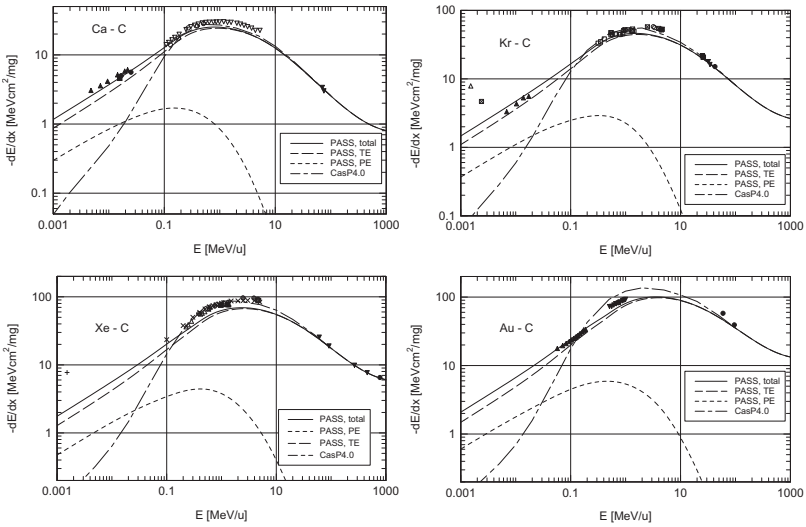

Fig. 4.11 Same as Fig. 4.9 for Ca, Kr, Xe and Au ions

Both theories have been geared toward intermediate and high projectile speeds and are not expected to be valid below the Bohr speed, i.e., below 25 keV/u. Nevertheless, plots have been extended down to 1 keV/u in order to allow an estimate of the error made if the theory is applied outside its prospective range of validity. It is seen that while CasP leads to an increasingly pronounced underestimate of the

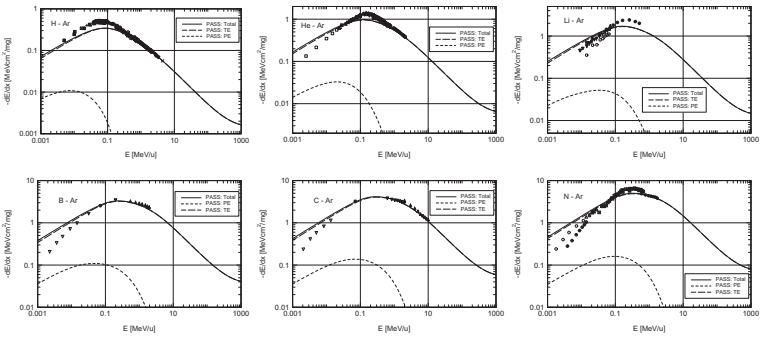

Fig. 4.12 Predicted stopping force for H, He, Li, B, C and N in argon. Standard version of PASS (ICRU, 2005) and Grande and Schiwietz (2010). Experimental data from Paul (2013)

stopping force at beam energies below 100 keV/u, the error in PASS is more moderate. Note that predictions at low speed lie below experimental data for He, C, O, Ar, Ca and Xe ions, yet above for Li and Kr ions, while there is surprisingly good agreement for H and Au ions. The lacking systematics reflects the overall accuracy of both theory and experiment in the low-velocity region.

The agreement between the two theoretical estimates and experiment is excellent at high speed. This mainly indicates the accuracy of the (f, ω) pairs and, in particular, the overall I-value in the database. In the intermediate-energy range, noticeable discrepancies are seen for both H, He and Li ions. This holds for both PASS and CasP. For PASS, the main reason is the use of (4.36). For CasP, lacking agreement for light ions indicates a weakness in the applied shell corrections.

Discrepancies of varying degree are also seen for heavier ions. In a few cases such as Kr and Xe, CasP comes closer to the experimental results than PASS, while the opposite is found for C and O ions. PASS calculations have all been performed with the Thomas-Fermi mean charge $\overline{q} = Z_1 \left(1 - \exp(-v/Z_1^{2/3} v_0)\right)$, while CasP calculations make use of an empirical expression for the mean charge (Schiwietz and Grande, 2001).

Figures 4.12 and 4.13 show similar results for an argon gas target. Significant deviations from experimental data are seen for H and He ions at low and intermediate projectile speeds. For heavier ions experimental data are sparse. Excellent agreement is found for O, S and Cl ions. For Li, N and Ne ions there are pronounced inconsistencies between different experimental data sets. For Xe, Pb and U experimental data lie consistently above the theoretical curves near the stopping maximum. A similar behaviour may be identified in Fig. 4.11. The adopted charge-state dependence is significant here (Fettouhi et al., 2006). A curve based on CasP has only been included for the O-Ar system. Here, CasP lies below the experimental data, while PASS lies above. While both discrepancies are rather large, the coverage with experimental data is quite sparse.

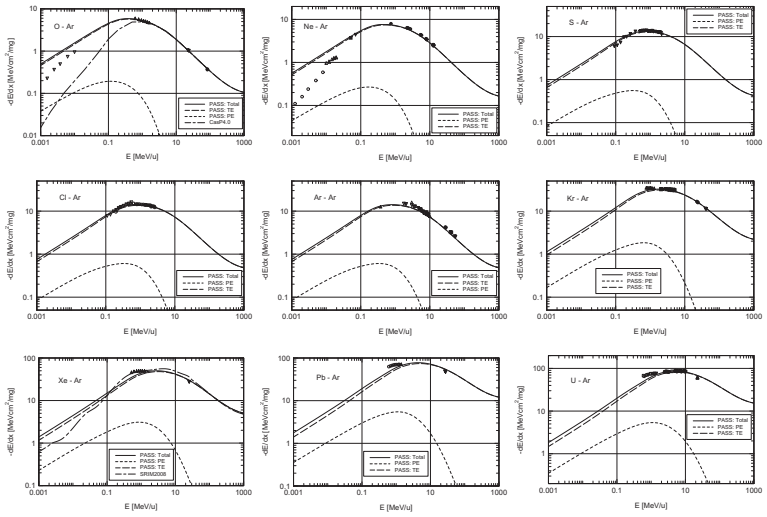

Fig. 4.13 Same as Fig. 4.12 for O, Ne, S, Cl, Ar, Kr, Xe, Pb and U ions. For O a prediction from Grande and Schiwietz (2010) has been added. For Xe a prediction from Ziegler et al. (2008) has been added

4.8.2 Equilibrium Stopping Forces from Empirical Tabulations

Until a few years ago the only available sources of stopping data for heavy ions were empirical tables or codes, based on interpolation between existing experimental data for selected ion-target combinations. An early attempt to produce a comprehensive table, based on effective-charge scaling, was presented by Steward and Wallace (1966). A set of tables by Northcliffe and Schilling (1970) was the dominating data source for many years. Later on several comprehensive data compilations were provided by Ziegler (1980) and Ziegler et al. (1985). Later versions have become available on the internet (Ziegler et al., 2008). Other empirical sources of heavy-ion stopping data were presented by Hubert et al. (1980, 1990) and Paul and Schinner (2001). For a discussion of the merits of these and other tabulations you are referred to ICRU (2005). Original experimental data have been compiled in an ongoing effort by Paul (2013).

For statistical analyses of their respective agreement with experimental data you may have a look at Paul and Schinner (2003). In general, discrepancies between empirical tabulations and experimental data are smaller than between theoretical calculations and experimental data. This must be so, since the data used for testing are in essence the same data that were used to produce the tabulations. The benefit of theoretical calculations such as CasP and PASS is the fact that predictions of stopping cross sections for ion-target combinations in a range where no or only few reliable data exist, have the same a priori accuracy as those where a comparison with experimental data is possible.

A special feature of empirical codes is the use of scaling relationships. The code MSTAR by Paul and Schinner (2001) uses a comparatively simple scaling relation with only few adjustable parameters. Therefore, predicted stopping cross sections are heavily dominated by ion-target combinations in the dark spots of Fig. 4.2. This has rather drastic consequences in low-velocity stopping, as we shall see in Chap. 8. Conversely, the fitting procedure in the SRIM code, which is not well documented, appears to allow for considerable structure in the predictions, as may be seen in Fig. 4.13 for the Xe-Ar system.

4.8.3 Charge-Dependent Stopping

The curves shown in Fig. 4.9–4.13 were determined on the basis of (4.36) as far as PASS is concerned, while curves found by CasP are based on the correct average equilibrium value, (4.34) for $x \to \infty$. In the present paragraph we shall have a closer look at the two approaches.

Figure 4.14 shows stopping cross sections of carbon for frozen charges of He^{q+} and Ar^{q+}. The contribution from target excitation/ionization is dominating. You may note that for Ar-C the stopping cross section increases by about one order of magnitude as the charge increases from 0 to 18. This increase is much weaker than the q^2 dependence which you may frequently see advocated in the literature (Ziegler et al., 1985).

Figure 4.15 shows equilibrium charge fractions and mean equilibrium charges for the two systems considered in Fig. 4.14. Evidently, high charge states increase in importance with increasing energy. Also included is the Thomas-Fermi estimate of the mean equilibrium charge,

$$q_{TF} = Z_1 \left(1 - \mathrm{e}^{-v/Z_1^{2/3} v_0}\right) . \tag{4.56}$$

It is seen that the two mean charges agree well with each other except at the low-energy end, where ETACHA yields significantly lower values. This is the energy range where ETACHA predicts sizable charge fractions for negative ions. Rozet et al. (1996) mention a lower validity limit of $\sim$ 1 MeV/u for predictions from ETACHA. This limit is presumably on the conservative side.

Figure 4.16 shows stopping cross sections found from the data underlying Fig. 4.14 and 4.15. As it must be, the two procedures, based on (4.34) and (4.36) lead to identical results at high energies where bare ions dominate the charge distribution. Differences occur at intermediate and low beam energies. These differences are sizable for He-C and negligible within the accuracy of the underlying theory in case of Ar-C.

This feature must be more general: For a heavy ion with many charge states the charge distribution is made up by only a small number of charges (cf. Fig. 4.15) at a given energy. The frozen-charge stopping cross section varies approximately linearly with the ion charge over this interval. Hence it makes little difference whether

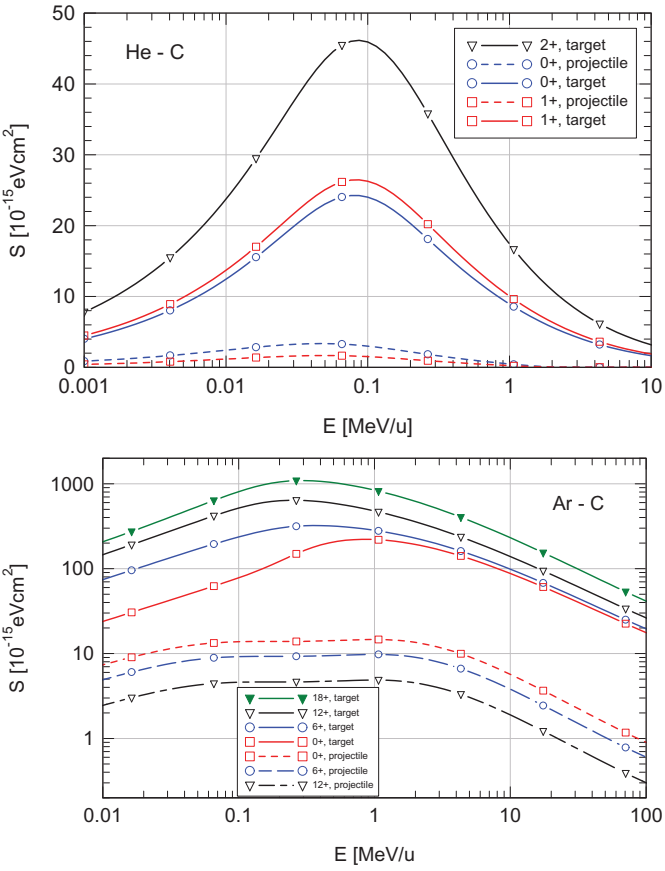

Fig. 4.14 Stopping cross section of carbon for frozen charges He^{q+} (top) and Ar^{q+} (bottom). Target excitation/ionization only. Calculated by the PASS code

the averaging is done over the stopping cross sections or the ion charge. This argument does not hold for light ions. The difference is not dramatic according to the left part of Fig. 4.16, but it is noticeable.

The standard procedure in the PASS code utilizes the Thomas-Fermi expression (4.56) for the mean charge. Figure 4.15 indicates that the difference between the two predictions for the mean equilibrium charge far exceeds the difference between the two ways of determining the mean stopping cross section. It is to be expected, therefore, that the standard procedure in the PASS code overestimates stopping cross sections for light ions such as H, He and Li. This does not concern antiprotons, which penetrate as bare ions.

Figures 4.15 and 4.16 concern target excitation only. Similar considerations apply to projectile excitation. Figure 4.14 shows pertinent frozen-charge stopping cross sections. Unlike target excitation/ionization, the contribution due to projec-

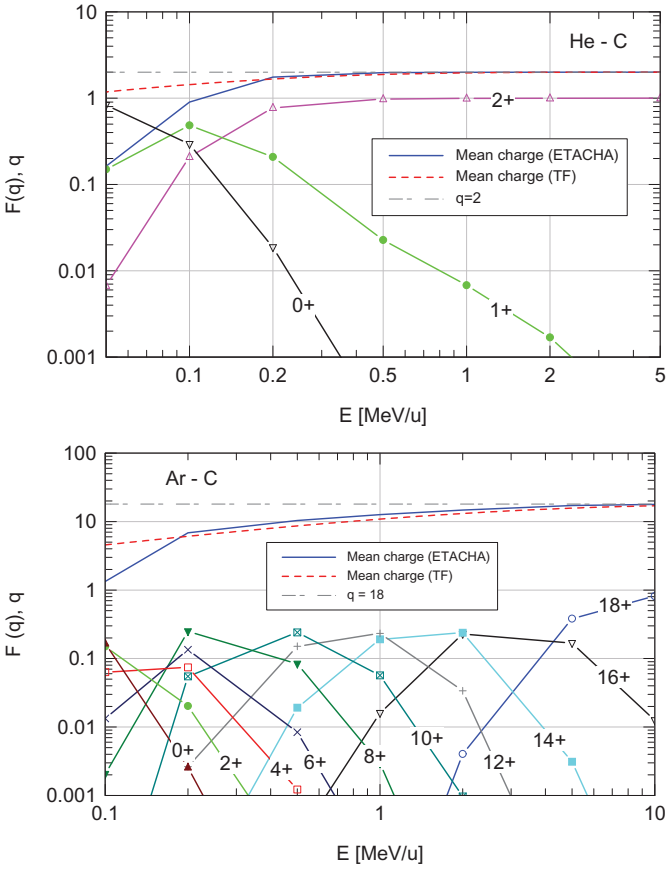

Fig. 4.15 Equilibrium charge fractions (indicated by $q+$) and mean equilibrium charges for He-C (top) and Ar-C (bottom) calculated by ETACHA (Rozet et al., 1996). Also included is the Thomas-Fermi estimate of the mean equilibrium charge, (4.56)

tile excitation/ionization increases with decreasing charge state. It is seen that target excitation/ionization dominates over the entire energy interval covered in the graph.

Direct measurements of charge-dependent stopping have been performed by several groups (Ogawa et al., 1991, Frey et al., 1996, Blazevic et al., 2000). Figure 4.17 shows an example. In measurements by Frey et al. (1996), the energy loss was measured of 1 MeV/u Ni^{q+} ions in C with equal entrance and exit charge for $q = 8$, 13, 16 and 18. Predicted stopping forces for frozen charge states from PASS and CasP agree reasonably well for $q \gtrsim 10$ but underestimate the measured energy loss. While the influence of projectile excitation is insignificant, you may note that inclusion of capture and loss contributes substantially and brings the theoretical prediction close to the experimental finding.

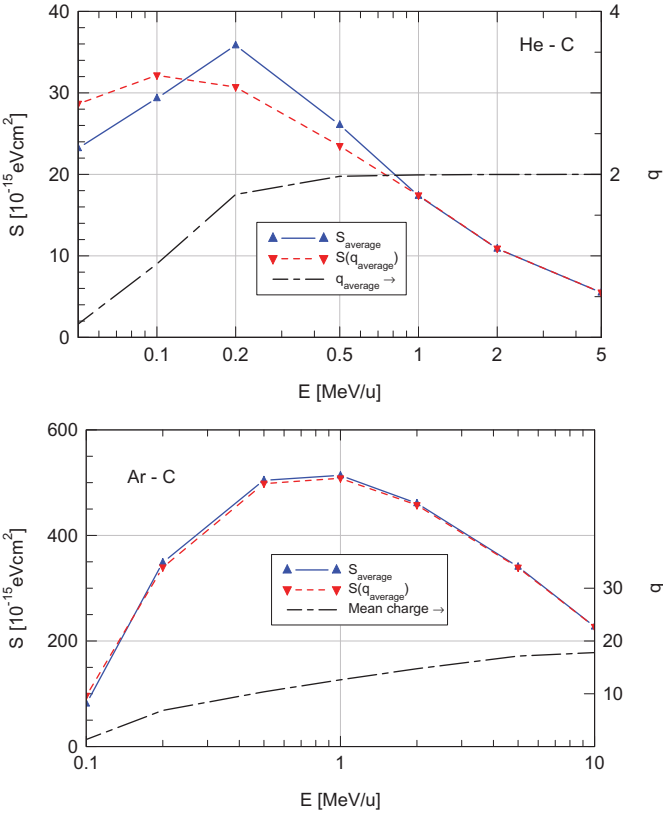

Fig. 4.16 Equilibrium stopping cross section for He-C (top) and Ar-C (bottom) calculated from PASS and ETACHA. Target excitation/ionization only. Solid lines: Average stopping cross section according to (4.34); dotted lines: Stopping cross section at average charge according to (4.36). Also included is the mean equilibrium charge (ETACHA) shown in Fig. 4.15

These measurements have been performed in an energy range where PASS and CasP tend to deliver reliable results. It is likely, therefore, that the measurements did not deal with frozen charges.

Similar comparisons have been performed by Blazevic et al. (2002).

Figure 4.18 shows calculated stopping forces of titanium for uranium ions for several charge states as a function of beam energy. Contributions due to target and projectile excitation/ionization are shown separately. It is seen that the difference is smallest at low beam energy for neutral ions. I increases significantly with increasing ion charge whereas it decreases slowly with increasing energy.

Extensive measurements on charge-dependent stopping were performed by Ogawa and coworkers, which will be discussed in the following chapter.

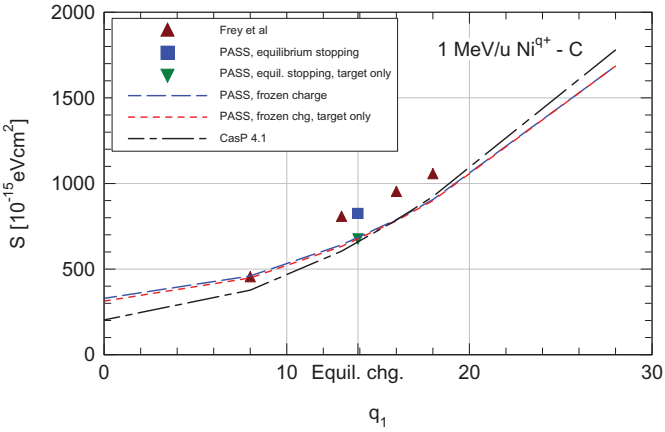

Fig. 4.17 Frozen-charge stopping cross sections for 1 MeV/u Ni^{q+}-C. Measurements from Frey et al. (1996). Compared with calculations by PASS and CasP4.1

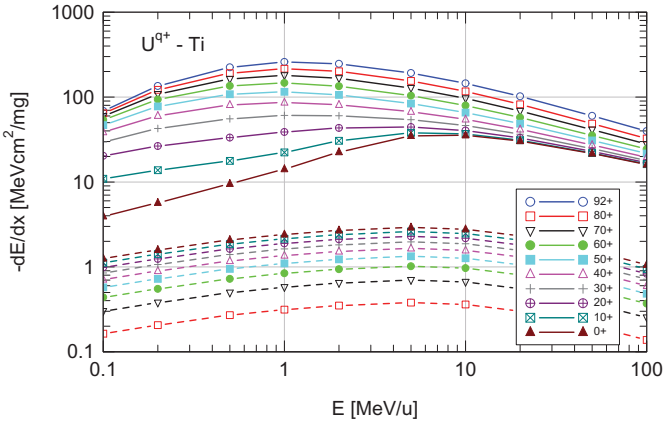

Fig. 4.18 Stopping force of Ti for U^{q+} calculated from PASS code. Solid lines: Target excitation/ionization only. Dotted lines: Projectile excitation/ionization only

4.8.4 Stopping in Compound Materials

To the extent that the energy loss of a penetrating particle is made up by a sum of energy losses in individual atomic collisions, the stopping cross section per molecule in a compound material $A_\ell B_m C_n \ldots$ is given by

$$S = \ell S_A + m S_B + n S_C \ldots , \tag{4.57}$$

where S_A is the stopping cross section of an A-atom corrected for changes of the electron structure as compared to a free A atom and correspondingly for B, C....

If uncorrected atomic stopping cross sections are inserted, (4.57) reduces to what commonly is called *Bragg's rule* after Bragg and Kleeman (1905)[3].

Differences in electron structure between bound and free atoms affect valence electrons. Within the PASS and CasP codes such differences are accounted for when measured or calculated dipole oscillator strengths are available (Palik, 2000, Berkowitz, 1979, 2002). In conducting materials the difference is primarily due to conduction electrons, which can be treated as a Fermi gas or the like. Semi-empirical schemes, based on the character of chemical bonds, have been developed by Powers et al. (1973), Powers (1980) and Thwaites (1983).

Bragg's rule is actually a good starting point in numerous cases. Based on explicit studies with binary stopping theory (Sigmund et al., 2003, Sharma et al., 2004) as well as physical reasoning, Sigmund et al. (2005) established a number of trends with regard to the magnitude of deviations from Bragg's rule:

If you are looking for pronounced deviations from Bragg's rule,

- look for a material with a high binding energy and
- a low atomic number, so that valence electrons make a large contribution to stopping.
- A good example would be LiF.

Moreover,

- Choose a low bombarding-ion energy, where inner-shell excitation channels may be closed or
- bombard with antiprotons, which do not experience screening and hence interact with all electrons inside the adiabatic radius.
- Heavy ions experience relatively more screening. Therefore, distant collisions tend to be suppressed. Hence, the accuracy of predictions based on Bragg's rule tends to increase with increasing Z_1.

In the SRIM code (Ziegler, 2012) it is assumed that deviations from Bragg's rule are independent of the bombarding ion. Since experimental data quoted above refer to protons and alpha particles, deviations from Bragg's rule tend to be overestimated in SRIM for heavier ions. For $Z_1 \geq 6$, Bragg's rule is a better option (Sigmund et al., 2005).

4.9 Impact-Parameter-Dependent Energy Loss ⋆

Almost all treatment of energy loss in this book as well as volume 1 has been based on impact-parameter dependencies, the only exception being the plane-wave Born

[3] W.H. Bragg performed a long series of experimental studies in radioactivity, in particular ranges of alpha and beta particles in matter, starting with Bragg (1904). One of his observations was that 'for all the materials examined the loss in traversing any atom is nearly proportional to the square root of the weight of that atom'. *Braggs law* was expressed as follows: 'The loss in the case of a complex molecule is proportional to the sum of the square roots of the weights of the constituents atoms.'

approximation presented in Sect. 4.4, Vol. 1. Integration over impact parameter leads to a more or less handy expression for the stopping cross section which allows incorporation of shell corrections via kinetic theory, cf. Sect. 4.5.5 and Sect. 6.6, Vol. 1.

Although the stopping cross section is a central quantity in particle penetration, it is not the only relevant integral over $T(p)$. Explicit expressions for impact-parameter-dependent energy loss are needed in case of slowing down in regular structures, e.g. under conditions of planar or axial channeling, or when a projectile is scattered from a plane surface under grazing incidence, cf. Fig. 1.3, Vol. 1. Impact-parameter dependencies are also needed in straggling, cf. the following chapter as well as Chap. 8, Vol. 1.

We know that the shell correction ensures incorporation of the orbital motion of electrons bound to the target atom or the projectile ion into the calculation of the energy loss. As far as the stopping cross section is concerned, this implies that the distribution in orbital velocity must be accounted for. If the impact-parameter dependence is of interest, also the distribution in configuration space needs to be accounted for.

4.9.1 Local-Density Approximation

A popular approach, particularly in the theory of channeling, is the local-density approximation discussed in Sect. 7.2.4, Vol. 1, where the mean energy transfer in an ion-atom collision is expressed by

$$T(\boldsymbol{p}) = \int_{-\infty}^{\infty} \mathrm{d}x\, \rho(x, \boldsymbol{p}) S\big(\rho(x, \boldsymbol{p})\big)\,, \tag{4.58}$$

where $\boldsymbol{p}$ is a vectorial impact parameter, $\rho(x, \boldsymbol{p}) \equiv \rho(\boldsymbol{r})$ is the electron density in the point $\boldsymbol{r} = (x, \boldsymbol{p})$, and $S(\rho)$ the stopping cross section per electron of a Fermi gas with an electron density ρ.

Equation (4.58) has typically been evaluated on the basis of the Lindhard dielectric function, (5.153), Vol. 1 or one of several modifications and simplifications. This has the advantage that orbital velocities are easily incorporated. However, there are at least two obvious limitations,

- The quantity dominating the dependence on p in (4.58) is the factor $\rho(x, \boldsymbol{p})$ in front of the stopping cross section. Therefore, the effective interaction range is the radius of the atom. On the other hand, we know that the effective interaction range is the adiabatic radius which, dependent on the speed, may far exceed atomic dimensions.
- Expressions for stopping in an electron gas used in the present context are based on the Born approximation, the applicability of which is severely limited for heavy ions.

4.9.2 Born Approximation

The Born approximation, in the form described in Sect. 4.3.2, Vol. 1, provides expressions for impact-parameter-dependent stopping to the lowest order in Z_1 with full allowance for shell corrections, at least in principle. Most explicit studies refer to light ions like protons, antiprotons and He ions (Mikkelsen and Sigmund, 1987, Kabachnik et al., 1988, Balashova et al., 1990, Mortensen et al., 1991, Kabachnik and Chumanova, 1994, Grande and Schiwietz, 1998, Azevedo et al., 2000).

For heavy ions, in the classical regime, calculations on the basis of the Born approximation retain their validity at large impact parameters. Likewise, the significance of shell and Barkas-Andersen corrections decreases with increasing impact parameter. Conversely, significant errors must be expected for close collisions. This suggests that in calculations addressing straggling—which is governed by close collisions, cf. Fig. 8.2, Vol. 1,—caution is indicated with regard to the Born approximation.

4.9.3 PCA/UCA Approximation

The unitary convolution approximation has been derived as an extension of the Born approximation in the original paper (Schiwietz and Grande, 1999) as well as in a more recent version (Grande and Schiwietz, 2009), but as described in Sect. 4.6, the shell correction has been ignored in the kernel and incorporated as a correction. The theory does not allow for a Barkas-Andersen correction.

4.9.4 Binary Theory

The scattering of an ion on electrons in motion has been treated in Sect. 6.5, Vol. 1. That treatment aimed at an expression for the stopping cross section and therefore ignored all spatial dependence. An extension of this treatment to allow for spatial dependencies has been presented by the author (Sigmund, 2000) and applied to the present problem by Schinner and Sigmund (2010).

Let us first consider the energy transfer in a binary collision between a heavy projectile with a velocity $\boldsymbol{v}$ and a free electron with an initial velocity $\boldsymbol{v}_e$. In a reference frame moving with the projectile the electron has a velocity $\boldsymbol{w} = \boldsymbol{v}_e - \boldsymbol{v}$. After scattering elastically on the projectile that velocity changes to

$$\boldsymbol{w}' = \boldsymbol{w}\cos\Theta + \frac{\boldsymbol{p}'}{p'} w \sin\Theta\,, \tag{4.59}$$

where $\boldsymbol{p}'$ and $\Theta(w, p')$ denote the vectorial impact parameter and the scattering angle, respectively, in the moving reference frame.

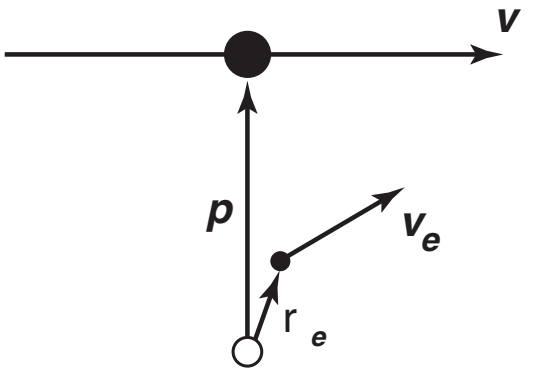

Fig. 4.19 Projectile interaction with moving target electron in lab frame. From Sigmund (2000)

In the laboratory frame the electron has a velocity $\boldsymbol{v}'_e = \boldsymbol{w}' + \boldsymbol{v}$ after the interaction, and the energy transfer can be expressed as

$$T = \frac{m}{2}\left(v_e'^2 - v_e^2\right) = m\boldsymbol{v}\cdot(\boldsymbol{v}-\boldsymbol{v}_e)(1-\cos\Theta) + m\frac{w}{p'}\boldsymbol{p}'\cdot\boldsymbol{v}\sin\Theta\,. \tag{4.60}$$

Note that $\boldsymbol{p}'$ is the impact parameter of a target *electron*, while we are interested in the impact parameter to the nucleus. The kernel of binary stopping theory is a mapping of the Bohr oscillator model on a binary scattering configuration. Within the Bohr model, the initial state of the target atom can be characterized by a harmonically-bound electron in motion on an elliptic orbit,

$$\boldsymbol{r}(t) = \boldsymbol{r}_\mathrm{e}\mathrm{e}^{\mathrm{i}\omega(t-t_0)} \tag{4.61}$$

$$\boldsymbol{v}(t) = \boldsymbol{v}_\mathrm{e}\mathrm{e}^{\mathrm{i}\omega(t-t_0)} \tag{4.62}$$

with $\boldsymbol{v}_\mathrm{e} = i\omega\boldsymbol{r}_\mathrm{e}$.

We may define t_0 as the time of closest approach between the projectile and the nucleus. Then the electron orbit may be approximated as

$$\boldsymbol{r}(t) \simeq \boldsymbol{r}_\mathrm{e} + \boldsymbol{v}_\mathrm{e}(t-t_0)\,. \tag{4.63}$$

for $t \simeq t_0$, see Fig. 4.19. Now this straight-line motion is taken as the incoming trajectory in a binary-scattering process. We may view this trajectory from a frame of reference moving with the projectile,

$$\boldsymbol{r}(t) = \boldsymbol{s} + \boldsymbol{w}(t-t_0) \tag{4.64}$$

where

$$\boldsymbol{s} = \boldsymbol{r}_\mathrm{e} - \boldsymbol{p}\,. \tag{4.65}$$

The impact parameter $\boldsymbol{p}'$ in the moving reference frame is given by the projection of $\boldsymbol{s}$ on the impact plane,

$$\boldsymbol{p}' = \boldsymbol{s} - (\boldsymbol{s}\cdot\hat{\boldsymbol{w}})\hat{\boldsymbol{w}} \tag{4.66}$$

with $\hat{\boldsymbol{w}} = \boldsymbol{w}/w$. The scattering angle in the moving reference frame can then be determined from the adopted potential with the initial speed $w = |\boldsymbol{v}_e - \boldsymbol{v}|$ and the impact parameter $p' = \sqrt{s^2 - (\boldsymbol{s} \cdot \hat{\boldsymbol{w}})^2}$.

Let us check whether we can reproduce the stopping cross section

$$S = \left\langle \int d^2\boldsymbol{p}\, T(p) \right\rangle_{\boldsymbol{v}_e} \tag{4.67}$$

that we know from Sect. 6.5.1, Vol. 1.

The relation between $d^2\boldsymbol{p}$ and $d^2\boldsymbol{p}'$ is given by the conservation of particle flux,

$$v\, d^2\boldsymbol{p} = w\, d^2\boldsymbol{p}' \,. \tag{4.68}$$

With this and (4.60), (4.67) reads

$$S = m \left\langle \int d^2\boldsymbol{p}' \, \frac{w}{v} \left[\boldsymbol{v} \cdot (\boldsymbol{v} - \boldsymbol{v}_e)(1 - \cos\Theta) + m \frac{w}{p'} \boldsymbol{p}' \cdot \boldsymbol{v}_e \sin\Theta, \right] \right\rangle_{\boldsymbol{v}_e} . \tag{4.69}$$

Integration of the second term over the impact parameter yields a vanishing result, while the first term leads to the transport cross section

$$\sigma^{(1)}(w) = \int d^2\boldsymbol{p}' \left[1 - \cos\Theta(w, p') \right] , \tag{4.70}$$

so that

$$S = m \left\langle \frac{w}{v} \boldsymbol{v} \cdot (\boldsymbol{v} - \boldsymbol{v}_e)\, \sigma^{(1)}(w), \right\rangle_{\boldsymbol{v}_e} . \tag{4.71}$$

in agreement with (6.71), Vol. 1.

4.9.5 Examples

Measuring impact-parameter-dependent energy losses would be a much more sensitive probe for the validity of different stopping models than measurements of stopping cross sections. However, data can be extracted mostly from measurements of stopping in channels and surface scattering at grazing incidence, i.e., at fairly large impact parameters. As the impact parameter decreases, the need to separate nuclear from electronic energy transfer introduces uncertainties. Conversely, the accuracy of existing calculations is not yet up to the standard of other aspects of particle penetration. Keep this in mind when studying the examples shown in this section.

Figure 4.20 shows an example of $T(p)$ evaluated by PASS and CasP. CasP results are based on the Born approximation and, therefore, are proportional to Z_1^2. This suggests to plot T/Z_1^2 in Rydberg units, $R = 13.6\,\text{eV}$. Excellent agreement is found at large impact parameters both between results for different ions and calculated by different codes, while differences are found at small impact parameters. Results for H ions lie in the Born regime and the two codes predict very similar results.

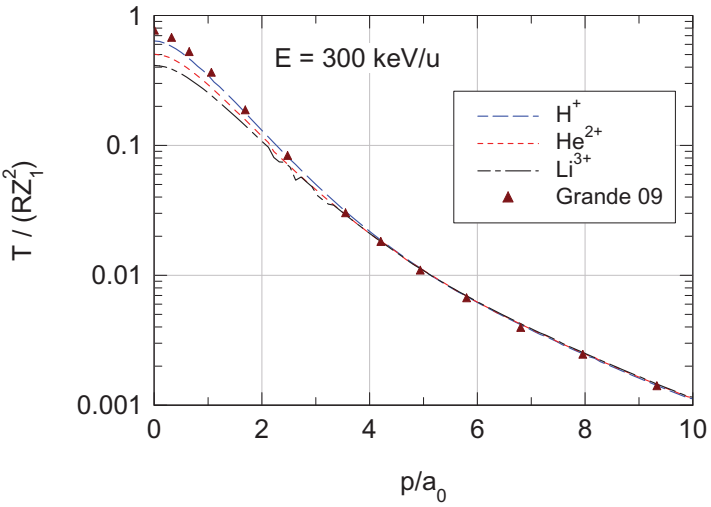

Fig. 4.20 Calculated mean energy loss of bare H, He and Li ions to atomic hydrogen at $E = 300$ keV/u. Lines: PASS results of Schinner and Sigmund (2010). Points: CasP results of Grande and Schiwietz (2009). From Schinner and Sigmund (2010)

Conversely, results for Li ions lie in the classical regime, and PASS results lie below those from CasP.

Figure 4.21 shows results for different charge states. The upper graph shows T/Z_1^2 in Rydberg units $R = 13.6\,\text{eV}$. As to be expected, all curves converge at small impact parameters, while increasing differences are found with increasing impact parameter. Conversely, the lower graph shows T/q_1^2, all curves show perfect agreement at large impact parameters, while a major variation is seen at $p = 0$.

4.10 Discussion and Outlook

This chapter has dealt with the stopping of swift heavy ions. Quantitative predictions in this area were, until around year 2000, based on Bethe theory combined with empirical scaling by the effective-charge postulate. You have seen that several theoretical schemes have now been developed that enable reliable predictions of stopping cross sections on the basis of existing atomic data, without introduction of adjustable parameters to be fitted by comparison with stopping data.

Most existing data—experimental and theoretical—refer to equilibrium stopping, which is of interest in numerous applications. While only few experimental data exist documenting transient effects in the stopping of heavy ions, all theoretical schemes discussed in this chapter allow theoretical predictions, provided that reliable data for charge-exchange cross sections are available.

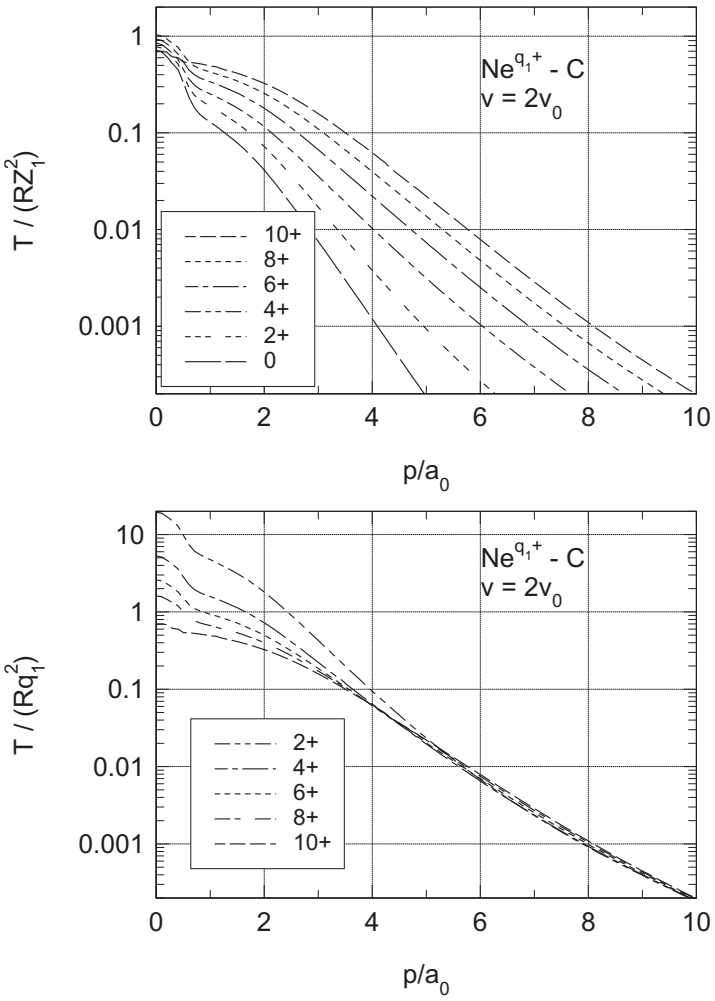

Fig. 4.21 Calculated mean energy loss of partially-screened neon ions Ne^{q+} to atomic carbon. $R = 13.61$ eV. $a_0 = 0.529$ Å. $v/v_0 = 2$. The upper graph shows absolute energy losses in units of RZ_1^2, while the lower graph shows energy losses divided by q_1^2. From Schinner and Sigmund (2010)

Also impact-parameter-dependent energy losses can be predicted. This is of significance not the least in the analysis of experimental channeling data.

The range of validity in terms of projectile speed of the schemes discussed here is broad. In the upper end it includes relativistic effects, except contributions from pair production and bremsstrahlung in the ultrarelativistic regime.

While the velocity range $v \simeq v_0$ has been deliberately omitted and will be covered in Chap. 8, caution is indicated with regard to stopping cross sections already

in the range of $v \simeq 2v_0$ and below, i.e., for $E \lesssim 100$ keV/u, where you will find significant scatter between experimental data and noticeable differences between theoretical predictions.

Problems

4.1. Derive the Fourier transform in three dimensions of the exponentially-screened Coulomb potential

$$\Phi(r) = \frac{e_1}{r} \mathrm{e}^{-r/a} \,. \tag{4.72}$$

4.2. Go through the derivation in Sect. 4.2.2, Vol. 1 by replacing straight Coulomb interaction by the charge-dependent potential (4.16) with the exponential screening function (4.9). Try to reproduce (4.18).

4.3. In the 'sudden approximation' the term $\exp(\mathrm{i}\omega_{j0}t')$ in (4.37) is set equal to 1, i.e., electronic binding is ignored. This approximation appears justified if the collision time τ obeys the condition

$$\omega_{j0} \simeq 2p/v \ll 1 \,. \tag{4.73}$$

Demonstrate that within this approximation you arrive at

$$T(p) \simeq \frac{2Z_1^2 e^4}{mv^2 p^2} \,. \tag{4.74}$$

If you need help, consult Grande and Schiwietz (1998).

4.4. Carry out the integral in (4.50).

References

Arista N.R. (2002): Energy loss of heavy ions in solids: non-linear calculations for slow and swift ions. Nucl Instrum Methods B **195**, 91–105

Arista N.R. and Lifschitz A.F. (1999): Nonlinear calculation of stopping powers for protons and antiprotons in solids: the Barkas effect. Phys Rev A **59**, 2719–2722

Arista N.R. and Lifschitz A.F. (2004): Non-linear approach to the energy loss of ions in solids. Adv Quantum Chem **45**, 47

Arista N.R. and Sigmund P. (2007): Stopping of ions based on semiclassical phase shifts. Phys Rev A **76**, 062902

Azevedo G.M., Grande P.L. and Schiwietz G. (2000): Impact-parameter dependent energy loss of screened ions. Nucl Instrum Methods B **164-165**, 203–211

Balashova L.L., Kondratyev V.N. and Kabachnik N.M. (1990): The impact-parameter dependence of antiproton energy loss. Nucl Instrum Methods B **48**, 18–20

Berkowitz J. (1979): *Photoabsorption, photoionization and photoelectron spectroscopy*. Academic Press, New York

Berkowitz J. (2002): *Atomic and molecular photoabsorption. Absolute total cross sections*. Academic Press, San Diego

Betz H.D. and Grodzins L. (1970): Charge states and excitation of fast heavy ions passing through solids: a new model for the density effect. Phys Rev Lett **25**, 211–214

Blazevic A., Bohlen H.G. and von Oertzen W. (2000): Charge-state changing processes for Ne ions passing through thin carbon foils. Phys Rev A **61**, 032901

Blazevic A., Bohlen H.G. and von Oertzen W. (2002): Stopping power of swift neon ions in dependence on the charge state in the non-equilibrium regime. Nucl Instrum Methods B **190**, 64–68

Bohr N. (1913): On the theory of the decrease of velocity of moving electrified particles on passing through matter. Philos Mag **25**, 10–31

Bohr N. (1940): Scattering and stopping of fission fragments. Phys Rev **58**, 654–655

Bohr N. (1941): Velocity-range relation for fission fragments. Phys Rev **59**, 270–275

Bragg W.H. (1904): On the absorption of alpha rays, and on the classification of the alpha rays from radium. Philos Mag **8**, 719–725

Bragg W.H. and Kleeman R. (1905): On the alpha particles of radium, and their loss of range in passing through various atoms and molecules. Philos Mag **10**, 318–341

Brandt W. and Kitagawa M. (1982): Effective stopping-power charges of swift ions in condensed matter. Phys Rev B **25**, 5631–5637

Brostrøm K.J., Bøggild J.K. and Lauritsen T. (1940): Cloud-chamber studies of fission fragment tracks. Phys Rev **58**, 651–653

Calera-Rubio J., Gras-Marti A. and Arista N.R. (1994): Stopping power of low-velocity ions in solids - inhomogeneous electron-gas model. Nucl Instrum Methods B **93**, 137–141

Carlson T.A., Nestor C.W., Wasserman N. and McDowell J.D. (1970): Calculated ionization potentials for multiply charged ions. Atomic Data **2**, 63–99

Cherubini A. and Ventura A. (1985): Stopping of light-ions in homogeneous electron gases. Lett Nuovo Cim **44**, 503–509

Cowern N.E.B., Read P.M., Sofield C.J., Bridwell L.B. and Lucas M.W. (1984): Charge-changing energy loss, higher-order Z_1 dependence, and pre-equilibrium behavior in the stopping power for energetic ions in solids. Phys Rev A **30**, 1682–1691

Datz S., Martin F.W., Moak C.D., Appleton B.R. and Bridwell L.B. (1972): Charge-changing collisions of channeled oxygen ions in gold. Radiat Eff **12**, 163–169

Dehmer J.L., Inokuti M. and Saxon R.P. (1975): Systematics of dipole oscillator-strength distributions for atoms of the first and second row. Phys Rev A **12**, 102–121

Fastrup B., Hvelplund P. and Sautter C.A. (1966): Stopping cross section in carbon of 0.1-1.0 MeV atoms with $6 < Z_1 < 20$. Mat Fys Medd Dan Vid Selsk **35 no. 10**, 1–28

Fettouhi A., Geissel H., Schinner A. and Sigmund P. (2006): Stopping of high-Z ions at intermediate velocities. Nucl Instrum Methods B **245**, 22–27

Finnemann J. (1968): En redegørelse for resultaterne af beregninger over spredning af elektroner med lav energi på afskærmede Coulombfelter. Master's thesis, Aarhus University

Frey C.M., Dollinger G., Bergmaier A., Faestermann T. and Maier-Komor P. (1996): Charge state dependence of the stopping power of 1 MeV/A ^{58}Ni ions. Nucl Instrum Methods B **107**, 31–35

Friedel J. (1952): The distribution of electrons round impurities in monovalent metals. Philos Mag **43**, 153–189

Grande P.L. and Schiwietz G. (1998): Impact-parameter dependence of the electronic energy loss of fast ions. Phys Rev A **58**, 3796–3801

Grande P.L. and Schiwietz G. (2002): The unitary convolution approximation for heavy ions. Nucl Instrum Methods B **195**, 55–63

Grande P.L. and Schiwietz G. (2008): CasP version 4.0. URL `www.hmi.de/people/schiwietz/casp.html`

Grande P.L. and Schiwietz G. (2009): Convolution approximation for the energy loss, ionization probability and straggling of fast ions. Nucl Instrum Methods B **267**, 859–865

Grande P.L. and Schiwietz G. (2010): CasP version 4.1. URL `www.casp-program.org/`

Grande P.L. and Schiwietz G. (2011): CasP version 5.0. URL `http://www.casp-program.org/`

Hubert F., Bimbot R. and Gauvin H. (1990): Range and stopping-power tables for 2.5 - 500 MeV nucleon heavy ions in solids. At Data and Nucl Data Tab **46**, 1–213

Hubert F., Fleury A., Bimbot R. and Gardès D. (1980): Range and stopping power tables for 2.5 - 100 MeV/nucleon heavy ions in solids. Ann de Phys **5 S**, 3–213

ICRU (2005): *Stopping of ions heavier than helium*, vol. 73 of *ICRU Report*. Oxford University Press, Oxford

Inokuti M., Dehmer J.L., T. B. and Hanson J.D. (1981): Oscillator-strength moments, stopping powers, and total inelastic- scattering cross sections of all atoms through strontium. Phys Rev A **23**, 95–109

Johnson R.E. (1982): *Introduction to atomic and molecular collisions*. Plenum Press, New York

Kabachnik N.M. and Chumanova O.V. (1994): Screening effects in the impact parameter dependence of electronic-energy loss of fast ions in collisions with atoms. Nucl Instrum Methods B **93**, 227–233

Kabachnik N.M., Kondratev V.N. and Chumanova O.V. (1988): The impact-parameter dependence of electron stopping in proton collisions with gas and solid atoms. phys stat sol B **145**, 103–116

Lifschitz A.F. and Arista N. (1998): Velocity-dependent screening in metals. Phys Rev A **57**, 200–207

Lindhard J. and Sørensen A.H. (1996): On the relativistic theory of stopping of heavy ions. Phys Rev A **53**, 2443–2456

Maynard G., Zwicknagel G., Deutsch C. and Katsonis K. (2001): Diffusion-transport cross section and stopping power of swift heavy ions. Phys Rev A **63**, 052903

Mikkelsen H.H. and Sigmund P. (1987): Impact parameter dependence of electronic energy loss: Oscillator model. Nucl Instrum Methods B **27**, 266–275

Moak C.D. and Brown M.D. (1963): Some stopping powers for iodine ions. Phys Rev Lett **11**, 284–285

Moak C.D. and Brown M.D. (1966): Some heavy-ion stopping powers. Phys Rev **149**, 244–245

Mortensen E.H., Mikkelsen H.H. and Sigmund P. (1991): Impact parameter dependence of light-ion electronic energy loss. Nucl Instrum Methods B **61**, 139–148

Nagy I. and Bergara A. (1996): A model for the velocity-dependent screening. Nucl Instrum Methods B **115**, 58–61

Northcliffe L.C. (1960): Energy loss and effective charge of heavy ions in aluminum. Phys Rev **120**, 1744–1757

Northcliffe L.C. and Schilling R.F. (1970): Range and stopping power tables for heavy ions. Nucl Data Tab **A 7**, 233–463

Ogawa H., Katayama I., Ikegami H., Haruyama Y., Aoki A., Tosaki M., Fukuzawa F., Yoshida K., Sugai I. and Kaneko T. (1991): Direct Measurement of fixed-charge stopping power for 32-MeV He^{3+} in a charge-state nonequilibrium region. Phys Rev B **43**, 11370–11376

Ormrod J.H. and Duckworth H.E. (1963): Stopping cross sections in carbon for low-energy atoms with $Z \leq 12$. Can J Physics **41**, 1424–1442

Ormrod J.H., MacDonald J.R. and Duckworth H.E. (1965): Some low-energy atomic stopping cross sections. Can J Physics **43**, 275–284

Palik E.D. (2000): *Electronic handbook of optical constants of solids – version 1.0*. SciVision – Academic Press

Paul H. (2013): *Stopping power graphs*. URL `https://www-nds.iaea.org/stopping/`

Paul H. and Schinner A. (2001): An empirical approach to the stopping power of solids and gases for ions from ^{3}Li to ^{18}Ar. Nucl Instrum Methods B **179**, 299–315

Paul H. and Schinner A. (2003): Judging the reliability of stopping power tables and programs for heavy ions. Nucl Instrum Methods B 252–258

Pierce T.E. and Blann M. (1968): Stopping powers and ranges of 5-90-MeV S^{32}, Cl^{35},Br^{79}, and I^{127} ions in H_2, He, N_2, and Kr: A semiempirical stopping power theory for heavy ions in gases and solids. Phys Rev **173**, 390–405

Powers D. (1980): Influence of molecular-structure on stopping power of chemical-species for he+-ions from a low-energy particle accelerator. Accouts of Chem Research **13**, 433–440

Powers D., Lodhi A.S., Lin W.K. and Cox H.L. (1973): Molecular effects in the energy loss of alpha particles in gaseous media. Thin Sol Films **19**, 205–215

Rozet J.P., Stephan C. and Vernhet D. (1996): ETACHA: a program for calculating charge states at GANIL energies. Nucl Instrum Methods B **107**, 67–70

Schinner A. and Sigmund P. (2000): Polarization effect in stopping of swift partially screened heavy ions: perturbative theory. Nucl Instrum Methods B **164-165**, 220–229

Schinner A. and Sigmund P. (2010): Impact-parameter-dependent electronic stopping of swift ions. 1. Binary theory. Europ Phys J D **56**, 41–50

Schiwietz G. and Grande P.L. (1999): A unitary convolution approximation for the impact-parameter dependent electronic energy loss. Nucl Instrum Methods B **153**, 1–9

Schiwietz G. and Grande P.L. (2001): Improved charge-state formulas. Nucl Instrum Methods B **175-177**, 125–131

Sharma A., Fettouhi A., Schinner A. and Sigmund P. (2004): Electronic stopping of swift ions in compounds. Nucl Instrum Methods B **218**, 19–28

Sigmund P. (1982): Kinetic theory of particle stopping in a medium with internal motion. Phys Rev A **26**, 2497–2517

Sigmund P. (1996): Low-velocity limit of Bohr's stopping-power formula. Phys Rev A **54**, 3113–3117

Sigmund P. (1997): Charge-dependent electronic stopping of swift nonrelativistic heavy ions. Phys Rev A **56**, 3781–3793

Sigmund P. (2000): Shell correction in Bohr stopping theory. Europ Phys J D **12**, 111–116

Sigmund P. (2004): *Stopping of heavy ions*, vol. 204 of *Springer Tracts of Modern Physics*. Springer, Berlin

Sigmund P. (2005): Interplay of classical and quantum mechanics in thetheory of charged-particle stopping. Adv Quantum Chem **48**, 91–110

Sigmund P. (2006): Stopping of swift ions: Solved and unsolved problems. Mat Fys Medd Dan Vid Selsk **52**, 557–593

Sigmund P., Fettouhi A. and Schinner A. (2003): Material dependence of electronic stopping. Nucl Instrum Methods B **209**, 19–25

Sigmund P. and Glazov L.G. (2003): Interplay of charge exchange and projectile excitation in the stopping of swift heavy ions. Europ Phys J D **23**, 211–215

Sigmund P. and Haagerup U. (1986): Bethe stopping theory for a harmonic oscillator and Bohr's oscillator model of atomic stopping. Phys Rev A **34**, 892–910

Sigmund P. and Schinner A. (2000): Binary stopping theory for swift heavy ions. Europ Phys J D **12**, 425–434

Sigmund P. and Schinner A. (2002): Binary theory of electronic stopping. Nucl Instrum Methods B **195**, 64–90

Sigmund P. and Schinner A. (2006): Shell correction in stopping theory. Nucl Instrum Methods B **243**, 457–460

Sigmund P., Sharma A., Schinner A. and Fettouhi A. (2005): Valence structure effects in the stopping of swift ions. Nucl Instrum Methods B **230**, 1–6

Smith D.Y., Inokuti M., Karstens W. and Shiles E. (2006): Mean excitation energy for the stopping power of light elements. Nucl Instrum Methods B **250**, 1–5

Sørensen A.H. (2007): On the nonperturbative contributions to the stopping of H- and He-like heavy ions. Nucl Instrum Methods B **264**, 240–248

Sternheimer R.M. (1952): The density effect for the ionization loss in various materials. Phys Rev **88**, 851–859

Steward P. (1968): Stopping power and range for any nucleus in the specific energy interval 0.01- to 500-MeV/amu in any nongaseous material. Ph.D. thesis, Univ. California, Berkeley. UCRL-18127

Steward P.G. and Wallace R. (1966): Calculation of stopping power and range-energy values for any heavy ion in nongaseous media. Tech. Rep. UCRL-17314, Univ. California, Berkeley

Thwaites D.I. (1983): Bragg's rule of stopping power additivity: a compilation and summary of results. Radiat Res **95**, 495–518

Ziegler J.F. (1980): The stopping and ranges of ions in matter. In J.F. Ziegler, editor, *Handbook of stopping cross-sections for energetic ions in all elements*, vol. 5 of *The Stopping and Ranges of Ions in Matter*, 1–432. Pergamon, New York

Ziegler J.F. (2012): *Particle interactions with matter*. URL `www.srim.org`

Ziegler J.F., Biersack J.P. and Littmark U. (1985): *The stopping and range of ions in solids*, vol. 1 of *The stopping and ranges of ions in matter*. Pergamon, New York

Ziegler J.W., Biersack J.P. and Ziegler M.D. (2008): *Stopping and Range of Ions in Matter*. Lulu Press Co, Morrisville, North Carolina

Chapter 5
Straggling

Abstract This chapter addresses energy-loss straggling of ions with $v > v_0$. The topic is divided up into uncorrelated or linear straggling, correlated straggling (bunching and packing) and charge-exchange straggling. The theory of linear straggling is developed in straight analogy with the stopping cross section. Bunching takes into account the spatial confinement of electrons in the atoms, while packing takes into account the spatial arrangement of atoms in molecules and solids. Charge-exchange straggling accounts for the dependence of elementary energy-loss processes on the ion charge. Significant gas-solid differences are pointed out in pertinent theory as well as experiment.

5.1 Introductory Comments

Electronic-energy-loss straggling has been analysed in Chaps. 8 and 9, Vol. 1 with a focus on swift point charges. Chapter 8 addressed the variance of an energy-loss profile which, for an atomic gas, reads

$$\Omega^2 = \left\langle (\Delta E - \langle \Delta E \rangle)^2 \right\rangle = N x \int T^2 \, \mathrm{d}\sigma(T) \,, \tag{5.1}$$

whereas Chap. 9 addressed the shape of the energy-loss profile $F(\Delta E, x)$ as a function of the travelled pathlength x.

The treatment of straggling to be presented here rests heavily on what has been discussed in Volume 1. However, we shall see that for heavier ions it is mostly the variance that is of interest, so that it is more important that you are familiar with the essentials of Chap. 8, Vol. 1 than with Chap. 9.

In the previous chapter the theoretical treatment of the stopping cross section has been presented as an extension of the theory of stopping of point charges presented in Volume 1. A similar extension will now be applied to the treatment of straggling presented in Chap. 8, Vol. 1.

P. Sigmund, *Particle Penetration and Radiation Effects Volume 2*,
Springer Series in Solid-State Sciences 179, DOI: 10.1007/978-3-319-05564-0_5,

However, the analogy is not complete, because straggling is more complicated for two fundamental reasons.

Firstly, straggling is not just a linear superposition of contributions from individual target electrons: The spatial correlation of the electrons plays a role. Indeed, if an ion hits an electron in a given atom, it has an increased chance to also hit another electron in the same atom. This is immaterial for the mean energy loss but it affects straggling. Correlation effects have already been considered in Sect. 8.9, Vol. 1, and they have been shown to go as the square of the stopping cross section. Since the stopping cross section increases with increasing Z_1, this aspect deserves increased attention here.

A second effect is absent in the stopping of point charges and, therefore, was not mentioned in Volume 1. Straggling due to charge exchange, discussed in Sect. 3.5.5, adds an extra dimension. Although charge exchange also contributes to the stopping cross section, its role in straggling is greatly enhanced, since *all* processes that lead to energy loss depend on the charge state: If the ion charge fluctuates, all energy losses fluctuate, not only those due to charge exchange.

5.2 General Considerations

Figure 5.1 shows five energy-loss spectra measured with 63.4 MeV Li^{2+} ions in carbon. With the target thickness increasing from 5 to 38 $\mu g/cm^2$ both peak and mean energy loss shift toward higher values as you would expect. However, a second peak develops which becomes dominating at 50 $\mu g/cm^2$, and at 109 $\mu g/cm^2$ the first peak has essentially vanished.

In order to understand what is going on here we have to appreciate that at the beam energy under consideration the charge-state distribution in equilibrium peaks at $q = 3$. Therefore, with increasing travelled pathlength an increasing fraction of the beam particles switches from $q = 2$ to $q = 3$, with an increased energy loss per pathlength as a consequence. Since the cross section for capture is small, switching back to $q = 2$ is unlikely. Therefore, from $\sim$ 100 $\mu g/cm^2$ we see essentially the energy-loss spectrum for a point charge $q = 3$. You may gain qualitative insight by looking at Problem 5.4.

We may extract the message from these results that an energy-loss spectrum can have more than one peak. Charge exchange is not the only possible reason for a multiple-peak structure: In fact, with sufficient energy resolution, *all* energy-loss spectra would exhibit a variety of major and minor peaks. The specific feature for charge exchange is that it takes a relatively large energy, $T_c \sim mv^2/2$ for a swift ion to capture an electron. Hence, for a beam energy of $uv^2/2 \simeq 10$ MeV you have $mv^2/2 \simeq 5$ keV. If the energy resolution of the detector is better than 5 keV, you have a chance to resolve adjacent peaks.

When considering the mean energy loss we always encounter a more or less pronounced difference between predictions based on classical dynamics and on Born approximation, respectively. We have seen in Sect. 8.2, Vol. 1, that this difference

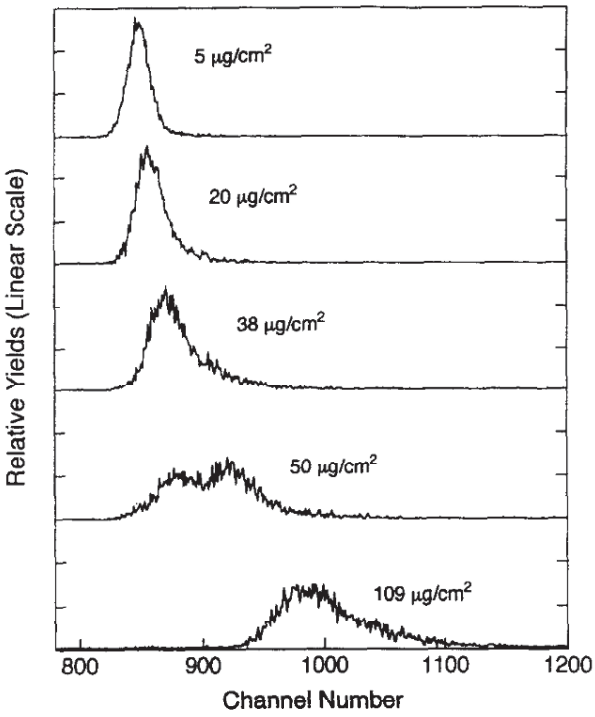

Fig. 5.1 Energy-loss spectrum for 63.4 MeV $^6Li^{2+}$ ions in carbon, from Ogawa et al. (1996)

is much less pronounced in straggling. Indeed, for a bare ion there is no equivalent of a Bloch correction in straggling in the nonrelativistic regime. This has the consequence that classical arguments often can be applied in straggling where a corresponding treatment of stopping would have required a quantal treatment.

A central result of straggling theory is (8.15), Vol. 1,

$$\Omega^2 = 4\pi Z_1^2 Z_2 e^4 N x\,, \tag{5.2}$$

derived by Bohr (1915) and commonly denoted as Bohr straggling. The range of validity of this formula is wide for a point charge, but deviations occur in the region around and below the stopping maximum as well as in the relativistic velocity regime. With increasing ion mass, both the limit between the classical and the Born regime and the stopping maximum move toward higher velocities. Therefore, classical scattering theory must be more widely applicable in studies of energy-loss straggling as Z_1 increases.

Heavy ions at relativistic velocities tend to be stripped of most of their electrons. While the theory of stopping and straggling of completely stripped heavy ions has already been reported in Sects. 8.4.3 and 8.8, Vol. 1, the regime of weak screening is important and will have to be considered.

5.2.1 Validity of the Gaussian Approximation

In Sect. 9.2, Vol. 1 we distinguished between thin, moderately-thick and very thick targets, where the specification of a thin target followed a criterion established by Bohr (1915, 1948),

$$T_{\max}^2 \gg \Omega^2 \,. \tag{5.3}$$

In the opposite case, $T_{\max}^2 \ll \Omega^2$, the spectrum is expected to approach Gaussian shape. We speak about moderately-thick targets as long as the spectrum is close to symmetric. At thicknesses where the projectile loses a significant fraction of its energy, the profile starts skewing again, in which case we talked about very thick targets.

Now, inserting $T_{\max} \simeq 2mv^2$ and (5.2) into (5.3) you obtain

$$Nx \ll \frac{(2mv^2)^2}{4\pi Z_1^2 Z_2 e^4} \tag{5.4}$$

as a condition for seeing a quasi-single-collision spectrum. This condition is increasingly hard to satisfy as Z_1 increases. It is for this reason that the opposite situation of a quasi-gaussian spectrum becomes increasingly common with increasing atomic number of the projectile. For numbers you are encouraged to look into Problem 5.1.

We have seen in the previous section that a necessary condition for a double-peaked energy-loss spectrum is a detector resolution better than $mv^2/2$. Another condition must be that this structure not be wiped out by straggling, i.e.,

$$\frac{mv^2}{2} \gg \Omega^2 \,. \tag{5.5}$$

Now, since $mv^2/2 \simeq T_{\max}/4$, (5.5) is a more severe condition than (5.3). Thus, the maximum thickness for seeing a multiple-peak structure is one quarter of the maximum thickness for what we call thin foils.

Actually, a closer analysis by Glazov and Sigmund (1997, 2000) of the spectra shown in Fig. 5.1 reveals that the observed width is mainly an expression of detector resolution rather than of energy-loss straggling. If a detector with higher energy resolution had been available to the experimenters, the peaks would be narrower.

5.2.2 Correlated and Uncorrelated Straggling

In Sect. 8.9, Vol. 1 the straggling parameter $W = \Omega^2/Nx$ of an atom was split into two parts according to

$$W = W_0 + \Delta W \tag{5.6}$$

with

$$W_0 = \int \mathrm{d}^2\boldsymbol{p} \sum_{i=1}^{Z_2} \left\langle T_i^2(\boldsymbol{p}_i) \right\rangle \tag{5.7}$$

and

$$\Delta W = \int \mathrm{d}^2\boldsymbol{p} \sum_{i \neq j}^{Z_2} \left\langle T_i(\boldsymbol{p}_i) T_j(\boldsymbol{p}_j) \right\rangle, \tag{5.8}$$

where $\boldsymbol{p}_i$ denotes the impact parameter to the ith target electron. Averages are taken over the distribution in real and velocity space of those electrons.

The term W_0 in (5.7) represents a linear superposition of contributions from all target electrons. We may call this 'uncorrelated' or 'linear' straggling. It differs from the corresponding expression for the stopping cross section only in the replacement of $\langle T_i(\boldsymbol{p}_i) \rangle$ by $\langle T_i^2(\boldsymbol{p}_i) \rangle$.

The term ΔW in (5.8) represents a double sum and, hence, must increase more strongly than linearly with the number of target electrons. We talk about 'correlated straggling' here. The dominating correlation is expressed by the impact parameter: It is the spatial proximity of the electrons in an atom that causes enhanced straggling compared with Bohr straggling. A quantitative treatment requires a theory of impact-parameter-dependent energy loss. We shall have to look into this topic.

5.3 Uncorrelated Straggling

Theoretical schemes used for evaluating stopping cross sections for swift heavy ions have been presented in Sects. 4.4–4.7. While all these schemes allow you to evaluate uncorrelated straggling parameters, results have been reported mainly for binary theory (Sigmund and Schinner, 2003, 2010) and the PCA-UCA model (Grande and Schiwietz, 2009).

Within the framework of binary stopping theory we may write

$$W_0 = Z_2 \sum_{n\ell} f_{n\ell} \int 2\pi p_i \, \mathrm{d}p_i \overline{T^2}_{n\ell}(p_i) \,, \tag{5.9}$$

where $f_{n\ell}$ denotes the bundled oscillator strength for the (n, ℓ)th shell, normalized according to $\sum f_{n\ell} = 1$, and $\overline{T^2}_{n\ell}(p)$ the square of the energy loss versus impact parameter, averaged over the velocity distribution of the respective shell[1].

In principle we also would have to average over the spatial distribution of the target electrons, yet this is immaterial because of the integration over the impact parameter.

A convenient reference standard is Fig. 5.2, taken over from Volume 1, which represents a universal plot of the electronic straggling parameter versus beam veloc-

[1] As in previous instances of this monograph, averages are expressed either by brackets, $\langle \ldots \rangle$ or bars, dependent on readability. There is no systematic difference in the physical significance, unless stated otherwise.

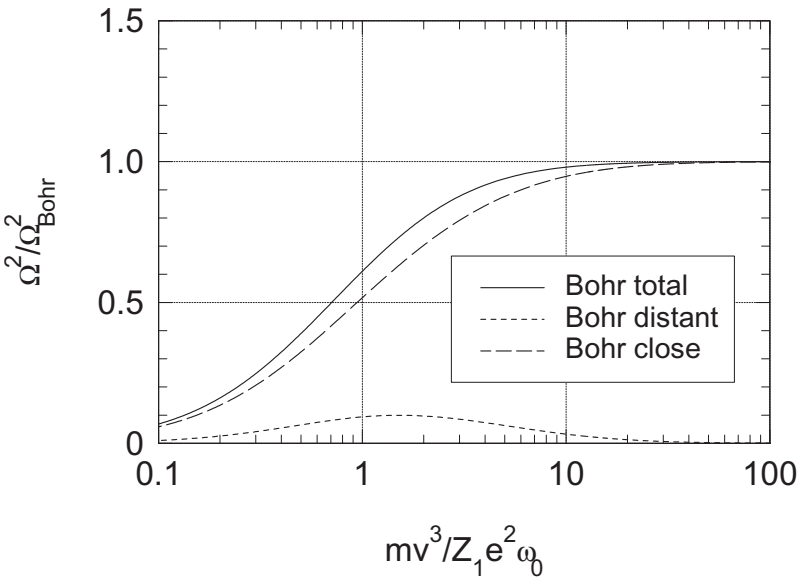

Fig. 5.2 Straggling in Bohr model. Ratio W/W_B for close and distant interactions and the sum. From Vol. 1 (Sigmund, 2006)

ity for an arbitrary fully-stripped ion hitting a one-electron atom characterized by a resonance frequency ω_0. Since the scaling property is linked to the Bohr variable $\xi = mv^3/Z_1e^2\omega_0$, that variable will be used also in the graphs to follow, with ω_0 replaced[2] by $I/\hbar$.

All those corrections to the Bohr theory of stopping which have been discussed in the previous chapter, are also relevant in straggling, albeit with different weights. Here follows a brief survey.

5.3.1 Screening

Screening reduces the contribution from distant interactions. Figure 5.2 shows that distant interactions play a rather minor role in straggling. Therefore, the reduction of straggling due to projectile screening must be significantly smaller than the corresponding reduction in the stopping cross section.

[2] According to (8.21), Vol. 1 the appropriate resonance frequency for straggling should be given by $I_1/\hbar$, where I_1 is defined by

$$\sum_j (\epsilon_j - \epsilon_0) f_j \ln I_1 = \sum_j (\epsilon_j - \epsilon_0) f_j \ln(\epsilon_j - \epsilon_0).$$

This would be relevant if different target materials were compared.

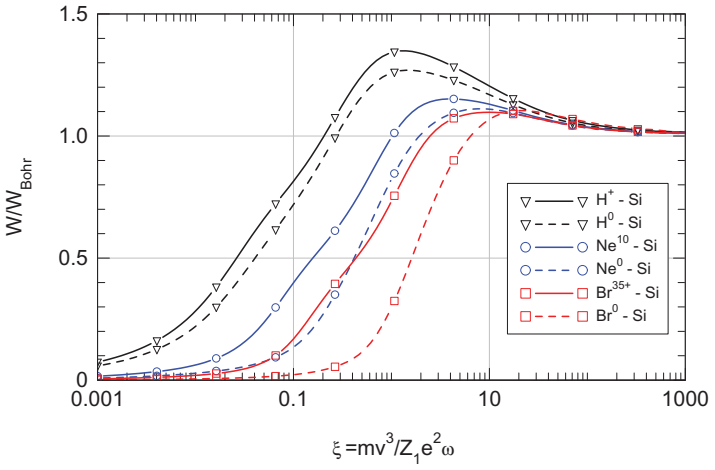

Fig. 5.3 Uncorrelated straggling for H, Ne and Br ions in Si according to binary stopping theory. Solid lines: fully-stripped ions. Dotted lines: neutral ions. Projectile excitation included

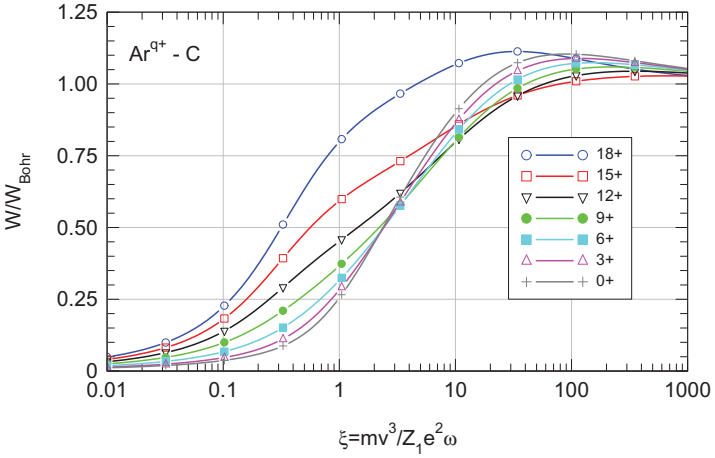

Fig. 5.4 Uncorrelated straggling parameter W_0 in units of W_{Bohr} of frozen-charge Ar^{q+} ions in carbon, calculated from binary theory. Target excitation/ionization only

Figure 5.3 shows a comparison of uncorrelated straggling between fully-stripped and neutral projectiles. Clearly, the difference between these two extreme charge states increases from hydrogen to bromine, yet it is much smaller than in case of the stopping cross section.

Figure 5.4 shows similar results for seven charge states of Ar in C, ranging from 0 to 18+. In comparison with the corresponding Fig. 4.14 which, roughly, showed a linear dependence of the stopping cross section on the ion charge, we see a much weaker dependence here. A noticeable difference is seen between bare argon and all other charge states. Evidently, screening by K electrons is significant over almost the

entire velocity range covered by the graph. Note also the nonmonotonic dependence on the ion charge at the upper end of the graph. This is related to the shell correction (see below).

5.3.2 Transition to the Bethe regime

We have seen in Sect. 8.2, Vol. 1 that there is no nonrelativistic Bloch correction in straggling for bare ions. Consequently there is no nonrelativistic inverse-Bloch correction either. That finding assumes bare-Coulomb interaction and cannot tacitly be adopted to screened ions.

However, screening becomes significant for $v \lesssim Z_1^{2/3} v_0$. In this velocity range, the Bohr kappa parameter is

$$\kappa = \frac{2Z_1 e^2}{\hbar v} \gtrsim 2Z_1^{1/3}\,, \tag{5.10}$$

which is greater than 1 for all Z_1. Therefore, the velocity range where screening plays a major role lies within the classical regime.

Now, our starting point is classical stopping theory, with screening taken into account. Extension into the Born regime requires an inverse-Bloch correction in principle, but since ions are essentially stripped in the Born regime, that correction must vanish.

Thus, even though the Bloch correction affects close interactions, no correction is necessary for straggling in charge equilibrium, if straggling is evaluated within classical theory.

5.3.3 Shell and Barkas-Andersen correction

These two corrections affect both distant and close interactions. Moreover, they are tightly intertwined, as can be seen in Sect. 8.7, Vol. 1.

Figure 5.5 shows uncorrelated straggling for H, Ne and Br in Si as well as for the corresponding mirror ions. The shell correction is seen to give rise to the familiar Bethe-Livingston shoulder which goes above Bohr straggling. As you may recall from Sect. 4.5.1, the shell correction becomes less important as Z_1 increases. Indeed, for Br-Si the shoulder has almost disappeared.

Also included in Fig. 5.5 are curves for mirror ions, i.e., antinuclei screened by the equivalent number of positrons. The difference between solid and dotted lines indicates the Barkas-Andersen effect, which becomes quite large in the low-velocity range and which increases in significance as Z_1 increases.

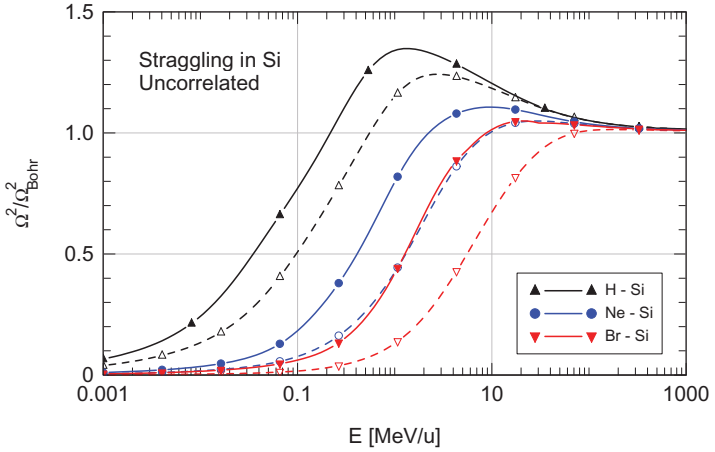

Fig. 5.5 Uncorrelated straggling for H, Ne and Br ions in Si. Target excitation/ionization only. Dashed lines (empty symbols) show results for mirror ions, i.e., antinuclei surrounded by the equivalent number of positrons

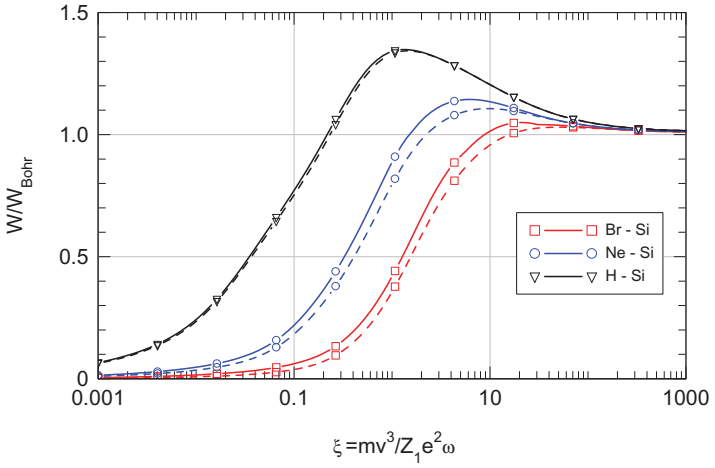

Fig. 5.6 Uncorrelated energy-loss straggling in silicon in charge equilibrium. Solid lines: Including projectile excitation. Dotted lines: Target excitation/ionization only

5.3.4 Projectile Excitation and Ionization

Figure 5.6 illustrates the influence of projectile excitation on uncorrelated straggling for H, Ne and Br ions in Si. For hydrogen ions this influence is negligible, while it is rather small for Ne and Br. This has to be so, because linear collisional straggling is dominated by large energy transfers. As was discussed in Sect. 4.5.3, large energy transfers do not change the velocity of the projectile. Hence, only energy transfers $T < U_1$ are taken into account.

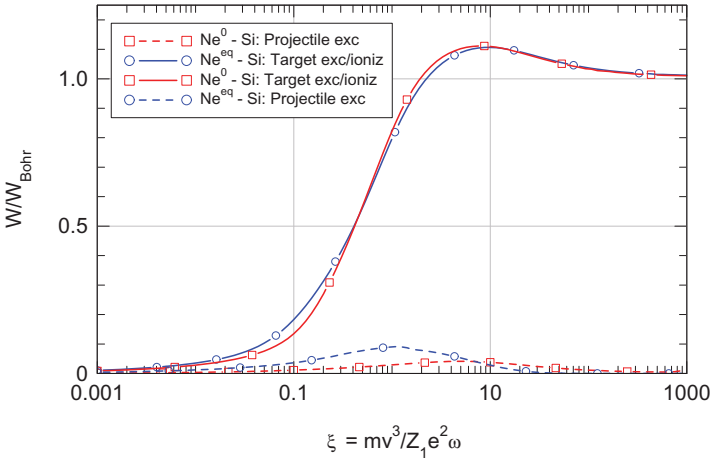

Fig. 5.7 Uncorrelated energy-loss straggling of neon ions in silicon. Solid lines: Charge equilibrium. Dotted lines: Neutral projectile. Circles (blue lines): Target excitation/ionization. Squares (red lines): Projectile excitation

Figure 5.7 demonstrates that the contribution of target excitation/ionization to linear collisional straggling is rather insensitive to the ion charge. While this is not the case for projectile excitation, that contribution is found to be small for both options of the ion charge, except at low velocities corresponding to $\xi = mv^3/Z_1e^2\omega < 0.1$.

5.3.5 Relativity

According to (8.33), Vol. 1, the primary relativistic correction is a multiplicative factor $(1-\beta^2/2)/(1-\beta^2)$ to Bohr straggling, (5.2), where $\beta = v/c$. This factor becomes significant for $\beta \gtrsim 0.5$. This is also the velocity range where the Lindhard-Sørensen correction, shown in Fig. 8.13, Vol. 1, becomes substantial.

At $v = 0.5c$, the mean equilibrium charge is given by

$$\overline{q_1} \simeq Z_1 \left(1 - \mathrm{e}^{-137/2Z_1^{2/3}}\right) . \tag{5.11}$$

This implies that $\overline{q_1} \simeq 53.5$ for a xenon ion and $\overline{q_1} \simeq 89$ for uranium. Dependent on the desired accuracy, a screening correction may be needed even in the relativistic regime.

Screening corrections in this energy range have been evaluated by Sørensen (2002) for hydrogen- and heliumlike heavy ions. Explicit screening corrections were given for stopping cross sections and found to have a substantial influence on charge-exchange straggling. Screening corrections in collisional straggling are small

in absolute terms, but as you may see from Fig. 8.13, Vol. 1, collisional straggling itself goes rapidly to zero at high beam energies. As it turns out, for $E \gtrsim 400$ MeV/u, collisional straggling for U^{91+} is closer to U^{92+} than to Pa^{91+} (Sørensen, 2010).

5.3.6 Electron Capture

Electron capture has been mentioned in Sect. 5.2 as a cause of multiple-peak structure, which can only be observed with ultrathin foils. For moderately-thick foils one may ask whether electron capture contributes to the straggling parameter $W = \int T^2 \, \mathrm{d}\sigma(T)$.

With $T_c \simeq mv^2/2$, we may compare the quantity

$$W_c = \left(\frac{m}{2} v^2\right)^2 \sigma_c \tag{5.12}$$

with Bohr straggling, $W_{\mathrm{Bohr}} = 4\pi Z_1^2 Z_2 e^4$. In terms of atomic parameters, the capture contribution is negligible if $W_c \ll W_{\mathrm{Bohr}}$ or

$$\frac{\sigma_c}{\pi a_0^2} \ll Z_1^2 Z_2 \left(\frac{2v_0}{v}\right)^4 . \tag{5.13}$$

From Chap. 2 we know that at high projectile speed the capture cross section decreases much faster than $\propto v^{-4}$. Conversely, at low projectile speed, where σ_c approaches a constant value, uncorrelated straggling decreases more slowly than $\propto v^4$ with decreasing v. Thus, there is an intermediate velocity range where the ratio of the capture contribution and uncorrelated collisional straggling goes through a maximum.

5.3.7 Short Summary of Linear Straggling

Figure 5.6 provides a good qualitative survey on uncorrelated straggling:

- Bohr straggling holds down to a value of $\xi = mv^3/Z_1 e^2 \omega \sim 100$,
- For $\xi \lesssim 100$ the Bohr parameter is not a suitable scaling parameter,
- The Bethe-Livingston shoulder is most pronounced for protons.

5.4 Bunching and Packing

Bunching and packing are effects caused by the spatial correlation of the electrons, which has been ignored in the treatment underlying the previous section. Bunching

addresses the correlation between electrons in an individual atom, while packing denotes the correlation between contributions from different atoms.

General expressions describing the two effects have been derived in Sect. 8.9, Vol. 1, except for the notation: No distinction was made there between bunching and packing. Instead, both effects were denoted as bunching.

Bunching is most directly studied in dilute atomic-gas targets such as noble gases. Bunching of electrons in atoms gives rise to fewer interactions but larger energy losses than for a random distribution of target electrons. This increases fluctuations in energy loss. A similar effect occurs when a molecular gas is compared with an atomic gas, although differences in electronic properties between bound and unbound atoms also need to be considered. In condensed matter, short-range order implies that the sequence of collisions undergone by a penetrating particle does not obey Poisson statistics. Instead, collisions take place at more regular intervals in time or space. This tends to *decrease* fluctuations in energy loss.

5.4.1 Statistics

Within the range of applicability of a classical-orbit picture of electronic energy loss, the basic statistical relations are strictly analogous for both bunching and packing, dating back to a paper by the author (Sigmund, 1976) and, in more general form, Sigmund (1978). The present derivation refers to bunching following Sigmund and Schinner (2010). Bunching was first treated explicitly by Besenbacher et al. (1980).

Let us introduce a probability $P(T, \boldsymbol{p})\,\mathrm{d}T$ for energy loss $(T, \mathrm{d}T)$ in a single collision as a function of a vectorial impact parameter $\boldsymbol{p}$ to the target *nucleus*. This defines the differential cross section for energy loss $(T, \mathrm{d}T)$ as

$$\mathrm{d}\sigma(T) = \mathrm{d}T \int \mathrm{d}^2\boldsymbol{p}\; P(T, \boldsymbol{p})\,. \tag{5.14}$$

From this follows the stopping cross section

$$S = \int T\,\mathrm{d}\sigma(T) = \int \mathrm{d}^2\boldsymbol{p}\,\overline{T}(\boldsymbol{p}) \tag{5.15}$$

and the straggling parameter

$$W^2 = \int \mathrm{d}^2\boldsymbol{p}\,\overline{T^2}(\boldsymbol{p})\,, \tag{5.16}$$

where $\overline{T}(\boldsymbol{p}) = \int \mathrm{d}T\; TP(T, \boldsymbol{p})$ and similarly for $\overline{T^2}$.

It is instructive to write (5.16) in the form (Grande and Schiwietz, 1991),

$$W = \int \mathrm{d}^2\boldsymbol{p}\,\left\{\left(\overline{T^2}(\boldsymbol{p}) - \left[\overline{T}(\boldsymbol{p})\right]^2\right) + \left[\overline{T}(\boldsymbol{p})\right]^2\right\}\,, \tag{5.17}$$

where the first two terms in the brackets denote the energy-loss fluctuation at a given impact parameter, whereas the last term determines straggling when no distinction is necessary between the impact parameter to the nucleus and the one to an electron, as is the case in Bohr's estimate presented in Sect. 2.3.3, Vol. 1.

Now consider a target atom with Z_2 electrons. In a classical-orbital description we may introduce an impact parameter $\boldsymbol{p}_\nu$ to the νth electron, so that

$$T(\boldsymbol{p}) = \sum_{\nu=1}^{Z_2} T_{j_\nu}(\boldsymbol{p}_\nu)\,, \tag{5.18}$$

where j_ν denotes the state of the νth electron, i.e., its distribution in real and velocity space.

With this, (5.15) reduces to

$$S = \sum_\nu \int \mathrm{d}^2\boldsymbol{p}_\nu\, \overline{T}_{j_\nu}(\boldsymbol{p}_\nu) \equiv \sum_\nu S_\nu\,, \tag{5.19}$$

where

$$S_\nu = \int \mathrm{d}^2\boldsymbol{p}\, \overline{T}_{j_\nu}(\boldsymbol{p}) \tag{5.20}$$

is the stopping cross section of the νth electron. Evidently, the spatial correlation of the target electrons has dropped out. The bar in (5.20) denotes an average over the distribution in orbital velocity, i.e., the shell correction.

In order to evaluate (5.16) we need

$$\overline{T^2}(\boldsymbol{p}) = \sum_{\nu\mu} \overline{T_{j_\nu}(\boldsymbol{p}_\nu) T_{j_\mu}(\boldsymbol{p}_\mu)}\,. \tag{5.21}$$

If we assume that the motion of electrons in the atom is uncorrelated, we may split the right-hand side according to

$$\overline{T^2}(\boldsymbol{p}) = \sum_\nu \overline{T^2_{j_\nu}(\boldsymbol{p}_\nu)} + \sum_{\nu\neq\mu} \overline{T_{j_\nu}(\boldsymbol{p}_\nu)}\;\overline{T_{j_\mu}(\boldsymbol{p}_\mu)}\,. \tag{5.22}$$

Here, the average of the second term factorizes into separate averages over individual electrons.

You may wonder why correlated motion of electrons can be neglected in estimating correlation effects. Well, there are several types of correlation, and the underlying assumption is that the most prominent, and certainly the most obvious type of correlation is bunching, i.e., the fact that the motion of the electrons is limited to a region of atomic dimensions.

Taking into account other correlations such as exchange effects requires a quantal treatment. A brief discussion within the Born approximation may be found in Fano's review (Fano, 1963).

Going back to (5.22) we may add and subtract the diagonal term missing in the second contribution to arrive at

$$W_{\mathrm{at}} = \sum_{\nu} \int \mathrm{d}^2\boldsymbol{p} \left\{ \overline{T_{j_\nu}^2(\boldsymbol{p}_\nu)} - \left(\overline{T_{j_\nu}(\boldsymbol{p}_\nu)}\right)^2 \right\} + \int \mathrm{d}^2\boldsymbol{p} \left(\sum_{\nu} \overline{T_{j_\nu}(\boldsymbol{p}_\nu)} \right)^2 \quad (5.23)$$

or, making use of (5.18),

$$W_{\mathrm{at}} = \sum_{\nu} \int \mathrm{d}^2\boldsymbol{p} \left(\overline{T_{j_\nu}^2}(\boldsymbol{p}) - \left(\overline{T_{j_\nu}}(\boldsymbol{p})\right)^2 \right) + \int \mathrm{d}^2\boldsymbol{p} \, \left(\overline{T}(\boldsymbol{p})\right)^2 . \quad (5.24)$$

With the notations

$$W_j = \int \mathrm{d}^2\boldsymbol{p} \, \overline{T_j^2}(\boldsymbol{p}) \quad (5.25)$$

and

$$V_j = \int \mathrm{d}^2\boldsymbol{p} \, \left(\overline{T_j}(\boldsymbol{p})\right)^2 \quad (5.26)$$

we may write (5.24) in the form

$$W = W_0 + \Delta W \,, \quad (5.27)$$

where

$$W_0 = \sum_{n,\ell} f_j W_j \quad (5.28)$$

and

$$\Delta W = \int \mathrm{d}^2\boldsymbol{p} \, \left[\overline{T}(\boldsymbol{p})\right]^2 - \sum_j f_j V_j \,, \quad (5.29)$$

where f_j is the number of target electrons in the jth shell, so that

$$\sum_j f_j = Z_2 \,. \quad (5.30)$$

Here W_0 represents uncorrelated straggling, while ΔW represents bunching. The bars denote averages over the distribution in real and velocity space of the target electrons.

In order to evaluate the integrals entering (5.29) we need expressions for the dependence of the mean energy transfer $\overline{T}_j(\boldsymbol{p})$ on impact parameter, cf. the discussion in Sect. 4.9.

5.4.2 Bunching: Atoms

Quantitative calculations on bunching corrections for light ions were first reported by Besenbacher et al. (1980) and later by Grande and Schiwietz (1991). Since the stopping cross section enters quadratically, the effect must increase in importance with increasing atomic number.

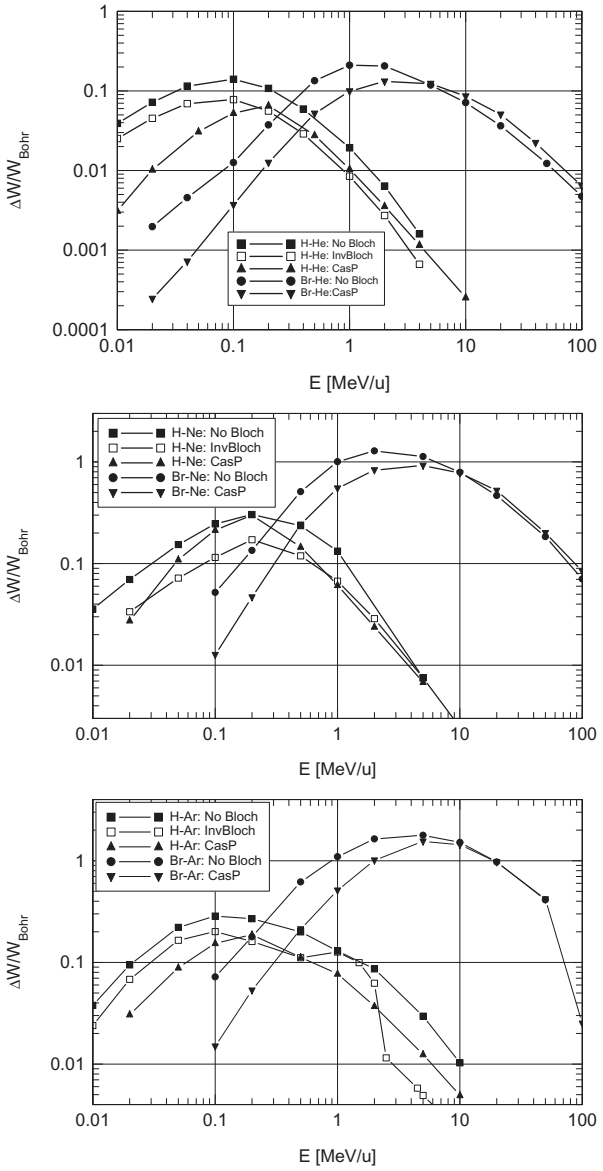

Fig. 5.8 Bunching correction $\Delta W / W_{\mathrm{Bohr}}$ versus beam energy for H and Br ions in He (top), Ne (middle) and Ar (bottom). Comparison of PASS calculations with and without inverse-Bloch correction and CasP calculations. From Sigmund and Schinner (2010)

Figure 5.8, taken from Sigmund and Schinner (2010), demonstrates this on the example of H and Br ions. As was to be expected, the bunching correction

has a maximum near the maximum of the stopping cross section, which lies at $\sim 100\,\mathrm{keV/u}$ for protons but at a considerably higher energy for bromine.

The same graph also shows a significant dependence on the target atom. The increase in magnitude from He to Ne must be due to the increasing number of electrons involved which gives rise to a higher electron density. Note that the bunching effect originates in small impact parameters. Further increase from Ne to Ar is rather small.

A word of caution is in place here. As you may notice, there are peculiar discontinuities in some of the curves, and there are significant differences between results computed from the PASS code and from CasP, indicating considerable uncertainties in the underlying computations. While a generous error margin should be kept in mind, there are clear trends as a function of Z_1 and Z_2. Also, the magnitude of the bunching correction does not seem to exceed $\Delta W/W_{\mathrm{Bohr}} \sim 2$, and the slope on both sides of the maximum appears steeper than in case of the stopping cross section. More quantitative details await more accurate computations.

5.4.3 Packing: Molecules

Packing in a molecular gas has been treated in detail in Sect. 8.9.3, Vol. 1. Interest at this point is directed at the variation with Z_1. Intuitively we may expect packing to be a smaller effect than bunching in view of the greater distances between electrons.

For a polyatomic molecule we have a packing correction

$$\Delta W = \sum_{\mu \neq \nu} \Delta W_{\mu\nu} \tag{5.31}$$

with

$$\Delta W_{\mu\nu} = \left\langle \int \mathrm{d}^2\boldsymbol{p} \int \mathrm{d}^2\boldsymbol{p}'\, \overline{T_\mu}(\boldsymbol{p})\overline{T_\nu}(\boldsymbol{p}')\, \delta\left(\boldsymbol{p} - \boldsymbol{p}' - \boldsymbol{b}_{\mu\nu}\right)\right\rangle , \tag{5.32}$$

where $\overline{T_\mu(\boldsymbol{p})}$ is the mean energy loss to atom μ at impact parameter $\boldsymbol{p}$ and $\boldsymbol{b}_{\mu\nu}$ is the projection of the internuclear distance $\boldsymbol{r}_{\mu\nu}$ on the impact plane. Angular brackets denote an average over all orientations of the molecule as well as, if allowed for, fluctuations in the spatial distribution due to zero-point and thermal vibrations. According to (8.93), Vol. 1, this can be written as

$$\Delta W_{\mu\nu} = \frac{1}{2\pi d_{\mu\nu}^2} \int \mathrm{d}^2\boldsymbol{p} \int \mathrm{d}^2\boldsymbol{p}' \frac{\overline{T_\mu}(\boldsymbol{p})\overline{T_\nu}(\boldsymbol{p}')}{\sqrt{1 - (\boldsymbol{p} - \boldsymbol{p}')^2/d_{\mu\nu}^2}} , \tag{5.33}$$

where $d_{\mu\nu}$ is the internuclear distance between the μth and the νth atom. Angular brackets have been omitted here, indicating that internal molecular motion has been neglected.

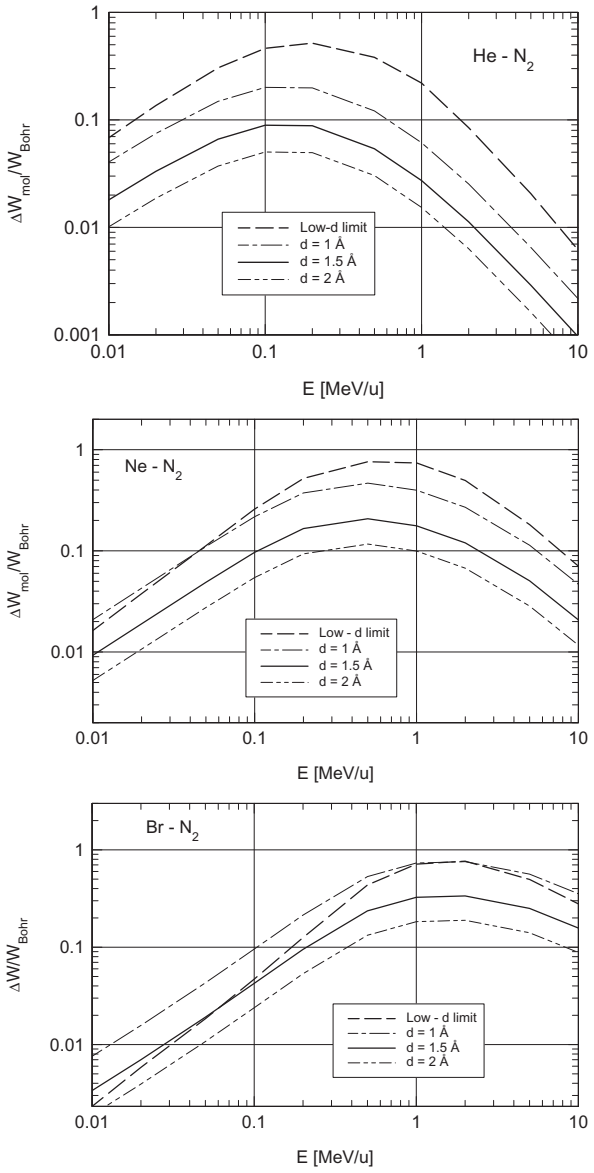

Fig. 5.9 Packing correction ΔW for He, Ne and Br ions (top to bottom) penetrating through molecular nitrogen. Solid line: $S^2/2\pi d^2$ for the equilibrium distance of the neutral molecule, $d = 1.5$ Å. Thin lines: Same for $d = 1.0$ and 2.0 Å. Dashed line: $\int \overline{T}^2 \mathrm{d}\sigma$. All expressions normalized to Bohr straggling. From Sigmund and Schinner (2010)

If the internuclear distance is large compared to the ion-atom interaction range, this reduces to

$$\Delta W_{\mu\nu} \simeq \frac{S_\mu S_\nu}{2\pi d_{\mu\nu}^2}, \qquad d_{\mu\nu} \text{ large}, \tag{5.34}$$

where S_μ is the stopping cross section for atom μ. In the opposite limit you find

$$\Delta W_{\mu\nu} \simeq \int \mathrm{d}^2\boldsymbol{p}\,\overline{T_\mu}(\boldsymbol{p})\overline{T_\nu}(\boldsymbol{p}), \qquad d_{\mu\nu} \text{ small}. \tag{5.35}$$

You are invited in Problem 5.3 to convince yourself that the formula

$$\Delta W_{\mu\nu} \simeq \mathrm{Min}\left(\frac{S_\mu S_\nu}{2\pi d_{\mu\nu}^2}, \int \mathrm{d}^2\boldsymbol{p}\,\overline{T_\mu}(\boldsymbol{p})\overline{T_\nu}(\boldsymbol{p})\right) \tag{5.36}$$

will give you a good overall estimate.

Figure 5.9 shows an example for molecular nitrogen. As Z_1 increases from 2 (He) to 53 (Br), the maximum of the packing correction is seen to increase and to move to higher energies. This is to be expected in view of the proportionality with the square of the stopping cross section. In accordance with (5.36) the magnitude depends sensitively on $d_{\mu\nu} \equiv d$. Noting that the option $d = 1.5\,\text{Å}$ is closer to reality, you may conclude that the low-d approximation (5.35) is of little importance except perhaps for Br-N_2 at energies below 0.1 MeV/u.

5.4.4 Packing: Solids

The packing correction for solids has been found to be negative long ago (Sigmund, 1978), but quantitative predictions have appeared only recently (Sigmund and Schinner, 2010).

We restrict ourselves to a monoatomic medium. The packing condition presented in Sect. 8.9.4, Vol. 1, refers to an amorphous medium. A slight generalization is necessary, if the theory is to be applied to a polycrystalline medium.

With reference to Fig. 5.10 we may write the average square of the energy loss in the form

$$\left\langle(\Delta E)^2\right\rangle = \frac{z}{A}W_0 + \frac{z}{A}{\sum_\nu}' \int \mathrm{d}^2\boldsymbol{p}\,T(\boldsymbol{p})T(\boldsymbol{p}+\boldsymbol{b}_\nu) \tag{5.37}$$

according to (8.106), Vol. 1, where z is the number of atoms in the target and A its area. $\boldsymbol{b}_\nu$ is the lateral component of the vectorial distance $\boldsymbol{r}_\nu$ of atom ν from an atom located in the origin, and the prime indicates omission of that atom from the sum.

From this we find the packing correction

$$\begin{aligned} Nx\Delta W &= \left\langle(\Delta E)^2\right\rangle - \langle\Delta E\rangle^2 - NxW_0 \\ &= \frac{1}{(2\pi)^2}Nx\int \mathrm{d}^2\boldsymbol{k}\,|S(\boldsymbol{k})|^2\left(\sum_\nu \mathrm{e}^{-\mathrm{i}\boldsymbol{k}\cdot\boldsymbol{b}_\nu} - N\int d^3\boldsymbol{r}\,\mathrm{e}^{-\mathrm{i}\boldsymbol{k}\cdot\rho}\right), \end{aligned} \tag{5.38}$$

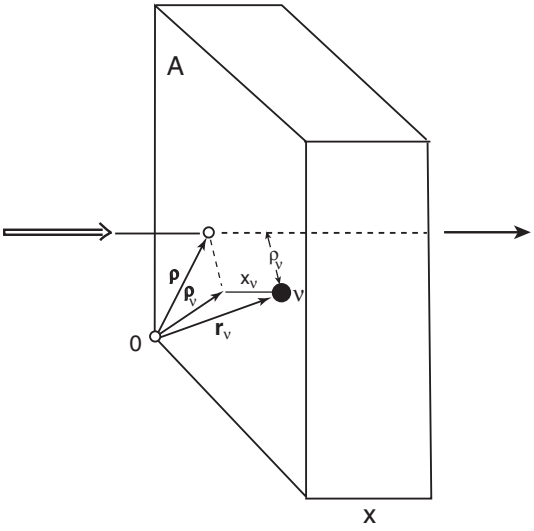

Fig. 5.10 Definition of geometric quantities determining energy loss in solids. From Vol. 1

where

$$S(\boldsymbol{k}) = \int \mathrm{d}^2 \boldsymbol{p} \overline{T}(\boldsymbol{p}) \mathrm{e}^{-\mathrm{i}\boldsymbol{k}\cdot\boldsymbol{b}} \tag{5.39}$$

and $\boldsymbol{\rho}$ is the lateral component of $\boldsymbol{r}$.

Writing

$$\int \mathrm{d}^2 k \, |S(k)|^2 \, \frac{\sin(kr)}{kr} = \frac{2\pi S^2}{r^2} \Psi(r) \tag{5.40}$$

we find

$$\Delta W = \frac{S^2}{2\pi} \left[\sum_{0<r_i<r_0} \frac{1}{r_i^2} \Psi(r_i) - N \int_0^{r_0} \mathrm{d}^3 \boldsymbol{r} \, \frac{1}{r^2} \Psi(r) \right] . \tag{5.41}$$

The function $\Psi(r)$ approaches unity at large values of r. In the opposite limit, $r \to 0$, $\Psi(r)$ approaches

$$\Psi(r) \to \frac{2\pi r^2}{S^2} \int \mathrm{d}^2 \boldsymbol{p} \left(\overline{T}(\boldsymbol{p}) \right)^2 . \tag{5.42}$$

Approximating this function by its limiting behaviour at both ends, as was done in (5.36), we find

$$\Delta W \simeq \Delta W_1 + \Delta W_2 \tag{5.43}$$

according to Sigmund and Schinner (2010) with

$$\Delta W_1 = \frac{S^2}{2\pi} \left[\sum_{r_i<r_0}{}' \frac{1}{r_i^2} - 4\pi N r_0 \right] \tag{5.44}$$

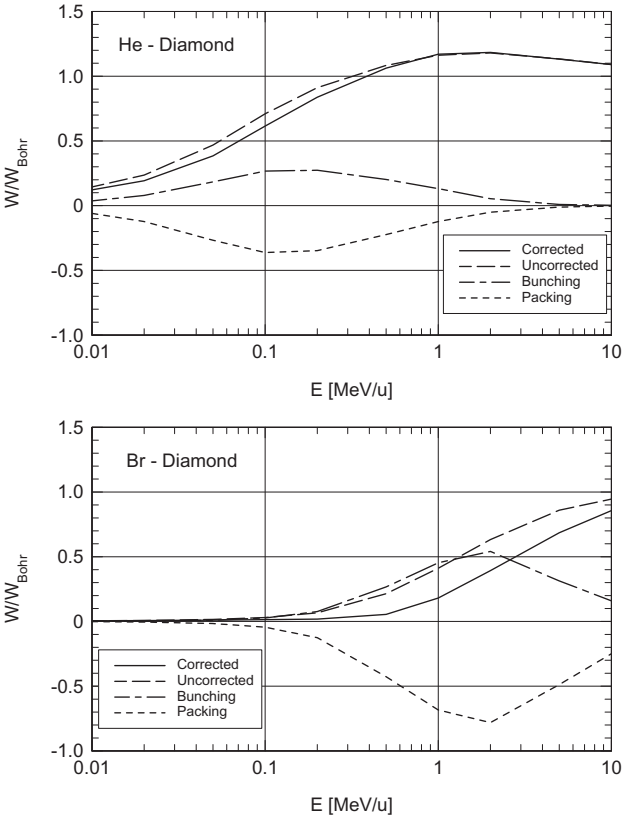

Fig. 5.11 Straggling of He (upper graph) and Br (lower graph) ions in diamond. Charge-exchange straggling and projectile excitation excluded. Curves labelled 'uncorrected' are based on (5.9) disregarding bunching correction. Curves labelled 'corrected' contain both bunching and packing correction

and

$$\Delta W_2 = \frac{4}{3} N S^2 d_0 \,. \tag{5.45}$$

r_0 is to be taken large enough to let the content of the square brackets come close to its asymptotic value. d_0 is defined by the cross-over of the low-r and the high-r limits,

$$d_0^2 = \left(\int \mathrm{d}^2 \boldsymbol{p} \overline{T}(\boldsymbol{p})^2 \right)^{-1} \frac{S^2}{2\pi} \,. \tag{5.46}$$

Note that $\Delta W_1 / S^2$ depends on the structure, while $\Delta W_2 / N$ depends on atomic parameters.

Examples shown in Figs. 5.11 and 5.12 have been evaluated assuming the high-d limit (5.34). This implies numerical evaluation of the quantity

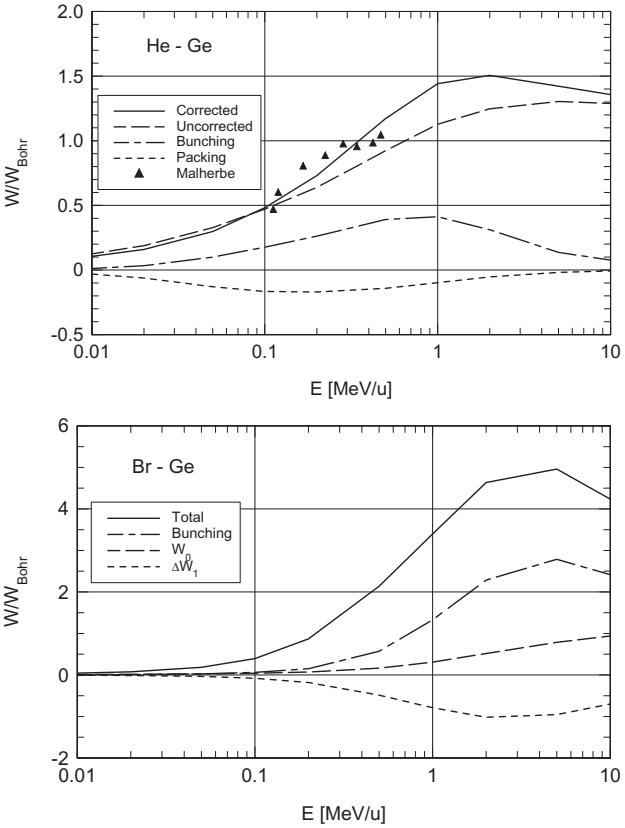

Fig. 5.12 Same as Fig. 5.11 for germanium. Experimental data from Malherbe and Alberts (1982) included in the upper graph

Table 5.1 The parameter $1/D^2$ defined in (5.47) in units of the cubic lattice constant d for four cubic structures and graphite. For graphite d is the in-layer lattice constant 2.456 Å; the height of the unit cell is 6.696 Å. From Sigmund and Schinner (2010)

Structure	$(d/D)^2$
simple cubic	8.8
graphite	9.3
body-centered cubic	14.4
face-centered cubic	22.8
diamond	33.9

$$\frac{1}{D^2} = \sum_{0<r_i<r_0}{}' \frac{1}{r_i^2} - N \int_0^{r_0} \mathrm{d}^3\boldsymbol{r}\, \frac{1}{r^2} \tag{5.47}$$

for several lattice structures, cf. Table 5.1.

In the case of He on diamond (Fig. 5.11, upper graph) the bunching and packing correction nearly cancel each other, while for Br ions the packing condition dominates and gives rise to an overall decrease in straggling.

In the corresponding graph for germanium (Fig. 5.12) the bunching correction is noticeably greater, as you may have expected by looking at Fig. 5.8. Here the net effect is an enhancement in straggling beyond the uncorrelated case. For Br in Ge this gives rise to a maximum straggling value of five times the Bohr value.

5.5 Charge-Exchange Straggling

Statistical expressions for charge-exchange straggling have been found in Sect. 3.5.5. The most general result—which includes the transient behaviour—is (3.133), which reduces to (3.137) for the stationary case. If only two significant states are involved, these relations simplify considerably, as discussed in Sect. 3.5.5.1. The number of input parameters increases rapidly as more states get involved, as demonstrated for three states by Sigmund (1992). Instead, the continuum approximation discussed in Sect. 3.5.5.2 is a convenient scheme to evaluate charge-exchange straggling at least in equilibrium.

5.5.1 Neglecting Energy Loss by Charge Exchange?

According to (3.138), charge-exchange straggling reduces to

$$\left(\frac{\mathrm{d}\Omega^2}{N\,\mathrm{d}x}\right)_{\mathrm{chex}} = \frac{2}{\sigma}\,(S_1 - S_2)\sum_{J=1}^{2} F_J\,(F_2 S_{J1} - F_1 S_{J2})\,. \tag{5.48}$$

in charge equilibrium, when only two states are active. In the literature, off-diagonal elements S_{12} and S_{21} have most often been ignored. Let us check to what degree this may be justified.

For clarity, consider hydrogen as the projectile and let 1 denote a bare proton and $2 \to 0$ a neutral hydrogen atom. Then,

$$S_1 - S_2 = (S_{11} - S_{00}) + S_{\mathrm{capt}} - S_{\mathrm{loss}} \tag{5.49}$$

and

$$\sum_J (F_2 S_{J1} - F_1 S_{J2}) = F_1 F_0\,(S_{11} - S_{00}) - F_1^2 S_{\mathrm{capt}} + F_0^2 S_{\mathrm{loss}}\,, \tag{5.50}$$

where $S_{\mathrm{loss}} \simeq T_{\mathrm{loss}}\sigma_{\mathrm{loss}}$ and $S_{\mathrm{capt}} \simeq T_{\mathrm{capt}}\sigma_{\mathrm{capt}}$ denote the stopping cross sections in a loss or capture event, respectively.

In (5.49), the importance of electron capture and/or loss is determined by the pertinent stopping cross sections. In (5.50) also the charge fractions play a role. This may change the relative weight of the three contributions substantially. For example, consider the limit of high energy, where $F_0 \ll 1$ and $F_1 \simeq 1$. If only stopping cross sections were considered, the three terms would typically be in decreasing order. Weighted by charge fractions, the first contribution would experience a substantial decrease, even more so the second one, whereas the third contribution, albeit small because of the small capture cross section, would be essentially unchanged.

Thus, energy loss by charge exchange cannot generally be neglected without a detailed analysis.

5.5.2 Examples

Figure 5.13 shows results from a detailed study of the two-state case by Besenbacher et al. (1981). Ω^2 was determined for hydrogen and helium ions in Ar and Kr for beam energies ranging from 70 to 500 keV/u. Dots in the two graphs show the difference $\left(\Omega^2/\Omega^2_{\mathrm{Bohr}}\right)_{\mathrm{He}} - \left(\Omega^2/\Omega^2_{\mathrm{Bohr}}\right)_{\mathrm{H}}$ for Ar and Kr targets, respectively. The lower solid curve in either graph shows an estimate of charge-exchange straggling, based on (5.48), ignoring energy loss by charge exchange and inserting known cross sections for charge exchange as well as frozen-charge stopping cross sections measured by Cuevas et al. (1964). The dot-dashed curve represents bunching, estimated on the basis of a local-density approximation. The dashed curve, representing the sum of the two, is seen to agree rather well with the experimental results.

The upper solid curve in the two graphs represents charge-exchange straggling, estimated on the basis of the assumption that the stopping cross section of singly-charged He should be identical with that for protons. Besenbacher et al. (1981) drew the important conclusion from this and similar results for other ion-target combinations that previously-reported results on charge-exchange straggling overestimated the effect.

Figure 5.14 shows an example for a very heavy ion (bismuth) at high beam energy. As was discussed in Sects. 6.7.2 and 8.8, Vol. 1, the theory of stopping and straggling of heavy bare nuclei at relativistic velocities needs to be amended by a Lindhard-Sørensen correction (Lindhard and Sørensen, 1996). Experimental results shown in Fig. 5.14 have been normalized to Lindhard-Sørensen straggling. It is seen that measured values of straggling agree well with the results of a Monte-Carlo simulation incorporating charge exchange based on measured cross sections for electron capture and loss, allowing for three charge states 83+, 82+ and 81+. Although the two graphs do not refer to exactly the same beam energy, the influence of screening is seen to be noticeable.

For a qualitative interpretation you are invited to look into Problem 5.5.

Figure 5.15 illustrates trends for sulphur ions in carbon. Equation (3.155) allows to separate charge-exchange straggling into two factors, one governed by the dependence of the energy loss on the ion charge, the other being governed by the

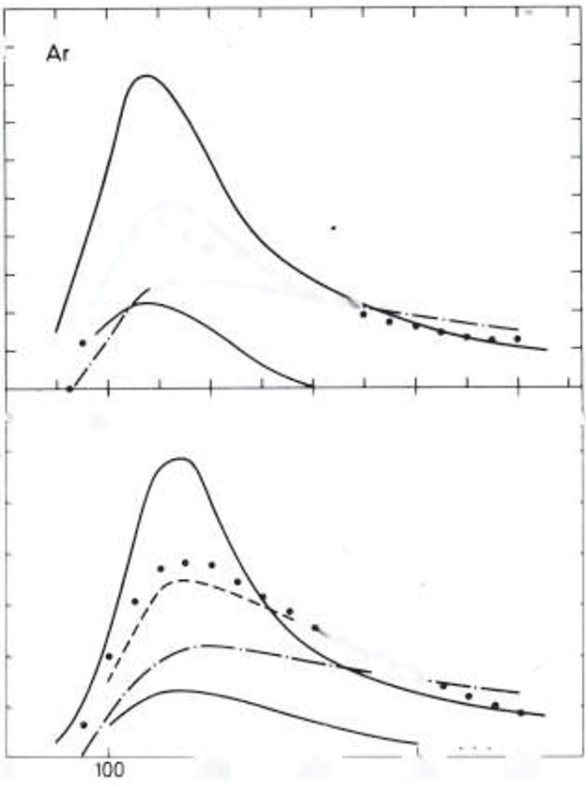

Fig. 5.13 Charge exchange and bunching in Ar and Kr. See text. From Besenbacher et al. (1981)

charge-state evolution. The top graph indicates that the dependence on beam energy is determined primarily by the charge fractions, while the charge dependence of the stopping cross section shows a comparatively slow decrease with energy. The large difference between results obtained from two different methods to arrive at charge fractions (Rozet et al., 1996, Osmani and Sigmund, 2011) indicates that charge-exchange straggling must be quite sensitive to input cross sections for electron capture and loss. Note in particular the difference between height and position of the maximum in the bottom graph. On the other hand, both estimates indicate charge-exchange straggling to far exceed the Bohr value around the maximum.

Moreover, note that the stopping maximum for S in C—which characterizes bunching and packing—lies at 0.8 MeV/u according to ICRU (2005), i.e. far below the maximum of charge-exchange straggling.

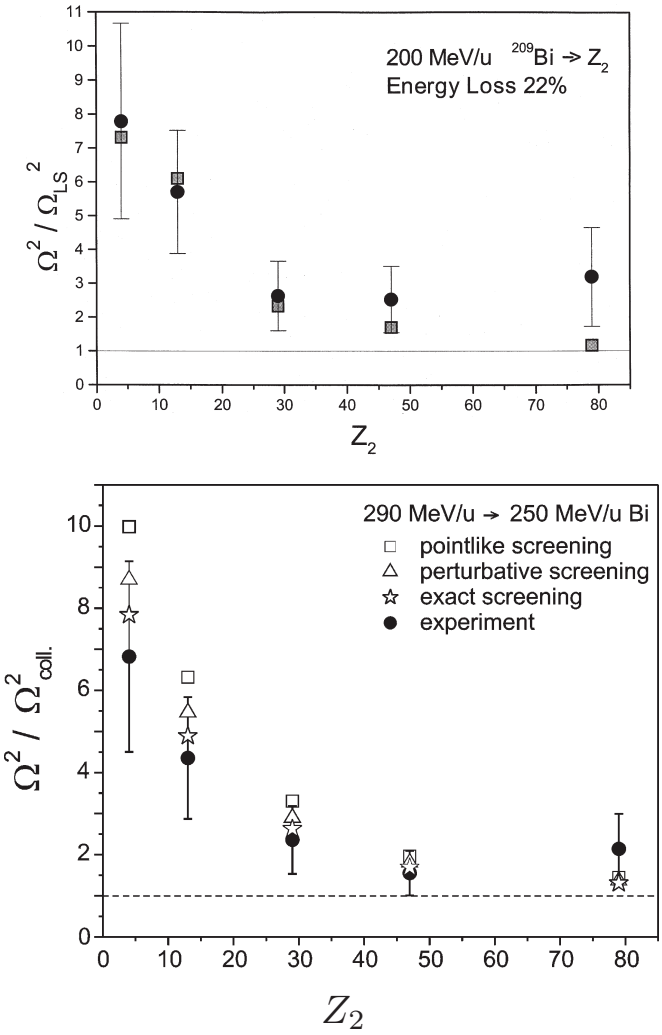

Fig. 5.14 Straggling of 200 (top) and $\mathbf{290 \rightarrow 250}$ (bottom) MeV/u bismuth ions in different solid materials, normalized to the prediction for collisional straggling of Lindhard and Sørensen (1996). Circles: Measurements of Weick et al. (2000). Other symbols: Different simulations accounting for charge-exchange straggling. Top: Calculation for bare ions. From Weick et al. (2000). Bottom: Calculation including screening correction in the stopping cross section. From Sørensen (2002)

5.6 Dielectric Theory

5.6.1 Recapitulation

According to (8.34), Vol. 1, Lindhard dielectric theory predicts straggling for a point charge $Z_1 e$ to be given by

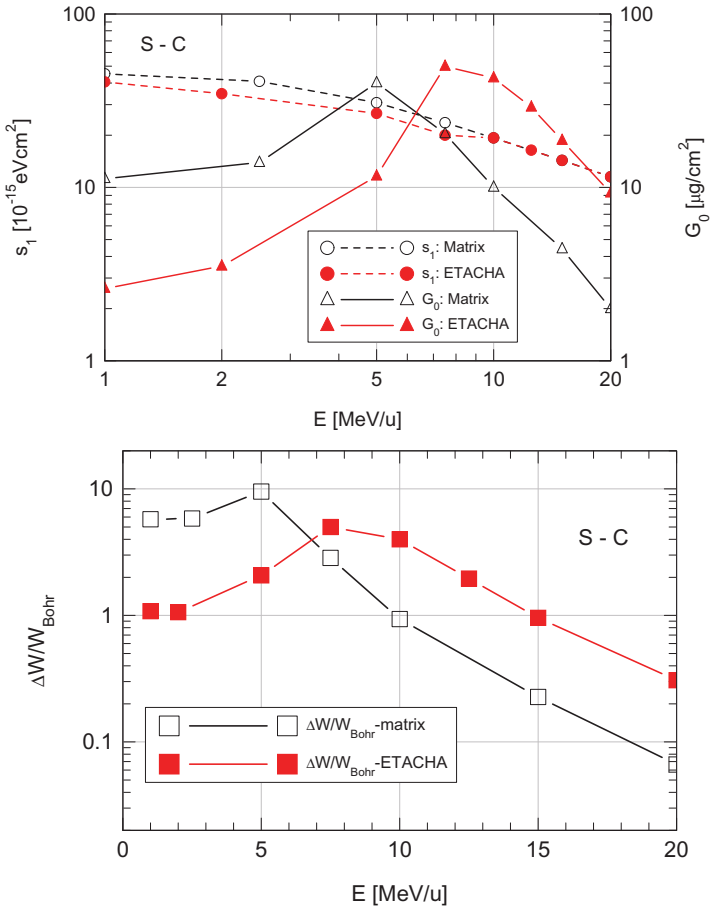

Fig. 5.15 Charge-exchange straggling in equilibrium of sulphur ions in carbon. Top: The functions $G_0 = \sum_J F_J(q_J - q)Q_J$ and $s_1 = (dS/dq_J)_{q_J=q}$ entering (3.155). Bottom: Two estimates of charge-exchange straggling ΔW_{chex}, based on two sets of charge fractions. From Sigmund et al. (2011). Energy loss in charge-changing events neglected

$$\frac{\mathrm{d}\Omega^2}{\mathrm{d}x} = -\frac{Z_1^2 e^2}{\pi v^2}\mathrm{Im}\int_0^\infty \frac{\mathrm{d}k}{k}\int_0^{kv}\mathrm{d}\omega\, 2\hbar\omega^2\left(\frac{1}{\varepsilon(k,\omega)} - 1\right) \tag{5.51}$$

in a medium characterized by a dielectric function $\varepsilon(k, \omega)$.

This expression has been evaluated by Bonderup and Hvelplund (1971), who reported results for four electron densities in Fig. 8.7, Vol. 1.

5.6.2 Local-Density Approximation

Bonderup and Hvelplund (1971) applied the local-density approximation of Lindhard and Scharff (1953) to evaluate the straggling parameter of an atom by setting

$$\frac{\Omega^2}{\Omega^2_{\text{Bohr}}} = \frac{\int 4\pi r^2 \mathrm{d}r\, \rho(r) \Omega^2\left(\rho(r), v\right)}{Z_2 \Omega^{2\prime}_{\text{Bohr}}}, \tag{5.52}$$

where $\rho(r)$ is the electron density of a target atom normalized to Z_2, and $\Omega^{2\prime}_{\text{Bohr}}$ is the asymptotic value of $\Omega^2\left(\rho(r), v\right)$ at high speed v.

While a formal justification of the local-density approximation in the theory of energy loss is not known to the author, one might argue that this approximation could be more well-founded in straggling on physical grounds, since straggling hinges on large energy transfers, i.e., close collisions.

Bonderup and Hvelplund (1971) evaluated (5.52) for protons and alpha particles and Lenz-Jensen electron densities for $\rho_{\text{atom}}(r)$ over a wide velocity range. The function $\Omega^2\left(\rho_{\text{atom}}(r), v\right)$ was divided into two branches governed by a high- and a low-speed expression, dependent on the ratio $v_F(r)/v$.

Chu (1976) evaluated the same scheme but replaced Lenz-Jensen electron distributions by Hartree-Fock densities according to Herman and Skillman (1963). Results are shown in Fig. 5.16. While there is good qualitative agreement between Hartree-Fock and Thomas-Fermi results, the former show an oscillatory behaviour similar to what is found for the stopping cross section, cf. Figs. 7.3 and 7.4, Vol. 1. Both densities lead to increasing deviations from Bohr straggling as Z_2 increases. This confirms that the critical beam speed at which straggling reaches Bohr straggling increases with increasing atomic number of the target.

5.6.3 Empirical Extension to Heavier Ions

Yang et al. (1991) extended the above scheme to heavier ions by the following steps:

- Calculated results of Chu (1976) were parameterized in terms of a 4-parameter fit.
- The projectile atomic number Z_1 was replaced by an effective charge $q_1 = \gamma Z_1$, where γ is the effective-charge ratio characterizing the stopping cross section.
- A resonance term depending on another four parameters was added to account for correlation effects. These parameters were determined by comparison to empirical data for straggling of light ions. Different parameter families were adopted for solids and gases.
- Finally, one more resonance term depending on another four parameters was added to account for charge-exchange straggling. These parameters were determined by comparison to available experimental straggling data for heavy ions.

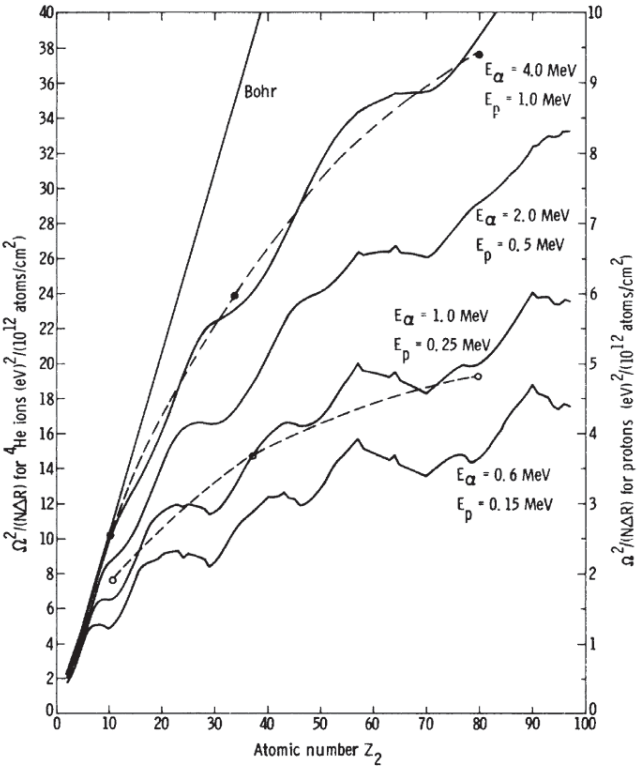

Fig. 5.16 Atomic straggling parameter versus atomic number Z_2 of the target for protons (scale on the right) and ^{4}He (scale on the left), calculated by local-density approximation. Solid lines: Hartree-Fock density. Dashed curves and points: Thomas-Fermi density. Straight line: Bohr straggling. From Chu (1976)

Different parameter families were adopted for atomic gases, molecular gases and solids.

Clearly, with such a large number of free parameters the experimental straggling data available at the time ought to be characterized with a reasonable accuracy. This is indeed seen to be the case for aluminium (lower graph). An interesting feature is seen in the upper graph, where curves for heavy ions such as gold and iodine seem to rise far above the Bohr value, even though supporting experimental data are not available.

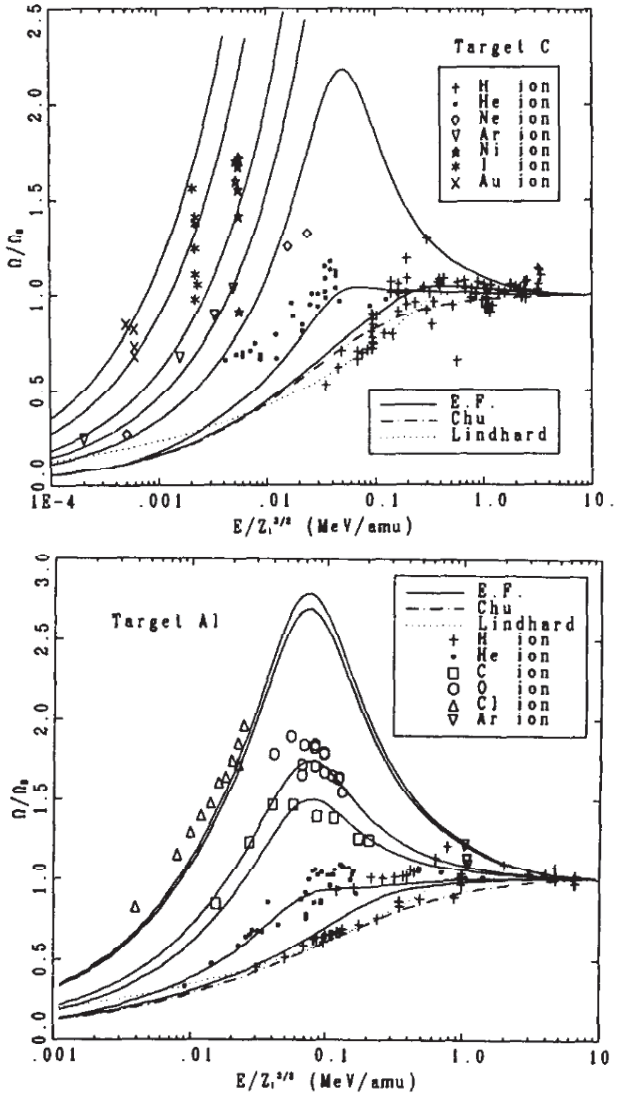

Fig. 5.17 $\Omega/\Omega_{\text{Bohr}}$ versus $E/Z_1^{3/2}$ for carbon (top) and aluminium target (bottom). Lines from the multi-parameter fit of Yang et al. (1991). From Yang et al. (1991)

5.7 Data

Experimental data for straggling of heavy ions have been compiled and condensed into an empirical interpolation formula by Yang et al. (1991). An example is shown in Fig. 5.17. You will find more recent data for solid targets in the literature, but I

hesitate to present specific references, because the analysis of many published data is affected by insufficient information about nonuniform foil thickness.

Increasing energy loss with increasing atomic number of the ion implies decreasing penetration depth and, hence decreasing film thickness for reliable measurements of mean energy loss and straggling. While the influence on the mean energy loss is limited, as long as the mean thickness of the foil is known with sufficient accuracy, the influence on straggling is potentially serious. In the worst scenario, where the target has a narrow hole over the entire thickness, some of the penetrating particles have zero energy loss. Surface roughness is frequently estimated from atomic-force micrographs of the target surface: Such an analysis does not necessarily discover a hole.

Sun et al. (2007) performed measurements at rather low beam energies, up to 0.25 MeV/u, on thin SiN films with high uniformity. Figure 5.18 shows measured maximum values of $\Omega^2/\Omega^2_{\rm Bohr} \lesssim 0.8$ in the energy range covered. On the other hand, scaling with the Bohr parameter $\xi = mv^3/Z_1e^2\omega$ is surprisingly well fulfilled, considering that several target-electron shells are involved. The agreement with the formula of Yang et al. (1991) is seen to be rather poor in the low-energy range, while the experimental data do not cover the energy range where that formula suggests a rapid increase in case of the heavier ions.

Vockenhuber et al. (2013) reported measurements with krypton ions up to 10 MeV in gas targets. Figure 5.19, showing data for Kr-He, indicates values of $W/W_{\rm Bohr} \lesssim 100$, up to a factor of ~ 2 above the formula of Yang et al. (1991). Comparison with PASS indicates that neither linear straggling nor bunching could explain such an effect. Charge-exchange straggling delivers the right order of magnitude, but uncertainties in the numerical evaluation are still too great to allow a quantitative comparison.

Straggling experiments in gases with low-energy ions will be discussed in Chap. 8.

5.8 Discussion and Outlook

This chapter focused on energy-loss straggling of medium to high energy ions. While theoretical formalism and computational tools are reasonably well developed, only few explicit quantitative predictions are available, and generally-valid scaling relations are essentially absent. This is not surprising, considering that theoretical understanding of the mean energy loss has emerged only since the beginning of the present millennium.

Uncorrelated (linear) straggling, treated in Sect. 5.3, is fairly well understood: Theoretical schemes aiming at stopping cross sections can be applied to evaluate straggling parameters. By and large, the influence of projectile screening, Barkas-Andersen and shell corrections is less pronounced than in case of the stopping cross section.

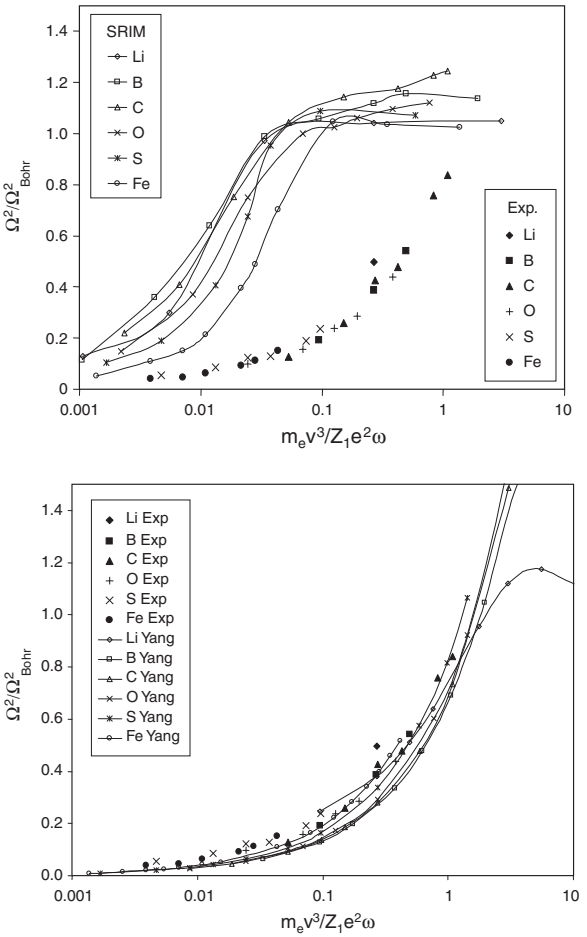

Fig. 5.18 Energy-loss straggling of several ions in the keV/u energy range in SiN films of high thickness uniformity. Measurements by Sun et al. (2007). Top: Scale as in Fig. 5.2. Also included are data extracted from the SRIM code. Bottom: Compared with interpolation formula of Yang et al. (1991). From Sun et al. (2007)

Bunching and packing corrections, on the other hand, appear significant, especially around the stopping maximum. Simple expressions for the packing correction in molecules and solids have been around for several decades (Sigmund, 1976, 1978), although there is still lacking experimental evidence whether this correction is negative for a solid, unlike the well documented case of an equivalent molecular gas, where this correction is positive.

First estimates of a bunching correction were performed on the basis of an electron-gas model (Besenbacher et al., 1980), and an early estimate employing impact-parameter-dependent energy loss was presented for protons (Grande and

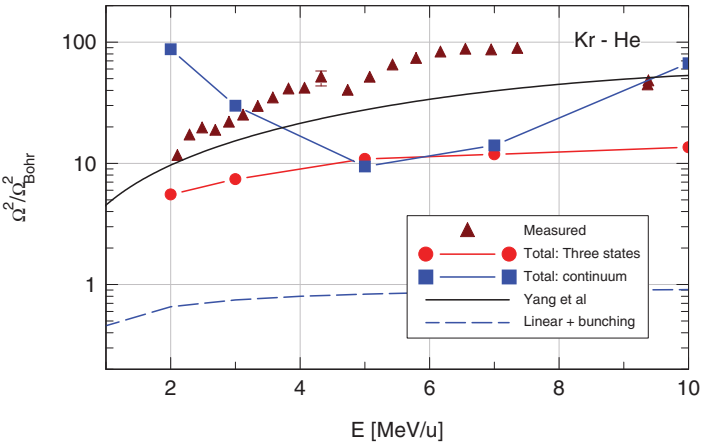

Fig. 5.19 Straggling of Kr ions in He gas. Measurements compared to calculations by PASS and to interpolation formula by Yang et al. (1991). From Vockenhuber et al. (2013)

Schiwietz, 1991). A more systematic study on the basis of the PASS code for heavy-ion stopping has now revealed some qualitative trends (Sigmund and Schinner, 2010).

Most pronounced is a peak near the stopping maximum, going roughly as the square of the stopping cross section, the magnitude of which increases with increasing Z_2—because of an increasing density of target electrons—and increasing Z_1 via the dependence on S^2. For solids, the bunching correction is counteracted by the packing correction, and examples shown in Sect. 5.4 indicate that the sum may be either positive or negative, dependent on the ion-target combination.

Unambiguous evidence for the significance of charge-exchange straggling may be found in the measurements of Ogawa et al., an example of which is shown in Fig. 5.1. These unique measurements refer to fairly light ions, high beam energy and thin foils. More frequent is the situation where the inherent structure of the spectrum cannot be resolved and where, instead, a gaussian-like spectrum is produced by charge exchange.

Charge-exchange straggling is predicted to go as $\propto (\mathrm{d}S/\mathrm{d}q)^2$ in charge equilibrium. This function goes through a maximum, but the position of that maximum differs from the maximum of S^2. In the example shown in Fig. 5.15, the maximum of charge-exchange straggling lies at a significantly higher energy than the maximum of bunching.

According to theoretical results summarized here as well as to numerous experimental findings, straggling may, dependent on ion-target combination and beam energy, be an order-of-magnitude higher than predicted by Bohr. It is a major challenge to experimentally distinguish between high values of straggling and experimental artifacts.

Problems

5.1. 1. An accelerator delivers singly-charged ions with $Z_1 = 1$ to 18 and $E = 10$ MeV. Assume Bohr straggling and find the maximum target thickness satisfying (5.4).
2. Make the same evaluation for stripped ions.

5.2. Carry out a calculation similar to (4.67)–(4.71) for the straggling parameter

$$W = \left\langle \int \mathrm{d}^2\boldsymbol{p}\, T^2(p) \right\rangle_{\boldsymbol{v}_e} \tag{5.53}$$

and check the result against (8.47), Vol. 1.

5.3. Justify the approximative expression (5.36) on the basis of (5.33). You may use a feasible model for the function $\overline{T_{\mu\nu}(\boldsymbol{p})}$ such as (8.98), Vol. 1. Further help may be found from Sigmund and Schinner (2010).

5.4. Treat the system depicted in Fig. 5.1 by the two-state approximation. Try to locate approximately the channel number corresponding to zero energy loss. Assume the energy loss to be $\propto q^2$ and extract a value of the electron-loss cross section assuming the capture cross section to be negligible.

5.5. For a qualitative explanation of trends emerging from Fig. 5.14 consider a two-state system with $q_1 = Z_1 = 83$ and $q_2 = Z_1 - 1 = 82$. Moreover, consider $F_1 \gg F_2$ and ignore energy loss to electron capture and loss. Assume $S(q_1) \simeq (q_1/Z_1)^2 S_{\mathrm{proton}}$ for simplicity and demonstrate, using nonrelativistic Bethe theory, that

$$\frac{(\Delta\Omega^2)_{\mathrm{chex}}}{\Omega^2_{\mathrm{Bohr}}} \simeq 8\frac{F_1 F_2}{\sigma}\frac{S_{\mathrm{proton}}}{mv^2\sigma_{12}}\,. \tag{5.54}$$

Convince yourself that this yields a steep increase with decreasing speed v. How do you explain the increase with decreasing Z_2?

References

Besenbacher F., Andersen H.H., Hvelplund P. and Knudsen H. (1981): Straggling in energy loss of swift hydrogen and helium ions in gases. Mat Fys Medd Dan Vid Selsk **40 no. 9**, 1–42

Besenbacher F., Andersen J.U. and Bonderup E. (1980): Straggling in energy loss of energetic hydrogen and helium ions. Nucl Instrum Methods **168**, 1–15

Bohr N. (1915): On the decrease of velocity of swiftly moving electrified particles in passing through matter. Philos Mag **30**, 581–612

Bohr N. (1948): The penetration of atomic particles through matter. Mat Fys Medd Dan Vid Selsk **18 no. 8**, 1–144

Bonderup E. and Hvelplund P. (1971): Stopping power and energy straggling for swift protons. Phys Rev A **4**, 562–589

Chu W.K. (1976): Calculation of energy straggling for protons and helium ions. Phys Rev A **13**, 2057–2060

Cuevas J., Garcia-Munos M., Torres P. and Allison S.K. (1964): Partial atomic and ionic stopping powers of gaseous hydrogen for helium and hydrogen beams. Phys Rev **135**, A335–345

Fano U. (1963): Penetration of protons, alpha particles, and mesons. Ann Rev Nucl Sci **13**, 1–66

Glazov L. and Sigmund P. (1997): Energy-loss spectra of charged particles in the presence of charge exchange. Nucl Instrum Methods B **125**, 110–115

Glazov L. and Sigmund P. (2000): Energy-loss spectra of charged particles in the presence of charge exchange: addendum on ^{6}Li spectra. Nucl Instrum Methods B **170**, 39–44

Grande P.L. and Schiwietz G. (1991): Impact-parameter dependence of electronic energy loss and straggling of incident bare ions on H and He atoms by using the coupled-channel method. Phys Rev A **44**, 2984–2992

Grande P.L. and Schiwietz G. (2009): Convolution approximation for the energy loss, ionization probability and straggling of fast ions. Nucl Instrum Methods B **267**, 859–865

Herman F. and Skillman S. (1963): *Atomic structure calculations*. Prentice Hall, New Jersey

ICRU (2005): *Stopping of ions heavier than helium*, vol. 73 of *ICRU Report*. Oxford University Press, Oxford

Lindhard J. and Scharff M. (1953): Energy loss in matter by fast particles of low charge. Mat Fys Medd Dan Vid Selsk **27 no. 15**, 1–31

Lindhard J. and Sørensen A.H. (1996): On the relativistic theory of stopping of heavy ions. Phys Rev A **53**, 2443–2456

Malherbe J.B. and Alberts H.W. (1982): Energy-loss straggling in C and Ge of p, D and alpha particles in the energy region 0.2 to 2.4 MeV. Nucl Instrum Methods **192**, 559–563

Ogawa H., Katayama I., Sugai I., Haruyama Y., Saito M., Yoshida K. and Tosaki M. (1996): Energy loss of high velocity $^{6}Li^{2+}$ ions in carbon foils in charge state non-equilibrium region. Nucl Instrum Methods B **115**, 66–69

Osmani O. and Sigmund P. (2011): Charge-state evolution of swift heavy-ion beams explored by matrix method. Nucl Instrum Methods B **269**, 813–816

Rozet J.P., Stephan C. and Vernhet D. (1996): ETACHA: a program for calculating charge states at GANIL energies. Nucl Instrum Methods B **107**, 67–70

Sørensen A.H. (2002): Stopping of relativistic hydrogen- and heliumlike heavy ions. Nucl Instrum Methods B **195**, 106–117

Sigmund P. (1976): Energy loss of charged particles to molecular gas targets. Phys Rev A **14**, 996–1005

Sigmund P. (1978): Statistics of particle penetration. Mat Fys Medd Dan Vid Selsk **40 no. 5**, 1–36

Sigmund P. (1992): Statistical theory of charged-particle stopping and straggling in the presence of charge exchange. Nucl Instrum Methods B **69**, 113–122

Sigmund P. (2006): *Particle penetration and radiation effects*, vol. 151 of *Springer Series in Solid-State Sciences*. Springer, Berlin

Sigmund P., Osmani O. and Schinner A. (2011): Charge-exchange straggling in equilibrium. Nucl Instrum Methods B **269**, 804–809

Sigmund P. and Schinner A. (2003): Barkas effect, shell correction, screening and correlation in collisional energy-loss straggling of an ion beam. Europ Phys J D **23**, 201–209

Sigmund P. and Schinner A. (2010): Impact-parameter-dependent stopping of swift ions. 3. Bunching and packing in energy-loss straggling. Europ Phys J D **58**, 105–116

Sørensen A.H. (2010): Private communication. Unpublished

Sun G., Döbeli M., Müller A.M., Stocker M., Suter M. and Wacker L. (2007): Energy loss and straggling of heavy ions in silicon nitride in the low MeV energy range. Nucl Instrum Methods B **256**, 586–590

Vockenhuber C., Jensen J., Julin J., Kettunen H., Laitinen M., Rossi M., Sajavaara T., Osmani O., Schinner A., Sigmund P. et al. (2013): Energy-loss straggling of 2-10 MeV/u Kr ions in gases. Europ Phys J D **67**, 145

Weick H., Geissel H., Scheidenberger C., Attallah F., Baumann T., Cortina D., Hausmann M., Lommel B., Münzenberg G., Nankov N. et al. (2000): Slowing down of relativistic few-electron heavy ions. Nucl Instrum Methods B **164-165**, 168–179

Yang Q., O'Connor D.J. and Wang Z. (1991): Empirical formulae for energy loss straggling of ions in matter. Nucl Instrum Methods B **61**, 149

Part III
Scattering

Chapter 6
Interatomic Potentials, Scattering and Nuclear Stopping

Abstract This chapter focuses on interatomic potentials of interest in single and multiple scattering of heavy charged particles and the associated energy loss. In the keV energy range and above it is commonly assumed that binary elastic scattering on central potentials makes up an adequate description. Limitations of this description are mentioned. Classical scattering for screened-Coulomb interaction is outlined, and special attention is given to scaling properties, in particular for Thomas-Fermi-type interaction. Power-law scattering is mentioned as a convenient tool for rough estimates. Comparisons between different theoretical estimates as well as between measured and calculated cross sections are presented, and attempts to directly invert a measured cross section into the underlying potential are reported. The chapter concludes with explicit results for nuclear stopping and straggling including pertinent experiments.

6.1 Introductory Comments

Elements of classical and quantal scattering theory for central-force potentials have been presented in Chap. 3, Vol. 1, with applications mainly to Coulomb interaction between point charges. The present chapter addresses interactions between screened ions and atoms as well as between neutral atoms. In the field of radiation physics such screened-Coulomb forces are most often expressed in terms of central pairwise potentials, but more sophisticated descriptions may be appropriate, in particular for collisions at energies in the eV and lower-keV range.

A simple estimate presented in Sect. 2.3, Vol. 1 suggests the stopping cross section for electronic collisions to exceed that for elastic nuclear collisions by 3–4 orders of magnitude. This result holds for interactions between practically free point charges within an energy regime where stopping cross sections decrease monotonically with increasing energy. You have seen in Chap. 4 that the electronic stopping cross section actually experiences a maximum and, from there, decreases monotonically toward zero with decreasing energy. We shall see that the nuclear stopping

P. Sigmund, *Particle Penetration and Radiation Effects Volume 2*,
Springer Series in Solid-State Sciences 179, DOI: 10.1007/978-3-319-05564-0_6,

cross section exhibits a similar behaviour, but at a lower energy and with a different height. In general there exists a cross-over point between electronic and nuclear stopping at some energy which, for not too light ions, lies in the keV or lower-MeV range. For collision cascades governing radiation effects such as defect formation and sputtering, discussed briefly in Chap. 1, Vol. 1, nuclear stopping is most often the dominating process.

At higher beam energies, where electronic stopping dominates energy loss, angular deflections are governed by the interaction with the nuclei, as you have seen in Chap. 2, Vol. 1. For small-angle deflections—which determine multiple scattering—it is essential that screening of the interaction be taken properly into account.

6.2 Potentials

Calculating the interaction force between two (neutral or charged) atoms is in principle a problem of quantum chemistry, but the type of questions asked in radiation physics is different from standard problems treated in quantum chemistry. Most of all, the range of internuclear distances of interest in scattering problems differs from that in molecular physics: Atoms moving with kinetic energies in the keV regime or above may approach each other to internuclear distances much smaller than those of atoms bound in a molecule. From this follows that interaction forces of interest are predominantly repulsive, while in traditional quantum chemistry it is more the equilibrium range that is of interest.

Moreover, the range of relative velocities of interacting atoms may lie several orders of magnitude above what is of interest in molecular spectroscopy and chemical reaction kinetics. In quantum chemistry and molecular-beam physics, adiabatic potentials, based on the ground-state configuration of the combined electron cloud of two collision partners, are typically a good first estimate. Conversely, once the relative speed between the colliding nuclei exceeds characteristic orbital velocities of the target and projectile electrons, it may be more appropriate to consider the opposite extreme, ignore any deformation of the electron clouds during collision and, instead, determine the interaction between undisturbed atomic-electron configurations.

Within the scope of this book, more emphasis will be laid on general behaviour than on element-specific details. Therefore, scaling laws valid for a wide range of elements and their experimental verification will receive attention. This, in fact, is dictated by necessity: There are about 10^4 ion-target systems if only atomic beams and elemental targets are taken into consideration. If molecular and cluster beams are allowed for as well as alloyed and compound targets, the variety of systems to be treated *ab initio* becomes rapidly prohibitive from the point of view of computational capacity and manpower.

The main justification of various adopted screening functions and screening radii is their ability to accurately describe pertinent experimental results. Those include measurements of elastic ion-atom scattering distributions under single- and/or

multiple-collision conditions as well as range distributions of ions in solids. Experiments in the former category will be mentioned later in this chapter, whereas the physics of ion ranges will be the subject of Chap. 9.

6.2.1 Bohr's Estimate

Bohr (1948) presented a first estimate of the interaction potential between two atoms on the basis of the electrostatic interaction energy of two stiff charge distributions,

$$\mathcal{V}(R) = -e \int \mathrm{d}^3\boldsymbol{r}\, \rho_1(\boldsymbol{r})\Phi_2(\boldsymbol{r})\,, \tag{6.1}$$

where $\rho_1(\boldsymbol{r}) = \rho_1(r_1)$ and $\phi_2(\boldsymbol{r}) = \phi_2(r_2)$ denote the charge density and electrostatic potential of the respective collision partners,

$$r_1 = |\boldsymbol{r} - \boldsymbol{R}_1| \quad r_2 = |\boldsymbol{r} - \boldsymbol{R}_2| \tag{6.2}$$

and $R = |\boldsymbol{R}_1 - \boldsymbol{R}_2|$ their internuclear distance. Yukawa-type charge distributions were assumed with Thomas-Fermi-type screening radii

$$a_1 = \frac{a_0}{Z_1^{1/3}}; \quad a_2 = \frac{a_0}{Z_2^{1/3}}\,. \tag{6.3}$$

You are encouraged to determine $\mathcal{V}(R)$ by solving Problem 6.1. If both collision partners are neutral atoms, the result is

$$\mathcal{V}(R) = \frac{Z_1 Z_2 e^2}{R}\, g(R) \tag{6.4}$$

$$g(R) = \frac{a_2^2 \mathrm{e}^{-R/a_1} - a_1^2 \mathrm{e}^{-R/a_2}}{a_2^2 - a_1^2}. \tag{6.5}$$

Equation (6.5) has been plotted in Fig. 6.1 for a series of values of the ratio a_1/a_2. The distance R is taken relative to the Bohr screening radius defined by

$$\frac{1}{a^2} = \frac{1}{a_1^2} + \frac{1}{a_2^2}\,. \tag{6.6}$$

As you could expect, for large values of a_1/a_2, atom 1 acts similar to a point charge, so that curves approach Bohr's expression

$$g(R) = \mathrm{e}^{-R/a}\,. \tag{6.7}$$

Scaling with a according to (6.6) is obeyed approximately for $R/a \lesssim 1$, but increasing differences are seen in the tails.

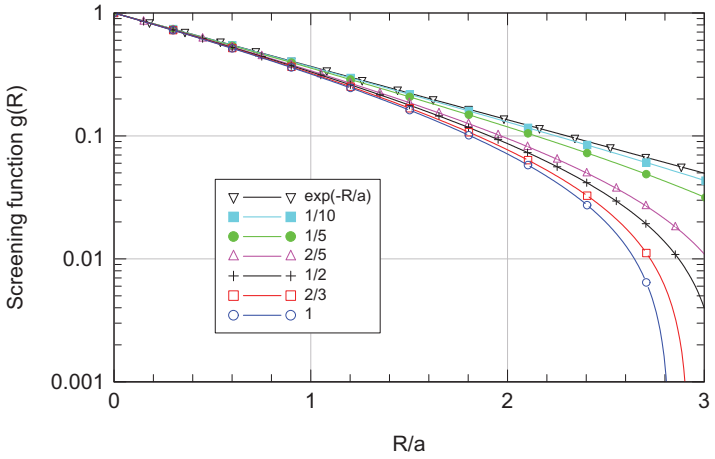

Fig. 6.1 Screening function $g(R)$ of the interaction potential between two neutral atoms according to (6.5). Numbers in the legend refer to different values of a_1/a_2. The solid curve refers to Bohr's estimate, (6.7)

The potential used in a series of papers by Lindhard and coworkers, especially Lindhard et al. (1968), differs from Bohr's estimate in two respects,

- The exponential screening function was replaced by the neutral-atom screening function either for the Thomas-Fermi or the Lenz-Jensen atom discussed in Sect. 1.4.4, and
- The screening radius was replaced by the $a_j = 0.8853a_0/Z_j^{1/3}$.

Figure 6.1 refers to the interaction between two neutral atoms. In the literature you will see potentials of this type also applied to interactions between positively and even negatively charged ions and atoms. This is plausible for not too highly-charged ions, since substantial deflection and/or energy transfer in elastic collisions implies impact parameters smaller than outer-shell radii.

To study this point further, you may use the result of Problem 6.1 which, for a nonvanishing ion charge $q_1 e$, yields a screening function

$$g(R) = \frac{1}{1 - a_1^2/a_2^2}\left[\left(1 - \frac{q_1}{Z_1}\right)\mathrm{e}^{-R/a_1} + \left(\frac{q_1}{Z_1} - \frac{a_1^2}{a_2^2}\right)\mathrm{e}^{-R/a_2}\right]. \qquad (6.8)$$

For a meaningful plot you need to make some assumptions on the dependence of the screening radius a_1 on the ion charge. This can be done by matching the screening functions shown in Fig. 1.8 by an exponential

$$g(r/a) \simeq (1 - q/Z)\mathrm{e}^{-r/a}\,. \qquad (6.9)$$

Within the accuracy of an exponential fit to the potential we may write (Sigmund, 1997)

$$a \simeq a_{\mathrm{TF}}(1 - q/Z)^{\alpha}\,. \qquad \alpha \simeq 1 \qquad (6.10)$$

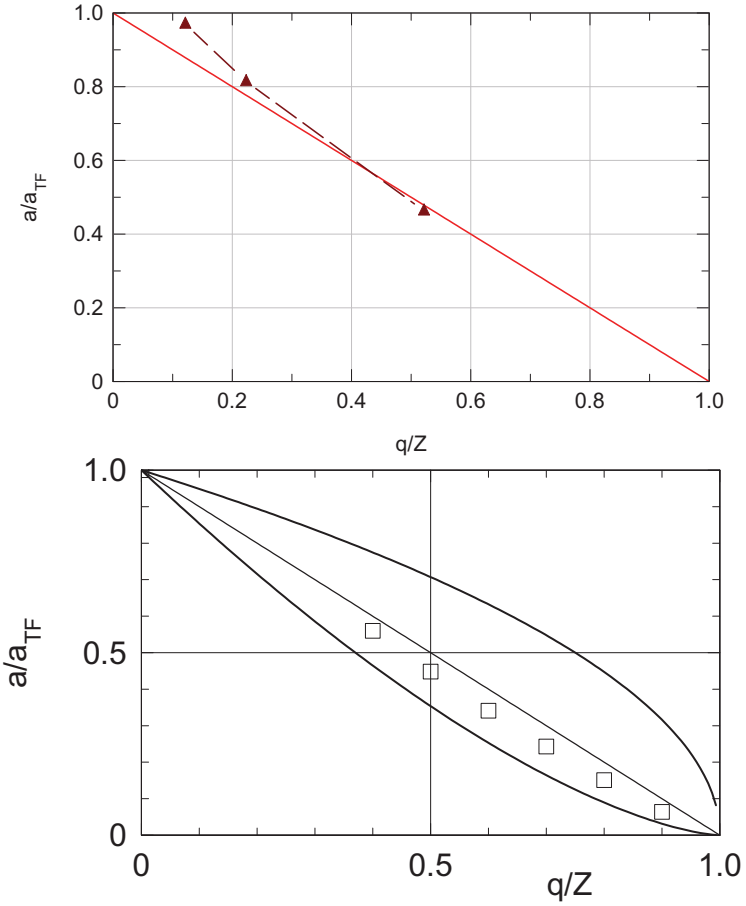

Fig. 6.2 Dependence of the Thomas-Fermi screening radius on the charge state of a positive ion. Upper graph: Comparison between (6.8) (triangles) and (6.9) (line). Lower graph: Points from Fermi and Amaldi (1934). Lines: $(1-q/Z)^{\alpha}$ with $\alpha = 0.5, 1$ and 1.5, cf. (6.10). From Sigmund (1997)

A more rigorous argument in support of (6.10), which does not make use of an exponential approximation, goes back to Fermi and Amaldi (1934). Their result is likewise shown in Fig. 6.2.

With this, Fig. 6.3 has been based on the relation

$$\frac{a_1}{a_2} = 1 - \frac{q_1}{Z_1}\,, \tag{6.11}$$

The dependence on Z_1 and Z_2 indicated in (6.3) is rather weak and has been ignored here. You may note that for a nearly-stripped ion the interaction potential depends

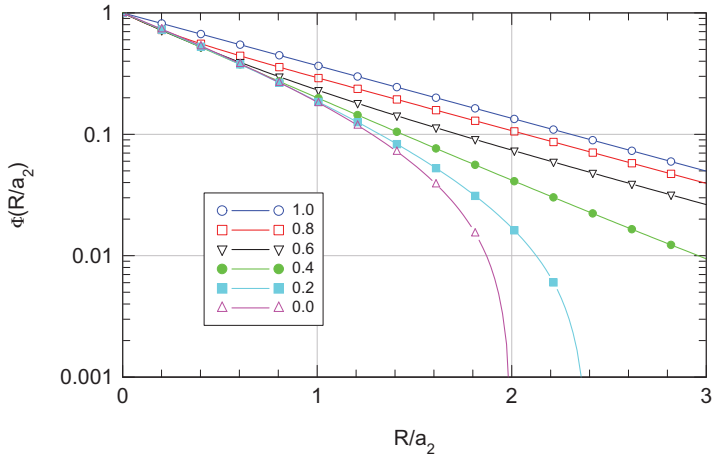

Fig. 6.3 Screening function for the interaction between a neutral atom and an ion with charge $q_1 e$ for $Z_1 = Z_2$ and $q_2 = 0$ according to (6.8)

sensitively on the charge, while such a dependence is barely visible for $R/a_2 \lesssim 0.5$ and quite small further up to $R/a_2 \sim 1.5$.

6.2.2 Thomas-Fermi Theory

Although a derivation of the interatomic potential proposed by Lindhard and Scharff was never published, an unpublished draft existed which, as far as the theoretical basis is concerned, was very similar to that underlying the theory of Firsov (1957b,a). Actually, both theories rely heavily on the work of Lenz (1932) and Jensen (1932) on the interaction between Thomas-Fermi atoms and ions as summarized by Gombas (1949).

You may recall from the discussion in Sect. 1.4 that the energy of a Thomas-Fermi atom contains a kinetic contribution, (1.15), in addition to potential (electrostatic) energy. This contribution also affects the interaction between two atoms but has been neglected in Bohr's estimate. It represents a quantum effect and takes into account that a straight overlap between stiff charge distributions may not be allowed by the Pauli principle, so that some electrons have to move up to higher (unoccupied) states.

Let us consider the energy of a diatomic molecule in the Thomas-Fermi model. An appropriate starting point is (1.18) which we may rewrite in a generalized form,

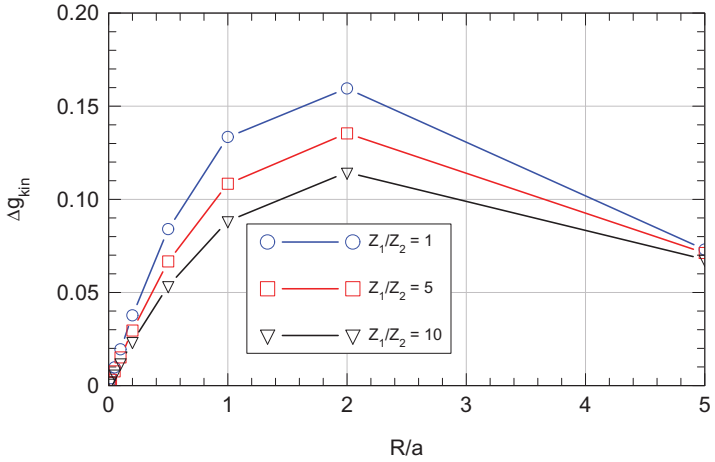

Fig. 6.4 The contribution of the kinetic-energy correction to the screening function for exponential atomic charge distributions

$$\mathcal{E} = \kappa_k \int \mathrm{d}^3\boldsymbol{r}\, \rho(\boldsymbol{r})^{5/3} - e \int \mathrm{d}^3\boldsymbol{r}\, \rho(\boldsymbol{r})\Phi_n(\boldsymbol{r}) + \frac{e^2}{2} \int \mathrm{d}^3\boldsymbol{r} \int \mathrm{d}^3\boldsymbol{r}'\, \frac{\rho(\boldsymbol{r})\rho(\boldsymbol{r}')}{|\boldsymbol{r}-\boldsymbol{r}'|} \tag{6.12}$$

for $v = 0$, where the potential $Z_1 e/r$ of the nucleus has been denoted by $\Phi_n(r)$. In this form (6.12) may also describe the electron energy of a molecule, with the replacement

$$\Phi_n(\boldsymbol{r}) = \frac{Z_1 e}{r_1} + \frac{Z_2 e}{r_2}\,. \tag{6.13}$$

You could try to determine an equilibrium configuration of the electrons in a molecule by applying the variational principle, just as has been done in case of an atom. The interaction energy between the two atoms/ions could then be found by adding the Coulomb interaction between the nuclei and subtracting the energies of the two isolated atoms. The resulting expression would represent an *adiabatic potential* in the Thomas-Fermi approximation.

Lenz (1932) and Jensen (1932) as well as Gombas (1949), aiming at this adiabatic potential, argued that a first approximation for this quantity could be found by superposition of undisturbed atomic charge distributions,

$$\rho(\boldsymbol{r}) \simeq \rho_0(\boldsymbol{r}) = \rho_1(r_1) + \rho_2(r_2)\,, \tag{6.14}$$

since the difference $\delta\rho = \rho - \rho_0$ will enter in the second order into the error in the energy.

As indicated above, with increasing relative velocity of two collision partners, straight superposition may become a more appropriate representation of the poten-

tial than adiabatic interaction. Therefore, the error made by adopting (6.14) will be even smaller in the present context.

Within this picture we may subtract the energies of the constituent atoms from (6.12) and obtain

$$\mathcal{V}(R) = \frac{Z_1 Z_2 e^2}{R} + \kappa_k \int \mathrm{d}^3\boldsymbol{r} \left[(\rho_1(r_1) + \rho_2(r_2))^{5/3} - \rho_1(r_1)^{5/3} - \rho_2(r_2)^{5/3}\right] - \int \mathrm{d}^3\boldsymbol{r} \left[\frac{Z_1 e^2}{r_1}\rho_2(r_2) + \frac{Z_2 e^2}{r_2}\rho_1(r_1)\right] + \int \mathrm{d}^3\boldsymbol{r} \int \mathrm{d}^3\boldsymbol{r}' \, \frac{e^2}{|\boldsymbol{r} - \boldsymbol{r}'|}\, \rho_1(r_1)\rho_2(r_2'). \quad (6.15)$$

for the interaction energy of two atoms. Figure 6.4 shows the contribution

$$\Delta g_{\mathrm{kin}} = \frac{R}{Z_1 Z_2 e^2} \times \kappa_k \int \mathrm{d}^3\boldsymbol{r} \left[(\rho_1(r_1) + \rho_2(r_2))^{5/3} - \rho_1(r_1)^{5/3} - \rho_2(r_2)^{5/3}\right] \quad (6.16)$$

to the screening function for a Yukawa-type charge density with Bohr's screening radius. With this choice, the result depends only on R/a and Z_1/Z_2, and the dependence on Z_1/Z_2 is not very pronounced.

Comparison of Fig. 6.4 to Fig. 5.17 indicates that the contribution of Δg_{kin} to the screened potential increases with increasing distance and eventually dominates. If you have difficulties in appreciating this, you are encouraged to look into Problem 6.3.

Equation (6.15) has served as the theoretical basis for numerous computations of interatomic potentials. Apart from computational details, theoretical schemes differ in the input, especially

- atomic charge distributions and
- possible inclusion of exchange and correlation terms.

This author is unaware of a fully analytical evaluation of the kinetic-energy contribution, (6.16). Although authors invested considerable effort in preparing the double integral for numerical evaluation, there is little reason to go into details, because straight numerical integration is no particular challenge on present-day computers.

6.2.2.1 Firsov's Estimate

The central study in the present context is the theory of Firsov (1957b,a). Note first that in quantum mechanics, an approximate solution of the Schrödinger equation leads to an overestimate of the energy of the considered system. This feature also prevails in Thomas-Fermi theory. A simple proof, following Firsov (1957b) has been

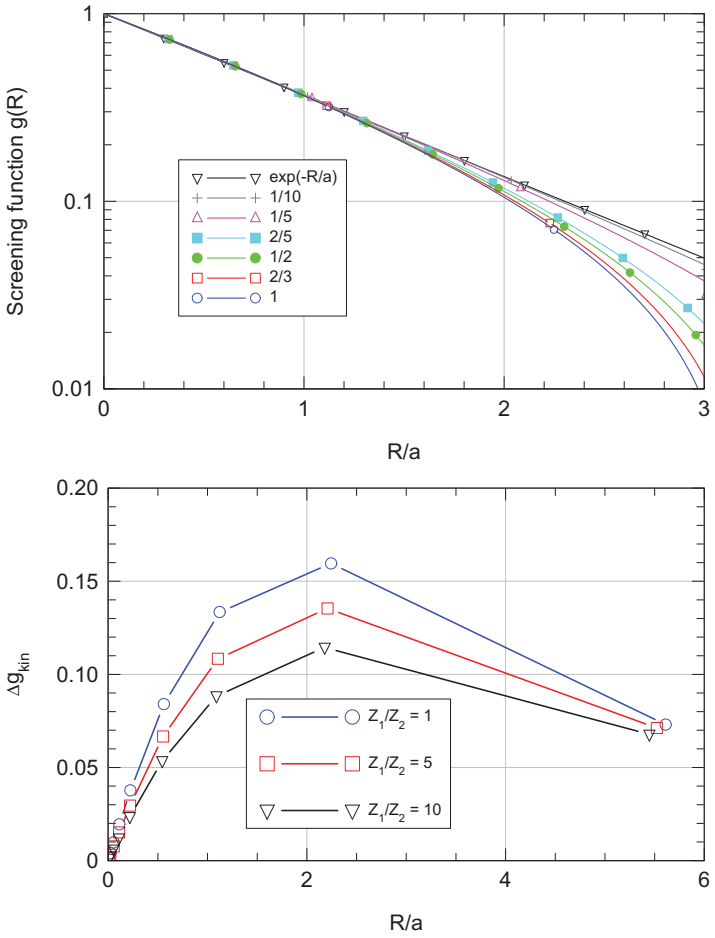

Fig. 6.5 Comparison between Bohr or Lindhard-Scharff and Firsov screening radii. Top: Figure 6.1 redrawn employing the Firsov screening radius as the abscissa variable. Bottom: Same as Fig. 6.4 for Firsov case

sketched in Problem 6.4. Superposition of atomic charge distributions is an approximation to the true charge density. Therefore, the resulting interaction potential must lead to an overestimate of the total electronic energy of the system of two atoms or ions. Firsov (1957b) also found an expression very similar to (6.15) which delivers an *upper bound* to the total energy. He also found that the difference between the two expressions, when evaluated with Thomas-Fermi input, does not exceed 5%. Note that this assumes the 'true' potential to be adiabatic.

Numerical evaluation of the two resulting potentials led Firsov (1957a) to propose

$$g(R) = g_0(R/a) \tag{6.17}$$

as an interpolation formula, where g_0 denotes the Thomas-Fermi screening function for a neutral atom and

$$a = \frac{0.8853 a_0}{\left(Z_1^{1/2} + Z_2^{1/2}\right)^{2/3}} . \tag{6.18}$$

Firsov's expression differs from Lindhard's choice only in the screening radius. You may easily convince yourself that the ratio $a_{\text{Lindhard}}/a_{\text{Firsov}}$ decreases from 1.12 to 1.04 for Z_1/Z_2 increasing from 1 to 100.

Figure 6.5 demonstrates the consequences on the scaling of the potential for Yukawa-type electron densities. The upper graph shows clearly improved scaling compared with Fig. 6.1, in particular for $R/a \lesssim 1$, where scaling is essentially perfect. On the other hand, no significant improvement of scaling is found in the kinetic contribution in comparison with Fig. 6.4.

6.2.2.2 Thomas-Fermi-Dirac Approach

Firsov's approach was extended by Abrahamson et al. (1961) to the Thomas-Fermi-Dirac scheme by including an exchange contribution in the Thomas-Fermi energy in accordance with Sect. 1.8.2. Again a maximization principle was employed in addition to the energy expression which provides a minimum. As a result of extensive numerical operations the authors suggested an interpolation formula,

$$\mathcal{V}(R) = \frac{Z_1 Z_2 e^2}{2R}\left[g_0\left(\frac{R}{a_1}\right) + g_0\left(\frac{R}{a_2}\right)\right] - \frac{\kappa_a^2}{120\kappa_k}(Z_1 + Z_2) + \bar{\Lambda}(R)\,, \tag{6.19}$$

where $a_j = 0.8853 a_0/Z_j^{1/3}$ are Thomas-Fermi radii and g_0 is the Thomas-Fermi function of a neutral atom. The last two terms in this expression, the first of which is independent of the internuclear distance R, represent the effect of the exchange term via the constant κ_a defined in (1.91).

Equation (6.19) has been applied to evaluate interaction potentials between rare-gas atoms by Abrahamson (1963b,a). The focus of those calculations was on internuclear distances far beyond the Thomas-Fermi screening radius, typically up to 6 Bohr radii, where potentials discussed here cannot be expected to provide a realistic estimate of the interaction.

Figure 6.6 shows an example for He-Ne. The potential is close to exponential for $R > a_0$, softer than Bohr's expression but harder than Thomas-Fermi screening.

As pointed out by Günther (1964), Firsov's variational principles lead to questionable results when applied to the Thomas-Fermi-Dirac model due to the finite dimensions of the atomic charge densities. Rather than abandoning the TFD model altogether, Nikulin (1971) proposed to keep the TFD functional and to insert Hartree-Fock atomic electron densities without the use of variational parameters.

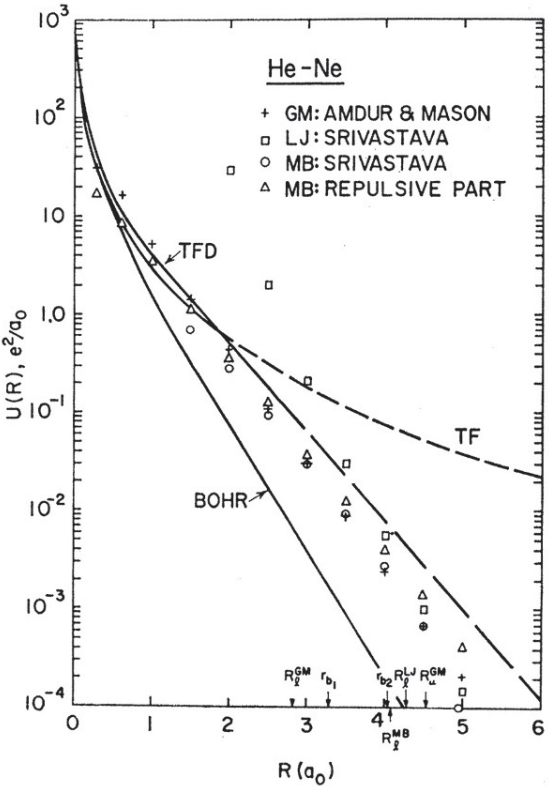

Fig. 6.6 Interaction potential between neutral He and Ne atoms according to the Thomas-Fermi-Dirac model. Also included potentials of Amdur and Mason (1956) and Srivastava (1958). From Abrahamson (1963a)

6.2.3 Other Binary Potentials

6.2.3.1 Hartree-Fock Estimates

If we accept the point of view of Firsov (1957b) that the electron density entering into the energy expression is a trial function, any physically acceptable expression for the electron density can be adopted, so that there is no reason to restrict to Thomas-Fermi-type input. Thus we can just as well apply accurate atomic electron distributions available from the literature. However, as long as interaction energies are determined by the Thomas-Fermi expression, with or without exchange-correlation, the error in such computations is substantial. In other words, subtleties in atomic wave functions will be immaterial.

The first attempt to improve the accuracy of the Thomas-Fermi model in this way were the calculations of molecular electron densities by Lenz (1932) and Jensen (1932), where a trial function, (1.59) was adopted which was not a solution of the Thomas-Fermi equation but a better approximation to reality. In the present context this idea was taken up by Wedepohl (1967) who applied electron densities calculated by Hartree and Hartree (1938) and empirical densities deduced from X-ray diffrac-

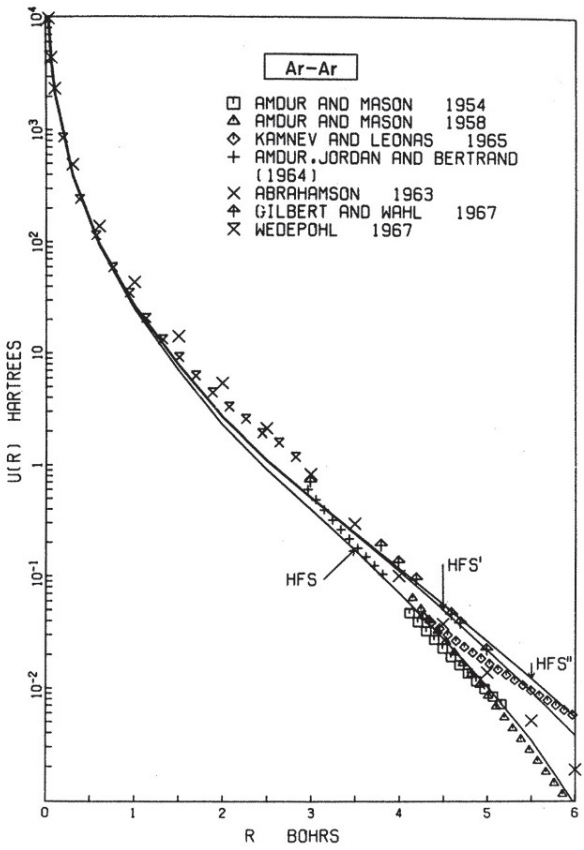

Fig. 6.7 Interaction potential between two argon atoms according to Wilson and Bisson (1971), compared with four potentials deduced from scattering measurements and three calculated potentials (Abrahamson, 1963b, Gilbert and Wahl, 1967, Wedepohl, 1967). From Wilson and Bisson (1971)

tion measurements (Witte and Wölfel, 1958). Interaction energies were calculated including the exchange term.

Wilson and Bisson (1971) applied the same scheme but used tabulations by Herman and Skillman (1963) for several homonuclear atom pairs. An example is shown in Fig. 6.7. This work was continued by Wilson et al. (1977), and results were parameterized in terms of a screening function

$$g(R) = \sum C_j \mathrm{e}^{-b_j R/a}\,, \tag{6.20}$$

which was first introduced by Molière (1947), who operated with three pairs of constants (C_j, b_j), cf. Table 6.1 and the Bohr screening radius. Results of Wilson et al. (1977) were plotted in terms of R/a_{Firsov} with $a_{\mathrm{Firsov}} = 0.8853 a_0/(Z_1^{1/2} +$

Table 6.1 Constants defining screening function (6.20) according to Molière (1947), Wilson et al. (1977) (Kr-C) and Ziegler et al. (1985) (ZBL)

Potential		Molière		Kr-C		ZBL	
C_1	b_1	0.35	0.3	0.190 945	0.278 544	0.028 17	0.201 62
C_2	b_2	0.55	1.2	0.473 674	0.637 174	0.280 22	0.402 90
C_3	b_3	0.10	6.0	0.335 381	1.919 249	0.509 86	0.942 29
C_4	b_4					0.181 75	3.199 8

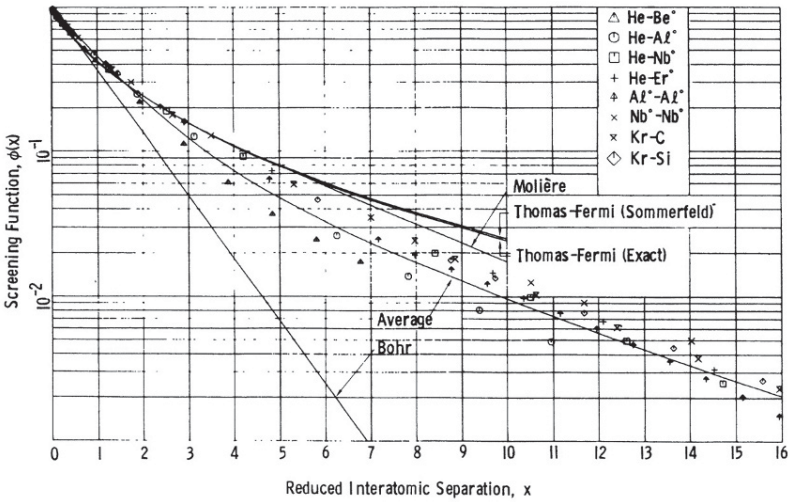

Fig. 6.8 Screening function for several atom pairs due to Wilson et al. (1977). See text. From Wilson et al. (1977)

$Z_2^{1/2})^{2/3}$, but with three pairs of constants (C_j, a_j) for each atom pair. The data set for the Kr-C pair (cf. Table 6.1) yields the so-called krypton-carbon potential, which has been frequently applied also to other atom-atom or ion-atom pairs. Examples are the data points in Fig. 6.8.

Similar computations were performed by numerous authors (Kim and Gordon, 1974, Dedkov, 1984, 1989), where also charged ions, in particular alkalis, were studied. A comprehensive review with a special emphasis on radiation physics is due to Dedkov (1995).

The work of Wilson et al. (1977) was extended to a large number of atom-atom pairs by Biersack and Ziegler (1982) and Ziegler et al. (1985), and an interpolation formula of the type of (6.20) was established with constants listed in Table 6.1 and commonly referred to as the ZBL potential.

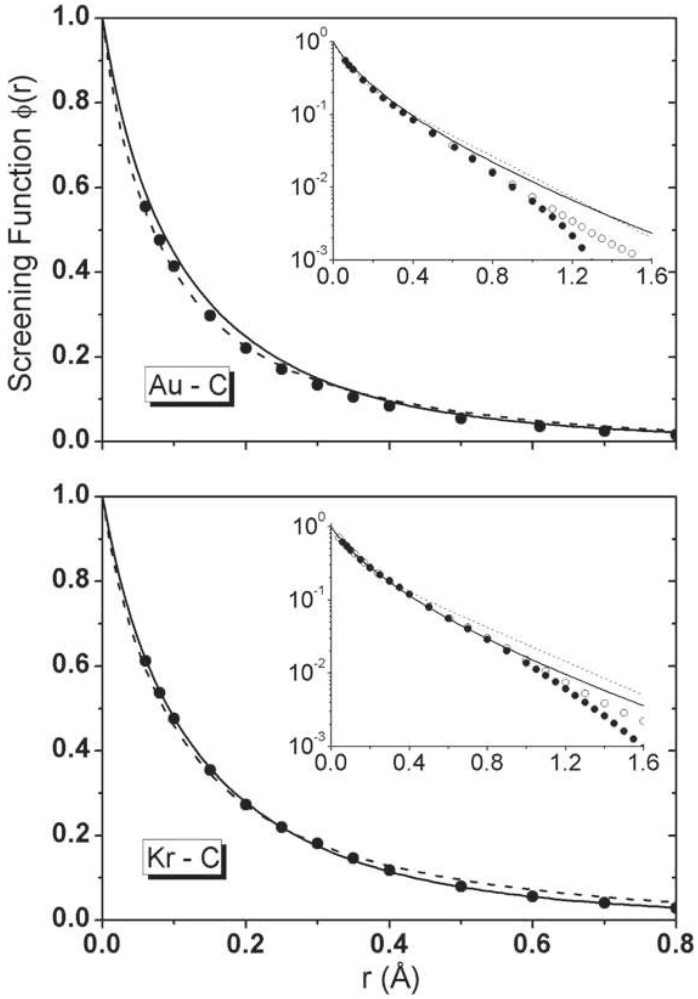

Fig. 6.9 Screening functions for Au-C and Kr-C interaction potentials. Solid circles: DFT(RESC); Empty circles: HF(RESC); solid lines: ZBL; dotted lines: Molière. From Kuzmin (2006)

6.2.3.2 Ab Initio Calculations

More recently, quantum chemistry codes have been applied to calculate interatomic potentials. The standard procedure here is to determine the ground-state energy of a molecule for a given configuration of the nuclei and to subtract the energy of the isolated atoms, i.e., one deals with *adiabatic potentials*. Apart from computational aspects the result of such calculations depends mainly on the basis set of atomic wave functions. Also relativistic effects may be taken into account.

Figure 6.9 shows two examples. Good agreement is found for $R \lesssim a_0$ between the results of two different codes, Density Functional Theory (TFD-RESC)[1] and Hartree-Fock (HF-RESC) as well as the Molière potential, whereas ZBL shows a slight difference. At larger distances substantial differences are found.

6.2.4 Nonbinary Potentials

6.2.4.1 Embedded-Medium Potentials

A useful theoretical basis for calculating interactions especially in *metals* is found in condensed-matter theory. The starting point is the problem of the electronic state of a foreign atom in a solid or at a solid surface. In the so-called effective-medium theory, the solid is replaced by a free electron gas (Nørskov, 1977, Nørskov and Lang, 1980, Stott and Zaremba, 1980, Nørskov, 1982, Daw and Baskes, 1983, 1984). The energy of such a system can be calculated by various methods, including density-functional theory. As a result one may find formation energies of point defects, chemisorption energies and the like.

Daw (1989), Adams and Foiles (1990) considered the effective interaction of two atoms embedded into an electron gas. This results in an embedded-atom potential taking proper care of the attractive part of the interaction force as well as the chemical properties of the interacting atoms.

This aspect will be discussed in some detail in connection with radiation effects in Volume 3 of this monograph.

6.2.4.2 Empirical Potentials

When simulating collision processes in solids or liquids you may need a realistic description of the equilibrium state of the medium. A convenient way to achieve such a description is to find a reasonable trial function with a number of parameters that can be fitted such as to match the known structure as well as mechanical and/or thermal properties of the material as closely as desirable. Such potentials must be attractive over a certain range of distances. An early example is the well-known Lennard-Jones or 6–12 potential (Lennard-Jones, 1924) with constants fitted to the van der Waals constants of real gases. Another empirical potential is the Born-Mayer potential, describing ionic crystals by a sum of a repulsive exponential and the Coulomb attraction between anions and cations (Born and Mayer, 1932).

More complicated structures may be described by means of many-body potentials. A useful example is the Stillinger-Weber potential characterizing silicon (Stillinger and Weber, 1985),

$$\mathcal{V} = \mathcal{V}_2 + \mathcal{V}_3 \,, \tag{6.21}$$

[1] Relativistic scheme of elimination of small components (RESC) of the four-component Dirac equation.

where $\mathcal{V}_2$ is a two-body potential with five free parameters and

$$\mathcal{V}_3(\boldsymbol{R}_i, \boldsymbol{R}_j, \boldsymbol{R}_k) = h(R_{ij}, R_{ik}, \theta_{jik}) + h(R_{ji}, R_{jk}, \theta_{ijk}) + h(R_{ki}, R_{kj}, \theta_{ikj}) \quad (6.22)$$

a three-body potential expressed by two interatomic distances and one angle, where θ_{jik} is the angle between $\boldsymbol{R}_{ji}$ and $\boldsymbol{R}_{ki}$. Expressing a three-body potential in this way facilitates the search for parameters reproducing the crystal structure.

For silicon, different sets of trial functions have become commonly used, developed by Stillinger and Weber (1985) and by Tersoff (1986). For monoatomic materials at least seven adjustable parameters enter, and a correspondingly higher number for heteroatomic substances.

Potentials describing material properties near equilibrium need to be amended such as to properly describe the behaviour at small internuclear distances. It is a requirement on the chosen parametrization that a smooth transition between the two regimes is obtainable.

6.2.5 Power Potentials

For rough estimates it is frequently useful to approximate the screening function in power form (Bohr, 1948),

$$g(\zeta) \simeq \frac{k_s}{s}\zeta^{1-s}. \quad (6.23)$$

Here the exponent s and the magnitude k_s can be determined in principle by matching (6.23) in power and slope to the actual potential. This, however, is rarely done in practice. A more efficient procedure will be mentioned in Sect. 6.4.2. Independent of the applied procedure, the exponent s depends on the range of distances where the screening function is supposed to be matched. For exponential screening, (6.5), s can take any value ≥ 1, while the Thomas-Fermi function mentioned in Sect. 6.2.2 behaves as $\propto R^{-3}$ at large distances, so the range of s-values is limited to $1 \lesssim 3$.

6.3 Screened-Coulomb Scattering

The basic tools for characterizing elastic scattering have been collected in Chap. 3, Vol. 1. The present section serves to provide specific results for ion-atom scattering under screened-Coulomb interaction.

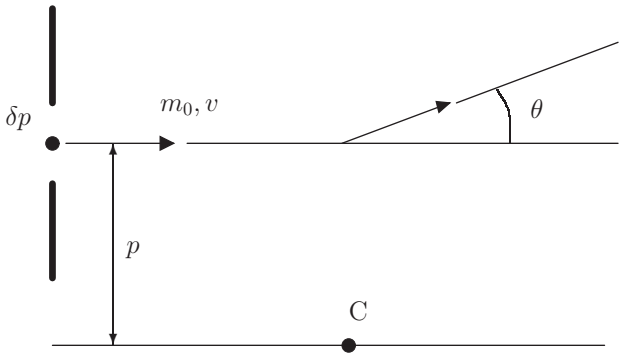

Fig. 6.10 Modified Bohr criterion for elastic scattering. See text

6.3.1 Limitations of Classical Elastic-Scattering Theory

It is a common procedure in the theory of heavy-ion penetration to treat nuclear scattering and stopping by classical scattering theory assuming elastic collisions. According to the Bohr criterion derived in Sect. 2.3.6, Vol. 1, classical scattering theory should be valid for

$$\frac{2Z_1 Z_2 e^2}{\hbar v} \gg 1 \,. \tag{6.24}$$

This defines an upper velocity limit, above which quantal scattering theory needs to be applied. That limit increases rapidly with increasing atomic numbers of the collision partners involved.

Nevertheless, some caution is indicated. Firstly, (6.24) has been derived for unscreened Coulomb interaction. An extension to screened-Coulomb interaction is evidently needed. Secondly, (6.24) assumes small-angle scattering. To what extent does it apply at large scattering angles? Thirdly, to what extent can electronic excitation and charge exchange be neglected? Let us briefly look into these aspects.

6.3.1.1 Generalization of the Bohr Criterion

A generalization of (6.24) was provided by Lindhard (1965). Figure 6.10 illustrates the scattering in the centre-of-mass frame of reference. A particle with reduced mass m_0 and velocity v passes through an aperture of width $2\delta p$ at an impact parameter p to a scattering centre C. According to the uncertainty principle, this implies a spread in transverse momentum

$$\delta P_1 \sim \frac{\hbar}{2\delta p} \,, \tag{6.25}$$

which is equivalent to a spread in scattering angle Θ,

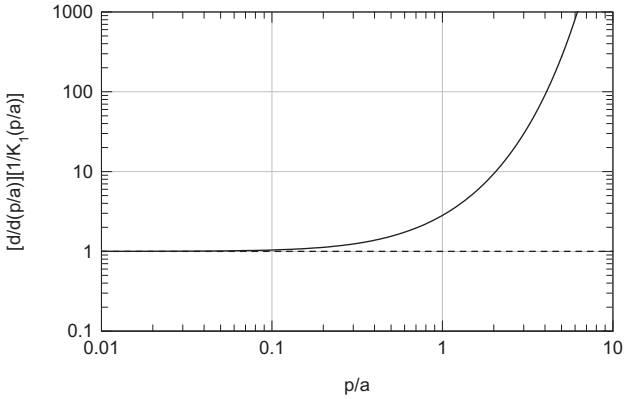

Fig. 6.11 Modified Bohr criterium. See text

$$\delta\Theta_1 \sim \frac{\delta P_1}{m_0 v}\,. \tag{6.26}$$

Conversely, the spread in impact parameter δp leads to a spread in scattering angle

$$\delta\Theta_2 = \left|\frac{\mathrm{d}\Theta}{\mathrm{d}p}\right| \delta p\,. \tag{6.27}$$

The total spread is then found as

$$\delta\Theta^2 = \delta\Theta_1^2 + \delta\Theta_2^2\,. \tag{6.28}$$

This quantity has a minimum at

$$\delta p^2 = \frac{\hbar}{2m_0 v|d\Theta/dp|}\,, \tag{6.29}$$

where

$$\delta\Theta^2_{\min} = \frac{\hbar|\mathrm{d}\Theta/\mathrm{d}p|}{m_0 v}\,. \tag{6.30}$$

According to Bohr (1948), a classical description is approximately valid if the spread in scattering angle $\delta\Theta$ is small compared to the scattering angle Θ itself. The resulting criterion can be written in the form

$$\left|\frac{\mathrm{d}}{\mathrm{d}p}\frac{1}{\Theta(p)}\right| \ll \frac{m_0 v}{\hbar}\,. \tag{6.31}$$

You can easily convince yourself that this reduces to (6.24) for Coulomb interaction. However, the fact that the scattering angle occurs in the denominator in (6.31) indicates a modification in particular at small angles.

As an example, consider two particles interacting via the Bohr potential

$$\mathcal{V}(R) = \frac{Z_1 Z_2 e^2}{R} \mathrm{e}^{-R/a} , \tag{6.32}$$

cf. (6.7). In problem 6.5 you will find that, for large impact parameters or small angles, (6.31) reduces to

$$\kappa \equiv \frac{2Z_1 Z_2 e^2}{\hbar v} \gg \left| \frac{\mathrm{d}}{\mathrm{d}(p/a)} \frac{1}{K_1(p/a)} \right| , \tag{6.33}$$

where $K_1(z)$ is a modified Bessel function in standard notation (Abramowitz and Stegun, 1964).

The function on the right-hand side of (6.33) has been drawn up in Fig. 6.11. You may note that the quantity on the left side of (6.33) is Bohr's kappa as introduced in (2.80), Vol. 1. For Coulomb interaction that quantity needs to exceed 1, the stipled line in Fig. 6.11. For screened interaction no change occurs at small impact parameters, $p \ll a$, where the potential is Coulomb-like (cf. the stipled line), while the solid line, valid for the Bohr potential, rises steeply from $p/a \sim 1$ on, thus making it increasingly difficult to fulfill the modified Bohr criterion. However, for heavy collision partners and $v \ll v_0$, a situation typical for applications in radiation damage, ion implantation etc, κ is much greater than 1. Therefore it makes sense to extend the ordinate scale in Fig. 6.11 to the level indicated in the graph.

6.3.1.2 Quantal Effects

The assumption of small-angle scattering is not critical to the derivation of the modified Bohr criterion presented in the previous section. Moreover, Fig. 6.11 does not give rise to concern about larger scattering angles (or smaller impact parameters). An exception is straight backscattering at 180°, where one might be concerned about interference between the incoming and outgoing wave (Sect. 7.8.3).

Quantal effects are, however, observable in the scattering of heavy particles. One of the most drastic ones is charge exchange, discussed in Chap. 2. Charge exchange may show pronounced variations with beam energy and scattering angle (Ziemba and Everhart, 1959, Lockwood et al., 1963). This implies that dependent on the detection device, measured distributions in angle or energy may deviate dramatically from the smooth spectra expected from classical scattering theory.

Inelastic energy loss by electron excitation or ionization affects conservation laws and thus angular as well as energy distributions of scattered particles. In fact, inelastic energy losses can be determined experimentally in this way, as was discussed in Problems 3.4 and 3.5, Vol. 1.

6.3.2 Recapitulation

6.3.2.1 Classical Scattering Integral

The central result of classical binary scattering theory is contained in (3.34) and (3.35), Vol. 1, which relates the scattering angle Θ in the centre-of-mass frame to the impact parameter p by

$$\Theta = \pi - 2p \int_{R_m}^{\infty} \frac{\mathrm{d}R}{R^2} \left(1 - \frac{\mathcal{V}(R)}{E_r} - \frac{p^2}{R^2}\right)^{-1/2} , \tag{6.34}$$

where $E_r = m_0 v^2/2$ is the relative kinetic energy and R_m the closest distance of approach that satisfies the relation

$$1 - \frac{\mathcal{V}(R_m)}{E_r} - \frac{p^2}{R_m^2} = 0 . \tag{6.35}$$

For screened-Coulomb interaction (6.4) or

$$\mathcal{V}(R) = \frac{Z_1 Z_2 e^2}{R} g(R/a) , \tag{6.36}$$

(6.34) reduces to

$$\Theta = \pi - 2p \int_{R_m}^{\infty} \frac{\mathrm{d}R}{R^2} \left[1 - \frac{a}{\epsilon R} g\left(\frac{R}{a}\right) - \frac{p^2}{R^2}\right]^{-1/2} \tag{6.37}$$

with

$$\epsilon = \frac{a E_r}{Z_1 Z_2 e^2} \tag{6.38}$$

in accordance with (3.50), Vol. 1. Introducing a dimensionless impact parameter

$$\xi = \frac{p}{a} \tag{6.39}$$

you find

$$\Theta = \pi - 2\xi \int_{\zeta_m}^{\infty} \frac{\mathrm{d}\zeta}{\zeta^2} \left(1 - \frac{g(\zeta)}{\epsilon\zeta} - \frac{\xi^2}{\zeta^2}\right)^{-1/2} , \tag{6.40}$$

where $\zeta_m = R_m/a$.

6.3.2.2 Scaling Properties

Equation (6.40) expresses the scattering angle as a function of ϵ and ξ,

$$\Theta = \Theta(\epsilon, p/a) . \tag{6.41}$$

You may write this relation in the form

$$p = ah\left(\epsilon, \sin\frac{\Theta}{2}\right), \tag{6.42}$$

and thus

$$\mathrm{d}\sigma = \left|\pi \mathrm{d}p^2\right| = \pi a^2 g_1\left(\epsilon, \sin^2\frac{\Theta}{2}\right)\mathrm{d}\sin^2\frac{\Theta}{2}, \tag{6.43}$$

where h and g_1 are functions determined by the screening function g.

The relation to the energy transfer is given by (3.8), Vol. 1,

$$T = \gamma E \sin^2\frac{\Theta}{2} \tag{6.44}$$

with

$$\gamma = \frac{4M_1M_2}{(M_1+M_2)^2} \tag{6.45}$$

for nonrelativistic collisions.

6.3.2.3 Classical Small-Angle Scattering

In Chap. 3.3.6, Vol. 1, an expansion of the classical scattering integral, (6.40) in powers of the interaction was found. The first term in this expansion, called momentum approximation, reads

$$\Theta = -\frac{1}{pE_r}\int_p^\infty \frac{\mathrm{d}r}{\sqrt{1-p^2/r^2}}\frac{\mathrm{d}}{\mathrm{d}r}\left[r\mathcal{V}(r)\right] \tag{6.46}$$

or, for screened-Coulomb interaction,

$$\Theta = -\frac{1}{\epsilon p/a}\int_{p/a}^\infty \frac{\mathrm{d}\zeta}{\sqrt{1-(p/a)^2/\zeta^2}}\frac{\mathrm{d}g(\zeta)}{\mathrm{d}\zeta}. \tag{6.47}$$

Equation (6.47) must be expected to accurately characterize the scattering law at sufficiently small angles.

6.3.3 Lindhard-Scharff Scaling

In addition to (6.43), which is an exact scaling property for classical elastic scattering on a screened Coulomb potential, Lindhard et al. (1968) derived an approximate scaling relationship which reduces the function $g(\epsilon, \sin^2\Theta/2)$ to a function of just one variable.

6.3.3.1 Power Potential

Following their argument, consider first the case of a power potential, where

$$g\left(\frac{R}{a}\right) = \frac{k_s}{s}\left(\frac{a}{R}\right)^{s-1}, \tag{6.48}$$

where $s > 1$ and k_s a constant. With this, (6.47) reduces to

$$\Theta = \frac{(s-1)k_s}{s\epsilon(p/a)^s}\int_1^\infty \mathrm{d}t\,\frac{t^{1-s}}{\sqrt{t^2-1}}\,. \tag{6.49}$$

The integral may be reduced to a standard form by substituting $t = 1/\sin u$. With this you find

$$\Theta = \frac{k_s\gamma_s}{\epsilon}\left(\frac{a}{p}\right)^s, \tag{6.50}$$

where

$$\gamma_s = \frac{1}{2}B\left(\frac{1}{2}, \frac{s+1}{2}\right) \tag{6.51}$$

and $B(x, y)$ is the beta function

$$B(x,y) = \int_0^1 \mathrm{d}t\,t^{x-1}(1-t)^{y-1} = \frac{\Gamma(x)\Gamma(y)}{\Gamma(x+y)}\,. \tag{6.52}$$

in the conventional definition (Abramowitz and Stegun, 1964).

6.3.3.2 Extrapolation

Equation (6.50) has a divergence at $p = 0$ instead of the expected result $\Theta = \pi$. In order to correct for this, Lindhard et al. (1968) made a bold wide-angle approximation by replacing

$$\Theta \to 2\sin\Theta/2 \tag{6.53}$$

$$p \to \sqrt{p^2 + p_0^2} \tag{6.54}$$

with a quantity p_0 to be determined by the requirement that $\Theta = \pi$ for $p = 0$, so that

$$2\epsilon = \frac{k_s}{2}B(1/2, (s+1)/2)(a/p_0)^s\,. \tag{6.55}$$

The substitution (6.54) has the convenience that p_0 drops out in the differential cross section with Θ as a variable, since

$$2\pi p\mathrm{d}p \equiv \pi\mathrm{d}p^2 \equiv \pi\mathrm{d}(p^2 + p_0^2)\,. \tag{6.56}$$

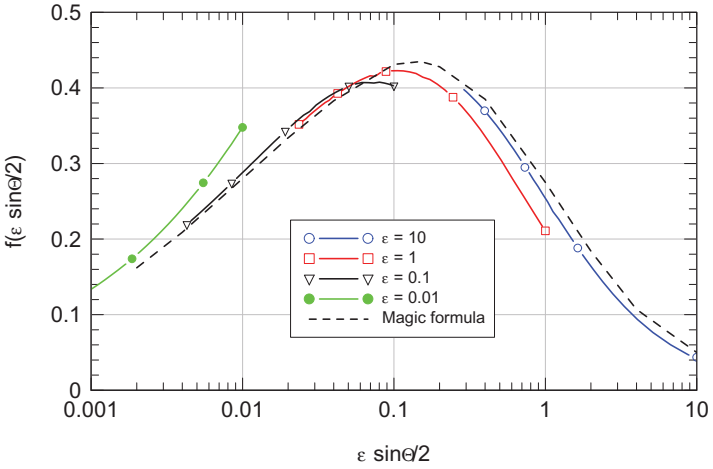

Fig. 6.12 Differential cross section for the Thomas-Fermi potential plotted in Lindhard-Scharff units. See text

With this, one may expect that the function $g(\epsilon, \sin\Theta/2)$ is approximately a function of the product $\epsilon \sin\Theta/2$, which approaches $\epsilon\Theta/2$ implied by (6.50) in the small-angle limit.

6.3.3.3 Verification

The standard form of the Lindhard-Scharff scaling relation reads as

$$\mathrm{d}\sigma(\Theta) = \pi a^2 \frac{\mathrm{d}\left(\epsilon \sin\frac{\Theta}{2}\right)}{\epsilon^2 \sin^2\frac{\Theta}{2}} f\left(\epsilon \sin\frac{\Theta}{2}\right) \tag{6.57}$$

with a yet unknown function $f(\epsilon \sin\Theta/2)$.

Scattering angles for the Sommerfeld approximation of the Thomas-Fermi potential have been evaluated numerically and tabulated by Robinson (1970). These cross sections have been plotted in Fig. 6.12 for ϵ ranging from 0.01 to 10. It is seen that Lindhard-Scharff scaling is fulfilled within a 10–20% error margin. A similar result was found for the Bohr potential in the original paper (Lindhard et al., 1968).

6.3.3.4 Magic Formula

While exact evaluation of scattering integrals is no longer a challenge, an accurate analytical approximation is still attractive. A ‘magic formula’ found by Lindhard et al. (1968) takes its starting point at the power law (6.50).

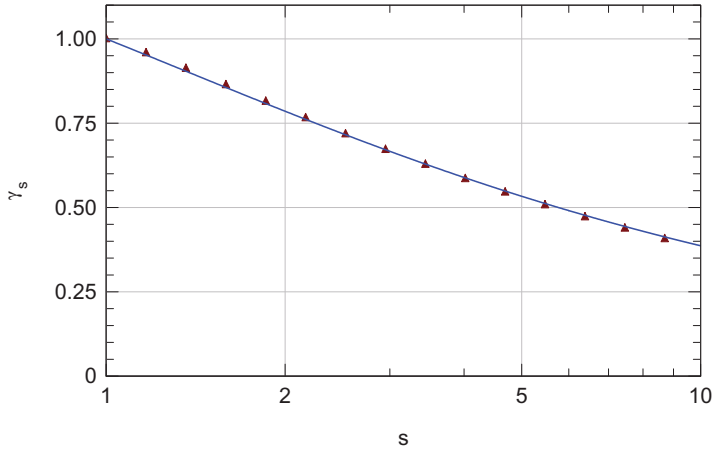

Fig. 6.13 The function γ_s, (6.51) (solid line) compared with the approximation γ'_s, (6.58) (points)

Figure 6.13 shows that the function γ_s is accurately approximated by the expression

$$\gamma'_s = \frac{1}{s}\sqrt{\frac{3s-1}{2}}\,. \tag{6.58}$$

Inserting γ'_s for γ_s and noting that the function $1/sp^s$ is proportional to the potential, you may write (6.50) in the form

$$\Theta^2 = -\frac{3}{4}p^3\frac{\mathrm{d}}{\mathrm{d}p}\left(p^{2/3}V(p)^2\right)\,. \tag{6.59}$$

This may be extrapolated to large angles in the way sketched in Sect. 6.3.3.2, but as mentioned there, this extrapolation does not affect the differential cross section.

The result of applying the magic formula to the Thomas-Fermi potential has been included in Fig. 6.12.

6.3.4 Comparison of Differential Cross Sections

The function $f(\eta)$ with

$$\eta = \epsilon \sin\frac{\Theta}{2} \tag{6.60}$$

is a convenient tool to compare differential cross sections originating in different scattering potentials. A convenient parametrization of $f(\eta)$ was found by Winterbon et al. (1970),

$$f(\eta) \simeq \frac{\lambda\eta^{1-2m}}{\left(1+\left[2\lambda\eta^{2(1-m)}\right]^q\right)^{1/q}}\,, \tag{6.61}$$

Table 6.2 Coefficients entering scaling function $f(\eta)$ for differential scattering cross section, (6.61) according to Winterbon (1972)

Screening function u	m	q	λ
Thomas-Fermi	0.333	0.667	1.309
Thomas-Fermi-Sommerfeld	0.311	0.588	1.70
Lenz-Jensen	0.191	0.512	2.92
Molière	0.216	0.570	2.37
Bohr	0.103	0.570	2.37

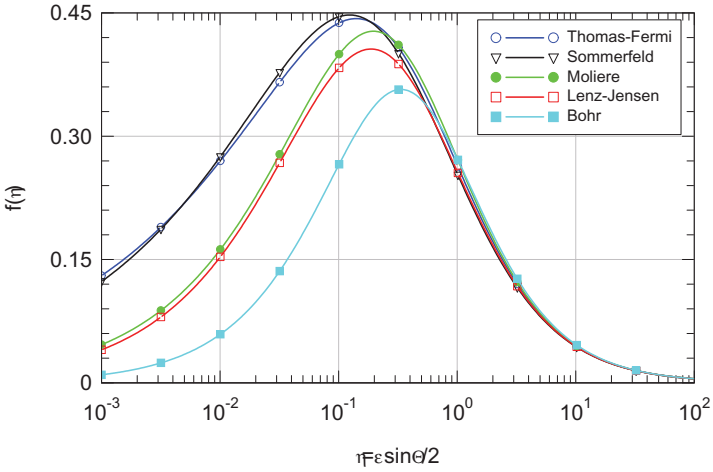

Fig. 6.14 Reduced differential cross section for several screened-Coulomb potentials, (6.61) with coefficients from Table 6.2

and parameters for several screening functions may be found in Table 6.2.

6.3.5 Inversion

Equation (6.34) expresses the scattering angle by the impact parameter and the beam energy, if the potential is given as a function of distance. You may ask whether that relation can be inverted, such that the potential can be determined from scattering measurements.

This type of inversion problem occurs in many fields of science. In the present context, relevant information can be found by varying the beam energy at a fixed scattering angle or vice versa, or a combination of the two. A scheme operating at a fixed scattering angle was proposed by Hoyt (1939), based on the solution of a related problem by Klein (1932). For the case of fixed beam energy and variable angle a similar scheme has been developed by Firsov (1953) and applied successfully in the analysis of experimental data.

In deriving Firsov's formula I am following Lane and Everhart (1960). Starting at (6.34) we may introduce a function

$$\Psi(R) = R^2 \left(1 - \frac{\mathcal{V}(R)}{E_r}\right), \tag{6.62}$$

so that

$$\Theta(p) = \pi - 2p \int_{R_m}^{\infty} \frac{\mathrm{d}R}{R} \frac{1}{\sqrt{\Psi(R) - p^2}} \tag{6.63}$$

Replacement of R by Ψ as the integration variable leads to

$$\Theta(p) = \pi - 2p \int_{p^2}^{\infty} \frac{\mathrm{d}\Psi}{\sqrt{\Psi - p^2}} \frac{\mathrm{d}(\ln R(\Psi))}{\mathrm{d}\Psi}, \tag{6.64}$$

since $\Psi(R_m) = p^2$, as follows from (6.34).

Now, the constant π can be expressed as

$$\pi = p \int_{p^2}^{\infty} \frac{\mathrm{d}\Psi}{\sqrt{\Psi - p^2}} \frac{\mathrm{d}\ln\Psi}{\mathrm{d}\Psi}, \tag{6.65}$$

as you may verify by carrying out the integration on the right-hand side. With this we arrive at

$$\Theta(p) = p \int_{p^2}^{\infty} \frac{\mathrm{d}\Psi'}{\sqrt{\Psi' - p^2}} \frac{\mathrm{d}}{\mathrm{d}\Psi'} \ln\left(\frac{\Psi'}{R(\Psi')^2}\right), \tag{6.66}$$

where the integration variable has been renamed to Ψ'.

After multiplying this equation by $1/\sqrt{p^2 - \Psi}$ and integrating from $p = \sqrt{\Psi}$ to infinity, and interchanging the order of integrations you find

$$\int_{\sqrt{\Psi}}^{\infty} \mathrm{d}p \frac{\Theta(p)}{\sqrt{p^2 - \Psi}} = \frac{1}{2} \int_{\Psi}^{\infty} \mathrm{d}\Psi' \frac{\mathrm{d}}{\mathrm{d}\Psi'} \left(\ln \frac{\Psi'}{R(\Psi')^2}\right) \int_{\Psi}^{\Psi'} \frac{\mathrm{d}p^2}{\sqrt{(\Psi' - p^2)(p^2 - \Psi)}}. \tag{6.67}$$

Since the integral over $\mathrm{d}p^2$ reduces to π, we arrive at

$$\int_{\sqrt{\Psi}}^{\infty} \mathrm{d}p \frac{\Theta(p)}{\sqrt{p^2 - \Psi}} = \frac{\pi}{2} \left(\ln \frac{\Psi'}{R(\Psi')^2}\right)_{\Psi'=\Psi}^{\infty} \equiv \frac{\pi}{2} \left(\ln \frac{\Psi(R')}{R'^2}\right)_{R'=R}^{\infty} \tag{6.68}$$

or

$$\int_{\sqrt{\Psi}}^{\infty} \mathrm{d}p \frac{\Theta(p)}{\sqrt{p^2 - \Psi}} = \frac{\pi}{2} \ln\left(\frac{R^2}{\Psi}\right). \tag{6.69}$$

Note that $\Psi(R)/R^2$ approaches 1 for large R according to the definition.

Equation (6.69) expresses R as a function of Ψ and, hence, of V/E_r. You may verify its validity on the example discussed in Problem 6.7.

Lane and Everhart (1960) have demonstrated that an interaction potential actually can be extracted by inversion of scattering data. However, the procedure is by no means trivial in practice. The first step is to express a measured differential cross section in centre-of-mass coordinates. The second step is an integration according to

$$\int_{\Theta'=\Theta}^{\pi} \mathrm{d}\sigma(\Theta') = \int_0^p 2\pi p' \mathrm{d}p' \,. \tag{6.70}$$

Typically the coverage with data points in the interval $0 \leq \Theta \leq \pi$ is incomplete. As a minimum, this limits the range of distances or energies covered by the deduced potential. Next, in order to allow integration as required in (6.69), some inter- or extrapolation may have to made, and finally, the potential has to be extracted from an implicit connection between Ψ and R.

The uniqueness of the inversion process has likewise been studied. Note first that Rutherford's cross section is identical for attractive and repulsive Coulomb interaction. Apart from that, a study by Demkov et al. (1971) indicates that the procedure becomes nonunique in case of cut-off potentials.

Figure 6.15 shows an example of a successful inversion. Lane and Everhart (1960) measured angular distributions of Ar^+ ions on Ar from about 1° to 40°. The top graph shows the data for 25 keV. The bottom graph shows potentials extracted from cross sections measured at 25, 50, and 100 keV (solid lines), as well as the Firsov (dotted) and Bohr (dashed) potentials. The near-coincidence of the three extracted potentials provides confidence both in the data and the procedure. Evidently, increasing the beam energy allows determination of the potential at smaller internuclear distances.

Potentials extracted from collision experiments are needed mostly for application in collision studies. Therefore, it appears more appropriate to compare measured to calculated cross sections, rather than comparing potentials found by inversion to calculated potentials.

6.3.6 Scattering Experiments

Direct measurements of differential cross sections are done on isolated target atoms. Data exist mainly for noble-gas targets. Early systematic measurements were performed by Everhart and coworkers, starting with Everhart et al. (1955), including the study of Lane and Everhart (1960) quoted above. The focus in this program, as well as in a parallel study by Fedorenko and coworkers (Kaminker and Fedorenko, 1955) changed gradually into inelastic processes.

Only few studies have been performed subsequently of ion-atom scattering aiming at interatomic potentials in the repulsive (keV) regime. Here I like to mention a couple of examples.

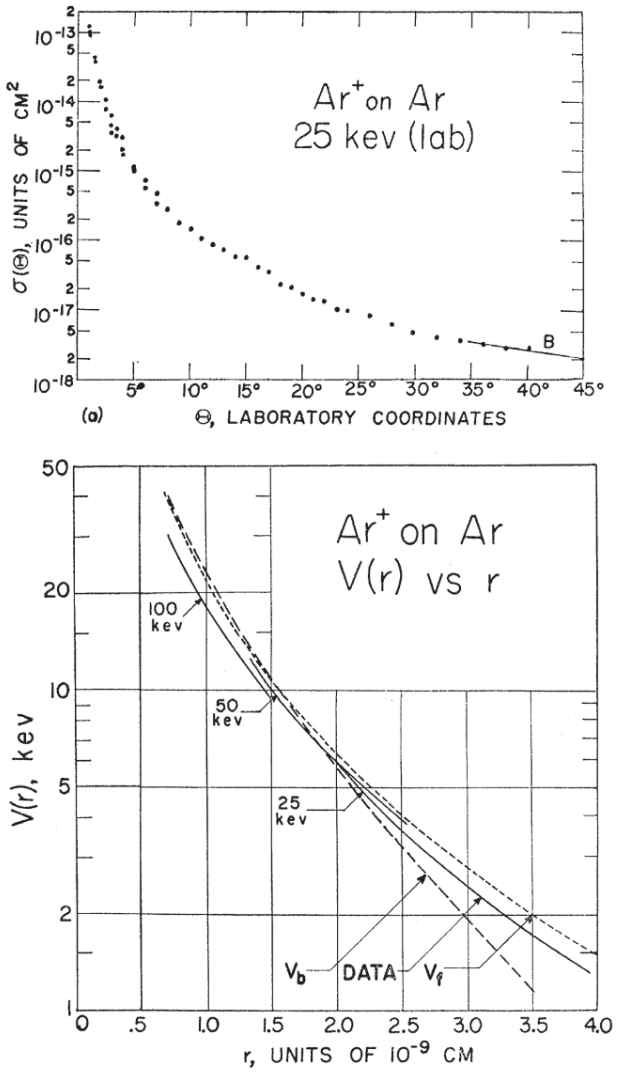

Fig. 6.15 Inversion of Ar^+-Ar differential scattering cross section (top) and the resulting potential (bottom). See text. From Lane and Everhart (1960)

6.3.6.1 Oscillatory Structure

Figures 6.16 and 6.17 show cross sections measured on xenon gas by Loftager et al. (1979). The abscissa variable is $\eta = \epsilon \sin \Theta$, and plotted is the ratio between the measured cross section in centre-of-mass variables and the Lenz-Jensen cross section. In Fig. 6.16, showing Ar on Xe, data referring to beam energies from 2.5 to

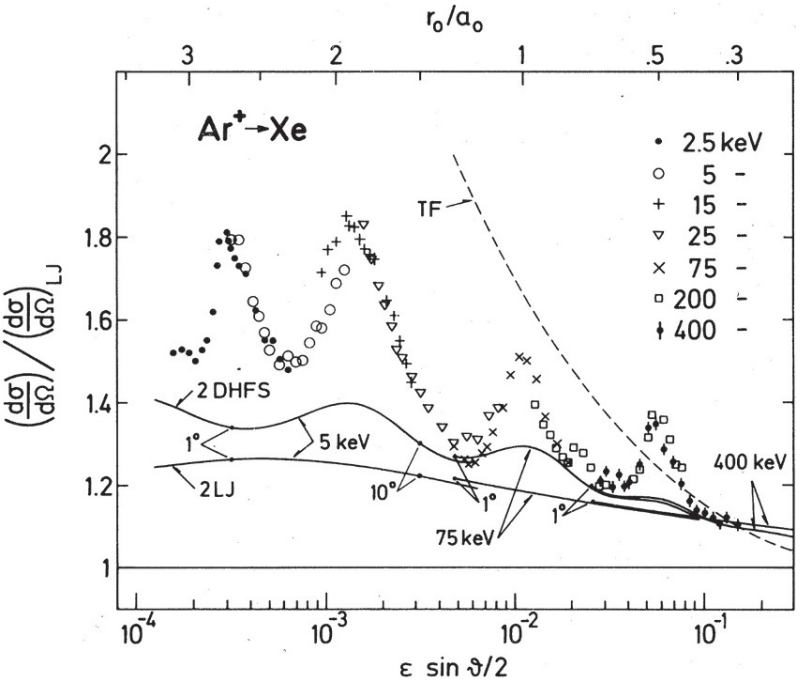

Fig. 6.16 Measured differential cross sections of Ar^+ on xenon. Plotted is the ratio between measurement and the Lenz-Jensen cross section (Lindhard et al., 1968) with the adopted screening radius $a = 0.8853a_0/\sqrt{Z_1^{2/3} + Z_2^{2/3}}$. Abscissa reduced to Lindhard variable $\eta = \epsilon \sin\Theta/2$. Also included: TF (Thomas-Fermi) (Lindhard et al., 1968). r_0 represents the closest distance of approach calculated for interaction potential based on superimposed LJ (2LJ) or Hartree-Fock (2DHFS) atomic charge densities. From Loftager et al. (1979)

400 keV fall essentially on one line, in agreement with the scaling relation (6.57). Loftager et al. (1979) concluded from this that scattering has been elastic.

Figure 6.17 shows data for C, Ne, Kr, Xe and Cd ions on Xe. You may first notice that with the exception of a small part of the C-Xe data, all experimental points fall in between the Thomas-Fermi and the Lenz-Jensen curve. Moreover, within a 20% margin, Lindhard-Scharff scaling is well obeyed for $\epsilon \sin\Theta/2 \gtrsim 0.002$, while major differences between different ions are found in the opposite end.

All data shown in Figs. 6.16 and 6.17 show an oscillatory structure which was found earlier (Loftager and Hermann, 1968, Afrosimov et al., 1972) and which has been ascribed to shell effects by Afrosimov et al. (1972). There are several possible reasons for such oscillatory structures. Very pronounced effects are found if scattered particles are recorded separately according to charge states (Ziemba and Everhart, 1959, Aberth et al., 1965). Loftager et al. (1979) found that differential cross sections for an interatomic potential allowing for shell structure (labelled DHFS in Fig. 6.17) show weak oscillations with a phase in good agreement with experiment.

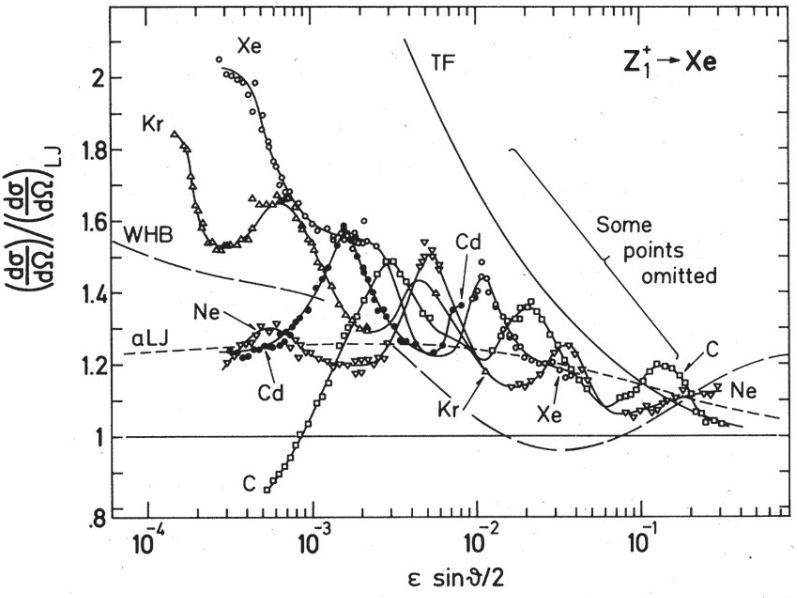

Fig. 6.17 Same as Fig. 6.16 for different ions on xenon. Also included: TF (Thomas-Fermi) (Lindhard et al., 1968), WHB (Wilson et al., 1977), aLJ (suggested average). From Loftager et al. (1979)

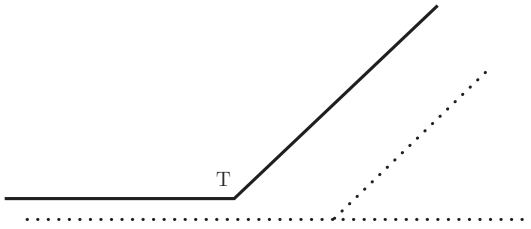

Fig. 6.18 Angular deflection in inelastic scattering. Schematic and exaggerated. See text

An explanation of the observations in Figs. 6.16 and 6.17 in terms of inelasticity (Afrosimov et al., 1972) appears most plausible: In Fig. 6.18 you find the sketch of an inelastic scattering event in the centre-of-mass frame. The only difference to the standard case of scattering on a central-force potential is an inelastic energy loss which, for simplicity, is assumed to take place at the apsis T. When arriving at T the particle has a certain angular momentum around the force centre which must be conserved. Since speed is reduced, the deflection angle and the impact parameter will increase. A quantitative discussion was given by Hartung et al. (1985) with near-perfect agreement between experiment and theory.

An experimental and theoretical study of pertinent processes and their respective contributions to the differential cross section, involving doubly-differential distributions in angle and energy as well as separation of charge states, has been performed on Na^+-Ne by Olsen et al. (1979). Figure 6.19 indicates that the contribution of

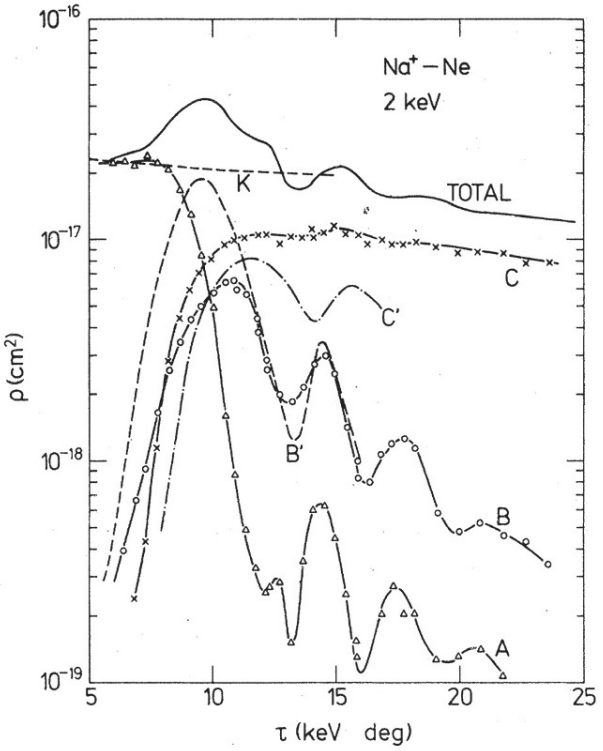

Fig. 6.19 Differential cross sections for 2 keV Na^+-Ne according to Olsen et al. (1979). A: Elastic; B: One-electron processes; C: Two-electron processes. K: Elastic scattering ignoring all electronic processes. From Olsen et al. (1979)

truly elastic collisions to the differential cross section (label A) may be very small—$\sim 1\%$ in this case—while ignoring all inelasticity (label K) may well lead to a result of the right order of magnitude (label TOTAL).

6.3.6.2 Inversion

An extensive effort to extract interatomic potentials from differential cross sections has been made by Zinoviev (2011). Literature data for a number of ion-target combinations were analyzed by the Firsov procedure described in Sect. 6.3.5. Figure 6.20 shows results plotted as a function of R/a_f, where a_f is a screening radius defined as

$$a_f = \frac{0.8853 a_0}{(Z_1^\alpha + Z_2^\alpha)^\beta} \tag{6.71}$$

with $\alpha = 1/2$ and $\beta = 2/3$.

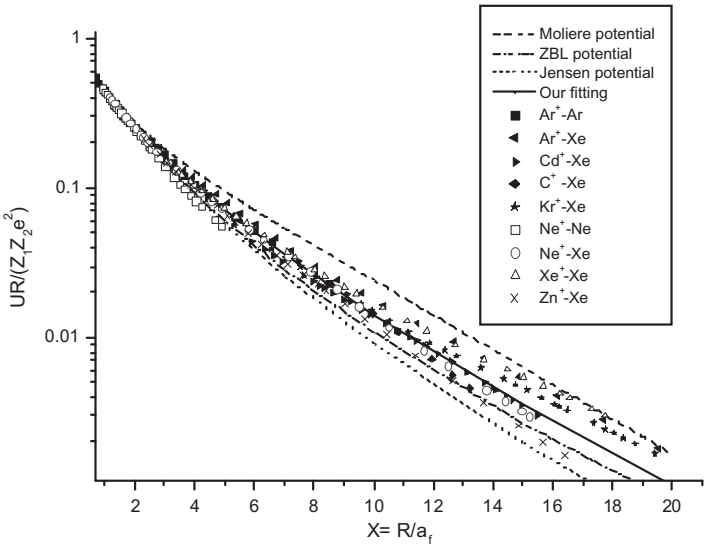

Fig. 6.20 Screening function $g(R/a)$ extracted from experimental scattering data by Firsov inversion. a_f denotes the Firsov screening radius. From Zinoviev (2011)

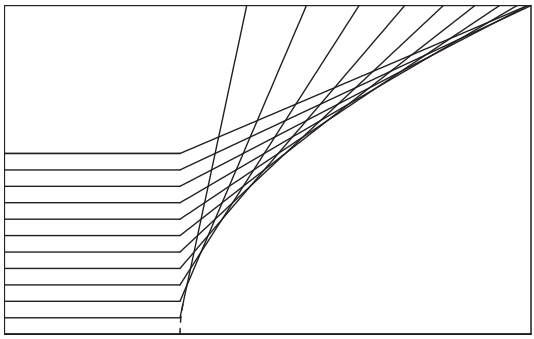

Fig. 6.21 Shadow cone in small-angle Rutherford scattering. See text

6.3.7 Shadow Cone

Imagine a homogeneous beam of particles scattered on a hard sphere of radius a with a mass much greater than the mass of a single projectile. Then, particles hitting the sphere will be scattered out of the beam. As a result there will be a cylindrical region behind the sphere where no moving particles will be detected. In other words, the sphere generates a cylindrical shadow of radius a.

What form of shadow can we expect when scattering obeys Rutherford's law rather than billiard-ball dynamics? This question was asked by Lindhard (1965), who provided an answer involving small-angle scattering.

Following Lindhard's argument, note first that for small scattering angles, (3.42), Vol. 1, reduces to

$$\Theta = \frac{b}{p}; \qquad b = \frac{2Z_1 Z_2 e^2}{M_0 v^2} \tag{6.72}$$

or, in the laboratory frame of reference,

$$\phi = \frac{Z_1 Z_2 e^2}{Ep}\,, \tag{6.73}$$

where ϕ is the scattering angle of the projectile, E the beam energy and p the impact parameter. Still assuming small angles we may place a coordinate system (x, y) in the impact plane, so that a single trajectory may be approximated by two straight lines

$$y = \begin{cases} p & \text{for } x < 0 \\ p + (Z_1 Z_2 e^2/Ep)x & \text{for } x > 0 \end{cases} \tag{6.74}$$

Such trajectories have been plotted in Fig. 6.21. Instead of a plain cylinder, we now find a parabolic cylinder which follows the relation

$$y = 2\sqrt{\frac{Z_1 Z_2 e^2}{E}x}\,. \tag{6.75}$$

Target particles lying within this 'shadow cone' will not be hit by the beam, regardless of the impact parameter. Specifically, if you want to hit a target particle at some distance $x = d$ behind the first target atom, you have to tilt the beam by an angle

$$\Delta\phi > \Theta_c = \frac{y(d)}{d} = 2\sqrt{\frac{Z_1 Z_2 e^2}{Ed}}\,. \tag{6.76}$$

This is a useful relation in the study of channeling, cf. Sect. 1.1.1, Vol. 1. We shall come back to this in Appendix 11.

The shadow cone has come to play an important role in ion-surface scattering at energies well below the Rutherford regime. Accurate calculations (Oen, 1983) may have to avoid the small-angle approximation and may need to take into account the time integral, cf. Sect. 3.3.4, Vol. 1. Alternatively, trajectories may be simulated (Yamamura and Takeuchi, 1984).

6.4 Nuclear Stopping

According to Sects. 2.2.3-.2.2.5, Vol. 1, the energy loss in an elastic binary collision may be characterized by the nuclear stopping force

$$\left(-\frac{\mathrm{d}E}{\mathrm{d}x}\right)_n = NS_n \tag{6.77}$$

with

$$S_n = \int T_n \, \mathrm{d}\sigma \tag{6.78}$$

and

$$T_n = \gamma E \sin^2 \frac{\Theta}{2} \,, \tag{6.79}$$

where $\gamma = 4M_1M_2/(M_1 + M_2)^2$.

If you have a tabulation of the scattering integral (6.34) for a given potential, the nuclear stopping cross section S_n can be found by integration,

$$S_n = \gamma E \int_0^\infty 2\pi p \, \mathrm{d}p \, \sin^2 \frac{\Theta(p)}{2} \tag{6.80}$$

without going over the differential cross section.

6.4.1 Scaling Properties

Conversely, making use of the scaling relations for the differential cross section in Sect. 6.3.2.2 you find

$$\left(-\frac{\mathrm{d}E}{\mathrm{d}x}\right)_n = N\pi a^2 \gamma E \int_0^\pi g\left(\epsilon, \sin^2 \frac{\Theta}{2}\right) \mathrm{d} \sin^2 \frac{\Theta}{2} \,. \tag{6.81}$$

This suggests the introduction of a dimensionless measure of the pathlength x,

$$\xi = N\pi a^2 \gamma x \,. \tag{6.82}$$

With this, (6.81) reduces to

$$-\frac{\mathrm{d}\epsilon}{\mathrm{d}\xi} = s(\epsilon) = \epsilon \int_0^\pi g\left(\epsilon, \sin^2 \frac{\Theta}{2}\right) \mathrm{d} \sin^2 \frac{\Theta}{2} \,. \tag{6.83}$$

This relation is general for elastic binary scattering on a screened-Coulomb potential in the nonrelativistic energy regime.

Specifically, with Lindhard-Scharff scaling, (6.57), this reduces to

$$\frac{\mathrm{d}\epsilon}{\mathrm{d}\xi} = \frac{1}{\epsilon} \int_0^\epsilon \mathrm{d}\eta \, f(\eta) \,, \tag{6.84}$$

where

$$\eta = \epsilon \sin^2 \frac{\Theta}{2} = \epsilon \frac{T}{\gamma E} \,, \tag{6.85}$$

and $f(\eta)$ is determined by the screening function of the potential.

Figure 6.22 shows $s_n(\epsilon)$ found by integration of the curves shown in Fig. 6.14 according to (6.84). In addition, the function

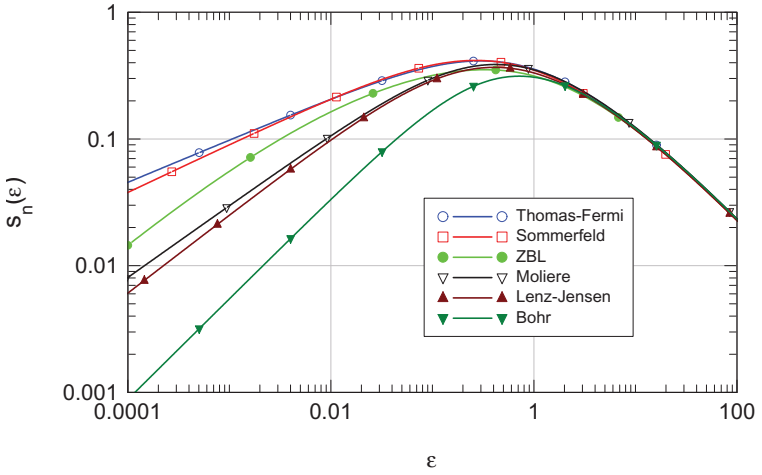

Fig. 6.22 Stopping cross sections in universal plot for the cross sections shown in Fig. 6.14. Also included is ZBL, i.e., the function adopted by Ziegler et al. (1985)

$$s_n = \frac{\ln(1 + a\epsilon)}{2(\epsilon + b\epsilon^c + d\sqrt{\epsilon})} \tag{6.86}$$

from Ziegler et al. (1985) with

$$a = 1.1383; \qquad b = 0.01321; \qquad c = 0.21226; \qquad d = 0.19593 \tag{6.87}$$

has been included. Note, however, that a comparison of the actual cross sections would have to take into account the adopted form of the screening radius.

6.4.2 Power Cross Section

Power cross sections have been introduced as a convenient tool in the derivation of the Lindhard-Scharff scaling relationship, (6.57). They have also been useful on their own as model cross sections in solving transport equations, as you will see in Chap. 9.

Going back to (6.57) and looking at Fig. 6.12 we may approximate $f(\eta)$ by

$$f_m(\eta) = \lambda_m \eta^{1-2m} \tag{6.88}$$

over a limited range of η-values, so that $m = 0$ yields a linear increase, applying to the low-η regime, while $m = 1$ characterizes the asymptotic behaviour at large η, i.e., Rutherford scattering.

Insertion of (6.88) into (6.57) yields

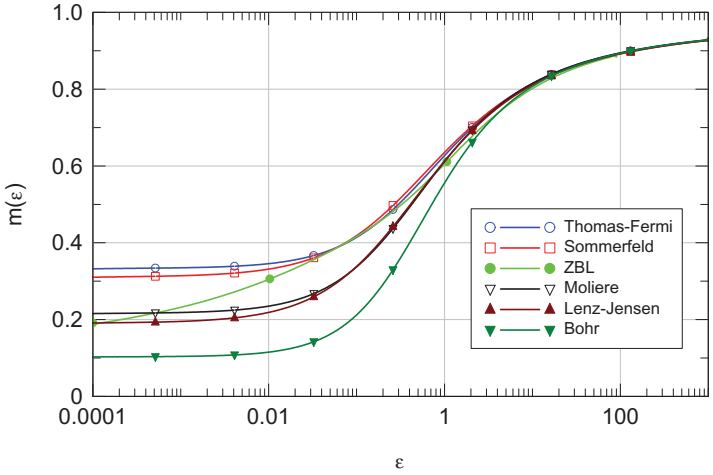

Fig. 6.23 Exponent m in power cross section extracted from stopping cross sections shown in Fig. 6.22

$$\mathrm{d}\sigma(E,T) = CE^{-m}T^{-1-m}dT \tag{6.89}$$

with

$$C = \frac{\pi}{2}\lambda_m a^2 \left(\frac{M_1}{M_2}\right)^m \left(\frac{2Z_1Z_2e^2}{a}\right)^{2m}, \tag{6.90}$$

where the numerical coefficient λ_m could be determined by going back to (6.23) and (6.50). It is, however, more efficient to determine λ_m by matching a power law to a more accurately determined scattering law. This could be either the function $f(\eta)$ or the stopping cross section. The latter takes the form

$$S = \int_0^{T_{\max}} T\,\mathrm{d}\sigma(E,T) = \frac{1}{1-m}C\gamma^{1-m}E^{1-2m}. \tag{6.91}$$

or, in dimensionless units,

$$s_n = \frac{\lambda_m}{2(1-m)}\epsilon^{1-2m}. \tag{6.92}$$

Figure 6.23 shows the variation of the exponent m found by matching the stopping cross sections shown in Fig. 6.22 in value and slope by the power form (6.91). You may note that there is a low-energy regime where a power law is a good approximation, and a high-energy regime close to Rutherford scattering.

The intermediate regime around $\epsilon \sim 1$ has frequently been characterized by $m = 1/2$ (Bohr, 1948, Nielsen, 1956, Firsov, 1958, Lindhard et al., 1963, Winterbon et al., 1970). Such a cross section is approximately equivalent with a potential $\propto 1/R^2$. Niels Bohr employed this potential to characterize the effect of 'excessive screening', i.e., interactions at distances $R \sim a$ and beyond. The corresponding

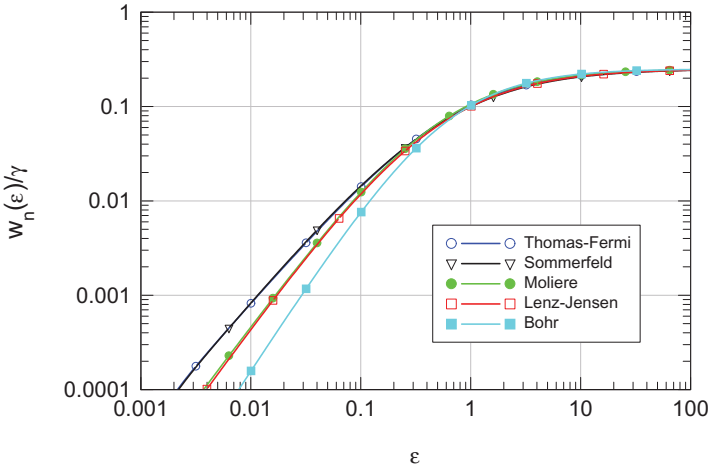

Fig. 6.24 Nuclear straggling in dimensionless units, (6.94)

differential cross section $\mathrm{d}\sigma(T) \propto \mathrm{d}T/T^{3/2}$ has convenient analytical properties. From (6.91) the particularly valuable property emerges that the stopping cross section becomes independent of energy for $m = 1/2$. The differential cross section expressed in the scattering angle becomes $\mathrm{d}\sigma(\Theta) \propto \mathrm{d}\Theta/\Theta^2$ at small angles. It will turn out that also this functional shape has convenient analytic properties.

The main drawback of the R^{-2} potential is that with its convenient analytic properties, numerous results can be derived that seemingly depend only on one parameter and frequently have the simple appearance of generally valid relationships. In other words, there is a temptation to ignore the limited range of validity of this particular interaction potential. This pitfall can be avoided with due care.

6.4.3 Straggling

The expression for straggling,

$$\frac{\mathrm{d}\Omega^2}{\mathrm{d}x} = \frac{\mathrm{d}}{\mathrm{d}x}\left\langle (\Delta E - \langle \Delta E\rangle)^2\right\rangle = N\int T^2 \mathrm{d}\sigma(E,T) \tag{6.93}$$

may, for Lindhard-Scharff scaling, be written in the form

$$\frac{\mathrm{d}}{\mathrm{d}\xi}\left\langle (\Delta\epsilon - \langle \Delta\epsilon\rangle)^2\right\rangle = w_n = \frac{\gamma}{\epsilon^2}\int_0^{\epsilon} \mathrm{d}\eta\, \eta^2 f(\eta)\,, \tag{6.94}$$

where according to (6.82)

$$\xi = N\pi a^2 \gamma x\,. \tag{6.95}$$

This is illustrated in Fig. 6.24 for the potentials shown in Fig. 6.14. This function approaches the value 1/4 at high energies (cf. Problem 6.8).

You may notice, by comparing Fig. 6.24 with Fig. 6.22, that $\sqrt{w_n}$ exceeds the stopping cross section s_n for $\epsilon > 1$. This is the regime where the differential cross section approaches the Rutherford cross section. If there were no electronic stopping, straggling would be governed by an analogue of the Landau distribution discussed in Sect. 9.3.2, Vol. 1.

6.4.4 Measurements of Nuclear Stopping

6.4.4.1 Experimental Aspects

Only a minute fraction of the experimental literature on stopping cross sections is devoted to nuclear stopping. This is by no means accidental.

Direct measurements of nuclear stopping have to take place at energies where electronic stopping is not dominating by several orders of magnitude, and accurate measurements require energies where nuclear stopping actually dominates. Even then, separating electronic from nuclear stopping is not a trivial task, as you will see in Chap. 7.

There are problems even in the absence of significant electronic stopping, which have been discussed in detail by Sidenius (1974):

- Nuclear energy loss is coupled to angular deflection. In the standard geometry the energy loss is measured in the beam direction with a narrow detection angle. Except for $M_1 \gg M_2$, ions with large energy losses will not be detected. While this simplifies the measurement of electronic stopping cross sections, nuclear stopping cross sections will be underestimated. Evidently, measurements of nuclear stopping require wide-angle detection. For $M_1 < M_2$ even detection in the backward direction may be necessary.
- In addition to beam particles the particle flux also contains energetic recoil atoms.

6.4.4.2 Results

In order to limit straggling to an acceptable limit, targets may have to be thin. Therefore, most direct measurements have been performed on gases.

Figure 6.25 shows measurements of Hvelplund (1975) with very heavy ions on hydrogen gas. The large mass ratio M_1/M_2 facilitates the detection of the entire scattered beam, and energies are low enough so that electronic stopping constitutes only a minor correction. Data for individual ions seem to fall on smooth curves which, by and large, lie in between the Thomas-Fermi and Lenz-Jensen predictions. Data for different ions differ significantly, more than what one would expect from universal scaling relations. Later time-of-flight data by Martini (1976) for the Pb-H_2 system (not shown in the graph) tend to agree with the data of Sidenius at the

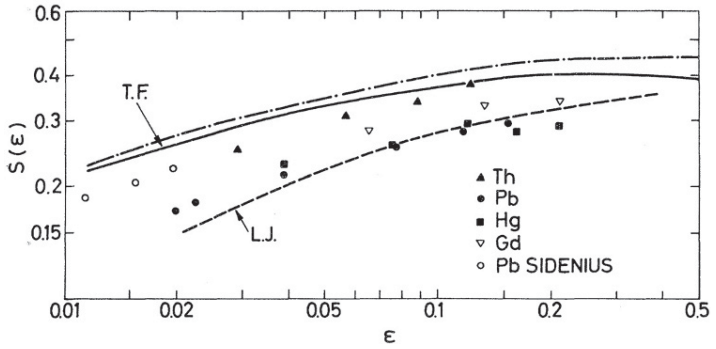

Fig. 6.25 Stopping cross section of heavy ions in hydrogen gas compared with theory. Data labelled Th, Pb, Hg and Gd: Stopping cross sections from Hvelplund (1975). Data labelled Sidenius from Sidenius (1963). Solid line: Thomas-Fermi nuclear stopping; dashed line: Lenz-Jensen nuclear stopping; dash-dotted curve: Total Thomas-Fermi stopping. From Hvelplund (1975)

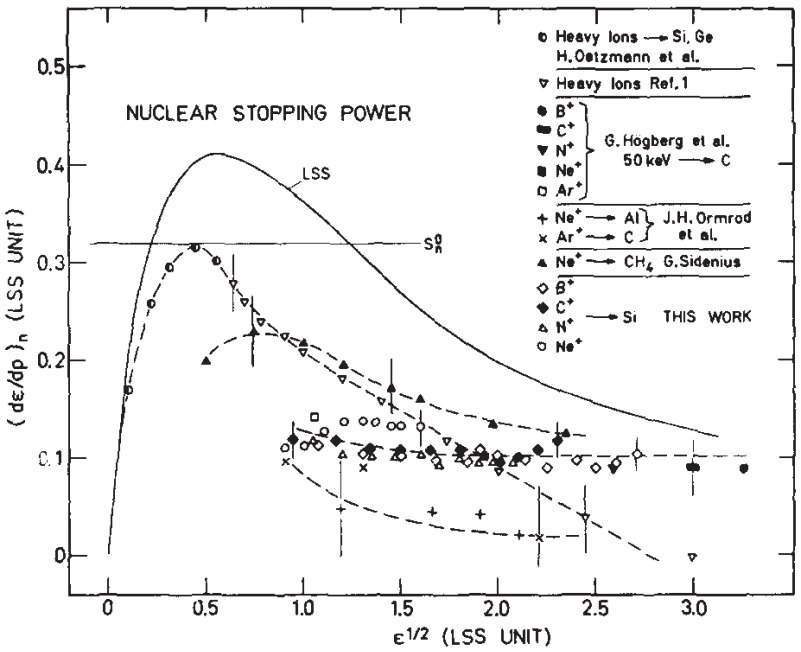

Fig. 6.26 Nuclear stopping cross section in Si. Comparison of various experimental results with universal stopping formula. See text. From Grahmann and Kalbitzer (1976)

low-energy end and with those of Hvelplund in the high-energy end. On the other hand, the difference between two data sets for Pb ions is as large as the difference between Th and Hg, suggesting that part of the deviation from scaling may be due to experimental error.

Figure 6.26 is another witness of the problematic nature of direct measurements of nuclear stopping. Experimental data for stopping of B, C, N, Ne and Ar ions in CH_4, C, Al, Si and Ge from several sources (Ormrod and Duckworth, 1963, Ormrod et al., 1965, Högberg and Skoog, 1972, Sidenius, 1974, Oetzmann et al., 1975, Grahmann and Kalbitzer, 1976) have been plotted in Lindhard-Scharff dimensionless units and compared with the Thomas-Fermi prediction of Lindhard et al. (1968). Apart from drastic deviations from the expected scaling behaviour you will notice that all experimental results lie significantly below the theoretical curve, even in the upper half of the abscissa variable, $\epsilon^{1/2} > 1.5$, where the stopping cross section should be independent of the adopted screening function according to Fig. 6.22.

What went wrong here? Firstly, data by Ormrod and Duckworth (1963), Ormrod et al. (1965), Högberg and Skoog (1972) had been taken with the aim of measuring electronic stopping. Nuclear stopping was minimized by choosing a detection angle that eliminated particles with a high nuclear energy loss. These data should not have been included in the graph. Secondly, data labelled 'this work' by Grahmann and Kalbitzer (1976) all refer to mass ratios $M_1/M_2 < 1$, where a noticeable fraction of the beam particles will suffer large-angle backscattering.

Conversely, the highest stopping cross sections listed in the graph refer to $M_1/M_2 > 1$ where this effect is much less pronounced. While the observed deviation from the Thomas-Fermi prediction fits well into the general pattern in the low-energy portion of the graph, the relatively small deviation found for the data of Sidenius (1974) can be ascribed to the fact that the target is CH_4, for which the scaling behaviour of atomic targets cannot be expected to be accurately fulfilled.

In brief, what remains of Fig. 6.26 is a scatter between relevant data of the same approximate magnitude as the one in Fig. 6.12, which serves as a theoretical basis for Lindhard-Scharff scaling.

The technique of Doppler-shift attenuation described briefly in Sect. 7.4.4, Vol. 1, has also been applied in low-energy stopping (Bister et al., 1975, Shane et al., 1976). While separation of nuclear from electronic stopping is not a trivial matter, comparisons with the Lindhard-Scharff predictions of the total stopping cross sections are much more favourable than what one might extract from Fig. 6.26.

6.5 Discussion and Outlook

The discussion in this chapter is based on Chap. 3, Vol. 1. Applications discussed there were dealing mainly with plain Coulomb interaction. Tools collected in the present chapter are quite adequate to treat scattering and nuclear stopping in the medium to upper keV regime and above. With equivalent knowledge of electronic stopping in this energy regime—to be discussed in Chap. 8—and suitable statistical tools—to be collected in Chap. 9—you will be well equipped to treat several aspects of particle penetration. Limitations prevail to lower energies especially in the medium and lower eV regime, where the many-body nature of collisions becomes exceedingly important, and where many-body potentials may be needed for quan-

titative predictions. These aspects become particularly important in the theory of radiation effects, the main subject of Volume 3 of this series.

Problems

6.1. Estimate the interaction potential between an ion 1 with a charge $q_1 e$ and a neutral atom 2 from the electrostatic interaction energy

$$\mathcal{V}(R) = -e \int \mathrm{d}^2 \boldsymbol{r}\, \rho_1(\boldsymbol{r}) \Phi_2(\boldsymbol{r}) \tag{6.96}$$

between two stiff charge distributions, characterized by potentials

$$\Phi_1(\boldsymbol{r}) = \frac{q_1 e}{r_1} + \frac{(Z_1 - q_1)e}{r_1} \mathrm{e}^{-r_1/a_1} \tag{6.97}$$

$$\Phi_2(\boldsymbol{r}) = \frac{Z_2 e}{r_2} \mathrm{e}^{-r_2/a_2}, \tag{6.98}$$

where r_1 and r_2 denote the distance from the respective nuclei, and a_1 and a_2 are arbitrary screening radii.

6.2. Figure 6.1 indicates that the screening function (6.5) turns negative at large values of R. Convince yourself, e.g. by looking at the limit $a_1/a_2 = 1$, that this is not a calculational error.

6.3. Consider a neutral Thomas-Fermi atom with a Yukawa-type charge density. Determine the kinetic energy per volume as well as the electrostatic energy per volume and compare the dependence on the distance r from the nucleus in the two cases. Show that regardless of atomic number and screening radius, electrostatic energy dominates at small r, while the opposite holds at large r.

6.4. Following Firsov (1957b) show that for a neutral system, the solution of the Thomas-Fermi equation minimizes the total energy. Hint: Set $\rho = \rho_0 + \delta\rho$, where ρ_0 is the charge density connected to an exact solution of the Thomas-Fermi equation for the potential. Insert this into (1.18) for $v = 0$ and expand in powers of $\delta\rho$. The zero-order term represents the exact energy, the linear term vanishes, and the quadratic term can be written in the form

$$\delta^2 \mathcal{E} = \frac{5}{9} \kappa_k \int \mathrm{d}^3 \boldsymbol{r}\, \frac{\delta\rho(\boldsymbol{r})^2}{\rho_0(\boldsymbol{r})^{1/3}} + \frac{e^2}{2} \int \mathrm{d}^3 \boldsymbol{r}\, \mathrm{d}^3 \boldsymbol{r}' \frac{\delta\rho(\boldsymbol{r}) \delta\rho(\boldsymbol{r}')}{|\boldsymbol{r} - \boldsymbol{r}'|}, \tag{6.99}$$

which is positive.

6.5. By solving Problem 3.8, Vol. 1, you will arrive at the scattering law for a Bohr potential, (6.32),

$$\Theta(p) = \frac{2Z_1Z_2}{m_0v^2} K_1\left(\frac{p}{a}\right) \tag{6.100}$$

for small scattering angles, where K_1 denotes a modified Bessel function in standard notation (Abramowitz and Stegun, 1964). Evaluate (6.31) for this scattering law.

Write the result in the form

$$\frac{2Z_1Z_2e^2}{\hbar v} \gg g_2(p/a), \tag{6.101}$$

and demonstrate that $g_2(p/a) \equiv 1$ for unscreened Coulomb interaction.

6.6. Khodyrev (2000) argues that the Bohr criterion (6.24) ought to be replaced by

$$2p \gg \lambda\!\!\!^{-}. \tag{6.102}$$

Identify the difference to Bohr's argument, and try to form an opinion on what is most relevant.

6.7. Problem 3.6, Vol. 1, concerns the scattering integral for the potential $\mathcal{V}(R) = A/R^2$, where A is a constant. Use the solution of that problem, $\Theta = \pi(1 - p/\sqrt{p^2 + A/E_r})$, to derive the potential by means of the Firsov inversion formula, (6.69).

6.8. Show that for Rutherford scattering, the function $w(\epsilon)/\gamma$ shown in Fig. 6.24 reduces to $w(\epsilon)/\gamma \equiv 1/4$.

References

Aberth W., Lorents D.C., Marchi R.P. and Smith F.T. (1965): Effect of nuclear symmetry in ion-atom scattering. Phys Rev Lett **14**, 776–778

Abrahamson A.A. (1963a): Repulsive interaction potentials between rare-gas atoms. heteronuclear two-center systems. Phys Rev **133**, A990–A1004

Abrahamson A.A. (1963b): Repulsive interaction potentials between rare-gas atoms. homonuclear two-center systems. Phys Rev **130**, 693–707

Abrahamson A.A., Hatcher R.D. and Vineyard G.H. (1961): Interatomic repulsive potentials at very small and intermediate separations. Phys Rev **121**, 159–171

Abramowitz M. and Stegun I.A. (1964): *Handbook of mathematical functions*. Dover, New York

Adams J.B. and Foiles S.M. (1990): Development of an embedded-atom potential for a bcc metal: Vanadium. Phys Rev B **41**, 3316–3328

Afrosimov V.V., Gordeev Y.S., Nikulin V.K., Polyanski A.M. and Shergin A.P. (1972): Singularities in scattering of atomic particles in collisions involving the excitation of inner electron shells. Zh Exp Teor Fiz **62**, 848–862. [Engl. Transl. in Sov. Phys. JETP 35, 449-456 (1972)]

Amdur I. and Mason E.A. (1956): Scattering of high velocity neutral particles .IX. Ne-A; A-Ne. J Chem Phys **25**, 632–634

Biersack J.P. and Ziegler J.F. (1982): Refined universal potentials in atomic collisions. Nucl Instrum Methods **194**, 93–100

Bister M., Anttila A. and Keinonen J. (1975): Method for determination of nuclear and electronic stopping power parameters. Phys Lett A **53**, 471–472

Bohr N. (1948): The penetration of atomic particles through matter. Mat Fys Medd Dan Vid Selsk **18 no. 8**, 1–144

Born M. and Mayer J.E. (1932): Zur Gittertheorie der Ionenkristalle. Physica B **75**, 1–18

Daw M.S. (1989): Model of metallic cohesion: The embedded-atom method. Phys Rev B **39**, 7441

Daw M.S. and Baskes M.I. (1983): Semiempirical, quantum-mechanical calculation of hydrogen embrittlement in metals. Phys Rev Lett **50**, 1285

Daw M.S. and Baskes M.I. (1984): Embedded-atom method – derivation and application to impurities, surfaces, and other defects in metals. Phys Rev B **29**, 6443–6453

Dedkov G.V. (1984): On the theory of the interatomic interaction potential at high projectile velocities. Radiat Eff Lett **86**, 127–132

Dedkov G.V. (1989): Interatomic interaction potentials in the electron gas approximation: Static case. Nucl Instrum Methods B **36**, 14–22

Dedkov G.V. (1995): The interatomic interaction potentials in radiation physics. phys stat sol A **149**, 453–514

Demkov Y.N., Ostrovskii V.N. and Berezina N.B. (1971): Uniqueness of the Firsov inversion method and focusing potentials. Zh Eks Teor Fiz **60**, 1604–1610. [Engl. Transl. in Sov. Phys. JETP 33, 867-870]

Everhart E., Carbone R.J. and Stone G. (1955): Differential cross-section measurements for large-angle collisions of helium, neon and argon ions with argon atoms at energies to 100 keV. Phys Rev **98**, 1045–1049

Fermi E. and Amaldi E. (1934): Le orbite degli elementi. Mem Accad Italia **6**, 119–149

Firsov O.B. (1953): Opredelenie sil, deistvuyushchikh mezhdu atomami, pri pomoshchi differentsialnogo effektivnogo secheniya uprugogo rasseyaniya. Zh Eksp Teor Fiz **24**, 279

Firsov O.B. (1957a): Calculation of the interaction potential of atoms. Zh Eksp Teor Fiz **33**, 696. [Engl. transl. Sov. Phys. JETP 6, 5340-537 (1958)]

Firsov O.B. (1957b): Interaction energy of atoms for small nuclear separations. Zh Eksp Teor Fiz **32**, 1464–1469. [Engl. transl. Sov. Phys. JETP **5**, 1192-1196(1957)]

Firsov O.B. (1958): Scattering of ions by atoms. Zh Eksp Teor Fiz **34**, 447. [Engl. transl. Soviet Physics Jetp 7, 308-311 (1958)]

Gilbert T.L. and Wahl A.C. (1967): Single-configuration wavefunctions and potential curves for ground states of He_2, Ne_2 and Ar_2. J Chem Phys **47**, 3425–

Gombas P. (1949): *Die Statistische Theorie des Atoms*. Springer, Vienna

Grahmann H. and Kalbitzer S. (1976): Nuclear and electronic stopping powers of low energy ions with $Z \leq 10$ in silicon. Nucl Instrum Methods **132**, 119–123

Günther K. (1964): Über die Existenz eines Maximalprinzips als äquivalente Formulierung des Thomas-Fermi-Dirac-Modells und das TFD-Wechselwirkungspotential v on Atomen. Ann Physik **14**, 296–309

Hartree D.R. and Hartree W. (1938): Self-consistent field with exchange for potassium and argon. Rev Mod Phys **166**, 450–464

Hartung H., Fricke B., Sepp W.D., Sengler W. and Kolb D. (1985): Theoretical evidence for quasi-molecular structure at small internuclear distances in elastic ion-atom scattering. J Phys B **18**, L433–L437

Herman F. and Skillman S. (1963): *Atomic structure calculations*. Prentice Hall, New Jersey

Högberg G. and Skoog R. (1972): Non-evidence for Z_1 oscillations of the nuclear ion-atom interaction in an amorphous target. Radiat Eff **13**, 197–202

Hoyt F.C. (1939): The determination of force fields from scattering in the classical theory. Phys Rev **55**, 664–665

Hvelplund P. (1975): Energy loss and straggling of 100-500 keV $_{90}$Th, $_{82}$Pb, $_{80}$Hg, and $_{64}$Gd in H_2. Phys Rev A **11**, 1921–1927

Jensen H. (1932): Die Ladungsverteilung in Ionen und die Gitterkonstante des Rubidiumbromids nach der statistischen Methode. Z Physik **77**, 722

Kaminker D.M. and Fedorenko N.V. (1955): Single scatter of argon ions during stripping in a gas. Zh Tekh Fiz **25**, 2239–2255

Khodyrev V.A. (2000): On the origin of the Bloch correction in stopping. J Phys B **33**, 5045–5056

Kim Y.S. and Gordon R.G. (1974): Ionrare gas interactions on the repulsive part of the potential curves. J Chem Phys **60**, 4323–4331

Klein O. (1932): Zur Berechnung von Potentialkurven für zweiatomige Moleküle mit Hilfe von Spektraltermen. Z Physik **76**, 226–235

Kuzmin V. (2006): Range parameters of heavy ions in carbon calculated with first-principles potentials. Nucl Instrum Methods B **249**, 13–17

Lane G.H. and Everhart E. (1960): Ion-atom potential functions obtained from keV scattering data. Phys Rev **120**, 2064–

Lennard-Jones J.E. (1924): On the determination of molecular fields. Proc Roy Soc A **106**, 463–477

Lenz W. (1932): Über die Anwendbarkeit der statistischen Methode auf Ionengitter. Z Physik **77**, 713

Lindhard J. (1965): Influence of crystal lattice on motion of energetic charged particles. Mat Fys Medd Dan Vid Selsk **34 no. 14**, 1–64

Lindhard J., Nielsen V. and Scharff M. (1968): Approximation method in classical scattering by screened Coulomb fields. Mat Fys Medd Dan Vid Selsk **36 no. 10**, 1–32

Lindhard J., Scharff M. and Schiøtt H.E. (1963): Range concepts and heavy ion ranges. Mat Fys Medd Dan Vid Selsk **33 no. 14**, 1–42

Lockwood G.J., Helbig H.F. and Everhart E. (1963): Measurements of resonant electron capture in He^+ on He collisions. Phys Rev **132**, 2078–2082

Loftager P., Besenbacher F., Jensen O.S. and Sørensen V.S. (1979): Experimental study of effective interaction potentials. Phys Rev A **20**, 1443

Loftager P. and Hermann G. (1968): Influence of Q values in atomic single collisions on observed scattering cross sections and som Q values. Phys Rev Lett **21**, 1623–1626

Martini V. (1976): Stopping cross-section measurements with heavy ions in keV energy-range in gases by time-of-flight spectroscopy. Nucl Instrum Methods **139**, 163–167

Molière G. (1947): Theorie der Streuung schneller geladener Teilchen I. Einzelstreuung am abgeschirmten Coulomb-Feld. Z Naturforsch **2a**, 133–145

Nielsen K.O. (1956): The range of atomic particles with energies about 50 keV. In M.L. Smith, editor, *Electromagnetically Enriched Isotopes and Mass Spectrometry*. AERE Harwell, Butterworth Sci. Pub., London

Nikulin V.K. (1971): Calculation of repulsive atomic-interaction potentials from statistical theory. Zh Tekh Fiz **41**, 33–40. [Engl. transl.: Sov. Phys. Techn. Phys. 16, 21-27 (1971)]

Nørskov J.K. (1977): Electronic structure of H and He in metal vacancies. Sol St Comm **24**, 691–693

Nørskov J.K. (1982): Covalent effects in the effective-medium theory of chemical binding: Hydrogen heats of solution in the 3d metals. Phys Rev B **26**, 2875–2885

Nørskov J.K. and Lang N.D. (1980): Effective-medium theory of chemical binding: Application to chemisorption. Phys Rev B **21**, 2131–2136

Oen O.S. (1983): Universal shadow cone expressions for an atom in an ion-beam. Surf Sci **131**, L407–L411

Oetzmann H., Feuerstein A., Grahmann H. and Kalbitzer S. (1975): Range parameters of heavy-ions in amorphous targets at LSS-energies of $0.0006 \leq \epsilon \leq 0.3$. Phys Lett A **55**, 170–172

Olsen J.O., Andersen T., Barat M., Courbin-Gaussorgues C., Sidis V., Pommier J., Agusti J., Andersen N. and Russek A. (1979): Excitation and charge transfer in low-energy Na^+-Ne collisions. Phys Rev A **19**, 1457–1484

Ormrod J.H. and Duckworth H.E. (1963): Stopping cross sections in carbon for low-energy atoms with $Z \leq 12$. Can J Physics **41**, 1424–1442

Ormrod J.H., MacDonald J.R. and Duckworth H.E. (1965): Some low-energy atomic stopping cross sections. Can J Physics **43**, 275–284

Robinson M.T. (1970): Table of classical scattering integrals. Tech. Rep. ORNL-4556, Oak Ridge National Laboratory

Shane K.C., Laumer H. and Seaman G.G. (1976): Energy loss of low-energy ^{40}Ca ions in C. J Appl Phys **47**, 2286–2288

Sidenius G. (1963): In M.R.C. McDowell, editor, *Proceedings of the 3rd International Conference on Atomic Collisions*, 709. North Holland, Amsterdam

Sidenius G. (1974): Systematic stopping cross section measurements with low energy ions in gases. Mat Fys Medd Dan Vid Selsk **39 no. 4**, 1–32

Sigmund P. (1997): Charge-dependent electronic stopping of swift nonrelativistic heavy ions. Phys Rev A **56**, 3781–3793

Srivastava K.P. (1958): Unlike molecular interactions and properties of gas mixtures. J Chem Phys **28**, 543–549

Stillinger F.H. and Weber T.A. (1985): Computer simulation of local order in condensed phases of silicon. Phys Rev B **31**, 5262–5271

Stott M.J. and Zaremba E. (1980): Quasiatoms: An approach to atoms in nonuniform electron systems. Phys Rev B **22**, 1564–1583

Tersoff J. (1986): New empirical model for the structural properties of silicon. Phys Rev Lett **56**, 632–635

Wedepohl P.T. (1967): Influence of electron distribution on atomic interaction potentials. Proc Phys Soc **92**, 79–93

Wilson W.D. and Bisson C.L. (1971): Inert gases in solids: Interatomic potentials and their influence on rare-gas mobility. Phys Rev B **3**, 3984–3992

Wilson W.D., Haggmark L.G. and Biersack J.P. (1977): Calculations of nuclear stopping, ranges and straggling in the low-energy region. Phys Rev B **15**, 2458–2468

Winterbon K.B. (1972): Heavy-ion range profiles and associated damage distributions. Radiat Eff **13**, 215–226

Winterbon K.B., Sigmund P. and Sanders J.B. (1970): Spatial distribution of energy deposited by atomic particles in elastic collisions. Mat Fys Medd Dan Vid Selsk **37 no. 14**, 1–73

Witte H. and Wölfel E. (1958): Electron distributions in NaCl, LiF, CaF_2, and Al. Rev Mod Phys **30**, 51–55

Yamamura Y. and Takeuchi W. (1984): Large-angle surface scattering of low-energy ions in the 2-atom scattering model. Radiat Eff **82**, 73–84

Ziegler J.F., Biersack J.P. and Littmark U. (1985): *The stopping and range of ions in solids*, vol. 1 of *The stopping and ranges of ions in matter*. Pergamon, New York

Ziemba F.P. and Everhart E. (1959): Resonance phenomena in large-angle helium ion-helium atom collisions. Phys Rev Lett **2**, 299–301

Zinoviev A.N. (2011): Interaction potentials for modeling of ion-surface scattering. Nucl Instrum Methods B **269**, 829–833

Chapter 7
Multiple Scattering

Abstract This chapter addresses multiple scattering of swift ions. Special attention is devoted to basic statistical tools. Angular profiles are considered in three dimensions (Goudsmit-Saunderson) as well as two and one dimension (small-angle approximation). Also lateral profiles as well as correlated angular-lateral distributions are considered. The correlation between energy loss and angular scattering is analysed mainly with a view to the separation of nuclear from electronic stopping.

7.1 Introductory Comments

The topic of multiple scattering[1] has been introduced in Sect. 2.4, Vol. 1. The fact that differential cross sections increase toward small laboratory scattering angles, and possibly diverge, implies that a given deflection angle typically is the result of several scattering events. Thus, multiple scattering is a statistical process. This is particularly true for small scattering angles.

From Volume 1 you may recall that there is a qualitative difference between multiple scattering of light and heavy particles. Large scattering angles are much more frequent for electrons and positrons than for protons and heavier particles. Moreover, multiple scattering of electrons and positrons is due to both target nuclei and electrons, whereas multiple scattering of protons and heavier particles is almost exclusively due to target nuclei[2]. Only within a very narrow angular range is there a noticeable contribution from target electrons. However, target electrons contribute indirectly by screening the ion-target interaction potential.

Following the general scope of this volume we shall focus on multiple scattering of ions. Although it is becoming more and more common to estimate multiple-scattering phenomena by computer simulation, statistical methods have been devel-

[1] Part of the text and many graphs have been taken over in more or less modified form from Sigmund (1991).

[2] An exception occurs in channelled motion, where angular deflection by nuclei is drastically reduced.

P. Sigmund, *Particle Penetration and Radiation Effects Volume 2*,
Springer Series in Solid-State Sciences 179, DOI: 10.1007/978-3-319-05564-0_7,

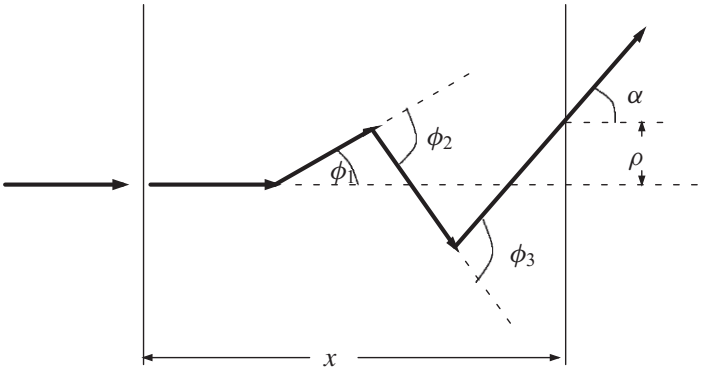

Fig. 7.1 Multiple scattering in a layer of thickness x: Notations

oped to a high degree of sophistication over the past century and are still competitive.

In Sect. 2.4.2, Vol. 1 the Bohr-Williams model for multiple scattering was introduced briefly, where the angular distribution of an initially well-collimated beam was divided up into a large-angle portion governed by Rutherford's law and a gaussian small-angle portion. Similar arguments were employed in Sect. 9.3.1 to characterize energy-loss straggling.

The analogy between energy loss and multiple angular deflection is not restricted to the Bohr-Williams theory. It applies to the general statistical theory of stopping and scattering as well as other approximation methods do. Therefore it will be helpful to let the structure of this chapter to some extent follow the outline of Chap. 9, Vol. 1.

7.2 Needs

The standard problem in multiple scattering deals with the angular distribution $F(\alpha, x)$ of an initially well-collimated beam after penetration of a slab of a given thickness x. The notation is defined in Fig. 7.1. Scattering angles in individual scattering events are denoted by $\boldsymbol{\phi}$, while the cumulative deflection angle is denoted by α.

In general, $\boldsymbol{\alpha}$ is to be understood as a vector on the unit sphere, but also its projection on a plane may be of interest, e.g. for visual inspection of trajectories in a cloud or bubble chamber, in photographic emulsion and the like.

Standard theory of multiple scattering ignores energy loss. For layer thicknesses where energy loss cannot be ignored, one may introduce an effective beam energy equal to the average between entrance and exit energy. However, energy loss can be incorporated rigorously by operating with velocity vectors in a three-dimensional description.

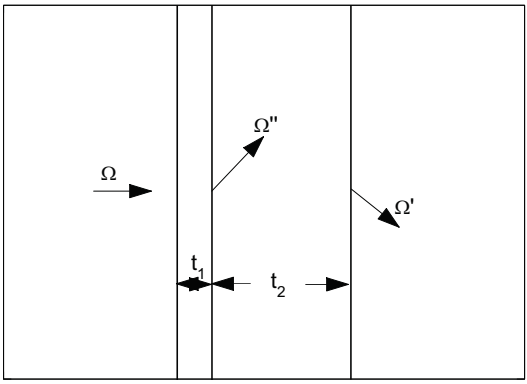

Fig. 7.2 Multiple scattering in two adjacent layers

In addition to the deflection angle also the lateral displacement from a straight trajectory may be of interest and readily measurable whenever trajectories are visualized. The lateral displacement is denoted by ρ in Fig. 7.1. Pronounced angular deflection may result in a noticeable lateral displacement. In other words, angular and lateral distributions must be expected to be correlated, and knowledge of correlated angular-lateral distributions may be needed in certain situations.

Figure 7.1 assumes force-free motion between collision events. Static or time-dependent electric and magnetic fields may complicate the matter. The disturbing influence of gravitation is most often too small to be measurable.

While the simple slab geometry may appear idealized, it may nevertheless serve as a most useful tool in the treatment of more complex experimental geometries: Knowledge of angular deflection and lateral spread over a finite pathlength may well be utilized in estimates of slit scattering on an aperture, reflection of a beam under grazing incidence on a planar or stepped surface, and similar situations.

Further complications are target nonuniformities such as inhomogeneous chemical composition, voids, bubbles and surface topography.

Finally, changes of the beam along its trajectory caused by charge exchange with the medium (Chap. 3) may be influential and have been found to be measurable.

7.3 Statistics: Angular Distributions

In this section, general relations determining energy-loss spectra derived in Chap. 9.2, Vol. 1, will be generalized to multiple-scattering distributions. A central underlying assumption is the statistical independence of successive collision events. This is considered to be justified for penetration through a random medium, as long as charge exchange can be considered negligible.

7.3.1 Two-Layer Argument

Consider a projectile penetrating through a homogeneous, isotropic and infinite medium, where it can be scattered but does not lose or gain kinetic energy. Let $F(\mathbf{\Omega}, \mathbf{\Omega}', t)\, \mathrm{d}^2\mathbf{\Omega}'$ be the probability for its direction of motion at time t to lie in the interval $(\mathbf{\Omega}', \mathrm{d}^2\mathbf{\Omega}')$, if it was $\mathbf{\Omega}$ at time zero. Here, $\mathbf{\Omega}$ and $\mathbf{\Omega}'$ are unit vectors.

In complete analogy to Sect. 9.2.1, Vol. 1, we may then write down a Chapman-Kolmogorov-type equation

$$F(\mathbf{\Omega}, \mathbf{\Omega}', t_1 + t_2) = \int \mathrm{d}^2\mathbf{\Omega}'' F(\mathbf{\Omega}, \mathbf{\Omega}'', t_1) F(\mathbf{\Omega}'', \mathbf{\Omega}', t_2)\,, \tag{7.1}$$

if we may assume statistical independence of the events taking place in the two time intervals. This relation expresses the fact that the angular distribution after time $t_1 + t_2$ is a convolution of the distributions characterizing scattering in the two time intervals t_1 and t_2.

Figure 7.2 illustrates the physics on a sandwich foil. We could have replaced the time variable t in (7.1) by the layer thickness x, implying small scattering angles, but by using time (or pathlength) as a variable we are independent of this restriction.

7.3.2 Expansion in Legendre Polynomials

For an isotropic medium the angular distribution depends only on the angle between the initial and final directions $\mathbf{\Omega}$ and $\mathbf{\Omega}'$, respectively. We may express this as

$$F(\mathbf{\Omega}, \mathbf{\Omega}', t) \equiv F(\mathbf{\Omega} \cdot \mathbf{\Omega}', t) \tag{7.2}$$

and expand the distribution in terms of Legendre polynomials in the variable $\cos\alpha = \mathbf{\Omega} \cdot \mathbf{\Omega}'$,

$$F(\mathbf{\Omega} \cdot \mathbf{\Omega}', t) = \sum_{\ell=0}^{\infty} (2\ell + 1) A_\ell(t) P_\ell(\cos\alpha) \tag{7.3}$$

with yet unknown coefficients $A_\ell(t)$, from which a factor $2\ell + 1$ has been split off for convenience. Insertion of (7.3) into (7.1) leads to

$$\sum_{\ell=0}^{\infty} (2\ell + 1) A_\ell(t_1 + t_2) P_\ell(\cos\alpha) = \sum_{\ell=0}^{\infty} \sum_{\ell'=0}^{\infty} (2\ell + 1)(2\ell' + 1) A_\ell(t_1) A_{\ell'}(t_2) \times \int \mathrm{d}^2\mathbf{\Omega}'' P_\ell(\mathbf{\Omega} \cdot \mathbf{\Omega}'') P_{\ell'}(\mathbf{\Omega}'' \cdot \mathbf{\Omega}'). \tag{7.4}$$

The integral over $\mathrm{d}^2\mathbf{\Omega}''$ may be evaluated after introduction of spherical coordinates. With the choice

$$\boldsymbol{\Omega} = (1, 0, 0) \tag{7.5}$$

$$\boldsymbol{\Omega}' = (\cos\alpha, \sin\alpha\cos\chi, \sin\alpha\sin\chi) \tag{7.6}$$

$$\boldsymbol{\Omega}'' = (\cos\theta, \sin\theta\cos\psi, \sin\theta\sin\psi) \tag{7.7}$$

it reads

$$\int \mathrm{d}^2\boldsymbol{\Omega}'' P_\ell(\boldsymbol{\Omega}\cdot\boldsymbol{\Omega}'') P_{\ell'}(\boldsymbol{\Omega}''\cdot\boldsymbol{\Omega}') = \int_{-1}^{1} \mathrm{d}\cos\theta \int_0^{2\pi} \mathrm{d}\psi \times P_\ell(\cos\theta) P_{\ell'}(\cos\alpha\cos\theta + \sin\alpha\sin\theta\cos(\psi-\chi)). \tag{7.8}$$

Now, insertion of the addition theorem for spherical harmonics, cf. (A.58), Vol. 1,

$$P_{\ell'}(\cos\alpha\cos\theta + \sin\alpha\sin\theta\cos(\psi-\chi)) = \frac{4\pi}{2\ell'+1}\sum_{m=0}^{\ell'} Y_{\ell' m}(\alpha,\chi) Y^*_{\ell' m}(\theta,\psi) \tag{7.9}$$

shows immediately that after integration over the azimuthal angle ψ only the terms for $m = 0$ remain, so that

$$\int \mathrm{d}^2\boldsymbol{\Omega}'' P_\ell(\boldsymbol{\Omega}\cdot\boldsymbol{\Omega}'') P_{\ell'}(\boldsymbol{\Omega}''\cdot\boldsymbol{\Omega}') = 2\pi P_{\ell'}(\cos\alpha)\int_{-1}^{1} \mathrm{d}\cos\theta P_\ell(\cos\theta) P_{\ell'}(\cos\theta) = \frac{4\pi}{2\ell+1}\delta_{\ell\ell'} P_\ell(\cos\alpha) \tag{7.10}$$

in view of the orthogonality relation for Legendre polynomials.

Insertion of (7.10) into (7.4), and noting that (7.1) has to be satisfied for arbitrary angles α you find

$$A_\ell(t_1 + t_2) = 4\pi A_\ell(t_1) A_\ell(t_2)\,. \tag{7.11}$$

Since this relation has to be satisfied for arbitrary values of t_1 and t_2, it has the general solution

$$A_\ell(t) = \frac{1}{4\pi}\mathrm{e}^{C_\ell t}\,, \tag{7.12}$$

with arbitrary coefficients C_ℓ that have to be determined from the physics involved.

We may now write (7.3) in the form

$$F(\boldsymbol{\Omega}\cdot\boldsymbol{\Omega}', t) = \sum_{\ell=0}^{\infty} \frac{2\ell+1}{4\pi}\mathrm{e}^{C_\ell t} P_\ell(\cos\alpha) \tag{7.13}$$

or, for a small time increment or pathlength,

$$F(\boldsymbol{\Omega}\cdot\boldsymbol{\Omega}',t)\simeq\sum_{\ell=0}^{\infty}\frac{2\ell+1}{4\pi}\left[1+C_\ell t\right]P_\ell(\cos\alpha);\quad t\text{ small}. \tag{7.14}$$

On the other hand, the scattering behaviour of a thin layer is governed by the differential cross section $d\sigma(\boldsymbol{\phi}) = K(\boldsymbol{\phi})\mathrm{d}^2\boldsymbol{\phi}$. In the single-collision limit we may write the angular distribution as

$$F(\boldsymbol{\Omega}\cdot\boldsymbol{\Omega}',t)=\left[1-Nvt\sigma\right]\frac{\delta(\cos\alpha-1)}{2\pi}+Nvt K(\alpha);\quad t\text{ small}, \tag{7.15}$$

where

$$\sigma=\int K(\boldsymbol{\phi})\,\mathrm{d}^2\boldsymbol{\phi} \tag{7.16}$$

is the total scattering cross section, N the number of scattering centres per volume and vt the travelled pathlength. Here the two terms on the right-hand side express the probabilities for zero and one collision, respectively, and the respective angular distributions.

After expansion of these expressions in terms of Legendre polynomials according to

$$\delta(\cos\alpha-1)=\sum_{\ell=0}^{\infty}\frac{2\ell+1}{2}P_\ell(\cos\alpha) \tag{7.17}$$

and

$$K(\alpha)=\sum_{\ell=0}^{\infty}\frac{2\ell+1}{2}P_\ell(\cos\alpha)\int K(\phi)P_\ell(\cos\phi)\,\mathrm{d}(\cos\phi)\,, \tag{7.18}$$

you recognize that the terms of zero order in t in (7.14) and (7.15) agree with each other already. Setting the terms of first order in t equal to each other leads to

$$C_\ell=-Nv\int K(\boldsymbol{\phi})\,\mathrm{d}^2\boldsymbol{\phi}\left[1-P_\ell(\cos\phi)\right]\,. \tag{7.19}$$

With this we have arrived at the following result for the angular distribution,

$$F(\alpha,t)\,2\pi\sin\alpha\,d\alpha=\sin\alpha\,d\alpha\sum_{\ell=0}^{\infty}(\ell+1/2)\mathrm{e}^{-Nvt\sigma_\ell}P_\ell(\cos\alpha) \tag{7.20}$$

with

$$\sigma_\ell=\int \mathrm{d}\sigma(\boldsymbol{\phi})\,\left[1-P_\ell(\cos\phi)\right]\,. \tag{7.21}$$

This result was derived by Goudsmit and Saunderson (1940). It is exact under the assumptions noted in the beginning of this section. It is equally valid for small and large deflection angles. Therefore its main application area lies in the scattering of electrons and positrons. The fact that the independent variable is the time or pathlength restricts the range of applicability of this formula to such situations where one of these quantities can be measured.

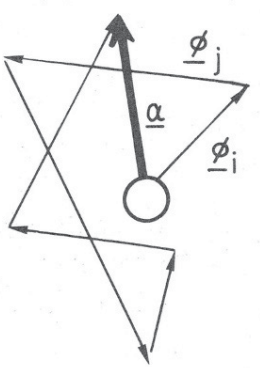

Fig. 7.3 Projection of a multiple-scattering trajectory on a plane perpendicular to the initial direction of motion. From Sigmund (1991)

7.3.3 Small-Angle Approximation

Multiple scattering of protons and heavier particles is mainly a small-angle phenomenon. In this case a small-angle approximation can be applied which constitutes a major simplification of the theory. This scheme implies that *all* angles, i.e., both the scattering angle ϕ in individual collisions and the total deflection angle α are small *in absolute terms*.

In order to specify the point, go back to (7.6) but expand up to first order in α,

$$\boldsymbol{\Omega}' \simeq (1, \alpha \cos\chi, \alpha \sin\chi) \equiv (1, \boldsymbol{e}') \,, \tag{7.22}$$

where we have introduced a two-dimensional vector

$$\boldsymbol{e}' = (\alpha \cos\chi, \alpha \sin\chi) \tag{7.23}$$

in the *impact plane*, i.e., a plane perpendicular to the initial direction of motion $\boldsymbol{\Omega}$ (Fig. 7.3).

Here is a summary of implications of this picture:

- The small-angle approximation must be expected to break down at angles where $\cos\alpha$ is significantly smaller than unity and α significantly larger than $\sin\alpha$.
- Within the range of validity of the small-angle approximation the penetration depth is equal to the travelled pathlength.
- $\boldsymbol{e}'$ is assumed to run over the entire impact plane, but discrepancies must be expected whenever α deviates significantly from $\tan\alpha$.

In other words, while the small-angle approximation is an extremely useful tool within its range of validity, repairing its deficiencies at deflection angles outside this range requires careful consideration of more than one type of correction.

7.3.4 Bothe Formula

The fact that the directional distribution only depends on the deflection angle was expressed by (7.2) in the rigorous description. In the small-angle approximation, the product $\boldsymbol{\Omega} \cdot \boldsymbol{\Omega}'$ reduces to unity. Instead, the deflection angle is expressed here as the difference $\boldsymbol{e}' - \boldsymbol{e}$. Hence,

$$F(\boldsymbol{e}, \boldsymbol{e}', t) \equiv F(\boldsymbol{e}' - \boldsymbol{e}, t) \tag{7.24}$$

for an isotropic scattering medium.

Instead of an expansion in Legendre polynomials, the appropriate transformation over an infinite plane is the Fourier transform,

$$F(\boldsymbol{e}' - \boldsymbol{e}, t) = \frac{1}{(2\pi)^2} \int \mathrm{d}^2\boldsymbol{k}\, \mathrm{e}^{\mathrm{i}\boldsymbol{k}\cdot(\boldsymbol{e}'-\boldsymbol{e})} F(\boldsymbol{k}, t)\,. \tag{7.25}$$

Insertion into (7.1) leads to

$$\frac{1}{(2\pi)^2} \int \mathrm{d}^2\boldsymbol{k}\, F(\boldsymbol{k}, t_1 + t_2) \mathrm{e}^{\mathrm{i}\boldsymbol{k}\cdot(\boldsymbol{e}'-\boldsymbol{e})} = \frac{1}{(2\pi)^4} \int \mathrm{d}^2\boldsymbol{k} \int \mathrm{d}^2\boldsymbol{k}' \int \mathrm{d}^2\boldsymbol{e}'' F(\boldsymbol{k}, t_1) F(\boldsymbol{k}', t_2) \mathrm{e}^{\mathrm{i}\boldsymbol{k}\cdot(\boldsymbol{e}''-\boldsymbol{e})} \mathrm{e}^{\mathrm{i}\boldsymbol{k}'\cdot(\boldsymbol{e}'-\boldsymbol{e}'')}. \tag{7.26}$$

Here the integration over $\mathrm{d}^2\boldsymbol{e}''$ can be carried out and leads to a delta function. With this you find that

$$F(\boldsymbol{k}, t_1 + t_2) = F(\boldsymbol{k}, t_1) F(\boldsymbol{k}, t_2)\,. \tag{7.27}$$

Since this relation has to be fulfilled for all t_1 and t_2, it follows that the function $F(\boldsymbol{k}, t)$ must be an exponential,

$$F(\boldsymbol{k}, t) = \mathrm{e}^{C(\boldsymbol{k})t}\,, \tag{7.28}$$

where $C(\boldsymbol{k})$ is an unknown function which can be determined from the single-scattering limit similar to the procedure applied in Sect. 7.3.2.

In that limit the angular distribution is given by

$$F(\boldsymbol{e}' - \boldsymbol{e}, t) \simeq [1 - Nvt\sigma]\, \delta(\boldsymbol{e}' - \boldsymbol{e}) + Nvt K(\boldsymbol{e}' - \boldsymbol{e})\,, \tag{7.29}$$

representing the probabilities for zero and one deflection event, respectively.

After inverse Fourier transform this reads

$$F(\boldsymbol{k}, t) = \int \mathrm{d}^2\boldsymbol{e}'\, \mathrm{e}^{-i\boldsymbol{k}\cdot(\boldsymbol{e}'-\boldsymbol{e})} F(\boldsymbol{e}' - \boldsymbol{e}, t) = 1 - Nvt \int \mathrm{d}^2\boldsymbol{\phi}\, K(\boldsymbol{\phi}) \left[1 - \mathrm{e}^{-i\boldsymbol{k}\cdot\boldsymbol{\phi}}\right], \tag{7.30}$$

where the integration variable $\boldsymbol{e}'$ has been replaced by

$$\boldsymbol{\phi} = \boldsymbol{e}' - \boldsymbol{e} \,. \tag{7.31}$$

Conversely, (7.28) reduces to

$$F(\boldsymbol{k}, t) \simeq 1 + C(\boldsymbol{k})t \tag{7.32}$$

for small t. Comparison with (7.30) then leads to

$$C(\boldsymbol{k}) = -Nv\sigma(\boldsymbol{k}) \,, \tag{7.33}$$

where

$$\sigma(\boldsymbol{k}) = \int \mathrm{d}^2\boldsymbol{\phi}\; K(\boldsymbol{\phi}) \left[1 - \mathrm{e}^{-i\boldsymbol{k}\cdot\boldsymbol{\phi}}\right] . \tag{7.34}$$

With this, (7.25) reads

$$F(\boldsymbol{\alpha}, t) = \frac{1}{(2\pi)^2} \int \mathrm{d}^2\boldsymbol{k}\; \mathrm{e}^{\mathrm{i}\boldsymbol{k}\cdot\boldsymbol{\alpha} - Nvt\sigma(\boldsymbol{k})} \,. \tag{7.35}$$

Making use of the azimuthal symmetry of the cross section and the relation

$$\int_0^{2\pi} \mathrm{d}\chi \mathrm{e}^{z\cos\chi} = 2\pi J_0(z) \,, \tag{7.36}$$

where $J_0(z)$ is a Bessel function of the first kind in standard notation, we may rewrite (7.35) in the form

$$F(\alpha, x)\, \mathrm{d}^2\boldsymbol{\alpha} = \alpha\, d\alpha \int_0^\infty k\, \mathrm{d}k\; J_0(k\alpha)\mathrm{e}^{-Nx\sigma(k)} \tag{7.37}$$

with

$$\sigma(k) = \int_0^\infty \mathrm{d}\sigma(\phi)\,[1 - J_0(k\phi)] \,, \tag{7.38}$$

where time has been replaced by the foil thickness $x = vt$. Equation (7.37) in conjunction with (7.38) has been derived by Bothe (1921b). It represents a straight extension to two dimensions of the Bothe-Landau formula (9.14), Vol. 1. It is a very powerful tool in the description of multiple scattering. However, the above derivation, while elegant, is not particularly transparent with regard to the underlying physics. The following section is intended to provide some clarification.

*7.3.5 Collision Counting**

Let us try an alternative way to derive (7.35), making use of statistical arguments presented in Sect. 2.2.2, Vol. 1.

For simplicity, let us group the multiplicity of vectorial scattering angles $\boldsymbol{\phi}$ into discrete bundles $\boldsymbol{\phi}_i$, $i = 1, \ldots, I$. If a projectile in a particular passage undergoes

n_i events with a scattering angle $\boldsymbol{\phi}_i$, the total deflection angle will be given by

$$\boldsymbol{\alpha} = \sum_{i=1}^{I} n_i \boldsymbol{\phi}_i \,. \tag{7.39}$$

If the probability for n_i events of type i is denoted as P_{n_i}, the angular distribution can be written as

$$F(\boldsymbol{\alpha}) = \sum_{n_1=0}^{\infty} P_{n_1} \sum_{n_2=0}^{\infty} P_{n_2} \cdots \sum_{n_I=0}^{\infty} P_{n_I} \delta \left(\boldsymbol{\alpha} - \sum_{i=1}^{I} n_i \boldsymbol{\phi}_i \right) . \tag{7.40}$$

7.3.5.1 Poisson Statistics

For a random medium, events of type i are mutually independent and hence may be assumed to be governed by Poisson's formula, (2.7), Vol. 1,

$$P_{n_i} = \frac{(Nx\sigma_i)^{n_i}}{n_i!} \mathrm{e}^{-Nx\sigma_i} \,. \tag{7.41}$$

Inserting this together with

$$\delta \left(\boldsymbol{\alpha} - \sum_{i=1}^{I} n_i \boldsymbol{\phi}_i \right) = \frac{1}{(2\pi)^2} \int \mathrm{d}^2 \boldsymbol{k} \, \mathrm{e}^{\mathrm{i}\boldsymbol{k}\cdot(\boldsymbol{\alpha} - \sum_{i=1}^{I} n_i \boldsymbol{\phi}_i)} \tag{7.42}$$

into (7.40) we find

$$\begin{aligned} F(\boldsymbol{\alpha}) = \frac{1}{(2\pi)^2} \int \mathrm{d}^2 \boldsymbol{k} \, \mathrm{e}^{\mathrm{i}\boldsymbol{k}\cdot\boldsymbol{\alpha}} \sum_{n_1=0}^{\infty} \frac{(Nx\sigma_1)^{n_1}}{n_1!} \mathrm{e}^{-Nx\sigma_1} \mathrm{e}^{-in_1\boldsymbol{k}\cdot\boldsymbol{\phi}_1} \\ \sum_{n_2=0}^{\infty} \frac{(Nx\sigma_2)^{n_2}}{n_2!} \mathrm{e}^{-Nx\sigma_2} \mathrm{e}^{-in_2\boldsymbol{k}\cdot\boldsymbol{\phi}_2} \cdots \\ \sum_{n_I=0}^{\infty} \frac{(Nx\sigma_I)^{n_I}}{n_I!} \mathrm{e}^{-Nx\sigma_I} \mathrm{e}^{-in_I\boldsymbol{k}\cdot\boldsymbol{\phi}_I} \end{aligned} \tag{7.43}$$

or, after summation of the exponential series,

$$F(\boldsymbol{\alpha}) = \frac{1}{(2\pi)^2} \int \mathrm{d}^2 \boldsymbol{k} \, \mathrm{e}^{\mathrm{i}\boldsymbol{k}\cdot\boldsymbol{\alpha} - Nx\sum_{i=1}^{I}\sigma_i + Nx\sum_{i=1}^{I}\sigma_i \mathrm{e}^{-i\boldsymbol{k}\cdot\boldsymbol{\phi}_i}} \,. \tag{7.44}$$

This has the form of (7.35) with

$$\sigma(\boldsymbol{k}) = \sum_{i=1}^{I} \sigma_i \left(1 - \mathrm{e}^{-i\,\boldsymbol{k}\cdot\boldsymbol{\phi}_i}\right) . \tag{7.45}$$

Making the transition to a continuous differential cross section,

$$\sigma_i \to \int \mathrm{d}\sigma(\boldsymbol{\phi}) \tag{7.46}$$

we arrive back at (7.34).

This derivation makes it clear that the number of scattering events may vary significantly from trajectory to trajectory.

7.3.5.2 Fixed Number of Interactions

In the literature you will often find arguments based on a fixed number, say n, of scattering events. Let us briefly look into this aspect. Instead of numbering *types of events* by an index i, it is now appropriate to number the events themselves by an index j. For a given event j the probability for a scattering angle $(\boldsymbol{\phi}, \mathrm{d}^2\boldsymbol{\phi})$ is given by

$$\frac{\mathrm{d}\sigma(\boldsymbol{\phi})}{\sigma} , \tag{7.47}$$

assuming the total cross section $\sigma = \int \mathrm{d}\sigma(\boldsymbol{\phi})$ to be finite. Then the distribution in total scattering angle $\boldsymbol{\alpha}$ is given by

$$F_n(\boldsymbol{\alpha}) = \int \frac{\mathrm{d}\sigma(\boldsymbol{\phi}_1)}{\sigma} \int \frac{\mathrm{d}\sigma(\boldsymbol{\phi}_2)}{\sigma} \ldots \int \frac{\mathrm{d}\sigma(\boldsymbol{\phi}_n)}{\sigma}\, \delta\left(\boldsymbol{\alpha} - \sum_{j=1}^{n} \boldsymbol{\phi}_j\right) \tag{7.48}$$

or, after inserting

$$\delta\left(\boldsymbol{\alpha} - \boldsymbol{\phi}_1 - \boldsymbol{\phi}_2 - \ldots - \boldsymbol{\phi}_n\right) = \frac{1}{(2\pi)^2} \int \mathrm{d}^2\boldsymbol{k}\; \mathrm{e}^{\mathrm{i}\boldsymbol{k}\cdot(\boldsymbol{\alpha}-\boldsymbol{\phi}_1-\boldsymbol{\phi}_2-\ldots-\boldsymbol{\phi}_n)} , \tag{7.49}$$

$$F_n(\boldsymbol{\alpha}) = \frac{1}{(2\pi)^2} \int \mathrm{d}^2\,\boldsymbol{k}\; \mathrm{e}^{\mathrm{i}\boldsymbol{k}\cdot\boldsymbol{\alpha}} \left(\int \frac{\mathrm{d}\sigma(\boldsymbol{\phi})}{\sigma} \mathrm{e}^{-i\,\boldsymbol{k}\cdot\boldsymbol{\phi}}\right)^n . \tag{7.50}$$

This expression is obviously different from (7.35). However, if we let the number n of scattering events be distributed according to Poisson's formula,

$$P_n = \frac{(N x \sigma)^n}{n!} \mathrm{e}^{-N x \sigma} . \tag{7.51}$$

the angular distribution

$$F(\boldsymbol{\alpha}) = \sum_{n=0}^{\infty} P_n\, F_n(\boldsymbol{\alpha}) \tag{7.52}$$

is readily seen to take on the form (7.35) with $\sigma(\boldsymbol{k})$ given by (7.34).

Thus, for large values of n, when the width of the Poisson distribution becomes small, we may expect (7.50) to approach (7.35). However, (7.50) does not appear more attractive either from a mathematical or a computational point of view than (7.35), and from a physical point of view it may even be undesirable since its utilization in practice requires the cross section to be finite.

Note that the total cross section drops out after application of (7.51). Therefore, σ need not be finite if the number of interactions is Poisson-distributed. Then, a necessary condition for a meaningful result is the convergence of $\sigma(\boldsymbol{k})$ as given by (7.34).

7.3.6 Excursion into Truncated Cross Sections*

The screened-Coulomb potentials that we deal with in this monograph all have an infinite interaction range, although the approach to zero may be more or less rapid. In classical scattering theory this implies that the differential cross section gets singular at scattering angle zero. In the analysis of energy loss this is not a fundamental obstacle, since an energy-loss spectrum hinges on the stopping cross section and higher moments, while the total cross section does not enter. Similarly, you may note that the integrand entering the transport cross section $\sigma(k)$ in the Bothe-Landau formula is regular at $\phi = 0$, provided that $\phi^2 \mathrm{d}\sigma(\phi)/\mathrm{d}\phi$ is finite.

There is a problem, however, if you try to predict a multiple-scattering profile by computer simulation. You can do this by defining probabilities of a given scatter process such as (7.47), where the denominator will be infinitely large. Alternatively you may operate with the scattering probability $|2\pi p\, \mathrm{d}p|$, in which you will have to treat an infinite range of impact parameters. An obvious way to solve this problem is to introduce a maximum impact parameter or a minimum scattering angle and to make sure that the final result is insensitive to the precise value of either quantity. Such values can be found in practice, whenever the corresponding transport equation has a well-defined solution.

However, you will also find physical arguments in the literature supporting a definite choice of a truncated interaction potential at least in the case of solid target materials. Such arguments rest on two undisputable facts,

- Strictly binary collisions are impossible in solids, and
- Interatomic potentials in solids differ from interatomic potentials in vacuum.

The proper solution to the first problem, when considered serious, is molecular-dynamics simulation, which is to be discussed in Volume 3 of this monograph. Solutions to the second problem have been discussed in Sect. 6.2.4.

A third way to circumvent these problems is to truncate the interaction potential at some distance less than half the nearest-neighbour distance in the target structure. This is unproblematic, if the scattering angle or energy loss are insignificant at this impact parameter, but an error is introduced if that is not the case. Note that the

statistical weight increases linearly with the impact parameter, so that even small scattering angles and/or energy losses may be significant. However, special tools such as perturbation theory may be valuable e.g. in the treatment of many-body collisions.

7.3.7 Transport Equation

Numerous treatments of multiple scattering in the literature are based on a transport equation of the type presented in (9.103) or (9.104), Vol. 1. The method will first be used to rederive Bothe's equation for the angular distribution and, subsequently, to find a relation governing the correlated angular-lateral distribution.

In order to find a suitable relationship for small-angle multiple scattering, consider the passage through a small pathlength interval δx. Let the angular distribution for small angles be given by $F(\boldsymbol{e}, x)$, where $x = vt$ is the penetration depth. Assuming δx sufficiently small so that the probability for two collisions can be ignored, you have

$$F(\boldsymbol{e}, x + \delta x) = F(\boldsymbol{e}, x)\left[1 - N\,\delta x \int \mathrm{d}\sigma(\boldsymbol{\phi})\right] + N\,\delta x \int \mathrm{d}\sigma(\boldsymbol{\phi})\, F(\boldsymbol{e} - \boldsymbol{\phi}, x), \quad (7.53)$$

where the two terms on the right-hand side express the probabilities for zero and one interaction, respectively, and the appropriate angular distribution. Expansion up to first order in δx leads to

$$\frac{\partial F(\boldsymbol{e}, x)}{\partial x} = -N \int \mathrm{d}\sigma(\boldsymbol{\phi})\,[F(\boldsymbol{e}, x) - F(\boldsymbol{e} - \boldsymbol{\phi}, x)]\,, \quad (7.54)$$

which is a transport equation or kinetic equation.

In Fourier space, specified by (7.25), this relation reads

$$\frac{\partial F(\boldsymbol{k}, x)}{\partial x} = -F(\boldsymbol{k}, x)\, N \int \mathrm{d}\sigma(\boldsymbol{\phi})\left[1 - \mathrm{e}^{-i\boldsymbol{k}\cdot\boldsymbol{\phi}}\right]. \quad (7.55)$$

Solution of this differential equation, together with the initial condition

$$F(\boldsymbol{e}, 0) = \delta(\boldsymbol{e}) \quad (7.56)$$

or

$$F(\boldsymbol{k}, 0) = 1 \quad (7.57)$$

leads you directly to (7.35).

7.3.8 Projected Distribution

Visual inspection of a trajectory e.g. in photographic emulsion, materials forming fission tracks, or cloud or bubble chambers warrants calculations of the distribution in projected scattering angle. Going back to (7.22), let us consider the distribution in projected deflection angle $\beta = \alpha \cos \chi$ within the small-angle approximation.

For small-angle scattering, the angular distribution projected on a plane containing the initial direction as an axis is easily found from Bothe's formula, (7.35), written in the form

$$F(\alpha_y, \alpha_z, x) = \frac{1}{(2\pi)^2} \int \mathrm{d}k_y \, d\, k_z \, \mathrm{e}^{\mathrm{i}k_y\alpha_y + ik_z\alpha_z - Nx\sigma\left(\sqrt{k_y^2+k_z^2}\right)} \,. \tag{7.58}$$

Integration over α_z then yields

$$F(\alpha_y, x) = \frac{1}{2\pi} \int \mathrm{d}k_y \, \mathrm{e}^{\mathrm{i}k_y\alpha_y - Nx\sigma(k_y)} \tag{7.59}$$

or, dropping the subscript y,

$$F(\alpha, x) = \frac{1}{2\pi} \int_{-\infty}^{\infty} \mathrm{d}k \, \mathrm{e}^{\mathrm{i}k\alpha - Nx\sigma(k)} \,. \tag{7.60}$$

Thus, the only difference between the two-dimensional and the one-dimensional distribution is in the replacement of the Bessel function $J_0(k\alpha)$ in (7.37) by $\exp(ik\alpha)$ in (7.60) (Snyder and Scott, 1949), while $\sigma(k)$ is unchanged.

7.3.9 Packing

In Sect. 5.4 we have seen that fluctuations in energy loss (straggling) are sensitive to the structure of the medium. An important example, discussed in Sect. 5.4.3, is energy loss in a molecular gas as compared to an atomic gas. A similar situation is found for multiple scattering (Sidenius et al., 1976, Sigmund, 1977).

In a molecular gas it is the molecules that are distributed at random, while atoms are correlated. Consider a diatomic gas made up by atoms A and B separated from each other by a vectorial distance $\boldsymbol{d}$. Then, the scattering angle in a collision may be written as

$$\boldsymbol{\phi} = \boldsymbol{\phi}_A(\boldsymbol{p}_A) + \boldsymbol{\phi}_B(\boldsymbol{p}_B) \,. \tag{7.61}$$

The Bothe formula retains the standard form

$$F(\boldsymbol{\alpha}, x) = \frac{1}{(2\pi)^2} \int \mathrm{d}^2\boldsymbol{k} \, \mathrm{e}^{\mathrm{i}\boldsymbol{k}\cdot\boldsymbol{\alpha} - Nx\sigma(\boldsymbol{k})} \,, \tag{7.62}$$

and the transport cross section can be written as

$$\sigma(\boldsymbol{k}) = \int \mathrm{d}^2\boldsymbol{p}\,(1 - \exp\left[-i\,\boldsymbol{k}\cdot(\boldsymbol{\phi}_A(\boldsymbol{p}_A) + \boldsymbol{\phi}_B(\boldsymbol{p}_B))\right]) \tag{7.63}$$

under the assumption of classical binary scattering, where

$$\boldsymbol{p}_A - \boldsymbol{p}_B = \boldsymbol{\rho}\,, \tag{7.64}$$

and $\boldsymbol{\rho}$ is the projection of $\boldsymbol{d}$ on the impact plane defined by the two vectorial impact parameters $\boldsymbol{p}_A$ and $\boldsymbol{p}_B$. These relations hold for a fixed orientation of all molecules, and a priori neither $\mathrm{d}\sigma(\boldsymbol{\phi})$ nor $F(\boldsymbol{\alpha})$ has azimuthal symmetry. If the molecules are oriented at random, the orientational average has to be taken over the distribution function $F(\boldsymbol{\alpha}, x)$, while it is not obvious whether that average already can be taken in the transport cross section.

We may, however, write the latter in the form

$$\sigma(\boldsymbol{k}) = \sigma_A(\boldsymbol{k}) + \sigma_B(\boldsymbol{k}) + \Delta\sigma(\boldsymbol{k})\,, \tag{7.65}$$

where $\sigma_A(\boldsymbol{k})$ and $\sigma_B(\boldsymbol{k})$ refer to isolated atoms and

$$\Delta\sigma(\boldsymbol{k}) = -\int \mathrm{d}^2\boldsymbol{p}\,\left(1 - \mathrm{e}^{-\boldsymbol{k}\cdot\boldsymbol{p}_A}\right)\left(1 - \mathrm{e}^{-\boldsymbol{k}\cdot\boldsymbol{p}_B}\right)\,. \tag{7.66}$$

For $\Delta\sigma(\boldsymbol{k}) = 0$, $\sigma(\boldsymbol{k})$ represents a random mixture of A and B atoms of density N each.

If the clusters are oriented at random, (7.62) has to be averaged over all orientations. We may tentatively assume that $\Delta\sigma(\boldsymbol{k})$ is a small perturbation, so that the integrand may be expanded up to the first order in $\Delta\sigma(\boldsymbol{k})$. This implies that the averaging only affects differential cross section,

$$\langle\Delta\sigma(\boldsymbol{k})\rangle_{\mathrm{av}} = -\int \mathrm{d}^2\boldsymbol{p}_A \int \mathrm{d}^2\boldsymbol{p}_B\,\left(1 - \mathrm{e}^{-\boldsymbol{k}\cdot\boldsymbol{p}_A}\right)\left(1 - \mathrm{e}^{-\boldsymbol{k}\cdot\boldsymbol{p}_B}\right) \times \langle\delta(\boldsymbol{p}_A - \boldsymbol{p}_B - \boldsymbol{\rho})\rangle_{\mathrm{av}}\,. \tag{7.67}$$

According to (8.92), Vol. 1, the Dirac function reduces to

$$\langle\delta(\boldsymbol{p}_A - \boldsymbol{p}_B - \boldsymbol{\rho})\rangle_{\mathrm{av}} = \frac{1}{2\pi\mathrm{d}^2\sqrt{1 - (\boldsymbol{p}_A - \boldsymbol{p}_B)^2/\mathrm{d}^2}} \simeq \frac{1}{2\pi\mathrm{d}^2}\,, \tag{7.68}$$

so that

$$\Delta\sigma(\boldsymbol{k}) \simeq -\frac{\sigma_A(\boldsymbol{k})\sigma_B(\boldsymbol{k})}{2\pi\mathrm{d}^2}\,. \tag{7.69}$$

The assumption that $(\boldsymbol{p}_A - \boldsymbol{p}_B)^2 \ll \mathrm{d}^2$ was also made in connection with the packing effect in straggling in Sect. 5.4.3. Typically the screening radius of the nuclear interaction is smaller than the adiabatic radius limiting the electronic interaction. Therefore this approximation is better justified in multiple scattering than in electronic straggling.

7.4 Statistics: Correlated Distributions ⋆

7.4.1 Lateral-Angular Distribution

Let us have a look at the combined distribution $F(\boldsymbol{e}, \boldsymbol{\rho}, x)$ for the angular deflection $\boldsymbol{e}$ and the lateral displacement $\boldsymbol{\rho} = (y, z)$ in the small-angle approximation. A suitable start is a transport equation (Scott, 1949). During passage through a thin layer δx, the lateral spread will increase even if no collision takes place. Hence, disregarding terms of higher than first order we find

$$F(\boldsymbol{\alpha}, \boldsymbol{\rho}, x + \delta x) = \left[1 - N\delta x \int \mathrm{d}\sigma(\phi)\right] F(\boldsymbol{\alpha}, \boldsymbol{\rho} - \boldsymbol{\alpha}\,\delta x, x) + N\delta x \int \mathrm{d}\sigma(\phi) F(\boldsymbol{\alpha} - \boldsymbol{\phi}, \boldsymbol{\rho}, x) \quad (7.70)$$

or, after expansion up to first order in δx,

$$\left(\frac{\partial}{\partial x} + \boldsymbol{\alpha} \cdot \boldsymbol{\nabla}_\rho\right) F(\boldsymbol{\alpha}, \boldsymbol{\rho}, x) = -N \int \mathrm{d}\sigma(\boldsymbol{\phi}) \left[F(\boldsymbol{\alpha}, \boldsymbol{\rho}, x) - F(\boldsymbol{\alpha} - \boldsymbol{\phi}, \boldsymbol{\rho}, x)\right], \quad (7.71)$$

where

$$\boldsymbol{\nabla}_\rho = \left(\frac{\partial}{\partial y}, \frac{\partial}{\partial z}\right). \quad (7.72)$$

In order to solve (7.71) we may try the ansatz

$$F(\boldsymbol{\alpha}, \boldsymbol{\rho}, x) = \frac{1}{(2\pi)^4} \int \mathrm{d}^2k \int \mathrm{d}^2\kappa\, \mathrm{e}^{\mathrm{i}\boldsymbol{k}\cdot\boldsymbol{\alpha} + i\boldsymbol{\kappa}\cdot(\boldsymbol{\rho} - x\boldsymbol{\alpha})} F(\boldsymbol{k}, \boldsymbol{\kappa}, x). \quad (7.73)$$

With this (7.71) reduces to

$$\frac{\partial F(\boldsymbol{k}, \boldsymbol{\kappa}, x)}{\partial x} = -N\sigma(\boldsymbol{k} - x\boldsymbol{\kappa}) F(\boldsymbol{k}, \boldsymbol{\kappa}, x), \quad (7.74)$$

with the solution

$$F(\boldsymbol{k}, \boldsymbol{\kappa}, x) = \mathrm{e}^{-N \int_0^x \mathrm{d}x' \sigma(\boldsymbol{k} - x'\boldsymbol{\kappa})}, \quad (7.75)$$

so that

$$F(\boldsymbol{\alpha}, \boldsymbol{\rho}, x) = \frac{1}{(2\pi)^4} \int \mathrm{d}^2k \int \mathrm{d}^2\kappa\, \mathrm{e}^{\mathrm{i}\boldsymbol{k}\cdot\boldsymbol{\alpha} + i\boldsymbol{\kappa}\cdot(\boldsymbol{\rho} - x\boldsymbol{\alpha}) - N \int_0^x \mathrm{d}x' \sigma(\boldsymbol{k} - x'\boldsymbol{\kappa})}. \quad (7.76)$$

By integrating over the angular variable we find a Bothe-type relation for the lateral displacement,

$$G(\boldsymbol{\rho}, x) = \int \mathrm{d}^2\boldsymbol{\alpha}\, F(\boldsymbol{\alpha}, \boldsymbol{\rho}, x) = \frac{1}{(2\pi)^2} \int \mathrm{d}^2\kappa\, \mathrm{e}^{\mathrm{i}\boldsymbol{\kappa}\cdot\boldsymbol{\rho} - N\int_0^x \mathrm{d}x'\sigma(\boldsymbol{\kappa}(x-x'))}\,. \quad (7.77)$$

7.4.2 Energy-Angular Distribution

For a particle beam penetrating through a thin layer, you may be interested in the dependence of the energy-loss spectrum on the angle of emergence from the foil. This is important not least in precision measurements of the electronic and nuclear energy loss. For small scattering angles and small energy losses $\Delta E \ll E$, the above derivation of Bothe's formula (7.35) can easily be generalized by replacing the unit vector $\boldsymbol{\alpha}$ by the full velocity vector $\boldsymbol{v}$, so that

$$F(\boldsymbol{v}, x)\,\mathrm{d}^3\boldsymbol{v} = \frac{\mathrm{d}^3\boldsymbol{v}}{(2\pi)^3} \int \mathrm{d}^3\boldsymbol{k}\, \mathrm{e}^{\mathrm{i}\boldsymbol{k}\cdot\boldsymbol{v} - Nx\sigma(\boldsymbol{k})}\,, \quad (7.78)$$

where

$$\sigma(\boldsymbol{k}) = \int \mathrm{d}\sigma(\boldsymbol{v}, \boldsymbol{v}') \left(1 - \mathrm{e}^{-i\boldsymbol{k}\cdot(\boldsymbol{v}'-\boldsymbol{v})}\right), \quad (7.79)$$

and $\mathrm{d}\sigma(\boldsymbol{v}, \boldsymbol{v}')$ is the differential cross section for scattering from a velocity $\boldsymbol{v}$ into a velocity interval $(\boldsymbol{v}', \mathrm{d}^3\boldsymbol{v}')$.

Since we normally use energy and angular variables, it will be more convenient to write

$$F(\Delta E, \boldsymbol{\alpha}, x)\,\mathrm{d}(\Delta E)\,\mathrm{d}^2\boldsymbol{\alpha} = \frac{\mathrm{d}(\Delta E)\,\mathrm{d}^2\boldsymbol{\alpha}}{(2\pi)^3} \int \mathrm{d}\kappa \int \mathrm{d}^2\boldsymbol{k}\, \mathrm{e}^{\mathrm{i}\kappa\Delta E + i\boldsymbol{k}\cdot\boldsymbol{\alpha} - Nx\,\sigma(\kappa,\boldsymbol{k})} \quad (7.80)$$

with

$$\sigma(\kappa, \boldsymbol{k}) = \int \mathrm{d}\sigma(T, \boldsymbol{\phi}) \left[1 - \mathrm{e}^{-i\kappa T - i\boldsymbol{k}\cdot\boldsymbol{\phi}}\right]. \quad (7.81)$$

You may integrate over the azimuthal variable in complete analogy to Sect. 7.3.4.

7.4.2.1 Mean Energy versus Angle

Individual energy-loss events are more or less accompanied by angular deflection. This effect is particularly important in case of nuclear energy loss. We may determine the mean energy loss as a function of scattering angle, a quantity of interest in case of negligible skewness.

From (7.80) we find

$$\int \mathrm{d}(\Delta E)\, \Delta E F(\Delta E, \boldsymbol{\alpha}, x) = \frac{1}{(2\pi)^2} \int \mathrm{d}^2\boldsymbol{k}\, \mathrm{e}^{\mathrm{i}\boldsymbol{k}\cdot\boldsymbol{\alpha} - Nx\sigma(\boldsymbol{k})} \left(-i N x \frac{\partial}{\partial \kappa} \sigma(\kappa, \boldsymbol{k}) \right)_{\kappa=0} . \quad (7.82)$$

This determines the mean energy loss $\overline{\Delta E}$ as a function of the scattering angle,

$$\overline{\Delta E}(\boldsymbol{\alpha}) = \frac{1}{F(\boldsymbol{\alpha})} \frac{1}{(2\pi)^2} \int \mathrm{d}^2\boldsymbol{k}\, \mathrm{e}^{\mathrm{i}\boldsymbol{k}\cdot\boldsymbol{\alpha} - Nx\sigma(\boldsymbol{k})} N x S(\boldsymbol{k}) , \quad (7.83)$$

where $F(\boldsymbol{\alpha}, x)$ is the energy-integrated angular distribution and

$$S(\boldsymbol{k}) = \int \mathrm{d}\sigma(T, \boldsymbol{\phi})\, T \mathrm{e}^{-i\boldsymbol{k}\cdot\boldsymbol{\phi}} \quad (7.84)$$

depends on the relative importance of electronic and nuclear stopping.

7.4.2.2 Angular Distribution at Moderate Target Thickness

For heavy ions you may encounter the situation that energy loss cannot be neglected, even though scattering angles are small. As a first approximation it may be sufficient to compute $\sigma(\boldsymbol{k})$ at the energy $E - \overline{\Delta E}/2$. If that is considered insufficient you may have to think of your target divided up into a number of layers, say n, with thickness x_j small enough so that the angular distribution in the jth foil can be described by a profile

$$F_j(E_j, \boldsymbol{\alpha}_j, x_j) = \frac{1}{(2\pi)^2} \int \mathrm{d}^2\boldsymbol{k}\, \mathrm{e}^{\mathrm{i}\boldsymbol{k}_j\cdot\boldsymbol{\alpha}_j - N x_j \sigma(E_j, \boldsymbol{k}_j)} , \quad (7.85)$$

where E_j is an energy between the mean entrance and exit energy of the jth foil. Assuming negligible energy-loss straggling you find

$$F(\boldsymbol{\alpha}, x) = \frac{1}{(2\pi)^2} \int \mathrm{d}^2\boldsymbol{k}\, \mathrm{e}^{\mathrm{i}\boldsymbol{k}\cdot\boldsymbol{\alpha} - N \sum_j x_j \sigma(E_j, \boldsymbol{k})} \quad (7.86)$$

by convolution, where $x = \sum x_j$ and $\alpha = \sum \boldsymbol{\alpha}_j$. Alternatively you may let n go to infinity and write (Sigmund, 1991)

$$F(\boldsymbol{\alpha}, x) = \frac{1}{(2\pi)^2} \int \mathrm{d}^2\boldsymbol{k}\, \mathrm{e}^{\mathrm{i}\boldsymbol{k}\cdot\boldsymbol{\alpha} - N \int_0^x \mathrm{d}x' \sigma(E(x'), \boldsymbol{k})} . \quad (7.87)$$

This point has been studied in detail by Valdes and Arista (1994).

7.4.3 Effect of Charge Exchange

Just as in energy-loss straggling, the charge of an ion may play a role in multiple scattering for at least two reasons. Firstly, electron capture and loss processes are accompanied by momentum change. Secondly, the cross section for elastic scattering is governed by the interatomic potential which depends on the ion charge. If we may ignore energy loss, calculating the contribution of charge exchange to the angular distribution becomes closely analogous to the theory of charge-exchange straggling sketched in Sect. 3.5. Indeed, within the small-angle approximation all that is necessary is to replace the one-dimensional, unidirectional energy-loss variables ΔE and T by the two-dimensional angular variables $\boldsymbol{\alpha}$ and $\boldsymbol{\phi}$, respectively. This implies that (3.95) turns into

$$F_{IJ}(\boldsymbol{\alpha}, x) = \frac{1}{(2\pi)^2} \int \mathrm{d}^2\boldsymbol{k}\, \mathrm{e}^{\mathrm{i}\boldsymbol{k}\cdot\alpha} \left(\mathrm{e}^{Nx(\mathbf{Q}-\boldsymbol{\sigma}(\boldsymbol{k}))}\right)_{IJ} , \tag{7.88}$$

where

$$\sigma_{IJ}(\boldsymbol{k}) = \int \mathrm{d}\sigma_{IJ}(\boldsymbol{\phi}) \left(1 - \mathrm{e}^{-i\boldsymbol{k}\cdot\boldsymbol{\phi}}\right) \tag{7.89}$$

and, from (3.8),

$$Q_{IJ} = \sigma_{IJ} - \delta_{IJ} \sum_L \sigma_{IL} . \tag{7.90}$$

A major simplification occurs if

$$\mathrm{d}\sigma_{IJ}(\boldsymbol{\phi}) \equiv \mathrm{d}\sigma_{IJ}(\phi) , \tag{7.91}$$

so that

$$\sigma_{IJ}(\boldsymbol{k}) \equiv \sigma_{IJ}(k) = \int \mathrm{d}\sigma_{IJ}(\phi)\,(1 - J_0(k\phi)) . \tag{7.92}$$

7.5 Approaches

7.5.1 Moments and Cumulants

Moments and cumulants do not play as important a role in multiple scattering as they do in the description of energy loss. Indeed, while energy loss is characterized primarily by the first moment, i.e., the stopping cross section, the first moment $\langle\boldsymbol{\alpha}\rangle$ over the multiple-scattering distribution most often vanishes for symmetry reasons. The second moment, on the other hand, diverges if evaluated uncritically in the small-angle approximation. Indeed, if (2.100), Vol. 1,

$$\langle\alpha^2\rangle = Nx \int \phi^2 \mathrm{d}\sigma(\phi) , \tag{7.93}$$

is evaluated on the basis of the small-angle version of Rutherford's law,

$$\mathrm{d}\sigma(\phi) \propto \frac{\phi\, d\phi}{\phi^4}\,, \tag{7.94}$$

a logarithmic divergence shows up both at small and large angles. While the former can be removed by allowing for a screening correction, the latter feature is inherent in the small-angle approximation. This problem can be overcome in an approximate way by the Bohr-Williams scheme to be presented below.

Moments and cumulants can, however, be evaluated in the Goudsmit-Saunderson description, (7.20) and (7.21). Making use of the relation

$$\int_{-1}^{1} \mathrm{d}\cos\alpha\; P_\ell(\cos\alpha) = 2\delta_{\ell 0} \tag{7.95}$$

and the recurrence relation for Legendre polynomials, (A.59), Vol. 1, and setting $R = vt$ you readily obtain

$$\int \mathrm{d}^2\boldsymbol{\alpha}\; F(\alpha, t) = 1, \tag{7.96}$$

$$\int \mathrm{d}^2\boldsymbol{\alpha}\; \cos\alpha\; F(\alpha, t) = \mathrm{e}^{-NR\sigma_1}, \tag{7.97}$$

$$\int \mathrm{d}^2\boldsymbol{\alpha}\; \cos^2\alpha\; F(\alpha, t) = \frac{1}{3} + \frac{2}{3}\mathrm{e}^{-NR\sigma_2}, \tag{7.98}$$

where σ_ℓ has been defined in (7.21). More relevant are the cumulants

$$\langle 1 - \cos\alpha\rangle = 1 - \mathrm{e}^{-NR\sigma_1}, \tag{7.99}$$

$$\langle (1 - \cos\alpha)^2\rangle = \frac{4}{3} - 2\mathrm{e}^{-NR\sigma_1} + \frac{2}{3}\mathrm{e}^{-NR\sigma_2}. \tag{7.100}$$

7.5.2 Diffusion Limit

In Chap. 9, Vol. 1, we learned that with increasing travelled pathlength the energy-loss distribution approaches a gaussian with a width determined by the straggling parameter. Let us have a look at the behaviour of the angular distribution with increasing travelled pathlength.

7.5.2.1 Goudsmit-Saunderson Distribution

Going first to the Goudsmit-Saunderson description (7.20) we note that all terms in the series except the one for $\ell = 0$ decrease toward zero with increasing pathlength. Dropping all terms $\ell \geq 1$ leads to an isotropic distribution $F(\alpha) = 1/4\pi$. The

relative magnitude of the subsequent terms depends on the cross section. However, we may note that $P_\ell(\cos\alpha)$ is an oscillating function, and the number of maxima and minima increases linearly with ℓ. Such oscillations will barely be visible in a situation where the angular distribution has become nearly isotropic.

Therefore, as a first approximation we may drop all terms with $\ell \geq 2$ and write

$$F(\alpha) \simeq \frac{1}{4\pi}\left(1 + 3\cos\alpha \mathrm{e}^{-NR\sigma_1}\right); \quad R \text{ large} \tag{7.101}$$

as an estimate of the approach to an isotropic distribution.

7.5.2.2 Small-Angle Scattering

Next, let us go to the small-angle approximation, (7.35). With increasing penetration depth x, the distribution will broaden in angle. This implies narrowing of the Fourier transform. Therefore, the distribution in angle will be predominantly determined by small values of k. Expansion of (7.34) in powers of k up to the leading order yields

$$\sigma(k) \simeq \frac{1}{2}\int (\boldsymbol{k}\cdot\boldsymbol{\phi})^2 \,\mathrm{d}\sigma(\boldsymbol{\phi}) = \frac{1}{4}k^2 \int \phi^2 \,\mathrm{d}\sigma(\phi)\,. \tag{7.102}$$

Let us assume a cross section that does not cause the integral to diverge and make use of

$$\langle\alpha^2\rangle = Nx\int \phi^2 \mathrm{d}\sigma(\phi)\,. \tag{7.103}$$

Then we may write

$$Nx\sigma(k) \simeq \frac{1}{4}k^2\langle\alpha^2\rangle\,. \tag{7.104}$$

With this, the integration in (7.35) can be carried out, so that the multiple-scattering profile assumes gaussian form

$$F(\alpha) \simeq \frac{1}{\pi\langle\alpha^2\rangle}\,\mathrm{e}^{-\alpha^2/\langle\alpha^2\rangle}\,. \tag{7.105}$$

7.5.2.3 Lateral Distribution

Application of the same procedure to the lateral distribution, (7.77), leads to

$$F(\rho, x) = \frac{1}{\pi\langle\rho^2\rangle}\mathrm{e}^{-\rho^2/\langle\rho^2\rangle} \tag{7.106}$$

with

$$\langle\rho^2\rangle = \frac{1}{3}Nx^3\int \phi^2 \,\mathrm{d}\sigma(\phi)\,. \tag{7.107}$$

7.5.2.4 Angular-Lateral distribution

You may also apply the diffusion approximation to the lateral-angular distribution, (7.80). After carrying out the fourfold integration you will arrive at

$$F(\alpha, \rho, x)\, \mathrm{d}^2\boldsymbol{\alpha}\, \mathrm{d}^2\boldsymbol{\rho} = \frac{3\mathrm{d}^2\boldsymbol{\alpha}\, \mathrm{d}^2\boldsymbol{\rho}}{(2\pi x^2 D)^2}\, \mathrm{e}^{-\alpha^2/Dx - 3\rho^2/Dx^3 + 3\boldsymbol{\alpha}\cdot\boldsymbol{\rho}/Dx^2}\,, \tag{7.108}$$

where

$$D = \frac{N}{4}\int \phi^2\, \mathrm{d}\sigma(\phi) \tag{7.109}$$

is a measure of the diffusion coefficient. According to Scott (1963), (7.108) was first found by Fermi.

7.5.3 An Integrable Example

Bothe (1921a) gave an example of an integrable two-dimensional distribution. Bothe made reference to a different physical application, but his calculation may nevertheless serve as a useful model for multiple scattering (Lindhard, 1970).

Consider the differential cross section

$$\mathrm{d}\sigma(\phi) = \mathcal{C}\,\frac{\mathrm{d}\phi}{\phi^2}, \qquad 0 \le \phi < \infty \tag{7.110}$$

with some constant $\mathcal{C}$. This refers to scattering on the R^{-2} potential mentioned in Sect. 6.4.2.

Insertion of (7.110) into (7.38) yields

$$\sigma(k) = \mathcal{C}k\,, \tag{7.111}$$

and subsequent integration of (7.37) leads to

$$F(\alpha, x) = \frac{1}{2\pi}\,\frac{N\mathcal{C}x}{(\alpha^2 + (N\mathcal{C}x)^2)^{3/2}}\,. \tag{7.112}$$

We first observe that this function is not gaussian, nor does it approach gaussian shape in the limit of large pathlengths. This does not constitute an inconsistency with the result of Sect. 7.5.2, since the integral $\int_0^\infty \phi^2 \mathrm{d}\sigma(\phi)$ does not exist.

Next, we note that despite the divergence of the cross section at small angles ϕ, the multiple-scattering profile remains finite at $\alpha = 0$, although it goes as $\propto (Nx)^{-2}$ and hence becomes large at small pathlengths.

Moreover, in the limit of large angles, $\alpha \gg N\mathcal{C}x$, the distribution (7.112) approaches the probability for a single scattering event specified by the cross section (7.110),

$$F(\alpha, x)\, \mathrm{d}^2\alpha \simeq N\mathcal{C}x\, \frac{d\alpha}{\alpha^2}\,. \tag{7.113}$$

Finally, the half-width of the distribution is given by

$$\alpha_{1/2} = \sqrt{2^{2/3} - 1}\, N\mathcal{C}x \tag{7.114}$$

i.e., proportional to the pathlength x. This finding is in striking contrast to the result of the diffusion approximation where $\alpha_{1/2} \propto \sqrt{Nx}$ according to (7.105) and (7.103).

7.5.4 Transition to Single Scattering

If we expand the exponential in (7.35) in terms of the penetration depth,

$$\mathrm{e}^{-Nx\sigma(k)} = 1 - Nx\sigma(k) + \frac{1}{2}(Nx)^2\,[\sigma(k)]^2 + \ldots\,, \tag{7.115}$$

we may get a measure of the relative significance of single, double, triple etc. collision events to the multiple-scattering distribution. We know already the two first terms in this expansion from (7.29). Going to the next order in Nx and integrating over $\mathrm{d}^2\boldsymbol{k}$ you will arrive at

$$\begin{aligned} F(\alpha) = \delta(\boldsymbol{\alpha}) + Nx \int \mathrm{d}\sigma(\boldsymbol{\phi})\,[\delta(\boldsymbol{\alpha} - \boldsymbol{\phi}) - \delta(\boldsymbol{\phi})] \\ + \frac{1}{2}(Nx)^2 \int \mathrm{d}\sigma(\boldsymbol{\phi}) \int \mathrm{d}\sigma(\boldsymbol{\phi}') \\ \times \left[\delta(\boldsymbol{\alpha} - \boldsymbol{\phi} - \boldsymbol{\phi}') - \delta(\boldsymbol{\alpha} - \boldsymbol{\phi}) - \delta(\boldsymbol{\alpha} - \boldsymbol{\phi}') + \delta(\boldsymbol{\alpha})\right] \ldots\,. \end{aligned} \tag{7.116}$$

As long as we keep away from the initial beam direction, i.e., for $\alpha \neq 0$, this reduces to

$$\begin{aligned} F(\alpha) = NxK(\alpha) + \frac{1}{2}(Nx)^2 \int \mathrm{d}^2\boldsymbol{\phi}\, K(\boldsymbol{\phi}) K(\boldsymbol{\alpha} - \boldsymbol{\phi}) \\ - (Nx)^2 K(\boldsymbol{\alpha}) \int \mathrm{d}^2\boldsymbol{\phi}\, K(\boldsymbol{\phi}) + \ldots\,. \end{aligned} \tag{7.117}$$

You may note that the second and third term on the right-hand side both diverge if $K(\phi)$ is singular at $\phi = 0$. However by limiting the integrations in the second and third term to a small interval around $\boldsymbol{\phi} = 0$ and $\boldsymbol{\phi} = \boldsymbol{\alpha}$, you can convince yourself that these divergencies cancel each other, so that the sum of the two terms of second order, originating in double-scattering events, remains finite even if the differential cross section diverges at small ϕ.

If the contribution from double scattering were characterized by only the first term on the right-hand side, it would normally be dominating over the single-

collision term, even for a finite total cross section. However, with the divergence removed we may conclude that the double-scattering term is made up predominantly by contributions from scattering angles ϕ and ϕ' not close to zero.

Hence, we may expect that for physically relevant cross sections the multiple-scattering distribution will approach the single-scattering law at large angles. This was found to be the case in the example discussed in Sect. 7.5.3.

7.5.5 Bohr-Williams Model

A physically very appealing model of multiple scattering was proposed by Williams (1939). According to Sect. 7.5.4 the angular distribution approaches the single-scattering distribution at large angles. Therefore we may introduce an angle $\alpha^\star$ which, approximately, separates the single-scattering from the multiple-scattering regime, so that

$$F(\alpha, x) \simeq Nx \frac{\mathrm{d}\sigma(\alpha)}{2\pi\alpha d\alpha} \text{ for } \alpha > \alpha^\star \,. \tag{7.118}$$

Deflections at angles $\phi < \alpha^\star$ occur more than once in the average and are treated in the diffusion approximation. For small-angle multiple scattering this implies

$$F(\alpha, x) = \frac{1}{\pi \langle \alpha^2 \rangle} \mathrm{e}^{-\alpha^2/\langle \alpha^2 \rangle} \tag{7.119}$$

with

$$\langle \alpha^2 \rangle = Nx \int_0^{\alpha^\star} \phi^2 \, \mathrm{d}\sigma(\phi) \,. \tag{7.120}$$

The integral in (7.120) diverges for Coulomb scattering but becomes finite when screening at small scattering angles is taken into account.

The diffusion approximation must be expected to be inadequate at angles $\alpha \sim \alpha^\star$, and the same must be true for the single-collision approximation. Evidently, some interpolation is necessary in the intermediate angular range.

We have not yet defined the limiting angle $\alpha^\star$. There are several options,

1. over the wide-angle part (Williams, 1939),

$$Nx \int_{\alpha^\star}^{\alpha_{\max}} \mathrm{d}\sigma(\phi) = 1 \,. \tag{7.121}$$

2. or over the small-angle part,

$$\alpha^{\star 2} = \langle \phi^2 \rangle = Nx \int_0^{\alpha^\star} \phi^2 \, \mathrm{d}\sigma(\phi) \tag{7.122}$$

3. or over the normalization,

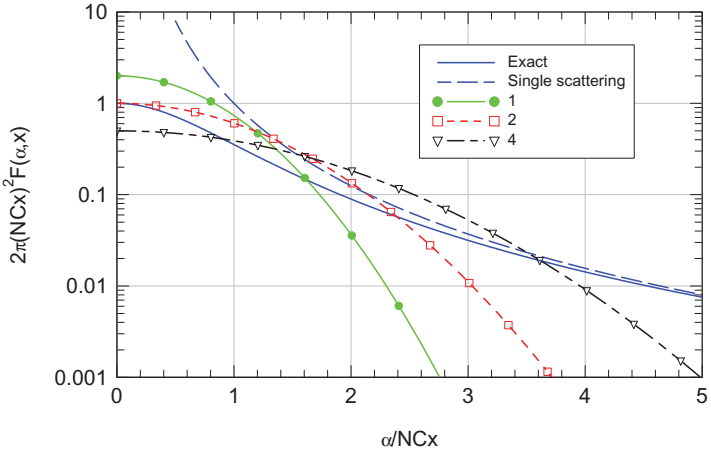

Fig. 7.4 Comparison between Bohr-Williams approximation and exact result for model distribution (7.112). Solid line: exact; dashed line: single-collision limit; lines with markers: diffusion limit; labels indicate the value of $\alpha^\star/NCx$.

$$\left[\int_0^{\alpha^\star} + \int_{\alpha^\star}^{\infty}\right] 2\pi\alpha \, \mathrm{d}\alpha F(\alpha, x) = 1 \,. \tag{7.123}$$

Let us first have a look at the example discussed in Sect. 7.5.3, where an exact solution is available. Here the Bohr-Williams scheme leads to

$$F(\alpha, x) \simeq \begin{cases} \frac{NCx}{2\pi\alpha^3} & \alpha > \alpha^\star \\ \text{for} & \\ \frac{1}{\pi NxC\alpha^\star} \exp\left(-\frac{\alpha^2}{NCx\alpha^\star}\right) & \alpha < \alpha^\star \end{cases} . \tag{7.124}$$

The two first options for $\alpha^\star$ mentioned above both yield

$$\alpha^\star = NCx \,, \tag{7.125}$$

while the third option cannot be fulfilled on the basis of (7.124).

Figure 7.4, which is an expanded version of Fig. 2.7, Vol. 1, shows (7.124) for three values of the parameter $\alpha^\star/NCx$. You may note that for all three values chosen, $\alpha^\star/NCx = 1$, 2 and 4, interpolation between the small-angle and the single-scattering limit is unproblematic. For $\alpha^\star/NCx = 1$ the scattered intensity for $\alpha = 0$ is overestimated by a factor of two. This problem does not occur for $\alpha^\star/NCx = 2$. The optimum choice appears to be close to $\alpha^\star/NCx = 2$, where the two cross-over points with the single-scattering curve almost merge, and where there is agreement with the exact curve at $\alpha = 0$. On the other hand, the agreement between the three diffusion profiles and the exact curve is not encouraging, and it seems fair to conclude that the Bohr-Williams scheme does not produce an accurate multiple-scattering profile for the cross section (7.110), which represents heavily-

screened Coulomb interaction. However, the approximation becomes powerful in high-energy scattering, in particular at target thicknesses where the single-scattering regime constitutes only a tiny fraction of the scattered beam, as you will see below.

7.5.6 Simulation

A major discussion of simulation techniques in particle penetration has been postponed to Volume 3. Simulation is particularly powerful in the field of radiation effects. However, since multiple-scattering problems can conveniently be analysed by simulation, a brief discussion has been included here.

Simulation techniques fall naturally into three categories:

- Monte-Carlo simulation (MC) operates with cross sections and is roughly equivalent to the theory presented in the present chapter.
- Binary-collision codes (BC) operate on a pre-installed target structure and utilize scattering laws relating impact parameters to scattering angle and energy transfer.
- Molecular-dynamics (MD) codes solve equations of motion for a many-body system comprising a given initial target structure and a projectile.

All methods are free of technical limitations such as small-angle approximation, neglecting energy loss, target geometry and the like. BC and MD codes allow to study the effects of crystal structure including thermal vibrations. Achieving adequate statistics may be a problem with BC and MD simulations.

On the other hand, care is indicated at small scattering angles. It is necessary to truncate interaction potentials at some impact parameter. As a consequence there is a minimum scattering angle which may affect the multiple-scattering profile.

By and large, simulation methods are particularly useful in cases where transport theory becomes problematic, at low beam energies, for large scattering angles and for complex geometries.

7.6 Angular Distribution

7.6.1 Scaling properties

In this section, estimates of multiple-scattering angular distributions will be analysed under the assumption of elastic screened-Coulomb scattering on a potential

$$\mathcal{V}(R) = \frac{Z_1 Z_2 e^2}{R} g\left(\frac{R}{a}\right), \tag{7.126}$$

characterized by a screening function g and a screening radius a. For the purpose of establishing scaling properties it is not required to specify g or a.

We shall focus here on small angles. It is tempting, therefore, to characterize single scattering by first-order perturbation theory.

7.6.1.1 Classical Scattering

Take first the classical expression, (3.76), Vol. 1, which may be expected to be valid for small angles,

$$\theta \simeq -\frac{1}{pE_r}\int_p^\infty \frac{\mathrm{d}r}{\sqrt{1-p^2/r^2}}\frac{\mathrm{d}}{\mathrm{d}r}\{r\mathcal{V}(r)\}\,. \tag{7.127}$$

The relations between laboratory and c.m.s. variables read

$$\phi \simeq \frac{M_2}{M_1+M_2}\theta; \quad E_r = \frac{M_2}{M_1+M_2}E \tag{7.128}$$

for small angles. Therefore the relation (7.127) remains valid if we replace θ by ϕ and E_r by E,

$$E_r\Theta = E\phi \quad \text{for small angles}\,. \tag{7.129}$$

After insertion of (7.126) you arrive at

$$\phi = -\frac{Z_1Z_2e^2}{Ea}g_1\left(\frac{p}{a}\right)\,, \tag{7.130}$$

where g_1 is a function determined by the screening function g. This suggests to introduce the scaled angular variable (Meyer, 1971)

$$\tilde{\phi} = \frac{Ea}{Z_1Z_2e^2}\phi\,. \tag{7.131}$$

The differential cross section then reads

$$\mathrm{d}\sigma(\phi) = |2\pi p\,\mathrm{d}p| = 2\pi a^2\frac{\mathrm{d}\tilde{\phi}}{\tilde{\phi}^3}\tilde{g}(\tilde{\phi})\,, \tag{7.132}$$

where the function $\tilde{g}(\tilde{\phi})$—which likewise depends on the screening function g—has been defined so that it reduces to unity for unscreened Coulomb scattering. This relation looks very similar to (6.57). You are welcome to analyse this similarity in detail by going to Problem 7.6.

A scaling relationship for small-angle multiple scattering can then be found by defining the scaled deflection angle

$$\tilde{\alpha} = \frac{Ea}{Z_1Z_2e^2}\alpha\,. \tag{7.133}$$

With this, (7.37) reduces to (Meyer, 1971)

$$F(\alpha, x)\mathrm{d}^2\boldsymbol{\alpha} = \tilde{\alpha}\,\mathrm{d}\tilde{\alpha}\int_0^\infty \tilde{k}\,\mathrm{d}\tilde{k}\,J_0(\tilde{k}\tilde{\alpha})\,\mathrm{e}^{-\tau\tilde{\sigma}(\tilde{k})} \tag{7.134}$$

with

$$\tilde{\sigma}(\tilde{k}) = 2\int_0^\infty \frac{\mathrm{d}\tilde{\phi}}{\tilde{\phi}^3}\tilde{g}(\tilde{\phi})\left(1 - J_0(\tilde{k}\tilde{\phi})\right), \tag{7.135}$$

where

$$\tau = \pi a^2 N x\,, \tag{7.136}$$

and $\tilde{k} = Z_1 Z_2 e^2 k/Ea$.

7.6.1.2 Born Approximation

At high projectile speeds it becomes more appropriate to characterize single scattering in the Born approximation. Then, from (3.94), Vol. 1 we may deduce that the function $\tilde{g}(\tilde{\phi})$ in (7.132) must be replaced by some function $\hat{g}_1(a\theta/\lambda\!\!\!^{-}) \equiv \hat{g}_1(M_1 va\phi/\hbar)$. It may then be more appropriate to introduce the scaled angular variable (Molière, 1948, Bethe, 1953)

$$\hat{\phi} = \frac{M_1 va}{\hbar}\phi \tag{7.137}$$

instead of $\tilde{\phi}$.

From (3.89) and (3.90) you find, for a screened-Coulomb potential with a screening function $g(r/a)$,

$$\mathrm{d}\sigma(\phi) = 2\pi a^2 \frac{\mathrm{d}\hat{\phi}}{\hat{\phi}^3}\hat{g}_1(\hat{\phi})\,, \tag{7.138}$$

where

$$\hat{g}_1(\hat{\phi}) = \left[\kappa_1\hat{\phi}\,f(\hat{\phi})\right]^2 \tag{7.139}$$

with

$$\kappa_1 = \frac{2Z_1 Z_2 e^2}{\hbar v} \tag{7.140}$$

and

$$f(\hat{\phi}) = \int_0^\infty \mathrm{d}\xi\; g(\xi)\sin(\xi\hat{\phi})\,, \tag{7.141}$$

as you may derive in Problem 7.7.

You may then introduce a dimensionless angle

$$\hat{\alpha} = \frac{M_1 va}{\hbar}\alpha\,. \tag{7.142}$$

This yields, then, the multiple-scattering profile

$$F(\alpha, x)\mathrm{d}^2\boldsymbol{\alpha} = \hat{\alpha}\,\mathrm{d}\hat{\alpha}\int_0^\infty \hat{k}\,\mathrm{d}\hat{k}\,J_0(\hat{k}\hat{\alpha})\,\mathrm{e}^{-\tau\hat{\sigma}(\hat{k})} \tag{7.143}$$

with

$$\hat{\sigma}(\hat{k}) = 2\int_0^\infty \frac{\mathrm{d}\hat{\phi}}{\hat{\phi}^3}\hat{g}_1(\hat{\phi})\left(1 - J_0(\hat{k}\hat{\phi})\right) \tag{7.144}$$

and $\hat{k} = \hbar k/M_1 v a$.

7.6.2 Relativity

In Chap. 2, Vol. 1, the angular deflection over a small scattering angle was determined via the momentum transfer perpendicular to the direction of motion. This quantity, when expressed by projectile *velocity*, invokes the impulse and hence is unaffected by effects of relativity. However, conversion of the momentum transfer $\Delta P_\perp$ into a scattering angle according to

$$\phi = \frac{\Delta P_\perp}{P_{||}} \tag{7.145}$$

involves the momentum $P_{||} = \gamma M_1 v$ of the projectile with

$$\gamma = \frac{1}{\sqrt{1 - v^2/c^2}}\,. \tag{7.146}$$

Therefore, the relations derived above remain valid in the relativistic regime if the projectile mass M_1 is replaced by $M_1\gamma$. In practice this implies the substitution

$$E \to \frac{1}{2}M_1\gamma v^2 \equiv \frac{1}{2}P_{||}v\,. \tag{7.147}$$

Note that the expression on the right-hand side is *not* the relativistic expression for the kinetic energy of the projectile.

7.6.3 Weak Screening

For fast electrons and light ions the differential scattering cross section is Rutherford-like except at very small scattering angles. You can easily convince yourself that the transport cross section, (7.38), diverges due to a singularity at $\phi = 0$, if you insert the straight Rutherford cross section. Thus, taking into account screening is essential. Molière (1948) showed how the effect of screening can be expressed by introducing a single parameter that he called the screening angle.

In classical scattering, screening becomes important when the impact parameter is not small compared to the screening radius, i.e.,

$$\phi \lesssim b_1/a = \frac{Z_1 Z_2 e^2}{Ea}\,, \tag{7.148}$$

where $b_1 = Z_1 Z_2 e^2/E$ is the collision diameter. Expressed in dimensionless variables this reads

$$\tilde{\phi} \lesssim 1\,, \tag{7.149}$$

where $\tilde{\phi}$ is defined by (7.131).

Within the range of validity of the Born approximation the equivalent regime is

$$p \lesssim \lambda\!\!\!^{-} \tag{7.150}$$

i.e.,

$$\phi \lesssim \frac{b_1}{\lambda\!\!\!^{-}} = \frac{2Z_1 Z_2 e^2}{\hbar v} \tag{7.151}$$

or, in dimensionless variables,

$$\hat{\phi} \lesssim 1\,, \tag{7.152}$$

where $\hat{\phi}$ is defined in (7.137).

Thus, within the regime of weak screening, the function $\tilde{g}(\tilde{\phi})$ governing the differential cross section (7.132) approaches unity not far above $\tilde{\phi} = 1$. A corresponding statement holds for $\hat{g}_1(\hat{\phi})$ in (7.138).

While scattering angles ϕ are $\ll 1$ here, scaled scattering angles $\tilde{\phi}$ or $\hat{\phi}$ may become large at high energies, as is evident from their definitions. We may, therefore, split the transport cross sections, (7.135) and (7.144) into two parts at some angle ϕ_1, so that screening only affects the integral from 0 to ϕ_1. This procedure, applied originally by Bohr (1913) and Bethe (1930) in classical and quantal stopping theory, respectively, was extended to multiple scattering by Molière (1948) and later by Bethe (1953).

Following Bethe (1953) we shall consider the Born regime, but since notations in Sects. 7.6.1.2 and 7.6.1.1 are analogous, the final result can easily be transcribed into the classical regime.

Let us write the scaled transport cross section in the form

$$\hat{\sigma}(\hat{k}) = \hat{\sigma}_1(\hat{k}) + \hat{\sigma}_2(\hat{k})\,, \tag{7.153}$$

where

$$\hat{\sigma}_1(\hat{k}) = 2\int_0^{\hat{\phi}_1} \frac{\mathrm{d}\hat{\phi}}{\hat{\phi}^3}\hat{g}_1(\hat{\phi})\left[1 - J_0(\hat{k}\hat{\phi})\right] \tag{7.154}$$

and

$$\hat{\sigma}_2(\hat{k}) = 2\int_{\hat{\phi}_1}^{\infty} \frac{\mathrm{d}\hat{\phi}}{\hat{\phi}^3}\left[1 - J_0(\hat{k}\hat{\phi})\right]\,. \tag{7.155}$$

Here it has been assumed that $\hat{\phi}_1 \gg 1$, so that $\hat{g}_1(\hat{\phi}) \equiv 1$ in (7.155).

Now, we know that the halfwidth of the multiple-scattering profile increases with the thickness. Let us assume the target to be thick enough so that the scaled halfwidth $\hat{\phi}_{1/2} \gg 1$. If so, we can assume that

$$1 \ll \hat{\phi}_1 \ll \hat{\phi}_{1/2} \,. \tag{7.156}$$

The factor $1 - J_0(\hat{k}\hat{\phi})$ draws its main contributions from $\hat{k}\hat{\phi}_{1/2} \sim 1$. With this, the argument in the Bessel function in (7.154) is always $\ll 1$, so that

$$\hat{\sigma}_1(\hat{k}) \simeq \frac{1}{2}\hat{k}^2 \int_0^{\hat{\phi}_1} \frac{\mathrm{d}\hat{\phi}}{\hat{\phi}} \hat{g}_1(\hat{\phi}) \,. \tag{7.157}$$

The second integral can be reduced by repeated partial integration to

$$\hat{\sigma}_2(\hat{k}) = \frac{1}{\hat{\phi}_1^2}\Big[1 - J_0(\hat{k}\hat{\phi}_1)\Big] + \frac{\hat{k}}{2\hat{\phi}_1} J_1(\hat{k}\hat{\phi}_1) + \frac{1}{2}\hat{k}^2 \left[-\gamma - \ln\frac{\hat{k}\hat{\phi}_1}{2} + O\left\{\hat{k}^2\hat{\phi}_1^2\right\}\right], \tag{7.158}$$

where $\gamma = 0.5772$ is Euler's constant. Ignoring terms of order $\hat{k}^2\hat{\phi}_1^2$ or higher we finally obtain

$$\hat{\sigma}_2(\hat{k}) \simeq \frac{1}{2}\hat{k}^2 \left[1 - \gamma - \ln\frac{\hat{k}\hat{\phi}_1}{2}\right] \tag{7.159}$$

and hence,

$$\hat{\sigma}(\hat{k}) = \frac{1}{2}\hat{k}^2 \left[\int_0^{\hat{\phi}_1} \frac{\mathrm{d}\hat{\phi}}{\hat{\phi}} \hat{g}_1(\hat{\phi}) + 1 - \gamma - \ln\frac{\hat{k}\hat{\phi}_1}{2}\right] . \tag{7.160}$$

Following Molière (1948), Bethe (1953) defines a screening angle $\hat{\phi}_a$ by the relation

$$-\ln\hat{\phi}_a = \lim_{\hat{\phi}_1 \to \infty} \left[\int_0^{\hat{\phi}_1} \frac{\mathrm{d}\hat{\phi}}{\hat{\phi}} \hat{g}_1(\hat{\phi}) + \frac{1}{2} - \ln\hat{\phi}_1\right] . \tag{7.161}$$

The reason for this particular choice is that for an exponential screening function the screening angle reduces to $\hat{\phi}_a = 1$, as you may verify by solving Problem 7.9. With this you find

$$\hat{\sigma}(\hat{k}) = \frac{1}{2}\hat{k}^2 \left[-\ln(\hat{k}\hat{\phi}_a) + \frac{1}{2} + \ln 2 - \gamma\right] , \tag{7.162}$$

where use has been made of the fact that

$$\int_{\hat{\phi}_1}^{\infty} \frac{\mathrm{d}\hat{\phi}}{\hat{\phi}} \Big(\hat{g}_1(\hat{\phi}) - 1\Big) = 0 \,. \tag{7.163}$$

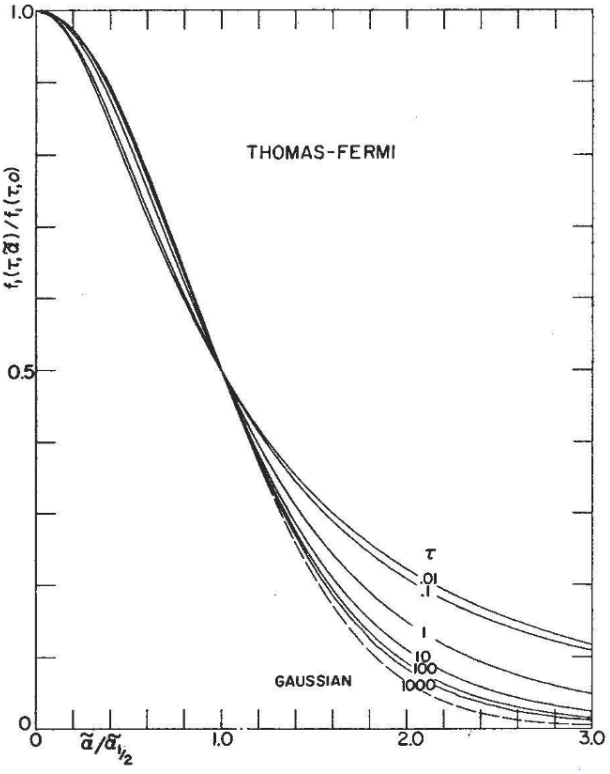

Fig. 7.5 Angular distributions evaluated in the small-angle approximation. The parameter $\tau = \pi N x a^2$ is a measure of the target thickness. From Sigmund and Winterbon (1974)

Evidently, the multiple-scattering profile (7.143) becomes independent of $\hat{\phi}_1$ and dependent only on the dimensionless thickness τ and the screening angle $\hat{\phi}_a$.

This approximation may yield reasonable results for $\hat{k} \lesssim 1$, i.e., for $\tau \gg 1$. Bethe (1953) expressed his results in terms of a few tabulated formulas, valid for high-energy electrons. In the following section we shall focus on ions.

7.6.4 Numerical Results

Multiple-scattering profiles for ions were evaluated by numerous authors over the years. Here I focus on three studies.

Meyer (1971) evaluated multiple-scattering profiles for exponential screening for both classical and Born scattering as well as for Thomas-Fermi interaction. His tabulations were based on a truncated potential, but it was found that the resulting halfwidths were insensitive to the choice of cut-off radius. There are, however, nu-

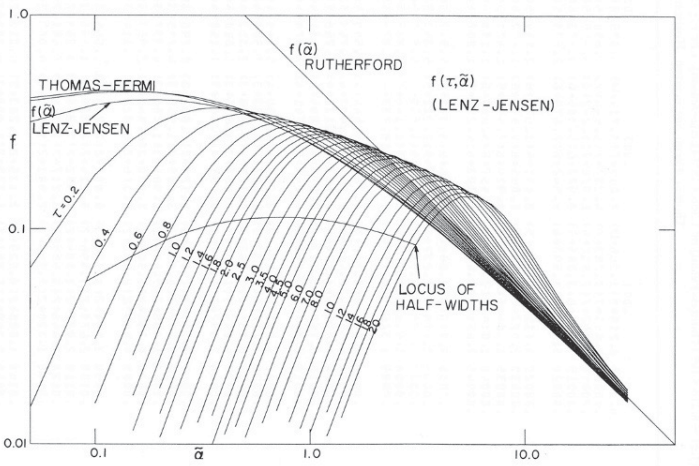

Fig. 7.6 Expanded version of Fig. 7.5 in Lindhard-Scharff units as in Fig. 6.12, that visualizes the transition to single scattering. From Sigmund and Winterbon (1974)

merical problems with large-angle scattering, where the reported profiles do not approach the single-scattering cross section.

Sigmund and Winterbon (1974) focused on classical scattering and produced tables for both Thomas-Fermi and Lenz-Jensen interaction. Truncation was avoided, and proper approach to single scattering was verified in all cases. A numerical error affecting tabulated low-thickness profiles was corrected subsequently (Sigmund and Winterbon, 1975). Also results for selected power cross sections were included for comparison.

Amsel et al. (2003) likewise produced tables for Thomas-Fermi and Lenz-Jensen interaction, but also studied projected profiles and supplied results of Monte Carlo simulations illustrating detailed trajectories. An attempt was made to compute multiple-scattering profiles by autoconvolution of the profiles from a number of thin layers, but that procedure was given up due to numerical problems in reproducing tails. Instead, their evaluation went over the Fourier transform as was done by previous authors.

Figure 7.5 shows multiple-scattering profiles evaluated in the small-angle approximation for Thomas-Fermi interaction. With available computer power at the time of publication in mind, the transport cross section $\tilde{\sigma}(\tilde{k})$ was evaluated analytically, so that only one numerical integration was necessary to determine the profile from (7.37).

The expected approach to gaussian shape is seen with increasing target thickness as expressed by $\tau = \pi N x a^2$, but for small values of τ, the profile looks more Lorentzian-like.

There are at least two observations to be kept in mind from Fig. 7.5,

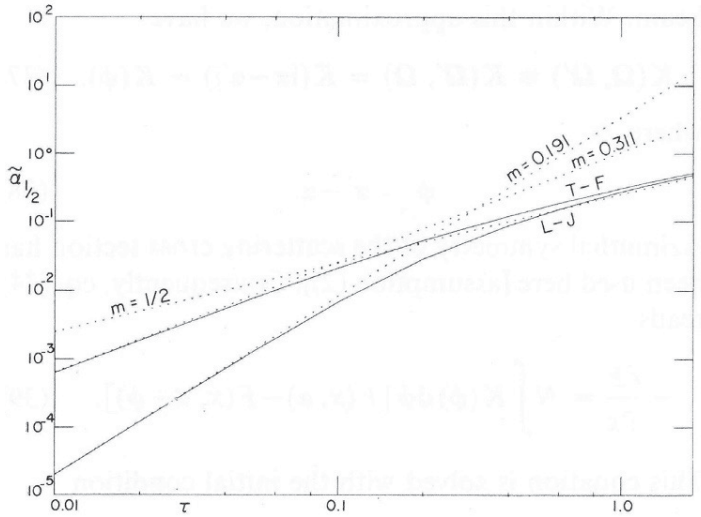

Fig. 7.7 Multiple-scattering halfwidths in the small-angle approximation for Thomas-Fermi and Lenz-Jensen screening and three power cross sections. Dimensionless units. From Sigmund and Winterbon (1974)

- Deviations from gaussian shape become pronounced in the wide-angle tails of the angular distribution. This was to be expected, since the profile must approach the single-scattering law here, as shown in Fig. 7.6.
- Experimentally, half-widths are frequently determined by fitting a measured profile to a gaussian. Dependent on how such a fit is performed, significant errors may arise. As an example, try to fit a parabola to the profile for $\tau = 0.01$ in the angular range $0 < \tilde{\alpha}_{1/2} \lesssim 0.5$. This would result in a significant underestimate of the halfwidth.

Figure 7.7 shows halfwidths versus thickness in dimensionless units, for several interaction potentials. The curves T-F and L-J represent Thomas-Fermi and Lenz-Jensen screening, respectively, while the curves for $m = 0.191$, 0.311 and 0.5 represent power scattering. Note that $m = 0.191$ and 0.311 reflect the behaviour of the Lenz-Jensen and Thomas-Fermi potential at large distances, respectively. This explains the behaviour at small values of τ. The curve for $m = 1/2$ represents (7.110).

The main conclusions to be drawn from Figs. 7.5–7.7 are as follows,

- Details of the screening behaviour become unimportant at large thickness, and
- At small thicknesses, the halfwidth appears to be very sensitive to the adopted screening function.

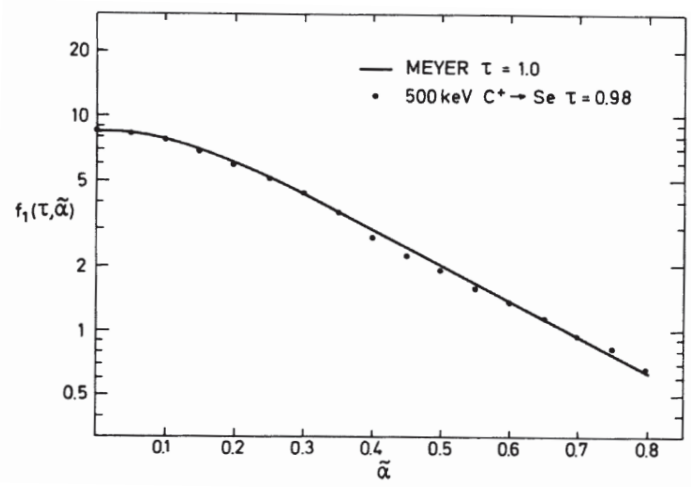

Fig. 7.8 Measured multiple-scattering profile for 500 keV C in 548 Å Se. Solid line: Meyer (1971). Points: Measured by Andersen et al. (1974). From Andersen et al. (1974)

7.6.5 Measurements

The experimental literature on multiple scattering of ions of all masses and energies is extensive, yet a comprehensive review is not known to the author. The present brief survey addresses primarily ions heavier than protons at moderate energies, where classical scattering provides an appropriate theoretical description.

Figure 7.8 shows a multiple-scattering profile measured by Andersen et al. (1974) compared with the calculation of Meyer (1971). Meyer's correction for truncation of the potential, mentioned in Sect. 7.6.4, has been ignored. Excellent agreement is found over an intensity range covering more than an order of magnitude.

Figure 7.9 shows a test on the scaling properties. Measurements from several groups representing different ions, targets and a wide range of energies, covering a τ-range of six orders of magnitude, confirm the validity of Thomas-Fermi scaling as far as the halfwidth is concerned. Moreover, excellent agreement is found with the theoretical prediction based on Thomas-Fermi interaction. The latter curve is taken from the table of Amsel et al. (2003) which goes to quite high τ-values but does not incorporate relativistic corrections. Such a correction is, however, included in Fig. 7.10, which was generated by Geissel et al. (2002).

Figure 7.11 shows the ratio $F(2\alpha_{1/2})/F(\alpha_{1/2})$, which characterizes the shape of a multiple-scattering profile. It is seen that this ratio is significantly higher than it would be for a gaussian profile. Deviations from strict Thomas-Fermi scaling are more pronounced here than in Fig. 7.9. Such deviations can be expected to increase if you go further out into the tails.

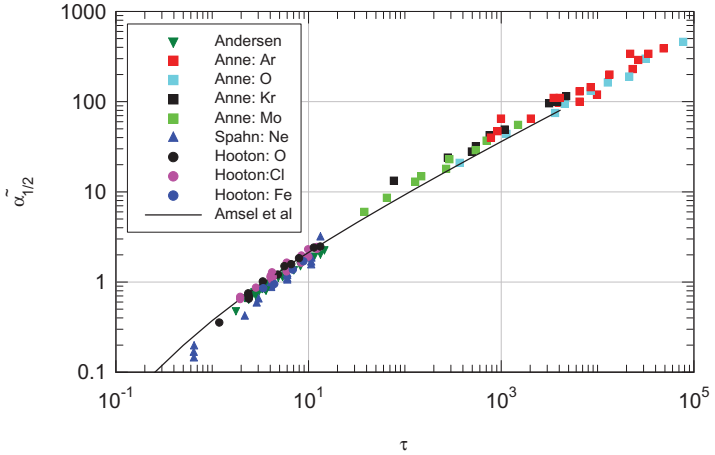

Fig. 7.9 Multiple-scattering halfwidths for a wide range of ions, targets and energies. Measurements of Andersen and Bøttiger (1971), Spahn and Groeneveld (1975), Hooton et al. (1975) and Anne et al. (1988). Solid line from Amsel et al. (2003). From ICRU (2005) (expanded)

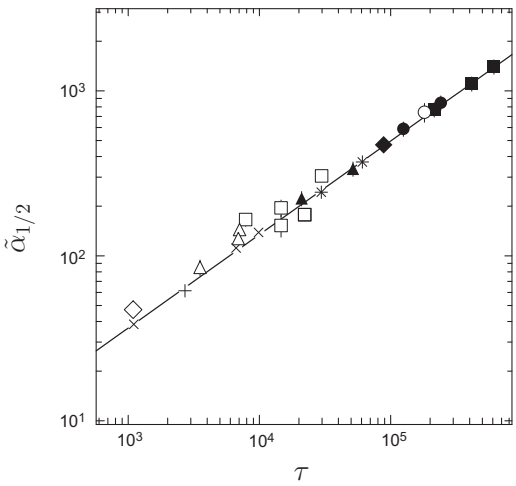

Fig. 7.10 Multiple scattering of relativistic heavy ions: Solid line: Theory of Sigmund and Winterbon (1974). Data from Anne et al. (1988), Schwab et al. (1990), Scheidenberger et al. (1998). 85 MeV/u Ar → Al (full circles), Pt (full square), Au (full triangles), 1500 MeV/u C → Pb (asterisk), 940 MeV/u U → Al (open circles), Ti (open squares), and Au (open triangles). From Geissel et al. (2002)

7.6.6 Special Aspects

In this section I like to list a few pertinent references on problems of a more technical nature which are encountered in practice but which, if treated here, would make this chapter unduly long.

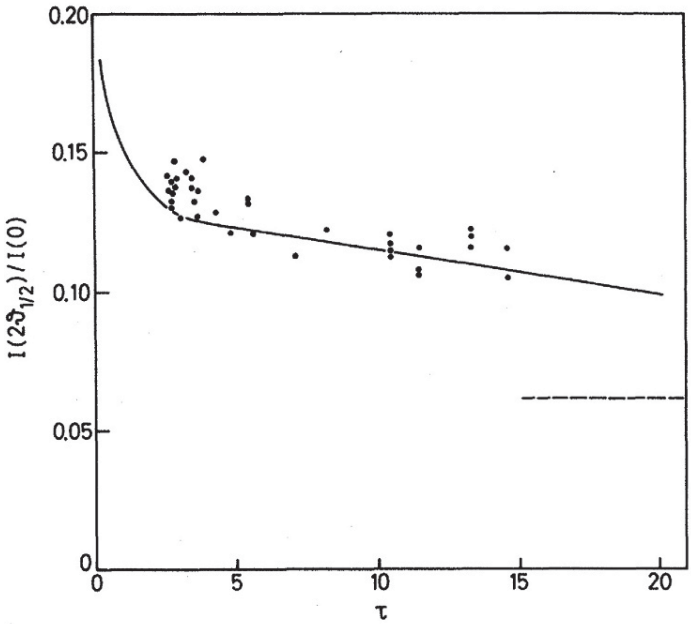

Fig. 7.11 Ratio $F(2\alpha_{1/2})/F(\alpha_{1/2})$ for numerous ions with $3 \leq Z_1 \leq 30$ in carbon foils of three different thicknesses and energies from 200 to 1000 keV, measured by Andersen and Bøttiger (1971). Solid line: Meyer (1971). The horizontal line represents a gaussian profile. From Andersen and Bøttiger (1971)

7.6.6.1 Projected Angular Distributions

Amsel et al. (2003) reevaluated multiple-scattering distributions for Thomas-Fermi and Lenz-Jensen interaction. Most of the tables in the printed paper refer to projected distributions, but cylindrical distributions of the type discussed here can be found in the internet on the homepage associated with the paper (Amsel et al., 2003).

The two distributions are quantitatively different, as you may recognize by solving Problem 7.10, but in the Gaussian limit they have the same half-width. Note, however, that the projection on an arbitrary plane can be constructed from the full cylindrically-symmetric distribution. The projection on a plane containing the plane of incidence, which is determined by (7.60) does not provide this option.

7.6.6.2 Heavy Ion in Light Material

If the ion mass M_1 exceeds the target mass M_2, the maximum scattering angle in a single-scattering event is given by

$$\sin \phi_{\max} = \frac{M_2}{M_1} \tag{7.164}$$

according to (3.6), Vol. 1. For $M_1 \gg M_2$ this may imply that the c.m.s. scattering angle is large even if the laboratory scattering angle is small. The small-angle approximation becomes then questionable, and discrepancies with experimental results have been found (Geissel et al., 1985). This situation has been treated on the basis of the approach of Goudsmit and Saunderson (1940) by Winterbon (1987, 1989).

7.6.6.3 Role of Charge Exchange

In the range of impact parameters characteristic of small-angle scattering, the Coulomb potential of the nucleus is more or less perfectly screened by electrons bound to the projectile. Therefore the influence of charge exchange on multiple scattering deserves attention.

Figure 7.12 shows a set of measurements for N ions in C by Kanter (1983). The incident energy $E = 3.7\,\mathrm{MeV}$ and the incident charge state $q = 1$ were kept constant, and the eight graphs represent multiple-scattering profiles for exit charge states $q = 0$–7. According to ETACHA (Rozet et al., 1996), the beam should be close to charge-equilibrated at the foil thickness $1.6\,\mu\mathrm{g/cm^2}$. The graph shows that a very large fraction of the ions is in charge states $q = 4$–6. Angular distributions for $q = 0$–5 all look very similar, whereas profiles for $q = 6$ and 7 are significantly broader, indicating that one or more collisions immediately before exit were more violent than average.

The main conclusion from Fig. 7.12 is that the influence of charge exchange is measurable in exit-charge-specific multiple-scattering profiles, while an influence on the total angular profile of the beam must be rather small.

While an explicit theoretical prediction on the basis of (7.92) is not available, Kanter (1983) included the results of a Monte-Carlo simulation in his work. Figure 7.12 indicates the occurrence of a ring structure around a minimum at zero scattering angle for the highest exit charge state. This appears to confirm the conclusion that deviations from average behaviour originate in the last collision.

7.7 Lateral Distribution

7.7.1 Scaling Properties

The lateral distribution, given by (7.77), may be rewritten in terms of the chord angle

$$\beta = \frac{\rho}{x} \tag{7.165}$$

illustrated schematically in Fig. 7.13. With the substitution

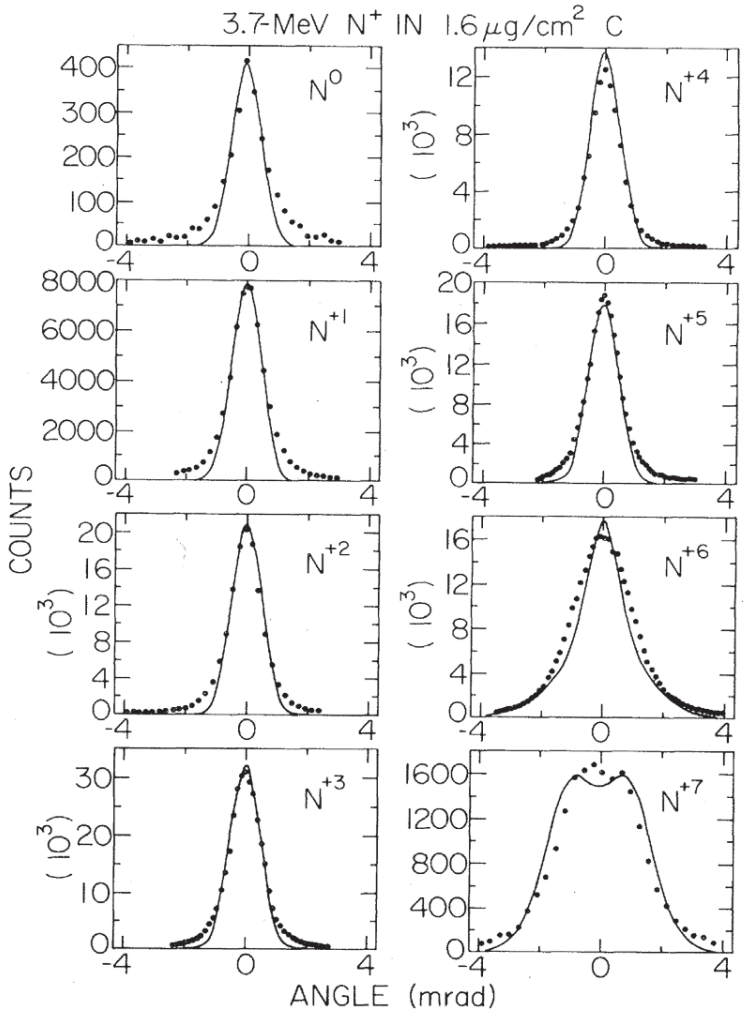

Fig. 7.12 Multiple-scattering profiles of 3.7 MeV N^+ ions in 1.6 μg/cm^2 carbon for exit charge states $q = 0$–7. Points: Measured. Lines: Monte Carlo simulation. From Kanter (1983)

$$k = \kappa x \tag{7.166}$$

you obtain

$$G(\boldsymbol{\rho}, x)\,\mathrm{d}^2\boldsymbol{\rho} \equiv G_\beta(\boldsymbol{\beta}, x)\,\mathrm{d}^2\boldsymbol{\beta} = \frac{\mathrm{d}^2\boldsymbol{\beta}}{(2\pi)^2}\int \mathrm{d}^2\boldsymbol{k}\,\mathrm{e}^{\mathrm{i}\boldsymbol{k}\cdot\boldsymbol{\beta} - Nx\frac{1}{k}\int_0^k \mathrm{d}k'\sigma(k')}. \tag{7.167}$$

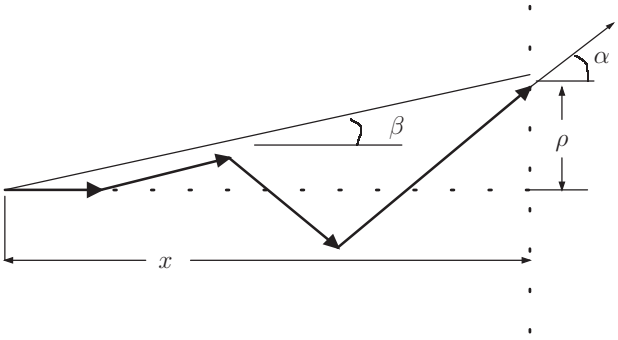

Fig. 7.13 Connection between lateral spread ρ, chord angle β, multiple-scattering angle α and penetration depth x

You may notice that the only difference to the angular multiple-scattering distribution is the replacement of the transport cross section $\sigma(k)$ by its average value $(1/k)\int_0^k \mathrm{d}k'\sigma(k')$.

7.7.2 Power Scattering

Marwick and Sigmund (1975) noted that for power scattering, where $\sigma(k) \propto k^{2m}$, angular profiles may be converted into lateral profiles by replacing $\sigma(k)$ with $\sigma(k)/(2m+1)$ or

$$\alpha = \Gamma_m \beta \equiv \Gamma_m \frac{\rho}{x} \tag{7.168}$$

with

$$\Gamma_m = (1+2m)^{1/2m} \; . \tag{7.169}$$

This implies, for example, that the lateral profile for $m = 1/2$ follows from (7.112) by substituting $\alpha = 2\rho/x$, i.e.,

$$F(\beta, x) = \frac{1}{2\pi} \frac{NCx/2}{(\beta^2 + (NCx/2)^2)^{3/2}} \, . \tag{7.170}$$

The quantity Γ_m decreases from 2.718 to 1.732 for m going from 0 to 1. It appears justified, for such a weak variation, to adopt power scattering with m dependent on the thickness. Quantitatively, such a dependence may be determined by matching a power-law profile to a Thomas-Fermi or Lenz-Jensen angular profile at angle zero. The two graphs in Fig. 7.14 show the variation of m and $\Gamma(\tau) \equiv \Gamma_m(\tau)$ with the dimensionless thickness parameter τ. You may note that the variation of Γ over a limited range of thicknesses is slow.

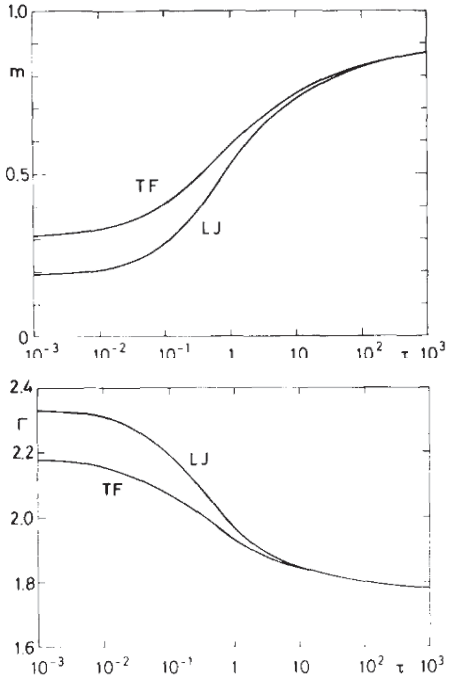

Fig. 7.14 Top: Effective exponent m for power scattering versus dimensionless target thickness τ. Bottom: Effective scaling factor Γ in (7.168). From Marwick and Sigmund (1975)

7.7.3 Numerical Results

Projected lateral profiles have been tabulated by Amsel et al. (2003) and may be downloaded from the homepage associated with that paper. Figure 7.15 shows a comparison between tabulated projected profiles for Thomas-Fermi interaction. Scaling has been tested by scaling the lateral profile, expressed through the chord angle β, to the angular profile at zero angle. This required a scaling factor $\Gamma = 1.94$, which is in perfect agreement with Fig. 7.14.

7.7.4 Measurements

Measurements of lateral distributions were performed by Sidenius and Andersen (1975) and by Knudsen et al. (1976). Figure 7.16 shows results for a large number of ions in the energy range 20–180 keV. Thomas-Fermi scaling appears well confirmed, and all results fall in between the Thomas-Fermi and the Lenz-Jensen prediction.

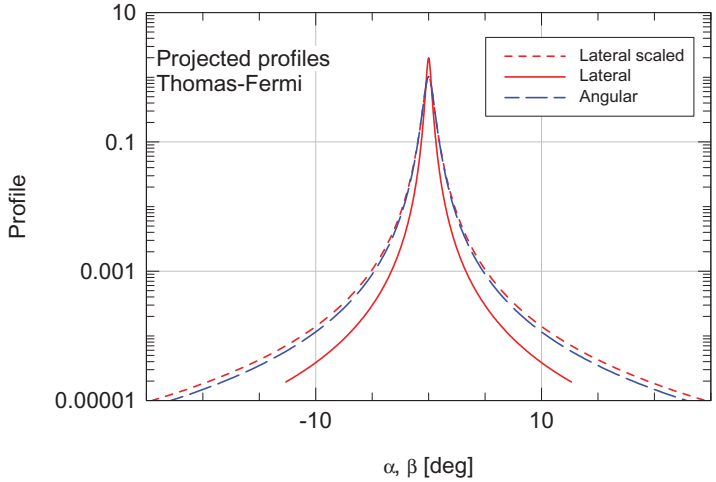

Fig. 7.15 Projected multiple-scattering profile for Thomas-Fermi interaction at thickness $\tau = 1$. Angular (blue) and lateral (red) profile according to Amsel et al. (2003). Dotted red line: Angular profile scaled by $\Gamma = 1.94$

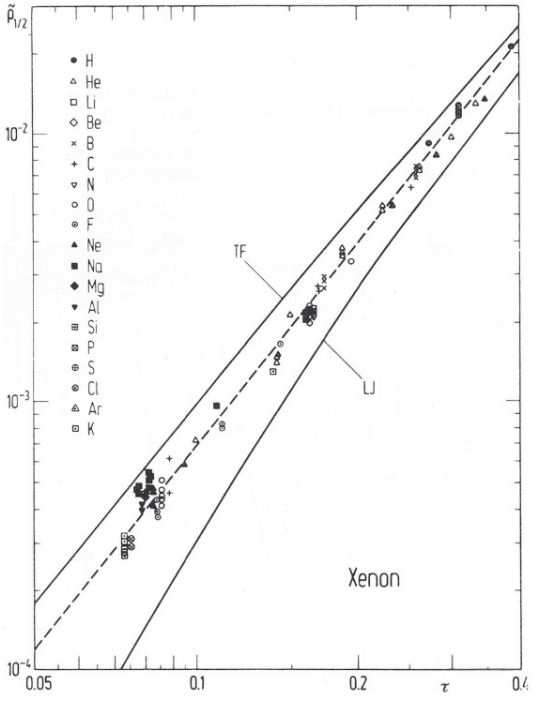

Fig. 7.16 Halfwidths of lateral profiles in xenon gas plotted in Thomas-Fermi units, measured by Sidenius and Andersen (1975) and compared with Thomas-Fermi and Lenz-Jensen prediction. Ions listed in the legend had energies between 20 and 180 keV. The stipled line serves to guide the eye. From Sidenius and Andersen (1975)

Lateral distributions in gases can be measured with good accuracy down to very low layer thicknesses in terms of atoms/area. This implies that when τ approaches

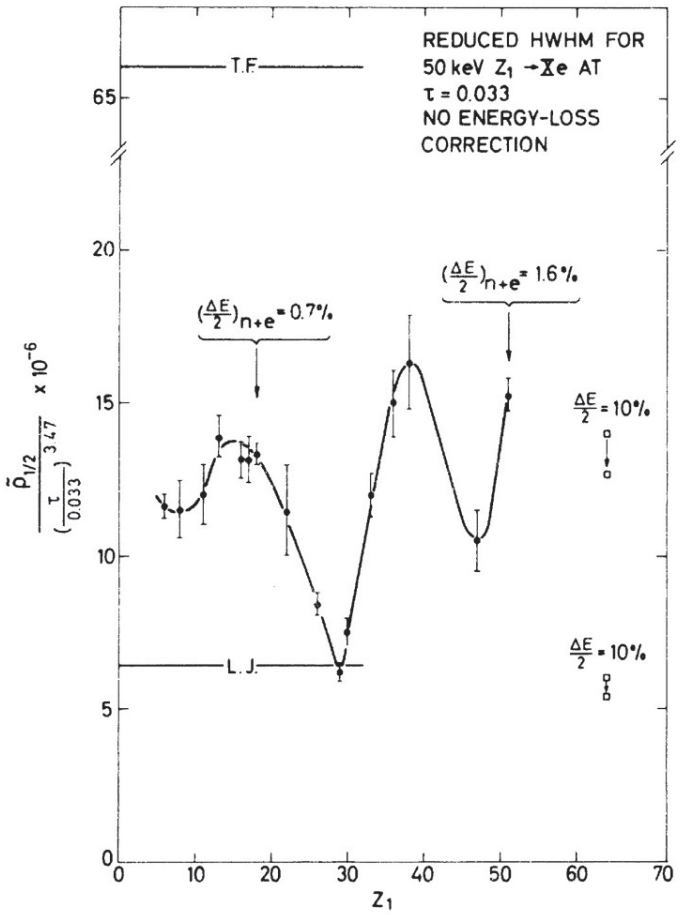

Fig. 7.17 Halfwidth of lateral profiles of ions in Xe gas measured by Knudsen et al. (1976) at very small target thickness corresponding to $\tau \simeq 0.033$. From Knudsen et al. (1976)

the single-collision regime, structure in the interatomic potential becomes visible when the profiles of ions with different atomic number Z_1 are compared. An example is shown in Fig. 7.17.

7.7.5 Packing

Unpublished measurements by Sidenius in the early 1970s of multiple scattering distributions in molecular gas revealed minor differences from the scaling prop-

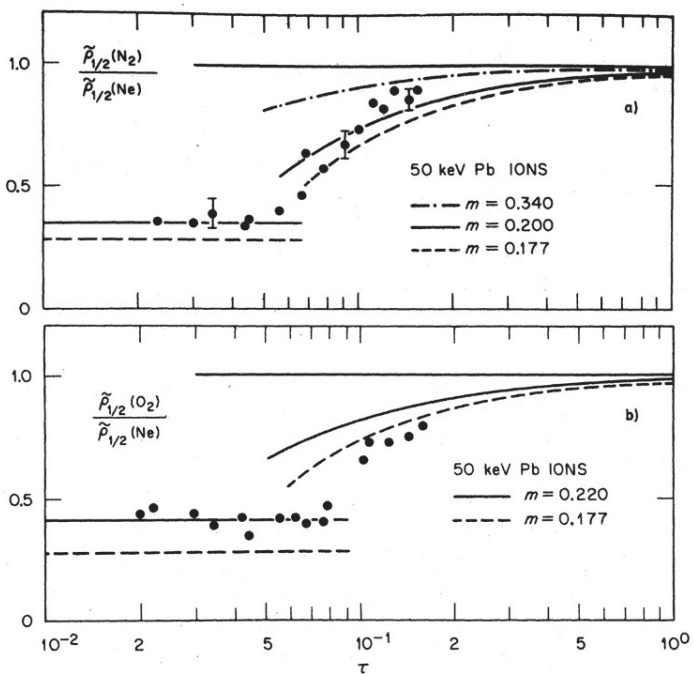

Fig. 7.18 Packing effect in multiple scattering. Ratio of multiple-scattering lateral half-widths of 50 keV Pb ions incident on nitrogen and neon (upper graph) and oxygen and neon (lower graph) gas targets. Calculations for power scattering from Sigmund (1977). Measurements and graph from Besenbacher et al. (1978)

erties predicted for atomic gases. These measurements initiated theoretical studies reported in Sects. 5.4 and 7.3.9.

Systematic measurements by Sidenius et al. (1976) and Besenbacher et al. (1978) revealed a substantial packing effect in molecular gases. Figure 7.18 shows a comparison of measured halfwidths with predictions based on (7.69) and power scattering (Sigmund, 1977). With decreasing layer thickness, pertinent scattering angles decrease, so representative impact parameters increase. With increasing impact parameter the potential of a molecule approaches the united-atom limit. This is indicated by the horizontal lines.

Unlike in the case of energy loss, the theory has not yet been generalized to solid targets. Multiple scattering distributions need to be characterized by the *distribution* rather than the second moment.

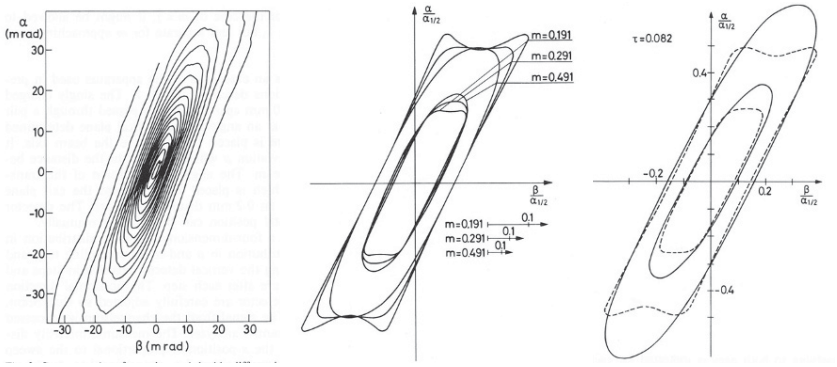

Fig. 7.19 Contours representing angular scans through a beam diameter. Left: Measured for 50 keV Ar in Xe at $\tau = 0.082$. Contours decreasing in 10% steps; Middle: Calculated for power scattering with exponents $m = 0.191$, 0.291 and 0.491. Right: Comparison of calculation (dashed curves) with experiment (solid curves) for contours 50 and 23%. From Sigmund et al. (1978)

7.7.6 Angular-Lateral Distribution

You can easily convince yourself that in the diffusion approximation, (7.108), the angular distribution in a given point $\boldsymbol{r} = (x, \boldsymbol{\rho})$ in space has contour lines

$$\left(\boldsymbol{\alpha} + \frac{3}{2}\boldsymbol{\beta}\right)^2 + \frac{3}{4}\beta^2 = \text{constant}\,, \tag{7.171}$$

i.e., a set of ellipses centered around the origin.

Approximate calculations for power scattering have been reported by Firsov et al. (1976) for the power potential with $m = 1/2$ and applied to measurements of energy spectra of ions reflected from plane surfaces after grazing incidence. Approximate calculations for arbitrary power potentials, $0 < m < 1$ were reported and compared with measurements by Sigmund et al. (1978), see Fig. 7.19.

More systematic calculations by Amsel et al. (2003) are likewise based on power scattering. Figure 7.20 shows the variation with the power exponent starting from the diffusion limit (upper-left graph).

7.8 Energy-Angular Distribution

Joint distributions in energy and angle are of interest in several areas. An aspect of considerable practical importance is the angular distribution at layer thicknesses large enough so that energy loss cannot be neglected. Several options to overcome this problem in cases where the energy loss is small compared to the beam energy have been mentioned in Sect. 7.4.2.2 and will not be discussed further here. Situa-

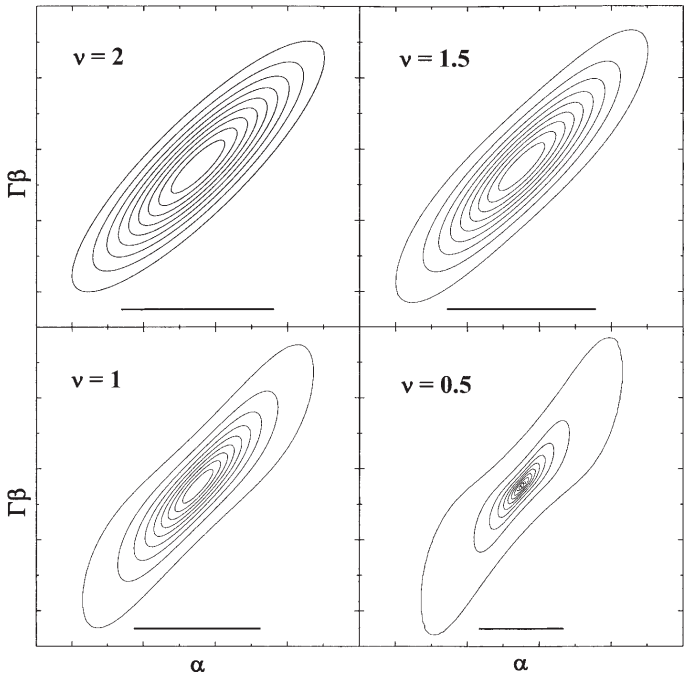

Fig. 7.20 Contour graphs (10%) for power scattering with exponent $m = \nu/2$. From Amsel et al. (2003)

tions where the energy loss is comparable to the beam energy belong into the topic of ion ranges to be discussed in Chap. 9.

Here are two specific situations, where correlated energy-angle distributions serve as a useful and, perhaps, necessary tool:

- Separating nuclear from electronic stopping in cases where both mechanisms contribute to stopping.
- Measurements involving resonance effects such as Doppler-shift attenuation to determine nuclear lifetimes, or inverted-Doppler-shift attenuation to measure stopping forces.
- A third situation, sometimes called the Ishiwari-effect, generated considerable theoretical activity because the effect, if real, would have cast doubt at the outcome of numerous measurements of electronic stopping.

I shall here briefly discuss the first of these three topics.

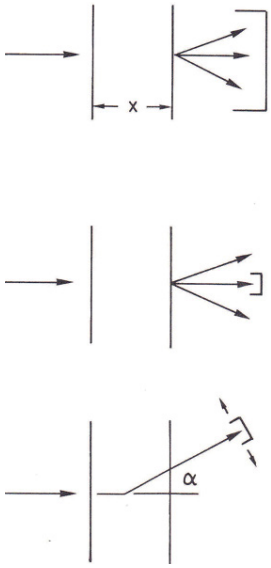

Fig. 7.21 Detector geometries in stopping measurements. From Sigmund (1991)

7.8.1 Separation of Nuclear from Electronic Stopping

While the energy loss of a particle along its path is determined by the sum of the electronic and the nuclear stopping cross section, the radiation effects caused by the two processes are different in both character and magnitude and, therefore, will typically be studied separately. Moreover, stopping theory delivers estimates of electronic and nuclear stopping cross sections. For both reasons, measurements are needed from which data on electronic and nuclear stopping can be extracted separately.

Figure 7.21 shows three characteristic geometries. In the upper graph the detecting device records the energy loss of all, or at least the majority of the incident particles. In such an experiment the quantity measured is the sum of the electronic and nuclear stopping cross section. This geometry is convenient for direct measurements of nuclear stopping in the energy regime where electronic stopping is negligible.

The middle graph shows the opposite extreme, where the detector records energy losses of particles scattered into a a narrow angular range around the direction of incidence. This is the standard geometry in electronic-stopping measurements. Nuclear energy losses in single collisions are small for small scattering angles and, dependent on the opening angle, negligible. However, multiple-scattering trajectories may involve larger angles. Therefore, nuclear stopping will not be completely suppressed.

The geometry sketched in the lower graph allows an angular scan of the energy loss. We shall get back to this case in Sect. 7.8.2.

Let us first find out some criteria regarding the importance of a nuclear-stopping correction. Roughly, nuclear stopping has its maximum at a dimensionless energy

$\epsilon \sim 1$ according to Fig. 6.22, or

$$\frac{1}{2}uv^2 \sim \left(\frac{1}{A_1} + \frac{1}{A_2}\right)\frac{Z_1 Z_2 e^2}{a} \sim (A_1 + A_2)\frac{e^2}{4a} = E_c\,, \tag{7.172}$$

if we set $A_1 \sim 2Z_1$ and $A_2 \sim 2Z_2$. At beam energies far above E_c, nuclear stopping will be a small correction. For lower beam energies, nuclear stopping will become a significant contribution for light ions, and dominating for heavier ions.

Next, let us look at the peak energy loss due to nuclear stopping in the beam direction. An elegant and efficient approximation was offered by Fastrup et al. (1966), based on the Bohr-Williams theory of multiple scattering with the limiting angle α^* defined by (7.122). Now, for small scattering angles, the relation $T = T_{\max} \sin^2 \Theta/2$ reduces to

$$T = \frac{M_1}{M_2} E\phi^2 \tag{7.173}$$

for $M_1 < M_2$. It is assumed, then, that the energy-loss spectrum at angles $\alpha > \alpha^*$ reflects the single-scattering cross section, while for $\alpha < \alpha^*$ one expects a gaussian-like spectrum centered around

$$T^* = \frac{M_1}{M_2} E\alpha^{*2}\,. \tag{7.174}$$

This is equivalent with

$$T^* = \int_0^{T^*} T\, \mathrm{d}\sigma(T)\,. \tag{7.175}$$

A rigorous description, based on the Bothe-Landau equation is due to Glazov and Sigmund (2003). Here (7.83) was solved numerically for Thomas-Fermi and Lenz-Jensen interaction neglecting electronic stopping. Figure 7.22 shows universal plots of nuclear-energy-loss profiles at angle zero. You may take note of considerable skewness and, in particular at the smallest τ-value, a major difference between Lenz-Jensen and Thomas-Fermi interaction which could be expected on the basis of Fig. 6.22.

Figure 7.23 shows a comparison between the two approaches, which indicates good quantitative agreement for τ-values down to $\tau \sim 1/2$.

What happens for $M_1 > M_2$? Here the energy-loss spectrum has two branches, one of which has its maximum at $\alpha = 0$. This binary-collision peak is well separated from what has been discussed in this section. Depending on target thickness it may even lie far above the electronic-energy-loss spectrum. Its presence may suggest inspection of the measured spectrum, but it should not preclude extraction of accurate stopping parameters.

For a detailed discussion both of the pertinent theory and examples of nuclear-stopping corrections applied in the literature the reader is referred to Glazov and Sigmund (2003).

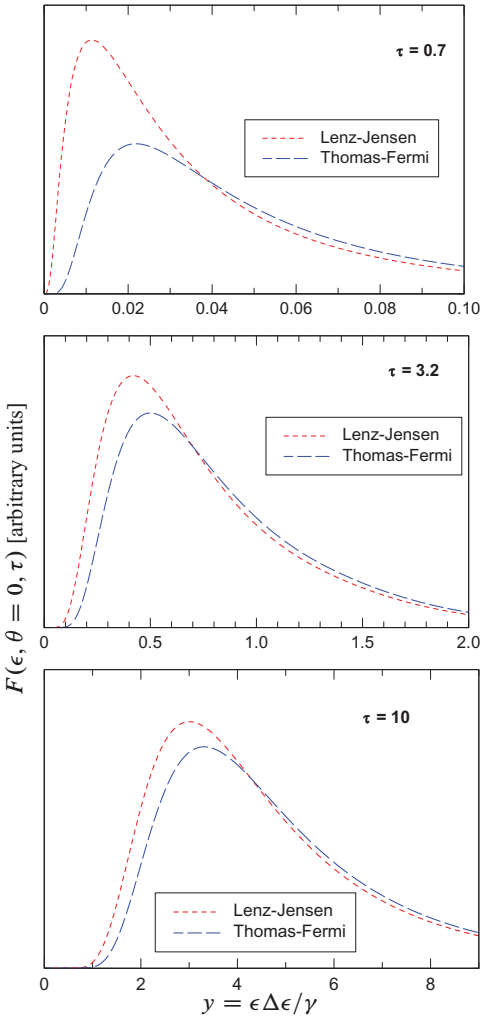

Fig. 7.22 Energy-loss spectra in forward direction. Nuclear stopping only. τ is the foil thickness in Thomas-Fermi units, (7.136). From Glazov and Sigmund (2003)

7.8.2 Angular Scan

Going back to Fig. 7.21 consider now the third of the three geometries, i.e., an angular scan of the energy-loss spectrum or related parameters such as the mean energy loss. At angles large enough to ensure single-collision conditions such measurements may provide information on differential cross sections. Conversely, only little variation of the energy-loss and related quantities is expected within the multiple-scattering angle.

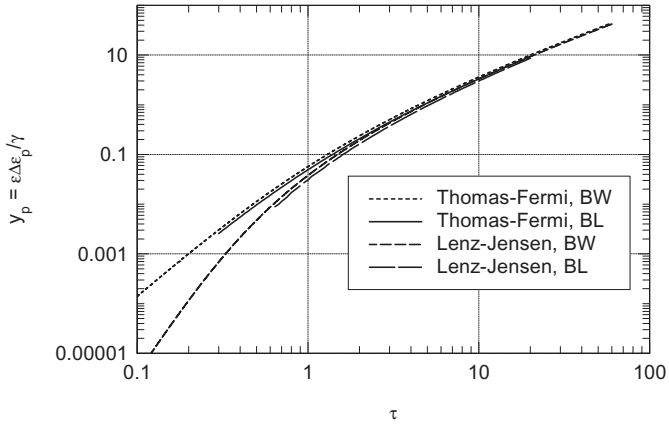

Fig. 7.23 Most probable energy loss in beam direction, calculated from (7.122) (BW) and (7.80) (BL). From Glazov and Sigmund (2003)

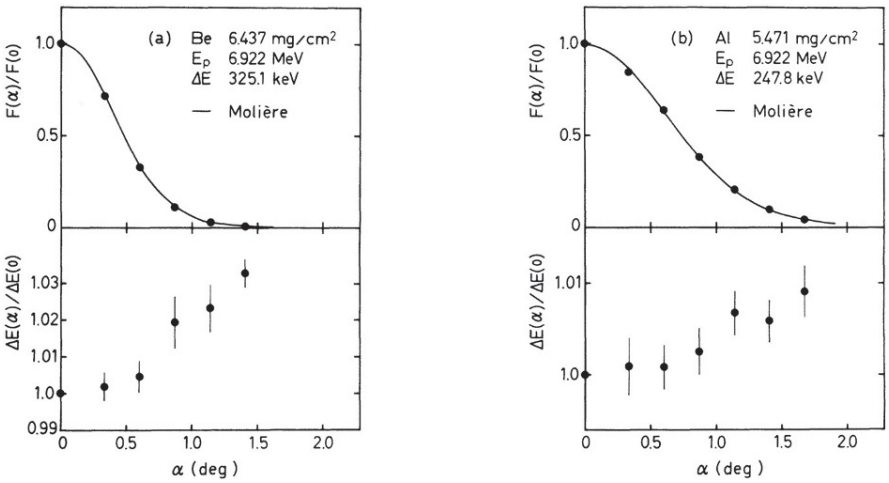

Fig. 7.24 Mean energy loss versus emergence angle of 7 MeV protons in Be and Ag foils. Also the multiple scattering distributions are shown. From Ishiwari et al. (1982)

It was a surprise, therefore, when Ishiwari et al. (1982) reported a variation in the mean energy loss of 7 MeV protons in metallic and organic foils. Figure 7.24 shows two examples, representing a light and a heavy target, Be and Ag, respectively. It was shown that this effect could not be explained in terms of nuclear stopping and was, therefore, tentatively ascribed to electronic stopping.

As a consequence, several attempts were made to explain the phenomenon theoretically by Meyer et al. (1977), Jakas et al. (1983, 1984a), Gras-Marti (1985), Sigmund and Winterbon (1985), starting at the Bothe-Landau formula or its exten-

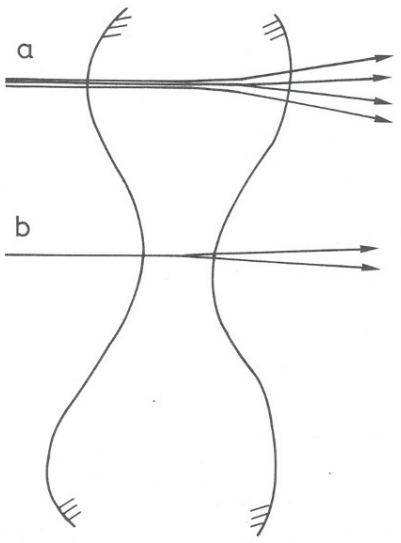

Fig. 7.25 Schematic illustration of the fact that for a nonuniform target, high energy loss tends to correlate with high multiple-scattering angles

sion, (7.80). These studies were useful theoretical exercises but did not explain the 'Ishiwari effect' indicated in Fig. 7.24.

A credible explanation was given by Lindhard (1984), stimulated by the similarity of $\Delta E(\Theta)$ with the multiple-scattering profile following Molière (1948), which is also shown in Fig. 7.24. Figure 7.25 shows a schematic view of a foil with a nonuniform thickness. For particles passing through the foil at point b, where the thickness is small, both energy loss and multiple scattering angle are relatively small, whereas the opposite is the case for particles passing through point a. Thus, the energy loss increases with increasing α.

Numerical estimates by Mertens and Krist (1986) confirmed the reality of the effect in principle. Subsequent measurements by Ishiwari et al. (1990) and Sakamoto et al. (1992) were performed with 5 MeV H^+ on Cu. Foil thickness nonuniformity was measured to be 4 and 2 pct. After correction for nonuniformity, a 0.75% increase in energy loss up to 3° remained, which was ascribed to impact-parameter-dependent electronic energy loss.

Figure 7.26 shows that for 5 MeV H^+ on Cu, a scattering angle $1° < \phi < 3°$ corresponds to an impact parameter $0.005 < p < 0.016$ Å. In this interval, the electronic energy loss shows a variation of 0.1 eV according to the CasP code (Grande and Schiwietz, 2010), while the nuclear energy loss varies between 20 and 200 eV. Both contributions, which have to be compared with a mean energy loss of 111.40 keV, have been included in Fig. 7.26. We may conclude, therefore, that angular variations in the energy loss of protons observed at these high energies do not reflect an unexpected dependence on impact parameter of the electronic energy loss.

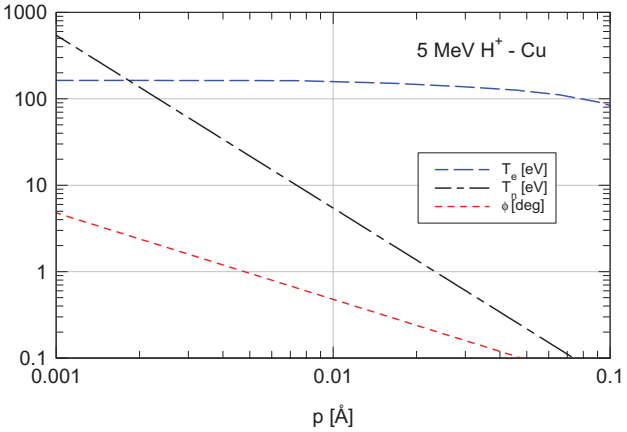

Fig. 7.26 Dependence of scattering angle ϕ (from Rutherford's law) and electronic energy loss T on impact parameter p in single collision of 5 MeV H^+ on Cu atom (from CasP (Grande and Schiwietz, 2010)

Several experiments have been carried out involving lower beam energies and/or heavier ions and supported by pertinent theory. While there is no doubt about the existence of angular-dependent stopping, such experiments have not led to surprising results or generated controversies. Studies by Jakas et al. (1984b), Geissel et al. (1984), Bednyakov et al. (1986), Lantschner et al. (1987) and Lennard and Geissel (1992) give an impression of this topic.

7.8.3 Trajectory Inversion

Another surprising effect was reported by Pronko et al. (1979). Figure 7.27 shows a Rutherford backscattering spectrum from a massive target, in casu 800 keV He^+ on copper. This spectrum is of the type shown in Fig. 1.7, Vol. 1, except that the penetration depth at which backscattering took place replaces the energy scale on the abscissa. A special feature in this experiment is the use of detectors that allow to study backscattering angles close to 180°. Two detectors have been employed with acceptance angles of 0.2 (narrow acceptance) and 4.5° (wide acceptance).

The spectrum for wide acceptance is seen to show the regular behaviour which is found for scattering angles off 180°, while a pronounced increase is observed for ions backscattered from the near-surface region into the narrow-acceptance detector. Evidently, the two curves have been normalized such as to agree in deeper layers.

It was observed immediately by Jakas and Baragiola (1980) and Crawford (1980) that the effect had to be related to reversibility: Consider a static material structure, regular or random, and disregard thermal vibrations. Then an ion backscattered from a target atom at 180° will undergo essentially the same trajectory as on the way

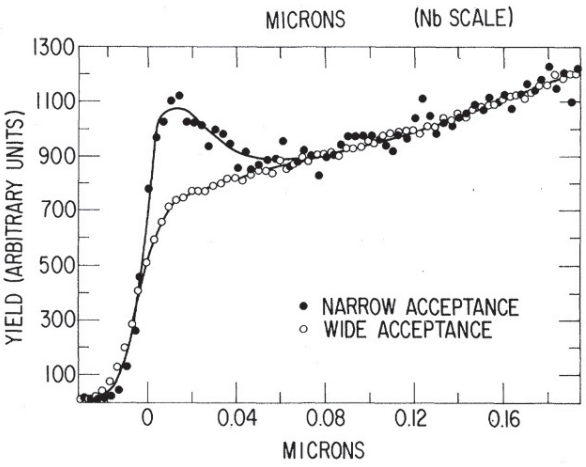

Fig. 7.27 Rutherford spectrum of 800 keV He^+ scattered from a thick Cu target. Instead of the energy of the backscattered ion the abscissa scale shows the depth of penetration at which backscattering has taken place. 'Narrow' and 'wide' acceptance indicate detector angles of 0.2 and 4.5°, respectively. From Pronko et al. (1979)

in, i.e., even though it undergoes multiple scattering it will emerge from the solid opposite to its incoming direction. Effects causing deviations from strict reversibility are

- Energy loss in the backscattering event, which changes all cross sections,
- Energy loss by electronic stopping, which changes cross sections gradually,
- Motion of recoil atoms in the time between scattering events on the way in and out, which changes impact parameters, and
- Thermal vibrations in the structure, which likewise changes impact parameters.

Here the first effect must be dominating at low penetration depth, while the others contribute to its gradual disappearance at larger depths due to increased pathlength and timespan.

All these effects can be accounted for in proper simulations, and good agreement with measurements has been achieved already by Barrett et al. (1980). A treatment by transport theory by Jakas et al. (1984a), assuming a random medium, allowed for energy change in the backscattering event. Reasonable agreement with measurements was achieved in the depth range where the effect is small, but the effect is underestimated at depth zero, presumably because both the change in velocity and the lateral displacement were treated as small perturbations.

7.9 Discussion and Outlook

Multiple scattering of ions is a comparatively well-developed area in the theory of particle penetration. With regard to the weakly-screened regime, i.e., protons and alpha particles, this has been so already half a century ago (Scott, 1963). Calculations and tabulations for heavier ions (Meyer, 1971, Sigmund and Winterbon, 1974, Amsel et al., 2003) provide fairly comprehensive coverage of both angular and lateral profiles, as far as penetration through unlimited media is concerned. Problems must be faced when surfaces are involved, such as in the scattering of particle beams at grazing incidence on a plane surface (Winter, 2002). There are analytical treatments on the topic, most notably by Firsov (1970), where the algebraic complexity is overcome by assuming $1/R^2$ interaction.

Limitations of the analytical schemes discussed in this chapter are most easily identified from the results: Caution is indicated when scattering angles and/or energy losses become large or when a profile overlaps with target inhomogeneities such as surfaces and voids. Monte Carlo simulation is the standard strategy to deal with such problems. This, however, hinges on a proper treatment of small-angle scattering and hence, requires careful consideration of how to truncate the interaction potential as mentioned in Sect. 7.3.6.

I have mentioned several types of correlation in this chapter, although in a more cursory form, mainly to illustrate the power of transport theory. While analytic solutions are not necessarily available, you should be aware that simulational solution may require excessive computation times, depending on the number of variables involved.

Problems

7.1. Derive the transport equation (7.54) from (7.1) by assuming one of the two layers to be infinitesimally small. If needed, get help from Sect. 9.5.1, Vol. 1.

7.2. Derive (7.35) and (7.34) explicitly, starting at (7.1) by going through the argument that led to the Bothe-Landau formula for the energy loss.

7.3. Evaluate the multiple-scattering distribution *versus* pathlength of a particle restricted to a plane and able to undergo scattering events with equal probability for $\phi = \pm 90°$. Write up the result as a sum of two standard Fourier series and generate a few representative plots.

7.4. Derive (7.59) and (7.60) from (7.40).

7.5. Determine the screening angle ϕ_a for Yukawa screening. Use the scattering law resulting from the Born approximation, (3.94), Vol. 1.

7.6. Show that Lindhard-Scharff scaling, defined in Sect. 6.3.3.2, holds rigorously within the small-angle approximation for any screened-Coulomb potential. Show that the function $\tilde{g}(\tilde{\phi})$ relates to the function $f(\epsilon \sin(\Theta/2))$ introduced in (6.57) as

$$\tilde{g}(\tilde{\phi}) = \tilde{\phi} f(\tilde{\phi}/2). \tag{7.176}$$

7.7. Derive (7.138)–(7.141) from (3.86), (3.89) and (3.90) in Volume 1.

7.8. Unlike (7.149), (7.152) does not involve the screening radius. Derive a condition for (7.152) to be a stronger restriction than (7.152) and draw a conclusion.

7.9. Show that for Born scattering on an exponentially-screened Coulomb potential the screening angle becomes $\hat{\phi} = 1$.

7.10. Evaluate the projected angular distribution for the cross section (7.110). Start from (7.60) and/or (7.112).

7.11. Convince yourself, on the basis of the Rutherford cross section, that the magnitude of $\Delta E(\alpha)$ shown in Fig. 7.24 cannot be explained by nuclear energy loss.

7.12. Construct a few diagrams of the type of Fig. 7.26 for 0.5 MeV H^+ and for 5 MeV C^+ on Cu.

7.13. Try to estimate the relative significance of recoil motion and thermal vibrations on the difference between impact parameters on the way in and out in the experiment shown in Fig. 7.27. Hint: Look at the distance travelled in the intervening time.

References

Amsel G., Battistig G. and L'Hoir A. (2003): Small angle multiple scattering of fast ions, physics, stochastic theory and numerical calculations. Nucl Instrum Methods B **201**, 325–388. URL `http://www.mfa.kfki.hu/ms/`

Andersen H.H. and Bøttiger J. (1971): Multiple scattering of heavy ions of keV energies transmitted through thin carbon films. Phys Rev B **4**, 2105–2111

Andersen H.H., Bøttiger J., Knudsen H., Petersen P.M. and Wohlenberg T. (1974): Multiple scattering of heavy ions of keV energies transmitted through thin films. Phys Rev A **10**, 1568–1577

Anne R., Herault J., Bimbot R., Gauvin H., Bastin G. and Hubert F. (1988): Multiple angular scattering of heavy ions (^{16,17}O, ^{40}Ar, ^{86}Kr and ^{100}Mo) at intermediate energies (20-90 MeV/u). Nucl Instrum Methods B **34**, 295–308

Barrett J.H., Appleton B.R. and Holland O.W. (1980): Role of reversibility in enhanced ion backscattering near 180° scattering angle. Phys Rev B **22**, 4180–4183

Bednyakov A.A., Chumanov V.Y., Chumanova O.V., Iferov G.A., Khodyrev V.A., Tulinov A.F. and Zhukova Y.N. (1986): Dependence of energy-loss of light-ions in au on scattering angle and target thickness in the energy interval 25 to 500 kev/amu. Nucl Instrum Methods B **13**, 146–151

Besenbacher F., Heinemeier J., Hvelplund P. and Knudsen H. (1978): Influence of spatial correlation between target atoms on the scattering of energetic ions: Multiple scattering in molecular gases. Phys Rev A **18**, 2470–2481

Bethe H. (1930): Zur Theorie des Durchgangs schneller Korpuskularstrahlen durch Materie. Ann Physik **5**, 324–400

Bethe H.A. (1953): Moliere's theory of multiple scattering. Phys Rev **89**, 1256–1266

Bohr N. (1913): On the theory of the decrease of velocity of moving electrified particles on passing through matter. Philos Mag **25**, 10–31

Bothe W. (1921a): Das allgemeine Fehlergesetz, die Schwankungen der Feldstärke in einem Dielektrikum und die Zerstreuung der alpha-Strahlen. Z Physik **5**, 63–69

Bothe W. (1921b): Theorie der Zerstreuung der α-Strahlen über kleine Winkel. Z Physik **4**, 300–314

Crawford O.H. (1980): Origin of the anomalous enhancement of 180-degrees backscattering yields for light-ions in solid targets. Phys Rev Lett **44**, 185–188

Fastrup B., Hvelplund P. and Sautter C.A. (1966): Stopping cross section in carbon of 0.1-1.0 MeV atoms with $6 < Z_1 < 20$. Mat Fys Medd Dan Vid Selsk **35 no. 10**, 1–28

Firsov O.B. (1970): Glancing-angle particle reflection from a solid for an inverse-square interaction potential. Zh Tekh Fiz **40**, 83. Engl. translation: Sov. Phys. Techn. Phys. 15, 57 (1970)

Firsov O.B., Mashkova E.S., Molchanov V.A. and Snisar V.A. (1976): Small-angle multiple particle scattering in the inverse-square interaction potential approximation. Nucl Instrum Methods **132**, 695–702

Geissel H., Lennard W.N., Andrews H.R., Jackson D.P., Mitchell I.V., Philips D. and Ward D. (1985): Energy-angle distribution measurements for 0.8 v_0 ^{20}Ne and ^{209}Bi ions. Nucl Instrum Methods B **12**, 38–42

Geissel H., Lennard W.N., Andrews H.R., Ward D. and Phillips D. (1984): Problems of interpreting energy loss data for non-zero emergent angles. Phys Lett A **106**, 371–373

Geissel H., Weick H., Scheidenberger C., Bimbot R. and Gardès D. (2002): Experimental studies of heavy-ion slowing down in matter. Nucl Instrum Methods B **195**, 3–54

Glazov L.G. and Sigmund P. (2003): Nuclear stopping in transmission experiments. Nucl Instrum Methods B **207**, 240–256

Goudsmit S. and Saunderson J.L. (1940): Multiple scattering of electrons. Phys Rev **57**, 24–29

Grande P.L. and Schiwietz G. (2010): CasP version 4.1. URL `www.casp-program.org/`

Gras-Marti A. (1985): Increased energy losses in off-beam directions for MeV protons traversing thin films. Nucl Instrum Methods B **9**, 1–5

Hooton B.W., Freeman J.M. and Kane P.P. (1975): Small angle multiple scattering of 12 – 40 MeV heavy ions from thin foils. Nucl Instrum Methods **124**, 29–39

ICRU (2005): *Stopping of ions heavier than helium*, vol. 73 of *ICRU Report*. Oxford University Press, Oxford

Ishiwari R., Shiomi N. and Sakamoto N. (1982): Geometrical effect on the measurement of stopping power: angle-dependent energy loss of 7-MeV protons in metallic and organice films. Phys Rev A **25**, 2524–2528

Ishiwari R., Shiomi-Tsuda N., Sakamoto N. and Ogawa H. (1990): Geometrical effect on the measurement of stopping powers - angle-dependent energy-loss of 5 mev protons in Cu. Nucl Instrum Methods B **51**, 209–215

Jakas M.M. and Baragiola R.A. (1980): Explanation for the 180-degrees Rutherford backscattering anomaly in solids. Phys Rev Lett **44**, 424–426

Jakas M.M., Lantschner G.H., Eckardt J.C. and Ponce V.H. (1983): Angular dependence of stopping power. phys stat sol B **117**, Kl31

Jakas M.M., Lantschner G.H., Eckardt J.C. and Ponce V.H. (1984a): Study of the angular dependence of the average energy loss for ions in solids. Phys Rev A **29**, 1838–

Jakas M.M., Lantschner G.H., Eckardt J.C. and Ponce V.H. (1984b): Study on the angular-dependence of the average energy-loss for ions in solids. Phys Rev A **29**, 1838–1843

Kanter E.P. (1983): Dependence of multiple-scattering distributions on the charge states of fast ions exiting from solid targets. Phys Rev A **28**, 1401–1604

Knudsen H., Besenbacher F., Heinemeier J. and Hvelplund P. (1976): Lateral multiple-scattering of energetic ions in very thin targets - Z_1 oscillations. Phys Rev A **13**, 2095–2105

Lantschner G.H., Eckardt J.C., Jakas M.M., Capuj N.E. and Ascolani H. (1987): Variation of peak energy for energy loss with angle of observation. Phys Rev A **36**, 4667

Lennard W.N. and Geissel H. (1992): Impact parameter dependent energy loss for heavy ions: an overview. In A. Gras-Marti, H.M. Urbassek, N.R. Arista and F. Flores, editors, *Interaction of charged particles with solids and surfaces*, 347. NATO ASI Series vol 271, Plenum Press, New York

Lindhard J. (1970): Classical directional effects for energetic electrons in crystals. In D.W. Palmer, M.W. Thompson and P.D. Townsend, editors, *Atomic Collision Phenomena in Solids*, 1. North Holland, Amsterdam

Lindhard J. (1984): unpublished

Marwick A.D. and Sigmund P. (1975): Small-angle multiple scattering of ions in the screened Coulomb region. 2. Lateral spread. Nucl Instrum Methods **126**, 317–323

Mertens P. and Krist T. (1986): The influence of foil inhomogeneities on the angular dependence of experimental stopping cross sections. Nucl Instrum Methods B **13**, 95

Meyer L. (1971): Plural and multiple scattering of low-energy heavy particles in solids. phys stat sol (b) **44**, 253–268

Meyer L., Klein M. and Wedell R. (1977): The energy-angle distribution of heavy particles penetrating solids. phys stat sol B **83**, 451

Molière G. (1948): Theorie der Streuung schneller geladener Teilchen. II. Mehrfach- und Vielfachstreuung. Z Naturforsch **3a**, 78–97

Pronko P.P., Appleton B.R., Holland O.W. and Wilson S.R. (1979): Anomalous yield enhancement for highly collimated 180-degrees scattering of He^+ in amorphous and polycrystalline materials. Phys Rev Lett **43**, 779–782

Rozet J.P., Stephan C. and Vernhet D. (1996): ETACHA: a program for calculating charge states at GANIL energies. Nucl Instrum Methods B **107**, 67–70

Sakamoto N., Ogawa H., Shiomi-Tsuda N. and Ishiwari R. (1992): Geometrical effect on the measurement of stopping power - angle-dependent energy-loss 5 Mev protons in Cu. Nucl Instrum Methods B **69**, 84–88

Scheidenberger C., Stöhlker T., Meyerhof W.E., Geissel H., Mokler P.H. and Blank B. (1998): Charge states of relativistic heavy ions in matter. Nucl Instrum Methods B **142**, 25

Schwab T., Geissel H., Armbruster P., Gillibert A., Mittig W., Olson R.E., Winterbon K.B., Wollnik H. and Munzenberg G. (1990): Energy and angular distributions for Ar-ions penetrating solids. Nucl Instrum Methods B **48**, 69–74

Scott W.T. (1949): Correlated probabilities in multiple scattering. Phys Rev **76**, 212–219

Scott W.T. (1963): Theory of small-angle multiple scattering of fast charged particles. Rev Mod Phys **35**, 231–313

Sidenius G. and Andersen N. (1975): Multiple-scattering of keV ions - lateral distributions in xenon. Nucl Instrum Methods **128**, 271–276

Sidenius G., Andersen N., Sigmund P., Besenbacher F., Heinemeier J., Hvelplund P. and Knudsen H. (1976): Effect of molecular geometry on multiple scattering of heavy energetic particles. Nucl Instrum Methods **134**, 597–599

Sigmund P. (1977): Classical scattering of charged particles by molecules, single and multiple collisions at small angles. Mat Fys Medd Dan Vid Selsk **39 no. 11**, 1–32

Sigmund P. (1991): Statistics of charged-particle penetration. In A. Gras-Marti, H.M. Urbassek, N. Arista and F. Flores, editors, *Interaction of charged particles with solids and surfaces*, vol. 271 of *NATO ASI Series*, 73–144. Plenum Press, New York

Sigmund P., Heinemeier J., Besenbacher F., Hvelplund P. and Knudsen H. (1978): Small-angle multiple scattering of ions in the screened-Coulomb region. III. Combined angular and lateral spread. Nucl Instrum Methods **150**, 221–231

Sigmund P. and Winterbon K.B. (1974): Small-angle multiple scattering of ions in the screened Coulomb region, I. Angular distributions. Nucl Instrum Methods **119**, 541–557

Sigmund P. and Winterbon K.B. (1975): Erratum. Nucl Instrum Methods **125**, 491

Sigmund P. and Winterbon K.B. (1985): Energy loss spectrum of swift charged particles penetrating a layer of material. Nucl Instrum Methods B **12**, 1–16

Snyder H.S. and Scott W.T. (1949): Multiple scattering of fast charged particles. Phys Rev **76**, 220–225

Spahn G. and Groeneveld K.O. (1975): Angular straggling of heavy and light ions in thin solid foils. Nucl Instrum Methods **123**, 425–429

Valdes J.E. and Arista N.R. (1994): Energy-loss effects in multiple-scattering distributions of ions in matter. Phys Rev A **49**, 2690–2696

Williams E.J. (1939): Concerning the scattering of fast electrons and of cosmic-ray particles. Proc Roy Soc A **169**, 531–572

Winter H. (2002): Collisions of atoms and ions with surfaces under grazing incidence. Phys Repts **367**, 387–582

Winterbon K.B. (1987): Finite-angle multiple-scattering. Nucl Instrum Methods B **21**, 1–7

Winterbon K.B. (1989): Finite-angle multiple-scattering revisited. Nucl Instrum Methods B **43**, 146–148

Part IV
Slow Ions

Chapter 8
Stopping of Slow Ions

Abstract This chapter addresses the stopping and straggling of ions at velocities up to the Thomas-Fermi speed $v_{TF} = Z_1^{2/3} v_0$, with the main focus on velocities up to the Bohr speed v_0.This topic is characterized by many unsolved problems both on the experimental and the theoretical side. Experimental findings play a more dominant role in this chapter than in other parts of this monograph. The newly found reciprocity principle is explored in the evaluation of data. Much existing theory is based directly or indirectly on electron-gas theory, especially Fermi-gas theory. The Lindhard-Scharff formula and Firsov's theory are discussed along with various extensions. The transport cross section approach is explored in conjunction with partial waves, Born approximation as well as linear and nonlinear dielectric theory. Stopping cross sections are known to show pronounced oscillations as a function of the atomic number Z_1 of the projectile, and presumably also of Z_2, where evidence is weaker.

8.1 Introductory Comments

Figure 4.1 indicates severe limitations of both Bohr and Bethe stopping theory toward low beam energies. For O in Al, the stopping cross section turns negative at $\sim$ 300 keV/u according to the Bohr formula and at $\sim$ 70 keV/u for the simple Bethe formula. We have seen in chapter 4 that a number of corrections extend the range of validity of both theories toward lower projectile velocities. Although excellent agreement with experimental results was found in some systems down to $\sim$ 1 keV/u, significant discrepancies were found in others.

The simple Bethe stopping formula assumes the orbital speed of the target electrons to be negligible compared to the projectile speed. Orbital speeds are not even considered in the original Bohr theory, which was developed before Bohr's atomic model. At energies below 100 keV/u we deal with projectile speeds of the order of the Bohr speed v_0 or less, i.e., a velocity range representative of outer-shell target electrons.

P. Sigmund, *Particle Penetration and Radiation Effects Volume 2*,
Springer Series in Solid-State Sciences 179, DOI: 10.1007/978-3-319-05564-0_8,

Orbital motion of target electrons is taken care of by the shell correction. Once a correction is not small but becomes the dominating feature, there is a strong motivation to build up the theory from the opposite end, in casu a projectile moving slowly compared to the orbital speed of the electrons.

Neglecting orbital motion is not the only limitation: Bethe's theory is based on the Born approximation which represents an expansion in terms of the Sommerfeld parameter $Z_1 e^2/\hbar v$. This parameter gets large when v gets small. Although we have learned that Bohr theory takes over at lower projectile speeds, the treatment of distant interactions in Bohr's theory (cf. Sect. 4.2.2, Vol. 1) rests on the 'sudden' approximation, i.e., the assumption that the displacement of a target electron during the interaction is negligible. Clearly, there must be a lower limit of the velocity range where such an assumption is valid.

We may conclude that stopping of slow ions needs a different theoretical basis, taking due account of the fact that the perturbation of the medium by the projectile may be substantial, that interaction times are not small, and that the electronic structure of the target in the vicinity of the projectile may be distorted significantly.

Major complications also exist on the experimental side. As you may see from Fig. 4.3, there is considerable scatter in the experimental data. Part of this is caused by the asserted scaling in the graph, where measurements employing oxygen on numerous target materials are involved. However, we shall see below that there is also substantial scatter between experimental data on one and the same system.

Stopping measurements in the conventional transmission geometry require thinner and thinner foils, the lower the beam energy. This is a severe limitation in particular for heavy ions, where the stopping force is large.

Moreover, the contribution from nuclear stopping to the total stopping cross section increases with decreasing energy. Therefore, separating nuclear from electronic stopping is essential in comparisons with theoretical predictions.

Finally, nuclear stopping is intimately connected to angular scattering. Therefore the proper correction for nuclear stopping depends on the experimental geometry.

At the time of writing a universal theory of electronic stopping for slow ions is not readily available. Just as in case of swift ions, stopping of light ions has received more interest both experimentally and theoretically. Since stopping of slow light ions such as protons and antiprotons has not been considered in detail in Volume 1, attention will be given to this subject here, although stopping of heavier ions is the main issue.

8.2 Velocity-proportional Stopping?

It may be useful to start with a rather general survey of experimental observations as well as theoretical considerations. More quantitative insight will be looked for in the following sections.

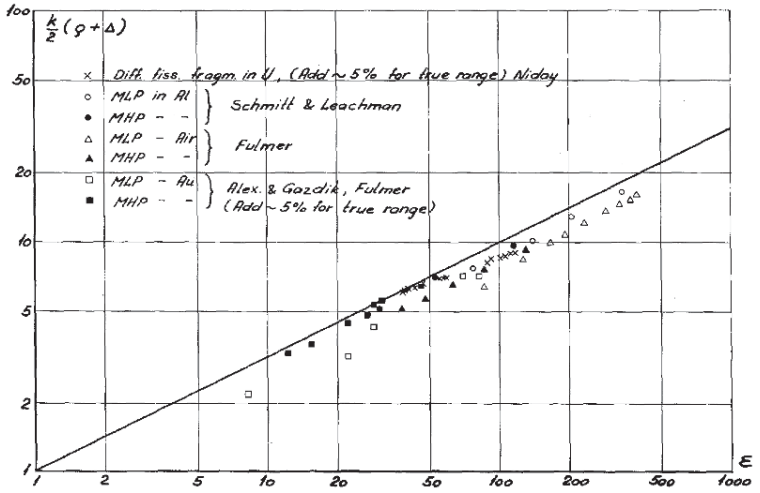

Fig. 8.1 Ranges of fission fragments in gaseous and solid materials compared to theoretical calculation by Lindhard et al. (1963b). $\rho = N\pi a^2 \gamma R$ and $\epsilon = E_r a / Z_1 Z_2 e^2$ denote dimensionless measures of the range and the initial energy in accordance with (6.82) and (6.38), respectively. The quantity Δ denotes a correction for the part of the range that does not generate enough ionization to produce a visible track, and k is a dimensionless constant. Experimental data from Alexander and Gazdik (1960), Fulmer (1957), Leachman and Schmitt (1954). From Lindhard et al. (1963b)

8.2.1 Stokes' Law

If you throw a steel ball into the air, and if there is no wind, the ball will, in addition to gravity, experience a friction force proportional to the velocity according to Stokes' law.

A simple theoretical explanation is provided by kinetic gas theory: The ball is hit by gas molecules with average speeds far in excess of the speed of the ball. Seen from the ball, the gas molecules have a net velocity opposite to the direction of motion of the ball, and hence will transfer a net momentum to the ball. If you neglect changes in air pressure around the ball, the resulting friction force will be proportional to the ball velocity.

This model is analogous to the movement of a heavy particle through a classical electron gas. Recalling that a friction force is synonymous with the loss of kinetic energy per pathlength, we may expect a range of beam energies where the stopping cross section is proportional to the projectile speed.

Fermi and Teller (1947) showed that velocity-proportional stopping also holds for a Fermi gas. That theory has undergone substantial development, as will be discussed below.

Evidence supporting the asserted proportionality of the stopping cross section with the projectile speed was first collected from measurements of the ranges of fission fragments, cf. Fig. 8.1. At this point we just note that the solid line represents the relation $R \propto \sqrt{E}$, from which you easily derive that

$$\frac{\mathrm{d}E}{\mathrm{d}R} = \frac{1}{\mathrm{d}R/\mathrm{d}E} \propto \sqrt{E}\,. \tag{8.1}$$

Direct measurements employing ion beams of a well-defined species and beam energy penetrating thin foils were reported from the 1960s on (Ormrod and Duckworth, 1963, Fastrup et al., 1966). The results of these as well as numerous subsequent studies may be inspected in Paul's internet album (Paul, 2013). The asserted proportionality of the stopping cross section with the beam speed has been confirmed in many of these measurements, but noticeable deviations have been observed. Such deviations have often been expressed in terms of a power law

$$\frac{\mathrm{d}E}{\mathrm{d}x} \propto E^p\,, \tag{8.2}$$

where p can range from 0.4 to 0.75 according to Fastrup et al. (1966).

8.2.2 Z_1 Structure

An interesting observation which emerged already from the first direct measurements (Ormrod and Duckworth, 1963, Ormrod et al., 1965) is an oscillatory structure of the stopping cross section as a function of the atomic number of the ion, called Z_1 structure or Z_1 oscillations. The phenomenon is illustrated in Fig. 8.2 in the dependence of the electronic stopping cross section S_e on Z_1 at a fixed beam speed. The relative amplitude of the oscillations appears to increase with decreasing velocity. These oscillations go along with an oscillatory dependence of the exponent p defined in (8.2) on Z_1 (Fastrup et al., 1966). This phenomenon became a major challenge to theoreticians for many years.

Once Z_1 oscillations had been found, experimentalists also looked for Z_2 oscillations. Pertinent experiments involve a variety of target materials. Comparing stopping measurements on different materials is, a priori, more tricky, since other material properties such as target structure and purity may vary significantly. We shall look for evidence in favour of Z_2 structure in the following section.

8.2.3 Reciprocity

Consider a collision between two neutral atoms 1 and 2 with atom 2 being initially at rest. Assume the energy to be low enough that ionization and charge exchange are negligible, but allow for electronic excitation of either atom or both with an excitation energy Q. This means that atom 1 has lost an energy

$$T \simeq Q \tag{8.3}$$

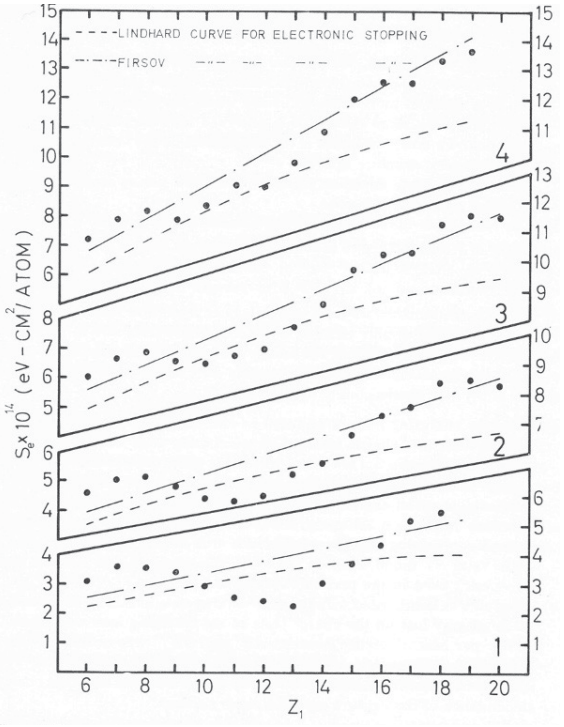

Fig. 8.2 Electronic stopping cross sections of various ions in carbon at four different beam speeds. Measurements by Fastrup et al. (1966) for $v/v_0 = 0.41$, 0.63, 0.91 and 1.1 (bottom to top). Also included are theoretical predictions from (8.73) and (8.80). From Fastrup et al. (1966)

in addition to a possible recoil loss.

The excitation energy Q follows a probability distribution $P(Q, \Theta)dQ$ which depends on the scattering angle. The electronic stopping cross section may then be determined from

$$S_e = \int \mathrm{d}\sigma(\Theta) \int \mathrm{d}Q \; QP(Q, \Theta) \,, \tag{8.4}$$

where Θ denotes the c.m.s. scattering angle.

This relation does notdistinguish between atom 1 and atom 2. Therefore we may expect that for a collision between two neutral atoms, in the absence of electron capture or loss,

$$S_e(1 \to 2) = S_e(2 \to 1) \,. \tag{8.5}$$

Equation (8.5) is a reciprocity relation (Sigmund, 2008a). It is strictly valid under conditions which are rarely satisfied in practice, but if you allow for minor deviations it is an extremely useful tool.

At low beam velocities the equilibrium charge is close to zero. Although the excitation probability of a C^+ ion hitting a neutral Si atom is not identical with that of a Si^+ ion hitting a neutral C atom, the difference will typically lie in the few-% range.

Figure 8.3 shows an example. Measured stopping cross sections reported in the literature for Si in C (red symbols) and C in Si (blue symbols) have been plotted

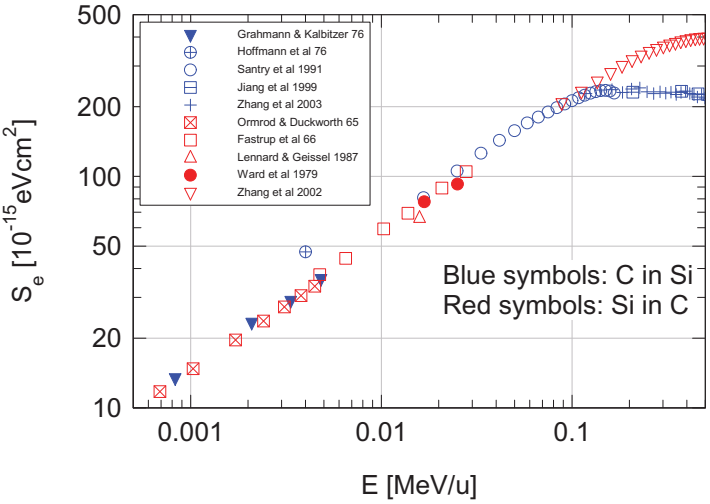

Fig. 8.3 Electronic stopping cross sections for C in Si (blue symbols) and Si in C (red symbols). Experimental data from Grahmann and Kalbitzer (1976), Hoffmann et al. (1976), Santry and Werner (1991), Jiang et al. (1999), Zhang and Weber (2003), Ormrod et al. (1965), Fastrup et al. (1966), Lennard and Geissel (1987), Ward et al. (1979), Zhang et al. (2002), compiled by Paul (2013). From Sigmund (2008a)

over three orders of magnitude in beam energy. With the exception of a single point (Hoffmann et al., 1976), reciprocity appears to be obeyed within experimental scatter up to $\simeq$ 100 keV/u. At 100 keV, the mean equilibrium charge is 2.7 for C in Si and 4.1 for Si in C. This difference appears to be insignificant, whereas at higher energies, the higher charge of Si gives rise to an increasing difference between the two data sets.

Reciprocity is a rather new principle at the time of writing, but numerous similar examples have been presented (Sigmund, 2008a), and a code to systematically analyse all ion-target combinations of the periodic table has been worked out by Kuzmin and Sigmund (2011).

The principle is not fulfilled rigorously, but it is nevertheless a useful tool in connection with experimental data:

- Reciprocity may be helpful in identifying experimental errors or errors in data analysis. As an example, inspection of Fig. 8.3 suggests caution regarding a single outlier.
- There are numerous ion-target combinations where measurements of ion 1 in target 2 are hard to perform, while ion 2 in target 1 is more accessible. Reciprocity may then provide a first estimate of the stopping cross sections.
- Reciprocity may also be helpful in testing theoretical predictions. It will normally be clear from the input whether or not reciprocity is inherent in a theory.

In Sect. 8.2 we had a first look at Z_1 oscillations in electronic stopping. As far as reciprocity is valid, there should be Z_2 oscillations with a similar magnitude and

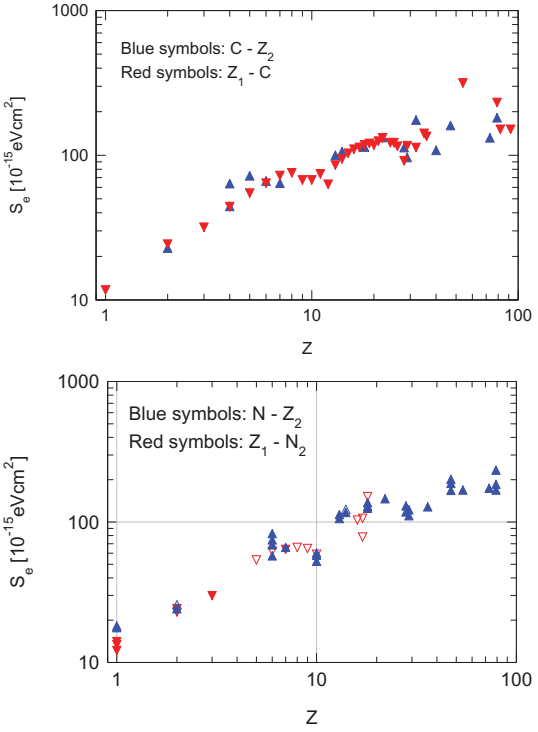

Fig. 8.4 Electronic stopping cross sections at $v = v_0$ for carbon ions in different materials and for different ions in carbon (upper graph). The same for nitrogen (lower graph). Experimental data that are not taken at v_0 were inter- or extrapolated toward v_0 by a power law. Empty symbols refer to cases where extrapolation is somewhat uncertain

similar positions of maxima and minima. Figure 8.4 illustrates two examples. The coverage with data is barely sufficient to allow a definite statement. More modestly we may conclude that existing data do not contradict the postulate that Z_2 and Z_1 structure are related phenomena.

8.2.4 Threshold Behaviour

Bohr (1948) argued that at beam velocities below the Bohr speed $v_0 = e^2/\hbar$, which is a measure of the velocity of the most loosely-bound electrons in the target, electronic collisions will be adiabatic. He therefore asserted that electronic stopping would decrease rapidly as the projectile speed dropped below $\sim v_0$. While the argument is valid, the decrease is less dramatic than one might have expected: Where visible at all, threshold effects tend to manifest themselves in a more or less abrupt change in the exponent p in (8.2).

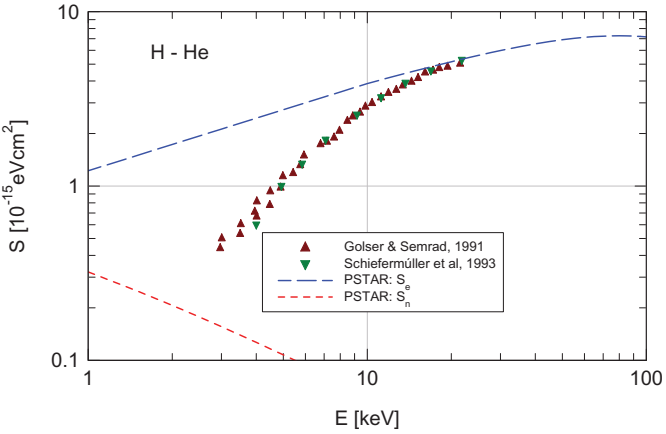

Fig. 8.5 Stopping cross section of helium for hydrogen ions. Data points from Golser and Semrad (1991) and Schiefermüller et al. (1993). Lines calculated by PSTAR code (ICRU, 1993)

Figure 8.5 shows an example reported by Golser and Semrad (1991) and confirmed by Schiefermüller et al. (1993).

8.3 Experimental Aspects

8.3.1 Problems and Tools

Most stopping cross sections reported in the literature were measured via energy spectra of ions after penetrating a thin foil or being reflected from a thick target. There are several ways to measure energy losses in reflection. A reasonably transparent method makes use of a thin layer of atoms heavier than the stopping medium, e.g. Au in Si, at a certain depth. Alternative options include Doppler-shift attenuation and penetration profiles (ranges). A common problem to all methods is the analysis.

If the energy loss is approximately proportional to $\sqrt{E}$, the *relative* energy loss goes as $1/\sqrt{E}$. At low beam energies this necessitates the use of exceedingly thin films in transmission measurements.

Nuclear stopping is substantial in the low-velocity range and becomes even dominating for all but the lightest ions below some critical beam energy. Figure 8.6 shows stopping forces for representative ions in silicon according to the SRIM tabulation (Ziegler, 2012). Both the electronic and the nuclear stopping force are seen to increase with the atomic number of the ion, the increase being more pronounced for the nuclear one. Consequently the cross-over between the two moves upward in energy with increasing atomic number.

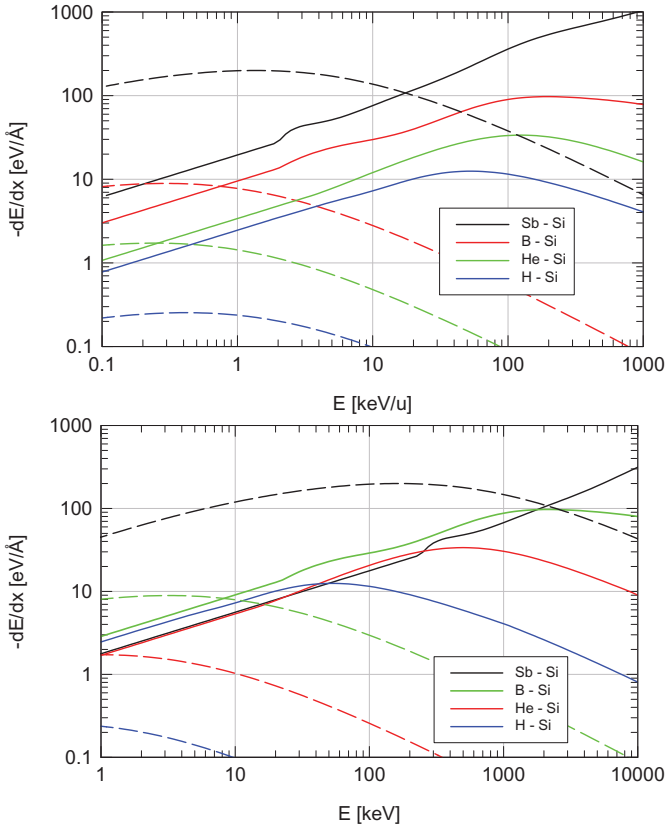

Fig. 8.6 Upper graph: Electronic stopping force (solid lines) and nuclear stopping force (broken lines) for Sb, B, He and H ions (top to bottom) in Si according to Ziegler (2012). Lower graph: Same with different abscissa unit

Figure 8.6 shows that hydrogen differs from other ions by the absence of a cross-over between nuclear and electronic stopping. Here, electronic stopping dominates over the entire depicted energy range. Moreover, in the energy range where stopping measurements are typically made, i.e. at energies above 10 keV, nuclear stopping accounts for $\sim$ 1% of the energy loss or less. Conversely, for Sb ions, nuclear stopping dominates up to $\sim$ 20 keV/u, and becomes a 1% correction only at energies above $\sim$ 1 MeV/u.

You may appreciate that in the vast majority of stopping measurements—which have been performed with protons and alpha particles at energies above and around the electronic-stopping maximum—nuclear stopping is only a matter of concern in precision measurements, i.e., at a level of accuracy of $\sim$ 1% or better (Andersen, 1991). Conversely, extracting an electronic stopping cross section from a measurement with Sb ions at energies below 1 MeV requires serious considerations about

the data analysis: Even a minor error in the treatment of nuclear stopping may result in a major error of the extracted electronic-stopping cross section.

The problem of separating electronic from nuclear stopping has been discussed in Sect. 7.8.1. As a general rule, the correction for nuclear stopping is smaller than the full nuclear-stopping cross section in the standard geometry for foil experiments, because those particles that have suffered large nuclear losses tend to be scattered out of the beam and do not enter the detector. In the experimental literature you may find three different procedures for applying such a correction,

- Subtracting some adopted nuclear-stopping cross section from the total measured stopping cross section,
- The same, but correcting for multiple scattering, or
- Monte-Carlo simulation with an adopted differential scattering cross section.

A survey of published data by Glazov and Sigmund (2003) revealed that very few authors presented enough documentation that would enable the reader to judge the quality of the nuclear-stopping correction, with the notable exception of Fastrup et al. (1966), where both uncorrected and corrected data are listed. When the correction is found by Monte-Carlo simulation, a minimum requirement is specification of the interatomic potential, but since small-angle multiple scattering is involved, also cut-off angles need to be specified, as discussed in Sect. 7.3.6.

8.3.2 Data

Published experimental data have been compiled by Paul (2013). This database lists data for protons, He ions and ions heavier than helium. This division has historical reasons, because the International Commission on Radiation Units and Measurements (ICRU) issued separate reports on the stopping of protons and alpha particles (ICRU, 1993) and of ions heavier than helium (ICRU, 2005). Unlike these two reports, which focus on stopping of swift ions, Paul's database lists stopping cross sections for the whole energy range where data have been published.

You may have noted above that protons play a special role in that there is no cross-over between electronic and nuclear stopping. There is another special feature of protons: According to Lindhard and Scharff (1961), the energy range for which the stopping cross section is approximately proportional to the velocity is defined by the Thomas-Fermi speed, i.e., for

$$E < \frac{1}{2} M_1 v_F^2 = \frac{1}{2} u v_0^2 A_1 Z_1^{4/3} , \tag{8.6}$$

where A_1 is the mass number of the projectile. This limiting energy increases more rapidly than with the square of the atomic number.

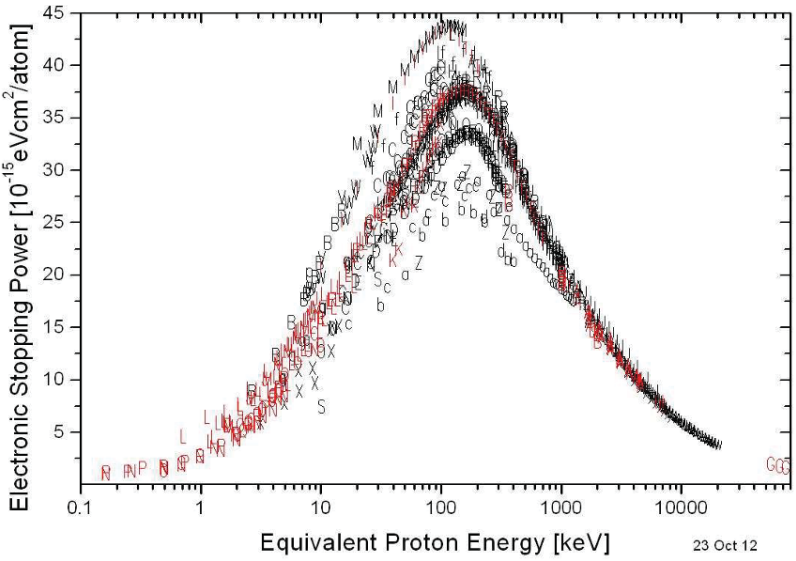

Fig. 8.7 Stopping cross sections of gold for protons or deuterons compiled by Paul (2013). Theoretical curves and numerous data references have been removed from the original graph of Paul (2013)

8.3.2.1 Protons

Paul's database lists stopping cross sections for protons in a large number of elemental and compound materials. Figure 8.7 shows the case of gold, where exceptionally many data exist. Gold is a material where impurity effects should play a minor role, and where preparation of thin foils is a well-established routine. Nevertheless, the scatter in the data from different sources is significant around and below the stopping maximum, even if a few outliers are ignored.

Figure 8.8 shows a reciprocity test involving hydrogen as projectile and target (H_2 gas). Despite an abundance of data, sufficiently many data for such a test have been found only for three pairs, all involving gas data. It is seen that data involving hydrogen as a target consistently lie $\sim$ 20% above those for hydrogen ions. Considering the difference between a naked proton and a neutral hydrogen atom or molecule in the present context, a violation of the reciprocity principle could well be expected in this case. Actually, with the small number of data (N-H_2 and O-H_2 from Weyl (1953), O-H_2 from Hvelplund (1971)), the observed deviation may be considered to lie within the error margin.

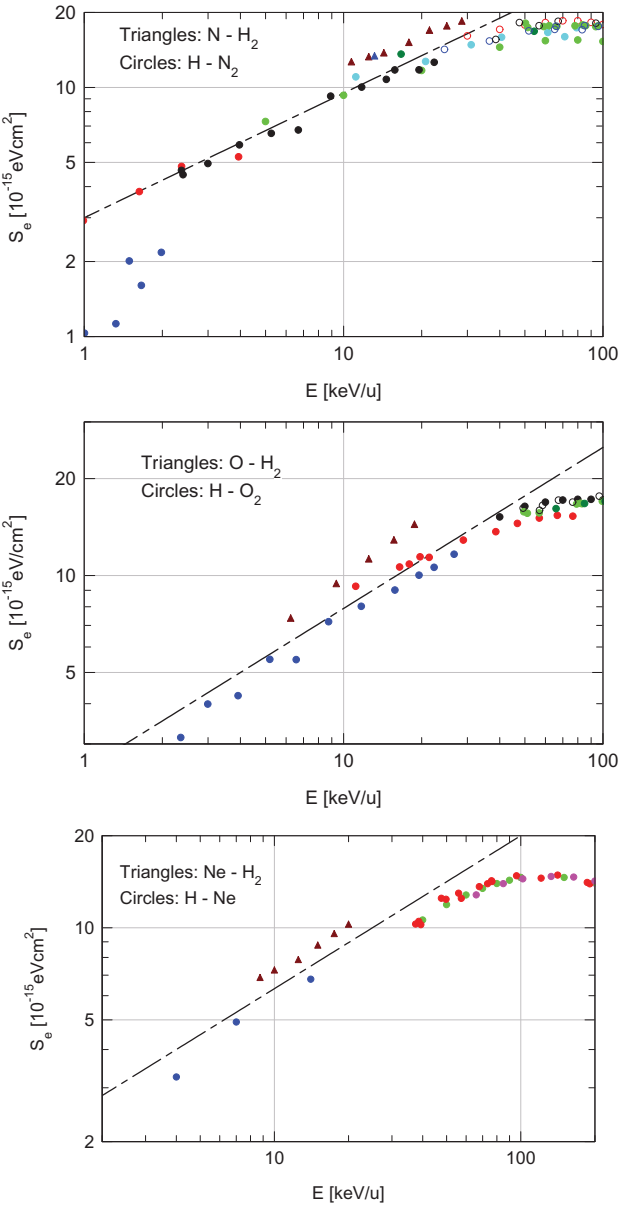

Fig. 8.8 Reciprocity test on H-N, H-O and H-Ne stopping cross sections. Lines indicate a E dependence. Data from Paul (2013)

8.3.2.2 Helium Ions

Figure 8.9 shows a graph equivalent to Fig. 8.7 but now for helium. While the scatter between data from different sources has reduced considerably around the stopping maximum, discrepancies from $\sim$ 300 keV downward prevail.

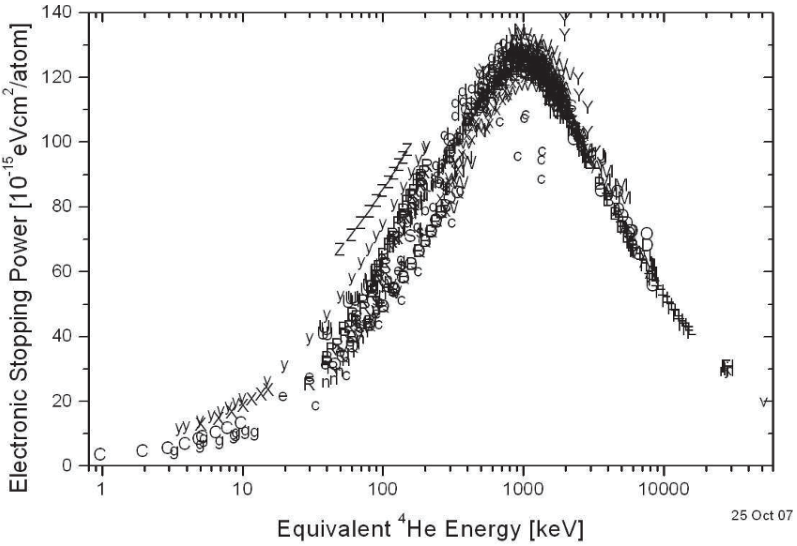

Fig. 8.9 Stopping cross sections of gold for ^{4}He or ^{3}He ions compiled by Paul (2013). Theoretical curves and numerous data references have been removed from the original graph in Paul (2013)

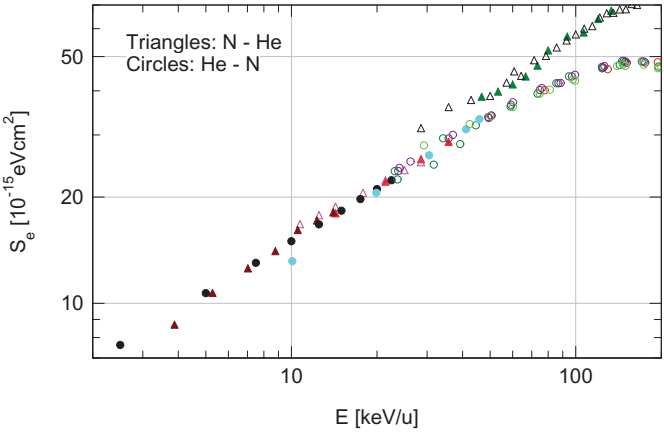

Fig. 8.10 Reciprocity test on He-N stopping cross sections. Data from Paul (2013)

Figure 8.10 shows a reciprocity test corresponding to Fig. 8.8. I have found only five ion-target combinations, where data are available that would allow such a test. The best coverage is for N-He, which is shown in the graph. Reciprocity is accurately fulfilled up to $\sim$ 30 keV/u, and deviations above that energy show consistently higher energy losses for nitrogen in helium than for helium in nitrogen, as has to be expected.

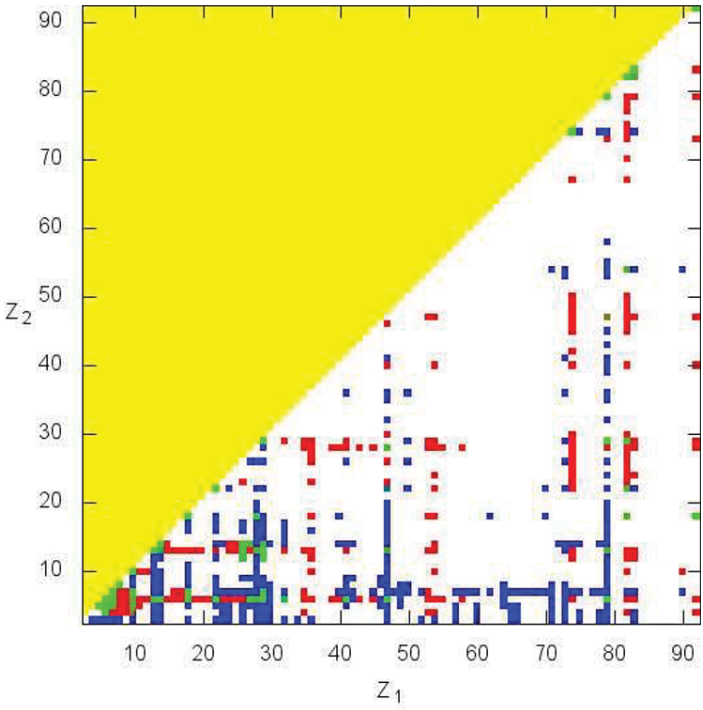

Fig. 8.11 Survey of experimental low-velocity stopping data. Every pair (Z_1, Z_2) for which stopping cross sections have been published for velocities below the Thomas-Fermi speed $v_{TF} = v_0 Z_1^{2/3}$ is marked by a point with a colour. For red squares only data for Z_1 in Z_2 are listed by Paul (2013). For blue squares only data for Z_2 in Z_1 are listed. Green squares indicate that both types of data are available. Output from REST code provided by V. Kuzmin

8.3.2.3 Heavier Ions

Figure 8.11 shows a survey of available data for $3 \leq Z_1, Z_2 \leq 92$ produced by the REST code (Kuzmin and Sigmund, 2011). This code, which reads data from Paul's database according to chosen selection criteria such as maximum and minimum beam energy as well as atomic numbers, was developed as a tool to study reciprocity. In Fig. 8.11, the Thomas-Fermi speed $v_{TF} = v_0 Z_1^{2/3}$ was chosen as the maximum. A green point on the graph indicates a stopping cross section close to linear in v. Colours approaching red indicate a steeper dependence. A flatter dependence is indicated by a colour closer to blue.

Clearly, for most ion-atom pairs (Z_1, Z_2), no stopping cross sections have been measured at low-velocities. While data exist for a variety of target materials. the number of ions for which data are available is very restricted, if you need to go beyond the most common materials such as carbon, aluminium, silver and gold.

Figure 8.12 shows reciprocity tests for four atom pairs (Z_1, Z_2), none of which is gaseous at room temperature. Although the number of supporting data is limited,

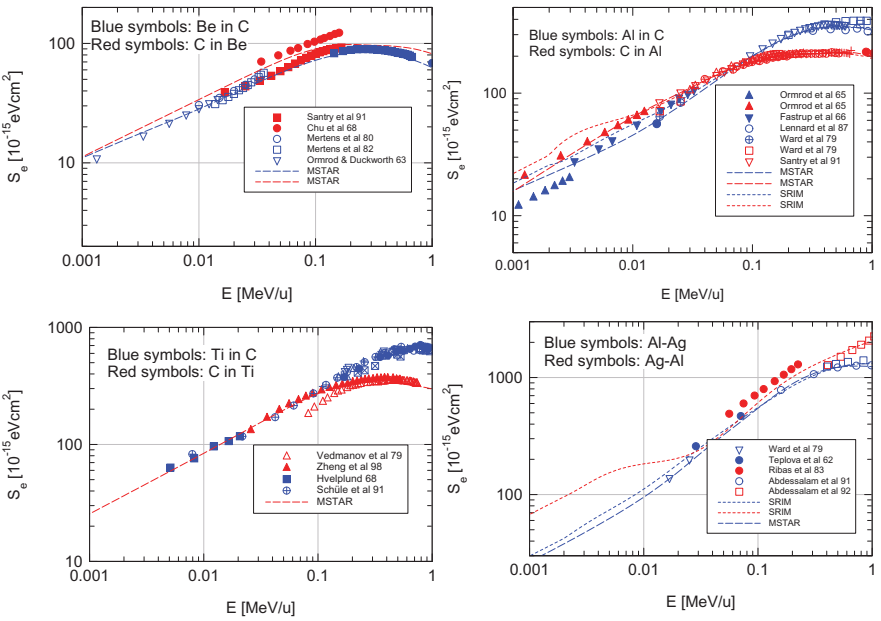

Fig. 8.12 Reciprocity test on solid materials. From Sigmund (2008a)

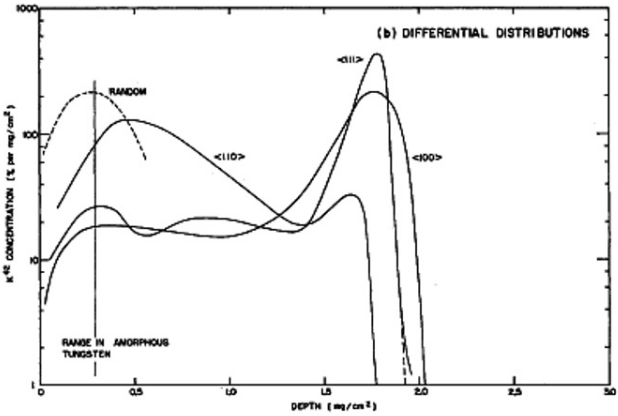

Fig. 8.13 Range profiles of 500 keV K^+ ions in W. From Eriksson et al. (1967)

reciprocity appears well fulfilled in all these cases. Several cases of major deviations from reciprocity have been reported (Sigmund, 2008a, Kuzmin and Sigmund, 2011).

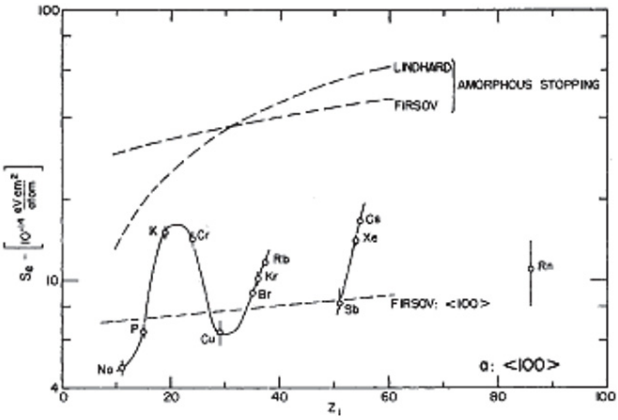

Fig. 8.14 Electronic stopping force on 11.6 keV/u ions moving through the ⟨100⟩ channel in tungsten. Extracted from range measurements. From Eriksson et al. (1967)

8.3.3 Stopping in Crystals

The topic of channeling will be taken up in the Appendix, where Sect. 11.10.1 has been devoted to energy loss. It is nevertheless useful to get into this topic here, because observations in this area have produced results that have greatly contributed to the understanding of random stopping.

Figure 8.13 shows range profiles of 500 keV K^+ ions in tungsten from Eriksson et al. (1967). Profiles are shown for penetration along three low-indexed directions as well as for random slowing-down. You may note that the ⟨110⟩, ⟨100⟩ and ⟨111⟩ profiles differ significantly from the random profile by a second peak at a larger depth and a very steep drop-off that allows the extraction of a maximum penetration depth. It is asserted that ions reaching the maximum penetration depth have travelled along nearly straight lines close to the potential minimum in the channel or, in other words, at a constant impact parameter to the target atoms enclosing the channel.

Figures 8.14 and 11.27 show stopping forces in tungsten, extracted from maximum *ranges* of ions slowing down along the ⟨100⟩ and ⟨110⟩ channels. According to (2.36), Vol. 1, the range $R(E_0)$ of an ion with an initial energy E_0 is given by

$$R(E_0) = \int_0^{E_0} \frac{\mathrm{d}E}{\mathrm{d}E/\mathrm{d}x}\,, \tag{8.7}$$

so that

$$\frac{\mathrm{d}R(E_0)}{\mathrm{d}E_0} = \frac{1}{(\mathrm{d}E/\mathrm{d}x)_{E_0}}\,. \tag{8.8}$$

Application of this to the *maximum* range determines the *minimum* energy loss during passage through the channel. Comparison of Fig. 11.27 with Fig. 8.14 reveals

- a very similar behaviour in the two channels,

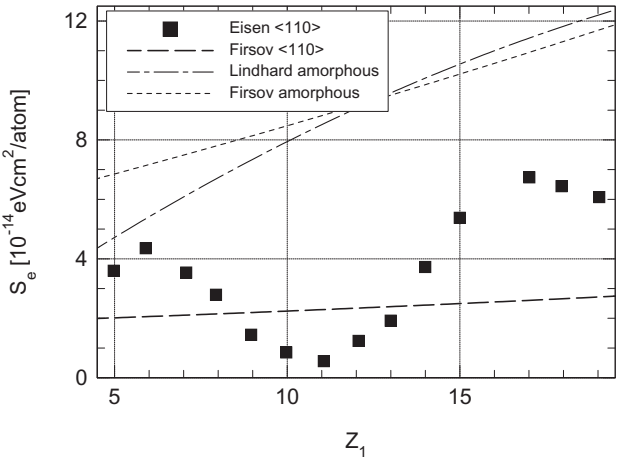

Fig. 8.15 Electronic stopping force on 11.6 keV/u ions moving through ⟨**110**⟩ channel in silicon. Redrawn after Eisen (1968)

- pronounced Z_1 oscillations for ions with $Z_1 \leq 55$, and
- reduced stopping compared to random, by comparison with estimates of Firsov (1959) and Lindhard and Scharff (1961) to be discussed below.

A similar, even more dramatic result was reported by Eisen (1968) on the basis of direct measurements of energy spectra of ions passing through the ⟨110⟩ channel in silicon, see Fig. 8.15. Also these measurements refer to minimum energy loss.

The essential new feature of these data is a very large amplitude ratio of the oscillations. Such observations trigger the interest of theoreticians. Indeed, there has been a flood of theoretical studies in this area ever since.

8.4 Limitations to Additivity ⋆

We have, so far, assumed the nuclear and electronic contributions to stopping and scattering to be strictly additive. This assumption is exactly fulfilled if the target is made up of independent electrons and nuclei. It is also well justified at energies where nuclear collisions do not contribute significantly to energy loss and electronic collisions do not contribute significantly to scattering. In the present chapter, where nuclear energy loss is significant and possibly dominating, it appears appropriate to look for possible interferences between nuclear and electronic energy loss.

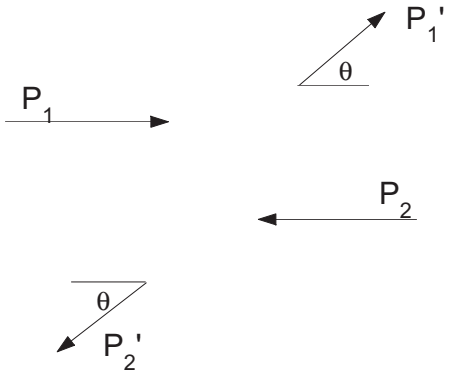

Fig. 8.16 Inelastic two-body collision

8.4.1 Conservation Laws in Inelastic Collisions

Figure 8.16 indicates a collision between two atomic particles with masses M_1 and M_2, respectively. The collision is viewed in the centre-of mass frame, where the sum of the two momenta $\boldsymbol{P}_1$ and $\boldsymbol{P}_2$ is zero. The two atoms are allowed to be excited as a result of the collision, and we allow for charge exchange in either direction while ionization is assumed to be forbidden. As a result, the masses have changed according to

$$M_1' = M_1 + \Delta M; \qquad M_2' = M_2 - \Delta M\,, \tag{8.9}$$

since no electrons are lost.

From energy conservation we find

$$\frac{P_1^2}{2M_1} + \frac{P_2^2}{2M_2} = \frac{P_1'^2}{2M_1'} + \frac{P_2'^2}{2M_2'} + Q\,, \tag{8.10}$$

where Q is the net excitation energy, taking into account excitation of both atoms including the energy balance of a possible charge-exchange event.

We may express (8.10) in terms of reduced masses μ, μ', so that

$$\frac{P_1^2}{2\mu} = \frac{P_1'^2}{2\mu'} + Q \tag{8.11}$$

or

$$P_1' = \sqrt{\frac{\mu'}{\mu}\left(P_1^2 - 2\mu Q\right)}\,. \tag{8.12}$$

We may express this relation in terms of the c.m.s. velocities $\boldsymbol{u}_1 = \boldsymbol{P}_1/M_1$ and $\boldsymbol{u}_1' = \boldsymbol{P}_1'/M_1'$ before and after the collision, respectively. In doing so, we linearize the relation with respect to the small parameter $\Delta M/\mu$ as well as the quantity $2\,\mu Q/P_1^2$. With this you obtain

$$u_1' \simeq u_1 \left(1 - \frac{\Delta M}{2\mu}\right)\left(1 - \frac{M_2 Q}{M_1 M u_1^2}\right), \tag{8.13}$$

where $M = M_1 + M_2$.

Now, view the collision in a reference frame where atom 2 is initially at rest. Then, the transformation presented in Sect. 3.2.1, Vol. 1, leads to

$$\boldsymbol{u}_1 = \boldsymbol{v}_1 - \boldsymbol{V}; \qquad \boldsymbol{u}_1' = \boldsymbol{v}_1' - \boldsymbol{V}, \tag{8.14}$$

where $\boldsymbol{V} = M_1 \boldsymbol{v}_1 / M$ is the centre-of-mass velocity. Then,

$$v_1'^{\,2} = V^2 + u_1'^{\,2} + 2 V u_1' \cos\Theta, \tag{8.15}$$

where Θ is the scattering angle in the c.m.s. frame, cf. Fig. 8.16. Insertion of (8.13) and linearization then lead to

$$T = \frac{M_1}{2}\left(v_1^2 - v_1'^{\,2}\right) = \gamma \frac{M_1}{2} v_1^2 \sin^2\frac{\Theta}{2} + \left(1 - \frac{2M_1}{M_1 + M_2}\sin^2\frac{\Theta}{2}\right)\left(Q + \frac{\Delta M}{2} v_1^2\right), \tag{8.16}$$

where $\gamma = 4M_1 M_2/(M_1 + M_2)^2$.

The physical model underlying the present paragraph is standard atomic-collision physics. An early reference is Fedorenko (1959). The present calculation, which is due to the author (Sigmund, 2008b), is geared toward stopping: You may have wondered why the energy loss was expressed as in the first line of (8.16) and not as $M_1 v_1^2/2 - M_1' v_1'^{\,2}/2$, i.e., the true loss of kinetic energy. The reason is that in particle stopping we always refer to the change in the velocity of the nucleus or, if you prefer, the centre-of-mass of the projectile.

8.4.2 Mean Energy Loss

Rearranging the contributions in (8.16) leads to

$$T = \gamma \frac{M_1}{2} v_1^2 \sin^2\frac{\Theta}{2}\left(1 - \frac{Q}{\mu v_1^2} - \frac{\Delta M}{2\mu}\right) + Q + \frac{\Delta M}{2} v_1^2. \tag{8.17}$$

Here,

$$T_n = \gamma \frac{M_1}{2} v_1^2 \sin^2\frac{\Theta}{2} \tag{8.18}$$

represents the elastic energy loss, while

$$T_e = Q + \frac{\Delta M}{2} v_1^2 \tag{8.19}$$

represents energy loss to excitation and charge exchange, i.e., electronic energy loss. With this we can write (8.17) in the form

$$T = T_n + T_e - \frac{T_n T_e}{2E_r}\,, \tag{8.20}$$

where $E_r = \mu v_1^2/2$ is the initial kinetic energy in the c.m.s.

Looking at the fractional energy loss,

$$\frac{T}{E_r} = \frac{T_n}{E_r} + \frac{T_e}{E_r} - \frac{1}{2}\frac{T_n}{E_r}\frac{T_e}{E_r} \tag{8.21}$$

you may note that the interference term is of second order, i.e., it becomes significant only when at least one of the first-order terms is not $\ll 1$. This can be the case for close collisions. The stopping cross section may then be written as

$$S = S_n + S_e - \Delta S \tag{8.22}$$

with

$$\Delta S = \frac{1}{2E_r}\int \mathrm{d}^2 p\, T_n(p) T_e(p) \tag{8.23}$$

in the impact-parameter representation, or

$$\Delta S = \frac{1}{2E_r}\int \mathrm{d}\sigma(\Theta) T_n(\Theta) T_e(\Theta)\,, \tag{8.24}$$

expressed via the differential cross section.

In the standard transmission geometry, where close collisions at most contribute to a high-loss peak that is ignored in the analysis, this correction will typically be negligible.

8.5 Free Target Electrons

8.5.1 Lindhard Theory

In Chap. 5, Vol. 1, the dielectric description of stopping has been presented. This theory allows a consistent description of stopping in a Fermi gas for weakly interacting particles, i.e., protons and other low-Z_1 ions.

We may write (5.30), Vol. 1, in the form

$$-\frac{\mathrm{d}E}{\mathrm{d}x} = \frac{\mathrm{i}Z_1^2 e^2}{\pi v^2}\int_{|\omega|<kv} \mathrm{d}k\,\mathrm{d}\omega\, \frac{\omega}{k}\frac{1}{\varepsilon(k,\omega)}, \tag{8.25}$$

where $\varepsilon(k,\omega)$ is the longitudinal dielectric function. The transverse part has been dropped, since we are interested in low projectile speeds ($v \ll c$) here.

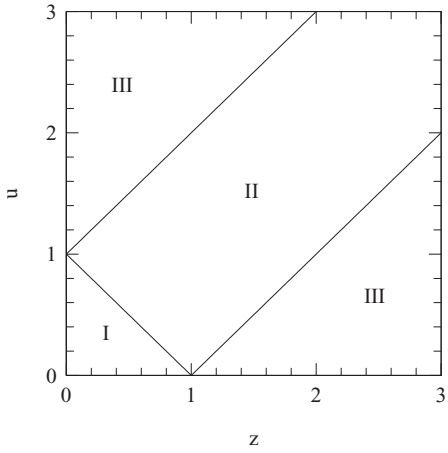

Fig. 8.17 Integration regimes defined in (8.28)

In Sects. 5.7.2 and 5.7.3, Vol. 1, you can find a derivation following Lindhard (1954) of the dielectric function for a Fermi gas,

$$\varepsilon(z,u) = 1 + \frac{\chi^2}{z^2}\Big[f_1(z,u) + \mathrm{i}\, f_2(z,u)\Big], \tag{8.26}$$

where

$$f_1(z,u) = \frac{1}{2} + \frac{1}{8z}\left[1-(z-u)^2\right]\ln\left|\frac{z-u+1}{z-u-1}\right| + \frac{1}{8z}\left[1-(z+u)^2\right]\ln\left|\frac{z+u+1}{z+u-1}\right| \tag{8.27}$$

and

$$f_2(z,u) = \begin{cases} \dfrac{\pi}{2}u & z+u<1 \qquad \text{I)} \\ \dfrac{\pi}{8z}\left[1-(z-u)^2\right] & \text{for } |z-u|<1<z+u \quad \text{II)} \\ 0 & |z-u|>1 \qquad \text{III)} \end{cases}. \tag{8.28}$$

Here

$$u = \frac{\omega}{k v_\mathrm{F}}; \qquad z = \frac{k}{2k_\mathrm{F}}; \qquad \chi^2 = \frac{e^2}{\pi\hbar v_\mathrm{F}}. \tag{8.29}$$

Writing (8.25) in (u,z) variables implies that

$$\frac{\omega}{k}\mathrm{d}k\,\mathrm{d}\omega = 4k_\mathrm{F}^2 v_\mathrm{F}^2 z u\,\mathrm{d}z\,\mathrm{d}u \tag{8.30}$$

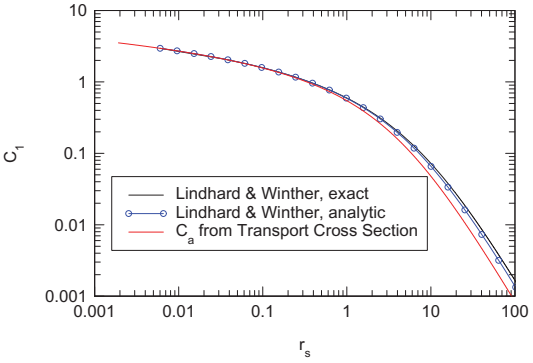

Fig. 8.18 The factor $C_1(v_F)$ determining the Lindhard-Winther low-speed stopping formula, (8.35). The abscissa is the Wigner-Seitz radius, $r_s = 1.919 v_0/v_F$. See text

with the limits

$$0 < z < \infty; \qquad |u| < v/v_F\,. \tag{8.31}$$

We may also write

$$\frac{\mathrm{i}}{\varepsilon(z,u)} = \frac{\mathrm{i}\varepsilon_1(z,u) + \varepsilon_2(z,u)}{\varepsilon_1^2(z,u) + \varepsilon_2^2(z,u)}\,, \tag{8.32}$$

where ε_1 and ε_2 represent the real and imaginary part of the dielectric function.

The imaginary part of the stopping force must drop out. Therefore, only ε_2 remains in the numerator. This limits the integration interval according to (8.28).

If we restrict ourselves to the leading order in v for small v, (8.28) tells us that only region I in Fig. 8.17 yields a nonvanishing contribution. We may then carry out the integration over u and arrive at

$$-\frac{\mathrm{d}E}{\mathrm{d}x} = \frac{4}{3\pi} Z_1^2 \frac{m v_0 v}{a_0} \int_0^1 \frac{\mathrm{d}z}{z} \frac{1}{(1 + \chi^2 f_1(z,0)/z^2)^2}\,. \tag{8.33}$$

Dividing by the electron density $n = k_F^3/3\pi^2$ we obtain the stopping cross section per target electron,

$$S = 4\pi Z_1^2 e^2 a_0 \frac{v}{v_0} \left(\frac{v_0}{v_F}\right)^3 C_1(v_F)\,, \tag{8.34}$$

where

$$C_1(v_F) = \int_0^1 \frac{\mathrm{d}z}{z} \frac{1}{(1 + \chi^2 f_1(z,0)/z^2)^2}\,. \tag{8.35}$$

Figure 8.18 shows C_1 found by numerical integration of (8.35). An accurate analytic expression[1] was given by Lindhard and Winther (1964),

[1] There is a misprint in the original paper: The denominator in Equ. (15) there, $2(1 + \chi^2/3)^2$ should be changed to the one in (8.36) here.

$$C_1 = \frac{1}{2(1-\chi^2/3)^2}\left[\ln\left(\frac{2}{3}+\frac{1}{\chi^2}\right) - \frac{1-\chi^2/3}{1+2\chi^2/3}\right]. \tag{8.36}$$

This expression is included in the figure. The origin of the third curve will be discussed below.

8.5.2 Transport Cross Section

Here we go a bit deeper into the analog to Stokes' law. Equation (6.71), Vol. 1, expresses the stopping cross section per target electron of a heavy particle with an arbitrary nonrelativistic velocity $\boldsymbol{v}$ in a gas of free electrons with a velocity distribution $f(\boldsymbol{v}_\mathrm{e})$ as

$$S = m\left\langle \frac{|\boldsymbol{v}_\mathrm{e}-\boldsymbol{v}|}{v}\boldsymbol{v}\cdot(\boldsymbol{v}-\boldsymbol{v}_\mathrm{e})\sigma^{(1)}(|\boldsymbol{v}_\mathrm{e}-\boldsymbol{v}|)\right\rangle_{\boldsymbol{v}_\mathrm{e}}, \tag{8.37}$$

where the brackets indicate an average over $\boldsymbol{v}_\mathrm{e}$ and

$$\sigma^{(1)}(v) = \int (1-\cos\Theta)\,\mathrm{d}\sigma(v,\Theta) \tag{8.38}$$

is the transport cross section per target electron at rest.

Expansion in powers of v/v_e up to the first order beyond the leading term yields

$$S \simeq \frac{m}{v}\left\langle\left(v_\mathrm{e}-\frac{\boldsymbol{v}_\mathrm{e}\cdot\boldsymbol{v}}{v_\mathrm{e}}\right)\left(-\boldsymbol{v}_\mathrm{e}\cdot\boldsymbol{v}+v^2\right)\left(\sigma^{(1)}(v_\mathrm{e})-\frac{\boldsymbol{v}_\mathrm{e}\cdot\boldsymbol{v}}{v_\mathrm{e}}\sigma^{(1)\prime}\right)\right\rangle_{\boldsymbol{v}_\mathrm{e}}, \tag{8.39}$$

where $\sigma^{(1)\prime} = \mathrm{d}\sigma^{(1)}(v_\mathrm{e})/\mathrm{d}v_\mathrm{e}$.

For an isotropic distribution, $f(\boldsymbol{v}_\mathrm{e}) \equiv f(v_\mathrm{e})$, averages over uneven powers of $\boldsymbol{v}_\mathrm{e}\cdot\boldsymbol{v}$ vanish, and $\left\langle(\boldsymbol{v}_\mathrm{e}\cdot\boldsymbol{v})^2\right\rangle_{\boldsymbol{v}_\mathrm{e}} = \langle v_\mathrm{e}^2\rangle v^2/3$. Then the leading nonvanishing term reduces to

$$S \simeq \frac{mv}{3}\left\langle 4v_\mathrm{e}\sigma^{(1)}(v_\mathrm{e}) + v_\mathrm{e}^2\sigma^{(1)\prime}\right\rangle_{\boldsymbol{v}_\mathrm{e}} \equiv \frac{mv}{3}\left\langle\frac{1}{v_\mathrm{e}^2}\frac{\mathrm{d}}{\mathrm{d}v_\mathrm{e}}\left(v_\mathrm{e}^4\sigma^{(1)}(v_\mathrm{e})\right)\right\rangle_{\boldsymbol{v}_\mathrm{e}}. \tag{8.40}$$

Finally, note that a projectile can transfer more energy to a moving electron than to an electron at rest. In a central collision between a heavy projectile with a speed v and an electron moving with a speed v_e towards the projectile, the energy transfer is

$$T_\mathrm{max} = 2mv(v+v_\mathrm{e}). \tag{8.41}$$

You may convince yourself of the correctness of this result by going to Problem 8.1. Here the low-speed limit, where

$$T_\mathrm{max} \simeq 2mvv_\mathrm{e}, \tag{8.42}$$

is of interest.

8.5.3 Fermi Gas

For a degenerate Fermi gas the velocity spectrum of the target electrons is given by

$$f(v_e) = \frac{3}{4\pi v_F^3}\theta(v_F - v)\,, \tag{8.43}$$

where θ indicates the Heaviside step function. In Problem 8.2 you may verify that (8.40) then reduces to the expression

$$S = mvv_F\sigma^{(1)}(v_F) \tag{8.44}$$

for the stopping cross section of a heavy particle moving slowly through a Fermi gas.

Equation (8.44) has become the starting point of numerous theoretical studies of stopping at low ion speeds. This formula was first proposed by Lindhard and utilized in the thesis of Finnemann (1968). The earliest quotation in a journal appears to be in a paper by Ferrell and Ritchie (1977) with reference to Finnemann (1968). Lindhard's derivation may be found in the lecture notes of Bonderup (1981).

8.5.4 Born Approximation

Consider a neutral atom with an atomic number Z_1 travelling at low speed through a Fermi gas. Let the disturbing potential of the projectile be a Yukawa potential with a screening radius a, and describe the scattering by the Born approximation. You may derive a transport cross section from (3.94), Vol. 1, by going to Problem 8.3 with the result that

$$\sigma^{(1)}(v_F) = \frac{\pi b^2}{2}\left\{\ln\left[1 + \left(\frac{2a}{\lambda\!\!\!^{-}}\right)^2\right] - \frac{1}{1 + (\lambda\!\!\!^{-}/2a)^2}\right\}\,, \tag{8.45}$$

where

$$b = \frac{2Z_1e^2}{mv_F^2}; \qquad \lambda\!\!\!^{-} = \frac{\hbar}{mv_F} \tag{8.46}$$

and, hence,

$$S = 4\pi Z_1^2e^2a_0\frac{v}{v_0}\left(\frac{v_0}{v_F}\right)^3 C_a(v_F), \tag{8.47}$$

where

$$C_a(v_F) = \frac{1}{2}\left[\ln\left(1 + \eta^2\right) - \frac{1}{1 + 1/\eta^2}\right] \tag{8.48}$$

with

$$\eta = \frac{2mv_Fa}{\hbar}\,. \tag{8.49}$$

8.5.5 Screening

The screening radius a introduced in the previous section is still undefined. Fermi and Teller (1947) suggested that it should be of the order of $\sqrt{a_0/k_\mathrm{F}}$. A more rigorous calculation goes back to Lindhard's lectures. It is reproduced here, following Bonderup (1981).

Consider a point charge $Z_1 e$ embedded in a Fermi gas with an electron density ρ. The charge will attract electrons, such that the electron density at distance r will be given by

$$\rho(r) = \rho + \delta\rho(r)\,. \tag{8.50}$$

As a consequence, the maximum electron momentum $\hbar k_\mathrm{F}$ will depend on r. Since the Fermi energy must be constant we have

$$\frac{\hbar^2 k_\mathrm{F}^2(r)}{2m} - e\Phi(r) = \frac{\hbar^2 k_\mathrm{F}^2}{2m}\,, \tag{8.51}$$

if we require the potential to vanish far away.

Making use of $\rho = k_\mathrm{F}^3/3\pi^2$ we may write this relation as

$$\frac{\hbar^2}{2m}\left(3\pi^2\right)^{2/3}\left(\rho^{2/3}(r) - \rho^{2/3}\right) = e\Phi(r)\,. \tag{8.52}$$

Assuming weak disturbance, i.e., small Z_1, $\rho^{2/3}(r) \simeq \rho^{2/3} + 2\delta\rho(r)/3\rho^{1/3}$ we find

$$\delta\rho(r) = \frac{emk_\mathrm{F}}{\pi^2\hbar^2}\Phi(r)\,. \tag{8.53}$$

The electron density must be connected to the potential via Poisson's equation,

$$\frac{1}{r}\frac{\mathrm{d}^2}{\mathrm{d}r^2}\left[r\Phi(r)\right] = -4\pi\left[Z_1\delta(\boldsymbol{r}) - e\delta\rho(r)\right]\,. \tag{8.54}$$

Insertion of $\delta\rho(r)$ from (8.53) yields

$$\frac{\mathrm{d}^2}{\mathrm{d}r^2}\left[r\Phi(r)\right] - \frac{1}{a^2}\left[r\Phi(r)\right] = 0 \text{ for } r > 0 \tag{8.55}$$

with

$$a^2 = \frac{\pi a_0}{4k_\mathrm{F}}\,. \tag{8.56}$$

Thus,

$$\Phi(r) = \frac{Z_1 e}{r}\mathrm{e}^{-r/a}\,. \tag{8.57}$$

This confirms that the self-consistent potential of a static point charge is a Yukawa potential in the limit of a weak disturbance, and it defines the screening radius a which is to be inserted into (8.49).

From (8.56) we find

$$\left(\frac{2a}{\lambda\!\!\!^{-}}\right)^2 = \frac{\pi v_\mathrm{F}}{v_0} \equiv \frac{1}{\chi^2}\,. \tag{8.58}$$

With this the stopping cross section is well defined. When expressed in terms of (8.34) we may write

$$C_a(v_\mathrm{F}) = \ln\frac{1+\chi^2}{\chi^2} - \frac{1}{1+\chi^2}\,. \tag{8.59}$$

It is seen that (8.59) agrees with (8.36) asymptotically at small χ or large v_F. This result has been included in Fig. 8.18. You may note very good agreement also outside the asymptotic regime.

8.5.6 Partial Waves

The method of partial waves in scattering theory has been presented in Sect. 3.4.4, Vol. 1. The transport cross section was expressed by

$$\sigma^{(1)} = \int (1-\cos\Theta)\mathrm{d}\sigma(\Theta) = \frac{4\pi}{k^2}\sum_\ell (\ell+1)\sin^2(\delta_\ell - \delta_{\ell+1}), \tag{8.60}$$

where δ_ℓ is a phase shift and $k = mv/\hbar$ a wave number, in casu of a target electron being scattered by a projectile ion.

Quantal scattering is of interest in the present context, because it is known to provide an explanation of the Ramsauer-Townsend effect, i.e., the experimental observation by Ramsauer (1921) and Bailey and Townsend (1921) of a nonmonotonic velocity dependence of the cross section of slow electrons scattered on gas atoms. A possible connection with Z_1-oscillations observed in electronic stopping, cf. Fig. 8.2, was pointed out by Lindhard and explored in an unpublished thesis by Finnemann (1968).

Calculations based on (8.60) have been published by numerous authors, starting with Briggs and Pathak (1973, 1974). A central aspect is the scattering potential. Finnemann (1968) employed Thomas-Fermi-type potentials of isolated atoms. However, quantal scattering cross sections are sensitive to the potential, and in case of $v \ll v_\mathrm{F}$ it appears important to take into account the screening of an ion or atom in an electron gas.

You may have seen this demonstrated in Sect. 8.5.5, where the screening radius $a = \sqrt{\pi a_0/4k_\mathrm{F}}$ differed drastically from that of an isolated atom, $a \simeq a_0/Z_1^3$. In that case, an energy argument was employed to derive a self-consistency condition. An equivalent procedure in the present case is use of Friedel's sum rule (Friedel, 1952), which will be introduced in Appendix 8.10.2, in conjunction with a trial potential with one free parameter (Apagyi and Nagy, 1987, Calera-Rubio et al., 1994).

A rigorous description of the potential of an external charge distribution embedded into a Fermi gas is provided by density functional theory (Kohn and Sham,

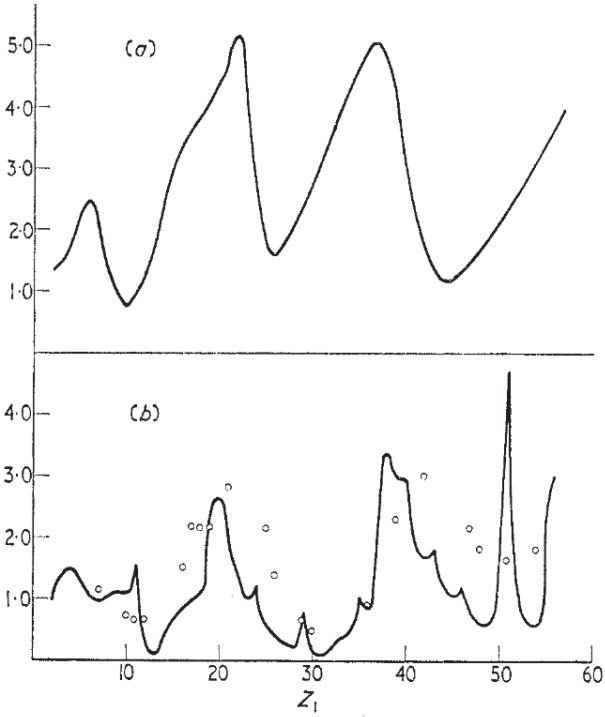

Fig. 8.19 Transport cross section at $v = 0.75v_0$ calculated by numerical evaluation of phase shifts for Thomas-Fermi potentials of neutral atoms (upper graph) and for Hartree-Fock potentials deduced from the tables of Clementi and Raimondi (1963), Clementi et al. (1967) (lower graph). The quantity plotted is $S_e/4\pi$. From Briggs and Pathak (1973)

1965), a sketch of which will be given in Appendix 8.10.3. Echenique et al. (1981, 1986) determined phase shifts for such a potential and calculated transport cross sections. This procedure has been applied successfully to a number of systems.

Only few examples were mentioned in Sect. 3.4.4, Vol. 1, where exact phase shifts are known, while nothing was said about determining phase shifts in general. Apart from perturbation expansions (Schiff, 1981), the quasiclassical (WKB) technique is a very attractive tool in this context (Ferrell and Ritchie, 1977). A brief introduction will be found in Appendix 8.10.1. Variational methods (Callaway, 1976, Gerjuoy et al., 1983) are powerful and used to be the most efficient tool before the general availability of powerful computers. Straight numerical solution of the time-independent Schrödinger equation is a ready-to-use option with present-day computers and used most frequently now.

8.5.6.1 Evaluation from Free-Atom Potential

Finnemann (1968) evaluated transport cross sections on the basis of the relation

$$-\frac{\mathrm{d}E}{\mathrm{d}x} = \rho m v v_\mathrm{F} \sigma^{(1)}(v_\mathrm{F}) = \frac{4}{3\pi} \frac{m v_\mathrm{F}^2}{a_0} \frac{v}{v_0} \sum_\ell (\ell+1) \left[\delta_\ell(v_\mathrm{F}) - \delta_{\ell+1}(v_\mathrm{F})\right] \quad (8.61)$$

by combination of (8.44) with (8.60). The Lenz-Jensen form of the Thomas-Fermi potential was utilized, and phase shifts were determined from the semiclassical (WKB) formula derived in Appendix 8.10.1 or by numerical integration of the radial Schrödinger equation.

Briggs and Pathak (1973) evaluated the transport cross section from the high-speed limit $v \gg v_0$ which, in the present notation, leads to

$$-\frac{\mathrm{d}E}{\mathrm{d}x} = \rho m v^2 \sigma^{(1)}(v) = \frac{4}{3\pi} \frac{m v_\mathrm{F}^3}{v_0 a_0} \sum_\ell (\ell+1) \left[\delta_\ell(v) - \delta_{\ell+1}(v)\right] . \quad (8.62)$$

This expression agrees with (8.61) for $v = v_\mathrm{F}$, but differences get increasingly pronounced for $v \neq v_\mathrm{F}$:

1. In (8.61) the phase of the Z_1 oscillations is determined by the density of the electron gas, while it is governed by the projectile speed in (8.62),
2. Equation (8.61) predicts a strictly linear dependence on projectile speed, while (8.62) tends to produce a quadratic dependence, cf. Problem 8.5,
3. Differences in absolute magnitude become significant: Briggs and Pathak (1973) were able to match positions of maxima and minima to measurements by Bøttiger and Bason (1969) on gold at $v = 0.75 v_0$, cf. Fig. 8.19. From the magnitude of the stopping force they deduce an electron density of about 4 electrons per gold atom. Conversely, if the low-speed formula is applied in the analysis, maxima and minima are matched at $v_\mathrm{F} = 0.75 v_0$. This is equivalent with an electron density of 1.6 electrons per gold atom. This value is significantly closer to the number of conduction electrons in gold.

In Problem 8.6 you may convince yourself that the first correction term to the linear dependence predicted by (8.44) is of third order in v. Thus, the linear dependence is fairly robust, as you may also see from Fig. 5.9, Vol. 1.

I have discussed this point in considerable detail, because you may find numerous comparisons with experimental results in a long series of papers by Pathak and coworkers in the literature. There is nothing astonishing if good agreement is achieved at $v \simeq v_\mathrm{F}$ or $v \gg v_\mathrm{F}$, but those predictions should not be extrapolated to lower projectile speeds.

8.5.6.2 Application of Friedel Sum Rule

As in the case of the Born approximation above, it appears appropriate to take into account the change in the electron density of the target due to a slowly moving ion. As a first approximation one may employ a stability condition derived by Friedel (1952) for a static impurity in a Fermi gas, which is known as the Friedel sum rule and sketched in Appendix 8.10.2,

$$\frac{2}{\pi}\sum_{\ell=0}^{\infty}(2\ell+1)\delta_\ell(v_\mathrm{F}) = Z_1\,. \tag{8.63}$$

The significance of the Friedel sum rule in the stopping of low-velocity ions appears to have been recognized first by Apagyi and Nagy (1987) and applied by the same authors in several studies of proton and antiproton stopping (Nagy and Apagyi, 2004).

Heavier ions, with a particular view at Z_1 structure, were considered by Calera-Rubio et al. (1994). Phase shifts were evaluated for a Yukawa potential by numerical solution of the Schödinger equation, and self-consistency was obtained by determining the screening radius so that the Friedel sum rule is satisfied.

8.5.6.3 Density Functional Method

The density functional method provides an accurate description of the potential of an impurity embedded into a Fermi gas. The Friedel sum rule, rather than being a tool to determine a free parameter in the potential, can be employed here as a final test on the accuracy of the calculation.

Features of the density-functional method are sketched in Appendix 8.10.3. Figure 8.20 shows electron densities around a proton embedded in a Fermi gas, calculated from density functional theory, and an otherwise equivalent linear approximation according to Almbladh et al. (1976). It is seen that the linear approximation underestimates the pile-up of electrons near the proton. The behaviour at larger distances, characterized by Friedel oscillations, is predicted very differently by the two schemes. Similar, possibly even more drastic features must be expected for other ions.

Stimulated by evidence of this kind, Echenique and coworkers developed stopping theory on the basis of density functional theory. A pioneering paper by Echenique et al. (1981) was followed up by a long series of studies. Much of the initial effort was devoted to proton and antiproton stopping, but work on heavier ions followed.

Figure 8.21 demonstrates significant differences for slow protons in a Fermi gas between the predictions of density functional theory and linear theory according to Lindhard and Winther (1964). In the most common density range, nonlinear theory predicts higher stopping.

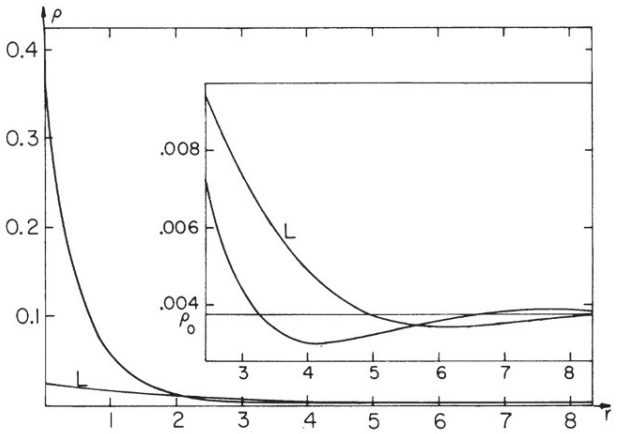

Fig. 8.20 Electron density around an embedded proton in a Fermi gas with $r_s = 4$. Calculated from density functional theory. The line denoted L represents the result of linear response theory. Abscissa and ordinate in atomic units. From Almbladh et al. (1976)

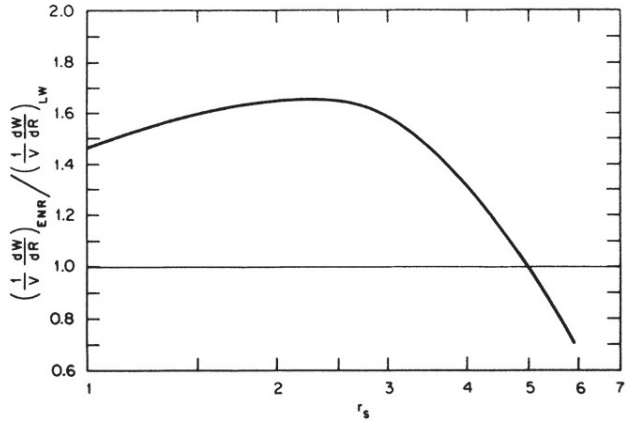

Fig. 8.21 Ratio of velocity-proportional stopping cross sections calculated from density functional theory and result of Lindhard and Winther (1964) as a function of the density parameter r_s. From Echenique et al. (1986)

Figure 8.22 shows predicted stopping forces on slow ions versus Z_1. Also included are experimental data from Fig. 8.15 (Eisen, 1968) on channeling of low-velocity ions in the ⟨110⟩ channel of silicon. The value $r_s = 2.38$ has been chosen to enforce agreement for $Z_1 = 5$. It is close to the value $r_s = 2.0$ that describes an electron gas with four electrons per silicon atom.

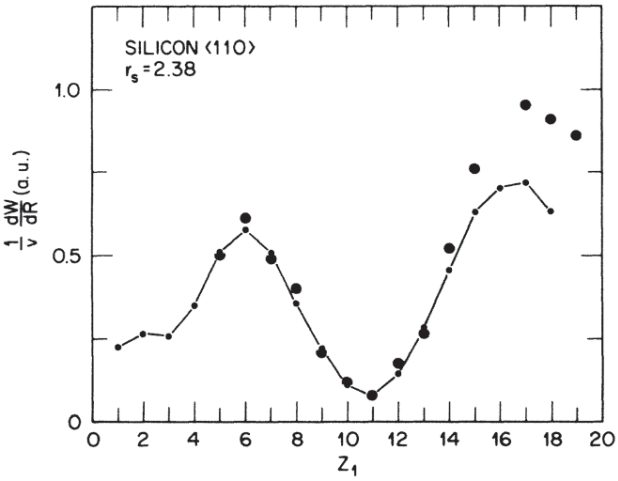

Fig. 8.22 Energy loss of low-energy ions in ⟨110⟩ channel of silicon. Small dots connected by lines: Calculated from density functional theory by Echenique et al. (1986). Large dots: Measurements by Eisen (1968). From Echenique et al. (1986)

8.5.7 Local-Density Approximation

In Sect. 7.2, Vol. 1, the local-density approximation was discussed. This scheme allows to evaluate atomic parameters from properties of a free-electron gas as a function of the electron density. For the electronic stopping cross section of an atom, (7.25) was derived which can be written in the form

$$S = \int_0^\infty 4\pi r^2 \, \mathrm{d}r \, \rho(r) S\big(\rho(r)\big) \,, \tag{8.64}$$

where $S(n)$ is the stopping cross section of a Fermi gas with a density n and $\rho(r)$ the electron density of the target atom. This relation assumes uniform motion of the projectile through the target atom. The present paragraph addresses the use of the local-density approximation in the low-velocity regime.

One may expect the local-density approximation to be justified when the electron density varies slowly over the effective range of interaction. While this is rarely the case, it appears nevertheless more appropriate than in case of swift ions, where interaction ranges may become very large. At this point the main criterion for the feasibility of the local-density approximation—which is a postulate—-is its success, i.e., whether its results are in accordance with experiment or with calculations based on first principles.

8.5.7.1 Nonuniform Projectile Motion

At low projectile speeds we have to worry about changes in magnitude and direction of the relative velocity between projectile and target *during the interaction*. The main purpose of the present paragraph is to identify the limits of the assumption of uniform motion. Once deviations become really serious, theoretical descriptions are influenced by specifics of the experimental setup to which an estimate is going to be applied.

Consider the relative motion of two colliding atoms and characterize it by a vector $\boldsymbol{r}(t)$ as a function of time. Let atom 1 experience a friction force $\boldsymbol{F}(r) = -F(r)\boldsymbol{v}/v$. Then the energy loss during the entire passage is given by

$$T = -\int \boldsymbol{F} \cdot \mathrm{d}\boldsymbol{r} = \int_{-\infty}^{\infty} \mathrm{d}t\, F(t)v(t)\,. \tag{8.65}$$

In Chap. 2, Vol. 1, we have learned that the trajectory is governed by the nuclear interaction. Ignoring the electronic interaction we may determine the trajectory from the theory of elastic collisions. With this we find

$$\frac{m_0}{2}v(t)^2 + \mathcal{V}(r) = \frac{m_0}{2}v^2\,, \tag{8.66}$$

where $\mathcal{V}(r)$ is the screened interatomic potential, v the initial speed and $m_0 = M_1M_2/(M_1 + M_2)$ the reduced mass. Moreover, from (3.31) and (3.32) we may deduce that

$$\mathrm{d}t = \pm\frac{\mathrm{d}r}{v}\left[1 - \frac{2\mathcal{V}(r)}{m_0v^2} - \frac{p^2}{r^2}\right]^{-1/2}\,, \tag{8.67}$$

where p is the impact parameter. The minus sign refers to the incoming trajectory, where $\mathrm{d}r/\mathrm{d}t < 0$. Hence,

$$T(p) = 2\int_{r_{\min}(p)}^{\infty} \mathrm{d}r\, F(r)\frac{1 - 2\mathcal{V}(r)/m_0v^2}{[1 - 2\mathcal{V}(r)/m_0v^2 - p^2/r^2]^{1/2}}\,, \tag{8.68}$$

where $r_{\min}(p)$ is determined by the root of the square root in the denominator.

The electronic stopping cross section of the atom may then be found by

$$S_e = \int_0^{\infty} 2\pi p\,\mathrm{d}p\, T(p) = \int_{r_{\min}}^{\infty} 4\pi r^2\,\mathrm{d}r\, F(r)\left[1 - \frac{2\mathcal{V}(r)}{m_0v^2}\right]^{3/2}\,, \tag{8.69}$$

where $r_{\min} = r_{\min}(0)$ is the distance of closest approach in a head-on collision.

After inserting $F(r) = \rho(r)S(\rho(r))$ we finally obtain

$$S_e = \int_{r_{\min}}^{\infty} 4\pi r^2\,\mathrm{d}r\, \rho(r)S(\rho(r))\left[1 - \frac{2\mathcal{V}(r)}{m_0v^2}\right]^{3/2}\,, \tag{8.70}$$

where $S(\rho)$ is the stopping cross section of a homogeneous Fermi gas.

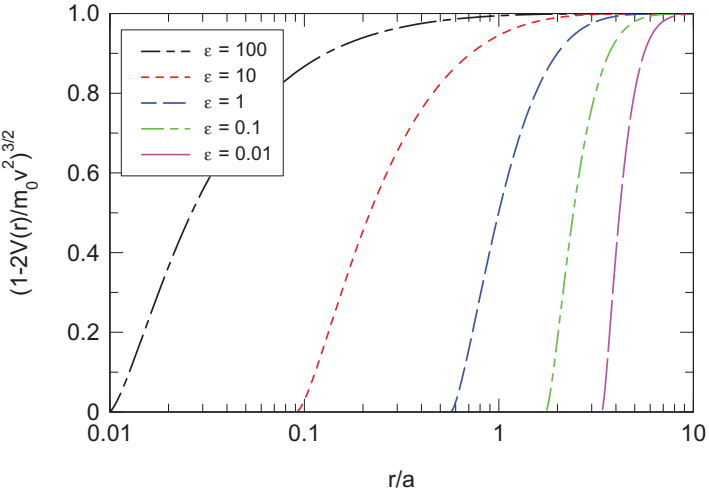

Fig. 8.23 The function $\left(1-2\mathcal{V}(r)/m_0v^2\right)^{3/2}$ appearing in (8.70) for various values of the Lindhard energy variable $\epsilon = m_0v^2a/Z_1Z_2e^2$ for exponential screening, $\exp(-r/a)$

In the limit of high speed v, the elastic interaction can be ignored. With that we arrive back at (8.64). The effect of the correction factor is manifested by a deviation from strict velocity-proportionality of the stopping cross section.

The importance of the factor $\left[1-2\mathcal{V}(r)/m_0v^2\right]^{3/2}$ in low-energy stopping was pointed out by Kishinevskii (1962). This function has been sketched in Fig. 8.23 for exponential screening, i.e., $\mathcal{V}(r) = \left(Z_1Z_2e^2/r\right)\exp(-r/a)$.

You may recall that the cross-over between nuclear and electronic stopping lies around $\epsilon \simeq 2$. Let us, therefore, restrict our attention to velocities equivalent to $\epsilon \gtrsim 10$, where nuclear stopping may be considered negligible. In that case, Fig. 8.23 tells us that deviations from straight-line motion cause changes mainly at $r/a \ll 1$. Note that the Thomas-Fermi radius responsible for the nuclear interaction, $a = 0.8853a_0/\sqrt{Z_1^{2/3}+Z_2^{2/3}}$, is always smaller than the Thomas-Fermi radius of either of the collision partners.

8.5.7.2 Tails in Electron Density

Equation (8.44), which represents the starting point for calculations in the low-velocity range employing the local-density approximation, has been derived under the assumption that $v \ll v_F$. According to Fig. 5.9, Vol. 1, the proportionality with v holds quite accurately up to slightly above v_F: For the case considered, $r_s = 2$, v_F is close to the Bohr speed. However, at $v \gg v_F$ the stopping cross section bends over and approaches the $\sim v^{-2}$ dependence following from the Bethe formula.

The integral (8.64) extends over the entire space. This includes regions where $\rho(r)$ is small but nonvanishing. When $\rho(r)$ becomes sufficiently small, the condition

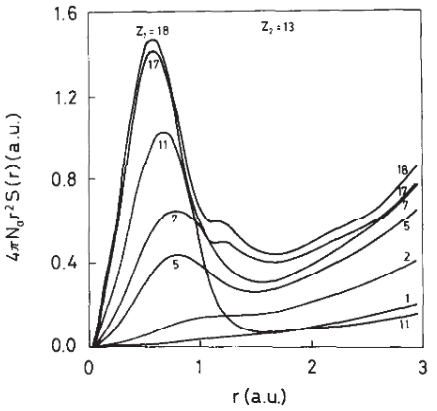

Fig. 8.24 Integrand of low-velocity stopping integral for aluminium in local-density approximation. Numbers on figures represent Z_1. From Calera-Rubio et al. (1994)

$v < v_F(r)$ will no longer be fulfilled. This implies that the second factor in the integral, $S\big(\rho(r)\big)$, will cause a more or less drastic overestimate of the integrand, if it is approximated by the linear expression following from (8.44).

If we wish to compute a stopping cross section at $v = v_0$, we are allowed to apply the linear formula as long as $v_F(r) > v_0$. For a simple Thomas-Fermi estimate, assume an exponential electron density

$$\rho(r) \simeq \frac{Z_2}{8\pi a^3} e^{-r/a} \tag{8.71}$$

with $a \simeq a_0 Z_2^{-1/3}$. With this, the above limitation reads

$$r < \frac{a_0}{Z_2^{1/3}} \ln\left(\frac{3\pi}{8} Z_2^2\right) . \tag{8.72}$$

Figure 8.24 shows an example, taken from Calera-Rubio et al. (1994). The integrand of (8.64), including the factor r^2 from the volume element, has been plotted for several ions in aluminium. All integrands have a maximum slightly below $r = a_0$, and all have a minimum slightly above $r = 1.5a_0$. All curves show a clear increase toward greater distances.

The work of Calera-Rubio et al. (1994) addressed solid aluminium. Therefore, the integration was limited to the interval $0 < r < r_a$, where $r_a = 3a_0$ is the atomic radius in the Al structure. While this prevents the integral from diverging, the procedure clearly overestimates the stopping cross section. Moreover, this argument would not apply to aluminium vapour.

This problem is clearly an artifact of the combination between the linear approximation, (8.44) and the local-density approximation. While the success of (8.44) is well documented in channeling, where use of the Fermi-gas model is justified to a certain extent, the local-density approximation, if accepted at all, should be applied in conjunction with the full, velocity-dependent stopping cross section for the Fermi gas, whether in the Lindhard approximation or in a more sophisticated scheme.

8.5.8 Lindhard-Scharff Formula

The formula

$$S = 8\pi\xi_e \frac{Z_1 Z_2}{Z} a_0 e^2 \frac{v}{v_0} \tag{8.73}$$

for the stopping cross section at low projectile speed with

$$Z = \left(Z_1^{2/3} + Z_2^{2/3}\right)^{3/2} \tag{8.74}$$

was published by Lindhard and Scharff (1961) without an explicit derivation. The proportionality with v was inferred from the Fermi gas, and the proportionality factors were found from Thomas-Fermi arguments. Empirically, the formula was 'not far in error'. Considering its impact for more than half a century, it would have been beneficial if a more quantitative derivation had been published. Amongst a number of valid causes for this omission, the main reason was the fact that by the time the formula became really interesting, Z_1 oscillations had been discovered, which were not predicted by the formula.

This author has never seen a complete derivation of (8.73). Various hints can be found in two earlier papers (Sigmund, 1975, 2008b), and a serious effort has been reported by Tilinin (1995), who also specified limits of validity of his approximative steps.

Equation (8.73) obeys the reciprocity criterion, apart from a numerical factor ξ_e which was inserted to improve the agreement of calculated ranges of fission fragments with experiment. This factor was given as $\xi_e \simeq Z_1^{1/6}$ to account for the increase of the projectile charge at higher velocities: As shown in Fig. 8.1, (8.73) was intended to cover a rather broad range of projectile speeds up to the Thomas-Fermi speed $v_{\mathrm{TF}} = Z_1^{2/3} v_0$.

Disregarding the empirical factor ξ_e you may conclude that the (Z_1, Z_2) symmetry of the stopping cross section implies that target and projectile excitation have been treated in an equivalent manner.

Consider the excitation of atom 2 by projectile 1. From (8.34) we find

$$\begin{aligned} S_{12} &= 4\pi Z_1^2 e^2 a_0 \frac{v}{v_0} \int \mathrm{d}^3\boldsymbol{r}\, \rho(r) \left(\frac{v_0}{v_{\mathrm{F}}}\right)^3 C_1(v_{\mathrm{F}}) \\ &= \frac{4}{3\pi} Z_1^2 e^2 a_0 \frac{v}{v_0} \int_0^\infty 4\pi \left(\frac{r}{a_0}\right)^2 \mathrm{d}\left(\frac{r}{a_0}\right) C_1(v_{\mathrm{F}}). \end{aligned} \tag{8.75}$$

In the Thomas-Fermi model, $C_1(v_{\mathrm{F}})$ is a function of Z_2 and r/a. If we set $a \simeq a_0/Z_2^{1/3}$, S_{12} becomes proportional to Z_1^2/Z_2 if the integral varies weakly with Z_2. The symmetrized expression, $S_{12} + S_{21}$ does not show the scaling properties shown in (8.73). However, Tilinin (1995) points out that the integrand approaches the contribution from atomic charge distributions at small r and from united-atom charge distributions at large r. This precludes simple scaling properties.

Tilinin (1995) writes his final result in terms of (8.73) multiplied by a function $\tau(\epsilon, \zeta)$, where $\epsilon = m_0 v^2 a / 2 Z_1 Z_2 e^2$ and $\zeta = Z_1 / Z_2$. This function, which is given in tabulated form (Tilinin, 1995), has generally very low values at small energies ($\epsilon \ll 1$) because of nonuniform projectile motion discussed in Sect. 8.5.7.1, but comes close to 1 for $\epsilon > 0.1$, depending somewhat on the ratio ζ.

8.5.8.1 Modifications

Modifications of the Lindhard-Scharff model aim at explaining oscillatory structure in the stopping cross section as a function of the atomic number Z_1 of the ion.

Bhalla and Bradford (1968) converted Lindhard's expression for the stopping force of a Fermi gas on a point charge at low speed into an expression for the inelastic energy loss in a binary collision, using intuitive arguments. This expression was evaluated on the basis of Hartree-Fock wave functions of Herman and Skillman (1963). Comparison with experiments showed good agreement in the phases of the oscillations. Reasonable absolute agreement was achieved with two (more or less) adjustable parameters.

A similar, but more transparent argument was applied by Pietsch et al. (1976), who noticed that it is primarily the factor $1/Z$ in (8.73) that represents the details of the charge distributions of the interacting atoms via the screening radius

$$a = \frac{0.8853 a_0}{Z^{1/3}} . \tag{8.76}$$

By a slight generalization,

$$Z^{2/3} \to [\alpha(Z_1, r_0)]^2 Z_1^{2/3} + [\alpha(Z_2, r_0)]^2 Z_2^{2/3} \tag{8.77}$$

with a function $\alpha(Z, r_0)$ to be adjusted to Hartree-Fock charge distributions according to Herman and Skillman (1963), surprisingly good agreement was achieved with measurements, when the free parameter r_0 was fixed to the value $r_0 = 2a_0$.

This idea was taken up again by Sugiyama (1981), who proposed an alternative way to determine the screening radius.

8.6 Bound Target Electrons

In this section the stopping problem is approached from an atomic-collision point of view. This implies that the primary standard of reference is theory and experiments of collisions between ions and isolated (gas) atoms. This discipline is a huge field of research on its own. Due to clever experimentation it has reached a degree of sophistication which, in some cases, is far beyond the resolution achieved in stopping measurements. On the other hand, much good physics can be learned from knowledge achieved there.

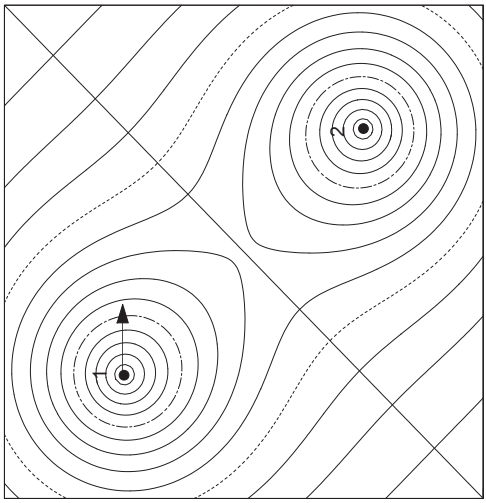

Fig. 8.25 Firsov's view of electronic energy loss for a homonuclear system, $Z_1 = Z_2$. See text

8.6.1 Electron Promotion

Electron promotion was discovered in the early days of quantum mechanics. It explains how colliding atoms may form molecules and how molecules may break up either spontaneously or under external action. In the mid 1960s it became clear (Fano and Lichten, 1965) that electron promotion also may explain how inner shells may be excited in collisions at energies too low for the processes considered until now in this monograph to be responsible.

As an example, take an L electron of argon. In order to overcome the binding energy $U \simeq 18^2/2^2$ Rydbergs, the ion must have a minimum energy of ~ 0.1 MeV/u, if the maximum energy transfer is given by (8.42) according to Problem 8.4. Actually, the observed threshold for X-ray excitation lies in the lower keV range, dependent on the incident ion.

8.6.2 Firsov Theory

Inspired by experiments by Fedorenko and coworkers, O.B. Firsov wrote a number of papers in the late 1950s on elastic and inelastic ion-atom collisions. As it turned out, these papers became more influential in the field of stopping of charged particles than in genuine atomic-collision physics.

The present section is taken over from a lecture by the author on the occasion of the 50th anniversary of this series of Firsov's papers (Sigmund, 2008b).

Consider an ion 1 with a speed v below the Bohr velocity v_0 colliding with a target atom 2 at rest. Firsov's view (Firsov, 1959) of such an event is indicated in Fig. 8.25:

- At any instant of time there exists a surface, the *Firsov surface*, which defines the respective domains of the collision partners.
- This surface is thought to be placed so that the normal component of the electric field vanishes everywhere.
- Electrons passing from the target domain to the projectile domain are taken as captured and hence transfer a momentum $-m\boldsymbol{v}$ to the projectile, thus causing it to slow down.
- The cross section for momentum transfer is determined by the electron flux from the target to the projectile domain.

From this, the basic Firsov expression is found for the electronic energy loss $T_e(p)$ in a single collision at impact parameter p,

$$T_e(p) = m \int \frac{\mathrm{d}\boldsymbol{R}}{\mathrm{d}t} \cdot \mathrm{d}\boldsymbol{R} \int \mathrm{d}^2\boldsymbol{r}\, \frac{1}{4}\rho(\boldsymbol{r}) v_e(\boldsymbol{r})\,, \tag{8.78}$$

where $\boldsymbol{R}(t)$ denotes the trajectory of the projectile, $\int \mathrm{d}^2 S$ an integration over the Firsov surface, $\rho(\boldsymbol{r})$ the electron density in the quasimolecular collision system and $v_e(\boldsymbol{r})$ the average electron speed. The factor $1/4$ originates in the assumption that the electron flux is isotropic.

There are numerous options in the implementation of this physical picture. In the original model, the following additional simplifications were made:

1. The Firsov surface was replaced by a plane,
2. That plane was placed midways between the collision partners,
3. The relative motion of the collision partners was taken as uniform,
4. The relation between mean electron speed v_e and density ρ in the quasi-molecule was determined by the Thomas-Fermi model, and
5. A simple approximation was adopted for the electron density which allowed (almost) analytic evaluation.

The somewhat awkward geometry of a colliding quasi-molecule tends to make analytic evaluation difficult or impossible. This hurdle is absent as long as we focus on a homonuclear collision with atomic numbers $Z_1 = Z_2 = Z$. Then the Firsov surface is indeed a plane midways between the nuclei as indicated in Fig. 8.25, and the two partners contribute equally to the integral over that plane. We then obtain

$$T_e(p) = mv \int_{-\infty}^{\infty} \mathrm{d}x \int 2\pi\rho_F \,\mathrm{d}\rho_F\, \frac{1}{4}\rho(r) v_e(r)\,, \tag{8.79}$$

where $R^2 = p^2 + x^2$, and ρ_F denotes the radial variable on the Firsov plane.

After integration over the impact parameter p we obtain the stopping cross section

$$S_e = \int_0^{\infty} 2\pi p\,\mathrm{d}p\, T_e(p) = \frac{4\pi^2}{3} mv \int_0^{\infty} r^4\,\mathrm{d}r\, \rho(r) v_e(r)\,. \tag{8.80}$$

The electron distribution has here tacitly been approximated as spherical around either collision partner, i.e., $\rho(r) \simeq 2\rho_{\mathrm{at}}(r)$, where $\rho_{\mathrm{at}}(r)$ refers to one atom. We

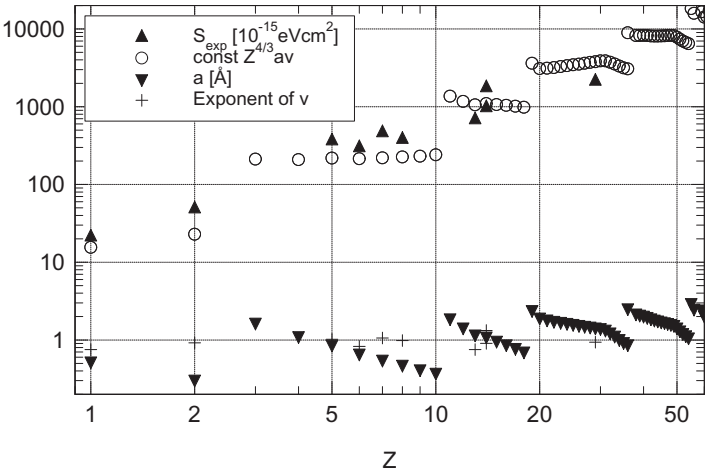

Fig. 8.26 Test of the a-dependence of the stopping cross section for $Z_1 = Z_2$. Stopping cross sections at $v = v_0$ and exponent $2p$ found by fitting measured values of S, extracted from Paul (2013). Atomic radii from Clementi and Raimondi (1963), Clementi et al. (1967). Circles show the Firsov prediction (8.82) with $C = 30$

may characterize $\rho_{\text{at}}(r)$ by a screening radius a so that

$$\rho_{\text{at}}(r) = \frac{Z}{a^3} g\left(\frac{r}{a}\right) \tag{8.81}$$

with some function g which may depend on Z. If we, moreover, adopt the Thomas-Fermi relation $v_e \propto \rho^{1/3}\hbar/m$, the stopping cross section reduces to

$$S_e = C\hbar Z^{4/3} a v\,, \tag{8.82}$$

where the dimensionless constant C is governed by the integral $\int_0^\infty y^4\,\mathrm{d}y\,[f(y)]^{4/3}$. Firsov's result is equivalent with (8.82) for $C = 20.4$ independent of Z. If the screening function f depends explicitly on Z, also C will depend on Z.

For $Z_1 \neq Z_2$, correction factors enter which depend on the details of the charge distribution. In Firsov's original calculation, Z has been replaced by $(Z_1 + Z_2)/2$ and a by $0.8853a_0/(Z_1 + Z_2)^{1/3}$.

For later consideration we keep in mind that the stopping cross section is proportional to the radius a of the charge distribution.

8.6.3 Dependence on Atomic Radius

Let us see to what extent measured stopping cross sections obey the scaling properties following from the Firsov and Lindhard & Scharff picture. Figure 8.26 shows

measured stopping cross sections for $Z_1 = Z_2$ at $v = v_0$, extracted from Paul (2013), atomic radii calculated from Hartree-Fock wave functions (Clementi and Raimondi, 1963, Clementi et al., 1967), and the prediction of (8.82) with $C = 30$, i.e., greater than the Firsov value $C = 20.4$. Also shown is an exponent $2p$ defined by (8.2) and determined by fitting a power law to the set of experimental data available for each Z.

The coverage with experimental stopping cross sections for $Z_1 = Z_2$ is far from comprehensive. Nevertheless, observed shell structure in S is surprisingly well represented by the atomic radii in the first power, as predicted by the Firsov model. Note also that the exponent $2p$ as extracted from measurements is quite close to $2p = 1$.

An attempt to directly relate the stopping cross section to the atomic radius was made by Pietsch et al. (1976). On the basis of the Lindhard-Scharff formula, (8.73), they arrived at $S_e \propto a^3$. Figure 8.26 indicates that such a result—-which deviates dramatically from Firsov scaling—is likely to exaggerate Z_1 and Z_2 structure.

8.6.4 Modifications

Firsov's model is sufficiently simple and transparent to allow for a variety of modifications. Such modifications appear justified to the extent that they match the qualitative nature of the model. Caution is indicated, if a modified theory aims at high precision, or if the degree of complexity of an addition far exceeds that of the original model. A concise review has been given by Akhiezer and Davidov (1979).

In the work of Kishinevskii (1962), Firsov's restriction to the range of $1/4 \lesssim Z_1/Z_2 \lesssim 4$ was dropped by allowing for nonuniform motion of the nuclei as mentioned in Sect. 8.5.7.1, by placing the Firsov surface in the potential minimum, by avoiding the R^{-2} potential and by a more stringent numerical evaluation.

Modified-Firsov theories primarily aim at explaining Z_1 structure. El-Hoshy and Gibbons (1968) observed that oscillations roughly followed the shell structure, with minima for Li, Na and Cu ions. A qualitative description was proposed by introducing an effective atomic number for the ion, otherwise following closely the Firsov model.

Quantitative descriptions without introduction of free parameters were proposed by Winterbon (1968) and Cheshire et al. (1968), who replaced Thomas-Fermi charge distributions by Hartree-Fock functions. The electron flux through the Firsov surface was expressed by $J = \rho v_e$. Winterbon, following Firsov, used the Thomas-Fermi expression

$$\frac{1}{2} m v_e^2 = \kappa_k \rho^{2/3} \tag{8.83}$$

to determine v, while Cheshire determined v_e from the expectation value of the kinetic energy for Slater orbitals,

$$\psi = \text{const}\, r^{n-1} \mathrm{e}^{-\xi r} Y_{\ell m}(\theta, \phi)\,. \tag{8.84}$$

Both authors inserted Hartree-Fock electron densities for individual orbitals from Clementi (1965). In addition, Winterbon also allowed for a spectrum of charge states, while Cheshire assumed the ion to be singly charged.

Both authors compared the resulting impact-parameter-dependent energy losses to stopping data for channelled ions from Eriksson et al. (1967) and Eisen (1968). While experimentally very pronounced Z_1 oscillations were found, calculated oscillation amplitudes were found to be much smaller. Winterbon (1968) made comparisons with data on stopping in amorphous carbon by Ormrod et al. (1965) and Fastrup et al. (1966). Although Z_1 oscillations are much less pronounced there, calculated oscillation amplitudes are still significantly smaller.

Cheshire's approach, unlike Winterbon's, suffers from an inconsistency: Although the electron velocity is determined from a quantal expectation value, the expectation value of the flux is not given by the product of the expectation values of ρ and v_e, as pointed out by Brice (1972). Indeed, Bhalla et al. (1970), following up on Cheshire's approach, found that the outcome of calculations following that scheme depended sensitively on the chosen parametrization of the Hartree-Fock input.

Nevertheless, Cheshire's scheme was employed by several authors, including Land and Brennan (1976) who, in a series of papers and a tabulation (Land and Brennan, 1978) found good agreement with measured stopping cross sections for random slowing-down by introduction of an adjustable constant, i.e., an effective impact parameter.

The approach of Kessel'man (1971) is similar to Winterbon's, but an analytical approximation to Hartree-Fock densities due to Green et al. (1969) was employed. Pronounced shell effects were predicted for related quantities, but no comparisons with stopping measurements were reported. In a recent even more simplified model of Kimura and Takeuchi (2009) the electron density was determined from the ZBL potential used in the SRIM code (Ziegler et al., 1985), and atomic structure was entered through the screening radius by the requirement that the average radius of the charge distribution matched that of a Hartree-Fock distribution. For random slowing-down, the magnitude of the computed stopping cross sections agrees with experiments about as well as the original Firsov formula, while the phases of the predicted Z_1 oscillations are close to opposite to those measured.

8.6.5 Numerical Procedures

Direct computation of collision processes by straight solution of the time-dependent Schrödinger equation has been possible for many years. Such computations operate typically within the semi-classical model, where the motion of the nuclei is characterized by classical trajectories, whereas electronic motion obeys Schrödinger's equation. This implies that the stopping cross section is given by the usual integral over the impact parameter. Since the computation of an individual collision event at a given energy, impact parameter and projectile state is computationally intensive,

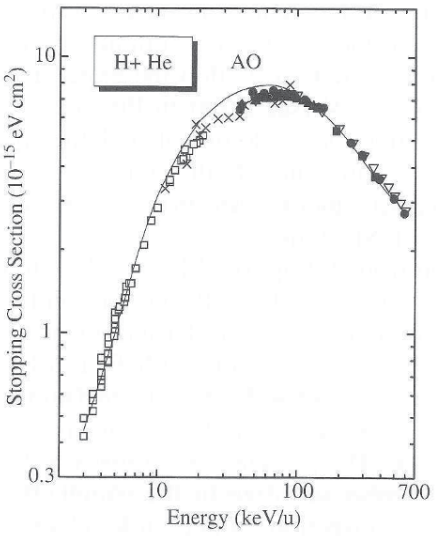

Fig. 8.27 Stopping cross section of He for H ions computed by the coupled-channel method compared with six sets of measurements. Shown is a weighted mean value for H^+ and H^0, where the contribution from H^- was found to be negligible. From Grande and Schiwietz (2004)

such calculations have been performed mainly to provide benchmarks for simplified models. While all these tools are potentially useful to study low-velocity stopping, none of them has been used systematically in this context. Especially, none of them has been employed to study Z_1 or Z_2 structure. Therefore this survey will be quite short.

8.6.5.1 Coupled-Channel Computations

The starting point of coupled-channel calculations, in the version proposed by Schiwietz (1990), is similar to that of semiclassical stopping theory, discussed in Sect. 4.3, Vol. 1, with the difference that no perturbation expansion is applied to the time-dependent expansion coefficients $c_j(t)$ that determine the amplitudes of the excited target states. Specifically, nuclear motion is characterized by classical trajectories, and electronic motion is described in terms of independent particles. A comprehensive survey of the method and its applications was given by Grande and Schiwietz (2004).

Coupled-channel calculations are computationally intensive, not the least because of the lack of sum rules that are useful in perturbation theory. The efficiency and reliability of this method depends on the number of states that contribute to the excitation spectrum. Applications reported by Grande and Schiwietz (2004) focused on the stopping of light ions (protons, antiprotons and alpha particles) in light targets (hydrogen and helium) in an energy range below the Bethe regime.

A particularly successful comparison with experimental data is shown in Fig. 8.27, where calculations and measurements extend down to 2 keV/u. At these energies, the energy loss in this system was found to be dominated by electron capture.

8.6.5.2 Electron-Nuclear Dynamics

Electron-nuclear dynamics, proposed by Deumens and Öhrn (1988) represents similar physics as the coupled-channel model. The formalism, developed for the treatment of chemical reactions, is presumably more powerful and versatile through the introduction of appropriate generalized coordinates into a quantal Lagrangian. Applications in atomic-collision and stopping theory, summarized by Cabrera-Trujillo et al. (2004), have likewise focused on the interaction between light ions and atoms.

Calculations have routinely been performed down to energies of 10 eV/u. While this is outside the scope of the present monograph—as well as that of stopping theory—this feature must be useful in other branches of collision physics and chemistry.

8.6.5.3 Time-Dependent Density Functional Theory

Time-dependent density functional theory is a generalization of the familiar density functional theory. The theoretical basis is a time-dependent generalization of the theorem of Hohenberg and Kohn (1964), derived by Runge and Gross (1984), see also Appendix 8.10.3. The scheme has become a powerful tool in the computation of static and dynamic properties of solids (Marques et al., 2006).

The method was applied to the stopping of protons and antiprotons in LiF by Pruneda et al. (2007). Even though the subject was one of intense discussion at the time, i.e., the seeming absence of an energy threshold in the stopping cross section of a high-bandgap material, the main merit of that work appears to be a new approach to the long-standing problem of low-energy stopping, going beyond the classical approaches of Lindhard-Scharff and Firsov on the one hand, and free-electron models on the other.

A successful application to the stopping of low-velocity heavy ions is due to Hatcher et al. (2008). This work addressed the motion of an ion through the $\langle 110 \rangle$ and $\langle 100 \rangle$ channels in silicon with the aim to compare with measurements by Eisen (1968). The calculation was performed as a molecular-dynamics simulation of the motion of an ion with initial velocity $v = 0.68 v_0$ through a layer of material initially in the ground state. Figure 8.28 shows an even better agreement between experiment and theory, compared to Fig. 8.21.

8.6.5.4 Classical-Trajectory Monte Carlo

The CTMC method (Classical-trajectory Monte Carlo) consists in numerical solutions of Newton's equations of motion for all or part of the electrons belonging to the system to be investigated. In its standard form the scheme was proposed by Olson and Salop (1977) as a tool to analyse ion-atom collisions with an arbitrary number of electrons. Atoms and ions are characterized by initial conditions mimicking pertinent quantum states, i.e., distributions in real and velocity space.

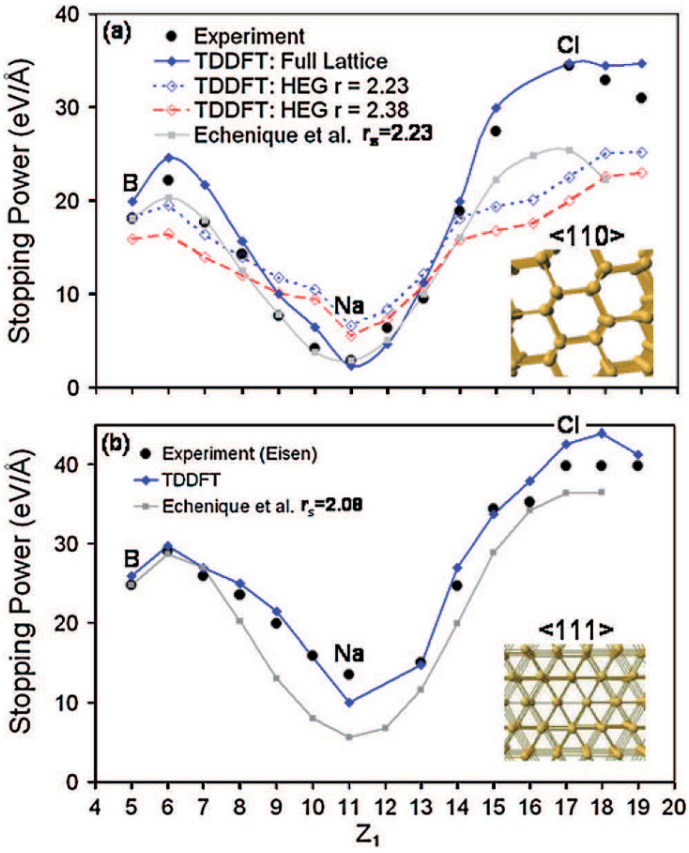

Fig. 8.28 Energy loss of ions with initial velocity $v = 0.68v_0$ in $\langle 110 \rangle$ (upper graph) and $\langle 111 \rangle$ (lower graph) channel in Si. Experimental data from Eisen (1968). Calculations from time-dependent density functional theory by Hatcher et al. (2008). HEG=homogeneous electron gas. Also included are results of Echenique et al. (1986). From Hatcher et al. (2008)

The scheme has proven successful in problems that are difficult to attack by other methods, in particular processes involving swift highly-charged ions. Its potential use in stopping problems has been examined by comparison with results from coupled-channel calculations (Grande and Schiwietz, 1995). For light ions, H, He and Li in atomic hydrogen, increasing discrepancies were found for beam energies from 300 keV/u downward. This was ascribed to the failure of classical theory to account for adiabaticity. As you may recall from the discussion in Chaps. 2 and 4, Vol. 1, this problem was circumvented in the classical Bohr theory by postulating a harmonic atomic binding force.

Calculations for a heavier ion have been performed by Liamsuwan and Nikjoo (2012), who analysed C in water. Figure 8.29 shows close coincidence of all theoretical curves above 2 MeV/u. At lower energies and down to 50 keV/u the CTMC

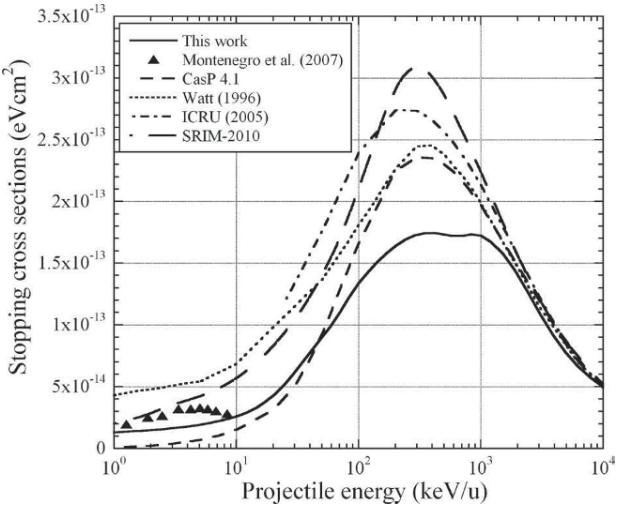

Fig. 8.29 Stopping cross section of liquid water for carbon ions. Experimental data from Montenegro et al. (2007) compared with calculations by CTMC ('this work') from Liamsuwan and Nikjoo (2012), Grande and Schiwietz (2010), Ziegler (2012), ICRU (2005) and Watt (1996). From Liamsuwan and Nikjoo (2012)

result is lower than all others. Drastic discrepancies are found between all data at even lower energies. This is the regime of dominating nuclear stopping.

8.6.5.5 Electronic Stopping in Collision Cascades

The theory of collision cascades aims at understanding phenomena such as radiation damage and sputtering and deals with the scattering and slowing down of primary and higher-order recoil atoms in the lower keV/u energy range and below. Except for target materials containing hydrogen or other very light materials, energy loss is dominated by nuclear stopping. However, energy transfer to target electrons may be the main process in the transport of energy away from the cascade volume, in particular under spike conditions, i.e., a region with high deposited-energy density.

The conventional treatment of electronic energy loss in collision cascades was initiated by Lindhard et al. (1963a) by allowing for a friction force acting on all moving particles, quantified by the Lindhard-Scharff formula, (8.73). This scheme has also been applied, either as it stands or slightly modified, in numerous simulation codes, although genuine quantal schemes are coming up such as Mason et al. (2011), Correa et al. (2012). A discussion of this development will be taken up in Volume 3.

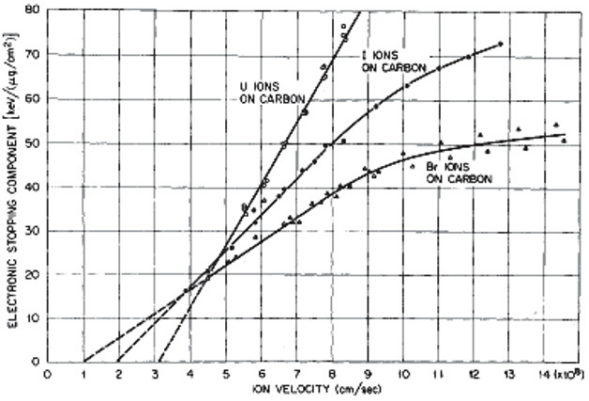

Fig. 8.30 Stopping force of C on U, I and Br ions. Lines inserted to guide the eye. From Brown and Moak (1972)

8.7 Transition to Higher Energies

At the time of publication, Fig. 8.1 was taken as a proof of the assertion that the regime of velocity-proportional stopping extends beyond the Bohr speed up to the region around the stopping maximum which, according to Lindhard and Scharff (1961), should lie close to the Thomas-Fermi velocity $v_{\mathrm{TF}} = Z_1^{2/3} v_0$. For this reason, the regime below the stopping maximum is usually called the regime of velocity-proportional or frictional stopping.

This assertion has become influential in the subsequent development. The LSS range theory, a main subject of the following chapter, as well as numerous computer codes implementing that theory, rest on frictional stopping. Extraction of stopping cross sections from range measurements (Simons et al., 1975) assumes velocity-proportional stopping, and the same is true when, in the analysis of Z_1 or Z_2 structure, measurements at different projectile speeds are scaled to a definite value, usually the Bohr speed v_0 (Paul, 2013).

An indication of deviations from this simple picture may already be found in the work of Fastrup et al. (1966), who tried to fit their measured stopping cross sections as well as those of Ormrod and Duckworth (1963) by a power law, $S_e = \mathrm{const} E^p$ and found values of p oscillating between 0.4 and 0.75 for $v \lesssim 1.1 v_0$.

Direct measurements of stopping cross sections for $v \gtrsim v_0$ revealed significant deviations from velocity-proportional stopping. Figure 8.30 shows stopping data for Br, I and U ions in C according to Brown and Moak (1972). Linear extrapolation leads to positive intercepts at virtual threshold energies that increase with the atomic number of the ion.

Lifschitz and Arista (2013) pointed out that these results are in qualitative agreement with heavy-ion stopping theory. Figure 8.31 shows calculations by the PASS code. Three expressions have been adopted for the mean equilibrium charge, the

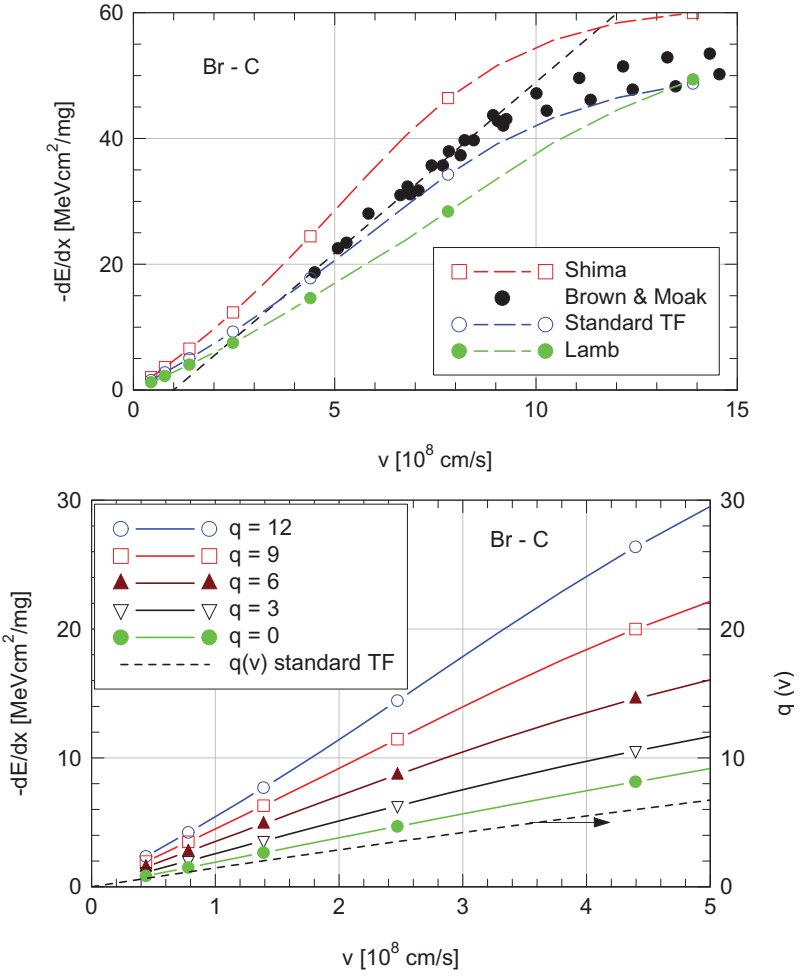

Fig. 8.31 Stopping force on Br ions in C. Calculation by PASS code. Upper graph: Three options of the mean equilibrium charge. Dots and dotted line: Measurements and linear extrapolation of Brown and Moak (1972). Lower graph: Frozen charges. Dotted line: Mean equilibrium charge

standard-Thomas-Fermi expression $q/Z_1 = 1 - \exp(-v/v_{\mathrm{TF}})$, the expression by Shima et al. (1982), and an implementation of the criterion of Lamb (1940) by Schinner (2013). In the upper graph, all three curves contain a region of approximately linear behaviour that results in an apparent threshold when extrapolated to lower speeds. The standard Thomas-Fermi charge yields the best agreement with the measurements and also reproduces the apparent threshold. The lower graph shows calculated stopping curves for frozen charges. These curves do not show an apparent threshold. You may, therefore, conclude that the behaviour observed by Brown and

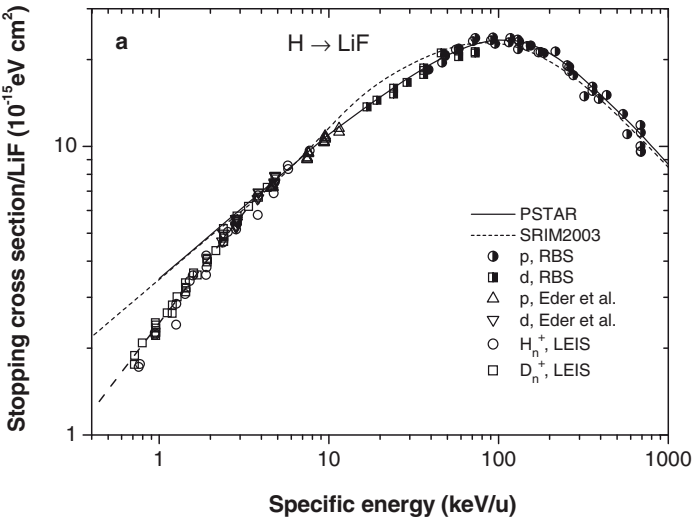

Fig. 8.32 Stopping force on atomic and molecular hydrogen ions in LiF. From Draxler et al. (2005)

Moak (1972) is caused by the increasing contribution of higher charge states with increasing velocity, and that it does not indicate a real threshold effect.

More recently such behaviour has also been found in experiments with protons and deuterons for both insulators and metals by several groups, including Draxler et al. (2005), Serkovic et al. (2007), Markin et al. (2008), Loli et al. (2010). An example is shown in Fig. 8.32.

8.8 Straggling ⋆

8.8.1 General Considerations

Figure 5.2 shows a universal plot for $\Omega^2 = \left\langle (\Delta E - \langle \Delta E \rangle)^2 \right\rangle$, predicted on the basis of the Bohr theory for a point charge. This graph falls naturally into three regimes, a high-energy regime for $mv^3/Z_1 e^2 \omega_0 \gtrsim 10$, a low-energy regime up to $mv^3/Z_1 e^2 \omega_0 \lesssim 1$ and an intermediate regime. We shall see below that according to both Lindhard and Firsov theory, the energy-loss straggling should approach a quadratic dependence on the beam speed v. With a linear dependence of the mean energy loss in the same regime this implies that the relative width of the energy-loss spectrum should become independent of v in the low-velocity range.

Qualitative results like this are well founded in theory, whereas quantitative predictions are scarce and incomplete.

The situation in the experimental area is equally problematic. Energy-loss measurements with low-energy ions are frequently performed by time-of-flight techniques. Proper analysis of such measurements involves conversion of measured time-of-flight spectra into energy spectra. If the extracted spectrum is close to gaussian, one may get an estimate of mean energy loss and straggling from peak and halfwidth, respectively.

This procedure invokes a number of pitfalls at low projectile speed. In the standard transmission geometry, those problems mentioned in connection with measurements of the mean energy loss in Sect. 8.3, in particular nuclear energy loss and multiple scattering, also affect the width of the energy distribution as well as the shape. Moreover, nonuniformities in foil thickness may be large on a relative scale and may dominate the measured width.

For the variance of the measured spectrum one may assume the relation

$$\left\langle (\Delta E - \langle \Delta E \rangle)^2 \right\rangle = \left\langle (\Delta E - \langle \Delta E \rangle)^2 \right\rangle_0 + \left\langle (\Delta E - \langle \Delta E \rangle^2 \right\rangle_{\text{foil}} + \Omega^2 \,, \qquad (8.85)$$

where $\left\langle (\Delta E - \langle \Delta E \rangle)^2 \right\rangle_0$ represents the energy spread of the incident beam,

$$\left\langle (\Delta E - \langle \Delta E \rangle)^2 \right\rangle_{\text{foil}} = \langle \delta x^2 \rangle \left(\frac{\mathrm{d}E}{\mathrm{d}x} \right)^2 \qquad (8.86)$$

the spread due to nonuniformity of the foil, and Ω^2 the (nuclear and electronic) straggling.

While the first term in (8.85) may be negligible, extracting separate information about the second and third term is a nontrivial task. Direct measurements of $\langle \delta x^2 \rangle$, when attempted at all, have typically not been considered accurate enough to extract data for extracting Ω^2. Therefore, trial and error procedures have been most common, where $\langle \delta x^2 \rangle$ enters as a fitting parameter in comparisons between measurements at varying ion type and beam energy.

Measurements in gases are less problematic than in solids. Here, foil thickness is equivalent with the pressure in the target chamber, and an important validity test is checking the proportionality of Ω^2 with pressure.

Straggling data are needed in practice in ion beam analysis with medium and low energy light ions. For heavy ions, where nuclear stopping and straggling are significant to dominating, electronic energy-loss straggling is of interest in connection with detectors. In low-energy ion implantation electronic straggling is commonly ignored, but an estimate of the error in this approximation might be of interest.

8.8.2 Free Target Electrons

8.8.2.1 Transport Cross Section

In Sect. 8.6, Vol. 1, the following expression was derived for the straggling parameter W per target electron,

$$W = \frac{\mathrm{d}\Omega^2}{N\,\mathrm{d}x} = \int T^2 \mathrm{d}\sigma$$
$$= \left\langle m^2 \frac{|\boldsymbol{v} - \boldsymbol{v}_e|}{v} \left\{ \left[(v^2 - \boldsymbol{v}\cdot\boldsymbol{v}_e)^2 - \frac{1}{2}\left(v^2 v_e^2 - (\boldsymbol{v}\cdot\boldsymbol{v}_e)^2\right) \right] \sigma^{(2)}(|\boldsymbol{v} - \boldsymbol{v}_e|) \right.\right.$$
$$\left.\left. + \left[v^2 v_e^2 - (\boldsymbol{v}\cdot\boldsymbol{v}_e)^2\right] \sigma^{(1)}(|\boldsymbol{v} - \boldsymbol{v}_e|) \right\} \right\rangle_{\boldsymbol{v}_e}, \quad (8.87)$$

where

$$\sigma^{(2)}(v) = \int (1 - \cos\theta)^2 \mathrm{d}\sigma(v, \theta) \quad (8.88)$$

is a higher-order transport cross section.

If all target electrons had a definite speed v_e, series expansion in powers of v/v_e would reduce (8.87) to

$$W = \frac{2}{3} m^2 v_e^3 \sigma^{(1)}(v_e) v \quad (8.89)$$

up to the leading term, independent of $\sigma^{(2)}$. This implies that for a Maxwell gas of classical electrons we may expect velocity-proportional straggling in the limit of low speed.

While we shall see below that this does not hold for a Fermi gas, this result is relevant for electronic straggling in a hot gas target. In principle it might also be relevant for nuclear straggling of a heavy projectile moving in a light gas target (Sigmund, 1982) after replacement of m and v_e by target mass and speed, respectively, albeit at energies lower than what is considered in this monograph.

8.8.2.2 Fermi Gas: Lindhard Theory

The low-speed limit of (8.87) can be evaluated for a Fermi gas along the same lines as was done with the stopping force in Sect. 8.5.1, leading to

$$\frac{\mathrm{d}\Omega^2}{n\,\mathrm{d}x} = 6\pi Z_1^2 e^4 \frac{v^2}{v_0^2} \int_0^1 \frac{z^4\,\mathrm{d}z}{\left[z^2 + \chi^2 f_1(0, z)\right]^2}, \quad (8.90)$$

for the straggling parameter per target electron, i.e., an expression proportional to v^2. Here, n represents the electron density. This above expression is seen in the

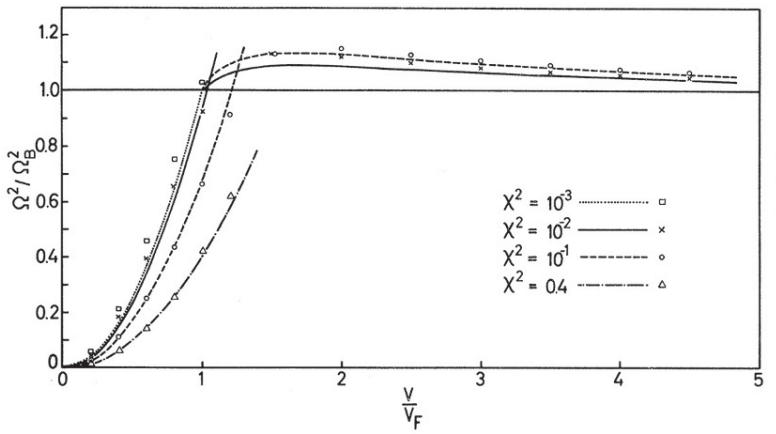

Fig. 8.33 Straggling ratio of Fermi gas for protons at different densities expressed by the parameter $\chi^2 = e^2/\pi\hbar v_F$. Points: numerical computations; lines: analytical approximations. From Bonderup and Hvelplund (1971)

low-speed limit of Fig. 8.33, which actually was evaluated directly from (5.51) by Bonderup and Hvelplund (1971).

Explicit expressions for low-and high-speed expansions were given by Sigmund and Fu (1982). The low-speed expansion reads

$$\frac{\Omega^2}{\Omega^2_{\text{Bohr}}} \sim \frac{3}{2}\frac{v^2}{v_F^2} C_2(\chi) \tag{8.91}$$

with

$$C_2(\chi) \simeq \frac{1}{(1-\chi^2/3)^2} \times \left[\frac{1+7\chi^2/6}{1+2\chi^2/3} - \frac{3\chi/2}{\sqrt{1-\chi^2/3}} \arctan\frac{\sqrt{1-\chi^2/3}}{\chi}\right]. \tag{8.92}$$

A number of modifications of this scheme may be found in the literature. Arista and Brandt (1981) applied the formalism to a non-degenerate plasma to estimate both mean energy loss and straggling for a high-temperature plasma. Several authors studied the effect of modified dielectric functions (Gras-Marti, 1985, Wang and Ho, 1995, Arbo et al., 2002).

8.8.2.3 Fermi Gas: Transport Cross Section

In Sect. 5.7.2, Vol. 1, it was mentioned that the Pauli principle is automatically satisfied in Lindhard dielectric theory. This is not necessarily the case in a theory based on the transport cross section, since that quantity rests on the interaction of an individual target electron with the projectile. As we shall see, this is without consequence for the stopping cross section, but it is significant for straggling.

For a degenerate Fermi gas, with

$$f(v_e) = \frac{3}{4\pi v_F^3} \quad \text{for } 0 < v_e < v_F \tag{8.93}$$

and zero otherwise, the velocity $\boldsymbol{v}'_e$ of a target electron after a collision must be outside the Fermi sphere, i.e., $v'_e > v_F$. In the centre-of-mass system, which is identical with the moving system since $M_1 \gg m$, we thus have

$$(\boldsymbol{u} + \boldsymbol{v})^2 \le v_F^2; \qquad (\boldsymbol{u}' + \boldsymbol{v})^2 \ge v_F^2 \,, \tag{8.94}$$

where $\boldsymbol{u}$ and $\boldsymbol{u}'$ are relative velocities before and after a collision. After introduction of spherical coordinates,

$$\begin{aligned} \boldsymbol{u} &= u(1,0,0), \\ \boldsymbol{u}' &= u(\cos\Theta, \sin\Theta\cos\psi, \sin\Theta\sin\psi), \\ \boldsymbol{v} &= v(\cos\chi, \sin\chi, 0), \end{aligned} \tag{8.95}$$

where $u' = u$ expresses the fact that the collision is elastic in the cms frame, the energy transfer $T = m\boldsymbol{v}\cdot(\boldsymbol{u}' - \boldsymbol{u})$ reduces to

$$T = 2mvu \sin\frac{\Theta}{2}\left(-\cos\chi\sin\frac{\Theta}{2} + \sin\chi\cos\frac{\Theta}{2}\cos\psi\right). \tag{8.96}$$

If $v \ll v_F$, v_e must lie close to the Fermi edge, i.e.,

$$v_e = v_F - \delta v \tag{8.97}$$

with $\delta v \ll v_F$, and

$$u \simeq v_e - v\cos\chi \,. \tag{8.98}$$

From this we find

$$S = \int \mathrm{d}^3\boldsymbol{v}_e \, f(v_e)\frac{u}{v}\int \mathrm{d}\sigma(u,\Theta)\int\frac{\mathrm{d}\psi}{2\pi}(2mvu)\sin\frac{\Theta}{2} \times\left(-\cos\chi\sin\frac{\Theta}{2} + \sin\chi\cos\frac{\Theta}{2}\cos\psi\right) \tag{8.99}$$

for the stopping cross section, and

$$W = \int \mathrm{d}^3 \boldsymbol{v}_e \, f(v_e) \frac{u}{v} \int \mathrm{d}\sigma(u, \Theta) \int \frac{\mathrm{d}\psi}{2\pi} (2mvu)^2 \sin^2 \frac{\Theta}{2} \times \left(-\cos\chi \sin\frac{\Theta}{2} + \sin\chi \cos\frac{\Theta}{2} \cos\psi \right)^2 \quad (8.100)$$

for the straggling parameter.

To the leading order we may set $u = v_F$, and the integration over v_e reduces to a thin shell near v_F with

$$0 \le \delta v \le 2v \sin\frac{\Theta}{2} \left(-\cos\chi \sin\frac{\Theta}{2} + \sin\chi \cos\frac{\Theta}{2} \cos\psi \right) \quad (8.101)$$

according to (8.94). Thus,

$$S = 6mv \int \mathrm{d}\sigma(v_F, \Theta) \sin^2\frac{\Theta}{2} \int \mathrm{d}\cos\chi \times \int \frac{\mathrm{d}\psi}{2\pi} \left(-\cos\chi \sin\frac{\Theta}{2} + \sin\chi \cos\frac{\Theta}{2} \cos\psi \right)^2 \quad (8.102)$$

and

$$W = 12m^2 v_F^2 v^2 \int \mathrm{d}\sigma(v_F, \Theta) \sin^3\frac{\Theta}{2} \int \mathrm{d}\cos\chi \times \int \frac{\mathrm{d}\psi}{2\pi} \left(-\cos\chi \sin\frac{\Theta}{2} + \sin\chi \cos\frac{\Theta}{2} \cos\psi \right)^3 . \quad (8.103)$$

For convenience, the angular integration over $\boldsymbol{v}_e$ has been replaced by averaging over the direction $\boldsymbol{v}$ of the incoming beam. This trick was also used in Sect. 4.4.4, Vol. 1, on the way to the Bethe formula.

Recognizing that the brackets above represent the scalar product of two unit vectors $(-\sin\Theta/2, \cos\Theta/2)$ and $(\cos\chi, \sin\chi\cos\psi)$, which has to be positive, integrations can easily be carried out and lead to

$$S = mv_F v \sigma^{(1)}(v_F) \quad (8.104)$$

in agreement with (8.44) and

$$W = 3(mv_F v)^2 \int \mathrm{d}\sigma(v_F, \Theta) \, \sin^3\frac{\Theta}{2} , \quad (8.105)$$

a result derived by the author (Sigmund, 1982). The dependence on v^2 is in agreement with (8.91) but differs from (8.89) which is proportional to v. This difference is due to the Pauli principle.

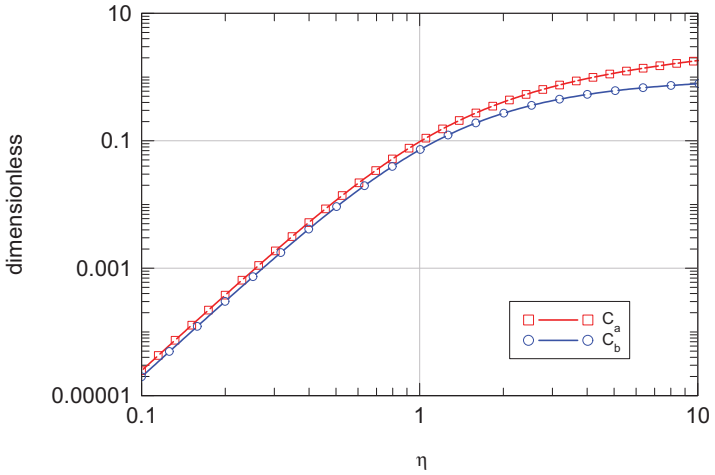

Fig. 8.34 Comparison of the functions $C_a(v_\mathrm{F})$ and $C_b(v_\mathrm{F})$ entering low-speed expressions for stopping cross section and straggling, (8.48) and (8.107), respectively, assuming Born approximation and exponentially-screened Coulomb scattering with $a = a_0$

8.8.2.4 Born Approximation

Evaluation of (8.105) along the same line as the stopping cross section in Sect. 8.5.4 yields

$$\frac{\Omega^2}{\Omega^2_\mathrm{Bohr}} = \frac{3}{2}\frac{v^2}{v_\mathrm{F}^2} C_b(v_\mathrm{F}) \tag{8.106}$$

with

$$C_b(v_F) = 1 - \frac{3}{2\eta}\arctan\eta + \frac{1/2}{1+\eta^2}\,, \tag{8.107}$$

where

$$\eta = \frac{2mv_\mathrm{F}a}{\hbar}\,. \tag{8.108}$$

Figure 8.34 shows that the function $C_b(v_F)$ is quite similar to the corresponding function $C_a(v_\mathrm{F})$ for the stopping cross section, (8.48).

Figure 8.35 shows a measure of the ratio Ω^2/v^2 for three screening radii. None of them resembles the Lindhard expression, which implicitly contains a density-dependent screening radius.

8.8.2.5 Partial Waves

Ashley et al. (1986) evaluated (8.105) by the method discussed in Sect. 8.5.6.3 for the stopping cross section. Results have been included in Fig. 8.36. Very pronounced

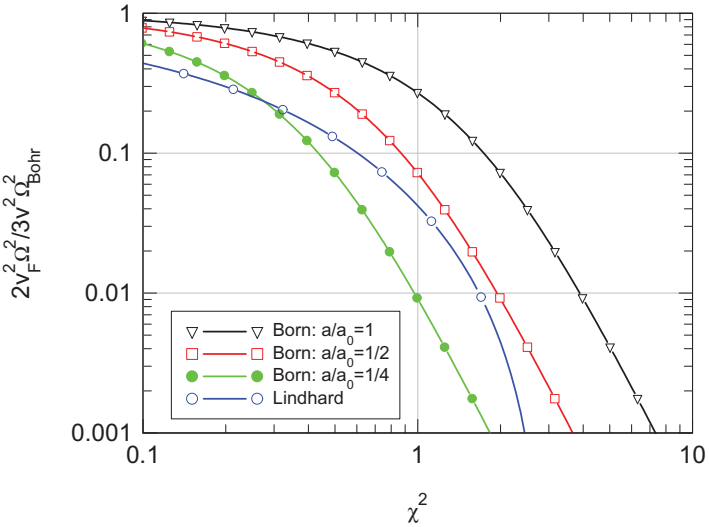

Fig. 8.35 Comparison of straggling in Fermi gas. Lindhard: From linear dielectric theory, (8.91); Born: From transport cross section, (8.106)

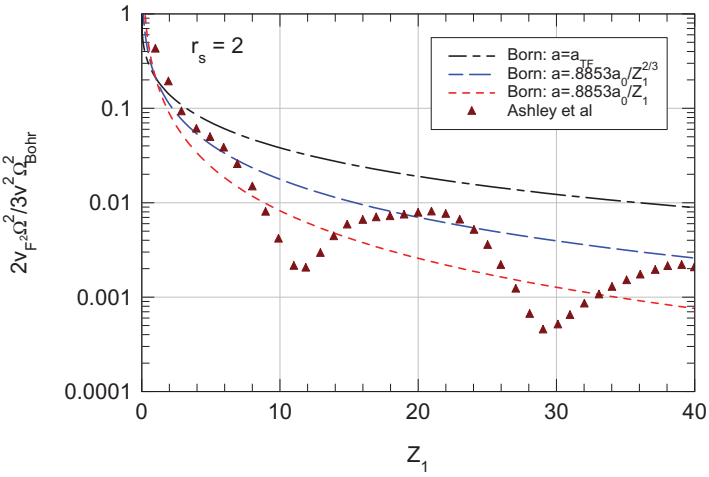

Fig. 8.36 The factor $C_b(v_F)$, (8.107) for $r_s = 2$ and three different dependencies of the screening radius on Z_1. Also included is the result of Ashley et al. (1986). Note that $r_s = 1.919v_0/v_F$

Z_1 structure shows up. Maxima and minima were found to move slowly towards lower values of Z_1 with decreasing electron density.

Such a structure should be expected to show up in measurements under channeling conditions. Pertinent measurements have not been published to the author's knowledge.

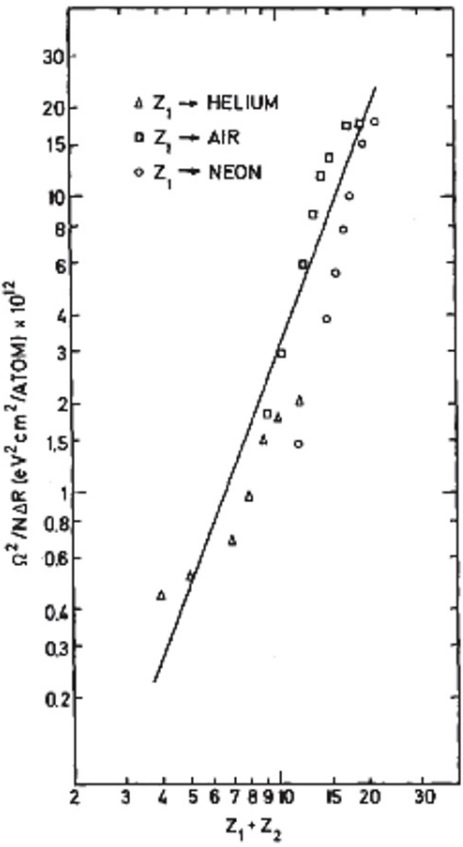

Fig. 8.37 Straggling parameters at $v = 0.9v_0$ for $2 \leq Z_1 \leq 12$ in He, Ne and air compared with (8.109). From Hvelplund (1971)

We have seen that Z_1 structure in the stopping cross section is much less pronounced under random slowing-down than in channeling. This feature must be expected to be even more pronounced in straggling because of decreased contribution of conduction electrons.

8.8.3 Bound Target Electrons

8.8.3.1 Firsov Theory

Hvelplund (1971), reporting measurements of straggling of several ions in gases, compared his results with an application of Firsov's formula to straggling. Assuming straight-line motion of the projectile through the target atom one finds

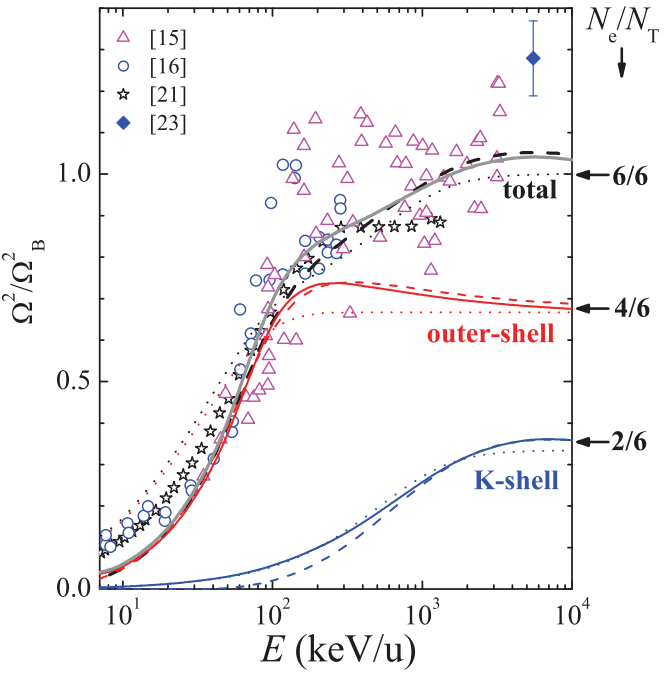

Fig. 8.38 Contributions from K and L shell of carbon to proton straggling. Experimental data from Yang et al. (1991), Shchuchinsky and Peterson (1984), Konac et al. (1998), Tosaki et al. (2005). Theoretical curves from MELF-GOS (dashed lines, see text), local-density approximation (solid lines) and an ad hoc expression due to Konac et al. (1998). From Montanari et al. (2007)

$$W = \int_0^\infty 2\pi p \, \mathrm{d}p \, [T(p)]^2 = 0.418 \, (Z_1 + Z_2)^{8/3} \, \frac{v^2}{v_0^2} e^4. \tag{8.109}$$

You may recall that Firsov's theory ascribes all energy loss to charge exchange. Nevertheless, the description above ignores charge-exchange straggling. You may ponder in Problem 8.8 about this paradox.

Figure 8.37 shows a qualitative agreement of (8.109) with experimental data, in particular an approximate scaling with $Z_1 + Z_2$, while quantitative agreement is barely better than a factor of two. There is a fairly pronounced oscillatory Z_1 structure for the He target, while such a structure is hardly identifiable for air or neon.

8.8.3.2 Quantal Estimates

In an extensive study of light-ion straggling by Montanari et al. (2007), calculations were compared with experiments on C, Al, Si and Cu over an energy range from

$\sim$10 keV/u to 10 MeV/u. Three calculational tools were employed. The MELF-GOS scheme, based on the Born approximation, employs generalized oscillator strengths matched to tabulated dipole oscillator-strength spectra at low wave numbers and extrapolated to high wave numbers in accordance with the Lindhard function (Lindhard, 1954) as amended by Mermin (1970).

While low-velocity straggling is not the main focus of that work, you may note in Fig. 8.38 a large discrepancy at the low-energy end below 100 keV/u. Apart from nuclear straggling and the break-down of the Born approximation, the most likely source of the discrepancy is foil inhomogeneity. In all cases, agreement with calculations is expected to improve at higher energies.

8.8.4 Comparison with Experiment

Figure 8.39 shows data from Hvelplund (1971) plotted as straggling ratios as is common for high-energy data. In the upper graph, for He ions, curves scale close to $\propto v^2$. The same is true in the intermediate energy range in the lower graph, for Ne ions, although curves flatten at the low- and high-energy ends of the graph.

In both graphs, curves for $5 \leq Z_1 \leq 12$ appear to coincide within experimental accuracy, whereas data for He and Li ions fall outside other data in this kind of plot.

Measurements of straggling for low-energy protons and antiprotons were reported by Møller et al. (2008). Figure 8.40 shows results for aluminium. Experimental data are as measured, i.e. have not been corrected for foil inhomogeneity. Dashed lines represent calculations by the PASS code for protons (upper) and antiprotons (lower), uncorrected for packing and bunching.

These curves lie about a factor of two below the experimental data. It was then assumed that the difference is predominantly due to foil inhomogeneity. Since the same foils were used for proton and antiproton measurements, an estimate for foil inhomogeneity δx was then found from (8.85) for the proton data. The value so determined was then utilized to determine a 'prediction' for the standard deviation for antiprotons (solid line). The dot-dashed line represents the adopted fit to the proton data. Considering experimental scatter, the agreement between theory and experiment appears reasonable.

The main lesson from this and similar graphs for Ni and Au is a substantial proton-antiproton difference (Barkas effect) in straggling. Both theoretical and experimental curves show energy dependencies $\propto v$ or steeper. This is to be expected for the contribution from foil inhomogeneity. With regard to the straggling parameter, Fig. 8.40 supports the predictions of both the Fermi-gas model as well as binary theory of $\Omega^2 \propto v^2$.

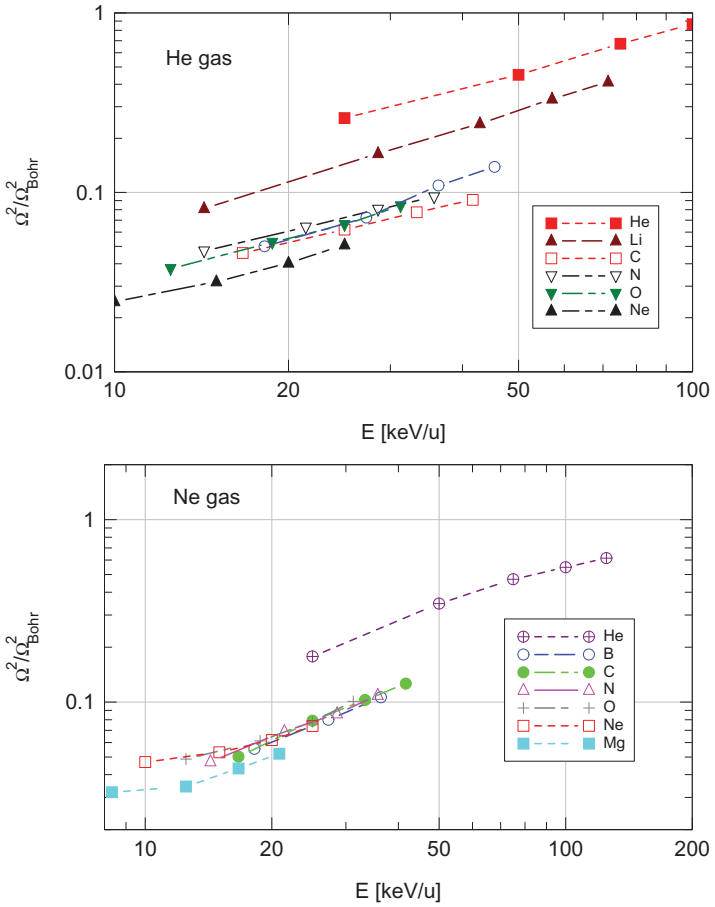

Fig. 8.39 Straggling for slow ions $2 \leq Z_1 \leq 12$ in helium (upper graph) and neon (lower graph). Measurements from Hvelplund (1971)

8.9 Discussion and Outlook

Low-energy electronic stopping has stimulated a surprising number of theoretical studies. This is unquestionably due to the discovery of Z_1 oscillations half a century ago. I have tried to sketch a variety of theoretical approaches, but I am fully aware of the fact that this survey is by no means complete.

While there are successes, such as the explanation of Z_1 structure in silicon under channeling conditions discussed in Sect. 8.5.6.3, and a reasonable characterization of the overall behaviour in random stopping by the Lindhard-Scharff formula as well as Teplova's extension of the Firsov formula, there are open questions:

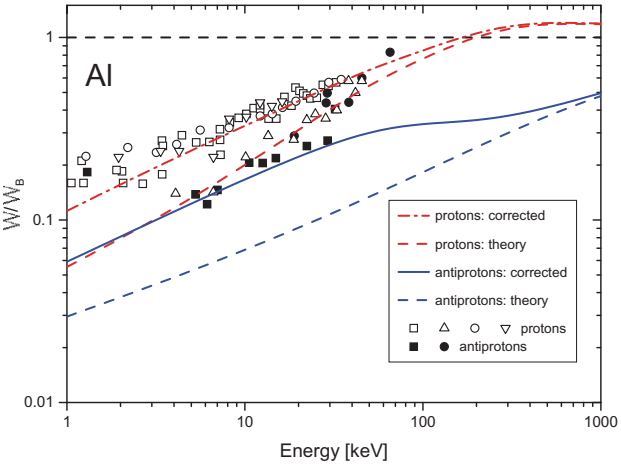

Fig. 8.40 Standard deviation of energy-loss spectrum of low-energy protons and antiprotons in Al. Empty symbols: Protons on different samples; filled symbols: Antiprotons; lines: see text. Redrawn after Møller et al. (2008)

- Very little is known about low-energy electronic stopping in insulators. This applies to both theory and experiment. And yet, the role of electronic processes in radiation effects is far more pronounced in insulators than in metals.
- Experimental scatter is large, and it is hard to distinguish between accurate and less accurate experiments. Nuclear-stopping corrections may be substantial, yet there is no agreement on how such corrections should be made, and most published papers do not contain sufficient documentation so that the reader could apply a chosen correction.
- The role of the ion charge in low-energy stopping has barely been mentioned, even though its significance in solid-state physics and chemistry of solid matter is well established.
- Threshold effects in stopping have been searched for since the 1960s. While few successes can be noted, there is missing a theory to predict where and where not a nontrivial threshold effect might be expected.
- Current attempts to establish powerful computer codes have a potential to solve many of the open questions. The problem here is, as in many other areas, to achieve a proper balance between adequate statistics and tolerable computation time.

8.10 Appendix

8.10.1 The WKB Method

The WKB (or JWKB or quasiclassical) method is the application to the Schrödinger equation of a mathematical technique that goes back to the early nineteenth century. It is a method to solve linear differential equations with slowly variable coefficients. JWKB stands for Jeffreys, Wenzel, Kramers and Brillouin. The application to calculate scattering phase shifts has been ascribed to Ford et al. (1959). You will find an instructive introduction to the method in the book of Bransden and Joachain (2000) with numerous applications, although the calculation of scattering phase shifts is not included explicitly. An explicit treatment of the application to scattering may be found in Landau and Lifshitz (1960).

The time-independent Schrödinger equation for a central symmetric potential,

$$-\frac{\hbar^2}{2m}\nabla^2\psi(\boldsymbol{r}) + \mathcal{V}(r)\psi(\boldsymbol{r}) = \epsilon\psi(\boldsymbol{r}) \tag{8.110}$$

has solutions of the form

$$\psi = A_\ell \frac{u_\ell(r)}{r} Y_\ell^\mu(\theta,\phi), \tag{8.111}$$

where A_ℓ is a constant, Y_ℓ^μ a spherical harmonic,

$$\epsilon = \frac{\hbar^2 k^2}{2m} \tag{8.112}$$

the total energy, and $u_\ell(r)$ obeys

$$\left[-\frac{\hbar^2}{2m}\frac{\mathrm{d}^2}{\mathrm{d}r^2} + \frac{\hbar^2\ell(\ell+1)}{2mr^2} + \mathcal{V}(r) - \epsilon\right] u_\ell(r) = 0. \tag{8.113}$$

In the region where $\mathcal{V}(r) = 0$, you may find in Chap. 3, Vol. 1, page 93, that $u_\ell = A_\ell \mathrm{e}^{\pm \mathrm{i}kr}$. Hence, if the potential varies 'slowly', it makes sense to make an ansatz

$$u_\ell(r) = A_\ell \mathrm{e}^{\frac{\mathrm{i}}{\hbar}S(r)}. \tag{8.114}$$

Insertion into (8.111) leads to

$$\frac{(S')^2}{2m} - \frac{\mathrm{i}\hbar}{2m}S'' + \frac{\hbar^2\ell(\ell+1)}{2mr^2} + \mathcal{V} - \epsilon = 0, \tag{8.115}$$

where a prime denotes the derivative with respect to r.

The trick in the WKB method is to make contact to classical motion by an expansion in powers of $\hbar$,

$$S = S_0 + \hbar S_1 + \frac{1}{2}\hbar^2 S_2 \ldots . \tag{8.116}$$

Insertion into (8.115) leads to

$$\left(S_0'\right)^2 = 2m\left[\epsilon - \frac{\hbar^2\ell(\ell+1)}{2mr^2} - \mathcal{V}(r)\right] \tag{8.117}$$

$$S_1' = \frac{\mathrm{i}}{2}\frac{S_0''}{S_0'} \tag{8.118}$$

$$S_2' = \mathrm{i}\frac{S_1''}{S_0'} - \frac{(S_1')^2}{S_0'} \tag{8.119}$$

with the solutions

$$S_0 = \pm\int_{r_0}^{r} \mathrm{d}r' \sqrt{2m\left[\epsilon - \frac{\hbar^2\ell(\ell+1)}{2mr'^2} - \mathcal{V}(r')\right]} + B_\ell\,, \tag{8.120}$$

where r_0 is the point where the the square root vanishes, B_ℓ is an arbitrary constant, and

$$S_1 = \frac{\mathrm{i}}{2}\ln S_0' + C_\ell. \tag{8.121}$$

Ignoring higher terms in $\hbar$ we then find

$$u_\ell(r) = \frac{A_\ell'}{\sqrt{S_0'}}\exp\left(\pm\mathrm{i}\int_0^r \mathrm{d}r' \sqrt{k^2 - \frac{\ell(\ell+1)}{r'^2} - \frac{2m}{\hbar^2}\mathcal{V}(r')}\right), \tag{8.122}$$

where $A_\ell' = A_\ell \exp(\mathrm{i}B_\ell/\hbar)$.

Consider first the case of a free particle, $\mathcal{V}(r) = 0$, where

$$S_0(r)/\hbar = \sqrt{k^2r^2 - \ell(\ell+1)} + \sqrt{\ell(\ell+1)}\left(\arcsin\frac{\sqrt{\ell(\ell+1)}}{kr} - \frac{\pi}{2}\right). \tag{8.123}$$

Asymptotically, for large values of kr this reduces to

$$S_0/\hbar \to kr - \sqrt{\ell(\ell+1)}\pi/2. \tag{8.124}$$

However, we know from (3.109), Vol. 1, that $\delta_\ell = (\ell + 1/2)\pi/2$. This discrepancy can be repaired by making the replacement

$$\ell(\ell+1) \to (\ell+1/2)^2 \tag{8.125}$$

in (8.115). The phase shift δ_ℓ is defined as the difference between the phase with and without the interaction, i.e.,

$$\delta_\ell = \int_{r_0}^{\infty} \mathrm{d}r \sqrt{k^2 - \frac{(\ell+1/2)^2}{r^2} - \frac{2m}{\hbar^2}\mathcal{V}(r)} - \int_{r_0}^{\infty} \mathrm{d}r \sqrt{k^2 - \frac{(\ell+1/2)^2}{r^2}}\,. \quad (8.126)$$

The dependence on r in these expressions is similar to but not identical with that of classical scattering integrals determining scattering angle and time integral, (3.34) and (3.61), Vol. 1.

8.10.2 Friedel Sum Rule

This section deals with the screening of a point charge embedded into a Fermi gas. The problem appeared in connection with the study of impurities in metallic solids. Friedel (1952) predicted that the change in electron density induced around an impurity shows radial oscillations when calculated quantally. These changes obey a sum rule which arises from the requirement that except for the induced charge the system as a whole must be electrically neutral.

Following Friedel (1954) and Ziman (1972), let us start with a single electron enclosed in a large spherical box with radius R. One solution of the stationary Schödinger equation is

$$\psi_{n\ell}(r, \cos\theta) = \text{const}\, j_\ell(kr) P_\ell(\cos\theta), \quad (8.127)$$

where

$$k = \sqrt{2m\epsilon/\hbar^2}\,, \quad (8.128)$$

ϵ the electron energy, θ the polar angle, $P_\ell(\cos\theta)$ a Legendre polynomial and

$$j_\ell(kr) = \sqrt{\pi/2kr}\, J_{\ell+1/2}(kr) \quad (8.129)$$

a spherical Bessel function in standard notation (Abramowitz and Stegun, 1964). Asymptotically, for large arguments $kr \gg 1$,

$$J_\ell \sim \sqrt{2/\pi kr}\, \cos(kr - \pi\ell/2 - \pi/4) \quad (8.130)$$

according to Abramowitz and Stegun (1964) and hence,

$$\psi_{n\ell}(r, \cos\theta) \sim \frac{\text{const}}{kr} \sin(kr - \ell\pi/2) P_\ell(\cos\theta)\,. \quad (8.131)$$

We want the wave function to vanish at the spherical boundary, $r = R$. This defines allowed values of the wave number k,

$$k_{n\ell} = \frac{(n + \ell/2)\pi}{R}\,. \quad (8.132)$$

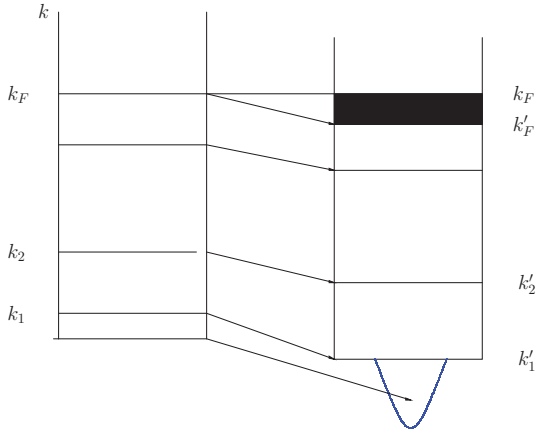

Fig. 8.41 A positively charged impurity embedded into a Fermi gas attracts electrons. This generates bound states in the bottom, indicated by a blue line and empty states in the top (black area). Redrawn after Friedel (1952)

Now, imagine a positive charge $Z_1 e$ in the origin. This will attract electrons into a number of bound states, and all energy levels will shift downwards, as indicated by a shift from left to right in Fig. 8.41. This implies that some states below the Fermi level will be vacated, as indicated by the black area in the figure. There will be no change far away from the origin. Therefore, the Fermi level will not be affected by embedding the point charge. To ensure neutrality, the black area will be filled with Z_1 electrons. Now, as is evident from Fig. 8.41, these electrons have wave numbers $k \simeq k_F$, i.e., they are characterized by asymptotic wave functions (8.131). Although the impurity potential changes the wave function, it does not change the asymptotic dependence on r, as you may recall from (3.109), Vol. 1. Hence, changes can be expected only in the phase. Writing

$$\psi_{n\ell}(r, \cos\theta) \sim \frac{\text{const}}{kr} \sin(kr - \ell\pi/2 + \delta_\ell) P_\ell(\cos\theta) \,. \tag{8.133}$$

instead of (8.131) we get a phase shift $\delta(k)$ for the various levels. The number of allowed levels between two wave numbers k and k' will be given by

$$\Delta\nu = 2(2\ell + 1)[\delta_\ell(k) - \delta_\ell(k')]/\pi \tag{8.134}$$

since there are $2\ell + 1$ allowed values of the azimuthal quantum number for every ℓ-value and 2 states for every orbital quantum number.

We must have $\delta_\ell(0) = 0$ in the absence of an impurity according to (8.131), since changes only occur in the near vicinity of the impurity. On the other hand, if you sum up $\Delta\nu$ over all k-values, all cancel except the uppermost one. Hence

$$\frac{2}{\pi} \sum_\ell (2\ell + 1)\delta_\ell(k_F) = Z_1, \tag{8.135}$$

which is Friedel's sum rule for a Fermi gas.

8.10.3 Density Functional Theory

According to (1.18), the Thomas-Fermi model expresses the energy of an atom or molecule as a functional of the electron density. This is also the case for the Thomas-Fermi-Dirac model including the exchange energy, (1.90), as well as various versions including correlation. While (1.18) is an approximation, it has an exact generalization due to Hohenberg and Kohn (1964).

Hohenberg and Kohn (1964) consider a stationary many-electron system in an external potential such as the Coulomb potential of a nucleus. Once you know the ground-state wave function—assuming that that state is non-degenerate—all properties of the system in the ground state, including the density $\rho(\boldsymbol{r})$, are defined uniquely. These authors then proved that the same is true if the electron density $\rho(\boldsymbol{r})$ is known. This may appear surprising, since the wave function depends on $3N$ variables, while $\rho(\boldsymbol{r})$ only depends on three variables $\boldsymbol{r} = (x, y, z)$.

This theorem has been generalized to a system governed by a time-dependent external potential by Runge and Gross (1984), who found that properties of such a system are determined by the time-dependent electron density $\rho(\boldsymbol{r}, t)$, but with the important addition that the state of the system at t depends on $\rho(\boldsymbol{r}, t')$ at all times $t' \leq t$.

These theorems have been converted into general schemes for the computation of electronic properties of atoms, molecules and solids denoted density functional theory and time-dependent density functional theory. In the basic paper, Kohn and Sham (1965) operate on the basis of the Thomas-Fermi energy functional,

$$\mathcal{E} = \int \mathrm{d}^3\boldsymbol{r}\big[\rho_{\mathrm{kin}}(\boldsymbol{r}) + \rho(\boldsymbol{r})\mathcal{V}(\boldsymbol{r}) + \rho_{\mathrm{xc}}(\boldsymbol{r})\big] + \frac{e^2}{2}\iint \mathrm{d}^3\boldsymbol{r}\,\mathrm{d}^3\boldsymbol{r}'\,\frac{\rho(\boldsymbol{r})\rho(\boldsymbol{r}')}{|\boldsymbol{r}-\boldsymbol{r}'|}, \quad (8.136)$$

where $\rho_{\mathrm{kin}}(\boldsymbol{r})$ and $\rho_{\mathrm{xc}}(\boldsymbol{r})$ denote the density of kinetic energy and of exchange-correlation energy, respectively. Variation, keeping the number of electrons constant, leads to

$$\frac{\partial\rho_{\mathrm{kin}}}{\partial\rho} + \mathcal{V} + \frac{\partial\rho_{\mathrm{xc}}}{\partial\rho} + e^2\int \mathrm{d}^3\boldsymbol{r}'\,\frac{\rho(\boldsymbol{r}')}{|\boldsymbol{r}-\boldsymbol{r}'|} = 0\,. \quad (8.137)$$

From this, Kohn and Sham (1965) showed that

$$\mathcal{V}_{\mathrm{eff}} = \mathcal{V} + \frac{\partial\rho_{\mathrm{xc}}}{\partial\rho} + e^2\int \mathrm{d}^3\boldsymbol{r}'\,\frac{\rho(\boldsymbol{r}')}{|\boldsymbol{r}-\boldsymbol{r}'|} \quad (8.138)$$

is an effective potential in which an individual electron moves independently.

Kohn and Sham (1965) used Slater determinants in the practical implementation, starting with a convenient set of single-particle wave functions, determining $\rho(\boldsymbol{r})$ and $\mathcal{V}_{\mathrm{eff}}(\boldsymbol{r})$, solving Schrödinger's equation for the potential $\mathcal{V}_{\mathrm{eff}}(\boldsymbol{r})$ and, from the N lowest-lying orbitals determining a new Slater determinant and, hence a new electron density $n(\boldsymbol{r})$. This can be used for another iteration.

The scheme has undergone rapid development over several decades and has found a wide range of applications in physics, chemistry and adjacent fields, and

you will easily find lots of pertinent reviews and textbooks as well as ready-to-use computer codes.

Problems

8.1. An electron hitting a heavy particle in a central collision at a velocity v' transfers a momentum $2mv'$ to the projectile. Use this result to calculate the change in kinetic energy of heavy particle moving with a velocity v hitting an electron moving with a velocity v_e toward the projectile in a central collision.

8.2. Derive (8.44) from (8.40) by inserting (8.43), performing partial integration and observing that $\mathrm{d}\theta(x)/\mathrm{d}x \equiv \delta(x)$.

8.3. Derive (8.45) from (8.44) and (3.94), Vol. 1.

8.4. Estimate the minimum energy for an ion to ionize the L shell of an argon atom. Set the binding energy $U = 18^2/2^2e^2/2a_0, mv_e^2/2 = U$ and assume the maximum energy transfer to be given by (8.42).

8.5. Illustrate the difference between $-\mathrm{d}E/\mathrm{d}x = nmv^2\sigma^{(1)}(v)$, the high-$v$ limit of the stopping force, and the low-v limit $-\mathrm{d}E/\mathrm{d}x = nmvv_\mathrm{F}\sigma^{(1)}(v_\mathrm{F})$ in case of the Born approximation, (8.45). Make plots of both curves for a couple of representative electron densities and demonstrate that the high-speed limit predicts a quadratic velocity dependence at low speed.

8.6. Extend the series expansion sketched in Sect. 8.5.2 to the next order in v and show that all terms vanish. If you feel fit, go to the subsequent term which leads to a nonvanishing contribution $\propto v^3$ to the stopping cross section.

8.7. Find exact phase shifts for the potential

$$V(r) = \begin{cases} -Z_1e^2\left(\frac{1}{r} - \frac{1}{a}\right) & r < a \\ 0 & r > a \end{cases} \tag{8.139}$$

and determine the total cross section as a function of the electron speed (Allis and Morse, 1931).

8.8. Consider a medium penetrated by an ion that can occupy one of two states 1 and 2. Introduce probabilities $F_{12}(p)$ and $F_{21}(p)$ as a function of impact parameter p for capture and loss, respectively. Determine a general expression for the mean energy loss $T(p)$ as well as the stopping cross section and straggling parameter in accordance with the Firsov model, where the energy loss in a capture event is given by $mv^2/2$, while all other energy loss is ignored. Next, still ignoring all other sources of energy loss, determine cross sections for capture and loss and find the straggling parameter according to the general expression, (3.138).

References

Abramowitz M. and Stegun I.A. (1964): *Handbook of mathematical functions*. Dover, New York

Akhiezer I.A. and Davidov L.N. (1979): Theory of electronic stopping of heavy ions in metals. Usp Fiz Nauk **129**, 239–254. [Engl. transl. Sov. Phys. Usp. 22, 804-812 (1979)]

Alexander J.M. and Gazdik M.F. (1960): Recoil properties of fission fragments. Phys Rev **120**, 874–886

Allis W.P. and Morse P.M. (1931): Theory of scattering of slow electrons on atoms. Z Physik **70**, 567–582

Almbladh C.O., v. Barth U., Popovic Z.D. and Stott M.J. (1976): Screening of a proton in an electron gas. Phys Rev B **14**, 2250–2254

Andersen H.H. (1991): Accelerators and stopping power experiments. In A. Gras-Marti, H.M. Urbassek, N.R. Arista and F. Flores, editors, *Interaction of charged particles with solids and surfaces*, vol. B 271 of *NATO ASI Series*, 145–192. Plenum, New York

Apagyi B. and Nagy I. (1987): A simple calculation of the stopping power of an electron gas for slow protons. J Phys C **20**, 1265–1268

Arbo D.G., Gravielle M.S., Miraglia J.E., Eckardt J.C., Lantschner G.H., Fama M. and Arista N.R. (2002): Energy straggling of protons through thin solid foils. Phys Rev A **65**, 042901

Arista N.R. and Brandt W. (1981): Energy loss and straggling of charged particles in plasmas of all degeneracies. Phys Rev A **23**, 1898–1905

Ashley J.C., Ritchie R.H., Echenique P.M. and Nieminen R.M. (1986): Nonlinear calculations of the energy loss of slow ions in an electron gas. Nucl Instrum Methods B **15**, 11–13

Bailey V.A. and Townsend J.S. (1921): The motion of electrons in gases. Philos Mag **42**, 873–891

Bhalla C.P. and Bradford J.N. (1968): Oscillating behavior of electron stopping power. Phys Lett A **27**, 318–319

Bhalla C.P., Bradford J.N. and Reese G. (1970): Critical examination of modified Firsov theory of inelastic energy loss in atomic collisions. In D.W. Palmer, M.W. Thompson and P.D. Townsend, editors, *Atomic collisions in solids*, 361–373. North Holland, Amsterdam

Bohr N. (1948): The penetration of atomic particles through matter. Mat Fys Medd Dan Vid Selsk **18 no. 8**, 1–144

Bonderup E. (1981): *Interaction of charged particles with matter*. Institute of Physics, Aarhus. URL `http://www.phys.au.dk/~ahs/EBnotes.htm`

Bonderup E. and Hvelplund P. (1971): Stopping power and energy straggling for swift protons. Phys Rev A **4**, 562–589

Bøttiger J. and Bason F. (1969): Energy loss of heavy ions along low-index directions in gold single crystals. Radiat Eff **2**, 105–110

Bransden B.H. and Joachain C.J. (2000): *Quantum Mechanics*. Prentice Hall, Harlow, 2 edn.

Brice D.K. (1972): Three-parameter formula for the electronic stopping cross section at nonrelativistic velocities. Phys Rev A **6**, 1791–1805

Briggs J. and Pathak A. (1973): Momentum transfer cross sections and the Z_1 oscillations in stopping power. J Phys C **6**, L153 – L157

Briggs J.S. and Pathak A.P. (1974): The stopping power of solids for low-velocity channelled heavy ions. J Phys C **7**, 1929–1936

Brown M.D. and Moak C.D. (1972): Stopping powers of some solids for 30-90-MeV ^{238}U ions. Phys Rev B **6**, 90–94

Cabrera-Trujillo R., Sabin J.R., Deumens E. and Öhrn Y. (2004): Dynamical processes in stopping cross sections. Adv Quantum Chem **45**, 109–124

Calera-Rubio J., Gras-Marti A. and Arista N.R. (1994): Stopping power of low-velocity ions in solids - inhomogeneous electron-gas model. Nucl Instrum Methods B **93**, 137–141

Callaway J. (1976): The variational method in atomic scattering. Phys Reports **45**, 89–173

Cheshire I.M., Dearnaley G. and Poate J.M. (1968): The Z_1-dependence of electronic stopping. Phys Lett A **27**, 304–305

Clementi E. (1965): Table of atomic functions. IBM J Res Devel **9 suppl.**

Clementi E. and Raimondi D.L. (1963): Atomic screening constants from SCF functions. J Chem Phys **38**, 2686–2689

Clementi E., Raimondi D.L. and Reinhardt W.P. (1967): Atomic screening constants from SCF functions. II. Atoms with 37 to 86 electrons. J Chem Phys **47**, 1300–1307

Correa A.A., Kohanoff J., Artacho E., Sanchéz-Portal D. and Caro A. (2012): Nonadiabatic forces in ion-solid interactions: The initial stages of radiation damage. Phys Rev Lett **108**, 213201

Deumens E. and Öhrn Y. (1988): Electron-nuclear dynamics with diabatic and adiabatic wave packets. J Phys C **92**, 3181–3189

Draxler M., Chenakin S., Markin S. and Bauer P. (2005): Apparent velocity threshold in the electronic stopping of slow hydrogen ions in LiF. Phys Rev Lett **95**, 113201

Echenique P.M., Nieminen R.M., Ashley J.C. and Ritchie R.H. (1986): Nonlinear stopping power of an electron gas for slow ions. Phys Rev A **33**, 897–904

Echenique P.M., Nieminen R.M. and Ritchie R.H. (1981): Density functional calculation of stopping power of an electron gas for slow ions. Sol St Comm **37**, 779–781

Eisen F.H. (1968): Channeling of medium-mass ions through silicon. Can J Physics **46**, 561–572

El-Hoshy A.H. and Gibbons J.F. (1968): Periodic dependence of the electronic stopping cross section for energetic heavy ions in solids. Phys Rev **173**, 454–460

Eriksson L., Davies J.A. and Jespersgaard P. (1967): Range measurements in oriented tungsten single crystals (0. 1-1. 0 MeV). I. Electronic and nuclear stopping powers. Phys Rev **161**, 219–234

Fano U. and Lichten W. (1965): Interpretation of Ar^+ – Ar collisions at 50 keV. Phys Rev Lett **14**, 627–629

Fastrup B., Hvelplund P. and Sautter C.A. (1966): Stopping cross section in carbon of 0.1-1.0 MeV atoms with $6 < Z_1 < 20$. Mat Fys Medd Dan Vid Selsk **35 no. 10**, 1–28

Fedorenko N.V. (1959): Ionization by collisions of ions with atoms. Usp Akad NAUK **68**, 481–511. [Engl. Transl. Sov. Phys. Uspekhi 2, 526 (1959)]

Fermi E. and Teller E. (1947): The capture of negative mesotrons in matter. Phys Rev **72**, 399–408

Ferrell T.L. and Ritchie R.H. (1977): Energy losses by slow ions and atoms to electronic excitation in solids. Phys Rev B **16**, 115–123

Finnemann J. (1968): En redegørelse for resultaterne af beregninger over spredning af elektroner med lav energi på afskærmede Coulombfelter. Master's thesis, Aarhus University

Firsov O.B. (1959): A qualitative interpretation of the mean electron excitation energy in atomic collsions. Zh Eksp Teor Fiz **36**, 1517–1523. [Engl. transl. Sov. Phys. JETP **9**, 1076-1080 (1959)]

Ford K.W., Hill D.L., Wakano M. and Wheeler J.A. (1959): Quantum effects near a barrier maximum. Ann Physics **7**, 239–258

Friedel J. (1952): The distribution of electrons round impurities in monovalent metals. Philos Mag **43**, 153–189

Friedel J. (1954): Electronic structure of primary solid solutions in metals. Adv Phys **3**, 446–507

Fulmer C.B. (1957): Scintillation response of CaI(Tl) crystals to fission fragments and energy vs. range in various materials for light and heavy fiission fragments. Phys Rev **108**, 1113–1116

Gerjuoy E., Rau A.R.P. and Spruch L. (1983): A unified formulation of the construction of variational principles. Rev Mod Phys **55**, 725–774

Glazov L.G. and Sigmund P. (2003): Nuclear stopping in transmission experiments. Nucl Instrum Methods B **207**, 240–256

Golser R. and Semrad D. (1991): Observation of a striking departure from velocity proportionality in low-energy electronic stopping. Phys Rev Lett **66**, 1831–1833

Grahmann H. and Kalbitzer S. (1976): Nuclear and electronic stopping powers of low energy ions with $Z \leq 10$ in silicon. Nucl Instrum Methods **132**, 119–123

Grande P.L. and Schiwietz G. (1995): On classical calculations of the electronic stopping power at intermediate energies. J Phys B **28**, 425–433

Grande P.L. and Schiwietz G. (2004): Ionization and energy loss beyond perturbation theory. Adv Quantum Chem **45**, 7–46

Grande P.L. and Schiwietz G. (2010): CasP version 4.1. URL `www.casp-program.org/`

Gras-Marti A. (1985): Increased energy losses in off-beam directions for MeV protons traversing thin films. Nucl Instrum Methods B **9**, 1–5

Green A.E.S., Sellin D.L. and Zachor A.S. (1969): Analytic independent-particle model for atoms. Phys Rev **184**, 1–9

Hatcher R., Beck M., Tackett A. and Pantelides S.T. (2008): Dynamical effects in the interaction of ion beams with solids. Phys Rev Lett **100**, 103201

Herman F. and Skillman S. (1963): *Atomic structure calculations*. Prentice Hall, New Jersey

Hoffmann I., Jäger E. and Müller-Jahreis U. (1976): Z_1-dependence of electronic energy straggling of light ions. Radiat Eff **31**, 57–59

Hohenberg P. and Kohn W. (1964): Inhomogeneous electron gas. Phys Rev **136**, B864–B871

Hvelplund P. (1971): Energy loss and straggling of 100-500 keV atoms with $2 \leq Z_1 \leq 12$ in various gases. Mat Fys Medd Dan Vid Selsk **38 no. 4**, 1–25

ICRU (1993): *Stopping powers and ranges for protons and alpha particles*, vol. 49 of *ICRU Report*. International Commission of Radiation Units and Measurements, Bethesda, Maryland

ICRU (2005): *Stopping of ions heavier than helium*, vol. 73 of *ICRU Report*. Oxford University Press, Oxford

Jiang W., Grötzschel R., Pilz W., Schmidt B. and Möller W. (1999): Random and channeling stopping powers and charge-state distributions in silicon for 0.2 – 1.2 MeV/u positive heavy ions. Phys Rev B **59**, 226–234

Kessel'man V.S. (1971): Stopping power of crystals for inelastic collisions with oscillatory dependence on ion charge. Zh Tekh Fiz **41**, 1708–1716. [English translation: Sov. Phys. Techn. Phys. **16**, 1346 (1972)]

Kimura H. and Takeuchi W. (2009): Dependence of electronic stopping power on incident ions using new Firsov formula. Nucl Instrum Methods B **267**, 2817–2822

Kishinevskii L.M. (1962): Cross sections for inelastic atomic collisions. Izv Akad NAUK SSSR **26**, 1410. [Engl. transl. Bull. Acad. Sci. USSR Phys. Ser. **20**,1433-1438 (1963)]

Kohn W. and Sham L.J. (1965): Self-consistent equations including exchange and correlation effects. Phys Rev **140**, A1133–A1138

Konac G., Klatt C. and Kalbitzer S. (1998): Universal fit formula for electronic stopping of all ions in carbon and silicon. Nucl Instrum Methods B **146**, 106–113

Kuzmin V. and Sigmund P. (2011): Exploring reciprocity as a tool in low-energy electronic stopping. Nucl Instrum Methods B **269**, 817–823

Lamb W.E. (1940): Passage of uranium fission fragments through matter. Phys Rev **58**, 696–702

Land D.J. and Brennan J.G. (1976): Sensitivity of the electronic stopping power to the shell structure of the target material. Nucl Instrum Methods **132**, 89–93

Land D.J. and Brennan J.G. (1978): Electronic stopping power of low-velocity ions. At Data Nucl Data Tab **22**, 235–247

Landau L.D. and Lifshitz E.M. (1960): *Quantum mechanics. Non-relativistic theory*, vol. 3 of *Course of theoretical physics*. Pergamon Press, Oxford

Leachman R.B. and Schmitt H.W. (1954): Fine structure in the velocity distribution of slowed fission fragments. Phys Rev **96**, 1366–1371

Lennard W.N. and Geissel H. (1987): Energy loss and energy loss straggling for heavy ions. Nucl Instrum Methods B **27**, 338–343

Liamsuwan T. and Nikjoo H. (2012): An energy-loss model for low- and intermediate-energy carbon projectiles in water. Int J Radiat Biol **88**, 45–49

Lifschitz A.F. and Arista N.R. (2013): The stopping of heavy ions in the low-to-intermediate energy range: The apparent velocity threshold. Nucl Instrum Methods B 245–248

Lindhard J. (1954): On the properties of a gas of charged particles. Mat Fys Medd Dan Vid Selsk **28 no. 8**, 1–57

Lindhard J., Nielsen V., Scharff M. and Thomsen P.V. (1963a): Integral equations governing radiation effects. Mat Fys Medd Dan Vid Selsk **33 no. 10**, 1–42

Lindhard J. and Scharff M. (1961): Energy dissipation by ions in the keV region. Phys Rev **124**, 128–130

Lindhard J., Scharff M. and Schiøtt H.E. (1963b): Range concepts and heavy ion ranges. Mat Fys Medd Dan Vid Selsk **33 no. 14**, 1–42

Lindhard J. and Winther A. (1964): Stopping power of electron gas and equipartition rule. Mat Fys Medd Dan Vid Selsk **34 no. 4**, 1–22

Loli L.N.S., Sanchez E.A., Grizzi O. and Arista N.R. (2010): Stopping power of fluorides and semiconductor organic films for low-velocity protons. Phys Rev A **81**, 022902

Markin S.N., Primetzhofer D., Prusa S., Brunmayr M., Kowarik G., Aumayr F. and Bauer P. (2008): Electronic interaction of very slow light ions in Au: Electronic stopping and electron emission. Phys Rev B **78**, 195122

Marques M.A., Ullrich C.A., Nogueira F., Rubio A., Burke K. and Gross E.K.U., editors (2006): *Time-Dependent Density Functional Theory*. Springer, New York

Mason D.R., Race C.P., Foulkes W.M.C., Finnis M.W., Horslfield A.P. and Sutton A.P. (2011): Quantum mechanical simulations of electronic stopping in metals. Nucl Instrum Methods B **269**, 1640–1645

Mermin N.D. (1970): Lindhard dielectric function in the relaxation-time approximation. Phys Rev B **1**, 2362–2363

Møller S.P., Csete A., Ichioka T., Knudsen H., Kristiansen H.P.E., Uggerhøj U.I., Andersen H.H., Sigmund P. and Schinner A. (2008): Antiproton and proton energy loss straggling at keV energies. Europ Phys J D **46**, 89–92

Montanari C.C., Miraglia J.E., Heredia-Avalos S., Garcia-Molina R. and Abril I. (2007): Calculation of energy-loss straggling of C, Al, Si, and Cu for fast H, He, and Li ions. Phys Rev A **75**, 022903

Montenegro E.C., Shah M.B., Luna H., Scully S.W.J., de Barros A.L.F., Wyer J.A. and Lecointre J. (2007): Water fragmentation and energy loss by carbon ions at the distal region of the Bragg peak. Phys Rev Lett **99**, 213201

Nagy I. and Apagyi B. (2004): Stopping power of an electron gas for heavy unit charges: Models in the kinetic approximation. Adv Quantum Chem **46**, 267–291

Olson R.E. and Salop A. (1977): Charge-transfer and impact-ionization cross sections for fully and partially stripped positive ions colliding with atomic hydrogen. Phys Rev A **17**, 531–541

Ormrod J.H. and Duckworth H.E. (1963): Stopping cross sections in carbon for low-energy atoms with $Z \leq 12$. Can J Physics **41**, 1424–1442

Ormrod J.H., MacDonald J.R. and Duckworth H.E. (1965): Some low-energy atomic stopping cross sections. Can J Physics **43**, 275–284

Paul H. (2013): *Stopping power graphs*. URL `https://www-nds.iaea.org/stopping/`

Pietsch W., Hauser U. and Neuwirth W. (1976): Stopping powers from the inverted Doppler shift attenuation method: Z-oscillations: Bragg's rule or chemical effects; solid and liquid state effects. Nucl Instrum Methods **132**, 79–87

Pruneda J.M., Sánchez-Portal D., Arnau A., Juaristi J.I. and Artacho E. (2007): Electronic stopping power in LiF from first principles. Phys Rev Lett **99**, 235501

Ramsauer C. (1921): Über den Wirkungsquerschnitt der Gasmoleküle gegenüber langsamen Elektronen. Ann Phys **64**, 513–540

Runge E. and Gross E.K.U. (1984): Density-functional theory for time-dependent systems. Phys Rev Lett **52**, 997–1000

Santry D. and Werner R. (1991): Measured stopping powers of ^{12}C and ^{14}N ions in thin elemental foils. Nucl Instrum Methods B **53**, 7–14

Schiefermüller A., Golser R., Stohl R. and Semrad D. (1993): Energy loss of hydrogen projectiles in gases. Phys Rev A **48**, 4467–4475

Schiff L.I. (1981): *Quantum mechanics*. McGraw-Hill, Auckland

Schinner A. (2013): *Implementation of the Lamb criterion for the equilibrium charge state of a heavy ion*. Unpublished

Schiwietz G. (1990): Coupled-channel calculation of stopping powers for intermediate-energy light ions penetrating atomic H and He targets. Phys Rev A **42**, 296–306

Serkovic L.N., Sanchez E.A., Grizzi O., Eckardt J.C., Lantschner G.H. and Arista N.R. (2007): Stopping power of fluorides for low-velocity protons. Phys Rev A **76**, 040901(R)

Shchuchinsky J. and Peterson C. (1984): Stopping power and energy-loss stragglings of slow protons moving in carbon, aluminum and gold - effective-charge fractions and straggling of heavy-ions. Radiat Eff **81**, 221–229

Shima K., Ishihara T. and Mikumo T. (1982): Empirical formula for the average charge-state of heavy ions behind various foils. Nucl Instrum Methods **200**, 605–608

Sigmund P. (1975): Energy loss of charged particles in solids. In C.H.S. Dupuy, editor, *Radiation damage processes in materials*, NATO Advanced Study Institutes Series, 3–117. Noordhoff, Leyden

Sigmund P. (1982): Kinetic theory of particle stopping in a medium with internal motion. Phys Rev A **26**, 2497–2517

Sigmund P. (2008a): Reciprocity in the electronic stopping of slow ions in matter. Europ Phys J D **47**, 45–54

Sigmund P. (2008b): Stopping of slow ions. Izv Russ Akad NAUK Ser Fiz **72**, 608–616. [Bulletin Russ. Acad. Sci. Phys. Ser. 72, 569-578 (2008)]

Sigmund P. and Fu D.J. (1982): Energy loss straggling of a point charge penetrating a free-electron gas. Phys Rev A **25**, 1450–1455

Simons D.G., Land D.J., Brennan J.G. and Brown M.D. (1975): Range, Distribution, and Stopping Power of 800-keV $^{14}N^{+}$ Ions Implanted in Metals from $Z_2 = 22$ to $Z_2 = 32$. Phys Rev A **12**, 2383

Sugiyama H. (1981): Modification of Lindhard-Scharff-Schiøtt formula for electronic stopping power. J Phys Soc Japan **50**, 929–932

Tilinin I.S. (1995): Quasiclassical expression for inelastic energy losses in atomic particle collisions below the Bohr velocity. Phys Rev A **51**, 3058–3065

Tosaki M., Ohsawa D. and Isozumi Y. (2005): An experimental evaluation of spatial distribution for deeply penetrating protons in carbon material. Nucl Instrum Methods B **230**, 59–62

Wang N. and Ho Y. (1995): Energy straggling of protons in solids. J Appl Phys **78**, 4830–4834

Ward D., Andrews H.R., Mitchell I.V., Lennard W.N., Walker R.B. and Rud N. (1979): Systematics for the Z_1-oscillation in stopping powers of varioussolid materials. Can J Phys **57**, 645–656

Watt D.E. (1996): *Quantities for dosimetry of ionizing radiations in liquid water*. Taylor & Francis, London

Weyl P.K. (1953): The energy loss of hydrogen, helium, nitrogen, and neon ions in gases. Phys Rev **91**, 289–296

Winterbon K.B. (1968): Z_1 oscillations in stopping of atomic particles. Can J Physics **46**, 2429–2433

Yang Q., O'Connor D.J. and Wang Z. (1991): Empirical formulae for energy loss straggling of ions in matter. Nucl Instrum Methods B **61**, 149

Zhang Y., Possnert G. and Weber W.J. (2002): High-precision measurement of electronic stopping powers for heavy ions using high-resolution time-of-flight spectrometry. Nucl Instrum Methods B **196**, 1–15

Zhang Y. and Weber W.J. (2003): Validity of Braggs' rule for heavy-ion stopping in silicon carbide. Phys Rev B **68**, 235317

Ziegler J.F. (2012): *Particle interactions with matter*. URL `www.srim.org`

Ziegler J.F., Biersack J.P. and Littmark U. (1985): *The stopping and range of ions in solids*, vol. 1 of *The stopping and ranges of ions in matter*. Pergamon, New York

Ziman J.M. (1972): *Principles of the theory of solids*. Cambridge University Press, Cambridge, 2 edn.

Chapter 9
Range and Energy Deposition

Abstract This chapter introduces the basic equations for range and energy profiles. Several range concepts such as vector range, projected and lateral range, pathlength and chord length are introduced as well as relations between these quantities. Input in the form of electronic and nuclear energy loss and scattering is taken from previous chapters, but the correlation between these quantities deserves attention in range and energy deposition profiles. Methods of solution including construction from moments and numerical solution of transport equations are discussed. Results are presented primarily in the form of more or less universal scaling relations indicating trends, and a few specific comparisons with experiment are shown to illustrate the degree of predictivity of various schemes.

9.1 Introductory Comments

Figure 1.1, Vol. 1, shows a photograph of the tracks of alpha particles in a cloud chamber. The range, or penetration depth, of such particles and its dependence on penetrating species, projectile energy and penetrated material is a quantity of central importance in most application areas. Accurate measurements and reliable predictions of particle ranges have been recognized to be necessary ingredients in all applications of radioactivity in the beginning of the past century and, later on, applications of all types of accelerators. It is the need to understand ion ranges that forms the main motivation to quantitatively study stopping forces and straggling, even though those topics have developed their own dynamics.

Penetration depths of alpha particles in a cloud chamber are of the order of centimeters. Ranges in condensed matter scale down inversely proportional with increasing density of the medium, so we arrive in the micrometer range. Ranges of heavy keV ions in solids—which are of interest in micro- and nanotechnology—may be down in the nanometer range. Conversely, heavy ions in the upper MeV and lower TeV range—which are used in particle therapy—come up into the 10-100 cm range in condensed matter.

P. Sigmund, *Particle Penetration and Radiation Effects Volume 2*,
Springer Series in Solid-State Sciences 179, DOI: 10.1007/978-3-319-05564-0_9,

By and large, experimental problems in measuring penetration profiles increase with decreasing energy. Reliable experimental methods became available in the late 1950s (Davies et al., 1960b) and have undergone refinement ever since.

On the theoretical side, the main problem is to find reliable input in terms of stopping and scattering cross sections. This has been the main subject of the previous eight chapters. Once such input has become available, tools are needed to study ion-range profiles as well as the spatial distribution of deposited energy. That aspect is nowadays taken care of mostly by suitable computer simulation codes. Therefore, the present chapter can focus on fundamental aspects as well as qualitative guidelines on the relative importance of stopping and scattering, of electronic versus nuclear stopping, and on their dependence on ion and target mass or atomic number.

9.1.1 Recapitulation

According to (2.35), Vol. 1, the quantity

$$R(E, E_1) = \int_{E_1}^{E} \frac{\mathrm{d}E'}{NS(E')} \tag{9.1}$$

represents an estimate of the mean pathlength travelled by a particle while slowing down from an initial energy E to some energy E_1. In the analysis of a cloud-chamber photograph, E_1 will be taken to be the energy below which the projectile does not leave a visible track.

The quantity specified by (9.1) is frequently called the 'csda range', where csda stands for *continuous slowing-down approximation*. It represents the pathlength in case of negligible straggling.

Figure 9.1 shows the electronic stopping cross section of aluminium for oxygen ions as a function of the beam energy E together with the total range down to zero energy[1]. You may identify a low-energy regime up to ~ 0.1 MeV/u, where the range goes approximately like the square root of the energy, and a high-energy regime from ~ 10 MeV/u upward, where the range is approximately $\propto E^2$. The behaviour in between these two regimes can very roughly be characterized as linear in energy.

Figure 9.1 also shows range straggling Ω_R computed from (2.38), Vol. 1,

$$\Omega_R^2 = \int_0^E \mathrm{d}E' \frac{NW(E')}{[NS(E')]^3} \,. \tag{9.2}$$

Both calculations neglect nuclear stopping and straggling, and electronic straggling has been approximated by Bohr straggling. You may note that in the high-energy

[1] For the calculation of the range the stopping cross section has been extrapolated down to zero energy.

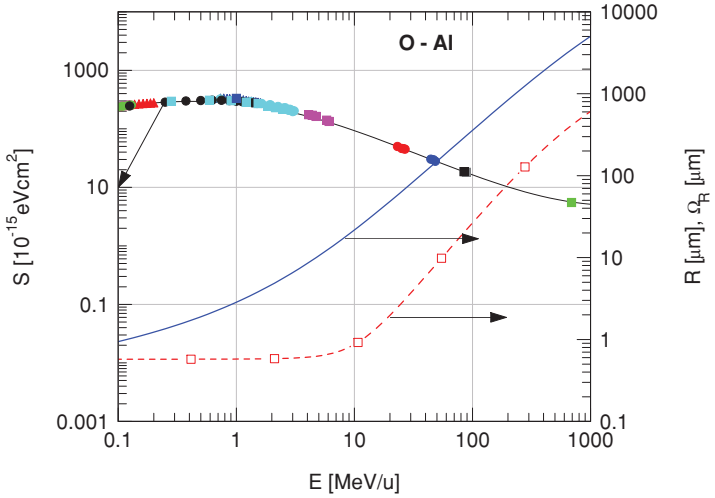

Fig. 9.1 Range R (solid curve), stopping cross section S (including measurements) and rms. range straggling Ω_R (dotted curve) for oxygen in aluminium. Measured stopping cross sections compiled by Paul (2013). Calculated stopping cross section from Sigmund and Schinner (2002). Pathlength calculated from (9.1) for $E_1 = 0$ and range straggling from (9.2). Nuclear stopping neglected

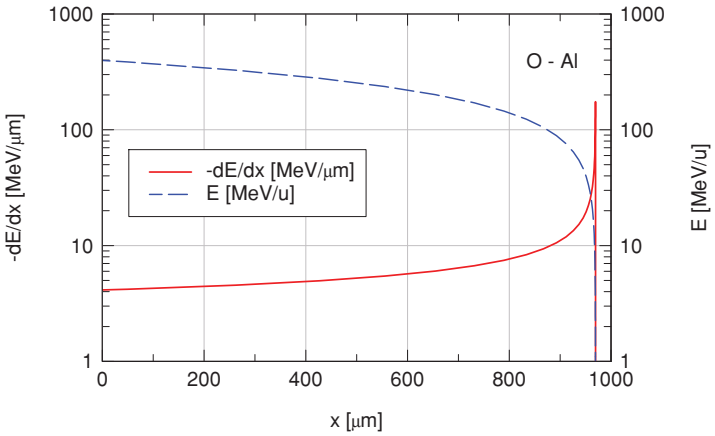

Fig. 9.2 Energy and stopping force versus pathlength for oxygen ion slowing down in aluminium from an initial energy 400 MeV/u to 0, calculated from (9.1) on the basis of the stopping cross section shown in Fig. 9.1. Nuclear stopping and scattering neglected

regime above 10 MeV, the relative fluctuation varies only slowly, whereas at lower energies it increases as the energy decreases.

These features are rather general for all ion-target combinations, except for the limiting energies which vary with Z_1 and Z_2.

Figure 9.2, which has been generated from (9.1) and the theoretical curve for $S(E)$ in Fig. 9.1, shows the beam energy and the mean energy loss as a function of

the travelled pathlength. You may notice that the beam energy degrades only slowly in the beginning of the trajectory, where the stopping force is small. Conversely, a sharp decrease is found when the beam energy approaches the stopping maximum. This behaviour is also reflected in the complementary quantity, the energy deposited per unit pathlength which goes through a sharp Bragg maximum before going to zero at the ion range.

9.1.2 Needs

Ion range and straggling as shown in Fig. 9.1 have been calculated under the simplifying assumption of negligible nuclear stopping and straggling. It has been tacitly assumed that (9.1) represents an average pathlength, whereas the derivation of this expression in Volume 1 does not account for statistical considerations. A proper statistical treatment should start at a penetration profile

$$F_{\mathrm{R}}(\boldsymbol{v}, \boldsymbol{r})\mathrm{d}^3\boldsymbol{r}\,, \tag{9.3}$$

defined as the probability for a projectile with an initial velocity $\boldsymbol{v}$ in the point $\boldsymbol{r} = \boldsymbol{0}$ to end up in a volume element $(\boldsymbol{r}, \mathrm{d}^3\boldsymbol{r})$ when coming to rest. This profile will depend on masses and atomic numbers of the species and the target atoms. Nuclear scattering and stopping need to be accounted for and may even be dominating. In a homogeneous medium, profiles will be translationally invariant, but in practical applications, symmetry breaking such as the existence of a (plane or rough) surface and other kinds of inhomogeneity may greatly complicate the matter.

Figure 9.2, showing an energy-deposition profile under the assumption of negligible nuclear stopping and scattering, needs to be generalized similarly. In addition, it is convenient to distinguish between deposition of nuclear and electronic energy, $F_{\mathrm{n}}(\boldsymbol{v}, \boldsymbol{r})\mathrm{d}^3\boldsymbol{r}$ and $F_{\mathrm{e}}(\boldsymbol{v}, \boldsymbol{r})\mathrm{d}^3\boldsymbol{r}$, respectively. Although all energy will ultimately end up as heat, i.e., nuclear motion, this distinction is relevant on a short timescale: The transfer of electronic energy to the atoms or molecules of a material is slow on the time scale of collision processes.

Defining a deposited-energy profile is meaningful as long as the penetration depth of the particles involved, electrons or atoms, decreases toward zero with decreasing energy.

9.2 Pathlength

A comprehensive scheme for calculating ion ranges in a homogeneous and isotropic medium has been outlined by Lindhard et al. (1963b). Unlike previous approaches, this scheme allows for both nuclear and electronic stopping, the basic equations are written down in general terms, and a clear distinction is made between pathlength

(range along the path) and vector range or related quantities. Following Lindhard et al. (1963b) we shall first have a look at the pathlength. This makes the procedure transparent and allows straight generalization to the vector range and related quantities.

9.2.1 Integral Equation

Following Lindhard et al. (1963b), let us define a function $F(E, R)$ such that $F(E, R)\,\mathrm{d}R$ is the probability for a projectile with initial energy E to come to rest after a travelled pathlength $(R, \mathrm{d}R)$. In order to find an equation governing $F(E, R)$, let the projectile travel over a pathlength increment δR. Let δR be so small that the probability for more than one collision is negligible. With the differential cross section $\mathrm{d}\sigma(E, T) = K(E, T)\,\mathrm{d}T$, there is a probability $N\delta R\,\mathrm{d}\sigma(E, T)$ for a collision with energy loss $(T, \mathrm{d}T)$ and a complementary probability for no collision, $1 - N\delta R \int \mathrm{d}\sigma(E, T)$. With this, $F(E, R)$ is now made up by two contributions,

$$F(E, R) = N\delta R \int \mathrm{d}\sigma(E, T) F(E - T, R - \delta R) + \left[1 - N\delta R \int \mathrm{d}\sigma(E, T)\right] F(E, R - \delta R) \quad (9.4)$$

by the rules of combined probabilities. Note the occurrence of $R - \delta R$ on the right-hand side, indicating that we still look for an end position $(R, \delta R)$ seen from the starting point of the trajectory.

After expanding

$$F(E, R - \delta R) \simeq F(E, R) - \delta R \frac{\partial}{\partial R} F(E, R) \quad (9.5)$$

you will recognize that terms of zero order in δR drop out from (9.4), and equating terms of first order leads to

$$-\frac{\partial}{\partial R} F(E, R) = N \int \mathrm{d}\sigma(E, T)\big[F(E, R) - F(E - T, R)\big]. \quad (9.6)$$

This is a linear homogeneous integro-differential equation, similar to but not identical with (9.103), Vol. 1. In order to find a unique solution we need a normalization condition. Since $F(E, R)$ is a probability density, an obvious requirement is

$$\int_0^\infty \mathrm{d}R\, F(E, R) = 1\,. \quad (9.7)$$

The above derivation assumes the total cross section $\int \mathrm{d}\sigma(E, T)$ to be finite. We have dealt with numerous situations where this assumption is not fulfilled. On the other hand, it is evident that a possible singularity of $\mathrm{d}\sigma(E, T)$ at $T = 0$ is counter-

acted in (9.6) by a factor

$$\big[F(E,R) - F(E-T,R)\big] \simeq T\,\frac{\partial}{\partial E}F(E,R) \qquad \text{for small } T\,. \tag{9.8}$$

If the differential cross section is truncated at some energy T_c, the above derivation is valid. According to (9.8), the integral on the right-hand side differs from (9.6) by a term

$$\int_0^{T_c} T\,\mathrm{d}\sigma(E,T)\,. \tag{9.9}$$

If this expression is finite and goes to zero for T_c going to zero, (9.6) should be valid even for an infinite total cross section.

9.2.2 Moments

Still following Lindhard et al. (1963b), introduce moments over the pathlength profile,

$$M^{(n)}(E) = \int \mathrm{d}R\, R^n F(E,R), \qquad n = 0,1,2\ldots \tag{9.10}$$

Multiplying (9.6) by R^n and integrating yields

$$nM^{(n-1)} = N\int \mathrm{d}\sigma(E,T)\big[M^{(n)}(E) - M^{(n)}(E-T)\big], \tag{9.11}$$

where it has been assumed that $F(E,\infty) = 0$, i.e., the projectile must have a finite pathlength.

From (9.7) we find that $M_0 = 1$. Thus, for the average pathlength $\langle R\rangle = M^{(1)}(E)$ we find

$$1 = N\int \mathrm{d}\sigma(E,T)\big[M^{(1)}(E) - M^{(1)}(E-T)\big]. \tag{9.12}$$

The equation for the second moment,

$$2M^{(1)} = N\int \mathrm{d}\sigma(E,T)\big[M^{(2)}(E) - M^{(2)}(E-T)\big], \tag{9.13}$$

can be rewritten in terms of the range straggling

$$\Omega_R^2(E) = M^{(2)}(E) - \Big[M^{(1)}(E)\Big]^2\,, \tag{9.14}$$

so that

$$N \int \mathrm{d}\sigma(E,T)\left[\Omega_R^2(E) - \Omega_R^2(E-T)\right] = 2M^{(1)}(E) - N \int \mathrm{d}\sigma(E,T)\left[M^{(1)}(E)^2 - M^{(1)}(E-T)^2\right]. \quad (9.15)$$

9.2.3 Simple Solutions

An approximate expression for the mean range may be found, based on the assumption that differential cross sections, whether electronic or nuclear, favour small energy transfers. Thus, after expanding

$$M^{(1)}(E-T) \simeq M^{(1)}(E) - T\frac{\mathrm{d}M^{(1)}(E)}{\mathrm{d}E}, \quad (9.16)$$

(9.12) reads

$$1 = NS(E)\frac{\mathrm{d}M^{(1)}(E)}{\mathrm{d}E} \quad (9.17)$$

or

$$\langle R \rangle = M^{(1)}(E) = \int_0^E \frac{\mathrm{d}E'}{NS(E')} \quad (9.18)$$

in agreement with (9.1). While a solution $M^{(1)}(E)$ of (9.12) is indeed an average pathlength, the last expression in (9.18) represents evidently an approximate solution, the accuracy of which depends on the cross section, as you may judge by solving Problem 9.1.

In an attempt to apply the same procedure to (9.15), consider first the term on the right-hand side. With

$$N \int \mathrm{d}\sigma(E,T)\left[M^{(1)}(E)^2 - M^{(1)}(E-T)^2\right] \simeq NS(E)2M^{(1)}(E)\frac{\mathrm{d}M^{(1)}(E)}{\mathrm{d}E} \simeq 2M^{(1)}(E), \quad (9.19)$$

the right-hand side of (9.15) vanishes. Thus, we have to go to the next order, yielding a term

$$\frac{1}{2}NW(E)\frac{\mathrm{d}^2}{\mathrm{d}E^2}M^{(1)}(E)^2 = NW(E)\left[\left(\frac{\mathrm{d}M^{(1)}(E)}{\mathrm{d}E}\right)^2 + M^{(1)}(E)\frac{\mathrm{d}^2M^{(1)}(E)}{\mathrm{d}E^2}\right]. \quad (9.20)$$

Equation (9.12) then expands to

$$1 = NS(E)\frac{\mathrm{d}M^{(1)}(E)}{\mathrm{d}E} - \frac{1}{2}NW(E)\frac{\mathrm{d}^2M^{(1)}(E)}{\mathrm{d}E^2}\,, \tag{9.21}$$

where $W(E) = \int T^2\,\mathrm{d}\sigma(E,T)$ is the straggling parameter. With this, (9.15) reduces to

$$NS(E)\frac{d\Omega_R^2(E)}{\mathrm{d}E} = NW(E)\left(\frac{\mathrm{d}M^{(1)}(E)}{\mathrm{d}E}\right)^2 \tag{9.22}$$

or

$$\Omega_R^2(E) = \int_0^E \mathrm{d}E'\,\frac{NW(E')}{[NS(E')]^3} \tag{9.23}$$

to the leading order, in agreement with Bohr's formula (9.2).

9.2.4 Profiles

At high beam energies, where straggling may be a small effect, range profiles can be approximated as gaussians,

$$F(R) \simeq \frac{1}{\sqrt{2\pi\,\Omega^2}}\exp\left(-\frac{(R-\langle R\rangle)^2}{2\Omega^2}\right). \tag{9.24}$$

However, the rigorous profile must always be skew, if not for other reasons since $F(E,R) = 0$ for $R < 0$.

Methods for reconstructing profiles from moments will be discussed below. Direct analytical solutions of the fundamental equation (9.6) for a feasible cross section have not been found to the author's knowledge. Numerical solutions have been found, but (9.6), which is very appropriate for generating moments recurrently, is not a good starting point for determining profiles numerically, since there are no initial conditions for $F(E,R)$ at $R = 0$ or elsewhere. An alternative would be Laplace transform according to

$$f(E,s) = \int_0^\infty \mathrm{d}R\,\mathrm{e}^{-sR}F(E,R)\,. \tag{9.25}$$

Here,

$$f(E,0) = 1 \tag{9.26}$$

according to (9.7) can serve as an initial condition.

An alternative is a numerical solution of the forward Boltzmann equation, (9.106), Vol. 1. In the present notation this reads

$$\frac{\partial F(E,R)}{\partial R} = N\int \mathrm{d}T\left[-K(E,T)\,F(E,R) + K(E+T)F(E+T,R)\right], \tag{9.27}$$

where $F(E, R)$ is the energy distribution at pathlength R. This defines an initial condition for

$$F(E, 0) = F_0(E)\,, \tag{9.28}$$

where $F_0(E)$ may be taken to be a narrow, e.g. gaussian profile. $F(E, R)$ can then be determined iteratively in suitable steps δR.

9.2.5 Input

According to (8.16), the energy loss in an individual collision event may be represented in the form

$$T = T_e + T_n + T_x\,, \tag{9.29}$$

where T_e is the electronic energy loss, T_n the energy loss in the absence of electronic processes, and T_x an interference term that is usually neglected. If so, we find the usual expression,

$$S(E) \simeq S_e(E) + S_n(E) \tag{9.30}$$

for the stopping cross section, while the straggling parameter,

$$W(E) = \int T^2 \mathrm{d}\sigma(E, T) = W_{ee} + 2W_{en} + W_{nn} \tag{9.31}$$

contains a mixed term,

$$W_{en} = \int \mathrm{d}\sigma(E, T)\, T_e T_n \tag{9.32}$$

or, in terms of an impact-parameter dependence,

$$W_{en} = \int 2\pi p\, dp\, T_e(p) T_n(p)\,, \tag{9.33}$$

If T_x is not negligible, up to three additional terms enter (9.31).

In the LSS theory (Lindhard et al., 1963b), which addresses low-energy heavy ions, only nuclear straggling as expressed by W_{nn} is taken into account. At high energies, where nuclear stopping is insignificant, only W_{ee} is usually considered. Evidently, W_{en} must be important in some transition regime.

9.2.6 Scaling Properties

Scaling properties for nuclear stopping have been introduced in Sect. 6.4.1. With a dimensionless variable ρ for the pathlength R we have

$$\epsilon = \frac{M_2 E a}{(M_1 + M_2) Z_1 Z_2 e^2}; \qquad \rho = N\pi a^2 \gamma R \tag{9.34}$$

for screened-Coulomb interaction and a screening radius a, where

$$\gamma = 4M_1M_2/(M_1 + M_2)^2 \,. \tag{9.35}$$

We may now write the total pathlength in terms of dimensionless variables in the form

$$\rho(\epsilon) = \int_0^\epsilon \frac{\mathrm{d}\epsilon'}{s_n(\epsilon') + s_e(\epsilon')} \,, \tag{9.36}$$

if the interference term discussed above can be omitted. In the absence of electronic stopping, this is a universal formula for all projectile and target atoms within the range of validity of a universal screening function such as Thomas-Fermi screening or exponential (Bohr) screening.

If electronic stopping cannot be neglected, universality gets lost, since

$$s_e(\epsilon) = \left(\frac{\mathrm{d}\epsilon}{\mathrm{d}\rho}\right)_e = \frac{\epsilon}{E}\frac{R}{\rho}\left(\frac{\mathrm{d}E}{\mathrm{d}R}\right)_e \,. \tag{9.37}$$

If we adopt the Lindhard-Scharff formula (8.73) for S_e, this reads

$$s_e(\epsilon) = k\epsilon^{1/2} \tag{9.38}$$

with

$$\begin{aligned} k &= \xi_e \left(\frac{2(M_1 + M_2)}{0.8853M_1}\right)^{3/2} \left(\frac{Z_1Z_2m}{ZM_2}\right)^{1/2} \\ &= 0.0795\xi_e \frac{(A_1 + A_2)^{3/2}}{A_1^{3/2}A_2^{1/2}} \left(\frac{Z_1Z_2}{Z}\right)^{1/2} \end{aligned} \tag{9.39}$$

with $Z^{2/3} = Z_1^{2/3} + Z_2^{2/3}$ in accordance[2] with Lindhard et al. (1963b). For rough orientation we may write $A_1 \simeq 2Z_1$ and $A_2 \simeq 2Z_2$, so that

$$k \sim 0.056\xi_e \frac{(Z_1 + Z_2)^{3/2}}{Z_1\left(Z_1^{2/3} + Z_2^{2/3}\right)^{3/4}} \,. \tag{9.40}$$

Figure 9.3 shows that k increases monotonically as a function of Z_2/Z_1, indicating that the relative importance of electronic stopping increases as Z_1 decreases.

Figure 9.4 shows plots of dimensionless pathlengths versus dimensionless energy for various screened-Coulomb potentials. Evidently, the difference between the Bohr potential—which has the lowest stopping cross section and hence the highest range—and the Thomas-Fermi potential in the other extreme is small at high energies but increases with decreasing energy and reaches almost two orders of magnitude at $\epsilon = 0.001$.

[2] Lindhard et al. (1963b) report a value 0.0793 for the numerical constant. Note that the definition of the atomic mass unit has changed since 1963.

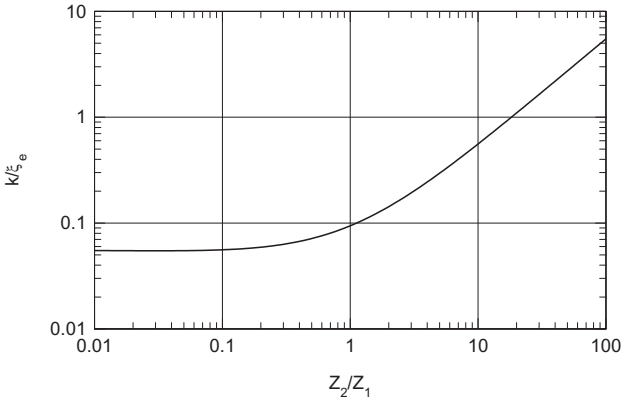

Fig. 9.3 Approximate behavior of the electronic-stopping constant k vs. Z_2/Z_1 according to (9.40)

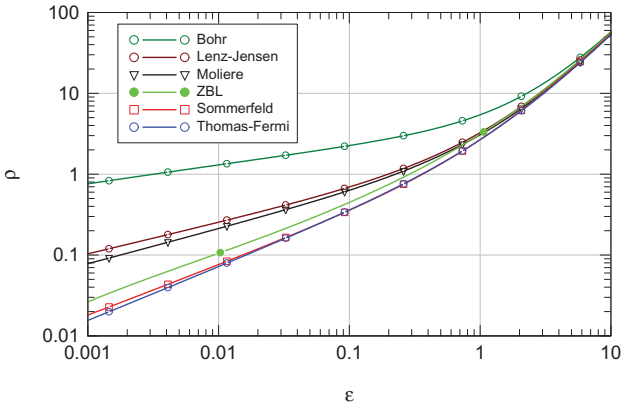

Fig. 9.4 Total pathlength based solely on nuclear stopping. Calculated from (9.36) for $s_e = 0$, employing nuclear stopping cross sections from Fig. 6.22

Figure 9.5, reconstructed after two similar graphs by Lindhard et al. (1963b), shows what happens when electronic stopping is included. The upper graph shows the range of low energies, $\epsilon \leq 1$. The difference between solid and dashed curves indicates the influence of electronic stopping, characterized by values of the constant k specified in (9.39). As you may expect, that difference gets smaller as k increases. Dotted lines show that ranges would be drastically overestimated if nuclear stopping were neglected.

The lower graph in Fig. 9.5 shows the high-energy behaviour for $\epsilon \geq 1$. Here the solid lines approach the dotted lines representing solely electronic stopping. You may note that this approach is quite slow, in particular for low values of k. Conversely, the difference between Thomas-Fermi and Lenz-Jensen nuclear stopping is barely visible.

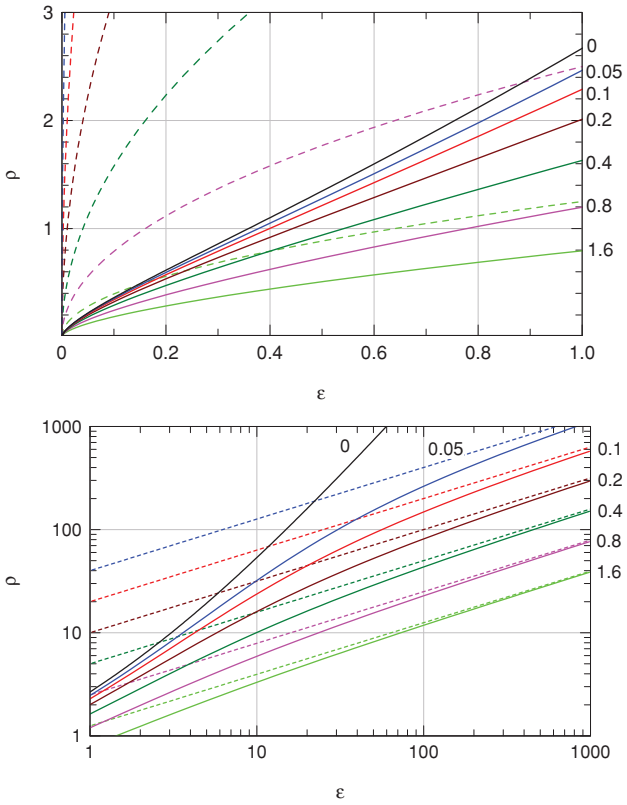

Fig. 9.5 Same as Fig. 9.4 for Thomas-Fermi nuclear stopping including Lindhard-Scharff electronic stopping (solid lines). Lenz-Jensen curves would be barely distinguishable on the scale of the graphs. Dotted lines: electronic stopping only. Numbers on the right axes indicate the factor k in the electronic-stopping formula as specified in (9.39)

Lindhard et al. (1963b) evaluated straggling in dimensionless units following (9.2). Figure 9.6 shows the energy dependence of pathlength straggling for a number of values of the parameter k determining the contribution of electronic stopping. It is seen that relative straggling depends only weakly on the beam energy in the regime of dominating nuclear stopping ($\epsilon \lesssim 1$), while there is a sharp drop-off at higher energies. You may look at Problem 9.3 to study the behaviour at higher energies.

9.2.7 Power Cross Section

Lindhard et al. (1963b) pointed out that exact solutions of the range equation can be found for power scattering, if electronic stopping is neglected. Write the cross

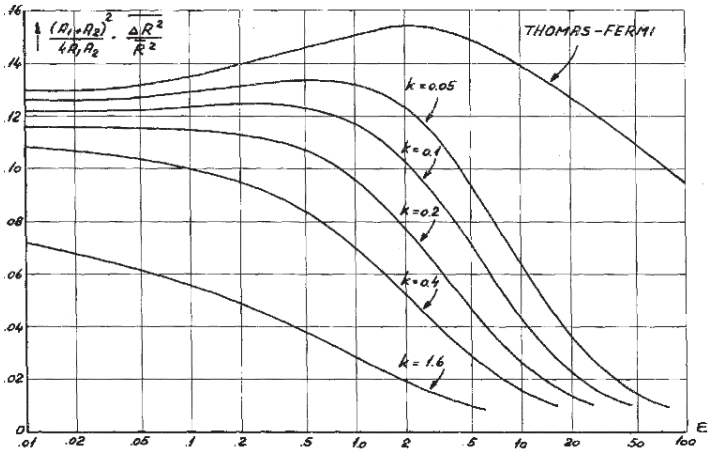

Fig. 9.6 Relative straggling of pathlength according to (9.2), based on nuclear and (Lindhard-Scharff) electronic stopping. Electronic straggling ignored. From Lindhard et al. (1963b)

section (6.89) in the form

$$\mathrm{d}\sigma(E,T) = CE^{-2m}\frac{\mathrm{d}t}{t^{1+m}}; \qquad 0 \le t \le \gamma \tag{9.41}$$

with $t = T/E$ and set

$$M^{(n)} = A_n\left(\frac{E^{2m}}{NC}\right)^n \tag{9.42}$$

with an unknown function $A_n = A_n(E)$. Then (9.11) reduces to

$$nA_{n-1} = A_n\int_0^\gamma \frac{\mathrm{d}t}{t^{1+m}}\left[1-(1-t)^{2mn}\right]. \tag{9.43}$$

Since $A_0 = 1$, it is seen that A_n is independent of E for all n, and that these coefficients can be determined recursively, starting from $n = 1$. A straightforward way to carry out the integral on the right-hand side involves partial integration with the purpose to remove the divergence at $t = 0$. This yields

$$nA_{n-1} = A_n\left[-\frac{1}{m}\gamma^{-m}\left(1-(1-\gamma)^{2mn}\right)+2nB_\gamma(1-m,2mn)\right], \tag{9.44}$$

where

$$B_\gamma(x,y) = \int_0^\gamma \mathrm{d}t\, t^{x-1}(1-t)^{y-1} \tag{9.45}$$

is the incomplete Beta function (Abramowitz and Stegun, 1964). Alternatively, assume for a moment that $m < 0$. This allows direct integration, so that

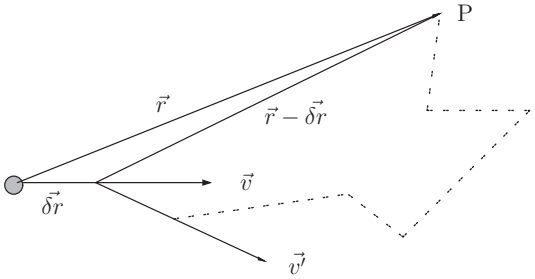

Fig. 9.7 Derivation of (9.49) for the vector-range profile. See text

$$nA_{n-1} = A_n \left[-\frac{1}{m}\gamma^{-m} - B_\gamma(-m, 1+2mn) \right] . \tag{9.46}$$

Since the term on the right-hand side remains regular at $m = 0$, analytical continuation into the regime of positive values of m is justified. You can easily verify from recursion formulae (Abramowitz and Stegun, 1964) that the two forms, (9.44) and (9.46), represent the same function.

9.3 Projected and Lateral Range

In the following we shall try to take account of angular deflection during slowing-down. This can conveniently be done by starting at the vector range $F_R(\boldsymbol{v}, \boldsymbol{r})$. The index R will be dropped for clarity in this section.

9.3.1 Integral Equation

Following the procedure outlined in Sect. 9.2.1 we ask for the probability $F(\boldsymbol{v}, \boldsymbol{r})\,\mathrm{d}^3\boldsymbol{r}$ for a projectile with an initial velocity $\boldsymbol{v}$ to end up in a volume element $(\boldsymbol{r}, \mathrm{d}^3\boldsymbol{r})$ surrounding a point P. Figure 9.7 indicates that the projectile travels for a short distance $|\delta\boldsymbol{r}|$ in the direction of $\boldsymbol{v}$. At this point there are two possibilities:

- The particle has undergone a collision and moves on with some velocity $\boldsymbol{v}'$. The probability for this to happen is $N|\delta\boldsymbol{r}|\,\mathrm{d}\sigma(\boldsymbol{v}, \boldsymbol{v}')$. We are now looking for the probability $F(\boldsymbol{v}', \boldsymbol{r} - \delta\boldsymbol{r})\,\mathrm{d}^3\boldsymbol{r}$ for the particle to end up near point P.
- The complementary probability for the projectile not to have undergone a collision is $1 - N|\delta\boldsymbol{r}| \int \mathrm{d}\sigma(\boldsymbol{v}, \boldsymbol{v}')$. In this case we look for the probability $F(\boldsymbol{v}, \boldsymbol{r} - \delta\boldsymbol{r})\,\mathrm{d}^3\boldsymbol{r}$ for the projectile to end up near point P.

This leads to

$$F(\boldsymbol{v},\boldsymbol{r}) = N|\delta\boldsymbol{r}| \int \mathrm{d}\sigma(\boldsymbol{v},\boldsymbol{v}')\, F(\boldsymbol{v}',\boldsymbol{r}-\delta\boldsymbol{r}) + \left[1 - N|\delta\boldsymbol{r}| \int \mathrm{d}\sigma(\boldsymbol{v},\boldsymbol{v}')\right] F(\boldsymbol{v},\boldsymbol{r}-\delta\boldsymbol{r}). \quad (9.47)$$

After expanding

$$F(\boldsymbol{v},\boldsymbol{r}-\delta\boldsymbol{r}) \simeq F(\boldsymbol{v},\boldsymbol{r}) - \delta\boldsymbol{r}\cdot\boldsymbol{\nabla}_{\boldsymbol{r}} F(\boldsymbol{v},\boldsymbol{r}) \quad (9.48)$$

the terms of zero order in $\delta\boldsymbol{r}$ drop out, and the terms of first order read

$$-\delta\boldsymbol{r}\cdot\boldsymbol{\nabla}_{\boldsymbol{r}} F(\boldsymbol{v},\boldsymbol{r}) = N|\delta\boldsymbol{r}| \int \mathrm{d}\sigma(\boldsymbol{v},\boldsymbol{v}') \left[F(\boldsymbol{v},\boldsymbol{r}) - F(\boldsymbol{v}',\boldsymbol{r})\right]. \quad (9.49)$$

With the unit vector

$$\boldsymbol{e} = \frac{\delta\boldsymbol{r}}{|\delta\boldsymbol{r}|} = \frac{\boldsymbol{v}}{|\boldsymbol{v}|} \quad (9.50)$$

this reads, finally,

$$-\boldsymbol{e}\cdot\boldsymbol{\nabla}_{\boldsymbol{r}} F(\boldsymbol{v},\boldsymbol{r}) = N \int \mathrm{d}\sigma(\boldsymbol{v},\boldsymbol{v}') \left[F(\boldsymbol{v},\boldsymbol{r}) - F(\boldsymbol{v}',\boldsymbol{r})\right]. \quad (9.51)$$

To connect this to the description involving a differential cross section expressed in terms of energy transfer it is convenient to replace velocities by energies. We may then write

$$-\boldsymbol{e}\cdot\boldsymbol{\nabla}_{\boldsymbol{r}} F(E,\boldsymbol{e},\boldsymbol{r}) = N \int \mathrm{d}\sigma(E,\boldsymbol{e},T,\boldsymbol{e}') \left[F(E,\boldsymbol{e},\boldsymbol{r}) - F(E-T,\boldsymbol{e}',\boldsymbol{r})\right]. \quad (9.52)$$

This is again a linear homogeneous integro-differential equation. In order to find a unique solution we need to impose a normalization condition,

$$\int \mathrm{d}^3\boldsymbol{r}\; F(\boldsymbol{v},\boldsymbol{r}) = \int \mathrm{d}^3\boldsymbol{r}\; F(E,\boldsymbol{e},\boldsymbol{r}) = 1\,. \quad (9.53)$$

9.3.2 Range Parameters

Figure 9.8 shows range parameters according to Lindhard et al. (1963b),

- The vector range $\boldsymbol{R}$ points from the origin to the end of a given trajectory,
- The projected range R_p represents the projection of $\boldsymbol{R}$ on the initial direction of motion,
- The lateral range $R_\perp$ represents the distance from the end point to the initial direction of motion,

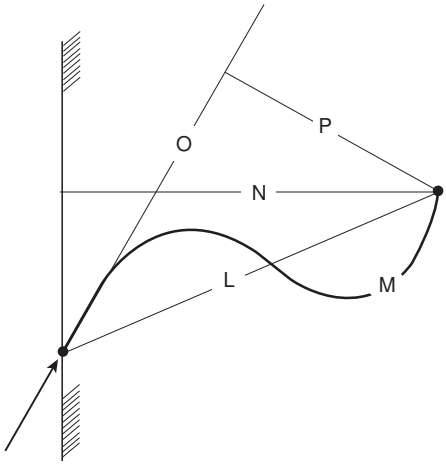

Fig. 9.8 Range concepts according to Lindhard et al. (1963b). See text. Figure from Sigmund (2004)

- The chord range $R_c = |\boldsymbol{R}| = \sqrt{R_p^2 + R_\perp^2}$ is the straight distance between the starting point and the end point of the trajectory,
- The penetration depth x represents the projection of $\boldsymbol{R}$ on a chosen direction, typically the surface normal of a target exposed to a beam incident at some angle, and
- The pathlength R represents the length of the trajectory.

All these quantities obey the laws of statistics and can be quantified by distribution functions that are related to each other. Most important in practical applications are the penetration depth and the lateral range. We shall look into these quantities separately and subsequently derive a relation between them.

9.3.3 Input

Evaluation of (9.52) requires a model for the differential cross section. The widely adopted model proposed by Lindhard et al. (1963b) has four ingredients,

1. Electronic and nuclear processes are decoupled,
2. Angular deflection in electronic processes is ignored,
3. Straggling in electronic energy loss is likewise ignored,
4. Electronic energy loss is taken to be proportional to the projectile speed.

The first two assumptions, although not rigorously valid, are consistent with what we have learned about quasielastic collisions in Chaps. 6–8. The third assumption is well justified at low beam energy but deserves attention in the high-energy range. The fourth assumption can easily be dropped to the extent that better input might be available.

If electronic energy loss is accounted for via its dependence on impact parameter, all these assumptions are much less restrictive than in the original formulation.

Going over for a moment to an impact-parameter representation we may write (9.52) in the form

$$-\boldsymbol{e}\cdot\boldsymbol{\nabla}_{\boldsymbol{r}}F(E,\boldsymbol{e},\boldsymbol{r}) = N\int \mathrm{d}^2\boldsymbol{p}\left[F(E,\boldsymbol{e},\boldsymbol{r}) - F(E-T_n(\boldsymbol{p})-T_e(\boldsymbol{p}),\boldsymbol{e}'(\boldsymbol{p}),\boldsymbol{r})\right], \quad (9.54)$$

where $T_n(\boldsymbol{p})$ and $T_e(\boldsymbol{p})$ represent nuclear and electronic energy loss, respectively. If we adopt the first assumption above, the scattered direction $\boldsymbol{e}'$ is unrelated to electronic processes. If electronic energy loss may be taken small compared to $E - T_n$, we may write

$$F(E-T_n(\boldsymbol{p})-T_e(\boldsymbol{p}),\boldsymbol{e}',\boldsymbol{r}) \simeq F(E-T_n(\boldsymbol{p}),\boldsymbol{e}',\boldsymbol{r}) - T_e(\boldsymbol{p})\frac{\partial}{\partial E}F(E-T_n(\boldsymbol{p}),\boldsymbol{e}',\boldsymbol{r}) + \frac{1}{2}T_e^2(\boldsymbol{p})\frac{\partial^2}{\partial E^2}F(E-T_n(\boldsymbol{p}),\boldsymbol{e}',\boldsymbol{r}). \quad (9.55)$$

If we neglect the coupling between electronic and nuclear energy loss, in accordance with the first assumption above, we may set $T_n = 0$ in the terms proportional to T_e and T_e^2,

$$F(E-T_n(\boldsymbol{p})-T_e(\boldsymbol{p}),\boldsymbol{e}',\boldsymbol{r}) \simeq F(E-T_n(\boldsymbol{p}),\boldsymbol{e}',\boldsymbol{r}) - T_e(\boldsymbol{p})\frac{\partial}{\partial E}F(E,\boldsymbol{e}',\boldsymbol{r}) + \frac{1}{2}T_e^2(\boldsymbol{p})\frac{\partial^2}{\partial E^2}F(E,\boldsymbol{e}',\boldsymbol{r}) \quad (9.56)$$

or, going back to the notation in terms of cross sections,

$$-\boldsymbol{e}\cdot\boldsymbol{\nabla}_{\boldsymbol{r}}F(E,\boldsymbol{e},\boldsymbol{r}) = N\int \mathrm{d}\sigma_n(E,T)\left[F(E,\boldsymbol{e},\boldsymbol{r}) - F(E-T,\boldsymbol{e}',\boldsymbol{r})\right] + NS_e(E)\frac{\partial}{\partial E}F(E,\boldsymbol{e},\boldsymbol{r}) - \frac{1}{2}NW_e(E)\frac{\partial^2}{\partial E^2}F(E,\boldsymbol{e},\boldsymbol{r}), \quad (9.57)$$

where S_e and W_e are the electronic stopping cross section and straggling parameter, respectively, and the differential cross section has reduced to the cross section for nuclear elastic scattering.

Equation (9.57) reduces to the LSS model if W_e is ignored[3].

[3] Including W_e at low velocity would not be meaningful: If a correction to nuclear straggling were necessary in the regime of dominating nuclear stopping, the first such correction would have to be a coupling term between T_n and T_e. However, at high energies, where electronic straggling dominates, (9.57) may become useful since it incorporates angular deflection by nuclear collisions.

9.3.4 Mean Range

Let us first have a look at mean ranges. We deal with slowing-down in a homogeneous, isotropic and infinite medium. If we assume cylindrical symmetry of the differential cross section, the mean vector range must point into the direction of the velocity, i.e., it reduces to the projected range, and the lateral component of the vector range must vanish in the average. Thus, after you have repeated the procedure applied to the pathlength in the previous section, (9.57) reduces to

$$1 = NS_e(E)\frac{\mathrm{d}R_p(E)}{\mathrm{d}E} + N\int \mathrm{d}\sigma_n(E,T)\left[R_p(E) - \cos\phi' R_p(E-T)\right], \quad (9.58)$$

where ϕ' is the laboratory scattering angle in a collision characterized by a differential cross section $\mathrm{d}\sigma(E,T)$. The factor $\cos\phi'$ in the second term in the brackets arises from the projection of the vector range $R_p(\boldsymbol{v}')$ on $\boldsymbol{v}$. The connection between $\cos\phi'$ and T for elastic collisions has been derived in Sect. 3.2.1, Vol. 1. In the present notation it reads

$$\cos\phi' = (1-t)^{1/2} + \alpha t(1-t)^{-1/2}, \quad (9.59)$$

where

$$\alpha = \frac{1}{2}\left(1 - \frac{M_2}{M_1}\right); \qquad t = \frac{T}{E}. \quad (9.60)$$

As you may have expected, α becomes substantial for large ratios M_2/M_1.

Once $R_p(E)$ has been found from (9.58), the mean penetration depth will be

$$\langle x\rangle(E) = \cos\theta R_p(E), \quad (9.61)$$

where θ is the angle between the direction of incidence and a given reference axis.

Comparison of (9.58) with (9.12), which you may also write in the form

$$1 = NS_e(E)\frac{\mathrm{d}R(E)}{\mathrm{d}E} + N\int \mathrm{d}\sigma_n(E,T)\left[R(E) - R(E-T)\right], \quad (9.62)$$

shows that the only difference to the mean pathlength is the factor $\cos\phi'$ in the brackets.

Application of (9.16) to (9.58) leads to

$$1 = N\left[S_e(E) + S^{(1)}(E)\right]\frac{\mathrm{d}R_p(E)}{\mathrm{d}E} + N\sigma^{(1)}(E)R_p(E) \quad (9.63)$$

according to Schiøtt (1966), which differs from (9.17) by an additive term containing the transport cross section

$$\sigma^{(1)}(E) = \int \mathrm{d}\sigma_n(E,T)\left[1 - \cos\phi'\right] \quad (9.64)$$

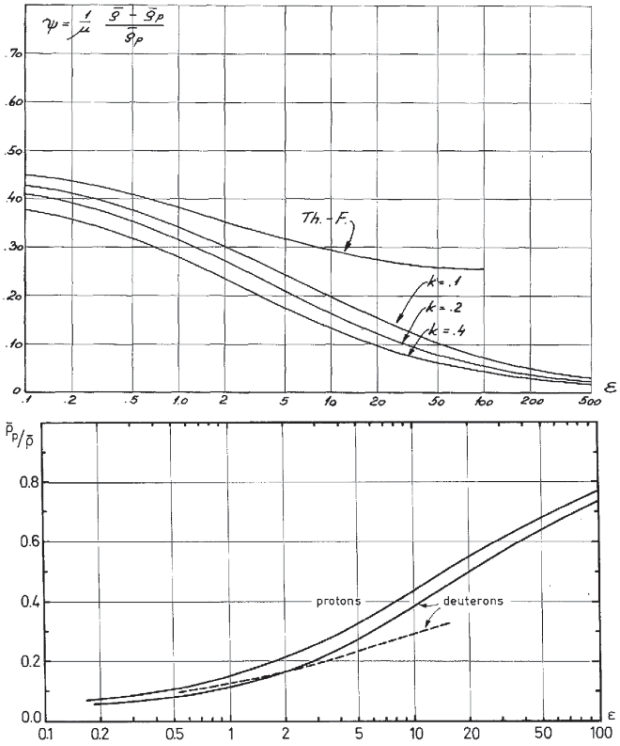

Fig. 9.9 Projected-range corrections according to Lindhard et al. (1963b) (upper graph) and Schiøtt (1966) (lower graph)

and the replacement of the stopping cross section by $S_e(E) + S^{(1)}(E)$ with

$$S^{(1)}(E) = \int T \cos\phi' \mathrm{d}\sigma(E, T). \tag{9.65}$$

With the approximation $T \ll E$, $\sigma^{(1)}(E)$ reduces to

$$\sigma^{(1)}(E) \simeq M_2 S_n(E)/(2M_1 E) \tag{9.66}$$

and $S^{(1)}(E) \simeq S_n(E)$. With this, (9.63) reduces to

$$1 = N\,[S_e(E) + S_n(E)]\,\frac{\mathrm{d}R_p(E)}{\mathrm{d}E} + N\,\frac{M_2}{2M_1}\,\frac{S_n(E)}{E}\,R_p(E)\,. \tag{9.67}$$

This equation is easily solvable. The difference from (9.18) increases with increasing mass ratio M_2/M_1. Figure 9.9 shows a couple of useful plots that allow a quick estimate of the importance of a projected-range correction. ρ_p is the projected

range in dimensionless units defined in (9.34). Note in particular the large correction in case of protons or deuterons.

9.3.5 Higher Moments

During the development of ion implantation in the 1960s and 1970s, range profiles were reconstructed from higher moments. Second moments, determining variance or standard deviation were most important, but skewed profiles were found experimentally early on. Thanks to the development of powerful computers—which is not the least due to ion implantation!—Monte Carlo and other simulation techniques nowadays provide a less painful procedure to arrive at reliable penetration profiles.

On the other hand, the mathematical formalism employed in the calculation of higher moments of range profiles, developed originally in the context of neutron diffusion, is distinguished by beauty and power and does not deserve to be abandoned. Much of this goes back to the Manhattan project during World War II. Amongst prominent scientists involved in this development I like to mention E. Fermi, E. Amaldi, H.A. Bethe, R.E. Marshak, G. Placzek and G.C. Wick.

9.3.5.1 Penetration Depth

Consider a monodirectional source of ions in a plane $x = 0$ in an infinite medium and look for the penetration profile $F(E, \boldsymbol{e}, x)$, which can be expressed as

$$F(E, \boldsymbol{e}, x) = \int \mathrm{d}y\, \mathrm{d}z\, F(E, \boldsymbol{e}, \boldsymbol{r})\,. \tag{9.68}$$

Equation (9.57) then reduces to

$$-\cos\theta \frac{\partial F(E, \boldsymbol{e}, x)}{\partial x} = N \int \mathrm{d}\sigma_n(E, T) \left[F(E, \boldsymbol{e}, x) - F(E - T, \boldsymbol{e}', x)\right] + N S_e(E) \frac{\partial F(E, \boldsymbol{e}, x)}{\partial E} - \frac{1}{2} N W_e(E) \frac{\partial^2 F(E, \boldsymbol{e}, x)}{\partial E^2}, \tag{9.69}$$

where θ is the angle between $\boldsymbol{e}$ and the x-axis[4].

A convenient way of attacking this type of equations was introduced by Wick (1949). You may first convince yourself, either by a physical argument or by looking at (9.69), that $F(E, \boldsymbol{e}, x)$ cannot depend on the azimuth of $\boldsymbol{e}$. We may decouple the angular and energy dependence by writing

$$F(E, \boldsymbol{e}, x) \equiv F(E, \cos\theta, x) = \sum_{\ell=0}^{\infty} (2\ell + 1) F_\ell(E, x) P_\ell(\eta)\,, \tag{9.70}$$

[4] Remember, however, the footnote 3 on page 433.

where $\eta = \cos\theta$ and $P_\ell(\eta)$ are Legendre polynomials discussed in Appendix A.2.3, Vol. 1.

With this, the term on the left-hand side of (9.69) reads

$$-\eta\frac{\partial F(E,\eta,x)}{\partial x} = -\sum_\ell \left[(\ell+1)P_{\ell+1}(\eta) + \ell P_{\ell-1}(\eta)\right]\frac{\partial F_\ell(E,x)}{\partial x}$$
$$\equiv -\sum_\ell \left[\ell\frac{\partial F_{\ell-1}(E,x)}{\partial x} + (\ell+1)\frac{\partial F_{\ell+1}(E,x)}{\partial x}\right] P_\ell(\eta) \quad (9.71)$$

by means of the recursion formula, (A.59), Vol. 1, and renumbering summation indices.

Amongst the terms on the right-hand side of (9.69) only the one involving the scattered ion needs special attention. Note first that the scattering angle ϕ' can be expressed as

$$\cos\phi' = \boldsymbol{e}\cdot\boldsymbol{e}'\,. \quad (9.72)$$

Next, the triple-differential cross section $\mathrm{d}\sigma$ can be written as (Holmes and Leibfried, 1960)

$$\mathrm{d}\sigma = \mathrm{d}\sigma(E,\boldsymbol{e},T,\boldsymbol{e}') = \mathrm{d}\sigma(T)\,\frac{\mathrm{d}^2\boldsymbol{e}'}{2\pi}\delta\left(\boldsymbol{e}\cdot\boldsymbol{e}' - \cos\phi'\right) \quad (9.73)$$

where the Dirac function expresses the connection between scattering angle and energy loss for elastic collisions, (9.59). See also Problem 9.4.

Now, according to (A.57), Vol. 1, you may write

$$\delta\left(\boldsymbol{e}\cdot\boldsymbol{e}' - \cos\phi'\right) = \sum_{\ell=0}^{\infty}\left(\ell+\frac{1}{2}\right)P_\ell(\boldsymbol{e}\cdot\boldsymbol{e}')P_\ell(\cos\phi') \quad (9.74)$$

and, according to (A.58), Vol. 1,

$$P_\ell(\boldsymbol{e}\cdot\boldsymbol{e}') = \frac{4\pi}{2\ell+1}\sum_{\mu=-\ell}^{\ell} Y^\star_{\ell\mu}(\boldsymbol{e}')Y_{\ell\mu}(\boldsymbol{e})\,, \quad (9.75)$$

where $Y_{\ell\mu}(\boldsymbol{e})$ are spherical harmonics with

$$Y_{\ell 0}(\boldsymbol{e}) = \sqrt{\frac{2\ell+1}{4\pi}}\,P_\ell(\eta)\,. \quad (9.76)$$

I shall leave it to you to collect the parts in Problem 9.5, you will take benefit from Appendix A.2.3, Vol. 1. You will arrive at

$$
\begin{aligned}
&-\ell\frac{\partial}{\partial x}F_{\ell-1}(E,x)-(\ell+1)\frac{\partial}{\partial x}F_{\ell+1}(E,x)\\
&\quad=(2\ell+1)N\left\{\int \mathrm{d}\sigma_n(E,T)\big[F_\ell(E,x)-P_\ell(\cos\phi')F_\ell(E-T,x)\big]\right.\\
&\qquad\left.+S_e(E)\frac{\partial F_\ell(E,x)}{\partial E}-\frac{1}{2}W_e(E)\frac{\partial^2 F_\ell(E,x)}{\partial E^2}\right\}. \qquad (9.77)
\end{aligned}
$$

Now, the normalization condition

$$
\int_{-\infty}^{\infty}\mathrm{d}x\; F(E,\eta,x)=1 \qquad (9.78)
$$

reduces to

$$
\int_{-\infty}^{\infty}\mathrm{d}x\; F_\ell(E,x)=\delta_{\ell 0}\,. \qquad (9.79)
$$

Defining moments, reminding that we deal with an infinite medium,

$$
M_\ell^n(E)=\int_{-\infty}^{\infty}\mathrm{d}x\; x^n F_\ell(E,x)\,, \qquad (9.80)
$$

we finally arrive at

$$
\begin{aligned}
&n\left[\ell M_{\ell-1}^{n-1}(E)+(\ell+1)M_{\ell+1}^{n-1}(E)\right]\\
&\quad=(2\ell+1)N\left\{\int \mathrm{d}\sigma_n(E,T)\big[M_\ell^n(E)-P_\ell(\cos\phi')M_\ell^n(E-T)\big]\right.\\
&\qquad\left.+S_e(E)\frac{dM_\ell^n(E)}{dE}-\frac{1}{2}W_e(E)\frac{d^2M_\ell^n(E)}{dE^2}\right\}. \qquad (9.81)
\end{aligned}
$$

This relation, together with (9.79) which now reads

$$
M_\ell^0(E)=\delta_{\ell 0}\,, \qquad (9.82)
$$

allows to determine all moments $M_\ell^n(E)$ recursively, starting from $n=0$.

9.3.5.2 Projected and Lateral Range

Higher-order averages of range profiles were calculated by Leibfried (1963) and Baroody (1964) assuming hard-sphere scattering for the elastic interaction. More general equations were established, and solved for elastic power-law scattering, by Sanders (1968a,b) and Winterbon et al. (1970).

Let us first have a look at the relation between the penetration depth and the projected range as well as the lateral range. Figure 9.10 shows the situation in the plane $z=0$. For a given trajectory, the coordinates of the end point P are (x, y) in a reference frame oriented along the x-axis. In a coordinate frame oriented along the

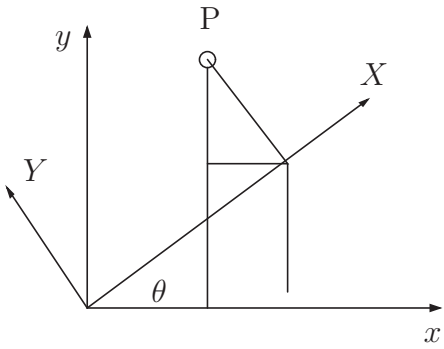

Fig. 9.10 Relation between penetration depth, projected range and lateral range. See text

initial velocity, the coordinates are (X, Y). These coordinates are related as

$$x = X\cos\theta - Y\sin\theta \tag{9.83}$$

$$y = X\sin\theta + Y\cos\theta, \tag{9.84}$$

see Fig. 9.10. From $\langle Y\rangle = 0$ we find

$$\langle x\rangle = \langle X\rangle\cos\theta = F_0^1 + 3M_1^1(E)P_1(\eta) \tag{9.85}$$

or

$$\langle X\rangle = 3M_1^1(E)\,, \tag{9.86}$$

whereas $F_0^1 = 0$. From

$$\begin{aligned}\langle x^2\rangle &= \langle X^2\rangle\cos^2\theta + \langle Y^2\rangle\sin^2\theta \\ &= M_0^2(E) + 3M_1^2(E)P_1(\eta) + 5M_2^2(E)P_2(E)\end{aligned} \tag{9.87}$$

you find

$$\langle X^2\rangle = \langle R_p^2\rangle = M_0^2(E) + M_2^2(E) \tag{9.88}$$

$$\langle Y^2\rangle = M_0^2(E) - \frac{1}{2}M_2^2(E) \tag{9.89}$$

or

$$\langle \Delta R_p^2\rangle = M_0^2(E) + M_2^2(E) - \left[3M_1^1(E)\right]^2 \tag{9.90}$$

$$\langle R_\perp^2\rangle = 2\langle Y^2\rangle = 2M_0^2(E) - M_2^2(E). \tag{9.91}$$

Relations between higher moments can be derived similarly.

9.3.5.3 Scaling Properties

Scaling properties can conveniently be studied on the example of power cross section

$$\mathrm{d}\sigma(E,T) = CE^{-m}\frac{\mathrm{d}T}{T^{1+m}} \quad \text{for } 0 < T \le \gamma E \tag{9.92}$$

found in (6.89). If you ignore electronic stopping, (9.81) reduces to

$$M_\ell^n = A_\ell^n \left(\frac{E^{2m}}{NC}\right)^n \tag{9.93}$$

with coefficients A_ℓ^n determined by

$$n\left(\ell A_{\ell-1}^{n-1} + (\ell+1)A_{\ell+1}^{n-1}\right) = (2\ell+1)A_\ell^n \int_0^\gamma \frac{\mathrm{d}t}{t^{1+m}}\left[1 - P_\ell(\cos\phi')(1-t)^{2mn}\right]. \tag{9.94}$$

Equationm (9.93) shows that within the range of validity of elastic nuclear scattering and power scattering, relative quantities such as the ratio between second moments and the square of the first moment become independent of the energy.

On the other hand, for $M_2/M_1 \neq 1$ such ratios depend on the masses involved, and this dependence enters both through the mass transfer factor $\gamma = 4M_1M_2/(M_1+M_2)^2$ and the scattering angle $\cos\phi'$ given by (9.59).

Figure 9.11 (lower part), showing the projected-range correction factor $\langle X\rangle/R$ as a function of the mass ratio M_2/M_1, confirms what we have already seen in Fig. 9.9: M_2/M_1 can become quite large, indicating that the trajectory of a light ion in a heavy target is very much diffusion-like. That conclusion is even more evident from the data for straggling: While relative straggling is small for $M_2/M_1 \ll 1$, mainly because γ is small, it becomes large for $M_2/M_1 \gg 1$ *despite* γ being small. Note in particular that $\langle \Delta X^2\rangle$ and $\langle Y^2\rangle$ approach each other, indicating that the penetration profile approaches a spherical shape centered around the mean projected range.

Figures 9.12 and 9.13 show third- and fourth-order averages. Here, the *skewness* of a distribution (Feller, 1966) is defined as

$$\frac{\left\langle (X - \langle X\rangle)^3\right\rangle}{\langle (X-\langle X\rangle)^2\rangle^{3/2}}, \tag{9.95}$$

and the *kurtosis* is

$$\frac{\left\langle (X - \langle X\rangle)^4\right\rangle}{\langle (X-\langle X\rangle)^2\rangle^{2}}. \tag{9.96}$$

The analysis of these graphs is left to Problems 9.6 and 9.7.

A more general screened-Coulomb cross section can be modelled approximately by a power cross section with an exponent m dependent on energy. If electronic energy loss is allowed for, the constant k in the LSS description will enter, or an equivalent parameter characterizing the electronic stopping cross section in Lindhard-

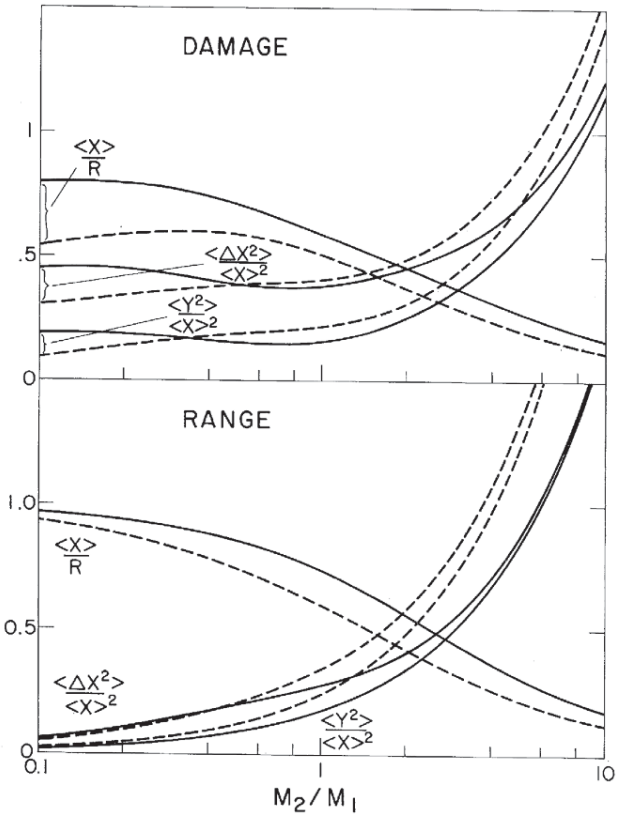

Fig. 9.11 Lower part: Projected-range correction factor and relative range straggling for power-law scattering and neglecting electronic stopping, as well as longitudinal and lateral straggling versus target/ion mass ratio M_2/M_1. Power exponent $m = 1/2$ (solid line) and 1/3 (dashed line). Upper graph: Same for deposited energy to be discussed in Sect. 9.4. From Winterbon et al. (1970)

Scharff units. With this number of parameters, the value of scaling relations becomes questionable, considering that there are basically only three parameters, i.e., Z_1, Z_2 and the beam energy E.

9.3.6 Charge Exchange

We have seen in Chap. 5 that charge exchange may contribute to energy-loss straggling. When this contribution is significant, it will also affect range straggling. Most often it will be adequate to include this as an additional contribution to straggling in the formalism discussed up till now. This assumes that the ion beam is in charge equilibrium over most of the trajectory. When that assumption is not satisfied, it may

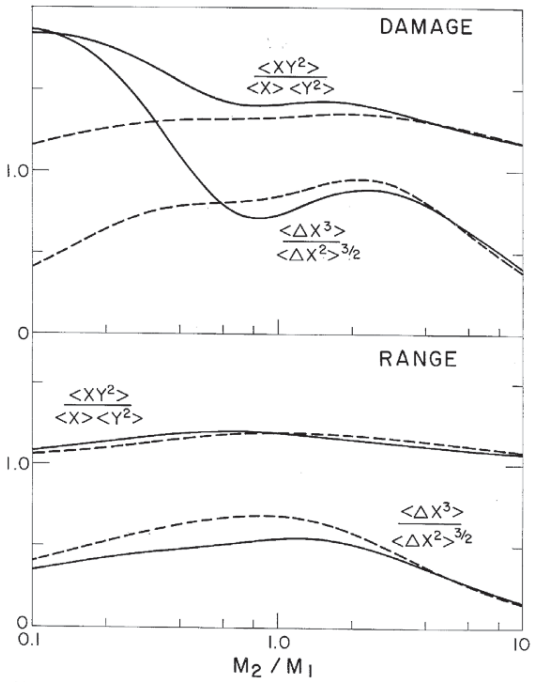

Fig. 9.12 Same as Fig. 9.11 for third-order moments. From Winterbon et al. (1970)

be appropriate instead to solve the transport problem with due account for charge-dependent stopping.

Pertinent integral equations were established in backward and forward form by Burenkov et al. (1992b). We shall here just look at the pathlength equation. Generalization to the vector range is straightforward.

With the notation for charge states introduced in Chap. 3 we may define a range profile $F_J(E, R)\,\mathrm{d}R$ as the probability for an ion with an energy E in a charge state J to come to rest after a pathlength $(R, \mathrm{d}R)$. Following the procedure leading to (9.4) we may write

$$F_J(E,R) = N\delta R \sum_K \int \mathrm{d}\sigma_{JK}(E,T) F_K(E-T, R-\delta R) + \left[1 - N\delta R \sum_K \int \mathrm{d}\sigma_{JK}(E,T)\right] F_J(E, R-\delta R) \quad (9.97)$$

and arrive at

$$-\frac{\partial}{\partial R} F_J(E,R) = N \sum_K \int \mathrm{d}\sigma_{JK}(E,T)\big[F_J(E,R) - F_K(E-T,R)\big]. \quad (9.98)$$

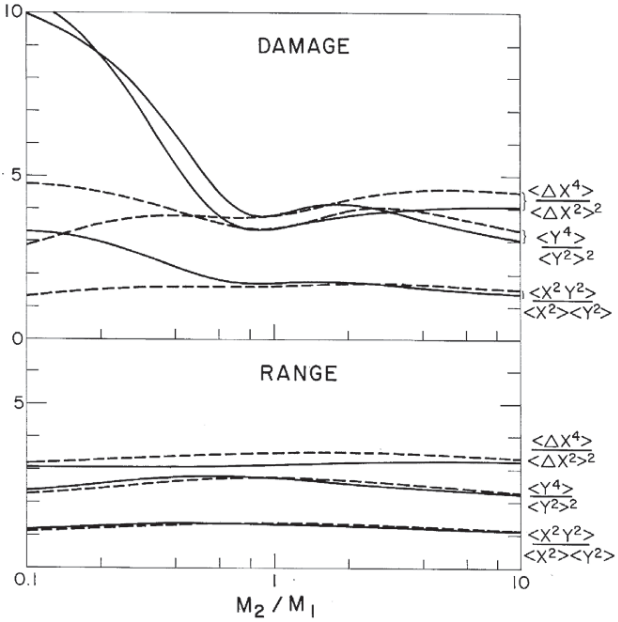

Fig. 9.13 Same as Fig. 9.11 for fourth-order moments. From Winterbon et al. (1970)

We may try to separate the cross section ignoring any interference between nuclear and electronic energy loss as well as charge exchange. This leads to

$$-\frac{\partial}{\partial R}F_J(E,R) = N\int \mathrm{d}\sigma_n(E,T)\big[F_J(E,R)-F_J(E-T,R)\big] + NS_J(E)\frac{\partial}{\partial E}F_J(E,R) - \frac{1}{2}NW_J(E)\frac{\partial^2}{\partial E^2}F_J(E,R) + N\sum_K \sigma_{JK}\big[F_J(E,R)-F_K(E,R)\big]. \quad (9.99)$$

This takes into account the variation of the stopping cross section and the straggling parameter with the charge state. If necessary, *equilibrium* values of mean energy loss and straggling due to charge exchange can be included in S_J and W_J.

Although these equations look very similar to those discussed in Chaps. 3 and 5, finding analytic solutions is much more complex, since the dependence of the cross sections on the beam energy cannot be neglected. Therefore, even the simplest case of a two-state system calls for numerical integration.

Aiming at high-energy ion implantation, Burenkov et al. (1992b) provided numerical solutions under conditions of negligible nuclear stopping, incorporating electronic straggling and ignoring energy loss in charge exchange. In a parallel attack, Burenkov et al. (1992a) provided an equivalent Monte-Carlo solution of the problem. Some caution is indicated with regard to the input: Little information was

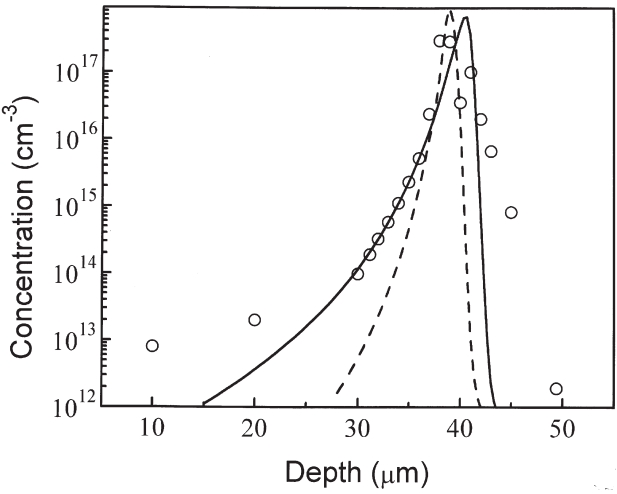

Fig. 9.14 Penetration profile of 100 MeV Al in Si. The influence of charge exchange is shown as the difference between the solid and the stippled line. Circles denote experimental results by Ferla et al. (1993). Profiles normalized to the ion fluence. From Komarov et al. (1999)

available at the time on charge-dependent stopping of heavy ions, i.e., the crucial parameter in that context. An example is shown in Fig. 9.14. For 100 MeV Al in Si, increasing the initial ion charge from 1 to 12 gave rise to a 2% decrease in mean penetration depth but a 12% increase in the width of the profile.

9.4 Deposited Energy

In Fig. 9.2 you have seen the energy-loss function $-\mathrm{d}E/\mathrm{d}x$ plotted as a function of the travelled pathlength. This is a qualitative measure of the distribution in depth of radiation effects such as ionization, dissociation and emission of photons. It is a qualitative measure, because the energy lost by electronic stopping may be transferred to high-energy electrons that dissipate their energy away from the point of impact. Energy transport by secondary and higher-generation electrons will thus result in a deposited energy profile which, together with angular deflection of the projectile, will cause more or less significant deviations from curves like the one shown in Fig. 9.2.

Similar effects occur when you make a plot of the nuclear stopping cross section as a function of pathlength: Nuclear energy loss goes into recoil atoms which may generate secondary and higher-order recoils and thus result in a recoil cascade, as mentioned in Sect. 1.1.2, Vol. 1.

Moreover, electrons and atoms experience both electronic and nuclear stopping, so cascades of electrons and recoil atoms must be coupled. This implies that not only the depth distribution shown in Fig. 9.2 is oversimplified: The normalization

to the total energy E will actually be an overestimate, since part of the energy will have been absorbed by recoil atoms.

Just as in the first part of this chapter, loss of electrons and nuclei through a target surface is ignored, since we deal with an infinite medium.

Here the concept of deposited energy enters as a central aspect in the theory of radiation effects. Energy is said to be deposited when it is no longer transferred to other particles by collision processes. A precise definition of the concept requires a distinction between collision processes and other types of energy transport or, preferably, reference to some measurable effect such as the amount of ionization or structural damage created in the medium.

The presentation below relies heavily on a pioneering study by Lindhard et al. (1963a).

9.4.1 Nuclear and Electronic Processes

According to Lindhard et al. (1963a) the energy of an atom with an initial energy E may be deposited amongst the nuclei of a medium, $\nu(E)$, and amongst the electrons in the medium, $\eta(E)$, so that

$$\nu(E) + \eta(E) = E\,. \tag{9.100}$$

In a polyatomic medium one may split $\nu(E)$ into contributions $\nu_j(E)$, $j = 1, 2\ldots$ for the species present in the medium. The fact that energy is considered conserved in (9.100) implies that deposited energy includes both kinetic and potential energy or, in other words, that all binding energies enter the balance.

9.4.2 Zero-Order Moments

9.4.2.1 Integral Equations

Consider an infinite homogeneous monoatomic medium, and let one of the atoms receive an energy E. This atom will dissipate its energy in interactions with the constituents of the target. As a result there will be recoil atoms and liberated electrons which, in turn, collide with the constituents of the medium and generate higher-order generations of recoils and liberated electrons. Such recoil and ionization cascades constitute a main topic in the theory of radiation effects to be discussed in Volume 3. The present, preliminary discussion serves to provide a basis for spatial energy-deposition profiles and their relation to range profiles.

In order to determine the average amount of energy $\nu(E)$ spent in nuclear motion, let the primary particle travel a distance δR short enough to let the probability for more than one collision be negligible. Following the procedure outlined in

Sect. 9.2.1 we may then write

$$\nu(E) = N\delta R \int \mathrm{d}\sigma(E, T_n, T_e)\Big[\nu(E - T_n - T_e) + \nu(T_n - U) + \sum_j \nu_e(T_{e,j} - U_j)\Big] + \Big[1 - N\delta R \int \mathrm{d}\sigma(E, T_n, T_e)\Big]\nu(E), \quad (9.101)$$

where $\nu_e(E)$ denotes the ν-function for an electron of energy E and U_j the ionization energy of an electron in the jth target shell. U represents the binding energy of a target atom to its equilibrium site. For a gas target we have $U = 0$.

After dropping all but first-order terms in δR we find

$$\int \mathrm{d}\sigma(E, T_n, T_e)\big[\nu(E) - \nu(E - T_n - T_e) - \nu(T_n - U) - \sum_j \nu_e(T_{e,j} - U_j)\big] = 0\,, \quad (9.102)$$

In their evaluation, Lindhard et al. (1963a) ignored $\sum_j \nu_e(T_{e,j} - U_j)$, although it was mentioned explicitly that there are cases where this is not justified. Following their route, let us drop that term for a moment. With that simplification, (9.102) reduces to a homogenous integral equation, so finding a unique solution requires an additional condition. Lindhard et al. (1963a) set the requirement that

$$\lim_{E\to 0} \nu(E)/E = 1\,. \quad (9.103)$$

This condition is feasible as long as the electronic stopping cross section $S_e(E)$ approaches zero more rapidly than the nuclear stopping cross section $S_n(E)$ at small energies. For the power form discussed in Chap. 6 this implies that $1 - 2m < 1/2$ at low energies or

$$m > 1/4 \quad (9.104)$$

for velocity-proportional electronic stopping. Only two of the cross sections listed in Table 6.61 fall into this category.

For an initial ion (Z_1, M_1) incident on a monoatomic medium (Z_2, M_2), you may introduce a quantity $\nu_{12}(E)$ as the average amount of energy ending up in nuclear motion of target atoms. Repeating the argument above, you arrive at

$$\int \mathrm{d}\sigma_{12}(E, T_n, T_e)\big[\nu_{12}(E) - \nu_{12}(E - T_n - T_e) - \nu_{22}(T_n - U)\big] = 0\,, \quad (9.105)$$

where $\mathrm{d}\sigma_{12}$ denotes the differential cross section for a 1-atom hitting a 2-atom, and $\nu_{22}(E)$ is determined by (9.102) in the form

$$\int \mathrm{d}\sigma_{22}(E, T_n, T_e)\big[\nu_{22}(E) - \nu_{22}(E - T_n - T_e) - \nu_{22}(T_n - U)\big] = 0\,. \quad (9.106)$$

You may note that unlike (9.106), (9.105) is an inhomogeneous equation, the solution of which is defined without a normalization condition, once $\nu_{22}(E)$ has been found from (9.106).

In ignoring the term $-\sum_j \nu_e(T_{e,j} - U_j)$ in (9.102) and subsequent relations we have assumed that energy deposited in electronic motion cannot be transferred from electronic to nuclear motion. There are at least two important cases where this is not justified:

- For high enough incident energies, primary or higher-generation electrons may have sufficient energy to generate recoil atoms.
- Ample evidence has accumulated since the 1970s that electronic processes may cause radiation damage, sputtering and similar processes that are related to nuclear motion at energies where binary collisions are not expected to give rise to these phenomena. One possible mechanism, pointed out already by Lindhard et al. (1963a), is conversion of bonding to antibonding states in covalent media with the result that the involved atoms repel each other. A much more detailed discussion of this point will be reserved to Volume 3.

If the quantity $\nu_e(E)$ is not negligible, it obeys the integral equation

$$\int \mathrm{d}\sigma_{e2}(E, T_n, T_e)\Big[\nu_e(E) - \nu_e(E - T_n - T_e) - \nu_{22}(T_n - U) - \sum_j \nu_e(T_{e,j} - U_j)\Big] = 0. \quad (9.107)$$

Evidently, (9.102) and (9.107) constitute a coupled system of integral equations even for self-bombardment, i.e., $Z_1 = Z_2$, of a monoatomic target material.

Energy deposition by electrons becomes even more important in the complementary quantity $\eta(E)$, the average amount of energy deposited in electronic motion. Especially for swift heavy ions, primary electrons may have larger ranges than the ion. Therefore, energy deposition profiles like the one shown in Fig. 9.2 may be affected substantially by energy transport via primary and secondary electrons.

Integral equations for $\eta(E)$ are, within the present view, identical with (9.102)–(9.107). As an example, the analog of (9.105) is

$$\int \mathrm{d}\sigma_{12}(E, T_n, T_e)\big[\eta_{12}(E) - \eta_{12}(E - T_n - T_e) - \eta_{22}(T_n - U) - \sum_j \eta_{e2}(T_{e,j} - U_j)\big] = 0, \quad (9.108)$$

if the last term in the brackets is not thrown away.

If $\eta_{e2}(E)$ can be ignored, (9.100) and (9.103) lead to

$$\lim_{E \to 0} \frac{\eta(E)}{E} = 0\,. \quad (9.109)$$

If $\eta_{e2}(E)$ is kept, (9.108) is an inhomogeneous equation governed by the analog of (9.107).

9.4.2.2 Solutions

Integral equations of the type discussed in the previous section can be solved step-by-step starting from energy zero on the basis of an initial condition such as (9.103). However, in applications it may be appropriate to apply this type of equations directly to measurable quantities such as the number of defects, inner-shell vacancies or ionizations, for which more specific initial conditions may be constructed from the threshold behaviour of those phenomena. Regardless of the specific threshold behaviour, once it is known, the pertinent integral equation can be solved numerically or, with suitable approximations, analytically.

Finding solutions for specific quantities is a main topic of radiation physics and belongs into Volume 3 of the present series. At this point we shall keep to quantities $\nu(E)$ and $\eta(E)$ and the initial conditions (9.103) and (9.109).

To find an approximate solution of the integral equation (9.102), apply (9.8) to $\nu(E)$, so that[5]

$$[S_n(E) + S_e(E)]\,\frac{\mathrm{d}\nu(E)}{\mathrm{d}E} - \int \mathrm{d}\sigma(E, T_n)\nu(T_n) = 0 \tag{9.110}$$

or

$$\nu(E) = \int_0^E \frac{\mathrm{d}E'}{S_n(E') + S_e(E')} \int \mathrm{d}\sigma(E', T_n)\nu(T_n)\,. \tag{9.111}$$

Approximating further so that

$$\int \mathrm{d}\sigma(E, T_n)\nu(T_n) \simeq \int \mathrm{d}\sigma(E, T_n)\,T_n = S_n(E) \tag{9.112}$$

you arrive at

$$\nu(E) \simeq \int_0^E \mathrm{d}E'\,\frac{S_n(E')}{S_n(E') + S_e(E')} \tag{9.113}$$

as a first approximation for $\nu(E)$.

Figure 9.15 shows an evaluation of (9.113) for power scattering, cf. Problem 9.15. In accordance with (9.104), the case of $m = 0.1$ does not provide a physically acceptable solution.

For $Z_1 \neq Z_2$, the analog of (9.111) is

$$\nu_{12}(E) = \int_0^E \frac{\mathrm{d}E'}{S_{n,12}(E') + S_{e,12}(E')} \int \mathrm{d}\sigma_{12}(E, T_n)\nu_{22}(T_n)\,, \tag{9.114}$$

[5] Indices introduced in $\nu(E)$ or $\eta(E)$ in the previous section will be omitted for clarity, where this is possible.

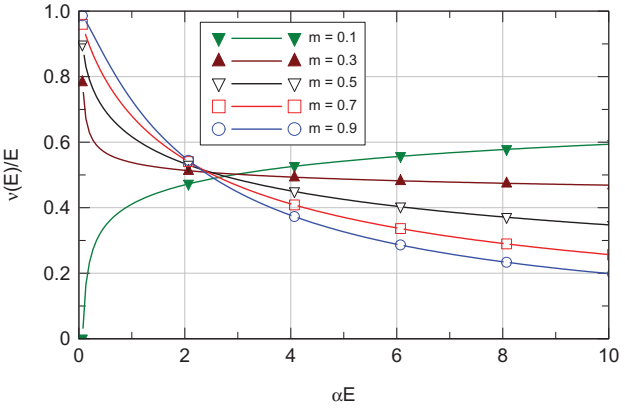

Fig. 9.15 Fraction $\nu(E)/E$ of energy deposited in nuclear motion according to approximate formula (9.113) for power cross section $\mathrm{d}\sigma = CE^{-m}T^{-1-m}\,\mathrm{d}T$ and $S_e = K\sqrt{E}$. The parameter α is defined as $\alpha = [(1-m)K/C]^{1/(2m-1/2)}$

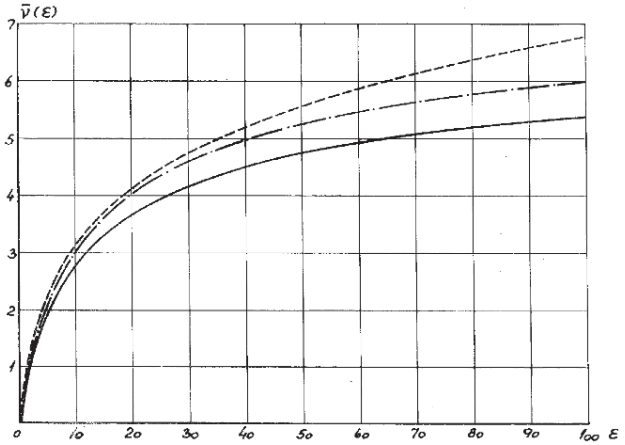

Fig. 9.16 Function $\nu(\epsilon)$ for equal-mass case in dimensionless units. Solid line: Numerical solution of (9.102) ignoring the ν_e-term for Thomas-Fermi scattering and with the electronic-stopping constant $k = 0.15$. The dot-dashed line reflects power scattering for $m = 3/4$. The stippled line is based on (9.113), likewise for power scattering with $m = 3/4$. From Lindhard et al. (1963a)

where $S_{n,12}(E)$ and $S_{e,12}(E)$ denote the nuclear and electronic stopping cross section, respectively, of particle 1 in species 2.

The quantity $\nu_{12}(E)/E$ has been evaluated for 24 representative ion-target combinations by Winterbon (1975). Figure 9.17 shows four examples. The full-drawn curves represent the Lindhard-Scharff value k_L of the constant k. The other curves indicate the sensitivity to the choice of k, i.e., the effect of Z_1 oscillations.

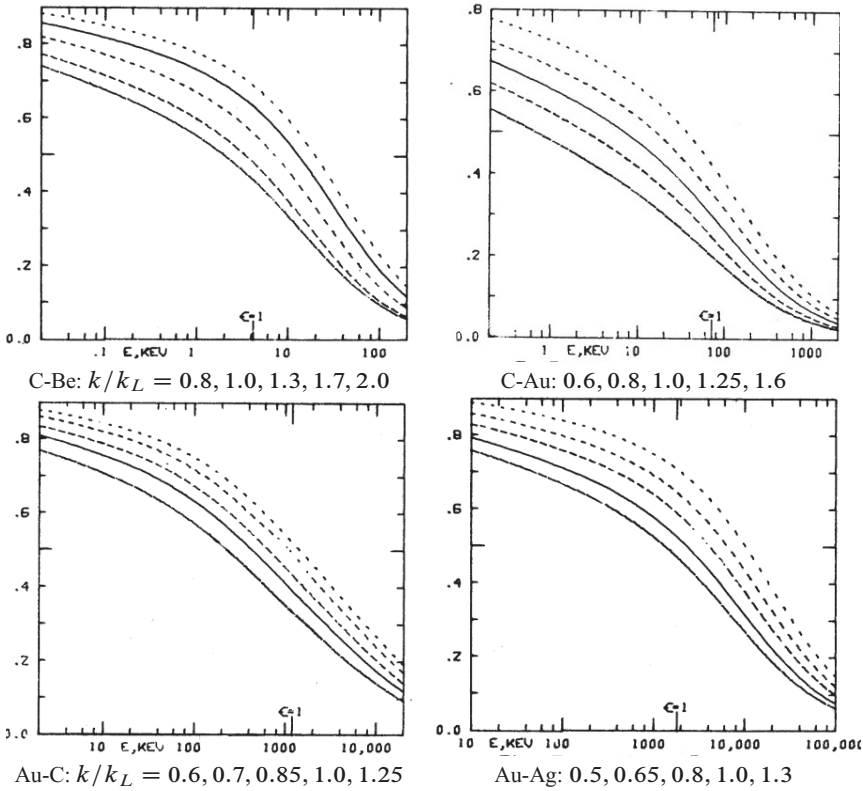

Fig. 9.17 The ratio $\nu(\epsilon)/\epsilon$ versus ϵ for four ion-target combinations. The point $\epsilon = 1$ has been marked on the abscissa. From Winterbon (1975)

Later, Winterbon (1986) developed a technique to solve moment equations iteratively, allowing for electronic-stopping input over a wide energy range including the stopping maximum as well as electronic straggling.

9.4.2.3 Measurements

Experimental tests of theoretical predictions concerning $\nu(E)$ and $\eta(E)$ rely mostly on measurements of $\eta(E)$.

Measurement of particle energies in proportional counters rely on the proportionality of the number of ion-electron pairs N_i generated in a gas-filled chamber with the energy E of the incident radiation, e.g. beta rays,

$$N_i \simeq \frac{E}{W}\,, \tag{9.115}$$

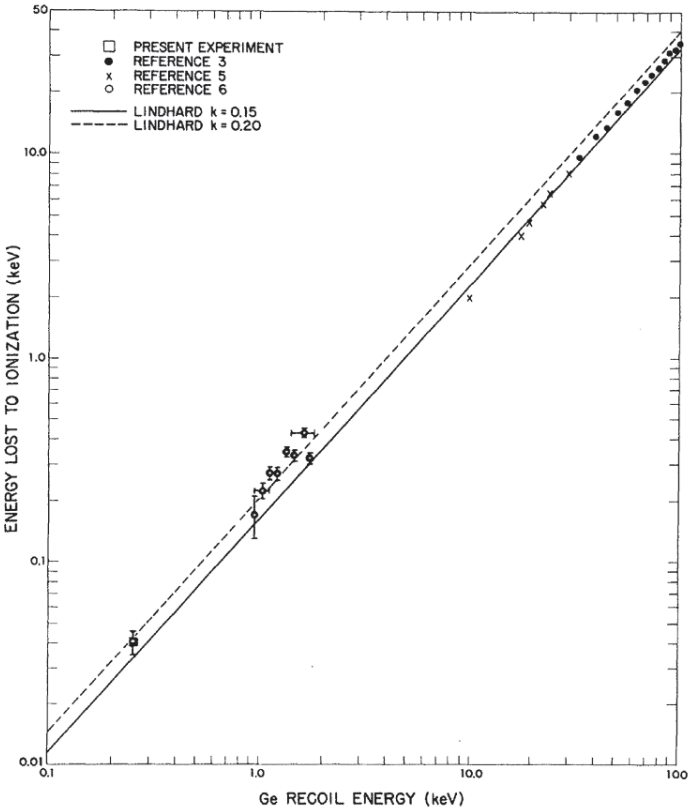

Fig. 9.18 Energy loss to electronic motion $\eta(E)$ compared to measurements of the ionization efficiency of Ge atoms in Ge. Solid and dotted lines according to Lindhard et al. (1963a) for $k = 0.15$ and 0.20, respectively. Experimental data from Chasman et al. (1965, 1968), Jones and Kraner (1971, 1975). From Jones and Kraner (1975)

where W, the 'W-value' or *energy to create an ion pair*, is an important parameter in radiation physics (ICRU, 1979), to be discussed in Volume 3 of this series.

Measurements on numerous ion-target combinations show that the ionization efficiency of heavy particles is not a universal material constant but also depends on the projectile and its energy. One relevant factor in this connection is energy transfer into nuclear motion, so that, instead of (9.115) one would use

$$N_i \simeq \frac{\eta(E)}{W}\,, \tag{9.116}$$

for comparison with measurements.

Figure 9.18 shows a comparison of $\eta(E)$ for Ge atoms in Ge with experimental values based on measured ionization efficiencies and involving a constant equivalent to $N_i = 2.96\,\text{eV}$ over an energy range from 0.25 to 100 keV. Considering that the

predicted ionization efficiency at the low-energy end is $\sim$ 10% below what would be expected from (9.115), and that even at the high-energy end it is still $\sim$ 0.3, the agreement between theory and experiment is impressive.

9.4.3 Higher Moments

9.4.3.1 Integral Equations

Now that we have a concept of deposited energy, let us look at the spatial distribution of that quantity. Define $F_n(\boldsymbol{v}, \boldsymbol{r})\,\mathrm{d}^3\boldsymbol{r}$ as the average density of energy deposited in nuclear motion in a volume element $(\boldsymbol{r}, \mathrm{d}^3\boldsymbol{r})$ as a consequence of a primary atom moving with a velocity $\boldsymbol{v}$ in $\boldsymbol{r} = 0$. The corresponding density of electronic energy is called $F_e(\boldsymbol{v}, \boldsymbol{r})\,\mathrm{d}^3\boldsymbol{r}$, and the two densities are normalized according to

$$\int \mathrm{d}^3\boldsymbol{r}\; F_n(\boldsymbol{v}, \boldsymbol{r}) = \nu(E), \tag{9.117}$$

$$\int \mathrm{d}^3\boldsymbol{r}\; F_e(\boldsymbol{v}, \boldsymbol{r}) = \eta(E). \tag{9.118}$$

When necessary, indices can be added to identify projectile and target target atoms.

Following the procedure described in Sect. 9.3.1 we can find an integral equation for $F_{12}(\boldsymbol{v}, \boldsymbol{r})$ which can stand for either F_n or F_e,

$$F_{12}(\boldsymbol{v}, \boldsymbol{r}) = N|\delta\boldsymbol{r}| \int \mathrm{d}\sigma \Big[F_{12}(\boldsymbol{v}', \boldsymbol{r} - \delta\boldsymbol{r}) + F_{22}(\boldsymbol{v}'', \boldsymbol{r} - \delta\boldsymbol{r}) + \sum_j F_{e2}(\boldsymbol{v}_j, \boldsymbol{r}) \Big] + \Big[1 - N|\delta\boldsymbol{r}| \int \mathrm{d}\sigma \Big] F(\boldsymbol{v}, \boldsymbol{r} - \delta\boldsymbol{r}), \tag{9.119}$$

where $\mathrm{d}\sigma$ denotes the cross section differential in the velocities of the scattered particle 1, the recoiling particle 2 and of ejected electrons. If the projectile is a target atom, we may replace the index 1 by 2. Following Sect. 9.3.1 we obtain a linear integral equation which, in terms of energy and angular variables reads

$$-\boldsymbol{e} \cdot \nabla_{\boldsymbol{r}} F_{12}(E, \boldsymbol{e}, \boldsymbol{r}) = N \int \mathrm{d}\sigma(E, \boldsymbol{e}, T_n, \boldsymbol{e}', T_e) \Big[F_{12}(E, \boldsymbol{e}, \boldsymbol{r}) - F_{12}(E - T_n, \boldsymbol{e}', \boldsymbol{r}) - F_{22}(T_n, \boldsymbol{e}'', \boldsymbol{r}) - \sum_j F_{e2}(\boldsymbol{v}_j, \boldsymbol{r}) \Big]. \tag{9.120}$$

9.4.3.2 Moments

Equations for higher moments are derived following the scheme outlined in Sect. 9.3.5.1 as far as the depth distribution of deposited energy is concerned, and correspondingly for the projected and lateral profiles discussed in Sect. 9.3.5.2, with the following changes and additions:

1. A recoil term representing $F_{22}(T_n, \boldsymbol{e}'', \boldsymbol{r})$ will have to be added,
2. Where necessary a term representing $\sum_j F_{e2}(T_e - U_j, \boldsymbol{e}_j, \boldsymbol{r})$ will have to be added,
3. In view of the normalization, (9.117) and (9.118), average values are found by dividing the appropriate moment by the respective zero-order moment.

As far as 1) is concerned, a term $-P_\ell(\cos\phi'')M_\ell^n(T_n - U)$ must be added in the brackets of (9.81), where

$$\cos\phi'' = \frac{T_n}{\gamma E} \tag{9.121}$$

and $\gamma = 4M_1M_2/(M_1 + M_2)^2$.

The term representing liberated electrons may be constructed similarly, although caution is indicated regarding the scattering angle ϕ'' of an ejected electron, except for beam velocities significantly higher than orbital velocities in the target.

Finally, the last item has the effect that relations such as (9.86) read

$$\langle X\rangle_n = \frac{3M_{n,1}^1(E)}{\nu(E)} \tag{9.122}$$

$$\langle X\rangle_e = \frac{3M_{e,1}^1(E)}{\eta(E)}. \tag{9.123}$$

9.4.3.3 Scaling Properties

As in case of range profiles, particularly simple scaling rules apply to the case of negligible electronic stopping coupled with power-law elastic scattering. Here, moments scale as

$$M_\ell^n(E) = B_\ell^n \frac{E^{1+2mn}}{(NC)^n}\,, \tag{9.124}$$

and the coefficients B_ℓ^n are, for equal masses, determined by

$$n\left(\ell B_{\ell-1}^{n-1} + (\ell+1)B_{\ell+1}^{n-1}\right) = (2\ell+1)B_\ell^\ell \int_0^\gamma \frac{\mathrm{d}t}{t^{1+m}} \times \left[1 - P_\ell(\cos\phi')(1-t)^{2mn+1} - \frac{C_{22}}{C_{12}}P_\ell(\cos\phi'')t^{2mn+1}\right] \tag{9.125}$$

under the assumption that the cross sections $\mathrm{d}\sigma_{12}$ and $\mathrm{d}\sigma_{22}$ obey a power law with the same exponent m but different constants C_{12} and C_{22} in the notation of (9.41).

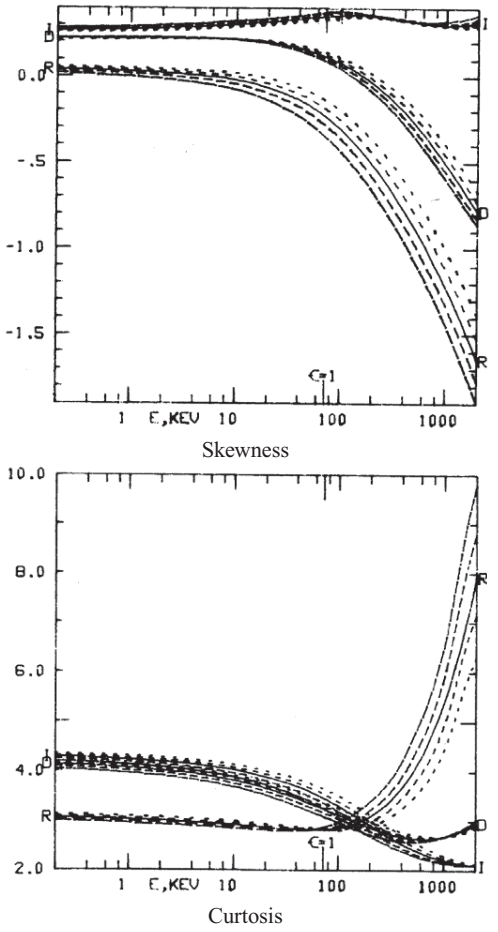

Fig. 9.19 Skewness (top) and kurtosis(bottom) for carbon ions in gold as a function of ϵ. R: Range; D: Nuclear motion $\nu(\epsilon)$; I: Electronic motion $\eta(\epsilon)$. Stipled curves indicate different k-values as in Fig. 9.17. From Winterbon (1975)

Results are shown in Figs. 9.11–9.13. When compared with ranges, average depths of energy deposition are slightly smaller than those of the ions, while the width of the energy deposition profile significantly exceeds the straggling of the ion range. More dramatic differences occur in higher moments shown in Figs. 9.12 and 9.13: Although range profiles show nonvanishing skewness and a kurtosis $\neq 3$, deviations from gaussian shape appear moderate, while in case of the deposited-energy profile this is true at most for $M_2/M_1 > 1$, where both profiles are strongly influenced by angular deflection of the projectile.

Winterbon (1975) has provided graphs of skewness and kurtosis versus beam energy for both range, nuclear and electronic motion and 24 ion-target combinations.

Figure 9.19 shows the case of C in Au. It is seen that for the range, a small positive skewness in the nuclear-stopping regime turns into a large negative skewness in the electronic-stopping regime. The damage distribution shows a significant positive skewness in the nuclear-stopping regime but turns likewise negative at higher energies. The ionization distribution is seen to have positive skewness at all energies.

The lower figure shows that the range profile has a kurtosis close to the gaussian value 3.0 up to $\epsilon \simeq 100$ but a strong increase at higher energies, while the two other profiles have a kurtosis $\simeq 4$ in the nuclear-stopping regime and a slow decrease at higher energies, following each other up to $\epsilon \simeq 100$. Caution is indicated with regard to higher energies since, for $Z_1 \ll Z_2$, the assumption of velocity-proportionality is no longer valid.

9.5 Range and Energy-Deposition Profiles

9.5.1 Construction from Moments

The problem of reconstructing a function from its moments does not necessarily have a unique solution, and the chance for finding a satisfactory solution in practice depends heavily on the kind of function you deal with. In the present context we deal with non-negative functions. This simplifies the task, as does the fact that typically we deal with unimodal profiles, i.e., profiles with only one maximum[6]. However, profiles may have discontinuities in value or slope. An obvious cause of discontinuity in ion bombardment is the presence of a surface, but discontinuities may have to be dealt with even in an infinite medium, to the extent that a projectile can be considered to start moving abruptly (Glazov, 1994). In the following we shall deal with an infinite medium. When a surface is marked, this marks the start of projectile motion. Discontinuities will be ignored. This is fully justified for the range profile. For energy and momentum profiles the matter will come up again in connection with sputtering in Volume 3.

9.5.1.1 Gram-Charlier and Edgeworth Expansion

There is ample evidence from early work with alpha particles that range profiles can be close to gaussian. However, Figs. 9.12 and 9.13 show that deviations occur. That figure assumes negligible electronic stopping. Moreover, deviations are more pronounced for the power-law exponent $m = 1/3$ than for $m = 1/2$. These two features indicate a tendency for deviations from gaussian shape to increase with decreasing energy. Minor to moderate deviations from gaussian shape are con-

[6] Bimodal profiles have, however, been found experimentally in case of slowing-down in single crystals by Eriksson et al. (1967), cf. Fig. 8.13 and the discussion in Sect. 11.10.1.

veniently described in terms of Hermite polynomial (Gram-Charlier) expansions (Feller, 1966).

A strictly gaussian range profile is characterized by

$$\psi = \frac{1}{\sqrt{2\pi}} \mathrm{e}^{-\xi^2/2} \tag{9.126}$$

with

$$\xi = \frac{x-a}{\alpha} \tag{9.127}$$

and

$$a = \langle x \rangle; \qquad \alpha = \sqrt{\langle (x - \langle x \rangle)^2 \rangle} \tag{9.128}$$

Following Winterbon et al. (1970) we may then write an ansatz

$$F(x) = \psi(\xi) \sum_{n=0}^{\infty} c_n \mathrm{He}_n(\xi)\,, \tag{9.129}$$

where $\mathrm{He}(\xi)$ are Hermite polynomials[7] in the notation of Abramowitz and Stegun (1964) and

$$c_n = \frac{1}{n!\alpha} \sum_{r=0}^{n} \alpha^{-r} M_r \mathrm{He}_{n-r}(-a/\alpha)\,, \tag{9.130}$$

where

$$M_r = \int_{-\infty}^{\infty} \mathrm{d}x\, x^r F(x) \tag{9.131}$$

From (9.128) follows that

$$\begin{aligned} c_0 &= \frac{1}{\alpha} \\ c_1 &= 0 \\ c_2 &= 0 \\ c_3 &= -\frac{1}{6\alpha} \frac{\langle (x - \langle x \rangle)^3 \rangle}{\langle (x - \langle x \rangle)^2 \rangle^{3/2}}, \end{aligned} \tag{9.132}$$

where you may note the skewness in the last expression.

The Edgeworth expansion represents a rearrangement of the individual terms in the Gram-Charlier expansion (Feller, 1966) in higher-order terms. As far as range profiles are concerned, deviations from gaussian shape are generally small and can most often be taken care of by the leading correction, i.e., the term determined by c_3. Skewness in the range profile is predominantly caused by angular deflection, which tends to shorten the range.

[7] The connection to the more conventional polynomials $\mathrm{H}_n(\xi)$ is given by $\mathrm{He}_n(\xi) = 2^{-n/2}(\xi/\sqrt{2})$ according to Abramowitz and Stegun (1964).

Energy-deposition profiles my deviate significantly from gaussian shape, as is evident from Fig. 9.2. Model examples for elastic collisions in the power approximation were studied by Winterbon et al. (1970). More realistic cases were studied by Winterbon (1972), and a number of examples were compiled by Winterbon (1975).

9.5.1.2 Pearson Distributions

Pearson distributions (Pearson, 1895) are four-parameter functions designed to fit skew probability densities. These functions are defined as solutions of differential equations of the type

$$\frac{\mathrm{d}F(x)/\mathrm{d}x}{F(x)} + \frac{P_1(x)}{P_2(x)} = 0\,, \tag{9.133}$$

where $P_1(x)$ and $P_2(x)$ are polynomials of first and second order, respectively. Pearson functions are classified into a number of families, dependent on the relation between the skewness and the kurtosis characterizing the distribution. There are two main groups, dependent on whether or not $P_2(x)$ has a root for real values of x. A gaussian profile is obtained in the limiting case of $P_2(x) = \text{constant}$.

Numerous authors employed Pearson functions in fitting measured range profiles or estimating range profiles from calculated moments. Following Hofker et al. (1975), several of them made reference to the Pearson IV family, which can be written as

$$F(x) = \text{const}\left[1 + y^2\right]^{-m} \mathrm{e}^{-\nu \arctan y}\,, \tag{9.134}$$

with

$$y = \left(\frac{x - x_0}{\alpha}\right), \tag{9.135}$$

where x_0 represents the peak of the distribution and ν and α are related to the width, the skewness and the kurtosis.

Winterbon (1983b) analysed a large number of calculated range moments from his compilation (Winterbon, 1975) and found that all results fell into a very narrow strip in a plot of kurtosis vs. skewness, marked by thick solid lines in Fig. 9.20, left graph. The Pearson IV curve falls outside this strip for the parameter range of negative skewness. Winterbon therefore found the Pearson VI distribution to be the most universally applicable ansatz, which can be written as

$$F(x) = \text{const}\left(1 + \frac{x - x_0}{\alpha_1}\right)^{m_1}\left(1 + \frac{x - x_0}{\alpha_2}\right)^{m_2}. \tag{9.136}$$

Negative skewness, equivalent with a tail towards low penetration depth, is characteristic of high-energy range profiles and caused mainly by elastic scattering. In the ion implantation regime, i.e., the range of dominating nuclear stopping, the Pearson IV distribution is not in contradiction with Winterbon's criterion. In that regime the skewness tends to be positive, in part because tails in the backward direction will be absent in case of noticeable reflection, partly because measuring techniques may be accompanied by diffusion and mixing.

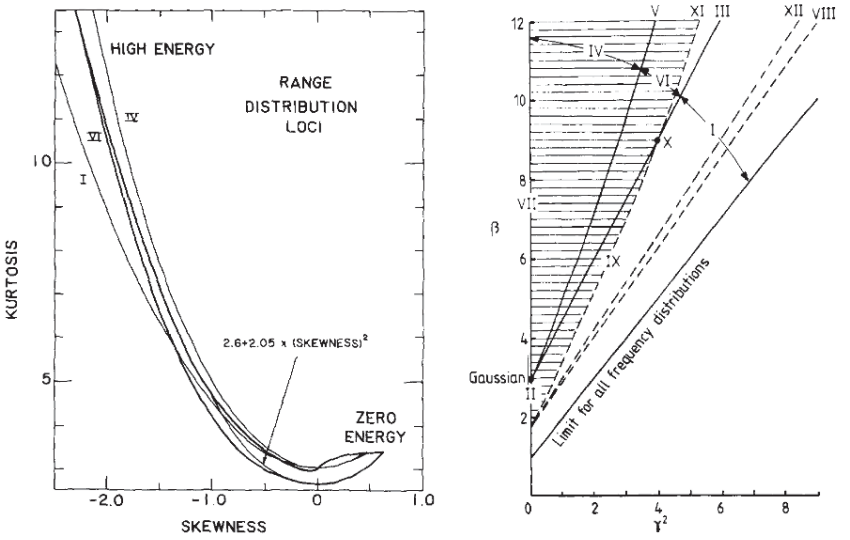

Fig. 9.20 Regions of validity of various Pearson distributions. Left graph from Winterbon (1983b). Right graph from Ashworth et al. (1990). γ = skewness. See text

In a thorough study including simulations of a large number of ion-target combinations, Ashworth et al. (1990) found that all Pearson families I–VII can be useful, dependent on the respective part of the parameter space in terms of atomic numbers and beam energy.

9.5.1.3 Padé Approximants

A Padé approximant is a rational function,

$$R(x) = \left(\sum_{\nu=0}^{m} a_\nu x^\nu\right)\left(\sum_{\nu=0}^{n} b_\nu x^\nu\right)^{-1} \quad ; \quad b_0 = 1 \tag{9.137}$$

to approximate some given function within a certain interval. Padé approximants have been useful in the construction of energy and, especially, momentum distribution functions (Littmark, 1974, Littmark and Sigmund, 1975).

9.5.2 Direct Methods

9.5.2.1 Transport Equation

Although fully numerical solution of the transport equation for a range or damage profile is an option, no examples in the literature are known to the author. Actually, the code BEST (Vicanek and Urbassek, 1988), standing for 'Boltzmann Equation Solving Tool' is a Monte Carlo code which, like numerous others, efficiently provides range profiles and related quantities that are roughly equivalent with what can be extracted from moments found by analytical methods with numerical methods.

9.5.2.2 Multigroup Methods

Multigroup methods, widely used in neutron transport theory, operate with a discrete number of energy steps. If the energy range between zero and the initial energy is divided up into n energies, the transport equation splits into n equations, describing the feeding of particles from every level to all lower ones. When applied to the slowing down of ions, this procedure neglects the fact that the mean free path decreases rapidly with decreasing energy. This problem has been overcome by Winterbon (1983a) by dynamically adjusting the interval size to the travelled pathlength, keeping the number of intervals constant.

A pathlength profile was constructed for power scattering on the basis of up to $n = 7$, requiring $2n - 1$ moments. Comparison with an accurately computed profile revealed good agreement already for $n = 5$ and perfect agrement for $n = 7$.

9.5.2.3 Brice's Method

A method to compute energy deposition distributions avoiding higher-order moments was proposed by Brice (1970). This scheme aims at high-energy implantation. Figure 9.2 shows a model for electronic energy deposition versus pathlength, neglecting straggling, multiple scattering and nuclear stopping. Evidently, an equivalent graph could be constructed for nuclear energy deposition versus pathlength.

In order to generate more realistic graphs for the two quantities, one needs to include nuclear energy loss from the beginning in the conversion from beam energy to travelled pathlength. Brice (1970) included multiple scattering by a correction factor determined from the ratio $R_p(E)/R(E)$ between projected range and pathlength, either on an integral or a differential basis. Statistics were incorporated via a modified range distribution $F(E, E', R)\mathrm{d}R$, which represents the probability for an ion of initial energy E to pass through the energy E' at a travelled pathlength $(R, \mathrm{d}R)$. Profiles $F(E, E', R)$ were assumed gaussian and determined by solving moment equations. Energy deposition was then incorporated as $\mathrm{d}E'/\mathrm{d}x$. In this form (Brice, 1974) the scheme does not allow for either secondary-electron or recoil transport.

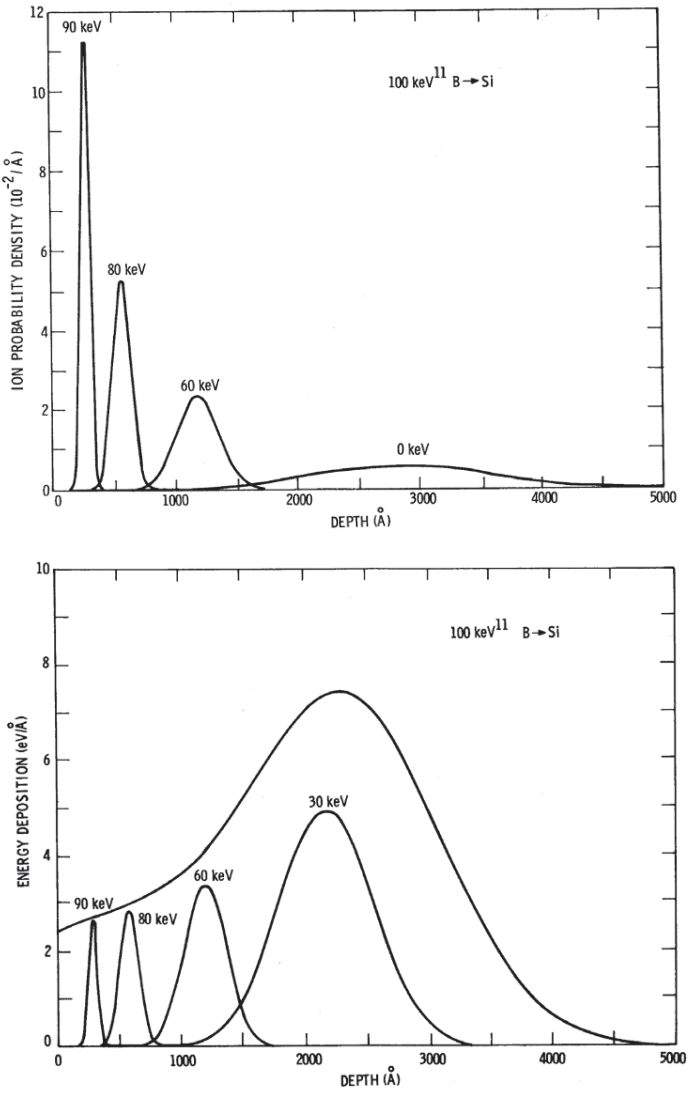

Fig. 9.21 Top: Depth distributions of 100 keV B ions in Si after slowing down to 90, 80, 60 keV and after coming to rest. Bottom: Depth deposition of *energy deposition rate* after slowing down to 90, 80, 60 and 30 keV and the overall deposited energy. From Brice (1975a)

Recoil transport was incorporated approximately later (Brice, 1975b). An example is shown in Fig. 9.21.

9.5.3 Simulation Codes

Computer simulation of particle penetration and radiation effects has, from the early days of computing in the 1950s, developed into a discipline with its own series of conferences and monographs. A characteristic feature of half a century's development is a trend towards minimizing external input.

As an example, the minimum input in a realistic Monte Carlo simulation is a differential cross section for nuclear collisions and a stopping cross section for electronic collisions. This was replaced in early molecular-dynamics simulations by an interatomic potential and a lattice structure. In more advanced simulations the lattice structure is output, provided that an appropriate potential has been adopted. In quantum molecular dynamics, electronic stopping is output rather than input, and with proper computing power and computational skill, most of the findings reported in this monograph might become replaced by numerical solution of Schrödinger's equation or relativistic equivalents.

Simulation techniques will be discussed explicitly in a separate chapter in Volume 3 of this series. Therefore only a very brief survey will be given here.

9.5.3.1 Monte Carlo Simulations

The physical model underlying Monte Carlo simulations is roughly equivalent with that represented by transport equations considered in the present chapter. Early work was devoted to electron penetration, summarized in an informative review by Berger (1963).

Most Monte Carlo schemes operate with a finite total cross section σ_{tot} which define a distribution in free pathlength ΔR,

$$f_1(\Delta R)\mathrm{d}\Delta R = \mathrm{e}^{-N\Delta R\sigma_{\text{tot}}}\mathrm{d}\Delta R\,. \tag{9.138}$$

From this, a random-number generator selects a sequence of free pathlengths. For a given pathlength, an elastic energy loss T_n is then selected from a probability distribution

$$f_2(T_n)\mathrm{d}T_n = \frac{\mathrm{d}\sigma_n(E,T)}{\sigma_{\text{tot}}}\,. \tag{9.139}$$

This defines a scattering angle at the same time. After subtraction of an electronic energy loss $N\Delta RS_e$ the simulator can go to the next iteration step, until the particle energy has come below some predefined value, whereafter another trajectory can be studied.

Early Monte Carlo simulations (Oen et al., 1963) involving heavy particles operated with hard-sphere cross sections, where a total cross section is readily available. For classical scattering cross sections for potentials utilized in this field and discussed in Chap. 6 the total cross section becomes infinite. I am aware of several obvious ways to circumvent this problem:

- Truncate the *cross section* at some minimum energy transfer $T_{\min}$ and choose this quantity small enough so that simulation results are unaffected within some prescribed error margin. This is the standard solution in most codes.
- Truncate the cross section at $T_{\min}$ and correct for the error by adding a quantity

$$\Delta S = \int_0^{T_{\min}} T \, \mathrm{d}\sigma(E, T) \tag{9.140}$$

  to the electronic stopping cross section. Remember that small energy transfers do not contribute significantly to straggling.
- Use a fixed free path. This solution has been adopted in the TRIM code (Wilson et al., 1977). This requires likewise an addition to the stopping cross section.

The predictive power of a Monte Carlo code must depend on the quality of the input and statistical accuracy. When applied to penetration in solids, common to all three categories is a breakdown at low energies, typically the sub-keV energy range, where the mean free path becomes comparable with the interatomic distance in the medium.

9.5.3.2 Binary Collision Codes

Although Monte Carlo codes operate with binary collisions, the term 'Binary collision code' denotes another kind of simulation, where input is a scattering integral instead of a cross section, and a lattice structure. This type of code proved very useful in early studies of channeling (Robinson and Oen, 1963, Beeler and Besco, 1964, Barrett, 1968). It simulates trajectories of a projectile and, most often, recoiling target atoms, in a prescribed structure.

Typically, the relation between scattering angle and impact parameter is given by the classical scattering integral, (6.34), involving an adopted potential. Positioning the trajectory in space—and possibly in time—requires the time integral discussed in Sect. 3.3.4, Vol. 1. Electronic stopping is added either via a stopping cross section or as an impact-parameter-dependent energy loss per collision.

Amongst powerful binary-collision codes I like to mention MARLOWE by Robinson and Torrens (1974), OKSANA by Shulga (1983) and ACAT by Yamamura and Takeuchi (1987).

Binary-collision codes are used for collisions in solids and mostly in crystals. Even though the structure of the target material is taken explicitly into account, often including thermal displacements, problems prevail at low energies, albeit less obvious than in Monte Carlo simulations. The main problem is the many-body nature of collisions in the sub-keV energy regime. Robinson (1981) offered a partial solution to this problem by incorporating scattering integrals for many-body collisions of Andersen et al. (1966). Shulga and Sigmund (1995), using the same procedure, built in an option to compute low-energy events by molecular-dynamics simulation.

9.5.3.3 Molecular Dynamics

Molecular-dynamics codes are based on Newton's second law or Hamilton's equation of motion which are solved numerically with a binary or many-body interaction potential as input. Electronic energy loss is most often added in the form of a stopping cross section, but projects to incorporate excitation and ionization a priori are under development.

The method was initiated by Alder and Wainwright (1959), who studied the thermal motion of particles interacting as hard spheres. A planar lattice of Cu atoms interacting via a potential of the form $\mathcal{V} = A\exp(-r/a)$ at energies up to 400 eV was simulated by Gibson et al. (1960). Further development was slow because of limited computing power and the absence of suitable graphical tools to visualize processes in three dimensions.

Molecular dynamics is complementary to binary-collision simulation in the sense that its limitations lie in the high-energy end of the energy scale, where the demands on computation times for individual events and reaching adequate statistics increase rapidly.

An illuminating review of the strengths and weaknesses of molecular dynamics, written by an interested observer, is due to Andersen (1987).

9.5.4 Measurements

Profiles of deposited energy, electronic or nuclear, are measured indirectly through associated radiation effects such as displaced lattice atoms, disorder, ionization as well as electron emission and sputtering. These topics will be reserved to Volume 3 in this series.

Much effort has been invested in the measurement of range profiles starting in the late 1950s (Nielsen, 1956, Davies et al., 1960b). These studies were motivated by the need to produce targets for nuclear-reaction studies by ion implantation. There is a maximum enrichment, dependent on the ion and its energy as well as the material, and one parameter determining this enrichment is the penetration depth.

From the mid 1960s on, interest turned into implantation in semiconductors with the development of integrated circuits. Since then the scope has been extended continuously to a wide variety of materials, including biologic material. With the growing interest in micro- and nanotechnology the main challenge has been to continuously improve depth resolution on the atomic scale.

9.5.4.1 Destructive Techniques

It is customary to distinguish between destructive and nondestructive techniques. In a destructive technique, the implanted target is typically etched in a controlled way. This can be done by chemical, e.g. electrochemical, etching (Davies et al.,

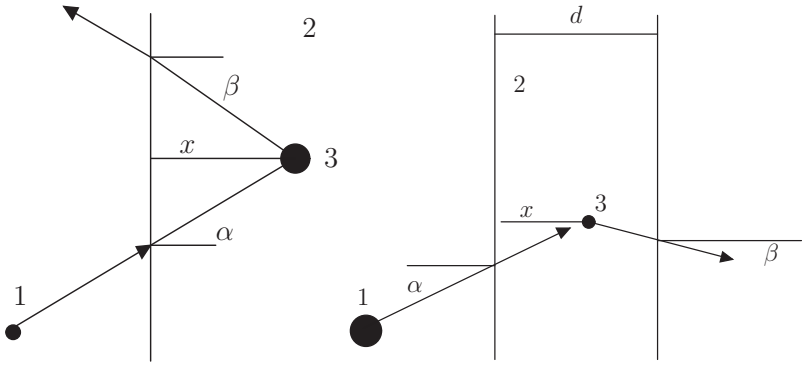

Fig. 9.22 Nondestructive depth profiling by Rutherford backscattering spectroscopy (RBS, left) and ERDA (Elastic recoil detection analysis, right), schematic

1960a) or sputtering (Lutz and Sizmann, 1963). The depth profile $F(x)\,\mathrm{d}x$ can then be measured in a number of ways:

- If the implanted species is radioactive, the residual activity of the target after each erosion step is a measure of the integral profile, $\int_x^\infty F(x')\,\mathrm{d}x'$ (Davies et al., 1960a).
- More generally, surface analysis by e.g. low-energy ion scattering or Auger spectroscopy (Feldman and Mayer, 1986) can be employed in situ to record the implant concentration at the surface during the etching process. This is a relative measure of the implant concentration $F(x)$.
- Similar information can be found by recording the sputtered flux by SIMS (Secondary Ion Mass Spectrometry) (Hofker et al., 1975).

Electrochemical etching played a central role in the development of ion implantation. Examples are shown in Figs. 9.23–9.25 below. The technique can have nanometer resolution, depending on the material, but it is applicable only to a small number of materials. Moreover, it is time-consuming since measurements cannot be performed in situ.

Measurements involving sputtering can be performed in situ, but since the sputter process causes distortions of the original profile, corrections are necessary. An important disturbing effect is atomic mixing (Andersen, 1979, Hofer and Littmark, 1979), a topic to be discussed in Volume 3.

9.5.4.2 Nondestructive Techniques

Figure 9.22 shows two examples of almost nondestructive depth profiling. In Rutherford backscattering (RBS), an incident ion 1 with an energy E is reflected from an impurity atom 3 in a matrix 2. The energy of the scattered ion is given by

$$E_{\mathrm{out}} = E - \Delta E_1 - \Delta E_2 - \Delta E_3, \tag{9.141}$$

where

$$\Delta E_1 = \frac{1}{\cos\alpha}\int_0^x \mathrm{d}x' N S_{12}\big(E(x')\big)\,, \tag{9.142}$$

$$\Delta E_2 = \gamma_{13}(E - \Delta E_1)\sin^2\frac{\Theta}{2}\,, \tag{9.143}$$

$$\Delta E_3 = -\frac{1}{\cos\beta}\int_x^0 \mathrm{d}x' N S_{12}\big(E(x')\big)\,. \tag{9.144}$$

Here, $S_{12}(E)$ is the stopping cross section of the material, Θ the c.m.s. scattering angle, which is related to the laboratory scattering angle ϕ_1 by

$$\sin^2\frac{\Theta}{2} = \frac{1}{2}\left(1 + \frac{M_1}{M_2}\sin^2\phi_1\right) \pm \frac{1}{2}\cos\phi_1\sqrt{1-(M_1/M_2)^2\sin^2\phi_1}\,, \tag{9.145}$$

i.e., the inverse of (3.5), Vol. 1, and given here by $\phi_1 = \pi - \alpha - \beta$, and

$$\gamma_{13} = \frac{4M_1M_3}{(M_1+M_3)^2}\,. \tag{9.146}$$

You may notice that for a given scattering angle, the term ΔE_2 depends on the implanted species. This implies that spectra of different species appear in different energy intervals. The terms ΔE_1 and ΔE_2, on the other hand, depend on the depth x of the implant. You may find a typical RBS spectrum in Fig. 1.7, Vol. 1.

This technique is particularly useful for heavy impurities in light targets, with H or He ions as preferred ions. Use of heavier ions increases the depth resolution because of higher stopping cross sections but diminishes the separation of different impurities. For $M_1 > M_3$, genuine backscattering ($\phi_1 > \pi/s$) is forbidden by conservation laws. This problem can be avoided by measuring Rutherford scattering in transmission on a thin foil or by grazing incidence.

However, in such cases the ERDA technique, indicated on the right part of Fig. 9.22 is often a better solution. In this technique, which was proposed by L'Ecuyer et al. (1976), it is the energy of the recoiling implant atom that is measured, which is given by

$$E' = \gamma_{13}\big[E - \Delta E_1\big)\sin^2\frac{\Theta}{2} - \frac{1}{\cos\beta}\int_x^d \mathrm{d}x N S_{31}\big(E(x)\big). \tag{9.147}$$

Equations 9.142–9.144 as well as (9.147) ignore multiple scattering and energy-loss straggling. Moreover, to determine absolute concentration profiles also the scattering cross section $\mathrm{d}\sigma_{13}$ enters the description. A number of elaborate computer codes have been developed to perfectionate these two as well as other ion-beam analytical techniques. A major biannual conference series on ion beam analysis has been held starting 1974, and several handbooks are on the market. For details the reader is referred to Wang and Nastasi (2010).

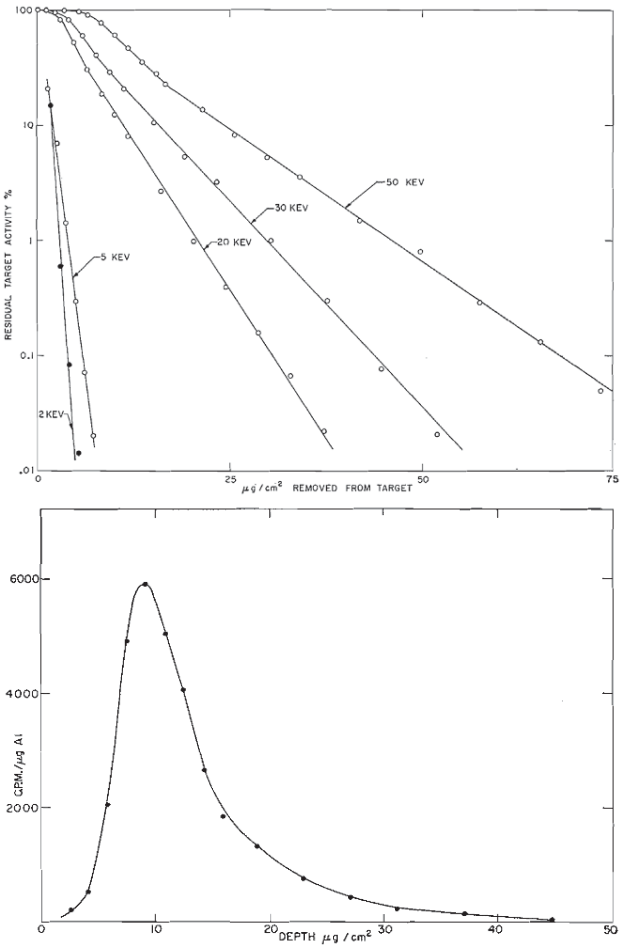

Fig. 9.23 Range profiles of ^{137}Cs ions in aluminium. Top: Integral profiles for 5–50 keV. Bottom: Differential profile for 50 keV. From Davies et al. (1960b)

9.5.4.3 Examples

Figure 9.23 shows one of the first range profiles measured for keV ions, measured by electrochemical stripping (Davies et al., 1960b). To appreciate the resolution, note that 1 μg/cm^2 is equivalent with 3.7 nm of aluminium. The lower graph shows a profile close to gaussian in the peak region and a distinct tail at greater depth. The upper graph shows that this tail is close to exponential.

Figure 9.24 demonstrates the influence of channeling on a range profile. The upper graph shows a comparison between a range profile in amorphous aluminium oxide with that in an aluminium polycrystal. The difference between the two profiles is not dramatic at small depths, up to about the 50% level. However, the deep tail

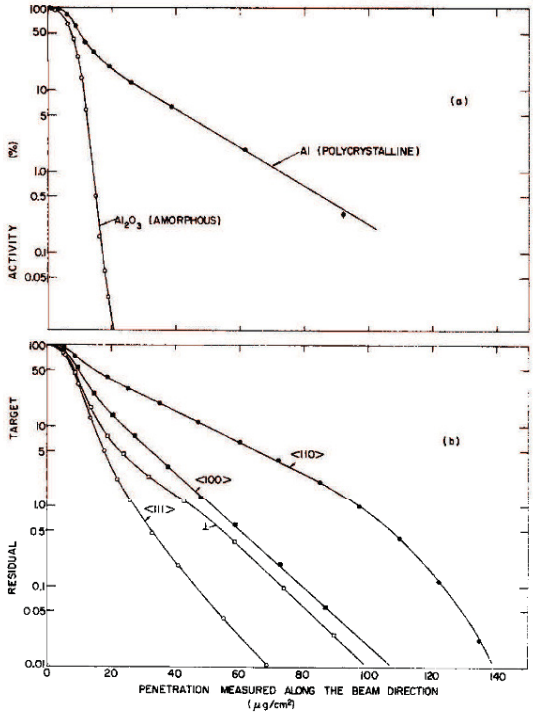

Fig. 9.24 Range profiles of 40 keV ^{85}Kr. Top graph: Integral profiles in amorphous Al_2O_3 and polycrystalline Al. Bottom graph: Al single crystal with the beam incident along ⟨111⟩, ⟨110⟩, ⟨100⟩ directions, and normal incidence, 7° off ⟨112⟩. From Piercy et al. (1963)

in aluminium is absent in the oxide. The lower graph demonstrates that this effect depends on the crystal direction, and the longest ranges are observed for the most open crystal direction, the ⟨100⟩ direction. This finding plays a central role in the discovery of the channeling effect to be discussed in Sect. 11.

Still another phenomenon shows up in Fig. 9.25 where, in addition to long-range channeling, an additional tail is observed in all profiles except the one in the amorphous target. A characteristic feature is an approximately equal slope for all crystal directions, indicating that it is not a collisional process.

Davies and Jespersgård (1966) concluded that the 'super tails' were due to diffusion of projectile particles after slowing down. Andersen and Sigmund (1965) suggested interstitial diffusion as the underlying mechanism by showing that for $M_1 < M_2$, projectiles could come to rest in a tungsten lattice without getting trapped in a lattice vacancy. The opposite behaviour was predicted for $M_1 > M_2$. Unpublished measurements by Domeij and Eriksson (1965) confirmed this assertion.

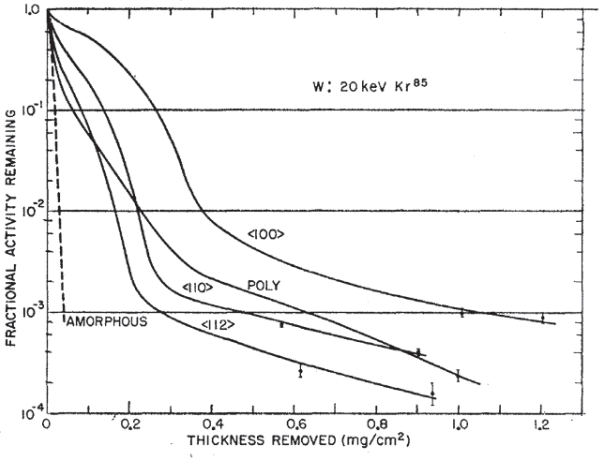

Fig. 9.25 Integral range profiles of 20 keV ^{85}Kr in W single crystal in three crystal directions, compared with a W polycrystal. Data for an amorphous crystal were derived from measurements on anodic tungsten oxide. From Kornelsen et al. (1964)

9.5.4.4 Comparison with Theory

As indicated in the introduction to this chapter, range calculations are nowadays performed with various simulation programs which, by and large, are based on theoretical concepts described in the foregoing sections. You may find an extensive list of literature references in a monograph by Eckstein (1991). Here I want to summarize some obvious pitfalls that should not be overlooked.

- Ion implantation profiles depend on the implant fluence. Increasing fluence implies a change in the composition of the target material, crystal damage, surface erosion by sputtering and mixing of previously implanted ions. In an early study by McCargo et al. (1963), previously measured ranges were reported too low by a factor of two because of high fluence.
- When comparing measured mean ranges with a Monte Carlo simulation, you may underestimate the range if there is a significant tail due to channeling. A comparison of the most probable range or, even better, the full profile is more appropriate in such a case.
- Experimental errors and artifacts may average out in mean ranges but tend to enhance fluctuations. If the measured range straggling turns out smaller than the calculation, there is likely to be an error in the theory, or perhaps in the analysis of the measurement.

All simulational models contain adjustable parameters, in particular the precise form of the screening radius and the screening function of the potential, as well as the precise energy dependence and proportionality factor of the electronic stopping

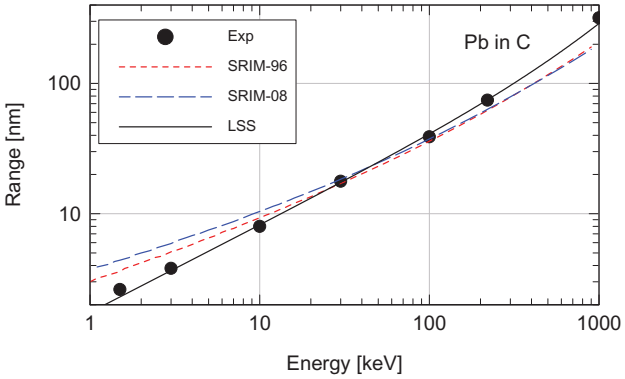

Fig. 9.26 Mean range of Pb ions in carbon. Measurement by Friedland et al. (1998). Simulations by two versions of the SRIM code (Ziegler et al., 2008). Theoretical curve (LSS) according to Lindhard et al. (1963b). From Sigmund (2013)

cross section. A crucial test on the validity of a given scheme, whether analytical or numerical, is its validity over a wide range of parameters. An example is shown in Fig. 9.26. It demonstrates, on a specific example, that the original LSS scheme (Lindhard et al., 1963b), with the original input, is still competitive with contemporary simulation codes.

9.6 Fluctuations and Correlations

While fluctuations in the ion range are fully accounted for in the transport equations discussed in Sects. 9.2.1 and 9.3.1, distributions in deposited energy are not. In contrast to a single bombarding ion, energy is shared amongst many particles in a recoil cascade and/or an ionization cascade, and both the sharing between nuclear or electronic motion, the respective distributions in space and the conversion into measurable quantities such as structural defects or inner-shell vacancies are subject to fluctuation. In particular, deposited-energy distributions discussed in Sect. 9.4.3.1 are mean values over many incident ions, while the distribution of deposited energy due to an individual ion may look very different.

Fluctuations in specific quantities like structural defects or inner-shell vacancies are central aspects of the theory of radiation effects and will be considered in Volume 3 of this series. Here, only one quantity will be mentioned briefly, which is tightly connected to the topics discussed in this chapter, the correlation between deposited energy and the penetration of the ion.

Slightly generalizing Westmoreland and Sigmund (1970), let us define a quantity $g_{n,e}(\boldsymbol{v}, \boldsymbol{r}, \boldsymbol{R})\,\mathrm{d}^3\boldsymbol{r}$ as the mean energy deposited in nuclear or electronic motion in a volume $(\boldsymbol{r}, \mathrm{d}^3\boldsymbol{r})$ by a projectile starting in $\boldsymbol{r} = \boldsymbol{0}$ with a velocity $\boldsymbol{v}$ *and coming to rest in* $\boldsymbol{R}$.

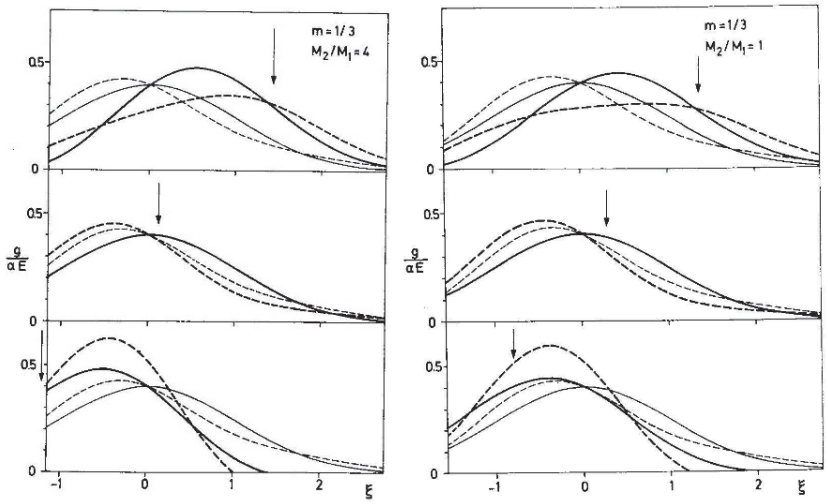

Fig. 9.27 Conditional distribution function of deposited energy $g_n(E, x)$ for normal incidence. Thick solid lines: Gaussian approximation; thick stippled lines: Including third-order moments. Thin lines denote the corresponding average energy deposition profiles. Abscissa variable $\xi = \alpha(x - \overline{x})$, so that $\xi = 0$ denotes the mean projected range; $\alpha = 1/\sqrt{\Delta x^2}$; arrows denote the actual penetration depth of the projectile; power scattering $m = 1/3$. Mass ratio $M_2/M_1 = 4$ (left) and 1 (right). From Westmoreland and Sigmund (1970)

We may also define a joint distribution in mean deposited energy and vector range,

$$F(\boldsymbol{v}, \boldsymbol{r}, \boldsymbol{R})\, \mathrm{d}^3\boldsymbol{r}\, \mathrm{d}^3\boldsymbol{R} = F(\boldsymbol{v}, \boldsymbol{R}) g_{n,e}(\boldsymbol{v}, \boldsymbol{r}, \boldsymbol{R})\, \mathrm{d}^3\boldsymbol{r}\, \mathrm{d}^3\boldsymbol{R}\,. \tag{9.148}$$

This function satisfies a backward transport equation of the type of (9.49) and (9.120). Following the procedure applied in the derivation of those relations you will obtain

$$-\frac{\boldsymbol{v}}{v} \cdot \nabla_r F(\boldsymbol{v}, \boldsymbol{r}, \boldsymbol{R}) - \frac{\boldsymbol{v}}{v} \cdot \nabla_R F(\boldsymbol{v}, \boldsymbol{r}, \boldsymbol{R}) = N \int \mathrm{d}\sigma(\boldsymbol{v}, \boldsymbol{v}', \boldsymbol{v}'') \times \left[F(\boldsymbol{v}, \boldsymbol{r}, \boldsymbol{R}) - F(\boldsymbol{v}', \boldsymbol{r}, \boldsymbol{R}) - F_R(\boldsymbol{v}', \boldsymbol{R}) F_{n,e}(\boldsymbol{v}'', \boldsymbol{r})\right]. \tag{9.149}$$

While it is possible in principle to find a transport equation for $g_{n,e}(\boldsymbol{v}, \boldsymbol{r}, \boldsymbol{R})$, cf. Problem 9.10, it is easier to find a solution for (9.149) and from there to find $g_{n,e}(\boldsymbol{v}, \boldsymbol{r}, \boldsymbol{R})$ from the definition, (9.148).

Approximate solutions can by found by the moment method starting from

$$\int \mathrm{d}^3\boldsymbol{r}\; F(\boldsymbol{v}, \boldsymbol{r}, \boldsymbol{R}) = F_R(\boldsymbol{v}, \boldsymbol{R}) \begin{Bmatrix} \nu(E) \\ \eta(E) \end{Bmatrix}\,, \tag{9.150}$$

depending on whether the nuclear or electronic energy distribution is of interest. Moreover,

$$\int \mathrm{d}^3\boldsymbol{R}\; F(\boldsymbol{v},\boldsymbol{r},\boldsymbol{R}) = F_{n,e}(\boldsymbol{v},\boldsymbol{r}). \tag{9.151}$$

Westmoreland and Sigmund (1970) derived moment equations and solutions for nuclear energy deposition governed by power scattering up to the third moment. Results are shown in Fig. 9.27. You may note that for $M_2/M_1 = 4$ (left group of graphs), where the projectile undergoes wide-angle scattering, there is a drastic difference between the energy deposition profile when the projectile comes to rest in $\overline{x} \pm \sqrt{\Delta x^2}$ (top and bottom graph, respectively). This difference is significantly smaller for $M_2/M_1 = 1$ (right group of graphs).

Equations of the type discussed in this section are well established in statistical physics. Equations first derived by Dederichs (1965), characterizing vacancy and interstitial distributions, were generalized by the present author (Sigmund et al., 1968) to power scattering and applied in particular in a theory of elastic-collision spikes (Sigmund, 1974). Winterbon et al. (1970) derived a transport equation for the probability density of deposited energy in space. Jakas (1979) determined solutions for the second moment. Large fluctuations were found, consistent with Fig. 9.27. Moreover, results turned out to be sensitive to the exponent m in the power cross section. The fact that solutions only could be found for $m < 1/2$ suggests caution.

9.7 Discussion and Outlook

This chapter is dominated by contributions of J. Lindhard and his coworkers, who developed the theory of ion penetration in the keV and lower-MeV energy range in the late 1950s. This effort has been documented in four seminal publications (Lindhard and Scharff, 1961, Lindhard et al., 1963a,b, 1968), which formed the ground for all subsequent work in the field, including numerous computer simulation codes. While there are better interaction potentials or cross sections for specific systems now, as well as electronic stopping cross sections based on measurements, little has changed in the basic concepts, in particular the definition of the quantities of interest. Also the hierarchy of processes to be considered in calculations is essentially the one adopted by Lindhard and coworkers, except in high-energy implantation where electronic straggling cannot be ignored.

Changes have occurred in the calculational techniques. Analytical methods are most suitable to provide moments over range and energy deposition profiles, but whenever a complete profile is needed, and deviations from gaussian shape are expected, direct methods are to be preferred, and computer simulation, in particular by the Monte Carlo method, has been the appropriate solution for many years. Achieving adequate statistics is no longer a problem, and to the extent that reliable input is available, potential sources of error are minor.

Challenges still exist in the treatment of ion slowing-down at lower energies, i.e., in the eV regime, where uncertainties pile up both in the general description and

the input. The dominating technique in this regime is molecular dynamics. Scaling relations found for the keV and MeV regime cannot be expected to be valid here. Therefore, every ion-target combination needs individual attention. This aspect will receive special attention in Volume 3 of this series.

Problems

9.1. Find an exact solution of (9.12) for the differential cross section

$$\mathrm{d}\sigma(E,T) = \frac{\sigma(E)}{E}\mathrm{d}T \text{ for } 0 \le T \le E \tag{9.152}$$

and show that it differs from (9.18) by a factor of two. Is this a serious objection to the approximation expressed by (9.16)?

9.2. Derive an equation for $\left\langle (R - \langle R\rangle)^3 \right\rangle$ by the procedure leading to (9.15). Find a solution by the method used to derive (9.23). The result is

$$\left\langle (R - \langle R\rangle)^3 \right\rangle = \int_0^E \mathrm{d}E' \left[3\frac{[NW(E')]^2}{[NS(E')]^5} - \frac{NQ(E')}{[NS(E')]^4} \right], \tag{9.153}$$

where $Q(E) = \int T^3 \mathrm{d}\sigma(E,T)$.

9.3. Show that in the energy regime of Bethe stopping and Bohr straggling, the quantity $\langle (R - \langle R\rangle)^2\rangle / \langle R\rangle^2$ exhibits a slow monotonic decrease as a function of the beam energy.

9.4. Where does the factor $1/2\pi$ in (9.73) arise from?

9.5. Fill in the details leading to (9.77), making use of Appendix A.2.3, Vol. 1.

9.6. Analyse Fig. 9.12. Why is the skewness positive everywhere? What is the reason for the decrease with increasing M_2/M_1? What can you conclude from the fact that the quantity $\langle XY^2\rangle / \langle X\rangle\langle Y^2\rangle$ is close to 1 for all mass ratios?

9.7. Analyse Fig. 9.13. Calculate the kurtosis of a gaussian profile. How does this compare to the data shown in the graph, and what can you conclude from this? What can you conclude from the fact that the quantity $\langle X^2Y^2\rangle / \langle X^2\rangle\langle Y^2\rangle$ is close to 1 for all mass ratios?

9.8. Establish integral equations analogous to (9.102) and (9.105) for a homogeneous polyatomic medium. Hint: Introduce the quantity $\nu_{jk}(E)$ which denotes the mean energy deposited in species k by a primary atom of species j.

9.9. Reproduce Fig. 9.15 on the basis of the information given in the caption.

9.10. Derive (9.149) for $Z_1 \neq Z_2$. Make sure to get the recoil term correctly. By inserting (9.148) find a transport equation for $g_{n,e}(\boldsymbol{v}, \boldsymbol{r}, \boldsymbol{R})$, where the range and energy deposition profile enter as input.

References

Abramowitz M. and Stegun I.A. (1964): *Handbook of mathematical functions*. Dover, New York

Alder B.J. and Wainwright T.E. (1959): Studies in molecular dynamics. I. General method. J Chem Phys **31**, 459–466

Andersen H.H. (1979): Depth resolution in sputter profiling. Appl Phys **18**, 131–140

Andersen H.H. (1987): Computer simulations of atomic collisions in solids with special emphasis on sputtering. Nucl Instrum Methods B **18**, 321–343

Andersen H.H., Garfinkel A.F., Hanke C.C. and Sørensen H. (1966): Stopping power of aluminium for 5-12 MeV protons and deuterons. Mat Fys Medd Dan Vid Selsk **35 no. 4**, 1–24

Andersen H.H. and Sigmund P. (1965): Defect distributions in channeling experiments. Nucl Instrum Methods **38**, 238–240

Ashworth D.G., Oven R. and Mundin B. (1990): Representation of ion implantation profiles by Pearson frequency distribution curves. J Phys D **23**, 870–876

Baroody E.M. (1964): Stopping by elastic collisions of particles from unidirectional plane source. J Appl Phys **35**, 2074–2085

Barrett J.H. (1968): Location of shoulders in channeling phenomena. Phys Rev **166**, 219–221

Beeler J.R. and Besco D.G. (1964): Effects of channeling on damage production in iron. Phys Rev **134**, A530–A532

Berger M.J. (1963): Monte Carlo calculation of the penetration and diffusion of fast charged particles. Methods Comp Phys **1**, 135–215

Brice D.K. (1970): Ion implantation depth distributions: Energy deposition into atomic processes and ion locations. Appl Phys Lett **16**, 103–106

Brice D.K. (1974): Heavy particle range and energy deposition distributions in solids. J Nucl Mater **53**, 123–219

Brice D.K. (1975a): *Ion Implantation Range and Energy Deposition Distributions*, vol. 1. Plenum, New York

Brice D.K. (1975b): Recoil contribution to ion-implantation energy-deposition distributions. J Appl Phys **46**, 3385–3394

Burenkov A.F., Komarov F.F. and Fedotov S.A. (1992a): The ion charge state fluctuation effect during high energy ion implantation: Monte-Carlo simulation. Nucl Instrum Methods B **67**, 35

Burenkov A.F., Komarov F.F. and Fedotov S.A. (1992b): The transport equation approach for the simulation of charge state fluctuation effects during ion implantation into solids. Nucl Instrum Methods B **67**, 30–34

Chasman C., Jones K.W., Kraner H.W. and Brandt W. (1968): Band-gap effects in stopping of Ge^{72} atoms in germanium. Phys Rev Lett **21**, 1430–1433

Chasman C., Jones K.W. and Ristinen R.A. (1965): Measurement of energy loss of germanium atoms to electrons in germanium at energies below 100 keV. Phys Rev Lett **15**, 245

Davies J.A., Friesen J. and McIntire J.D. (1960a): A radiochemical technique for studying range-energy relationships for heavy ions of keV energies in aluminium. Can J Chem **38**, 1526–1534

Davies J.A. and Jespersgård P. (1966): Anomalous penetration of xenon in tungsten crystals – a diffusion effect. Can J Physics **44**, 1631

Davies J.A., McIntyre J.D., Cushing R.L. and Lounsbury M. (1960b): The range of alkali metal ions of kiloelectron volt energies in aluminum. Can J Chem **38**, 1535–1546

Dederichs P.H. (1965): Die räumliche Struktur einer Defektkaskade im Gasmodell. phys stat sol **10**, 303

Domeij B. and Eriksson L. (1965): Radon implant in tungsten. Private communication

Eckstein W. (1991): *Computer simulation of ion-solid interactions*. Springer-Verlag, Berlin

Eriksson L., Davies J.A. and Jespersgaard P. (1967): Range measurements in oriented tungsten single crystals (0. 1-1. 0 MeV). I. Electronic and nuclear stopping powers. Phys Rev **161**, 219–234

Feldman L.C. and Mayer J.W. (1986): *Fundamentals of surface and thin film analysis*. North Holland, New York

Feller W. (1966): *An introduction to probability theory and its applications*, vol. 2. Wiley, New York

Ferla A.L., Torrisi L., Galvagno G., Rimini E., Ciavola G., Carnera A. and Gasparotto A. (1993): Implants of aluminum in the 5 -120 MeV energy range into silicon. Nucl Instrum Methods B **73**, 9–13

Friedland E., Kalbitzer S., Hayes M., Klatt C., Konac G. and Langpape C. (1998): Range parameters of gold and lead in carbon and of carbon in gold at reduced energies of $10^{-3} < \epsilon < 1$. Nucl Instrum Methods B **136**, 147–152

Gibson J.B., Goland A.N., Milgram M. and Vineyard G.H. (1960): Dynamics of radiation damage. Phys Rev **120**, 1229–1253

Glazov L.G. (1994): Solution of the kinetic equation for the deposited energy distribution in the power cross section model. J Phys Cond Matter **6**, 4181–4196

Hofer W.O. and Littmark U. (1979): Theoretical treatment of cascade mixing in depth profiling by sputtering. Phys Lett A **71**, 457–460

Hofker W.K., Oosthoek D.P., Koeman N.J. and De Grefte H.A.M. (1975): Concentration Profiles of Boron Implantations in Amorphous and Polycrystalline Silicon. Radiat Eff **24**, 223–231

Holmes D.K. and Leibfried G. (1960): Range of radiation induced primary knockons in the hard core approximation. J Appl Phys **31**, 1046–1056

ICRU (1979): *Average energy to produce an ion pair*, vol. 31 of *ICRU Report*. International Commission of Radiation Units and Measurements, Bethesda, Maryland

Jakas M.M. (1979): Fluctuation in the spatial-distribution of energy deposited by atomic particles. Phys Lett A **72**, 423–426

Jones K.W. and Kraner H.W. (1971): Stopping of 1- to 1.8-keV Ge-73 atoms in germanium. Phys Rev C **4**, 125

Jones K.W. and Kraner H.W. (1975): Energy lost to ionization by 254-eV ^{73}Ge atoms stopping in Ge. Phys Rev A **11**, 1347–1353

Komarov F.F., Komarov A.F. and Mironov A.M. (1999): Influence of initial charge and charge state fluctuations on high-energy ion ranges and track formation. Nucl Instrum Methods B **148**, 159–163

Kornelsen E.V., Brown F., Davies J.A., Domeij B. and Piercy G.R. (1964): Penetration of heavy ions of keV energies into monocrystalline tungsten. Phys Rev **136**, A849–858

L'Ecuyer J., Brassard C., Cardinal C., Chabbal J., Deschenes L., Labrie J.P., Tereault B., Martel J.G. and Jacques R.S. (1976): An accurate and sensitive method for the determination of the depth distribution of light elements in heavy metals. J Appl Phys **47**, 381–382

Leibfried G. (1963): Higher order average of primary recoil distributions. Z Physik **171**, 1–18

Lindhard J., Nielsen V. and Scharff M. (1968): Approximation method in classical scattering by screened Coulomb fields. Mat Fys Medd Dan Vid Selsk **36 no. 10**, 1–32

Lindhard J., Nielsen V., Scharff M. and Thomsen P.V. (1963a): Integral equations governing radiation effects. Mat Fys Medd Dan Vid Selsk **33 no. 10**, 1–42

Lindhard J. and Scharff M. (1961): Energy dissipation by ions in the keV region. Phys Rev **124**, 128–130

Lindhard J., Scharff M. and Schiøtt H.E. (1963b): Range concepts and heavy ion ranges. Mat Fys Medd Dan Vid Selsk **33 no. 14**, 1–42

Littmark U. (1974): En løsning til det reducerede momentproblem og dennes anvendelse på impulsdeponering ved ionbeskydning. Ph.D. thesis, University of Copenhagen

Littmark U. and Sigmund P. (1975): Momentum deposition by heavy-ion bombardment and an application to sputtering. J Phys D **8**, 241–245

Lutz H. and Sizmann R. (1963): Super ranges of fast ions in copper single crystals. Phys Lett **5**, 113–114

McCargo M., Brown F. and Davies J.A. (1963): A reinvestigation of the range of Na^{24} ions of keV energies in aluminium. Can J Chem **41**, 2309–2313

Nielsen K.O. (1956): The range of atomic particles with energies about 50 keV. In M.L. Smith, editor, *Electromagnetically Enriched Isotopes and Mass Spectrometry*. AERE Harwell, Butterworth Sci. Pub., London

Oen O.S., Holmes D.K. and Robinson M.T. (1963): Ranges of energetic atoms in solids. J Appl Phys **34**, 302–312

Paul H. (2013): *Stopping power graphs*. URL `https://www-nds.iaea.org/stopping/`

Pearson K. (1895): Contributions to the Mathematical Theory of Evolution. II. Skew Variation in Homogeneous Material. Phil Trans Roy Soc London **186**, 343–414

Piercy G.R., Brown F., Davies J.A. and McCargo M. (1963): Experimental evidence for the increase of heavy ion ranges by channeling in crystalline structure. Phys Rev Lett **10**, 399–400

Robinson M.T. (1981): Theoretical aspects of monocrystal sputtering. In R. Behrisch, editor, *Sputtering by Particle Bombardment*, vol. 1, 73. Springer, Heidelberg

Robinson M.T. and Oen O.S. (1963): Computer studies of the slowing down of atoms in crystals. Phys Rev **132**, 2385–2398

Robinson M.T. and Torrens I.M. (1974): Computer simulation of atomic-displacement cascades in solids in the binary-collision approximation. Phys Rev B **9**, 5008–5024

Sanders J.B. (1968a): On penetration depths and collision cascades in solid materials. Ph.D. thesis, Leiden University

Sanders J.B. (1968b): Ranges of projectiles in amorphous materials. Can J Physics **46**, 455

Schiøtt H.E. (1966): Range-energy relations for low-energy ions. Mat Fys Medd Dan Vid Selsk **35 no. 9**, 1–20

Shulga V.I. (1983): Computer simulation of single crystal and polycrystal sputtering. 1. Radiat Eff **70**, 65–83

Shulga V.I. and Sigmund P. (1995): Simulation of energy-dependent isotope sputtering. Nucl Instrum Methods B **103**, 383–386

Sigmund P. (1974): Energy density and time constant of heavy-ion-induced elastic-collision spikes in solids. Appl Phys Lett **25**, 169–171

Sigmund P. (2004): *Stopping of heavy ions*, vol. 204 of *Springer Tracts of Modern Physics*. Springer, Berlin

Sigmund P. (2013): Elements of sputtering theory. In T. Som, D. Kanjilal and Y. Huang, editors, *Nanofabrication by Ion-Beam Sputtering: Fundamentals and Applications*, chap. 1, 1–40. Pan Stanford Publishing, Singapore

Sigmund P., Scheidler G.P. and Roth G. (1968): Spatial distribution of defects in cascades. Black spot defects in electron irradiated copper. In *Solid-State Research with Accelerators*, vol. BNL-50083, 374–395. Brookhaven National Laboratory

Sigmund P. and Schinner A. (2002): Binary theory of electronic stopping. Nucl Instrum Methods B **195**, 64–90

Vicanek M. and Urbassek H.M. (1988): Energy and angular distributions of sputtered particles: A comparison between analytical theory and computer simulation results. Nucl Instrum Methods B **30**, 507–513

Wang Y. and Nastasi M. (2010): *Handbook of modern ion beam materials analysis*. Cambridge University Press, Cambridge

Westmoreland J.E. and Sigmund P. (1970): Correlation functions in the theory of atomic collision cascades: Ion location and distribution in depth and size of damage clusters. Radiat Eff **6**, 187–197

Wick G.C. (1949): On the Space Distribution of Slow Neutrons. Phys Rev **75**, 738–756

Wilson W.D., Haggmark L.G. and Biersack J.P. (1977): Calculations of nuclear stopping, ranges and straggling in the low-energy region. Phys Rev B **15**, 2458–2468

Winterbon K.B. (1972): Heavy-ion range profiles and associated damage distributions. Radiat Eff **13**, 215–226

Winterbon K.B. (1975): *Ion Implantation Range and Energy Deposition Distributions*, vol. 2. Plenum Press, New York

Winterbon K.B. (1983a): New method of solution of a Boltzmann equation. Phys Rev Lett **50**, 1723–1725

Winterbon K.B. (1983b): Pearson distributions for ion ranges. Appl Phys Lett **42**, 205–206

Winterbon K.B. (1986): Calculating moments of range distributions. Nucl Instrum Methods B **17**, 193–202

Winterbon K.B., Sigmund P. and Sanders J.B. (1970): Spatial distribution of energy deposited by atomic particles in elastic collisions. Mat Fys Medd Dan Vid Selsk **37 no. 14**, 1–73

Yamamura Y. and Takeuchi W. (1987): Monocrystal sputtering by the computer simulation code ACOCT. Nucl Instrum Methods B **29**, 461–470

Ziegler J.W., Biersack J.P. and Ziegler M.D. (2008): *Stopping and Range of Ions in Matter*. Lulu Press Co, Morrisville, North Carolina

Part V
Penetration of Aggregates

Chapter 10
Penetration of Molecules and Clusters

Abstract The main part of this chapter addresses the penetration of diclusters, i.e., diatomic molecules that enter a stopping medium and move in a more or less correlated manner. Topics of prime interest are Coulomb explosion, multiple scattering, energy loss and charge state. Specific results refer to beams of initially random orientation and to clusters aligned with the beam direction. Selected results are also discussed for larger clusters, mainly hydrogen clusters.

10.1 Introductory Comments

Modern accelerators can deliver beams of molecular ions over a wide energy range. The interaction of such beams with gaseous and solid materials is an active area of both basic and applied research. The penetration properties of such beams are an important aspect of the field of particle penetration.

Interest in the field started with a study by Poizat and Remillieux (1972) of the penetration of swift (MeV) H_2^+ ions through a gold single crystal. Until then the general expectation was that molecules would break up shortly after entering the material and that the fragments would move independently. The observation of a small fraction of molecules in the exiting beam generated a discussion of whether those molecules had penetrated the crystal intact, or whether they had formed by recombination after exiting the foil.

While both possibilities seem realistic, the difference is not necessarily well defined, since the state of binding of a molecule must be more or less affected by the presence of the medium. Caution is indicated, therefore, in talking about penetrating molecules. Instead it has become customary to speak about penetration of clusters of atoms, even when the 'cluster' is made up by only two atoms, commonly called a *dicluster*.

Penetration properties of clusters can be studied by applying the tools used for atomic projectiles. Here the pertinent standard of reference is an atomic beam with the same velocity. Quantities to study are equilibrium charge states, mean energy

P. Sigmund, *Particle Penetration and Radiation Effects Volume 2*,
Springer Series in Solid-State Sciences 179, DOI: 10.1007/978-3-319-05564-0_10,

loss and straggling, multiple scattering as well as radiation effects to be discussed in Volume 3.

Molecular fragments tend to be charged. Therefore, a penetrating cluster experiences *Coulomb explosion*. This implies a gradually increasing internuclear distance with increasing dwell-time in the target as well as an increasing difference in the velocities of the fragments as compared to that of the centre of mass. As a result one may find a multiple-peak structure in the energy-loss spectrum of a penetrating dicluster (Golovchenko and Lægsgaard, 1974, Gemmell et al., 1975).

These observations gave rise to extensive studies of cluster penetration by means of coincidence techniques which reveal the combined influence of Coulomb explosion, energy loss and multiple scattering (Gemmell, 1982). A direct outcome of such studies is the option to deduce the structure of the incident molecular ion from the distribution in phase space of the emerging fragments (Gaillard et al., 1978). This technique developed to a useful tool in the study of molecular ions (Gemmell, 1981).

Another important application area of swift molecular ion beams is the deposition of high densities of energy, giving rise to heating, electron emission, sputtering and associated phenomena. Ion beams may well be competitive with lasers in this respect, the main difference being a strong localization of the deposited energy around the trajectory of the cluster or its fragments.

It will be evident from these introductory remarks that penetration of clusters is a fairly complex phenomenon. I shall, therefore, try to focus on various effects one by one and consider their combined effect in a more cursory manner.

10.2 Coulomb Explosion

10.2.1 Dynamics

As a start, let us treat a simple model of Coulomb explosion. Consider two atomic ions with atomic masses M_1 and M_2 and charges q_1 and q_2 at an internuclear distance $r = r_0$ at time $t = 0$ in vacuum. Due to the mutual Coulomb repulsion, r will increase with time. Energy conservation requires that

$$\frac{\mu}{2}\left(\frac{\mathrm{d}r}{\mathrm{d}t}\right)^2 + \frac{q_1 q_2}{r} = \frac{q_1 q_2}{r_0}\,, \tag{10.1}$$

where $\mu = M_1 M_2/(M_1 + M_2)$ is the reduced mass.

From this you obtain the relative speed $w(r) = \mathrm{d}r/\mathrm{d}t$ as a function of distance,

$$\frac{w(r)}{w_\infty} = \sqrt{1 - \frac{r_0}{r}}\,, \tag{10.2}$$

where

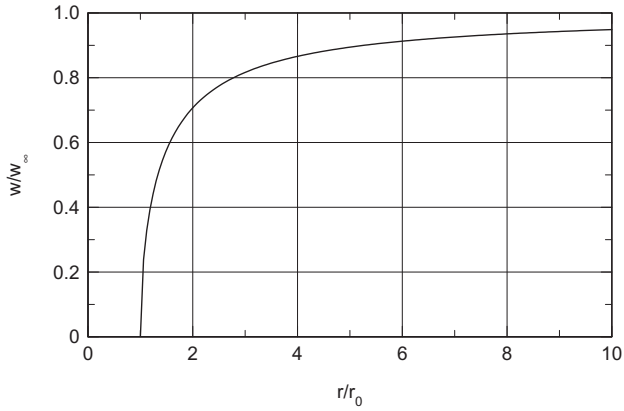

Fig. 10.1 Relative speed $w(r) = \mathrm{d}r/\mathrm{d}t$ of an exploding dicluster according to (10.2)

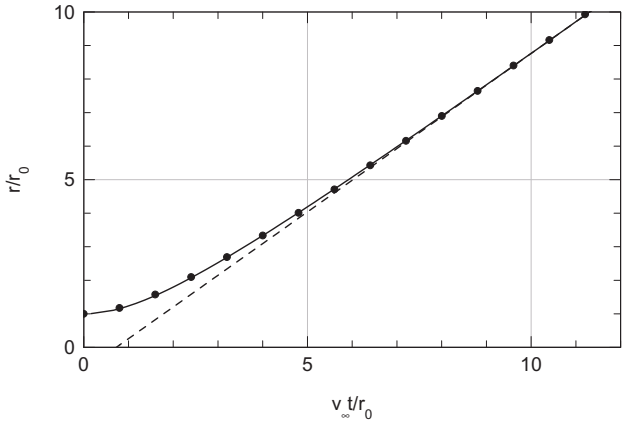

Fig. 10.2 Relative separation of an exploding dicluster according to (10.4). The dashed line shows the asymptotic behaviour. The round symbols indicate the analytical approximation, (10.5)

$$w_\infty = \sqrt{\frac{2q_1q_2}{\mu r_0}} \tag{10.3}$$

is the asymptotic relative speed.

This relation—which is a universal scaling law valid for unscreened Coulomb interaction—is illustrated in Fig. 10.1. It is seen that by the time when the internuclear distance r has doubled, $r = 2r_0$, the relative speed has reached 70% of its asymptotic value.

The distance as a function of time is determined by

$$\frac{w_\infty t}{r_0} = \sqrt{\frac{r}{r_0}\left(\frac{r}{r_0} - 1\right)} + \ln\left(\sqrt{\frac{r}{r_0}} + \sqrt{\frac{r}{r_0} - 1}\right). \tag{10.4}$$

This relation is illustrated in Fig. 10.2. Also (10.4) is a universal scaling law in case of unscreened Coulomb interaction. You may appreciate that a simple analytical interpolation formula,

$$\frac{r}{r_0} \simeq 1 + \frac{(w_\infty t/r_0)^2}{w_\infty t/r_0 + 2.86} \tag{10.5}$$

describes the behaviour accurately over the entire time range.

10.2.2 Time Constant

According to (10.4), Coulomb explosion is characterized by a time constant

$$\tau = \frac{r_0}{w_\infty} \,. \tag{10.6}$$

Let the cluster move with an initial speed v. Then, the pathlength travelled by the projectile during the time τ may be expressed as

$$\frac{v\tau}{a_0} = \frac{1}{\sqrt{2Z_1 Z_2}} \sqrt{\frac{\mu}{m}} \left(\frac{r_0}{a_0}\right)^{3/2} \frac{v}{v_0} \,, \tag{10.7}$$

if we may set $q_1 = Z_1 e$ and $q_2 = Z_2 e$. According to Fig. 10.2, Coulomb explosion is essentially complete at $t \sim 5\tau$. Evidently, for swift particles, where $v \gg v_0$, the right-hand side of (10.7) may become $\gg 1$. This implies that for penetration through a thin solid target, only a minor part of the Coulomb explosion takes place while the cluster moves inside (cf. Problem 10.2).

10.2.3 Transformation to the Laboratory Frame

Consider now a measurement of the final velocity distribution of the two particles, analysed with a detector some distance away from the target. In a reference frame where the molecule is at rest, particle 1 will have a velocity

$$\boldsymbol{w}_1 = \frac{M_2}{M} w_\infty \boldsymbol{e} \,, \tag{10.8}$$

where $M = M_1 + M_2$ is the total mass and $\boldsymbol{e}$ a unit vector defining the initial orientation of the molecule.

In the laboratory frame of reference, atom 1 has the velocity $\boldsymbol{v}_1 = \boldsymbol{v} + \boldsymbol{w}_1$ or the energy

$$E_1 = \frac{M_1}{2} \left(v^2 + w_1^2 + 2w_1 v \cos\phi\right) \,, \tag{10.9}$$

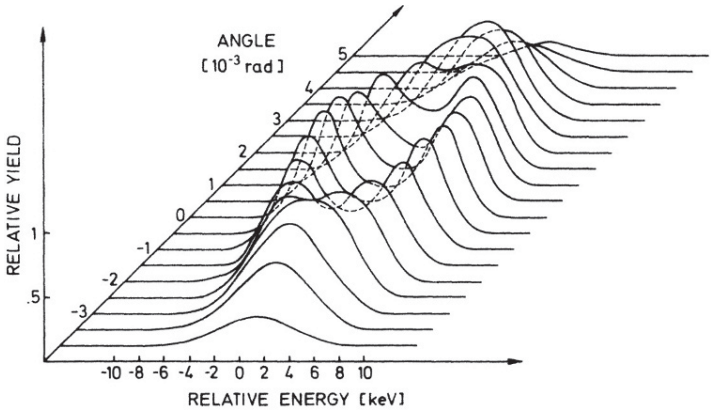

Fig. 10.3 Distribution in energy and angle of H^+ ions resulting from Coulomb explosion of 2 MeV H_2^+ incident on a 2 μg/cm^2 carbon foil. Energy measured relative to 1 MeV. From Golovchenko and Lægsgaard (1974)

where ϕ is the angle between $\boldsymbol{v}$ and $\boldsymbol{e}$, i.e., between the molecular orientation and the beam direction. This reduces to

$$E_1 = \frac{M_1}{2}v^2 + \mu v w_\infty \cos\phi + \frac{M_2}{M}\frac{q_1 q_2}{r_0}\,, \tag{10.10}$$

whereas atom 2 has an energy

$$E_2 = \frac{M_2}{2}v^2 - \mu v w_\infty \cos\phi + \frac{M_1}{M}\frac{q_1 q_2}{r_0}\,. \tag{10.11}$$

Consider the important case of a homonuclear molecule with $M_1 = M_2$ and $q_1 = q_2$. According to (10.10) and (10.11), Coulomb explosion causes the energy spectrum to split into two branches for all orientations except for $\phi = \pi/2$, i.e., when the molecule is oriented perpendicular to the beam.

This is illustrated in Fig. 10.3 which represents the result of measurements by Golovchenko and Lægsgaard (1974) with 2 MeV H_2^+ ions penetrating through a thin carbon foil. The sharp peaks predicted by (10.10) and (10.11) are broadened due to multiple scattering and other effects to be discussed below, but the splitting of the energy spectrum is clearly visible as well as the fact that it is most pronounced in the forward direction corresponding to an orientation $\phi = 0$. The two peaks merge into one at some finite scattering angle θ_0 corresponding to the orientation $\phi = \pm\pi/2$. You are encouraged to evaluate θ_0 in Problem 10.3.

10.2.4 Energy and Angular Spectra

For a given orientation the energy spectrum of atom 1 may be written as

$$f(E_1)\mathrm{d}E_1 = \delta\left(E_1 - M_1 v^2/2 - M_1 w_1^2/2 - M_1 w_1 v\cos\phi\right)\mathrm{d}E_1\,. \tag{10.12}$$

For random orientation we find an energy spectrum

$$\begin{aligned} F(E_1)\mathrm{d}E_1 &= \mathrm{d}E_1 \frac{1}{2}\int_{-1}^{1} \mathrm{d}\cos\phi\; f(E_1) \\ &= \begin{cases} (M_1 w_1 v)^{-1}\mathrm{d}E_1 & \text{for } \frac{M_1}{2}(v-w_1)^2 \le E_1 \le \frac{M_1}{2}(v+w_1)^2 \\ 0 & \text{otherwise.} \end{cases} \end{aligned} \tag{10.13}$$

This represents a constant energy distribution within limits defined by (10.13).

Next, consider the distribution in energy and angle of the emerging particles. In the following we shall deal with swift ion beams, where

$$v \gg w_\infty\,. \tag{10.14}$$

This is encountered most often in the literature, especially in the case considered in Fig. 10.3.

For a given orientation, atom 1 receives a momentum component

$$\Delta P = M_1 w_1 \sin\phi \tag{10.15}$$

perpendicular to the beam direction. Hence, within the small-angle approximation it is deflected by an angle

$$\theta_1 \simeq \frac{w_1}{v}\sin\phi\,. \tag{10.16}$$

We may thus expand (10.12) into

$$\begin{aligned} f(E_1,\theta_1)\mathrm{d}E_1\mathrm{d}\theta_1 = {} & \delta\left(E_1 - M_1 v^2/2 - M_1 w_1 v\cos\phi\right) \\ & \times \delta\left(\theta_1 - \frac{w_1}{v}\sin\phi\right)\mathrm{d}E_1\mathrm{d}\theta_1 \end{aligned} \tag{10.17}$$

where the term $M_1 w_1^2/2$ has been neglected.

Introducing the solid angle $\mathrm{d}^2\Omega_1 = 2\pi\theta_1\,\mathrm{d}\theta_1$ (in the small-angle approximation) and averaging over ϕ you obtain a double-differential distribution

$$F(E_1,\theta_1)\mathrm{d}E_1\,\mathrm{d}^2\Omega_1 = \frac{\mathrm{d}E_1\,\mathrm{d}^2\Omega_1}{2\pi M_1 w_1 v}\delta\left(\theta_1^2 - \left(\frac{w_1}{v}\right)^2 + \left(\frac{\Delta E_1}{M_1 v^2}\right)^2\right)\,, \tag{10.18}$$

where

$$\Delta E_1 = E_1 - \frac{M_1}{2}v^2\,. \tag{10.19}$$

Integration over the solid angle leads back to (10.13). Conversely, integration over the energy leads to

$$F(\theta_1)\mathrm{d}^2\Omega_1 = \frac{\mathrm{d}^2\Omega_1}{2\pi}\frac{v/w_1}{\sqrt{(w_1/v)^2-\theta_1^2}} \tag{10.20}$$

for $\theta_1 \le w_1/v$, and zero otherwise. This distribution was derived by Golovchenko and Lægsgaard (1974). It is characterized by a broad valley around the beam axis and a sharp peak toward the maximum scattering angle w_1/v.

All these features agree qualitatively with Fig. 10.3. A more quantitative analysis requires taking into account multiple scattering as well as the distribution of internuclear distances r_0 and, perhaps, stopping.

10.3 Multiple Scattering

In this section we shall look at the effect of multiple scattering on the motion of a dicluster. Coulomb explosion will be ignored here. The combined effect of Coulomb explosion and multiple scattering will be considered in Sect. 10.6.2.

10.3.1 Independent Atoms

Consider a diatomic cluster entering a foil of thickness x. We want to know the distribution $F_0(\boldsymbol{\alpha}_1, \boldsymbol{\alpha}_2, x)\,\mathrm{d}^2\boldsymbol{\alpha}_1\,\mathrm{d}^2\boldsymbol{\alpha}_2$ of the scattering angles after emergence from the target. Here, $\boldsymbol{\alpha}_1$ and $\boldsymbol{\alpha}_2$ are vectorial scattering angles in the small-angle approximation.

For reference, assume the two atoms to scatter independently of each other, so that

$$F_0(\boldsymbol{\alpha}_1, \boldsymbol{\alpha}_2, x) = F(\alpha_1, x)F(\alpha_2, x) \tag{10.21}$$

or, by (7.35),

$$F_0(\boldsymbol{\alpha}_1, \boldsymbol{\alpha}_2, x) = \frac{1}{(2\pi)^4}\int \mathrm{d}^2\boldsymbol{k}_1 \int \mathrm{d}^2\boldsymbol{k}_2\, \mathrm{e}^{\mathrm{i}[\boldsymbol{k}_1\cdot\boldsymbol{\alpha}_1+\boldsymbol{k}_2\cdot\boldsymbol{\alpha}_2]-Nx[\sigma_1(k_1)+\sigma_2(k_2)]}\,, \tag{10.22}$$

$$\sigma_i(k) = \int \mathrm{d}\sigma_i(\boldsymbol{\phi})\left[1-\mathrm{e}^{-\mathrm{i}\boldsymbol{k}\cdot\boldsymbol{\phi}}\right]; \qquad i = 1, 2\,, \tag{10.23}$$

where $\mathrm{d}\sigma_i(\boldsymbol{\phi})$ is the differential scattering cross section of atom i in the small-angle approximation.

It is convenient to introduce the scattering angle of the centre-of-mass,

$$\boldsymbol{\alpha} = \frac{M_1}{M}\boldsymbol{\alpha}_1 + \frac{M_2}{M}\boldsymbol{\alpha}_2\,, \tag{10.24}$$

where $M = M_1 + M_2$, and the relative scattering angle

$$\Delta\boldsymbol{\alpha} = \boldsymbol{\alpha}_1 - \boldsymbol{\alpha}_2 \,. \tag{10.25}$$

As we have seen in the previous section, the quantity of prime interest is the relative motion of the two atoms. This implies that we are mostly interested in the distribution

$$F_0(\Delta\alpha, x) = \int \mathrm{d}^2\boldsymbol{\alpha}\; F(\boldsymbol{\alpha}_1, \boldsymbol{\alpha}_2, x) = \frac{1}{(2\pi)^2} \int \mathrm{d}^2\boldsymbol{k}\; \mathrm{e}^{\mathrm{i}\boldsymbol{k}\cdot\Delta\boldsymbol{\alpha} - Nx[\sigma_1(k)+\sigma_2(k)]} \,. \tag{10.26}$$

In other words, the distribution in relative scattering angle reflects single scattering governed by the differential cross section

$$\mathrm{d}\sigma(\boldsymbol{\phi}) = \mathrm{d}\sigma_1(\boldsymbol{\phi}) + \mathrm{d}\sigma_2(\boldsymbol{\phi}) \,. \tag{10.27}$$

10.3.2 Correlated Scattering

The assumption of independent scattering cannot be justified in general: If the cluster is aligned with the beam direction, the two atoms will scatter on a target atom at approximately the same impact parameter. Therefore, let us go one step further and take into account the orientation of the dicluster. We may define a differential cross section $\mathrm{d}\sigma(\boldsymbol{\phi}_1, \boldsymbol{\phi}_2)$ for scattering of atom 1 by an angle $(\boldsymbol{\phi}_1, \mathrm{d}^2\boldsymbol{\phi}_1)$ and atom 2 by an angle $(\boldsymbol{\phi}_2, \mathrm{d}^2\boldsymbol{\phi}_2)$ in a collision with a single target atom. With this, the multiple-scattering distribution reads

$$F(\boldsymbol{\alpha}_1, \boldsymbol{\alpha}_2, x) = \frac{1}{(2\pi)^4} \int \mathrm{d}^2\boldsymbol{k}_1 \int \mathrm{d}^2\boldsymbol{k}_2\, \mathrm{e}^{\mathrm{i}(\boldsymbol{k}_1\cdot\boldsymbol{\alpha}_1 + \boldsymbol{k}_2\cdot\boldsymbol{\alpha}_2) - Nx\sigma(\boldsymbol{k}_1, \boldsymbol{k}_2)} \tag{10.28}$$

with

$$\sigma(\boldsymbol{k}_1, \boldsymbol{k}_2) = \int \mathrm{d}\sigma(\boldsymbol{\phi}_1, \boldsymbol{\phi}_2) \left[1 - \mathrm{e}^{-\mathrm{i}(\boldsymbol{k}_1\cdot\boldsymbol{\phi}_1 + \boldsymbol{k}_2\cdot\boldsymbol{\phi}_2)}\right] \tag{10.29}$$

in complete analogy with the single-particle distribution.

To find the differential cross section, vectorial impact parameters $(\boldsymbol{p}_1, \boldsymbol{p}_2)$ are defined according to Fig. 10.4, and the projection of the internuclear-distance vector $\boldsymbol{r}$ on the impact plane is denoted as $\boldsymbol{\rho}$. With this the differential cross section reads

$$\mathrm{d}\sigma(\boldsymbol{\phi}_1, \boldsymbol{\phi}_2) = \mathrm{d}^2\boldsymbol{\phi}_1\, \mathrm{d}^2\boldsymbol{\phi}_2 \int \mathrm{d}^2\boldsymbol{p}_1 \int \mathrm{d}^2\boldsymbol{p}_2 \\ \delta\left(\boldsymbol{\phi}_1 - \boldsymbol{\phi}_1(\boldsymbol{p}_1)\right) \delta\left(\boldsymbol{\phi}_2 - \boldsymbol{\phi}_2(\boldsymbol{p}_2)\right) \delta\left(\boldsymbol{p}_1 - \boldsymbol{p}_2 + \boldsymbol{\rho}\right) . \tag{10.30}$$

The transport cross section now reads

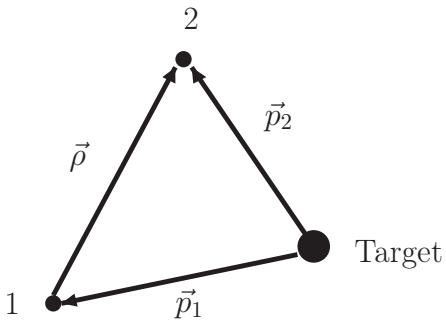

Fig. 10.4 Small-angle scattering of dicluster on target atom viewed in the impact plane perpendicular to the beam direction

$$\sigma(\boldsymbol{k}_1, \boldsymbol{k}_2) = \int \mathrm{d}^2\boldsymbol{p}_1 \int \mathrm{d}^2\boldsymbol{p}_2\, \delta\left(\boldsymbol{p}_1 - \boldsymbol{p}_2 + \boldsymbol{\rho}\right) \left(1 - \mathrm{e}^{-\mathrm{i}[\boldsymbol{k}\cdot\boldsymbol{\phi}_1(\boldsymbol{p}_1) + \boldsymbol{k}\cdot\boldsymbol{\phi}_2(\boldsymbol{p}_2)]}\right). \quad (10.31)$$

Consider again the distribution in the relative scattering angle $\Delta\boldsymbol{\alpha}$. In straight analogy with the calculation in the previous section you find

$$F(\Delta\boldsymbol{\alpha}, x) = \int \mathrm{d}^2\boldsymbol{\alpha}\, F(\boldsymbol{\alpha}_1, \boldsymbol{\alpha}_2, x) = \frac{1}{(2\pi)^2} \int \mathrm{d}^2\boldsymbol{k}\, \mathrm{e}^{\mathrm{i}\boldsymbol{k}\cdot\Delta\boldsymbol{\alpha} - Nx\sigma(\boldsymbol{k}, -\boldsymbol{k})}. \quad (10.32)$$

It is of interest to identify the deviation from the uncorrelated case, (10.26). With that in mind, write (10.32) as

$$F(\Delta\boldsymbol{\alpha}, x) = \frac{1}{(2\pi)^2} \int \mathrm{d}^2\boldsymbol{k}\, \mathrm{e}^{\mathrm{i}\boldsymbol{k}\cdot\Delta\boldsymbol{\alpha} - Nx[\sigma_1(k) + \sigma_2(k) + \Delta\sigma(\boldsymbol{k})]} \quad (10.33)$$

with

$$\Delta\sigma(\boldsymbol{k}) = -\int \mathrm{d}^2\boldsymbol{p}_1 \int \mathrm{d}^2\boldsymbol{p}_2\, \delta\left(\boldsymbol{p}_1 - \boldsymbol{p}_2 + \boldsymbol{\rho}\right) \left[1 - \mathrm{e}^{-\mathrm{i}\boldsymbol{k}\cdot\boldsymbol{\phi}_1(\boldsymbol{p}_1)}\right] \left[1 - \mathrm{e}^{\mathrm{i}\boldsymbol{k}\cdot\boldsymbol{\phi}_2(\boldsymbol{p}_2)}\right]. \quad (10.34)$$

10.3.3 Examples

10.3.3.1 Alignment

In case of perfect alignment we have

$$\boldsymbol{\rho} = 0 \quad (10.35)$$

and hence,

$$\Delta\sigma(\boldsymbol{k}) = -\int \mathrm{d}^2\boldsymbol{p}\left[1-\mathrm{e}^{-\mathrm{i}\boldsymbol{k}\cdot\boldsymbol{\phi}_1(\boldsymbol{p})}\right]\left[1-\mathrm{e}^{\mathrm{i}\boldsymbol{k}\cdot\boldsymbol{\phi}_2(\boldsymbol{p})}\right]. \tag{10.36}$$

10.3.3.2 Random Orientation

In the case of random orientation we may assume that only a small fraction of the beam is affected by correlation. Hence, we may assume $\Delta\sigma(\boldsymbol{k})$ to be small, so that $\exp[-Nx\Delta\sigma(\boldsymbol{k})] \simeq 1 - Nx\Delta\sigma(\boldsymbol{k})$. This allows to carry out the angular average,

$$\langle\delta(\boldsymbol{p}_1-\boldsymbol{p}_2+\boldsymbol{\rho})\rangle = \frac{1}{2\pi r\sqrt{r^2-(\boldsymbol{p}_1-\boldsymbol{p}_2)^2}}, \tag{10.37}$$

cf. (8.92), Vol. 1. For not too low beam energy the effective interaction range of the nuclear interaction is small compared to the internuclear distance. Hence,

$$\langle\delta(\boldsymbol{p}_1-\boldsymbol{p}_2+\boldsymbol{\rho})\rangle \simeq \frac{1}{2\pi r^2}. \tag{10.38}$$

Then we find

$$F(\Delta\boldsymbol{\alpha}, x) = F_0(\Delta\boldsymbol{\alpha}, x) + F_1(\Delta\boldsymbol{\alpha}, x) + \ldots \tag{10.39}$$

with

$$F_1(\Delta\alpha, x) = \frac{Nx}{(2\pi)^3 r^2}\int \mathrm{d}^2\boldsymbol{k}\,\sigma_1(k)\sigma_2(k)\,\mathrm{e}^{\mathrm{i}\boldsymbol{k}\cdot\Delta\boldsymbol{\alpha}-Nx[\sigma_1(k)+\sigma_2(k)]}. \tag{10.40}$$

10.3.3.3 $\boldsymbol{\phi^{-2}}$ Scattering

For qualitative orientation, consider a homonuclear dicluster and a scattering law

$$\mathrm{d}\sigma(\phi) = C\frac{\mathrm{d}\phi}{\phi^2}. \tag{10.41}$$

With this we find

$$\sigma(k) = Ck \tag{10.42}$$

$$\Delta\sigma(k) = -2Ck, \tag{10.43}$$

For the perfectly-aligned case this leads to

$$F(\Delta\alpha, x) \equiv \delta(\Delta\boldsymbol{\alpha}), \tag{10.44}$$

as it must be.

For the orientational average we have

$$F_0(\Delta\alpha, x) = \frac{2NCx}{2\pi} \frac{1}{[(2NCx)^2 + \Delta\alpha^2]^{3/2}} \tag{10.45}$$

$$F_1(\Delta\alpha, x) = \frac{2NCx}{2\pi} \frac{3NC^2x}{2\pi r^2} \frac{2(2NCx)^2 - 3\Delta\alpha^2}{[(2NCx)^2 + \Delta\alpha^2]^{7/2}} . \tag{10.46}$$

This may be written in the form

$$\frac{F_1(\Delta\alpha, x)}{F_0(\Delta\alpha, x)} = \frac{3}{4\pi r^2 Nx} \frac{1}{\alpha_1^2} \frac{1 - 3(\Delta\alpha/\alpha_1)^2/2}{1 + (\Delta\alpha/\alpha_1)^2}, \tag{10.47}$$

where $\alpha_1 = 2NCx$ is close to the halfwidth. This function decreases rapidly with α_1 and with x.

10.4 Energy Loss

Correlation effects of the kind experienced in multiple scattering are also observed in energy loss. They tend to be more pronounced here, because the interaction range of electronic stopping is larger than that of elastic scattering. In the literature you find the terminologies 'proximity effect' or 'vicinage effect', both of which refer to correlations in pertinent impact parameters.

We consider the mean energy loss of a swift n-atomic cluster. To establish a reference, assume the atoms to interact independently with the target atoms. Then the total energy loss will be

$$\frac{\mathrm{d}E}{\mathrm{d}x} = N \sum_{s=1}^{n} S_s , \tag{10.48}$$

where S_s is the stopping cross section for an individual atomic ion s. Deviations from this expression are conventionally expressed by the stopping ratio

$$R = \frac{S}{\sum_s S_s} , \tag{10.49}$$

where S is the stopping cross section for the cluster.

Indications of deviations from $R = 1$ were first reported by Ewing (1962). Calculations and measurements by Brandt et al. (1974) confirmed the existence of the effect[1]. Extensive measurements have been performed with swift proton clusters. According to a compilation by Arista (2000), stopping ratios for H_2^+ in carbon have been measured by several groups and are reported to lie between $R = 0.8$ and 1.4, dependent on beam energy and target thickness.

[1] However, Shubeita et al. (2011) found significantly lower enhancement factors than those reported by Brandt et al. (1974)

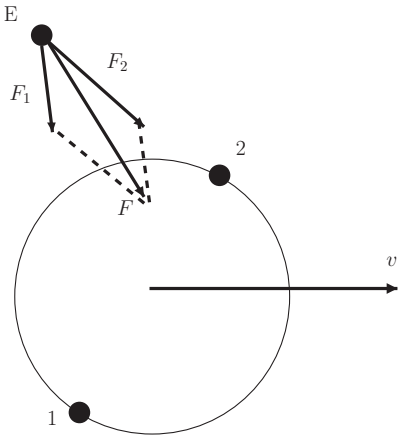

Fig. 10.5 Proximity effect in energy loss. See text. From Schinner and Sigmund (2012)

10.4.1 Qualitative Considerations

If the range of interaction between the projectile atoms and the target electrons far exceeds the internuclear distance of the cluster, the latter will effectively act as one particle with the combined charge $\sum_s q_s$, as far as distant interactions are concerned. This is conventionally called the 'united-atom limit'. As regards close interactions, the atoms in the cluster tend to act independently. Therefore, the actual stopping cross sections must be expected to lie below that of the united atom.

In the opposite case of a short interaction range, a proximity effect can only be expected for specific orientations of a cluster, such as has been seen in the case of a dicluster aligned with the beam direction in case of multiple scattering, analysed in Sect. 10.3.

Consider first a diatomic cluster. Identifying the interaction range with the adiabatic radius we may expect a significant proximity effect for

$$\frac{v}{\omega} \gtrsim r \,, \tag{10.50}$$

where r is the instantaneous internuclear distance in the cluster and ω a representative resonant frequency of weakly-bound target electrons. With $\hbar\omega \sim e^2/2a_0$ (10.50) reads

$$\frac{v}{v_0} > \frac{1}{2}\frac{r}{a_0} \sim 1 \tag{10.51}$$

for $r \sim 2a_0$.

We may conclude that the proximity effect in energy loss must have an onset around $v \sim v_0$, and it can be treated by the Born approximation or classical theory dependent on Bohr's kappa parameter $\kappa = 2Z_1 v_0/v$.

Next, consider a molecule made up by two atoms 1 and 2 interacting with a classical electron E (Fig. 10.5). The force acting on the electron is given by the vector sum $\boldsymbol{F} = \boldsymbol{F}_1 + \boldsymbol{F}_2$ of the forces from the two constituents. A similar relation

holds for the momentum transfer $\boldsymbol{P}$. Hence, the kinetic-energy transfer is greater than the sum of individual energy transfers if $\boldsymbol{P}_1 \cdot \boldsymbol{P}_2 > 0$, i.e., the angle between $\boldsymbol{P}_1$ and $\boldsymbol{P}_2$ must be less than 90°. Thus, for electrons located outside the circle indicated in Fig. 10.5 the energy loss is enhanced, while it is weakened for electrons located inside the circle.

Since the effective interaction range increases with the beam speed v, the relative significance of the region of enhanced energy loss increases with increasing speed if r is constant. Conversely, as r increases because of Coulomb explosion, the region of decreased energy loss increases, resulting in a decrease in the stopping ratio R. Moreover, screening of the interaction due to electrons accompanying the projectile ions must diminish the relative significance of the region of enhanced stopping. Therefore, R must be expected to decrease with decreasing charge state.

The first theoretical treatments (Brandt et al., 1974, Arista, 1978) as well as numerous subsequent ones—see Arista (2000) for a comprehensive review—are based on dielectric stopping theory. We shall come back to this formalism below, but as Fig. 10.5 indicates, the origin of non-additive stopping is the vector nature of the ion-electron interaction. For that reason it appears most instructive to treat the problem first as an interaction with an isolated target atom.

In Bethe theory, where the stopping cross section is $\propto Z_1^2$, an upper bound for enhanced stopping may be found via the united-atom limit, i.e., an atom with atomic number $\sum_s Z_s$. This suggests

$$R_{\max} = \frac{\left[\sum_s Z_s\right]^2}{\sum_s Z_s^2} \,. \tag{10.52}$$

For a homonuclear cluster this would be $R_{\max} = n$, the number of atoms in the cluster. At the velocities where measurements have been made, observed values are not anywhere near this limit.

10.4.2 Born Approximation

Treatments of the proximity effect in stopping on the basis of the Bethe theory were reported by Steinbeck and Dettmann (1978), Basbas and Ritchie (1982), Ray et al. (1992) for bare cluster ions and by Jensen and Sigmund (2000) for screened cluster ions.

The interaction between a swift point charge $Z_1 e$ and an atom was treated within the Born approximation in Sect. 4.3.2, Vol. 1. We may extend this treatment to the interaction of two point charges $Z_1 e$, $Z_2 e$ with an atom by making the replacement

$$\mathcal{V}(\boldsymbol{r}, t) = \sum_{\nu=1}^{Z_0} \frac{-Z_1 e^2}{|\boldsymbol{r}_\nu - \boldsymbol{R}(t)|} \Rightarrow \sum_{\nu=1}^{Z_0} \left(\frac{-Z_1 e^2}{|\boldsymbol{r}_\nu - \boldsymbol{R}_1(t)|} + \frac{-Z_2 e^2}{|\boldsymbol{r}_\nu - \boldsymbol{R}_2(t)|} \right) , \tag{10.53}$$

where Z_0 now denotes the atomic number of the target atom.

Introducing relative coordinate vectors,

$$\boldsymbol{R}_1(t) = \boldsymbol{R}(t) + \frac{M_2}{M}\boldsymbol{r}(t); \quad \boldsymbol{R}_2(t) = \boldsymbol{R}(t) - \frac{M_1}{M}\boldsymbol{r}(t)\,, \tag{10.54}$$

we may assume the time dependence in $r(t)$ by Coulomb explosion to be small for the duration of the interaction, so that

$$r(t) \simeq r = \text{constant}\,. \tag{10.55}$$

We may repeat the derivation presented in Sects. 4.3.2 and 4.3.4, Vol. 1 (cf. Problem 10.4) on the basis of (10.53) and (10.54). Instead of (4.5.2), Vol. 1, we then arrive at the expression

$$\sigma_j = \frac{4e^4}{\hbar^2 v}\int \frac{\mathrm{d}^3\boldsymbol{q}}{q^4}\left|F_{j0}(\boldsymbol{q})\right|^2 \delta\left(\omega_{j0} - \boldsymbol{q}\cdot\mathbf{v}\right) \times\left[Z_1^2 + Z_2^2 + 2Z_1Z_2\cos(\boldsymbol{q}\cdot\boldsymbol{r})\right] \tag{10.56}$$

for the excitation cross section of state j of the target atom.

By solving Problem 10.5 you will convince yourself that the factor in the square brackets may be generalized to an n-atomic cluster according to

$$Z_1^2 + Z_2^2 + 2Z_1Z_2\cos(\boldsymbol{q}\cdot\boldsymbol{r}) \to \sum_s Z_s^2 + \sum_{s\neq s'} Z_sZ_{s'}\cos\left(\boldsymbol{q}\cdot\boldsymbol{r}_{ss'}\right)\,. \tag{10.57}$$

The term $\propto \sum_s Z_s^2$ represents the sum of the uncorrelated cross sections of the moving atoms leading to (10.48). The remaining terms, which are $\propto 2Z_sZ_{s'}$, contain factors $\cos(\boldsymbol{q}\cdot\boldsymbol{r}_{ss'})$ in the integrand and thus depend on the angle between $\boldsymbol{v}$ and the distance vector $\boldsymbol{r}_{ss'} = \boldsymbol{R}_s - \boldsymbol{R}_{s'}$.

Going back for a moment to the dicluster, you may expect, based on the discussion of multiple scattering, that two cases offer themselves for straight evaluation of (10.56),

1. random orientation, where we may replace $\cos(\boldsymbol{q}\cdot\boldsymbol{r})$ by

$$\langle\cos(\boldsymbol{q}\cdot\boldsymbol{r})\rangle = \frac{\sin(qr)}{qr}\,, \tag{10.58}$$

2. complete alignment with the beam, where

$$\cos(\boldsymbol{q}\cdot\boldsymbol{r}) = \cos\left(\frac{\omega_{j0}r}{v}\right)\,. \tag{10.59}$$

You may then follow the derivation of the stopping cross section described in Sects. 4.3.4 and 4.5.3, Vol. 1, with the result

$$S = \frac{2\pi Z_1^2 e^4}{mv^2} \sum_j \left(\epsilon_j - \epsilon_0\right) \int \frac{\mathrm{d}Q}{Q^2} \left|F_{j0}(q)\right|^2 \left[Z_1^2 + Z_2^2 + 2Z_1 Z_2 u(r)\right] , \tag{10.60}$$

and correspondingly for an n-atomic cluster. The function $u(r)$ reads

$$u(r) = \begin{cases} \dfrac{\sin(qr)}{qr} & \text{random orientation} \\ \text{for} & \\ \cos\left(\frac{\omega_{j0} r}{v}\right) & \text{perfect alignment.} \end{cases} \tag{10.61}$$

You are encouraged to derive a more general expression in Problem 10.6.

10.4.2.1 Bethe Limit

In the Bethe limit, i.e., when shell corrections are ignored, the stopping cross section reduces to

$$S = \frac{2\pi Z_0 e^4}{mv^2} \sum_j f_{j0} \int_{(\hbar\omega_{j0})^2/2mv^2}^{2mv^2} \frac{\mathrm{d}Q}{Q} \times \left[\sum_s Z_s^2 + 2 \sum_{s<s'} Z_s Z_{s'} g(r_{ss'})\right] \tag{10.62}$$

in the notation of Sect. 4.5.4, Vol. 1.

10.4.2.2 Random Orientation

For random orientation, (10.62) can be integrated (Steinbeck and Dettmann, 1978, Basbas and Ritchie, 1982) and expressed in terms of integral cosine functions (Abramowitz and Stegun, 1964). This calculation has been left to the reader as Problem 10.7. In the limit of $2mv^2 \gg \hbar\omega_{j0}$ you will then find

$$\Delta S = 2 \sum_{s<s'} Z_s Z_{s'} \frac{4\pi Z_0 e^4}{mv^2} \sum_j f_{j0} \left[\ln \frac{1}{q_{\min} r_{ss'}} + 1 - \gamma\right] , \tag{10.63}$$

where

$$q_{\min} = \omega_{j0}/v \tag{10.64}$$

and $\gamma = 0.57721$ is Euler's constant.

You may note that the upper limit, $q_{\max} = 2mv/\hbar$, does not appear in (10.63). This reflects the fact that the proximity effect results from distant interactions.

Insertion of (10.64) leads to an expression containing the I-value,

$$\ln I = \sum_j f_{j0} \ln(\hbar\omega_{j0}) \tag{10.65}$$

according to (4.119), Vol. 1. Thus, (10.63) reduces to

$$\Delta S = 2 \sum_{s<s'} Z_s Z_{s'} \frac{4\pi Z_0 e^4}{mv^2} \ln \frac{1.526\hbar v}{I r_{ss'}} . \tag{10.66}$$

In this form this result was found by Arista (1978) for the Fermi gas. Here the logarithmic term increases monotonically with the beam velocity. However, the increase is slower than that of the Bethe logarithm, $\ln(2mv^2/I)$.

10.4.2.3 Alignment

For perfect alignment, (10.62) leads to

$$\Delta S = 2 \sum_{s<s'} Z_s Z_{s'} \frac{4\pi Z_0 e^4}{mv^2} \sum_j f_{j0} \cos \frac{\omega_{j0} r_{ss'}}{v} \ln \frac{2mv^2}{\hbar\omega_{j0}} . \tag{10.67}$$

Note the oscillatory term $\cos(\omega_{j0} r_{ss'}/v)$. Consider a system with only one significant resonance ω. In this case, ΔS will oscillate around zero as the ratio $r_{ss'}/v$ varies. For a dicluster the stopping cross section itself will have maximum and minimum values $(S_1 \pm S_2)^2$, respectively.

For complete alignment, impact parameters are perfectly correlated. A negative interference must, therefore, come from the time sequence of the two interactions (Arista and Ponce, 1975). For a dicluster, the impulses exerted by the two atoms act coherently for $\omega r/v = 2\pi\mu$, $\mu = 0, 1, 2 \ldots$. Note the adiabatic radius v/ω, mentioned in (10.50) above. Conversely, for $\omega r/v = 2\pi(\mu + 1/2)$ the two impulses are in antiresonance.

10.4.2.4 Harmonic Oscillator

It is useful to evaluate an example for a case where rigorous evaluation is uncomplicated. Such an example is a harmonic-oscillator target atom. The interaction between a single point charge and an oscillator has been presented in Sects. 4.5.3 and A.4.3, Vol. 1.

Starting at (10.60) and inserting the matrix elements $F_{j0}(q)$ for the oscillator, (A.181), Vol. 1, you arrive at

$$\Delta S = \frac{4\pi e^4}{mv^2} \sum_{s<s'} Z_s Z'_s \Delta L_{ss'} , \tag{10.68}$$

where

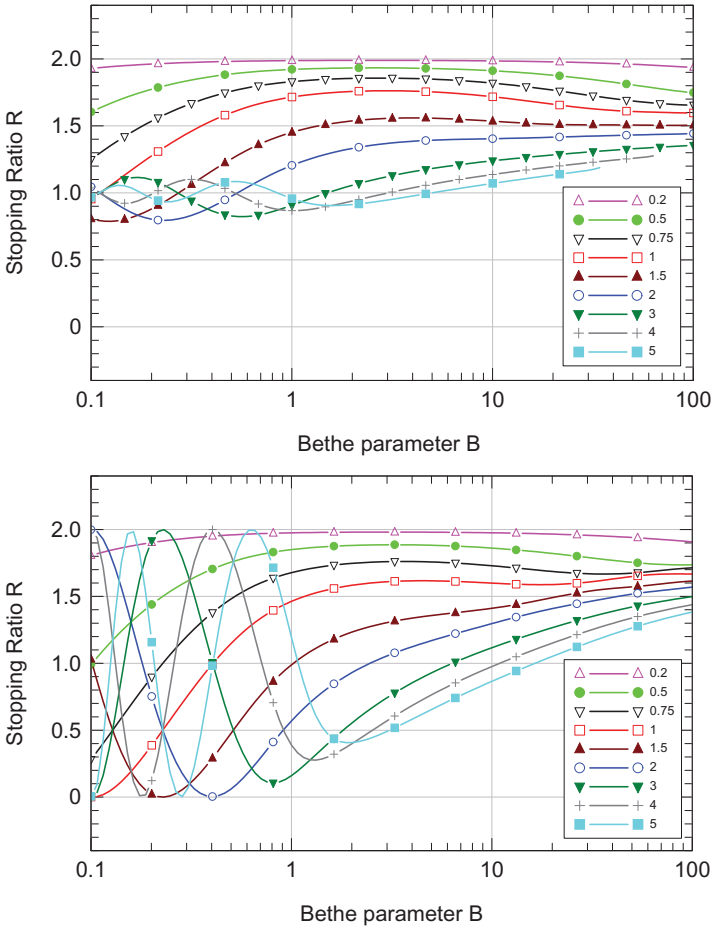

Fig. 10.6 Stopping ratio R versus Bethe parameter $B = 2mv^2/\hbar\omega_0$ for a beam of proton di-clusters oriented randomly (top) and aligned in the beam direction (bottom), interacting with a 3D quantum oscillator with a resonance frequency ω_0. Numbers in the inset indicate the value of the factor $\gamma_0 = r\sqrt{2m\omega_0/\hbar}$. From Sigmund and Schinner (2010)

$$\Delta L_{ss'} = \sum_{\nu=1}^{\infty} \frac{1}{(\nu-1)!} \int_{\nu^2/B}^{\infty} \mathrm{d}t\, t^{\nu-2} \mathrm{e}^{-t} u(r) \tag{10.69}$$

and $u(r)$ is given by (10.61).

With this, proximity is characterized by a dimensionless parameter

$$\gamma_j = r\sqrt{2m\omega_{j0}/\hbar}\,. \tag{10.70}$$

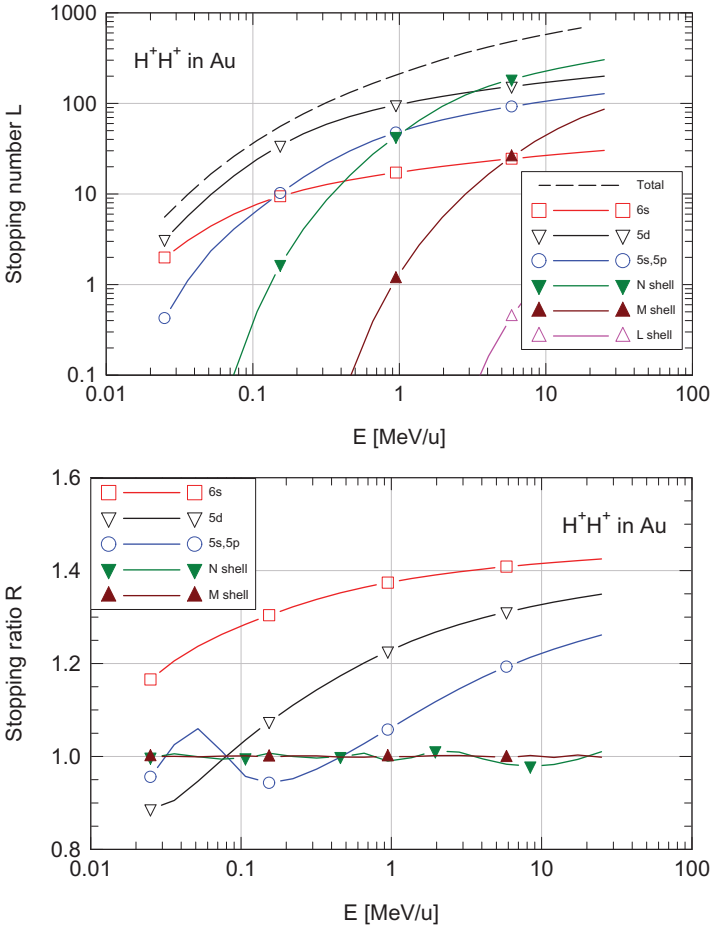

Fig. 10.7 H_2 clusters penetrating through gold. Upper graph: Stopping numbers L for individual shells and the sum. Lower graph: Stopping ratios of individual shells. Evaluated from (10.69) with resonance frequencies and occupation numbers of individual shells taken from ICRU (2005)

Figure 10.6 shows stopping ratios R for a dicluster for a series of values of the parameter γ_0, (10.70). For small values of γ_0, i.e., small internuclear distances r, the stopping ratio is close to the united-atom value $R = 2$. As r increases, R decreases, and at the same time an oscillatory dependence on projectile speed develops, which has been mentioned above and first predicted by Arista and Ponce (1975). These oscillations are most pronounced when the molecule is oriented parallel to the beam (lower graph).

Figure 10.7 shows the case of H_2 diclusters in gold as an example. The upper graph shows stopping numbers for individual shells, including the proximity cor-

rection evaluated from the oscillator model, (10.69), whereas the lower graph shows stopping ratios for individual shells.

It is seen that the dominating contribution to the stopping number—and, hence, to the stopping cross section—stems from target electrons in the 5th and 6th shell up to $\sim$ 1 MeV/u. At higher energies the contribution of inner-shell electrons increases, just as in case of penetrating atomic ions. Conduction electrons contribute significantly only at energies $\lesssim$ 0.1 MeV/u, but they eventually take over at energies not covered in the graph where the Born approximation becomes questionable.

Conversely, the lower graph in Fig. 10.7 shows that stopping ratios > 1 are found for 6s and 5d electrons and, for energies $\gtrsim$ 1 MeV/u, for 5s and 5p electrons. As a consequence, the overall enhancement of the stopping ratio is less than 10% over a wide energy range, in agreement with recent measurements by Shubeita et al. (2011), and contrary to early measurements reported by Brandt et al. (1974).

10.4.3 Classical Theory

Stopping measurements were reported with heavier ions such as N_2 (Steuer et al., 1982) and C_n (Baudin et al., 1994) in a velocity regime near the Bohr speed. In this energy range the validity of the Born approximation is questionable. Moreover, projectile screening becomes important.

Before going into an extension of the Bohr stopping model presented in Sect. 4.2, Vol. 1, have a look at (10.63) together with (10.64). You will notice that these equations do not contain Planck's constant $\hbar$ if you interpret ω_{j0} as a classical resonance frequency. This suggests that essentially the same interference term in the energy loss ought to be derivable from Bohr theory as from the Born approximation.

To appreciate this, remind that in the simple Bethe limit, the stopping cross section of an atom is determined by a logarithmic integral governed by a lower and an upper limit in the wave number q, where $q_{\min}$ reflects Bohr's adiabatic limit which appears both in quantum and classical theory. The upper limit $q_{\max}$, on the other hand, reflects the maximum energy transfer to a target electron. The difference between the atomic stopping cross section and the interference term lies in the factor $2Z_1Z_2u(r)$ in (10.60) with $u(r)$ defined by (10.61). Now, this reduces the effective integration interval to $q \lesssim 1/r$, in agreement with (10.50). Thus, for random orientation the contribution from close collisions to the proximity effect in energy loss is unimportant.

With this, the following treatment will be rather concise. If you are interested in the details, go to Problem 10.8.

10.4.3.1 Extension of Bohr Theory

Bohr theory was extended to clusters of point charges by Basbas and Ritchie (1982) and to clusters of screened atoms by Jensen and Sigmund (2000).

According to (4.11), Vol. 1, the energy transfer in a single interaction between a projectile and a harmonically-bound target electron with a resonant frequency ω_0

can be written as

$$T = \frac{1}{2m}\left|\int \mathrm{d}t\ \boldsymbol{F}(t)\,\mathrm{e}^{\mathrm{i}\omega_0 t}\right|^2 , \tag{10.71}$$

where the time-dependent force $\boldsymbol{F}(t) = -\nabla\mathcal{V}$ is determined by a potential

$$\mathcal{V}(t) = \int \mathrm{d}^3\boldsymbol{q} \sum_s V_s(q)\mathrm{e}^{\mathrm{i}\boldsymbol{q}\cdot(\boldsymbol{r}-\boldsymbol{p}-\boldsymbol{v}t-\boldsymbol{r}_s)} , \tag{10.72}$$

and $\boldsymbol{r}_s$ is the distance of the sth cluster atom from some reference point moving with the cluster. $\boldsymbol{p}$ is the vectorial impact parameter taken from the reference point and $\mathcal{V}_s(r)$ a screened potential characterizing the interaction between the sth cluster atom and a target electron.

From (10.71) you then find

$$\begin{aligned} T(p) = \frac{(2\pi)^2 e^2}{2m} \sum_{s,s'} \int \mathrm{d}^3\boldsymbol{q} \int \mathrm{d}^3\boldsymbol{q}'\,(\boldsymbol{q}\cdot\boldsymbol{q}')V_s(q)V_{s'}(q') \\ \times \mathrm{e}^{\mathrm{i}\boldsymbol{q}\cdot(\boldsymbol{r}-\boldsymbol{p}-\boldsymbol{r}_s)}\mathrm{e}^{-\mathrm{i}\boldsymbol{q}'\cdot(\boldsymbol{r}-\boldsymbol{p}-\boldsymbol{r}_{s'})}\delta(\omega_0 - \boldsymbol{q}\cdot\boldsymbol{v})\delta(\boldsymbol{q}'\cdot\boldsymbol{v} - \boldsymbol{q}\cdot\boldsymbol{v}). \end{aligned} \tag{10.73}$$

Integration over the impact plane yields

$$\begin{aligned} S_{\mathrm{dist}}(v) &= \int \mathrm{d}^2\boldsymbol{p}\, T(p) \\ &= \frac{8\pi^4}{mv} \sum_{ss'} \int \mathrm{d}^3\boldsymbol{q}\, q^2 V_s(q)V_{s'}(q)\mathrm{e}^{\mathrm{i}\boldsymbol{q}\cdot(\boldsymbol{r}_s-\boldsymbol{r}_{s'})}\delta(\omega_0 - \boldsymbol{q}\cdot\boldsymbol{v}) \end{aligned} \tag{10.74}$$

within the dipole limit, i.e., for distant interactions.

We may split (10.74) according to

$$S_{\mathrm{dist}}(v) = \sum_s S_{\mathrm{dist},s}(v) + \sum_{s\neq s'} \Delta S_{\mathrm{dist},ss'}(v) , \tag{10.75}$$

where $S_{\mathrm{dist},s}(v)$ is the distant part of the stopping cross section for an isolated s-projectile and

$$\Delta S_{ss'}(v) = \frac{8\pi^4}{mv} \int \mathrm{d}^3\boldsymbol{q}\, q^2 V_s(q)V_{s'}(q)\mathrm{e}^{\mathrm{i}\boldsymbol{q}\cdot(\boldsymbol{r}_s-\boldsymbol{r}_{s'})}\delta(\omega_0 - \boldsymbol{q}\cdot\boldsymbol{v}), \tag{10.76}$$

an interference term.

10.4.3.2 Random

For random orientation of the projectile we may take the average

$$\left\langle \mathrm{e}^{\mathrm{i}\boldsymbol{q}\cdot(\boldsymbol{r}_s-\boldsymbol{r}_{s'})}\right\rangle = \frac{\sin(qr_{ss'})}{qr_{ss'}}\,, \tag{10.77}$$

where $r_{ss'} = |\boldsymbol{r}_s - \boldsymbol{r}_{s'}|$. Averaging over the orientation of $\boldsymbol{v}$ leads to

$$\langle\delta(\omega_0 - \boldsymbol{q}\cdot\boldsymbol{v})\rangle = \begin{cases} 1/2qv & \text{for } q > \omega_0/v \\ 0 & \text{otherwise.} \end{cases} \tag{10.78}$$

With this we arrive at

$$\Delta S_{ss'} = \frac{4\pi^4}{mv^2 r_{ss'}} \int_{\omega_0/v}^{q_1} 4\pi q^2\,\mathrm{d}q\; V_s(q) V_{s'}(q) \sin(qr_{ss'})\,, \tag{10.79}$$

where q_1 is an unspecified upper limit for the integration. Equation (10.79) reduces to the low-q part of the interference term in (10.71), as you may demonstrate by solving Problem 10.9. As argued above, the upper limit q_1 will be set to infinity. Before actually doing so, let us look at the integral for screened-Coulomb interaction. Following (4.16) we may set

$$V_s(r) = -\frac{q_s e^2}{r} - \frac{(Z_s - q_s)e^2}{r}\, g_s(r/a_s)\,. \tag{10.80}$$

Setting the screening function g_s to

$$g_s(r/a) = \mathrm{e}^{-r/a} \tag{10.81}$$

we find

$$V_s(q) = -\frac{Z_s e^2}{2\pi^2}\,\frac{q^2 + \beta_s/a_s^2}{q^2(q^2 + 1/a_s^2}\,, \tag{10.82}$$

where $\beta_s = q_s/Z_s$. With this we may write (10.79) in the form

$$\Delta S_{ss'} = \frac{2\pi Z_s Z_{s'}}{mv^2} I_{ss'} \tag{10.83}$$

with

$$I_{ss'} = \int_{\omega_0/v}^{q_1} \frac{\mathrm{d}q}{q^2} \sin(qr_{ss'}) \frac{(q^2 + \beta_s/a_s^2)(q^2 + \beta_{ell}/a_{s'}^2)}{(q^2 + 1/a_s^2)(q^2 + 1/a_{s'}^2)}\,. \tag{10.84}$$

This integral is conveniently evaluated numerically. Figure 10.8 shows examples. Except for a slightly oscillatory behaviour, the interference term decreases as the ratio between the internuclear distance and the screening radius increases. The integral is largest for bare ions and negligible for neutral ions. The four graphs differ in the ratio a_{ad}/a, i.e. indicate increasing projectile speed.

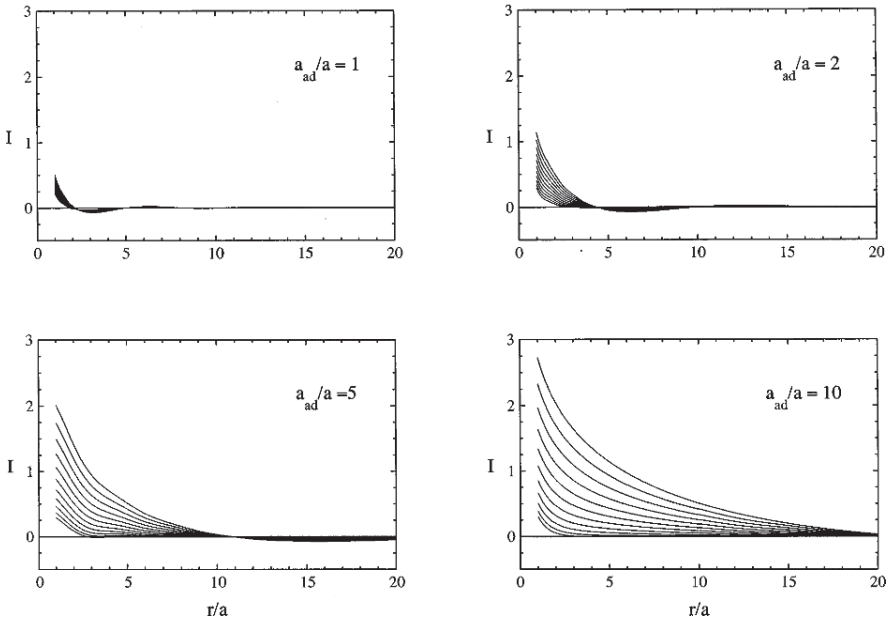

Fig. 10.8 The function $I_{ss'}$ defined in (10.84) for a homonuclear molecule with $r_{ss'} = r$, $a_s = a_{s'} = a$, $a_{\mathrm{ad}} = v/\omega_0$ the adiabatic radius. Charge fractions β/Z in steps of 0.1 from bottom to top. The upper limit in the integral has been set to infinity. From Jensen and Sigmund (2000)

10.4.3.3 Alignment

Going back to (10.76), consider now the case of a diatomic atom oriented along the direction of motion so that

$$\Delta S_{12}(v) = \frac{8\pi^4}{mv} \int \mathrm{d}^3\boldsymbol{q}\, q^2 V_1(q) V_2(q) \mathrm{e}^{\mathrm{i}q_x r_{12}} \delta(\omega_0 - q_x v)\,, \tag{10.85}$$

or

$$\Delta S_{\mathrm{dist},12}(v) = \frac{8\pi^4}{mv} \cos\frac{\omega_0 r_{12}}{v} \int \mathrm{d}^2\boldsymbol{q}\, (q^2 + \omega_0^2/v^2) \\ V_1(\sqrt{q^2 + \omega_0^2/v^2}) V_2(\sqrt{q^2 + \omega_0^2/v^2}), \tag{10.86}$$

where the subscript indicates that this is only the part from distant interactions: If you insert (10.82) you will find that the integral has the usual logarithmic divergence, i.e., close collisions need separate attention in the aligned case.

A proper theory of the close-collision part of the stopping integral on the basis of the Bohr model, operating with free-Coulomb scattering of an electron on a two-centre potential, has not been developed to the author's knowledge. You can, however, get a hint on what results may look like from studies of Steuer and Ritchie

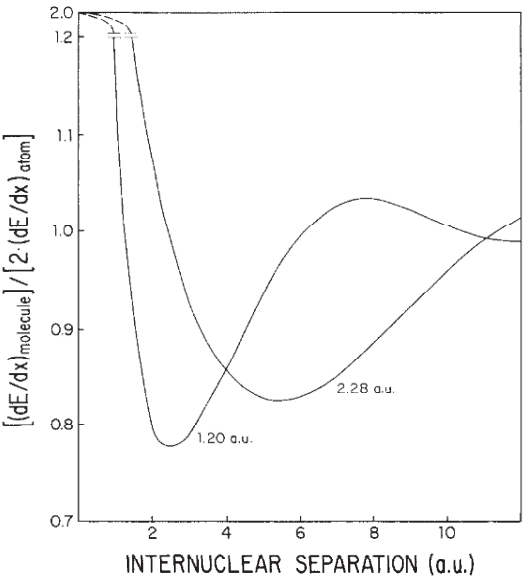

Fig. 10.9 Calculated stopping ratio for N_2 molecular ions in carbon, aligned in the direction of motion and in charge equilibrium for $v/v_0 = 1.20$ and 2.28. From Steuer and Ritchie (1989)

(1988, 1989), based on the Born approximation and screened-Coulomb potentials of the type of (10.72). From Fig. 10.9 you may note the oscillatory behaviour expressed by the factor $\cos(\omega_0 r_{12}/v)$ in (10.86).

10.4.4 Dielectric Theory

Chapter 5, Vol. 1, is devoted to the dielectric theory of stopping. This theory, which was initiated in a classic paper by Fermi (1940), considers the stopping of a charged particle as an aspect of electromagnetic field theory. The interaction between a penetrating particle and the medium induces a polarization field. In electrostatics, such a field is directed opposite to the field of the external charge. For a time-dependent field, the inertia of the target electrons gives rise to a retardation which complicates the matter. Stimulated by Fermi (1939, 1940), and others, early studies focused on the relativistic velocity regime.

The polarization field, which was employed to estimate the influence of the stopping medium on the charge state of an atomic ion in Sect. 1.5.1, offers an alternative way to derive stopping cross sections: Instead of computing the energy transfer to the constituents of the medium you may determine the force exerted on the projectile by the induced field. This procedure was applied by Aa. Bohr (Bohr, 1948a) for distant collisions. Lindhard (1954) generalized it to both distant and close collisions by introducing a wave-number-dependent dielectric function. This was particularly useful for a free electron gas, where stopping cross sections would diverge in the absence of a binding frequency. Lindhard's evaluation demonstrated the correctness of

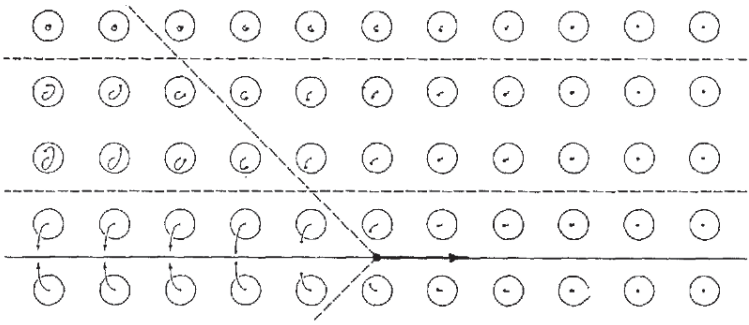

Fig. 10.10 Schematic illustration of the displacement of target electrons during passage of a charged particle. From Bohr (1948b)

Kramers' assertion (Kramers, 1947) that the stopping cross section of a free electron gas is characterized by the plasma frequency ω_P.

10.4.4.1 Qualitative Considerations

As pointed out by Fermi (1939, 1940), the polarization field induced by a swift point charge gives rise to a gas-solid difference in the energy loss of a charged particle: In condensed matter, the range of the Coulomb interaction may be much larger than the interatomic distance. The polarization in the medium will reduce the local field acting on the target electrons and hence give rise to reduced stopping. This density effect is particularly pronounced at relativistic projectile velocities, as discussed in Sect. 5.6.4, Vol. 1.

Bohr (1948b) has given a beautiful illustration of this polarization, which is shown in Fig. 10.10. Electrons are displaced from their equilibrium positions mainly within a cone with its top at the moving particle. The orientation of the displacement shifts as a function of the distance from the trajectory. In the lateral direction the displacement becomes negligible outside the adiabatic radius. Note in particular that there is a pronounced asymmetry in the longitudinal direction.

In Sect. 5.3.3, Vol. 1, it has been shown that the density effect on the stopping force is very small at nonrelativistic velocities. Therefore, a description of energy loss of a point charge in terms of the polarization wake, while illuminating, does not promise new features in addition to what we know from the conventional picture in terms of energy transfer to individual atoms. Especially, in the limit of zero target density, the results are identical, as was shown in Sect. 5.3.2, Vol. 1.

This is different in the context of penetration of composite particles, where the induced field acts on each of the constituent particles. As an example, consider a penetrating dicluster. In Sect. 10.2 the mutual repulsion between the two moving atoms was treated in terms of Coulomb interaction in free space. This ignores the effect of the induced field, in particular a possible orientation effect. Along the same line, electrons bound to a moving point charge experience a modified electric field.

For strongly bound electrons this may imply a Stark shift of the energy levels (Rozet et al., 1987), while for weakly-bound electrons the ionization energy may change.

10.4.4.2 Energy Loss and Induced Field

Consider a cluster of point charges $Z_s e, s = 1, 2, \ldots, n$ penetrating through a homogeneous medium. Then a given charge $Z_{s'}$ experiences the following forces,

$$\boldsymbol{F}_s = Z_s e \boldsymbol{E}^{\text{ind}}_{ss} + \sum_{s' \neq s} Z_s e \boldsymbol{E}^{\text{Coul}}_{s's} + \sum_{s' \neq s} Z_s \boldsymbol{E}^{\text{ind}}_{s's} , \tag{10.87}$$

where $\boldsymbol{E}^{\text{Coul}}_{s's}$ is the Coulomb field of charge s' at the position of charge s and correspondingly for $\boldsymbol{E}^{\text{ind}}_{s's}$.

Summing up over s yields the total stopping force on the cluster,

$$\boldsymbol{F} = \sum_{s} Z_s e \boldsymbol{E}^{\text{ind}}_{ss} + \sum_{s' \neq s} Z_s e \boldsymbol{E}^{\text{ind}}_{s's} , \tag{10.88}$$

where the Coulomb forces have cancelled, since $Z_s e \boldsymbol{E}^{\text{Coul}}_{s's} = -Z_{s'} e \boldsymbol{E}^{\text{Coul}}_{ss'}$.

The first term in (10.88) represents the incoherent superposition of the stopping forces on the constituents of the cluster. The second term represents the proximity effect. Because of the asymmetry of the induced forces that you have seen in Fig. 10.10, this sum will normally be nonvanishing.

Conversely, inspecting (10.87) you will recognize that Coulomb explosion will be modified by the induced force.

10.4.4.3 General Relations

The fundamental equations for the induced field have been derived in Chap. 5, Vol. 1. The scalar potential of the electromagnetic field follows from (5.19), Vol. 1,

$$\Phi(\boldsymbol{r}, t) = \int \mathrm{d}^3\boldsymbol{k}\, \Phi(\boldsymbol{k}, \boldsymbol{k} \cdot \boldsymbol{v})\, \mathrm{e}^{\mathrm{i}(\boldsymbol{k}\cdot\boldsymbol{r} - \omega t)} . \tag{10.89}$$

with

$$\Phi(\boldsymbol{k}, \omega) = \frac{4\pi}{k^2 \varepsilon_l(k, \omega)} \rho_{\text{ext}}(\boldsymbol{k}, \omega) , \tag{10.90}$$

where $\rho_{\text{ext}}(\boldsymbol{k}, \omega)$ represents the charge distribution of the projectile and $\varepsilon_l(k, \omega)$, denoted as $\varepsilon(k, \omega)$ in the following, is the longitudinal dielectric function.

Subtracting the Coulomb potential from (10.90) you find the induced potential

$$\Phi_{\text{ind}}(\boldsymbol{k}, \omega) = \frac{4\pi}{k^2} \left(\frac{1}{\varepsilon(k, \omega)} - 1 \right) \rho_{\text{ext}}(\boldsymbol{k}, \omega) . \tag{10.91}$$

Equations (10.90) and (10.91) assume linear response. The reader interested in an extension to the next order in Z_1 may have a look at Esbensen and Sigmund (1990).

The relation to the stopping force was described in Sect. 5.2.3, Vol. 1. The result for a point charge is

$$-\frac{\mathrm{d}E}{\mathrm{d}x} = \frac{iZ_1^2e^2}{2\pi^2 v}\int \frac{d^3\boldsymbol{k}'}{k^2}\boldsymbol{k}\cdot\boldsymbol{v}\left(\frac{1}{\varepsilon(k,\boldsymbol{k}\cdot\boldsymbol{v})}-1\right). \tag{10.92}$$

according to Lindhard (1954). For an arbitrary stiff charge distribution

$$\rho_{\mathrm{ext}}(\boldsymbol{r}-\boldsymbol{v}t) = \int \mathrm{d}^3\boldsymbol{k}\;\rho_{\mathrm{ext}}(\boldsymbol{k})\,\mathrm{e}^{\mathrm{i}\boldsymbol{k}\cdot(\boldsymbol{r}-\boldsymbol{v}t)} \tag{10.93}$$

you may derive, correspondingly,

$$-\frac{\mathrm{d}E}{\mathrm{d}x} = \frac{4\pi i}{v}(2\pi)^3\int \frac{\mathrm{d}^3\boldsymbol{k}}{k^2}\boldsymbol{k}\cdot\boldsymbol{v}\,|\rho_{\mathrm{ext}}(\boldsymbol{k})|^2\left(\frac{1}{\varepsilon(k,\boldsymbol{k}\cdot\boldsymbol{v})}-1\right). \tag{10.94}$$

For a cluster of atoms, $s = 1,\ldots,n$ located at points $\boldsymbol{r}_s$ relative to a reference points we have

$$\begin{aligned}|\rho_{\mathrm{ext}}(\boldsymbol{k})|^2 &= \sum_s |\rho_s(k)|^2 + \sum_{s\neq s'}\rho_s^*(\boldsymbol{k})\rho_{s'}(\boldsymbol{k})\,\mathrm{e}^{\mathrm{i}\boldsymbol{k}\cdot(\boldsymbol{r}_s-\boldsymbol{r}_{s'})}\\ &= \sum_s |\rho_s(k)|^2 + 2\sum_{s<s'}\rho_s^*(\boldsymbol{k})\rho_{s'}(\boldsymbol{k})\cos\left(\boldsymbol{k}\cdot(\boldsymbol{r}_s-\boldsymbol{r}_{s'})\right)\end{aligned} \tag{10.95}$$

For the special case of a dicluster of two equal point charges this leads to

$$\begin{aligned}\frac{\mathrm{d}E}{\mathrm{d}x} = \frac{-\mathrm{i}e^2}{2\pi^2 v}\int \frac{d^3\boldsymbol{k}}{k^2}(\boldsymbol{k}\cdot\boldsymbol{v})\left(\frac{1}{\varepsilon(k,\boldsymbol{k}\cdot\boldsymbol{v})}-1\right)\\ \times\left[Z_1^2+Z_2^2+2Z_1Z_2\cos(\boldsymbol{k}\cdot\boldsymbol{r})\right],\end{aligned} \tag{10.96}$$

an expression established by Arista (1978).

10.4.4.4 Fermi Gas

Starting with Arista (1978) numerous authors have evaluated integrals like (10.96), either to study the effect of the chosen dielectric function or to model stopping in real media. Calculations by Arista (1978) refer to the dielectric function of Lindhard (1954) which has been discussed in Sect. 5.7.3, Vol. 1. Approximate analytic solutions were offered in the limits of high and low velocities, respectively. You are welcome to study the high-speed limit by looking into Problem 10.11.

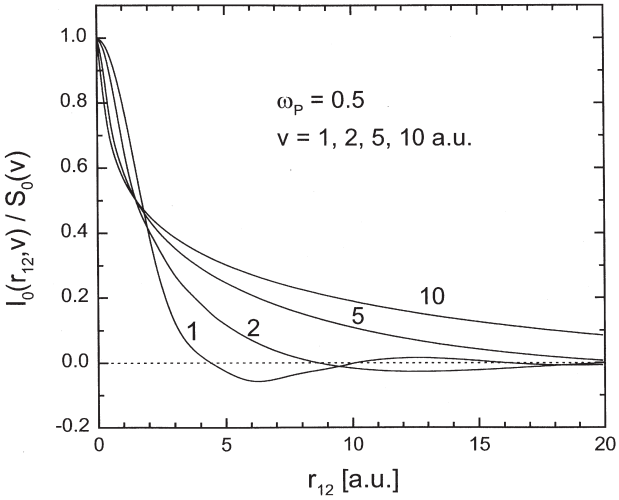

Fig. 10.11 Relative enhancement in stopping cross section of a dicluster of two randomly oriented point charges, $R-1$, in Fermi gas with $\hbar\omega_P = 13.6$ eV as a function of the internuclear distance r_{12}/a_0 for v/v_0 =1, 2, 5 and 10. From Arista (2000)

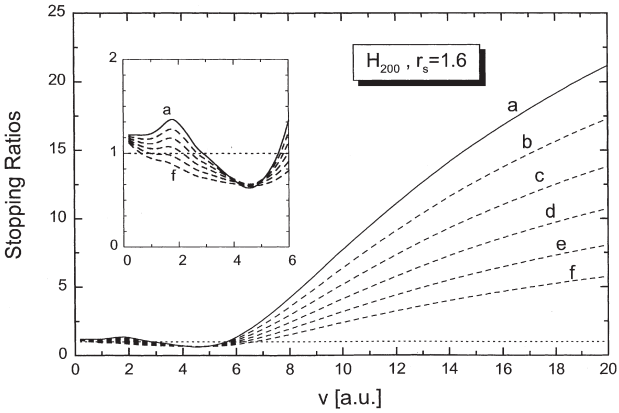

Fig. 10.12 Stopping ratio R for a cluster of 100 H_2 molecules in a Fermi gas with $r_s = 1.6$ versus projectile speed v/v_0. Letters a...f indicate neutral fractions 0...50% in steps of 10%. From Arista (2000)

Figure 10.11, showing numerical results for four beam velocities, confirms that enhancement factors tend to decrease with increasing internuclear distance except at low projectile speed, where oscillatory effects must be expected.

Figure 10.12 shows calculated enhancement factors for a cluster of 100 H_2 molecules in a Fermi gas with $r_s = 1.6$, demonstrating that very large enhancement factors must be expected at high enough projectile speeds. These calculations bear relevance to experiments by Ray et al. (1992) with carbon clusters of low charge.

For $v/v_0 \lesssim 5$ and up to 25 atoms per cluster, enhancement factors up to $R \sim 1.3$ were found in those measurements.

10.4.4.5 Oscillator Gas

Although the Fermi gas is a popular model for calculations in the theory of stopping, it is characterized by only one parameter, its density which, at the same time, determines an effective binding frequency ω_P, the plasma frequency. In the Drude-Lorentz model known from classical electrodynamics (Jackson, 1975), at least two parameters enter, namely the plasma frequency and at least one resonance frequency of an individual isolated oscillator. Varying the density and keeping the atomic resonance frequency constant would enable you to isolate the effect of the medium on the proximity effect.

We cannot evaluate (10.96) on the basis of the Drude-Lorentz model, since the absence of a k dependence in the dielectric function causes a divergence at large k. We can, however, evaluate the interference term $\propto Z_1 Z_2$, where the factor $\langle \cos \boldsymbol{k}\cdot\boldsymbol{r} \rangle$ removes the divergence at large k. If you solve Problem 10.12, you will arrive at

$$\Delta\left(\frac{\mathrm{d}E}{\mathrm{d}x}\right) = -\frac{4Z_1 Z_2 e^2 \omega_P^2}{v^2}\left[\frac{\sin\eta}{\eta} - \mathrm{Ci}(\eta)\right], \tag{10.97}$$

where Ci represents the integral cosine (Abramowitz and Stegun, 1964) and

$$\eta = \frac{\sqrt{\omega_0^2 + \omega_P^2}\, r}{v}. \tag{10.98}$$

In the limit of high projectile speed this reduces to

$$\Delta\left(\frac{\mathrm{d}E}{\mathrm{d}x}\right) = -\frac{4Z_1 Z_2 e^2 \omega_P^2}{v^2}\left[1 - \gamma - \ln\eta\right]. \tag{10.99}$$

This is very similar to (10.63). You may note that the main difference is the replacement of the transition frequency ω_{j0} by a frequency $\sqrt{\omega_0^2 + \omega_P^2}$, which indicates the density effect known from Drude-Lorentz theory (Jackson, 1975).

You may be in doubt about the range of validity of the Drude-Lorentz estimate. This problem is overcome by replacing the Drude-Lorentz function by its quantal analog that has been established by Belkacem and Sigmund (1990) and described in Sect. 5.5, Vol. 1.

Figure 10.13 shows stopping ratios evaluated with this model by Sigmund and Schinner (2011). You may appreciate that the highest enhancement factor is predicted for the lowest target density over the entire energy range covered, and at the highest density shown, for $\omega_P^2/\omega_0^2 = 10$, negative enhancement is found for $B = 2mv^2/\hbar\omega_0 < 10$.

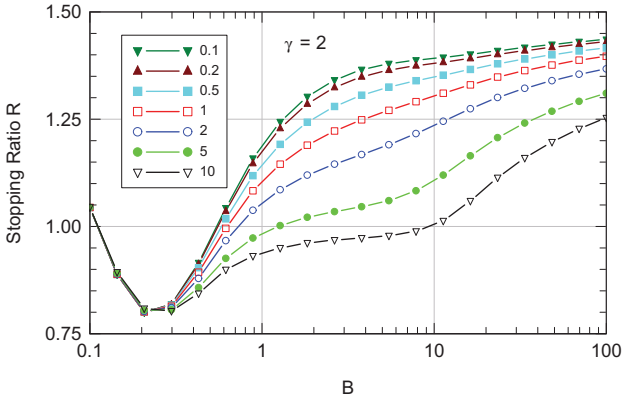

Fig. 10.13 Stopping ratio for randomly oriented dicluster of two point charges versus $B = 2mv^2/\hbar\omega_0$, calculated within the Born approximation for a gas of quantum-oscillator atoms. Numbers in the legend indicate the density of the medium expressed by ω_P^2/ω_0^2. The parameter $\gamma = r\sqrt{2m\omega_0/\hbar}$ is a measure of the internuclear distance. From Sigmund and Schinner (2011)

You will frequently find in the literature the claim that it is the wake force that is the cause of the proximity effect in stopping. Evidently, the opposite is true: The proximity effect in the stopping cross section of a molecular ion is biggest in the absence of a wake, i.e., in vacuum (Sigmund and Schinner, 2011).

10.4.5 Large Clusters

10.4.5.1 Proximity Effect

As the number n of atoms in the cluster increases, the number of neighbours per cluster atom and, hence, the proximity effect increases. If the projectile speed is high enough to ensure a stopping ratio $R_n > 1$, R_n will tend to increase with n until there are internuclear distances exceeding the adiabatic radius, whereafter one expects R_n to saturate at some value $n_{\max}$ which must depend on the projectile speed. Details depend on the adopted geometrical structure as well as the charge distribution in the cluster.

Ray et al. (1992) performed measurements for hydrogen clusters H_n^+ with $n = 2 - 25$ in carbon foils of different thicknesses over an energy range of 10–120 keV/u. Measured stopping ratios ranged from $\sim$ 0.7 to $\sim$ 1.3. Calculations were performed on the basis of the quantum harmonic oscillator model described in Sect. 4.5.2, Vol. 1. Figure 10.14 confirms that the proximity effect increases with n at high speed. The figure on the right shows qualitative agreement with one set of measurements.

Similar calculations were performed by Abril et al. (1992) on the basis of dielectric theory. This, as well as subsequent work by Pérez-Pérez et al. (1996) demon-

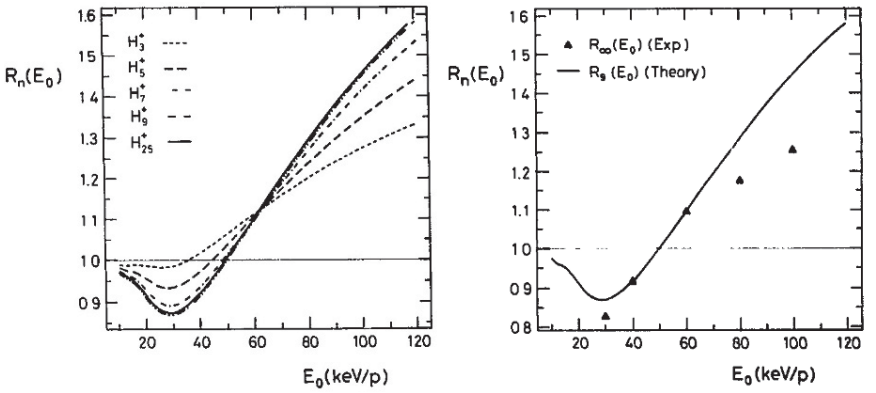

Fig. 10.14 Stopping ratio R_n for H_n cluster in carbon versus beam energy per proton. Left: Calculation for $n = 3, 5, 7, 9$ and 25. Right: Comparison of R_n with limiting values R_∞ extrapolated from measured values. From Ray et al. (1992)

strated that the stopping ratio depends sensitively on the adopted dielectric function. In particular, a pronounced difference was predicted in the energy dependence of the stopping ratio between aluminium and carbon targets. No measurements have yet been reported that would confirm or disprove such an effect.

Measurements with carbon clusters including fullerene were performed by Baudin et al. (1994). No significant proximity effect was found for fullerene in an energy range up to ~ 0.5 MeV/u, while moderate enhancements of up to 10% were found for smaller carbon clusters with $n \leq 8$. More recent experiments by Tomita et al. (2010) with carbon clusters near the Bohr speed showed pronounced negative enhancements, as one would expect on the basis of graphs like Fig. 10.14.

A detailed analysis of such measurements is complex and involves the charge state, Coulomb explosion, multiple scattering and the geometrical structure of the incident cluster.

10.4.5.2 Nonlinearities

Penetration of a large cluster implies a major disturbance of the stopping medium. This disturbance may well have a feedback on the penetration properties. This shows up in the *clearing-the-way effect*, first observed by Yamamura (1988) in computer simulations of sputtering, where it was found that Ar_n clusters with $n = 10 - 200$ and energies of 100 eV/atom penetrated about twice as deeply as single argon atoms. The simple explanation was that at such low energies, target atoms recoiling from nuclear collisions with the frontrunners of the cluster can move away from the point of impact, so that backrunners meet a diluted target (Sigmund, 1989).

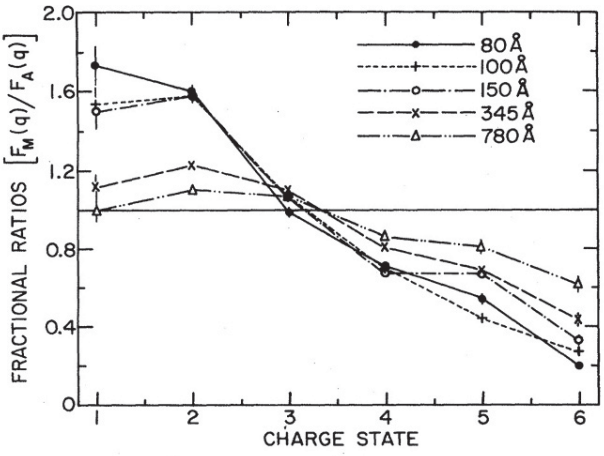

Fig. 10.15 Ratio $F_M(q)/F_A(q)$ of charge fractions for 4.2 MeV N_2^+ ($F_M(q)$) and 2.1 MeV N^+ ($F_A(q)$) ions after penetrating through carbon foils of thickness 80–750 Å. From Maor et al. (1985)

Much more pronounced nonlinearities are observed in radiation effects such as track formation, displacement damage, sputtering and electron emission. Such phenomena will be discussed in Volume 3 of this series.

10.5 Charge State

While it is obvious that the trajectories of the constituents of a cluster must depend on the various charge states, evidence has evolved gradually that those charges themselves are also affected by proximity effects.

10.5.1 Observations

Early observations appeared as by-products from studies of beam-foil spectroscopy (Bickel, 1975), but in connection with studies of Coulomb explosion the need to study charge states became evident (Gaillard et al., 1977, Breskin et al., 1979).

Maor et al. (1985) measured charge distributions of atomic nitrogen ions emerging from carbon foils for incident 4.2 MeV N_2^+ and for incident N^+ atomic ions at the same speed, i.e., at 2.1 MeV. They found that lower charges were more abundant for molecular than for atomic bombardment. Foil thicknesses were chosen sufficiently large so that charge equilibrium was ensured in case of atomic bombardment. Notwithstanding, charge distributions depended on thickness for molecular

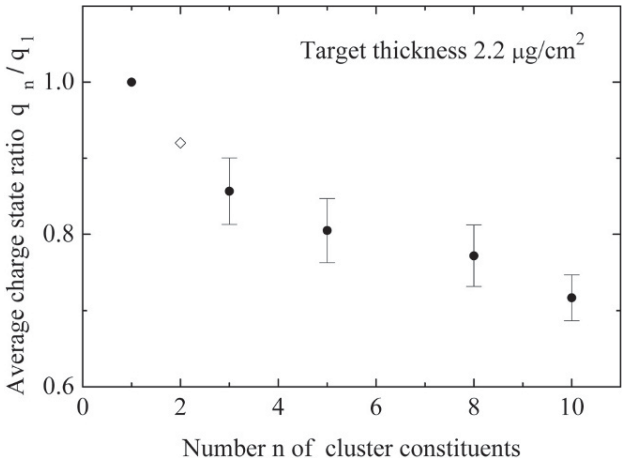

Fig. 10.16 Relative average charge per emerging carbon atom for incident 2 MeV/atom C_n cluster after penetration through 2.2 μg/cm^2 carbon foil. From Brunelle et al. (1999)

projectiles, as is seen in Fig. 10.15. A trend toward equilibrium is seen as thickness increases, and that equilibrium appears to be that found for bombardment with atomic ions.

One may conclude that the presence of a nearby atomic ion lowers the equilibrium charge state, and that this effect diminishes gradually, as the ions move apart as a consequence of Coulomb explosion and/or multiple scattering.

Similar measurements were performed by Brunelle et al. (1999) with carbon clusters of varying size. Figure 10.16 demonstrates that the decrease in the mean equilibrium charge per atomic C ion gets more pronounced with increasing cluster size.

Amongst subsequent reported experimental studies I like to mention Chiba et al. (2011) who, in coincidence measurements, determined a clear correlation between the ejection angle of the fragments of incident C_2^+ ions with the charge state and, in this way, were able to correlate the initial internuclear distance with the exit charges of the fragments.

10.5.2 Qualitative Considerations

All observations point at an increased fraction of emerging neutrals and, more generally, a shift of the charge spectrum toward lower charges. Initial attempts aimed at an explanation in terms of a surface effect, but with the observation of significant proximity effects in energy loss it became clear that the behaviour in the bulk could not be neglected.

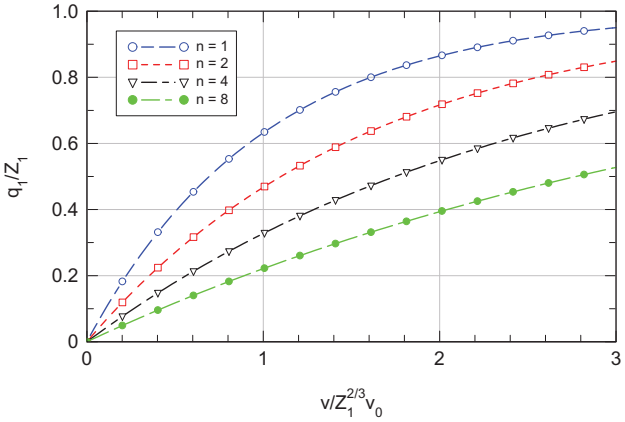

Fig. 10.17 Very qualitative estimate of the mean equilibrium charge per atomic ion of an n—atomic cluster in the united-atom limit, (10.100)

Let us consider an atomic nitrogen ion at a velocity where the mean equilibrium charge is 4. This implies that for penetration through a gas, two electrons tend to occupy the K shell with a binding energy of 404 eV while a third electron may occupy the 2s shell with a binding energy of 20 eV. Now consider an N_2 molecule at the same velocity and, for qualitative orientation, go to the united-atom limit, i.e., a silicon ion. Let us assume for a moment that there are 2×3 electrons. Then, two would occupy the K shell with a binding energy of 1844 eV, another two the 2s shell with a binding energy of 154 eV, and the last two would be in the 2p shell with a binding energy of 104 eV. Clearly, the atomic ion has a much lower ionization energy and hence a higher ionization cross section. Thus, the molecular ion will tend to capture more electrons in order to lower its charge state. This argument must exaggerate the actual phenomenon, but it indicates the direction of the effect.

10.5.3 Estimates

From an energetic point of view, a proximity effect in charge state must be expected in penetration through both solid and gaseous matter, although reported measurements that I am aware of all refer to solids.

10.5.3.1 United-Atom Limit

Keeping to the united-atom limit for a moment we may find an upper bound for the effect by making recourse to the simple Thomas-Fermi formula for the equilibrium charge state, (1.6) which, for an n-atomic cluster in the united-atom limit reads

$$q/n = Z_1 \left(1 - \mathrm{e}^{-v/(nZ_1)^{2/3}v_0}\right) . \tag{10.100}$$

This relation is shown in Fig. 10.17 for $n = 1, 2, 4$ and 8. In agreement with the experimental finding the mean charge state decreases with increasing cluster size. This upper limit exceeds the experimental result shown in Fig. 10.16 as had to be expected.

10.5.3.2 Perturbation Limit

Consider an atomic ion 1 in charge equilibrium. According to the Bohr stripping criterion, all states with orbital velocities exceeding the projectile speed $> v$ are occupied (with N electrons) and all those with velocities $< v$ are empty.

Now let another atomic ion 2 be located in a distance R from ion 1. The perturbation caused by this ion may be expressed by a potential $\phi_2(|\boldsymbol{r} - \boldsymbol{R}|)$, which will cause a change in the energy levels of ion 1. In a single-electron picture, the νth level will be lowered by an energy

$$\Delta E_\nu = -e\langle\nu|\phi(|\boldsymbol{r} - \boldsymbol{R}|)|\nu\rangle \tag{10.101}$$

to first order in the perturbation.

Charge equilibrium is now achieved when the newly available states are occupied with electrons. If we characterize these electron states by a density of states $\rho_1(v) = (d\nu/\mathrm{d}E)_v$, the change in ion charge can be expressed by

$$\Delta q_1 = \rho_1(v)\Delta E_(N) \simeq -e\phi(R)\rho_1(v) , \tag{10.102}$$

where it has been assumed that R is large enough so that the variation of ϕ_2 over the spatial extension of ion 1 is negligible. Estimates of this type have been used in computer simulations of cluster penetration (Nardi et al., 2002).

10.5.3.3 Effective-Charge Estimate

Following Heredia-Avalos et al. (2001), consider an atomic ion 1 in an n-atomic cluster moving with a constant speed v. The potential seen by an electron on atom 1 is given by

$$\mathcal{V}(r) = \frac{Z_1 e}{r} + \sum_{j=2}^{n} V_j\left(\left|\boldsymbol{r} - \boldsymbol{R}_j\right|\right) , \tag{10.103}$$

disregarding electron-electron interaction, where $V_j(r)$ is the effective interaction potential of atom j which could be given by (4.19). Internuclear distances R_j are large enough so that the screened core potential of the atoms $j = 2, \ldots, n$ can be neglected, so that

$$V_j(r) \simeq \frac{q_j e}{r}\mathrm{e}^{-r/a_{\mathrm{ad}}} , \tag{10.104}$$

where $a_{\mathrm{ad}} = v/\omega$ according to (4.19), with ω denoting a characteristic resonance frequency of the target. With this, we find

$$\mathcal{V}(r) = \frac{e}{r}\left[Z_1 + \sum_{j=2}^{n} q_j \frac{r}{\left|\boldsymbol{r} - \boldsymbol{R}_j\right|} \mathrm{e}^{-\left|\boldsymbol{r}-\boldsymbol{R}_j\right|/a_{\mathrm{ad}}}\right], \tag{10.105}$$

Now, approximating

$$\left|\boldsymbol{r} - \boldsymbol{R}_j\right| \simeq R_j \tag{10.106}$$

$$r \simeq \langle r \rangle , \tag{10.107}$$

we can introduce an effective nuclear charge $\mathcal{Z}_j$ through

$$\frac{\mathcal{Z}_1 e}{r} = \mathcal{V}(r) = \frac{e}{r}\left[Z_1 + \sum_{j=2}^{n} q_j \frac{\langle r \rangle}{R_j} \mathrm{e}^{-R_j/a_{\mathrm{ad}}}\right] \tag{10.108}$$

or

$$\mathcal{Z}_1 = Z_1 + \sum_{j=2}^{n} q_j \frac{\langle r \rangle}{R_j} \mathrm{e}^{-R_j/a_{\mathrm{ad}}} , \tag{10.109}$$

where

$$q_j = \mathcal{Z}_j \left(1 - \mathrm{e}^{-v/(v_0 Z_j^{2/3})}\right) \tag{10.110}$$

in accordance with (1.6).

Writing similar relations for the remaining $n-1$ atoms, you arrive at a system of equations for $\mathcal{Z}_j$ which determines the charges q_j of the cluster constituents,

$$\sum_{\ell} \mathcal{Z}_\ell = \sum_{\ell} Z_\ell + \sum_{\ell \neq j} q_j \frac{\langle r_\ell \rangle}{R_j} \mathrm{e}^{-R_j/a_{\mathrm{ad}}} . \tag{10.111}$$

There are various options for evaluating this expression:

1. If $\mathcal{Z}_\ell - Z_\ell$ is a small correction, you may wish to insert Z_ℓ for $\mathcal{Z}_\ell$ everywhere in the correction term on the right-hand side, including the ionic radius $\langle r_\ell \rangle$.
2. If you leave $\mathcal{Z}_j$ in (10.110) but otherwise replace $\mathcal{Z}_\ell$ with Z_ℓ, you get a linear system.
3. If you insert $\mathcal{Z}_\ell$ everywhere in the correction term, the system gets highly nonlinear.

As an example, consider a homonuclear cluster and assume, additionally, that the charge is uniformly divided amongst the cluster constituents. Then the second assumption leads to

$$n\mathcal{Z}_1 = nZ_1 + \mathcal{Z}_1 \left(1 - \mathrm{e}^{-v/(v_0 Z_1^{2/3})}\right) \langle r_1 \rangle \sum_{j \neq \ell} \frac{1}{R_{\ell j}} \mathrm{e}^{-R_{\ell j}/a_{\mathrm{ad}}} \tag{10.112}$$

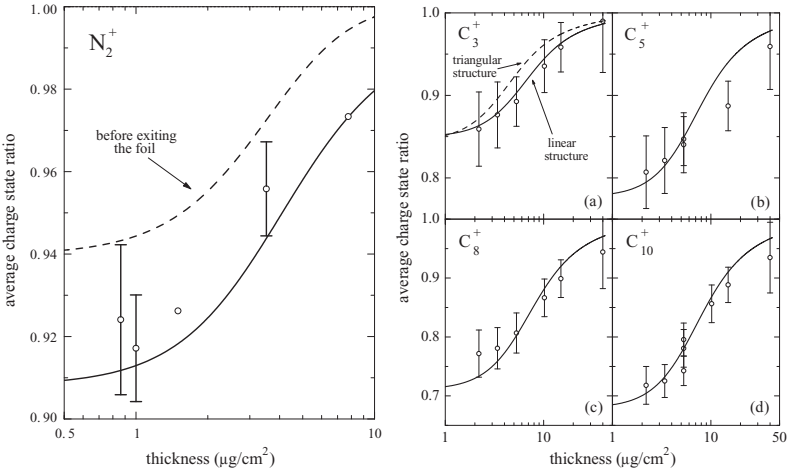

Fig. 10.18 Average charge ratio q/Z_1 versus target thickness for 2 MeV/atom N_2^+ (left (Maor et al., 1985)) and for 2 MeV/atom C_n^+ ions (right, (Brunelle et al., 1999)) in carbon compared with calculations by Heredia-Avalos et al. (2001). From Heredia-Avalos et al. (2001)

or

$$\mathcal{Z}_1 = Z_1 \left[1 - \left(1 - \mathrm{e}^{-v/(v_0 Z_1^{2/3})} \right) \langle r_1 \rangle \frac{1}{n} \sum_{j \neq \ell} \frac{1}{R_{\ell j}} \mathrm{e}^{-R_{\ell j}/a_{\mathrm{ad}}} \right]^{-1} . \qquad (10.113)$$

If you identify $\langle r_1 \rangle$ with the screening radius $a_{\mathrm{sc}} = a_{\mathrm{TF}}(1 - q_1/Z_1)$, you may recognize that $\mathcal{Z}_1 \to Z_1$ for high projectile speeds v, even though the other terms in the denominator increase monotonically.

Heredia-Avalos et al. (2001) used different input in the evaluation of their scheme:

- Instead of (10.110), an empirical relation extracted from the effective stopping charge (Ziegler et al., 1985) was utilized,
- For the screening radius, the expression $a = \frac{1}{\omega_P}\sqrt{v^2 + v_F^2/3}$ was employed, thus ensuring an acceptable behaviour at low projectile speeds.
- For the ionic radius an expression extracted from Brandt and Kitagawa (1982) was inserted, and
- Z_ℓ was replaced by $\mathcal{Z}_\ell$ in the correction term, i.e., the third option was applied.

Figure 10.18 shows results for N_2^+ and C_n^+ clusters in carbon. Considering the overall simplicity of the model, the agreement achieved with experimental findings appears surprisingly good.

10.5.3.4 Thomas-Fermi Estimate

According to the Thomas-Fermi atomic model, the electron density $\rho(\boldsymbol{r})$ is related to the potential $\phi(\boldsymbol{r})$ as

$$\rho(\boldsymbol{r}) = A\,(\phi(\boldsymbol{r}) - \zeta)^{3/2}\ , \tag{10.114}$$

where ζ, the chemical potential, is a constant and

$$A = \frac{(2me)^{3/2}}{3\pi^2\hbar^3}\,. \tag{10.115}$$

For an isolated ion 1 this relation must be satisfied with $\rho(\boldsymbol{r}) = \rho_1(r)$ and $\phi(\boldsymbol{r}) = \phi_1(r)$.

In the presence of a second ion 2, (10.114) reads

$$\rho_1(r) + \Delta\rho_1(\boldsymbol{r}) = A\,[\phi_1(\boldsymbol{r}) + \phi_2(|\boldsymbol{r}_1 - \boldsymbol{R}|) - \zeta]^{3/2}\ . \tag{10.116}$$

To the first order in ϕ_2 this reduces to

$$\Delta\rho_1(\boldsymbol{r}) \simeq \frac{3}{2}A\,(\phi_1(r) - \zeta)^{1/2}\,\phi_2(\boldsymbol{r}) \tag{10.117}$$

or

$$\Delta\rho_1(\boldsymbol{r}) \simeq \frac{3}{2}A^{2/3}\,[\rho_1(r)]^{1/3}\,\phi_2\,(|\boldsymbol{r} - \boldsymbol{R}|)\ . \tag{10.118}$$

The number of additional electrons is then given by

$$\begin{aligned} -\Delta q_1 = \int \mathrm{d}^3\boldsymbol{r}\,\Delta\rho_1(\boldsymbol{r}) &= \frac{3}{2}A^{2/3}\int \mathrm{d}^3\boldsymbol{r}\,[\rho_1(r)]^{1/3}\,\phi_2\,(|\boldsymbol{r} - \boldsymbol{R}|) \\ &\simeq \frac{3me}{(3\pi^2)^{2/3}\hbar^2}\phi_2\,(R)\int 4\pi r^2\,\mathrm{d}r\ [\rho_1(r)]^{1/3}\,. \end{aligned} \tag{10.119}$$

Setting

$$\rho_1(r) = \frac{Z_1 - q_1}{4\pi a^2}\frac{a}{r}\mathrm{e}^{-r/a} \tag{10.120}$$

you find

$$-\Delta q_1 = A_2\frac{me}{\hbar^2}a^2(Z_1 - q_1)^{1/3}\phi_2(R) \tag{10.121}$$

with

$$A_2 = \frac{15\cdot 2^{7/3}\Gamma(2/3)}{\pi^{2/3}}\,. \tag{10.122}$$

10.5.3.5 Dielectric Theory

Various aspects of the problem were discussed in a series of papers starting with Miskovic et al. (2000). These studies are based on the energy criterion and inspired

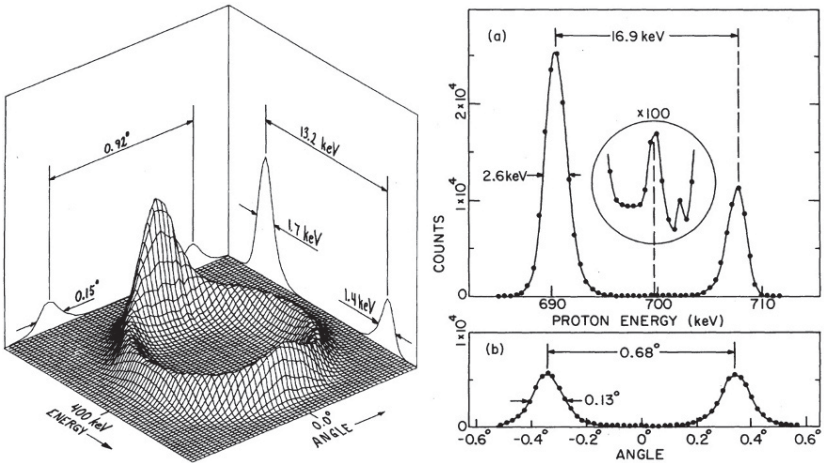

Fig. 10.19 *Ring pattern* showing the distribution in energy and angle of emerging protons from 2.0 MeV (left) and 3.5 MeV(right) $^4HeH^+$ ions incident on carbon foils of thickness 8.5 nm (left) and 20 nm (right). From Cooney et al. (1981)

by the theory of Brandt and Kitagawa (1982). Properties of the material enter explicitly through the dielectric function. The initial approach operates with a *spherical-ball* model of a cluster with an adopted minimum distance between atoms. A significant influence of wake forces was found on equilibrium charge states (Miskovic et al., 2001a). An interesting qualitative feature is the prediction of Li et al. (2002) of an asymmetric distribution of the charge between leading and trailing cluster atoms due to the wake force.

All these studies address rather slow massive cluster ions, which by no means can be expected to act as a small perturbation of the electronic structure of the target. Considerable caution is indicated here, and even more with regard to further studies (Miskovic et al., 2001b) addressing Na clusters with n up to 200 at $v = 3v_0$.

10.6 Correlations

Coincidence measurements have revealed more detailed information about penetration of molecules and clusters than what can be deduced from measurements of energy loss or multiple scattering.

10.6.1 Ring Patterns

Figure 10.19 shows two examples on similar systems but plotted differently. The two graphs refer to swift $^4HeH^+$ diclusters incident on carbon films. Both graphs show combined energy-angle distributions of emerging *protons*. The left graph shows a ring pattern of the type of Fig. 10.3. You may notice a pair of peaks oriented along the direction of motion, specified by by scattering angle zero. The two peaks have different heights. Most pronounced is the peak at the smallest energy which represents trailing protons. The graph on the right shows equivalent information in a less illuminating but more quantitative manner.

These graphs suggest that Coulomb explosion is the dominating process here. Note, however, that such measurements are performed with very thin foils, were a major portion of the Coulomb explosion takes place after the molecular fragments have left the foil, while disturbing effects like multiple scattering, energy loss, wake force, straggling and electron capture become inactive shortly after the fragments have left the target. As a consequence, measurement of only the neutral component of the emitted flux would show a less pronounced ring structure.

In view of the manifold of processes that determine ring patterns of the type shown in Fig. 10.19, a comprehensive theoretical treatment needs to be based on computer simulation (Plesser, 1982, Kemmler et al., 1985, Zajfman et al., 1990, Zajfman, 1990, Denton et al., 2007, Miskovic et al., 2007), while analytical estimates should assist in judging the relative importance of various effects. Nevertheless, attention has also been given to correlations and synergy between Coulomb explosion, multiple scattering, energy loss and wake field (Kagan et al., 1978, Sigmund, 1992b,a, Sigmund et al., 1996, Miskovic et al., 2007).

10.6.2 Coulomb Explosion and Multiple Scattering

Coulomb explosion is a deterministic process, where the statistics is defined by the initial conditions, i.e., the initial configuration in real and velocity space of the impinging molecule, in particular its orientation relative to the beam direction. In the absence of competing effects it will result in a ring pattern determined by the masses and charges of the fragments and broadened by fluctuations in internal configuration of the molecule at the point of incidence.

Multiple scattering, on the other hand, is a stochastic process which, in a homogeneous medium, gives rise to a broadening of the average straight-line trajectory in the lateral direction. To this adds energy loss which gives rise to a broadening in the longitudinal direction as well as slowing down.

For simplicity, consider a homonuclear dicluster, $q_1 = q_2 = Z_1$. From (10.4) you can easily extract that the speed of Coulomb explosion goes as

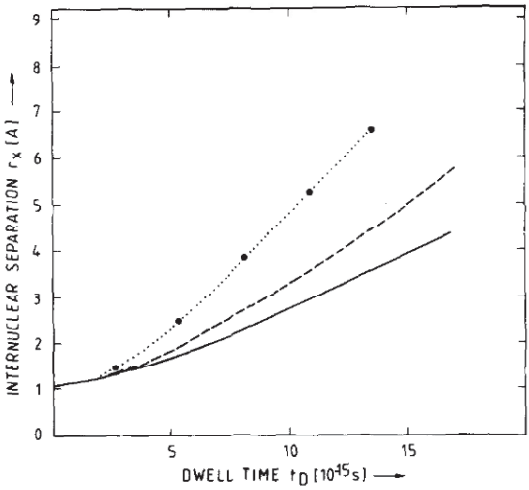

Fig. 10.20 Calculated internuclear distance of a 2 MeV CO dicluster penetrating through carbon. Dashed line: Unscreened-Coulomb explosion, no multiple scattering; solid line: Screened-Coulomb explosion without multiple scattering; line with markers: Screened-Coulomb explosion plus multiple scattering. From Kemmler et al. (1985)

$$\frac{\mathrm{d}r}{\mathrm{d}t} \simeq \begin{cases} w_\infty^2 t/r_0 & w_\infty t \ll r_0 \\ \qquad \text{for} & \\ w_\infty & w_\infty t \gg r_0 \ , \end{cases} \tag{10.123}$$

where $w_\infty = \sqrt{2Z_1^2 e^2/\mu r_0}$ for bare projectile ions with atomic number Z_1, r_0 is the initial internuclear distance and $\mu = M_1/2$ the reduced mass.

By piecewise fitting of the data shown in Fig. 7.9 by power laws you can approximate the multiple scattering halfwidth by

$$\tilde{\alpha}_{1/2} = \begin{cases} \tau/6 & \tau \simeq 1 \\ \qquad \text{for} & \\ 1.71\sqrt{\tau} & \tau \gg 1 \end{cases} \tag{10.124}$$

with

$$\tilde{\alpha}_{1/2} = (Ea/\sqrt{2}Z_1 Z_2 e^2)\alpha_{1/2} \tag{10.125}$$

$$\tau = \pi a^2 N v t \ . \tag{10.126}$$

If you wonder about the origin of the factor $\sqrt{2}$, go to Problem 10.13. Z_2 denotes the atomic number of the target material.

The lateral spread follows, then, from

$$\frac{\mathrm{d}\rho}{\mathrm{d}t} \sim \alpha_{1/2} v \tag{10.127}$$

We may then make a rough comparison,

$$\frac{(\mathrm{d}r/\mathrm{d}t)_{\mathrm{CoulExpl}}}{(\mathrm{d}\rho/\mathrm{d}t)_{\mathrm{Multiscat}}} \simeq \begin{cases} 2.7 Z_1/Z_2 N r_0^2 a & t \text{ small} \\ \text{for} & \\ 0.23\sqrt{M_1 v/Z_2^2 e^2 N r_0 t} & t \text{ large} . \end{cases} \tag{10.128}$$

Hence, the ratio of the two rates is constant initially but decreases gradually with time. The ratio $1/r_0^2 aN$ will typically be > 1, and considering the numerical factor, we may conclude that Coulomb explosion dominates initially except for $Z_1 \ll Z_2$, i.e., light ions in heavy targets where scattering angles and cross sections become large. Figure 10.20 shows the results of a computer simulation which confirms these features.

Multiple scattering and Coulomb explosion interfere, since a scattering event experienced by one fragment typically causes rotation of the axis and, hence, the direction of Coulomb explosion. This gives rise to a change in the lateral motion of the other fragment, even though that fragment has not been affected by the scattering event. In other words, individual fragments will experience more scattering events, so the angular and lateral profile will be broader than expected (Sigmund, 1992b).

If a dicluster is aligned in the direction of motion, the constituent atoms will undergo small-angle scattering at very similar impact parameters. At least for homonuclear diclusters this will cause similar scattering angles or *coherent scattering*. This effect results in a peak in the ring pattern in the forward or backward direction.

10.6.2.1 Transmission of Molecules

Poizat and Remillieux (1971) found that the flux of particles transmitted after bombardment of a carbon foil by H_2^+ molecular ions contained a small fraction of H_2^+. This observation was found surprising, since it was assumed that incident molecules would dissociate immediately after entering the foil, and that Coulomb explosion would cause the fragments to move away from one another, so they would never meet again.

Figure 10.21 shows results from extensive measurements by Cue et al. (1980). Clearly, the fraction of transmitted molecules decreases with increasing dwelltime x/v in the foil, but after an initial fast decay, all three curves get flatter.

Dwell times up to 10^{-14} s are equivalent with foil thicknesses of micron size. Hence, experiments of this type trace a very different regime of molecular-ion bombardment from what we have seen in Fig. 10.19. In particular, multiple scattering must play an important role.

A qualitative interpretation (Gaillard et al., 1976, Cue et al., 1980) is indicated in Fig. 10.22. Initially, fragments move apart under Coulomb explosion. Therefore, the probability for two fragments to exit from a thin foil at the same spot is very small. With increasing foil thickness, multiple scattering will give rise to a small region of overlap. This causes a flatter survival curve.

This process has been simulated by several groups (Cue et al., 1980, Zajfman, 1990, Jakas and Capuj, 1995) by Monte Carlo codes allowing for Coulomb explosion and multiple scattering as well as wake forces.

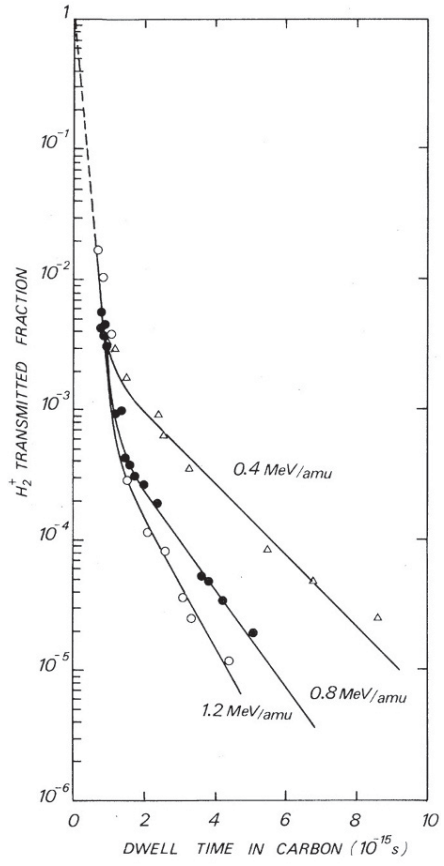

Fig. 10.21 Measured transmission yield of H_2^+ molecules for bombardment with H_2^+ molecules in carbon foils. From Cue et al. (1980)

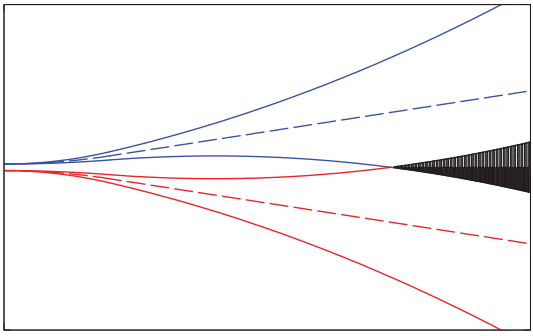

Fig. 10.22 Schematic view of recombination of a dicluster: Dashed lines: Trajectories undergoing Coulomb explosion only. Solid lines indicate the half-widths of an added multiple-scattering profile. The shaded area indicates the regime where recombination becomes likely

An essential part of such simulations is the recombination probability which hinges on the probability for the cluster to carry an electron at emergence. We know

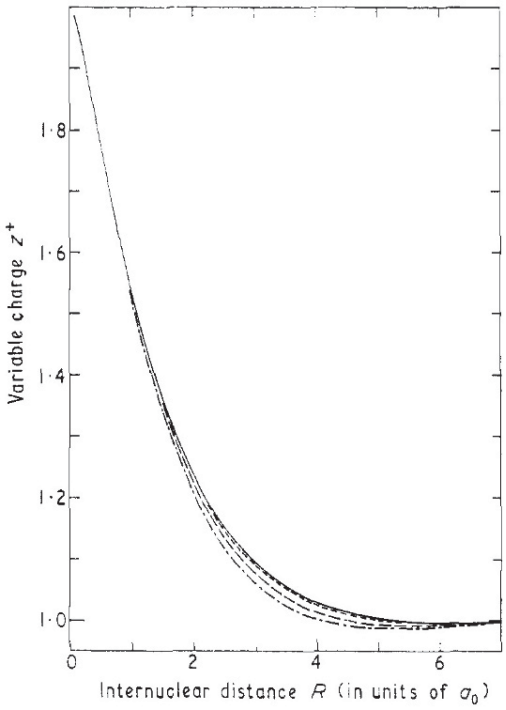

Fig. 10.23 Calculated effective charge $Z_g(R)$ for charge transfer for H_2^+. From McCarroll et al. (1970)

from Sect. 10.5 that the equilibrium charge may differ from that of an atomic projectile. This is accounted for by Cue et al. (1980) by an effective-charge factor $Z_g(R)$ in accordance with Nikolaev (1966). A calculated expression for H_2^+ (McCarroll et al., 1970) for the $1s\sigma$ state is shown in Fig. 10.23 which indicates a substantial proximity effect for $R \lesssim 3a_0$.

For the configuration to be stable, the total energy $E_r + U(R)$ must be negative, where E_r is the relative kinetic energy and $U(R)$ the binding energy in the given state. If the total energy is positive, a neutral hydrogen atom will emerge. Thus, Cue et al. (1980) asserted that H^0 and H_2^+ emission are related processes.

Simulated results (Gaillard et al., 1976, Cue et al., 1980, Zajfman, 1990, Jakas and Capuj, 1995) show reasonable agreement with experiment. An example is shown in Fig. 10.24.

10.6.3 Coulomb Explosion and Energy Loss

Consider a dicluster with atomic charges (q_1, q_2) moving with velocity $\boldsymbol{v}$. If you neglect all interactions except Coulomb explosion, the velocity component of atom 1 in the beam direction will be given by

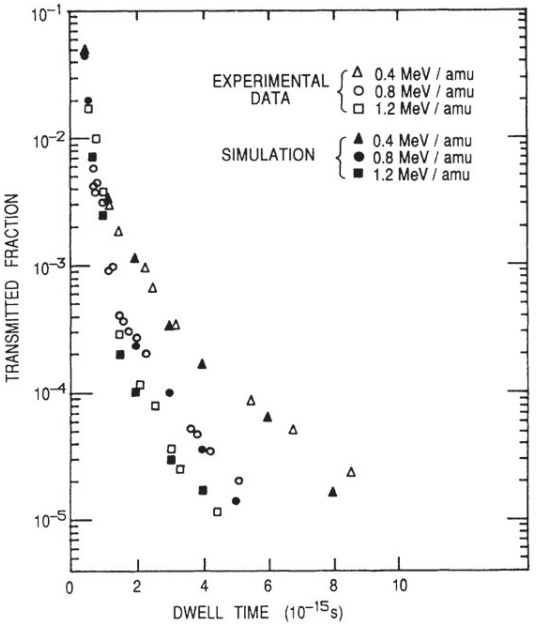

Fig. 10.24 Comparison of simulated and measured transmission fraction of H_2^+ molecules. Open symbols: Measurements (Cue et al., 1980); solid symbols: Simulated (Gaillard et al., 1976); solid line: Simulated (Cue et al., 1980); dashed line: Simulated (Zajfman, 1990). From Zajfman (1990)

$$v(t) = v + \frac{M_2}{M} w(t) \cos\theta \tag{10.129}$$

as a function of time, where $M = M_1 + M_2$ and θ the angle between the axis and $\boldsymbol{v}$. Averaging the kinetic energy $E(t) = (M_1/2)v(t)^2$ over all orientations you can determine a mean energy change

$$\langle \Delta E(t) \rangle = \begin{cases} \frac{1}{3E} \left(\frac{q_1 q_2}{r_0} \right)^2 \left(\frac{x}{r_0} \right)^2 & t \text{ small} \\ & \text{for} \\ \frac{1}{3} \frac{M_2}{M} \frac{q_1 q_2}{r_0} & t \text{ large} \end{cases}, \tag{10.130}$$

where E is the initial energy and $x = vt$ the travelled pathlength.

Note that $\langle \Delta E \rangle$ is a positive quantity. This must be so, since Coulomb explosion converts potential energy into kinetic energy of the fragments. On a relative scale this contribution decreases with increasing pathlength.

The situation is different for the straggling, where you find

$$\left\langle (\Delta E(t) - \langle \Delta E(t) \rangle)^2 \right\rangle = \begin{cases} \frac{4}{3} (q_1 q_2 / r_0)^2 (x/r_0)^2 & t \text{ small} \\ & \text{for} \\ 4E \langle \Delta E \rangle & t \text{ large,} \end{cases} \tag{10.131}$$

where $\langle \Delta E \rangle$ is given by (10.130).

This phenomenon has been studied experimentally by Fadanelli et al. (2005, 2006), who found a $\sim 20\%$ increase in Ω^2 for 500 keV/u H_2^+ as compared to H^+. By

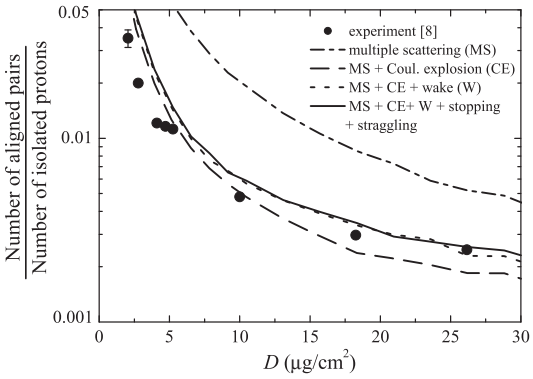

Fig. 10.25 Fraction of aligned proton pairs transmitted through carbon foils of various thicknesses for incident H_2^+ ions with energy 0.5 MeV/u. Alignment is defined by a detector with an opening angle of 0.04°. Solid dots are experimental data of Susuki et al. (2000). From Denton et al. (2007)

analyzing the angular dependence it was possible to separate the effect of Coulomb explosion from the proximity effect in energy loss. The authors conclude that the two effects contribute almost equally to Ω^2.

10.6.4 Wake Effects

The term *wake potential* is considered synonymous with *induced potential* in this monograph. This implies that no wake exists as long as a particle travels through vacuum. Be aware that this notation is not universal in the literature.

If you are unfamiliar with wake theory, it might be an advantage to have a look at Appendix 10.9 before going on with the present section.

Graphs like Fig. 10.29 suggest to classify wake phenomena into two groups,

- Dynamic screening of the near-field of moving ions,
- Long-range effects due to the oscillating tail.

The first effect has great practical importance and is almost ubiquitous in experiments with molecule and cluster beams. Its dominating feature is the reduction of proximity effects which would be more pronounced in penetration through vacuum. A characteristic example is the proximity effect in the energy loss which, according to Fig. 10.13, is most pronounced for penetration through a dilute stopping medium but decreases monotonically as the wake force increases with increasing electron density. Many computer simulation codes for molecules and clusters incorporate an estimate of the wake force. Therefore, dynamic screening is incorporated.

Identifying long-range effects of wake forces has been a challenge, and several routes have been followed.

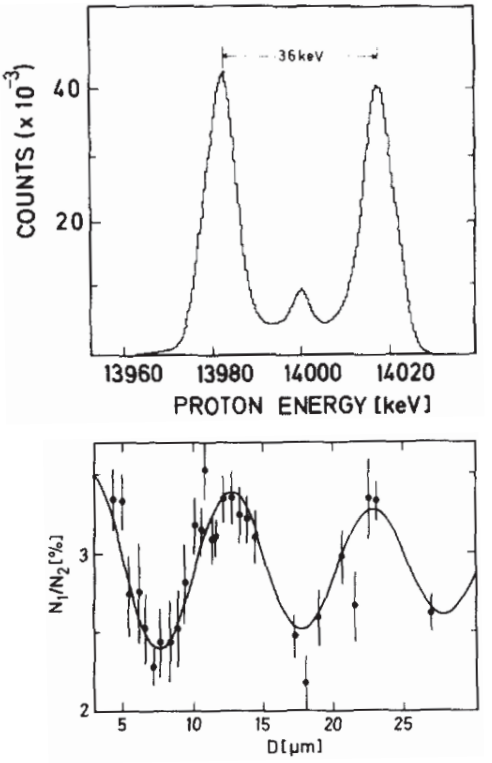

Fig. 10.26 Two-foil experiment with 14MeV/u H_2^+ ions. First foil: 4-8 μg/cm^2 C; second foil: 20 μg/cm^2 Al. Upper graph: Proton energy spectrum at 0°. Lower graph: Intensity ratio between trailing and leading peak versus free space between foils. From Kumbartzki et al. (1982)

10.6.4.1 Alignment

Figure 10.28 shows a deep trough in the potential surface behind a moving ion, enabling the trailing ion in a dicluster to *fall* into it. This is equivalent with a torque trying to align the cluster in the beam direction. Such an effect was suggested by Eckardt et al. (1978) on the basis of measured energy losses.

The effect has been confirmed experimentally by Susuki et al. (2000) with 0.2–0.5 MeV/u H_2^+ ions. Aligned proton pairs were identified as pairs that entered a detector with an opening angle of 0.04°. Figure 10.25 shows experimental results compared with computer simulations by Denton et al. (2007). You may note that in comparison with the transmission yield in Fig. 10.21 the fraction of aligned pairs is fairly large and it falls off rather slowly.

Amongst the simulated curves, the one label MS represents *uncorrelated* multiple scattering as a reference standard. The curve including CE lies lower, because Coulomb explosion acts against alignment. The curve including W demonstrates a

slightly increased alignment due to the wake force, which appears to be unaffected by energy loss and straggling. Correlated multiple scattering was not allowed for in the code.

10.6.4.2 Ring Pattern

Kagan et al. (1978) presented a thorough analytical approach to the effect of the wake force on ring patterns, which was reformulated in terms of kinetic equations by Gorbunov et al. (1996). Kagan et al. (1978) note that unlike the uncorrelated stopping force or the Coulomb force between the fragments of a dicluster, the wake force—which does not obey Newton's third law—exerts a torque on the cluster. This gives rise to a rotation and thus is a contributing factor in the formation of ring patterns like those shown in Fig. 10.19. In particular, this suggests that the asymmetry between the forward and backward peak in the ring pattern is caused by the wake potential.

The theory of Kagan et al. (1978) considers a dicluster of bare ions, the stopping force is assumed to be proportional to the square of the atomic number, and the equations of motion are solved in the small-t limit introduced in (10.130). Moreover, with a view to the experiments on HHe mentioned above, it was found necessary to take into account the fact that the centre-of-mass experiences a net deflection due to a nonvanishing lateral component of the total wake force. Therefore, the theory operates with three frames of reference, the laboratory frame, the c.m.s. frame, and a frame in uniform motion with the initial velocity.

As it stands, the theory is deterministic and does not account for either multiple scattering or energy-loss straggling. The basic idea has been reformulated in terms of the classical Liouville equation by Gorbunov et al. (1996). Such a formulation would allow to incorporate both multiple scattering and energy straggling, but also this approach has remained unfinished. Therefore, comparisons with experiment have not been possible.

10.6.4.3 Two Foils

The wavelength of the wake,

$$\lambda = 2\pi v/\omega\,, \tag{10.132}$$

is typically much larger than the internuclear distance r_0 of an impinging molecule. One possibility to trace the influence of the wake force in the oscillatory part is to increase the initial distance r_0 between the constituent atoms of a dicluster. This can be done in a double-foil experiment, where the first foil serves to initiate a Coulomb explosion which can proceed in the vacuum between the two foils. The internuclear distance r_0 that determines the trajectories in the second foil can then be regulated by varying the free space between the two foils.

The trailing ion in a well-aligned dicluster experiences a wake force which may be positive or negative, dependent on the distance from the leading ion. Therefore, the energy loss of the trailing ion will be greater or smaller than that of the leading ion, respectively. The lateral component of the wake force—which determines alignment—will likewise depend on the free space between the foils. Thus, the intensity of the second peak will oscillate, while that of the leading peak will be independent of the spacing between the foils. Figure 10.26 shows that at 14 MeV/u the effect is rather weak (upper graph), but with the experimental accuracy achieved in an experiment by Kumbartzki et al. (1982), oscillations become clearly visible.

Gorbunov et al. (1996) addressed this phenomenon on the basis of a Liouville equation describing the motion of a dicluster in configuration and velocity space Kagan et al. (1978), allowing for wake force and Coulomb explosion. Because of the neglect of multiple scattering in the theory a comparison with experiment is not promising and was indeed not reported.

10.7 Applications

The survey of applications of ion beams given in Volume 1 of this monograph focused on atomic ions. This is to briefly mention a few applications of molecular and cluster beams.

10.7.1 Energy Deposition

Obviously, bombardment with a molecular or cluster beam results in an enhancement of the energy deposited per volume in comparison with an otherwise identical atomic beam at the same speed. As a first approximation this enhancement may be taken to be proportional to the number of atoms in the target. Even greater enhancements may be due to proximity effects in stopping, while effects like Coulomb scattering and clearing-the-way effect act in the opposite direction.

While comparing cluster bombardment as a function of the number n of atoms in the cluster at constant v is the obvious choice from a physics point of view, this is normally not the situation met by an experimentalist, who has access to one or perhaps two accelerators with limited ranges of acceleration voltage. Here the obvious comparison will be at constant beam energy E, since the initial charge cannot differ substantially from one unit for stable clusters. This implies that for large clusters you will compare different stopping regimes.

Enhanced *electronic* energy deposition is of interest in inertial-confinement fusion, i.e., the generation of high-temperature plasmas by particle bombardment (Tahir et al., 1994). The choice of the atomic species Z_1 and cluster size involves an optimization between different trends:

- In order to achieve a desired initial velocity v, increasing cluster size implies increasing acceleration voltage,
- Above a certain threshold speed, the proximity effect in stopping increases with increasing v,
- The stopping cross section of an isolated ion decreases above the stopping maximum,
- Coulomb explosion causes decreased energy deposition density with depth.

Since hydrogen is the stopping medium in such experiments, multiple scattering is of minor significance.

Conversely, enhanced *nuclear* energy deposition is of interest in secondary ion mass spectrometry (SIMS). This makes use of enhanced sputter yields for molecule (Andersen and Bay, 1974) or cluster bombardment (Bouneau et al., 2002) as well as enhanced ion fractions (Szymczak and Wittmaack, 1994). Applications initially addressed biomolecular mass spectrometry (Mahoney et al., 1991), but from 2003 on the technique has been used more generally in mass spectrometry (Toyoda et al., 2003) as well as in other areas such as etching and smoothing (Matsuo et al., 1996).

Bombardment with cluster ions is thought to optimize the density of energy deposition, and hence the ion yield, at a given *incident charge*. This is important for insulators, where charging up of the target needs to be minimized.

10.7.2 Coulomb Imaging

You may note from (10.2) that the initial internuclear distance r_0 enters critically into the final speed achieved by the fragments of a diatomic cluster, and hence the angular and energy distribution observed in the detecting system. Therefore, measured Coulomb explosion patterns can be utilized to extract information on r_0. If the penetrated foil is just thin enough to ensure near-complete ionization of the impinging ion, disturbing effects like multiple scattering, stopping and straggling as well as wake effects can be ignored. The resulting emission pattern will then reflect the initial structure, expanded by Coulomb explosion, and observed fluctuations reflect the vibrational structure of the molecule in its initial state.

Similar considerations apply to more complex molecules, except that the possibility of a simple analytical formulation of the relation between the initial configuration and the final observation, as indicated in Sect. 10.2 drops rapidly to zero when there are more than two atoms in the cluster. Therefore, the analysis of such experiments is based on molecular-dynamics simulation applied to various presumed structures and final selection by trial and error.

The first application was a determination of the structure of H_3^+ by Gaillard et al. (1978). On the basis of an equilateral triangular structure as a working hypothesis it was easy to generalize (10.1) to a triatomic molecule (cf. Problem 10.15). Measurements were reported from three laboratories with different apparatus, and it was concluded that the results were compatible with the assumption of a triangular structure.

The experimental technique was developed by means of wire planes, thus enabling coincident detection of both position and velocities (Faibis et al., 1986) applied to a number of small molecules. Information can be gained on both geometrical and vibrational structures (Vager et al., 1989).

10.8 Discussion and Outlook

As you may have noticed, the field of molecule and cluster penetration offers challenges on both the experimental and the theoretical side. Initial motivations came from experiments, in particular molecule transmission, cluster sputtering and enhanced electronic stopping. Theory provided feedback on all these topics and added predictions on wake phenomena. Fascinating experiments were designed that demonstrated ring patterns and reduced charge states. Experiments with polyatomic molecules enabled determination of the structures of molecular ions. Theory and simulation are in reasonable agreement with experiment, with the exception of wake-bound electronic states which have been predicted a long time ago but never unambiguously identified.

On the applied side, it seems that Coulomb imaging—despite considerable success—has not become a standard technique, simply because of its cost. Conversely, the use of large clusters has become accepted as a tool to deposit large energy densities, not the least in surface analysis and fusion research.

10.9 Appendix: Polarization Wake

We have met the polarization wake repeatedly in this and previous chapters. The present appendix presents a few pertinent results in some detail. Although recognized early on as an important aspect of particle penetration (Bohr, 1948b, Neufeld and Ritchie, 1955), massive interest in wake forces arose in connection with the study of molecule and cluster penetration. Although the role of polarization wakes in that topic may occasionally have been overemphasized, there is no question that its significance deserves to be estimated.

10.9.1 Point Charge

In this section we shall have a look at wake potentials of a moving point charge $Z_1 e$, evaluated within linear response theory on the basis of (10.89) and (10.90) for a few representative dielectric functions. Results from this section have already been mentioned in Sect. 1.5.1. With

$$\rho_{\text{ext}}(\boldsymbol{k},\omega) = \frac{Z_1 e}{(2\pi)^3}\delta(\omega - \boldsymbol{k}\cdot\boldsymbol{v}) \tag{10.133}$$

you find

$$\Phi_{\text{ind}}(\boldsymbol{r},t) = \frac{Z_1 e}{2\pi^2}\int \frac{\mathrm{d}^3\boldsymbol{k}}{k^2}\mathrm{e}^{\mathrm{i}\boldsymbol{k}\cdot(\boldsymbol{r}-\boldsymbol{v}t)}\left(\frac{1}{\varepsilon(k,\omega)} - 1\right) \tag{10.134}$$

Following Neufeld and Ritchie (1955) we introduce cylindric coordinates $\boldsymbol{r} = (x,\boldsymbol{\rho})$. After integration over the azimuth you find

$$\Phi_{\text{ind}}(\boldsymbol{r},t) = \frac{Z_1 e}{\pi}\int_0^\infty k\,dk\,J_0(k\rho)\int_{-\infty}^{\infty}\frac{\mathrm{d}\kappa}{k^2+\kappa^2} \times\left(\frac{1}{\varepsilon\left(\sqrt{k^2+\kappa^2},\kappa v\right)} - 1\right)\mathrm{e}^{\mathrm{i}\kappa(x-vt)}, \tag{10.135}$$

where $J_0(z)$ is a Bessel function in standard notation (Abramowitz and Stegun, 1964).

10.9.1.1 Drude-Lorentz Oscillator

If you are interested in the potential at large distances, you may approximate the dielectric function by its long-wavelength limit $k = 0$. For a classical Drude-Lorentz oscillator with a frequency ω_0,

$$\varepsilon(0,\omega) = 1 + \frac{\omega_P^2}{\omega_0^2 - \omega^2 - i\omega\gamma} \tag{10.136}$$

according to Jackson (1975) or (5.54) in Volume 1, and hence

$$\frac{1}{\varepsilon(0,\omega)} - 1 = \frac{\omega_P^2}{\omega^2 + i\omega\gamma - \omega'^2} \tag{10.137}$$

with

$$\omega'^2 = \omega_0^2 + \omega_P^2\,, \tag{10.138}$$

you find

$$\Phi_{\text{ind}}(\boldsymbol{r},t) = \frac{Z_1 e\omega_P^2}{\pi v^2}\int_0^\infty k\,dk\,J_0(k\rho) \times\int_{-\infty}^{\infty}\mathrm{d}\kappa\,\frac{\mathrm{e}^{\mathrm{i}\kappa(x-vt)}}{(\kappa^2+k^2)(\kappa^2 + i\gamma\kappa/v - \omega'^2/v^2)}. \tag{10.139}$$

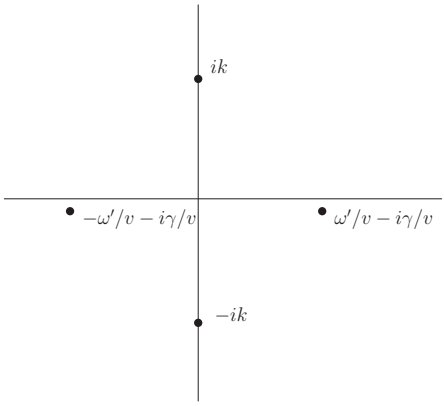

Fig. 10.27 Poles of the integrand in (10.139)

The integral over dκ is similar to one that has been evaluated in Sect. A.2.5, Vol. 1. The location of the poles of the denominator is indicated in Fig. 10.27. For $x - vt > 0$ the integrand approaches zero on a large semicircle in the upper half-plane. For $x - vt < 0$ it approaches zero on a large semicircle in the lower half-plane. Deforming the integration path into such a semicircle leaves the residues at the respective poles.

For $x - vt > 0$ the pertinent pole is at $\kappa = ik$. You then obtain

$$\Phi_{\text{ind}}(\boldsymbol{r}, t) = -\frac{Z_1 e \omega_P^2}{v^2} \int_0^\infty \frac{dk}{k^2 + \omega'^2/v^2} J_0(k\rho)\, \mathrm{e}^{-k(x-vt)}\,. \tag{10.140}$$

For $x - vt < 0$ the three poles in the lower half-plane of Fig. 10.27 deliver nonvanishing residues. Here you find

$$\begin{aligned}\Phi_{\text{ind}}(\boldsymbol{r}, t) = &-\frac{Z_1 e \omega_P^2}{v^2} \int_0^\infty \frac{dk}{k^2 + \omega'^2/v^2} J_0(k\rho)\, \mathrm{e}^{k(x-vt)} \\ &+ \frac{2 Z_1 e \omega_P^2}{v\omega'} \sin\left(\frac{\omega'}{v} x - \omega' t\right) \int_0^\infty dk\, \frac{k}{k^2 + \omega'^2/v^2} J_0(k\rho).\end{aligned} \tag{10.141}$$

Thus, the induced potential consists of two parts,

$$\Phi_{\text{ind}}(\boldsymbol{r}, t) = \Phi_{\text{ind}}^{(1)}(\boldsymbol{r}, t) + \Phi_{\text{ind}}^{(2)}(\boldsymbol{r}, t)\,, \tag{10.142}$$

where

$$\Phi_{\text{ind}}^{(1)}(\boldsymbol{r}, t) = -\frac{Z_1 e \omega_P^2}{v^2} \int_0^\infty \frac{dk}{k^2 + \omega'^2/v^2} J_0(k\rho)\, \mathrm{e}^{-k|x-vt|} \tag{10.143}$$

for all $x - vt$, and

$$\Phi_{\text{ind}}^{(2)}(\boldsymbol{r},t) = \frac{2Z_1 e\omega_P^2}{v\omega'} \sin\left(\frac{\omega'}{v}x - \omega' t\right) K_0\left(\frac{\omega'}{v}\rho\right) \tag{10.144}$$

for $x - vt < 0$, where $K_0(z)$ is a modified Bessel function in standard notation (Abramowitz and Stegun, 1964).

All these results are due to Neufeld and Ritchie (1955), who considered the case of $\omega_0 = 0$, i.e., $\omega' = \omega_P$.

You may note that $\Phi_{\text{ind}}^{(2)}(\boldsymbol{r},t)$ factorizes into an oscillatory function of x with the wavelength $v/2\pi\omega'$ and a monotonically decreasing function of ρ with a decay length v/ω'. You may recognize the Bohr adiabatic radius. The calculation reported here refers to the long-wavelength limit, i.e., (10.144) may become invalid as ρ gets small. On the other hand there appears to be an undamped oscillatory dependence on $x - vt$ which has received much interest in the past.

Consider now the function $\Phi_{\text{ind}}^{(1)}(\boldsymbol{r},t)$ in a reference frame moving with the projectile. With the substitution $k = \zeta\omega'/v$, you obtain

$$\Phi_{\text{ind}}^{(1)}(\boldsymbol{r},t) = -\frac{Z_1 e\omega_P^2}{\omega' v}\int_0^\infty \frac{\mathrm{d}\zeta}{\zeta^2+1} J_0\left(\frac{\omega'\rho}{v}\zeta\right) \mathrm{e}^{-(\omega' x'/v)\zeta}\,, \tag{10.145}$$

where $x' = x - vt$. The integrand is =1 at $\zeta = 0$ and falls off over a decay length $\sim v/\omega' r'$, where $r' = \sqrt{x'^2 + \rho^2}$. Thus, a rough estimate leads to

$$\Phi_{\text{ind}}^{(1)}(\boldsymbol{r},t) \sim -\frac{Z_1 e\omega_P^2}{\omega'^2 r'}\,. \tag{10.146}$$

For a free electron gas, where $\omega' = \omega_P$, this is the negative of the Coulomb potential of the bare ion. Thus, $\Phi_{\text{ind}}^{(1)}(\boldsymbol{r},t)$ represents screening of the projectile potential to within the adiabatic radius.

10.9.1.2 Quantum Oscillator

The spherical harmonic oscillator has served as a useful model for stopping calculations in Volume 1. Unlike in the case of the classical oscillator a restriction to long wavelengths is not required. Within the Born approximation, the main part of the theory can be carried out analytically.

The longitudinal nonrelativistic dielectric function (Belkacem and Sigmund, 1990) is given in (5.90),

$$\varepsilon_l(k,\omega) = 1 + \frac{m\omega_{\text{P}}^2}{\hbar k^2}\mathrm{e}^{-\omega_k/\omega_0}\sum_{j=1}^{\infty}\frac{1}{j!}\left(\frac{\omega_k}{\omega_0}\right)^j \times\left(\frac{1}{j\omega_0 - \omega - \mathrm{i}\Gamma} + \frac{1}{j\omega_0 + \omega + \mathrm{i}\Gamma}\right), \tag{10.147}$$

where $\omega_k = \hbar k^2/2m$.

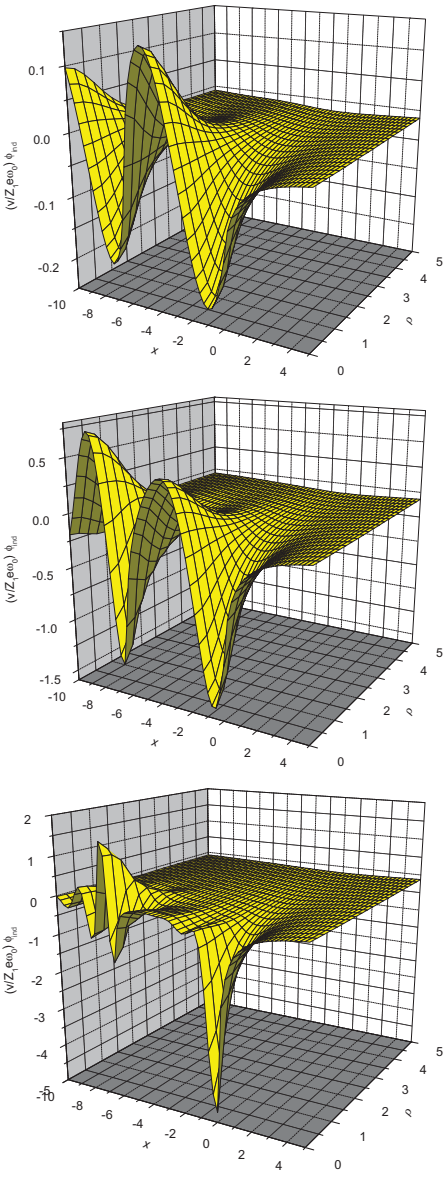

Fig. 10.28 Induced potential for a medium of quantum oscillators for $B = 2mv^2/\hbar\omega_0 = 10$ and $\omega_P^2/\omega_0^2 = 10, 1$ and 0.1 (top to bottom). From Schinner and Sigmund (2012)

Wake potentials may be calculated by insertion of (10.147) into (10.134) and evaluated numerically. Figure 10.28 shows induced potentials for $B = 2mv^2/\hbar\omega_0 = 10$ for three densities, expressed by $\omega_P^2/\omega_0^2 = 0.1, 1$ and 10. Qualitative features

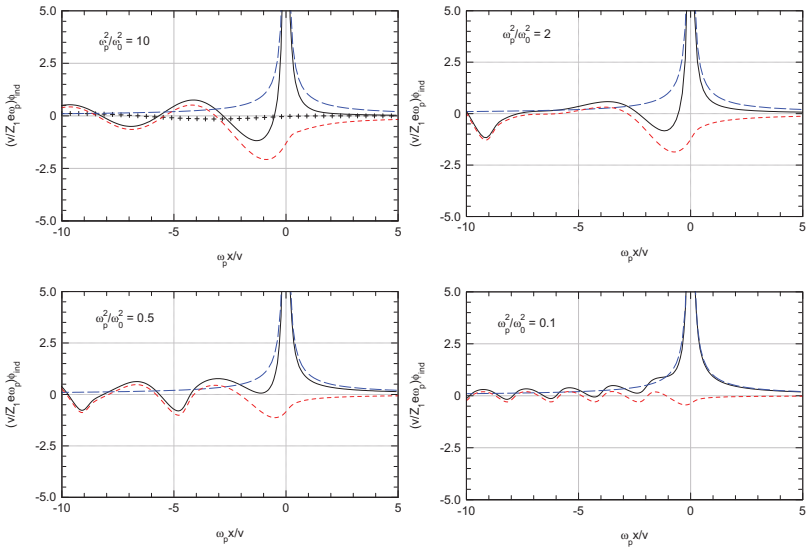

Fig. 10.29 Induced potential (red dotted lines), Coulomb potential (blue dashed lines) and total potential (solid black lines) at $\rho = 0$ for $B = 2mv^2/\hbar\omega_p = 10$. Results for an ensemble of oscillators for $\omega_p^2/\omega_0^2 = 10$, 2, 0.5 and 0.1. From Schinner and Sigmund (2012)

found already for the Drude-Lorentz oscillator go again, such as the strong forward-backward asymmetry, a periodic behaviour in the longitudinal direction behind the projectile and an exponential decrease in the lateral direction. The amplitude of the oscillations increases with increasing density, while the wavelength decreases.

Figure 10.29 shows induced potentials together with the Coulomb potential and the total wake potential in the core ($\rho = 0$) at $B = 2mv^2/\hbar\omega_0 = 10$ for four electron densities expressed by the parameter ω_P^2/ω_0^2. Two main effects are seen:

- As in the static case, the polarization causes screening of the Coulomb potential near the projectile,
- A pronounced oscillatory potential develops further behind the projectile with a wavelength of the order of the adiabatic radius v/ω_P, i.e., the effective interaction radius in the lateral direction.

Both effects are most pronounced for $\omega_P^2/\omega_0^2 \gg 1$, i.e., for high electron densities. Note in particular that the potential may significantly exceed the static Coulomb interaction. At low densities the Coulomb interaction appears to be only lightly disturbed by a weak oscillation with wavelengths of the order of v/ω_0.

10.9.1.3 Fermi Gas

Models of the free electron gas have served as the main tool in the study of wake fields and their applications, starting with Neufeld and Ritchie (1955) and, later, Neelavathi et al. (1974), Vager and Gemmell (1976). Explicit calculations for a Fermi gas became available from Echenique et al. (1979) on the basis of the plasmon-pole approximation discussed in Sect. 5.4.5, Vol. 1.

Figure 10.30 shows results based on Lindhard's dielectric function, discussed in Sect. 5.7.3, Vol. 1 and specified in (5.154)–(5.157). Input parameters are similar to those in Fig. 10.28. The Fermi gas is characterized by only one parameter. Hence, these potentials are very similar except for the scale.

10.9.1.4 Implications

Wake phenomena are of interest in many connections, especially in the relativistic regime but also the interaction of charged particles moving close and nearly parallel to a plane surface (Winter, 2002). In the present context only their influence on the penetration of molecules is considered.

It follows from Figs. 10.29 and 1.14 that the force on the projectile ions depends on the orientation of the cluster. This must affect Coulomb explosion and multiple scattering, although the effect is small for internuclear distances well below the adiabatic radius.

There is an interesting relation between wake forces and energy loss. We have seen in Chap. 5, Vol. 1, that the stopping force on a point charge is related to the work performed against the induced field. Let us generalize this relation and consider the work performed by a projectile characterized by some charge distribution

$$\rho(\boldsymbol{r},t) = \rho_0(\boldsymbol{r} - \boldsymbol{v}t)\,. \tag{10.148}$$

The net force on the projectile is given by

$$\boldsymbol{F} = \int \mathrm{d}^3\boldsymbol{r}\;\rho(\boldsymbol{r},t)\boldsymbol{E}_{\mathrm{ind}}(\boldsymbol{r},t)\,. \tag{10.149}$$

For a dicluster we may approximate

$$\rho_0(\boldsymbol{r}) = \rho_1(|\boldsymbol{r} - \boldsymbol{R}_1|) + \rho_2(|\boldsymbol{r} - \boldsymbol{R}_2|)\,, \tag{10.150}$$

assuming straight superposition of two atomic charge densities. Then we have

$$\boldsymbol{F} = \boldsymbol{F}_{11} + \boldsymbol{F}_{22} + \boldsymbol{F}_{12} + \boldsymbol{F}_{21}\,, \tag{10.151}$$

where

$$\boldsymbol{F}_{\mu\nu} = \int \mathrm{d}^3\boldsymbol{r}\;\rho_\mu(\boldsymbol{r},t)\boldsymbol{E}_{\mathrm{ind},^\circ}(\boldsymbol{r},t) \tag{10.152}$$

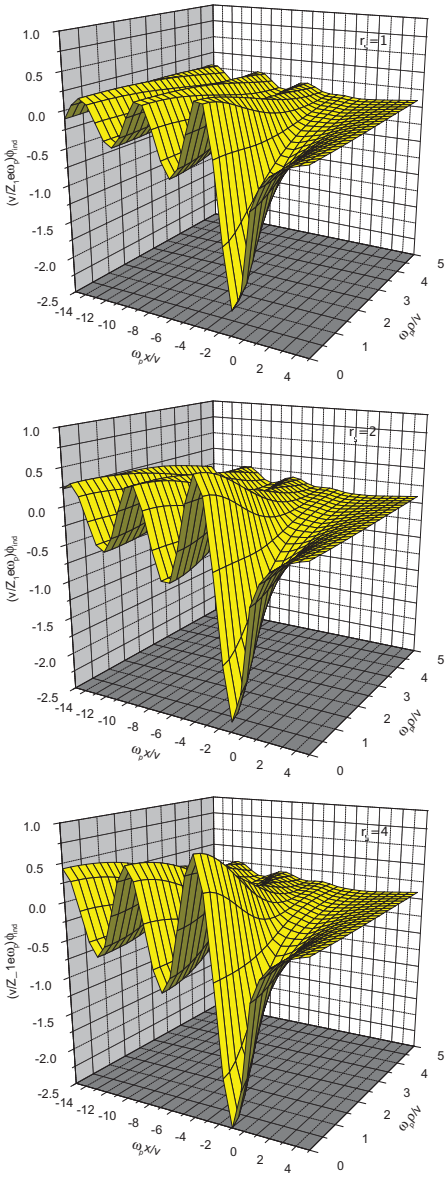

Fig. 10.30 Induced potential for Fermi gas at $2mv^2/\hbar\omega_p = 10$ and $r_s = 1, 2, 4$ (top to bottom). From Schinner and Sigmund (2012)

or, in Fourier space,

$$\boldsymbol{F}_{\mu\nu} = -32\pi^4 i \int \frac{\boldsymbol{k}\,\mathrm{d}^3\boldsymbol{k}}{k^2\varepsilon(k, \boldsymbol{k}\cdot\boldsymbol{v})}\,\rho_\mu(k)\rho_\nu(k)\,\mathrm{e}^{\mathrm{i}\boldsymbol{k}\cdot(\boldsymbol{R}_\mu - \boldsymbol{R}_\nu)}\,. \tag{10.153}$$

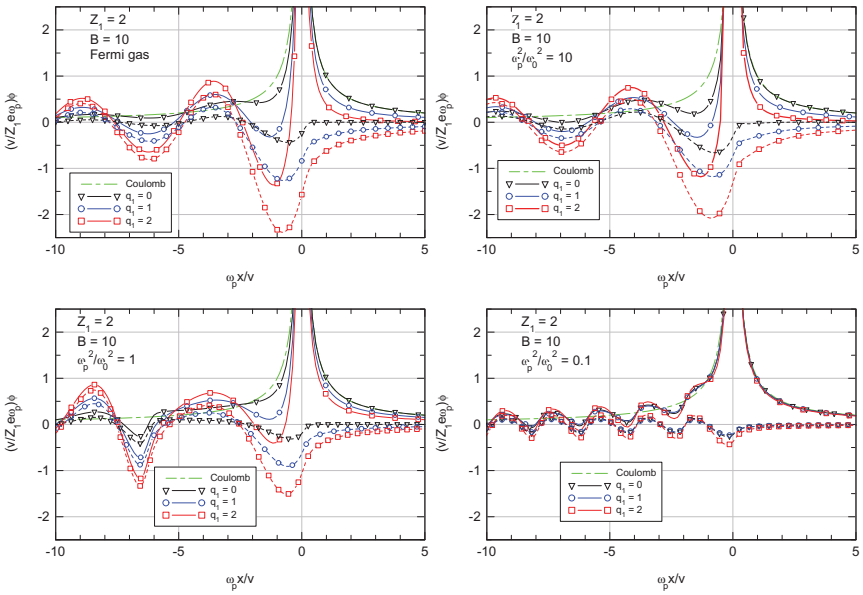

Fig. 10.31 Charge-state dependence of the wake potential: Dashed lines: induced potential. Solid lines: Total potential; Dot-dashed line: Bare Coulomb potential. Fermi gas (top left) and oscillator model; $B = 2mv^2/\hbar\omega_p = 10$; $Z_1 = 2$; $\hbar\omega_0 = 13.6$ eV. $\omega_p^2/\omega_0^2 = 10$, 1 and 0.1

In (10.151), the first two terms represent stopping forces on isolated atomic ions 1 and 2, while the last two terms reflect the interference effect.

While the treatment presented in Sect. 10.4 produces the total energy loss of the molecule, (10.151) identifies the change in stopping force of atom 1 due to the presence of atom 2 and vice versa. This allows an estimate of the effect of the polarization wake on Coulomb explosion.

10.9.2 Screened Ions

The influence of the ion charge on the wake potential has been studied by Schinner and Sigmund (2012). The potential of the screened projectile charge has been expressed by (4.16) with exponential screening and the screening radius

$$a = (1 - q_1/Z_1)\, a_{TF} = (1 - q_1/Z_1)\, 0.8853 a_0/Z_1^{1/3}\,. \tag{10.154}$$

Screening enters the integrand in (10.134) via the replacement

$$\frac{Z_1}{k^2} \to \frac{q_1}{k^2} + \frac{Z_1 - q_1}{k^2 + 1/a^2}\,. \tag{10.155}$$

This results in an additional factor

$$f(k,a,\beta) = \frac{k^2a^2 + q_1/Z_1}{k^2a^2 + 1}\,. \tag{10.156}$$

in the integrand.

The two upper graphs in Fig. 10.31 show induced potentials, Coulomb potential and total potential for He^{++}, He^{+} and He^{0} in a Fermi gas (left) and an oscillator gas (right) both with $\omega_p^2/\omega_0^2 = 10$, i.e., high electron density. These graphs are very similar, and they show that the magnitude of the induced field decreases with decreasing charge. This implies that

- The screening of the Coulomb potential near the projectile by the polarization charge is *reduced* as the ion charge gets smaller, and
- The oscillatory potential far behind the projectile gets suppressed.

These features are still visible for $\omega_p^2/\omega_0^2 = 1$ (lower graph left), whereas effects due to the induced field are barely visible at low density, $\omega_p^2/\omega_0^2 = 0.1$ (lower graph right).

Problems

10.1. Derive (10.2) and (10.4) from (10.1).

10.2. Determine the relative change $(r(x/v) - r_0)/r_0$ in internuclear distance during passage through a foil with thickness x in the experiment described by Golovchenko and Lægsgaard (1974).

10.3. Determine the scattering angle θ_0, where the two peaks in the energy spectrum shown in Fig. 10.3 merge into one. Hint: When the molecule is oriented perpendicular to the beam, each H atom receives a certain momentum perpendicular to the beam.

10.4. Derive (10.56), following the procedure outlined in Sects. 4.3.2 and 4.3.4 of Volume 1.

10.5. Follow the procedure in Sect. 10.4.2 to derive (10.57).

10.6. Consider (10.56) for an arbitrary angle ϕ between $\boldsymbol{r}$ and $\boldsymbol{v}$. If you aim at the stopping cross section, you will have to sum over all j at some stage. Assume you have carried out the summation over all *degenerate* states. This implies that the factor $\left|F_{j0}(\boldsymbol{q})\right|^2$ becomes independent of the direction of $\boldsymbol{q}$. Under this assumption, carry out the integration over the angular variables of $\boldsymbol{q}$, and show that this is equivalent with the replacement

$$\delta\left(\omega_{j0} - \boldsymbol{q}\cdot\mathbf{v}\right)\cos(\boldsymbol{q}\cdot\boldsymbol{r}) \Rightarrow J_0\left(r\sin\phi\sqrt{q^2-\omega_{j0}^2/v^2}\right)\cos\left(\frac{r\omega_{j0}}{v}\cos\phi\right) \quad (10.157)$$

in (10.56). [Hint: Use cylindric coordinates with $\boldsymbol{v}$ as the axis].

A derivation of this result, based on dielectric theory, was presented by Brandt et al. (1974).

10.7. Derive (10.62) from (10.60) for random orientation, i.e., $u(r) = \sin(qr)/(qr)$. Remind that $Q = \hbar^2 q^2/2m$. Express the result in terms of the integral cosine function

$$Ci(\xi) = -\int_{\xi}^{\infty} \mathrm{d}t\,\frac{\cos t}{t}\,. \quad (10.158)$$

Apply appropriate expansions for small and large arguments and arrive at (10.66) to the leading order.

10.8. Develop an expression for the stopping cross section of a diatomic molecule by generalizing Bohr's calculation, following Sects. 4.2.1 and 4.2.2 in Volume 1. If you need help, consult Basbas and Ritchie (1982) Sect. IBID or Jensen and Sigmund (2000) Sect. ILIA.

10.9. Show that (10.79) reduces to a part of (10.62) for Coulomb interaction, where $V(q) = -Z_j e^2/2\pi^2 q^2$.

10.10. Derive (10.94).

10.11. Evaluate (10.96) for a beam of swift clusters of two protons oriented at random, penetrating through a free electron gas, approximated as a static gas using the dielectric function defined in (5.60) of Volume 1,

$$\varepsilon(k,\omega) = 1 + \frac{\omega_P^2}{\omega_k^2 - (\omega + \mathrm{i}\Gamma)^2}\,. \quad (10.159)$$

If you need help, check Arista (1978).

10.12. Repeat Problem 10.11 for a Drude-Lorentz dielectric function

$$\varepsilon(\omega) = 1 + \frac{\omega_P^2}{\omega_0^2 - (\omega + \mathrm{i}\gamma)^2}\,. \quad (10.160)$$

Important: Evaluate only the interference term $\propto Z_1 Z_2$.
Hint: First carry out the integral over k and subsequently use Cauchy's theorem to evaluate the integral over ω.

10.13. Show that for a homonuclear dicluster with atomic number Z_1, the relative multiple scattering is found from the atomic multiple scattering distribution by replacing $Z_1 \to \sqrt{2}Z_1$.

10.14. Derive (10.130) and (10.131).

10.15. Assume a regular ring of n atomic ions with charges $Z_1 e$ and masses M_1 at a radius $r(0)$. Determine the ring radius $r(t)$ as a function of time as well as the final velocity $v(\infty)$. What is the minimum area of the detector placed 1 m behind the target, if you want to detect all emerging particles? Take, as an example, $Z_1 = 6$, $n = 6$ and $E = 1$ MeV/u.

References

Abramowitz M. and Stegun I.A. (1964): *Handbook of mathematical functions*. Dover, New York

Abril I., Vicanek M., Gras-Marti A. and Arista N.R. (1992): Large hydrogen cluster stopping in carbon. Nucl Instrum Methods B **67**, 56–61

Andersen H.H. and Bay H.L. (1974): Nonlinear effects in heavy-ion sputtering. J Appl Phys **45**, 953–954

Arista N.R. (1978): Energy loss of correlated charges in an electron gas. Phys Rev B **18**, 1–8

Arista N.R. (2000): Stopping of molecules and clusters. Nucl Instrum Methods B **164-165**, 108–138

Arista N.R. and Ponce V.H. (1975): The energy loss of correlated protons in channeling. J Phys C **8**, L001–L004

Basbas G. and Ritchie R.H. (1982): Vicinage effects in ion-cluster collisions with condensed matter and with single atoms. Phys Rev A **25**, 1943–1962

Baudin K., Brunelle A., Chabot M., Della-Negra S., Depauw J., Gardès D., kansson P.H., LeBeyec Y., Billebaud A., Fallavier M. et al. (1994): Energy loss by MeV carbon clusters and fullerene ions in solids. Nucl Instrum Methods B **94**, 341–344

Belkacem A. and Sigmund P. (1990): Stopping power and energy loss spectrum of a dense medium of bound electrons. Nucl Instrum Methods B **48**, 29–33

Bickel W.S. (1975): Molecular effects in beam-foil spectroscopy. Phys Rev A **12**, 1801–1807

Bohr A. (1948a): Atomic interaction in penetration phenomena. Mat Fys Medd Dan Vid Selsk **24 no. 19**, 1–52

Bohr N. (1948b): The penetration of atomic particles through matter. Mat Fys Medd Dan Vid Selsk **18 no. 8**, 1–144

Bouneau S., Brunelle A., Della-Negra S., Depauw J., Jacquet D., Le Beyec Y., Pautrat M., Fallavier M., Poizat J.C. and Andersen H.H. (2002): Very large gold and silver sputtering yields induced by keV to MeV energy Au-n clusters (n=1-13). Phys Rev B **65**, 144106

Brandt W. and Kitagawa M. (1982): Effective stopping-power charges of swift ions in condensed matter. Phys Rev B **25**, 5631–5637

Brandt W., Ratkowski A. and Ritchie R.H. (1974): Energy loss of swift proton clusters in solids. Phys Rev Lett **33**, 1325–1328

Breskin A., Faibis A., Goldring G., Hass M., Kaim R., Vager Z. and Zwang N. (1979): Charge-state dependence of the Coulomb explosion of 10-MeV OH^+. Phys Rev Lett **42**, 369–372

Brunelle A., Della-Negra S., Depauw J., Jacquet D., LeBeyec Y. and Pautrat M. (1999): Reduced charge state of MeV carbon cluster constituents exiting thin carbon foils. Phys Rev A **59**, 4456–4460

Chiba A., Saitoh Y., Narumi K., Takahashi Y., Yamada K. and Kaneko T. (2011): Measurement of divergence angle classified by charge-state combination of C_2^+ constituents passing through a thin carbon foil. Nucl Instrum Methods B **269**, 824–828

Cooney P.J., Gemmell D.S., Pietsch W.J., Ratkowski A.J., Vager Z. and Zabransky B.J. (1981): Interactions of fast HeH^+ beams with matter. Phys Rev A **24**, 746–757

Cue N., de Castro-Faria N.V., Gaillard M.J., Poizat J.C. and Remillieux J. (1980): Transmission of fast H_2^+ through thin foils. Phys Rev Lett **45**, 613–617

Denton C.D., Abril I., Garcia-Molina R. and Heredia-Avalos S. (2007): Alignment effects in the interaction of H_2^+ molecules with thin foils. Nucl Instrum Methods B **256**, 137–140

Echenique P.M., Ritchie R.H. and Brandt W. (1979): Spatial excitation pattern induced by swift ions in condensed matter. Phys Rev B **20**, 2567–2580

Eckardt J.C., Lantschner G., Arista N.R. and Baragiola R.A. (1978): Electronic stopping of slow molecular-ions in solids. J Phys C **11**, L851–L855

Esbensen H. and Sigmund P. (1990): Barkas effect in a dense medium: Stopping power and wake field. Ann Physics NY **201**, 152–192

Ewing R.I. (1962): Response of silicon surface barrier detectors to hydrogen ions of energies 25 to 250 keV. IRE Trans Nucl Sci **NS-9 no. 2**, 207–210

Fadanelli R.C., Grande P.L., Behar A., Dias J.F. and Schiwietz G. (2005): The influence of the Coulomb explosion on the energy loss of H^{2+} and H^{3+} molecules channeling along the Si(100) direction. Nucl Instrum Methods B **230**, 96–99

Fadanelli R.C., Grande P.L., Behar M., Dias J.F., Czerski K. and Schiwietz G. (2006): Interplay between the Coulomb explosion and vicinage effects studied using H^{2+} molecules under channeling conditions. Physical Review B **73**, 245336

Faibis A., Koenig W., Kanter E.P. and Vager Z. (1986): MUPPATS—a multiparticle 3D imaging detector system. Nucl Instrum Methods B **13**, 673–677

Fermi E. (1939): The absorption of mesotrons in air and in condensed materials. Phys Rev **56**, 1242–1242

Fermi E. (1940): The ionization loss of energy in gases and in condensed materials. Phys Rev **57**, 485–493

Gaillard M.J., Gemmell D.S., Goldring G., Levine I., Pietsch W.J., Poizat J.C., Ratkowski A.J., Remillieux J., Vager Z. and Zabransky B.J. (1978): Experimental determination of the structure of H^{3+}. Phys Rev A **17**, 1797–1803

Gaillard M.J., Poizat J.C., Ratkowski A. and Remillieux J. (1976): The dependence of H_2^+ molecular-ion yields on the proton neutral fraction. Nucl Instrum Methods **132**, 69–73

Gaillard M.J., Poizat J.C., Ratkowski A., Remillieux J. and Auzas M. (1977): Nonequilibrium effects in the proton neutral fraction emerging from solids bombarded with MeV H^0, H^+, H_2^+, and H_3^+ beams. Phys Rev A **16**, 2323–2335

Gemmell D.S. (1981): The coulomb-explosion technique for determining geometrical structures of molecular-ions. Nucl Instrum Methods **191**, 425–431

Gemmell D.S. (1982): Collisional effects in the passage of fast molecular-ions through thin foils. Nucl Instrum Methods **194**, 255–267

Gemmell D.S., Remillieux J., Poizat J.C., Gaillard M.J., Holland R.E. and Vager Z. (1975): Evidence for an alignment effect in motion of swift ion clusters through solids. Phys Rev Lett **34**, 1420–1424

Golovchenko J. and Lægsgaard E. (1974): Correlated scattering of protons impinging as hydrogen molecules. Phys Rev A **9**, 1215–1219

Gorbunov L.M., Nersissian H.B. and Matevossian G.G. (1996): On the theory of a dicluster-ion beam propagation through a thin foil. J Phys C **8**, 2513–2517

Heredia-Avalos S., Garcia-Molina R. and Arista N.R. (2001): Vicinage effects in the charge state of swift molecular constituents traversing thin foils. Europhys Lett **54**, 729–735

ICRU (2005): *Stopping of ions heavier than helium*, vol. 73 of *ICRU Report*. Oxford University Press, Oxford

Jackson J.D. (1975): *Classical electrodynamics*. John Wiley & Sons, New York

Jakas M.M. and Capuj N. (1995): Wake forces and the transmission yield of H_2^+ through thin carbon foils. Phys Rev A **51**, 2277–2280

Jensen J. and Sigmund P. (2000): Electronic stopping of swift partially stripped molecules and clusters. Phys Rev A **61**, 032903–1–14

Kagan Y., Kononets Y.V. and Dzhamankyzov N.K. (1978): Dynamic-interaction effects in the decay of fast molecules in thin films. Zh Eksp Teor Fiz **74**, 288–299. [English Translation: Sov. Phys. JETP **47**, 148 (1978)]

Kemmler J., Koschar P., Burkhard M. and Groeneveld K.O. (1985): Wake effects in the stopping power of molecular ions. Nucl Instrum Methods B **12**, 62–66

Kramers H.A. (1947): The stopping power of a metal for alpha-particles. Physica **13**, 401–412

Kumbartzki G.J., Neuburger H., Kohl H.P. and Polster W. (1982): Measurements of the wavelength of the polarization wake in carbon and aluminium. Nucl Instrum Methods **194**, 291–293

Li H.W., Wang Y.N. and Miskovic Z.L. (2002): Influence of wake-potential asymmetry on charge states, and Coulomb explosion of fast molecular ions in solids. Nucl Instrum Methods B **193**, 204–208

Lindhard J. (1954): On the properties of a gas of charged particles. Mat Fys Medd Dan Vid Selsk **28 no. 8**, 1–57

Mahoney J.F., Perel J., a. Ruatta S., a. Martino P., Husain S. and Lee T.D. (1991): Massive cluster impact mass spectrometry: A new desorption method for the analysis of large biomolecules. Rapid Comm Mass Spectrometry **5**, 441–445

Maor D., Cooney P.J., Faibis A., Kanter E.P., Koenig W. and Zabransky B.J. (1985): Charge-state distributions of nitrogen ions resulting from the foil-induced dissociation of 4.2-MeV N_2^+ ions. Phys Rev A **32**, 105–111

Matsuo J., Toyoda N. and Yamada I. (1996): Nanofabrication technology by gas cluster ion beams. J Vac Sci Technol B **14**, 3951–3954

McCarroll R., Piacentini R.D. and Salin A. (1970): Differential cross sections in proton-hydrogen collisions. J Phys B **3**, 137–148

Miskovic Z.L., Davison S.G., Goodman F.O., Liu W.K. and Wang Y.N. (2000): Vicinage effect on the charge state of fast clusters in solids. Physical Review A **61**, 062901

Miskovic Z.L., Davison S.G., Goodman F.O., Liu W.K. and Yang Y.N. (2001a): Stopping power of fast, partially stripped molecules and clusters: Vicinage effects in charge states. Phys Rev A **63**, 022901

Miskovic Z.L., Liu W.K., Goodman F.O. and Wang Y.N. (2001b): Ion-charge distribution in fast, partially stripped clusters passing thin foils. Phys Rev A **64**, 064901

Miskovic Z.L., Wang Y.N. and Song Y.H. (2007): Dynamics of fast molecular ions in solids and plasmas: A review of recent theoretical developments. Nucl Instrum Methods B **256**, 57–65

Nardi E., Zinamon Z., Tombrello T.A. and Tanushev N.M. (2002): Simulation of the interaction of high-energy C-60 cluster ions with amorphous targets. Phys Rev A **66**, 013201

Neelavathi V.N., Ritchie R.H. and Brandt W. (1974): Bound electron states in the wake of swift ions in solids. Phys Rev Lett **33**, 302–305

Neufeld J. and Ritchie R.H. (1955): Passage of charged particles through plasma. Phys Rev **98**, 1632–1642

Nikolaev V.S. (1966): Calculation of effective cross sections for proton charge exchange in collisions with multi-electron atoms. Zh Eks Teor Fiz **51**, 1263. English translation: Sov. Phys. JETP **24**, 1263 (1967)

Pérez-Pérez F.J., Abril I., Garcia-Molina R. and Arista N. (1996): Collective effects in the energy loss of large hydrogen clusters. Phys Rev A **54**, 4145–4152

Plesser I. (1982): The interpretation of molecular-ion dissociation experiments. Nucl Instrum Methods **194**, 269–275

Poizat J.C. and Remillieux (1972): Channeling effects on transmission of MeV H^{2+} ions through a thin gold single-crystal. J Phys B **5**, L94

Poizat J.C. and Remillieux J. (1971): Dissociation of a fast H_2^+ molecular ion beam colliding with thin carbon targets. Phys Lett A **34**, 53–54

Ray E., Kirsch R., Mikkelsen H.H., Poizat J.C. and Remillieux J. (1992): Slowing down of hydrogen clusters in thin foils. Nucl Instrum Methods B **69**, 133–141

Rozet J.P., Chetioui A., Bouisset P., Vernhet D., Wohrer K., Touati A., Stephan C. and Grandin J.P. (1987): Anomalous population of deep capture states of fast ions emerging from solid foils. Phys Rev Lett **58**, 337–340

Schinner A. and Sigmund P. (2012): Polarization wake of penetrating ions: Oscillator model. Europ Phys J D **66**, 56

Shubeita S.M., Grande P.L., Dias J.F., Garcia-Molina R., Denton C.D. and Abril I. (2011): Energy loss of swift H_2^+ and H_3^+ molecules in gold: Vicinage effects revisited. Phys Rev B **83**, 245423

Sigmund P. (1989): Collision cascades and sputtering induced by larger cluster ions. J de Physique **C2-50**, 175–192

Sigmund P. (1992a): Scaling laws governing the multiple scattering of diatomic molecules under Coulomb explosion. Phys Rev A **46**, 2596–2606

Sigmund P. (1992b): Scattering and stopping of swift diatomic molecules under Coulomb explosion. Nucl Instrum Methods B **67**, 11–16

Sigmund P., Bitensky I.S. and Jensen J. (1996): Molecule and cluster bombardment: energy loss, trajectories, and collision cascades. Nucl Instrum Methods B **112**, 1–11

Sigmund P. and Schinner A. (2010): Impact-parameter-dependent stopping of swift ions. 3. Bunching and packing in energy-loss straggling. Europ Phys J D **58**, 105–116

Sigmund P. and Schinner A. (2011): Stopping of swift hydrogen diclusters: Oscillator model. Europ Phys J D **61**, 39–50

Steinbeck J. and Dettmann K. (1978): Energy loss of fast H_2^+ molecules in solids: I. J Phys C **11**, 2907–2916

Steuer M.F., Gemmell D.S., Kanter E.P., Johnson E.A. and Zabransky B.J. (1982): Diminished stopping powers for fast nitrogen and oxygen diclusters in carbon. Nucl Instrum Methods **194**, 277–279

Steuer M.F. and Ritchie R.H. (1988): Energy loss of aligned nitrogen molecular ions in an electron gas. Nucl Instrum Methods B **33**, 170–173

Steuer M.F. and Ritchie R.H. (1989): Intermediate-velocity molecular and atomic ions in solids. Nucl Instrum Methods B **40/41**, 372–375

Susuki Y., Fritz M., Kimura K., Mannami M., Garcia-Molina R. and Abril I. (2000): Energy loss of fragment protons dissociated from 0.2- and 0.5-MeV/amu H_2^+ ions incident in carbon foils. Phys Rev A **62**, 012902

Szymczak W. and Wittmaack K. (1994): Evidence for strongly enhanced yields of negative molecular secondary ions due to bombardment with SF_n cluster ions. Nucl Instrum Methods B **88**, 149–153

Tahir N.A., Hoffmann D.H.H., Maruhn J.A. and Deutsch C. (1994): Indirect drive inertial fusion using heavy ion cluster beams. Nucl Instrum Methods B **88**, 127–130

Tomita S., Murakami M., Sakamoto N., Ishii S., Sasa K., Kaneko T. and Kudo H. (2010): Reduction in the energy loss of 0.5-MeV-per-atom carbon cluster ions in thin carbon foils. Phys Rev A **82**, 044901

Toyoda N., Matsuo J., Aoki T., Yamada I. and Fenner D.B. (2003): Secondary ion mass spectrometry with gas cluster ion beams. Appl Surf Sci **203-204**, 214–218

Vager Z. and Gemmell D.S. (1976): Polarization induced in a solid by the passage of fast charged particles. Phys Rev Lett **37**, 1352–1355

Vager Z., Naaman R. and Kanter E.P. (1989): Coulomb explosion imaging of small molecules. Science **24**, 426–431

Winter H. (2002): Collisions of atoms and ions with surfaces under grazing incidence. Phys Repts **367**, 387–582

Yamamura Y. (1988): Sputtering by cluster ions. Nucl Instrum Methods B **33**, 493–496

Zajfman D. (1990): Effect of coherent multiple scattering on the transmission of H_2^+ through thin foils. Phys Rev A **42**, 5374–5377

Zajfman D., Both G., Kanter E.P. and Vager Z. (1990): Multiple scattering of MeV atomic and molecular tions traversing ultrathin films. Phys Rev A **41**, 2482–2488

Ziegler J.F., Biersack J.P. and Littmark U. (1985): *The stopping and range of ions in solids*, vol. 1 of *The stopping and ranges of ions in matter*. Pergamon, New York

Part VI
Penetration through Crystals

Chapter 11
Channeling and Blocking of Energetic Particles in Crystals

Jens Ulrik Andersen[1]

Department of Physics and Astronomy, University of Aarhus
8000 Aarhus C, Denmark

Abstract

The development of channeling and blocking since the foundation of the field was laid by Jens Lindhard in his classical paper in 1965 is discussed[2], and the question is asked whether this theory has passed the test of time. Have important aspects of the theory been challenged? Where has the theory needed modification or extension? Are there still open questions to be solved?

A basic theoretical issue is the applicability of classical mechanics in the description. Lindhard showed that for particles heavy compared with the electron classical orbital pictures may always be applied. However, for electrons and positrons there are strong quantal features, like Bragg interference. The quantal description introduced by Lindhard and co-workers has been used as the basis for a comprehensive treatment of the channeling of MeV electrons and positrons and of channeling radiation. At very high energies, GeV and TeV, the motion becomes classical, due to the relativistic increase of the field seen by the particles in the reference frame following

[1] Updated and slightly edited from J. U. Andersen's contribution to *Ion Beam Science*. Solved and Unsolved Problems. Part II, P. Sigmund, editor. Published in Mat. Fys. Medd. Dan. Vid. Selsk. 52:2, 655-698 (2006), http://www.sdu.dk/Bibliotek/matfys. Reprinted with kind permission of the Royal Danish Academy of Sciences and Letters.

[2] If this is your first encounter with the field of channeling, it will be an advantage for you to have easy access to Lindhard's paper (Lindhard, 1965)

P. Sigmund, *Particle Penetration and Radiation Effects Volume 2*,
Springer Series in Solid-State Sciences 179, DOI: 10.1007/978-3-319-05564-0_11,

their longitudinal motion. Channeling radiation in this regime is still an active field of research.

For channeling and blocking of ions, the concept of statistical equilibrium plays a central part in Lindhard's theory. The application of this concept has met with two important challenges, the first based on computer simulations and the second on experiments with the transmission of heavy ions through thin crystals. In both cases the challenges have been met and new insight has been gained but there are still problems to be solved. Channeling and blocking of ions have found very many interesting applications, and a few problems and opportunities worth pursuing are suggested.

11.1 Introduction

Channeling was discovered a few years before I in 1964 began my graduate studies at the University of Aarhus, and I was lucky to be supervised by one of the pioneers in the field, John Davies, who brought the field to Aarhus. The local interest was stimulated by many lively 'Saturday meetings' where new experimental developments were analysed and discussed. Most important was the strong involvement of Jens Lindhard, who with an impressive intellectual effort provided a theoretical foundation of the field in his famous paper from 1965 (Lindhard, 1965). Before publication he presented the theory in a series of lectures, and I still remember these as a thrilling experience. There had been earlier theoretical work on channeling, including both computer simulations and analytical theory, but Lindhard's theory far surpassed this earlier work in depth of analysis, in generality of concepts, and in breadth of coverage of the phenomena. Lindhard presented his theory at the first of a series of International Conferences on Atomic Collisions in Solids (ICACS), and later developments in channeling were usually reported at these meetings. Figure. 11.1 shows Lindhard at ICACS in Hamilton, 1979, in a characteristic pose, using his pipe to make a point.

This is a brief review of the development of channeling during the following about forty years, based very much on my personal experience. I shall emphasize developments which I have found of particular interest and mainly refer to work in which I have been involved and therefore know best. I shall try to give credit where needed to pioneering efforts by other groups but many more would have deserved to be mentioned. A main theme will be the further development of the theory of channeling on the basis of Lindhard's original paper. Have some of the basic concepts been challenged? Where has the theory been extended and where are new developments needed?

After an introduction of the basic features of channeling, the continuum potential and the continuum model, the question of quantum versus classical mechanics is considered. The quantum world of electron channeling and channeling radiation was for many years at the centre of my interest. This is an aspect of channeling that was hardly touched upon in Lindhard's paper from 1965. He later published a paper

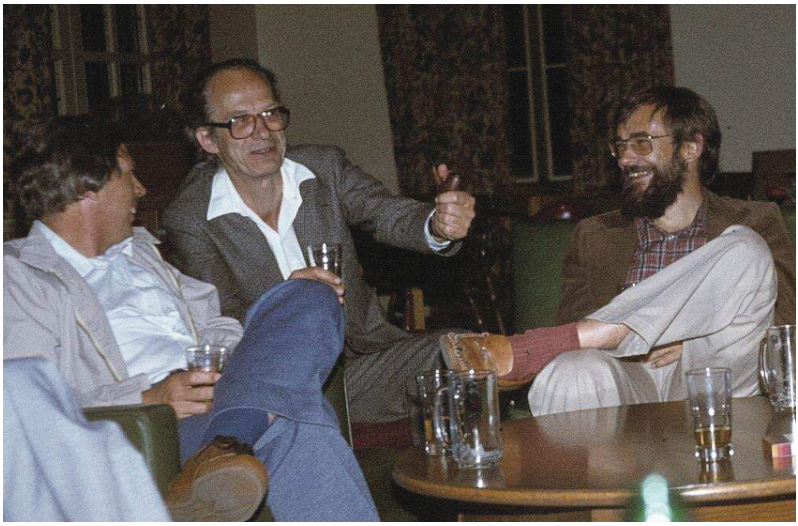

Fig. 11.1 Jens Lindhard gesturing with his pipe; with Larry Howe and the author. ICACS, Hamilton, Canada, 1979

on the quantum theory of channeling (Lervig et al., 1967), and I shall briefly discuss how this paper has provided a basis for a comprehensive, quantitative description of channeling radiation from MeV electrons and positrons. The physics at very high energies (GeV or TeV) is an active area of its own.

For ion channeling the focus will be on a key concept in Lindhard's theory. As a student I was especially impressed by the powerful applications of the concept of statistical equilibrium. Lindhard admired Gibbs' work on statistical mechanics and liked to quote Niels Bohr saying something like "this is how theory should be, at first very general and mathematical but then with great predictive power". Two attacks on application of the hypothesis of statistical equilibrium in channeling will be discussed, the first based on computer simulations and the second on experiments. Because so fundamental concepts were challenged, the resolution of the problems has given important new insights.

The field of channeling covers an enormous area of experience, and in this brief review it has been necessary to be selective. I have listed a few references to reviews covering in much more detail various aspects of channeling (Gemmell, 1974, Gibson, 1975, Feldman et al., 1982, Davies, 1983, Andersen et al., 1983b, Sørensen and Uggerhøj, 1987, Hofsäss, 1996, Krause and Datz, 1996, Cohen and Dauvergne, 2004, Uggerhøj, 2005). They may also be consulted for a more complete bibliography.

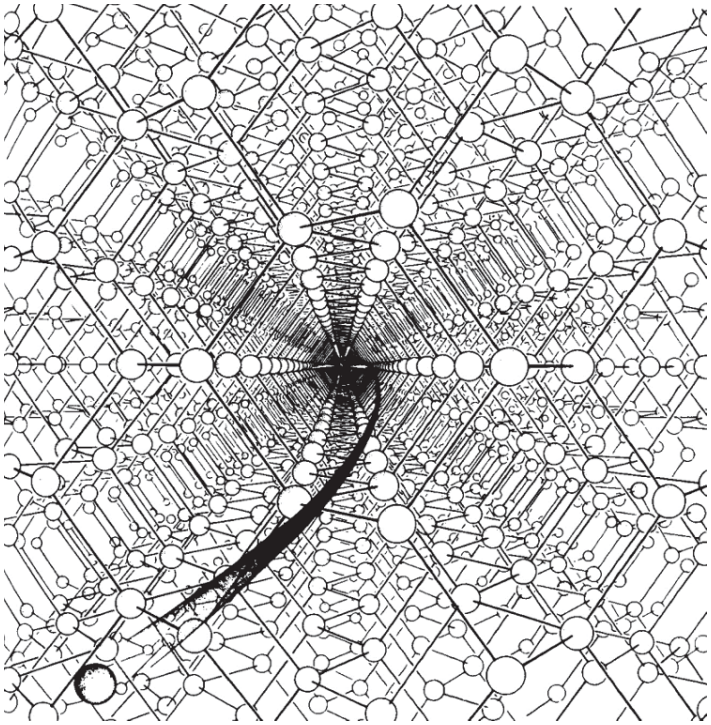

Fig. 11.2 From "Channeling in Crystals" by W. Brandt, Sci. Am. 218, 90 (1968)

11.2 Collision with String of Atoms

When Lindhard first saw the picture in Fig. 11.2 of an artist's perception of the passage of an ion through the open channels in a crystal lattice, his comment was: "this is not channeling!"

It is important to distinguish channeling from transparency. For channeling along a crystal axis, the motion is governed by correlated collisions with atoms aligned as pearls on a string, as illustrated in Fig. 11.3. If many atoms contribute, the discrete deflections may be replaced by the force corresponding to the continuum string potential obtained by integration of the atomic interaction potential,

$$U(\boldsymbol{r}) = \frac{1}{d}\int \mathrm{d}z\, \mathcal{V}_{\mathrm{at}}(\boldsymbol{r}, z) \tag{11.1}$$

Here z is the coordinate parallel to the string of atoms and $\boldsymbol{r} = (x, y)$ is the transverse coordinate vector. At large distances r, contributions from atoms on several strings must be included in the continuum potential.

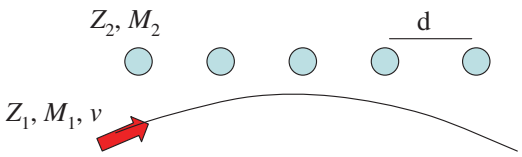

Fig. 11.3 Deflection of ion by string of atoms

11.2.1 Continuum Model

In this continuum model there is a separation between the motion along the axis and the transverse motion, which is governed by a transverse Hamiltonian,

$$H(\boldsymbol{P}_\perp, \boldsymbol{r}) = \frac{P_\perp^2}{2M_1} + U(\boldsymbol{r}) \tag{11.2}$$

with conservation of transverse energy $E_\perp$. (For relativistic particles, $M_1 \to \gamma M_1$; (Lervig et al., 1967)).

The string potential is repulsive and channeled ions are kept away from the atomic strings. The allowed area ($U(\boldsymbol{r}) < E_\perp$) within one unit cell in the transverse lattice of strings is denoted $A(E_\perp)$, and the total area per string is $A_0 = (Nd)^{-1}$ where N is the number density of the crystal. As illustrated in Fig. 11.4, the motion is only for very low transverse energy confined to a single unit cell in the transverse lattice. In a classical *statistical equilibrium* at fixed $E_\perp$, with constant density on an energy shell in transverse phase space, the spatial density is in two dimensions constant in the allowed area.

When the particle motion is restricted, the particle is said to be channeled. Channeled particles do not have hard collisions with atoms and move through a gas of loosely bound atomic electrons. For particle incidence parallel to an axis there is therefore a very strong reduction in the yield of processes requiring a hard collision with an atom, like nuclear reactions or backscattering. Also energy loss and capture and loss of electrons are strongly modified.

11.2.2 Screened Potential

The Coulomb force between projectile and target nuclei is screened by electrons. A great simplification is obtained with Thomas-Fermi scaling:

$$U(r) = \frac{Z_1 Z_2 e^2}{d} g(r/a)\,. \tag{11.3}$$

The distance is scaled with the Thomas-Fermi screening radius a, which for $Z_1 \ll Z_2$ is given in terms of the Bohr radius $a_0 = 0.53$ Å by

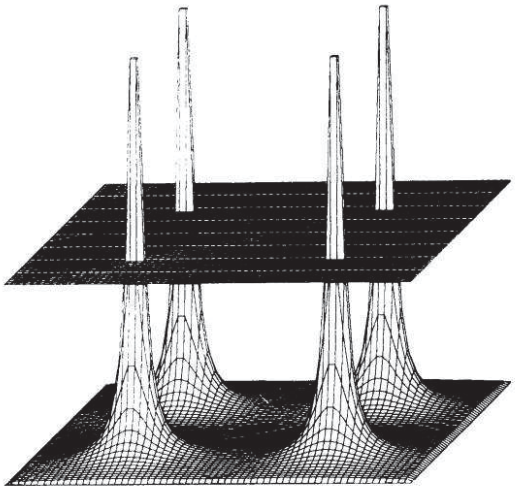

Fig. 11.4 Axial continuum potential

$$a = 0.8853 a_0 Z_2^{-1/3} . \tag{11.4}$$

A convenient approximation for analytical estimates is Lindhard's standard potential (Lindhard, 1965),

$$U(r) = \frac{Z_1 Z_2 e^2}{d} \ln\left(\frac{(Ca)^2}{r^2} + 1\right) , \tag{11.5}$$

with $C \cong \sqrt{3}$. For distances r of order a, the potential is proportional to $1/r$, changing to $1/r^2$ at larger distances. Another commonly used and more accurate analytical approximation is the Molière potential. If the projectile charge is small and the screening is due only to the target electrons, a very accurate potential can be obtained from analytical approximations to the screened potential obtained from Hartree-Fock calculations of electron densities (for example the Doyle-Turner potential (Doyle and Turner, 1968) used often in calculations of electron diffraction and electron channeling (Andersen et al., 1983b).

The question of the screening of the ion-atom potential is complex. It depends both on the atomic numbers of projectile and target and on the velocity of the projectile. According to the simple Bohr criterion, electrons bound to the ion with orbital velocities smaller than the ion velocity are stripped off. A characteristic velocity, separating between low velocities with nearly neutral projectiles and high velocities with only few electrons remaining on the ion, is therefore the Thomas-Fermi-scaled Bohr velocity, $Z_1^{2/3} v_0$.

The simplest case is for particles with $Z_1 \ll Z_2$ in the limit of high velocities, where the screening radius, a, is determined by target electrons, alone. If a few inner electrons with $\langle r \rangle \ll a$ remain on the projectile, giving it a net number of charges, Q, we may write the continuum potential $U^{(Q)}$ in terms of the potential $U^{(1)}$ for a proton as

$$U^{(Q)}(r) \cong Q U^{(1)}(r)\,. \tag{11.6}$$

The number of charges, Q, can change by capture and loss but for well-channeled ions the cross sections are small and we may speak of 'frozen charge states' for not too thick crystals (see Fig. 11.28 below).

In the opposite limit of high Z_1 and low velocities the ion carries many electrons, is nearly neutral, and the screening is due to electrons on both target and projectile atoms. The screening is described fairly well by introduction of an effective atomic number, $Z^{-1/3} = \left(Z_1^{2/3} + Z_2^{2/3}\right)^{-1/2}$, in the formula for the Thomas-Fermi screening radius, (11.4) (Lindhard, 1965).

In the intermediate range, heavy ions at high velocity but carrying many electrons, the situation is not clear and further studies would be desirable. As discussed below, there is empirical evidence from blocking of fission fragments that in a high-Z material there is only a small contribution from projectile electrons to the screening. On the other hand, observations of 'cooling' and 'heating' of heavy ion beams transmitted through thin crystals give clear evidence of an influence of the ion charge state on the interaction potential.

11.2.3 Lindhard's Critical Angle

Channeling requires incidence nearly parallel to a crystal axis. A limit to the incidence angle ψ is obtained from the expression for the string potential. The transverse momentum of a particle with angle ψ is $P_\perp = p \sin\psi \cong p\psi$, and hence the kinetic energy in the transverse motion is $E\psi^2$. The barrier for penetration into a string is of order $2Z_1 Z_2 e^2/d$, (11.5), and hence the critical angle is of order of the Lindhard angle,

$$\psi_1 = \left(\frac{2Z_1 Z_2 e^2}{Ed}\right)^{1/2}. \tag{11.7}$$

For relativistic particles with total energy $\gamma M_1 c^2$, the kinetic energy in the transverse motion is $P_\perp^2/2M_1\gamma$, and the formula (11.7) holds with the replacement $E \to pv/2 = \gamma M_1 v^2/2$ (Lervig et al., 1967).

Lindhard introduced a rough distinction between 'channeled beam' ($\psi < \psi_1$) and 'random beam' ($\psi > \psi_1$). Transition from channeled to random is denoted "dechanneling" and the reverse transition "feeding-in". For random beam many aspects of the motion are like in an amorphous medium because there is no restriction of the transverse motion. However, at very high energies the correlated scattering with string atoms extends to angles much larger than the critical angle and this has important consequences, for example for the multiple scattering and for radiation from electrons and positrons.

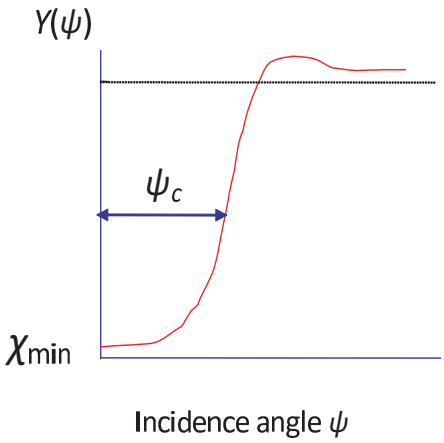

Fig. 11.5 Axial dip in close-encounter yield

11.2.4 Thermal Vibrations

Thermal vibrations play an important role. On the time scale of the ion motion the displacements of atoms can be considered static. The atomic recoil can be ignored in the evaluation of the scattering angle and, except for questions of coherence in electron channeling, we need not be concerned about the quantisation of atomic motion into phonons. The rms vibrational amplitude in two dimensions, ρ, is typically of order 0.1 Å. When a particle can penetrate to a distance of order ρ from strings it is able to hit atoms. With a Gaussian distribution of the thermal displacements r, $\mathrm{d}P(r) = \exp(-r^2/\rho^2)\mathrm{d}r^2/\rho^2$, an ion with minimum distance of approach to strings equal to $\rho\sqrt{\ln 2}$ will have the probability for a head-on collision with an atom reduced by a factor of two compared with a random target. A more precise estimate of the critical angle is therefore

$$\psi_c = \left(\frac{U\left(\rho\sqrt{\ln 2}\right)}{E} \right)^{1/2} . \tag{11.8}$$

With the standard potential in (11.5) we obtain

$$\psi_c = \psi_1 \left[\frac{1}{2} \ln \left(\frac{(Ca)^2}{\rho^2 \ln 2} + 1 \right) \right]^{1/2} . \tag{11.9}$$

The factor on ψ_1 is close to unity.

The vibrational displacements also modify the continuum potential. Instead of the logarithmic divergence at small r the thermally averaged potential U_T has a finite maximum at $r = 0$, close to $U(\rho/\sqrt{2})$, but replacement of U by U_T leads only to a very small change in (11.9) (Andersen and Feldman, 1970).

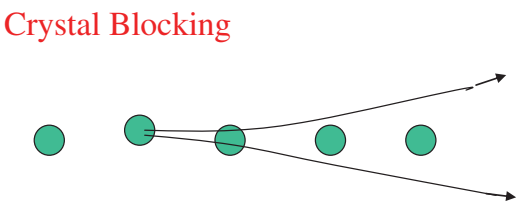

Fig. 11.6 Blocking in the direction of a string of particles emitted from a lattice site

11.2.5 Dip in Yield

The most dramatic consequence of channeling is the nearly complete extinction of processes requiring a small impact parameter with a crystal atom, as illustrated in Fig. 11.5. Particles incident at zero angle and at distance r from a string acquire a transverse energy $U(r)$, and they can later hit a fraction $\exp(-r^2/\rho^2)$ of the vibrating atoms. With the assumption of a rapid trend towards statistical equilibrium in the allowed area (a uniform distribution), we therefore obtain

$$\chi_{\min} = \frac{1}{A_0} \int_{A_0} 2\pi r \, \mathrm{d}r \, \exp(-r^2/\rho^2) = \pi\rho^2/A_0 \,. \tag{11.10}$$

This minimum yield $\chi_{\min}$ is of order $\leq 1\%$, only. Roughly, the result may be interpreted as immediate dechanneling of the ions which hit the surface inside a distance ρ from a string. As discussed below, there are corrections, mainly due to effects of crystal planes containing the axis, which increase the minimum yield by a factor of order 2-3, the so-called Barrett factor first established in computer simulations (Barrett, 1973b).

Since recoils can be ignored the particle trajectories can be calculated as motion in a fixed potential. They are reversible in time if energy loss can be ignored, and this has several important consequences. One is the equivalence between channeling and blocking. Blocking occurs when charged particles are emitted from a lattice site in an axial direction, as illustrated in Fig. 11.6. The emitted particles are blocked by the string and prevented from exiting the crystal in the axial direction. Reversibility implies that the width and minimum yield of the blocking dip are identical to those for the channeling dip. Pioneering work on blocking was carried out especially by Tulinov and his group in Moscow (Tulinov et al., 1965).

11.3 Planar Channeling

Also for particles incident on a crystal nearly parallel to a major crystallographic plane the motion can be guided by a continuum potential, given by

$$\mathcal{V}(x) = N d_p \int \mathrm{d}y \, \mathrm{d}z \, V_{\mathrm{at}}(x, y, z) \,, \tag{11.11}$$

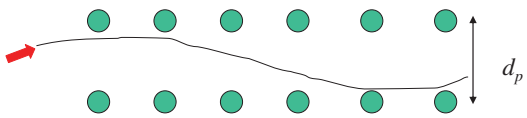

Fig. 11.7 Planar channeling

for a plane with spacing d_p. The density of atoms in a plane is Nd_p.

The critical angle for planar channeling is smaller by factor of order 3 than for axial channeling. The motion is one-dimensional oscillation, as illustrated in Fig. 11.7. Planar channeling gives rise to a dip in yield with a narrower width and a higher minimum yield than for axial channeling. Planar effects are therefore normally less useful for applications. At very high energies, planar channeling in a bent crystal can be used to bend beams of charged particles, as first suggested by Tsyganov (Tsyganov, 1976b,a).

A special situation is the motion of particles nearly parallel to a set of close packed strings in the plane. The planar channelling in this region, which Lindhard called channeling by a string of strings, is weakened because the particles can penetrate the planes between the strings. As we shall discuss below, channeling by planes is still important for the behaviour of axially channeled particles and it is a major cause of the Barrett factor on minimum yields mentioned above.

11.4 Channeling of Electrons and Positrons

An important issue is the question whether classical mechanics can be applied to describe ion channeling. Lindhard carried out an elegant analysis analogous to Bohr's famous argument concerning the use of classical orbital pictures in binary Coulomb scattering, which lead to the condition

$$\kappa = \frac{2Z_1 Z_2 e2}{\hbar v} > 1\,. \tag{11.12}$$

For correlated scattering on string atoms Lindhard showed that for particles heavy compared with the electron the transverse motion is always classical. A particle scattering off a string can be described by a wave packet with extension small enough to give a well defined scattering angle and still large enough for the spread in direction of the motion, deriving from the uncertainty principle, to be insignificant. Qualitatively, the reason is that the parameter Z_2 in the above formula, giving the strength of the scattering potential, is in effect increased by the concerted participation of many string atoms.

Channeling of electrons and positrons was hotly debated in the late sixties and early seventies. The essentially classical features of blocking of electrons and positrons were demonstrated by Uggerhøj by observation of the emission of both particles from radioactive ^{64}Cu implanted into a copper crystal (Uggerhøj, 1966, Uggerhøj and Andersen, 1968). The beautifully simple experiment is illustrated

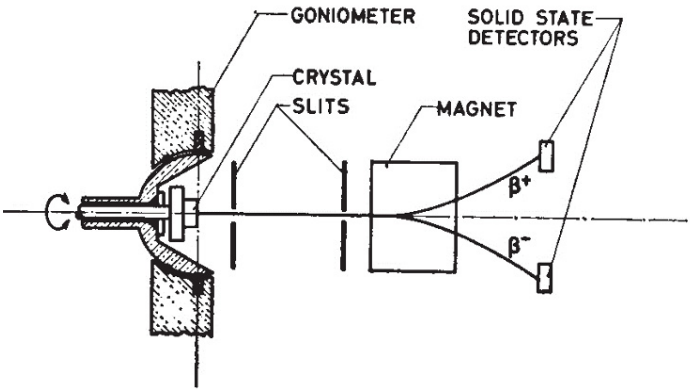

Fig. 11.8 Set-up for observation of the emission of electrons and positrons from ^{64}Cu implanted into a copper crystal (Uggerhøj and Andersen, 1968)

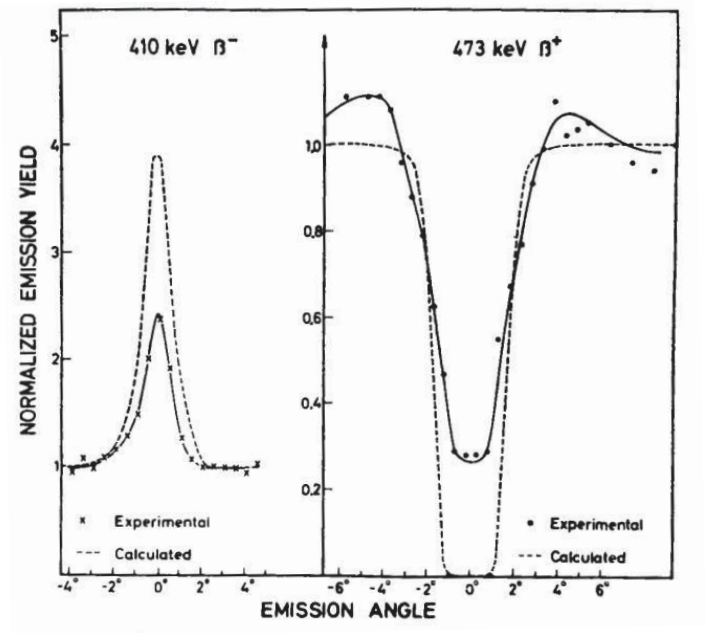

Fig. 11.9 Observed yields along an axis, compared with continuum model calculations (Uggerhøj and Andersen, 1968)

in Figs. 11.8 and 11.9. The crystal is mounted in a goniometer, and two collimators determine the emission direction for both electrons and positrons. As shown in Fig. 11.9, there is a strong decrease in yield along the axis for positrons, similar to observations for heavier particles like alpha particles. In contrast, there is a strong

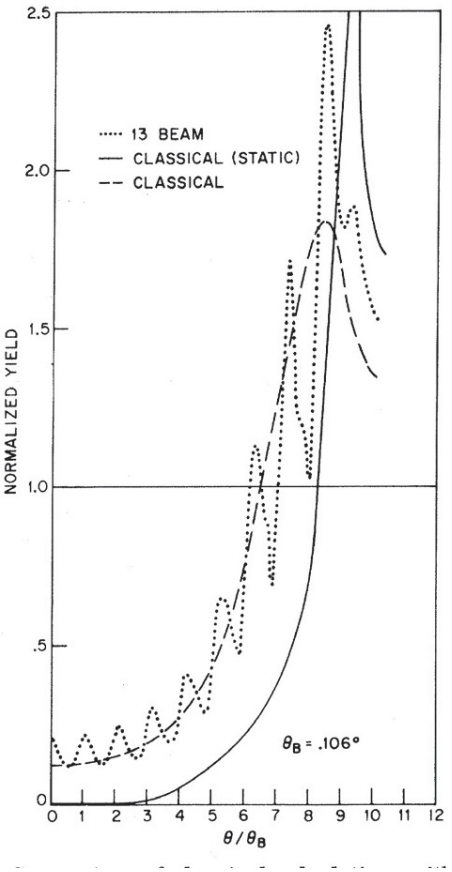

Fig. 11.10 Comparison of classical calculations of a {111} Au planar dip in yield for 1-MeV positrons with a quantum, so-called many-beam calculation. The Bragg angle is given by the positron wavelength divided by twice the planar spacing, $\theta_B = \lambda/2d_p$, (Andersen et al., 1971)

increase in the yield of electrons, as would be expected classically from the reversed sign of the interaction with string atoms.

The classical interpretation of these experiments was criticised and it was argued that, as known from electron microscopy, the transmission of electrons through thin crystals is dominated by coherent Bragg reflection. However, it was soon realized that this quantisation of transverse momentum does not in itself imply the absence of strong classical features. The decisive question is again whether the localization of an electron to move close to a string or plane gives too much spread in direction of motion via the uncertainty principle to allow a classical description by orbital pictures. This is determined by the number of bound states in the transverse motion, which becomes large for relativistic electrons (Andersen et al., 1977).

The phase space for bound states in a planar potential is larger for positrons, which oscillate in the open space between planes, and hence channeling is more classical for positrons than for electrons. Figure 11.10 shows a comparison between classical calculations, without and with thermal vibrations, and a quantum calculation (13-beam) of a planar dip in yield of wide angle scattering for 1 MeV positrons

in a thin gold crystal (Andersen et al., 1971). The dip has an essentially classical envelope with fine structure from Bragg interference. A classical dip with wiggles from interference was later measured for positron channelling in a thin Si crystal (Pedersen et al., 1972).

11.5 Channeling Radiation

The discovery of channeling radiation should be accredited mainly to Kumakhov, who was the first to derive the correct relativistic transformation (Kumakhov, 1976). The simplest way is to consider first the emission of radiation in the so-called rest system following the electron motion along a string or plane, and then make a Doppler transformation to the laboratory system. The outcome is that the Bohr relation between the photon frequency and the electron energy jump is modified by approximately a factor $2\gamma^2$ for emission in the forward direction. A line spectrum of planar channeling radiation was first presented by the Livermore group at the ICACS conference in Hamilton, 1979 (Alguard et al., 1980), and shortly afterwards we observed in Aarhus the first line spectra for axially channeled electrons (Andersen et al., 1983b). As illustrated by the spectrum in Fig. 11.11, the lines of channelling radiation are particularly sharp in diamond because of the very small thermal vibrations in this material (Guanere et al., 1982).

For not too high energies (MeV) a quantum treatment must be applied, and a systematic description can be based on the formalism developed by Lindhard and co-workers (Lervig et al., 1967, Andersen et al., 1983b). Spin effects are not important and the Klein-Gordon equation for a spinless particle with total relativistic energy E may be used as a starting point,

$$\left\{\left[-i\hbar\nabla - \frac{e}{c}\boldsymbol{A}(\boldsymbol{R})\right]^2 c^2 + m^2c^4\right\}\psi(\boldsymbol{R},\dots) = [E - H_{\text{rad}} - H_{\text{latt}} - \mathcal{V}(\boldsymbol{R},\dots)]^2\,\psi(\boldsymbol{R},\dots)\,. \quad (11.13)$$

Here the terms H_{rad} and H_{latt} are the independent Hamiltonians of the radiation field and the crystal, while $\boldsymbol{A}$ represents the vector potential of the radiation field. The trick is now to separate off a phase factor corresponding to the total momentum and not just to its z component,

$$\psi\,(\boldsymbol{R}\dots)) = \mathrm{e}^{\mathrm{i}Kz}w(\boldsymbol{r},z,\dots) \quad \text{with } \hbar^2K^2c^2 + m^2c^4 = E^2\,. \quad (11.14)$$

This gives an approximate equation of first order in the time-like parameter $t = z/v$. Neglecting terms of second order, like $\partial^2/\partial z^2$ and $\mathcal{V}^2$, we obtain

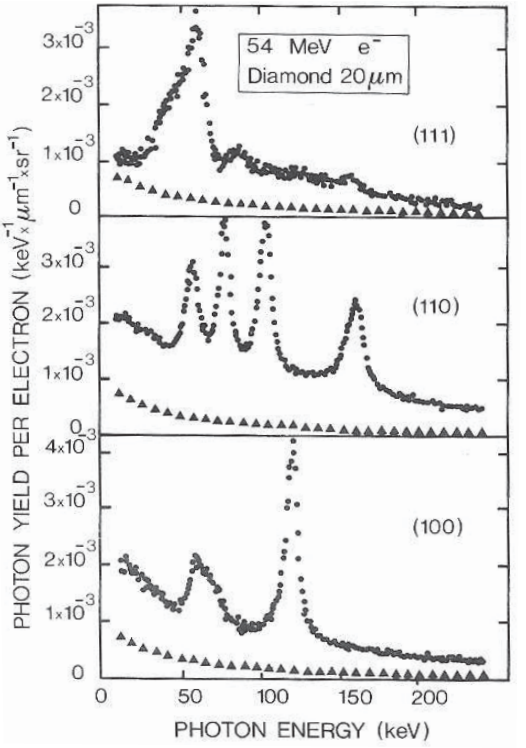

Fig. 11.11 Photon spectra in the beam direction for 54 MeV electrons along different planes in diamond. Triangles show spectrum for incidence in a random direction (Guanere et al., 1982)

$$\mathrm{i}\hbar v\frac{\partial}{\partial z}w = \left[-\frac{\hbar^2}{2\gamma m}\Delta_r + \mathcal{V}(\boldsymbol{r}, z, \ldots) + H_{\mathrm{rad}} + H_{\mathrm{latt}} + H_{e,r}\right] w(\boldsymbol{r}, z, \ldots)\,, \tag{11.15}$$

$$H_{e,r} = -e\left(\beta A_z + \frac{1}{\gamma mc}\boldsymbol{A}\cdot\boldsymbol{p}\right).$$

The equation has the form of a non-relativistic Schrödinger equation in two dimensions, and the wave function describes the transverse channeling state. The radiation operator $H_{e,r}$ can be treated as a perturbation, and also the interaction potential can be simplified by a series of perturbation approximations. For example, the electronic excitations are treated by a replacement of $\mathcal{V}$ by its expectation value $\langle\mathcal{V}\rangle$ in the electronic ground state and a perturbation calculation of the inelastic transitions induced by the difference $\mathcal{V} - \langle\mathcal{V}\rangle$. Similarly, vibrational excitations of the lattice are treated by the introduction of a thermally averaged potential, with Fourier components reduced by a Debye-Waller factor. In the final step, the potential is approximated by the thermally averaged axial or planar continuum potential.

Measurements of axial channeling radiation for 4 MeV electrons along a Si [111] direction are shown in Fig. 11.12 (Andersen et al., 1982). Four lines are clearly distinguished, from 2s-2p, 3d-2p, 2p-1s, and 3p-1s transitions. The angular dependence

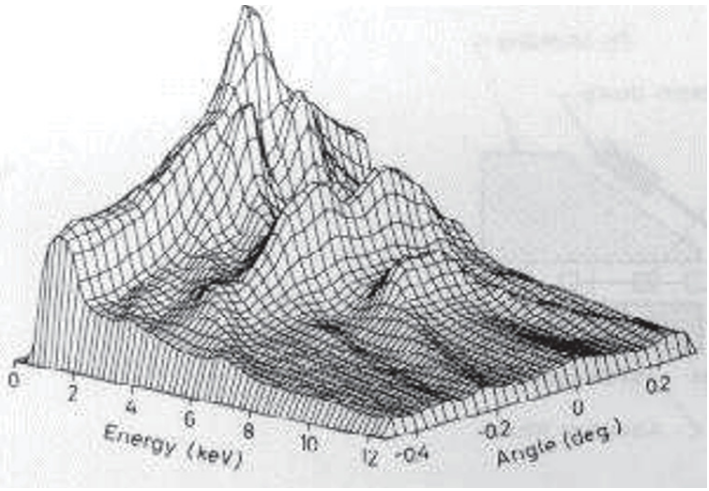

Fig. 11.12 Photon spectra vs angle of incidence to a $\langle 111 \rangle$ axis for 4 MeV electrons in a 0.5 μm thick Si crystal (Andersen et al., 1982)

of the intensities reflects the overlap of the incoming plane wave with the initial states of the transitions, i.e., the intensity is proportional to the square of a Fourier component of the transverse wave function. The ridges at larger angles are from free-to-bound transitions.

Radiative transitions between the bound levels give photon energies in the direction of the axis equal to $h\nu = 2\gamma\Delta E_R$, where E_R is the energy level in the reference system moving with the particle in the z direction, the so-called rest system. Here the mass is unrelativistic and the potential is multiplied by a factor of γ due to the Lorentz contraction of the spacing, d, of atoms on a string. Hence the Hamiltonian is just multiplied by the factor γ. The measurements are in Fig. 11.13 seen to be reproduced quite well by calculations. Transitions along three different axes are included. The potential scales with γ/d, see (11.3), and hence measurements for channeling along three different axes can be included in one graph with scaled units. The agreement is quite good when an accurate potential (Doyle-Turner, for example) is used.

The line spectrum of channeling radiation reveals the energy spectrum of bound states, just like the Rydberg series revealed to Niels Bohr the discrete states of the hydrogen atom. Observation of the energies combined with the perturbation calculations can give quite accurate information about crystal properties like the crystal potential and the thermal vibrations (Datz et al., 1986, Hau et al., 1990). It is also possible to calculate the coherence properties from up to third order perturbation theory and reproduce the observed line widths (Andersen et al., 1983a, Hau and Andersen, 1993a,b).

After a hectic period in the 1980s with many active groups, both in theory and in experiments, the activity in low-energy channeling radiation has subsided, and today

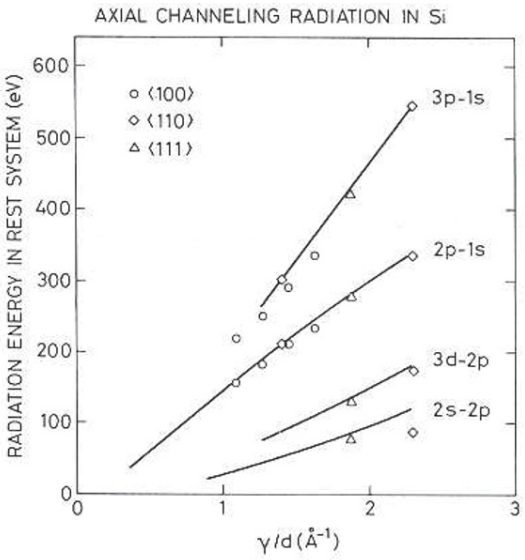

Fig. 11.13 Comparison between calculated transition energies in the rest frame and measurements, at varying electron energy, $E = \gamma mc^2$, and for axes with different atomic spacing, d (Andersen et al., 1982)

it is rare to see a paper in this field. Perhaps the field is too well established. Also, the early promises of application of MeV electron beams in crystals as a radiation source seem not to have materialized. In contrast, there has been a continued interest in radiation phenomena in crystals for high-energy electrons (GeV). The physics in this region is very different, with essentially classical motion of the electrons, and other processes like creation of particle-antiparticle pairs have been studied. Like the Bethe-Heitler bremsstrahlung spectrum for a random medium, the radiation spectrum extends up to the kinetic energy of the particle, and the photon yield can be very strongly enhanced. The production of hard photons for particle physics is therefore an interesting application. The effective electrical field generating the radiation corresponds to the continuum potential in the 'rest system', and since it is proportional to the relativistic factor γ it becomes huge at extreme relativistic energies. This opens up for fundamental studies in strong-field electrodynamics (Uggerhøj, 2005).

11.6 Dechanneling

Multiple scattering is strongly reduced for channeled particles. There remain force fluctuations due to thermal vibrations and electronic scattering. One can derive a differential equation for the distribution in transverse energy, $g\,(E_\perp, z)$, as a function of the depth z,

$$\frac{\partial}{\partial z} g(E_\perp, z) = \frac{\partial}{\partial E_\perp} A(E_\perp) D(E_\perp) \frac{\partial}{\partial E_\perp} \frac{g(E_\perp, z)}{A(E_\perp)} \,. \tag{11.16}$$

This is a diffusion equation with diffusion function $D(E_\perp)$. The diffusion equation may be derived from the more general master equation through a second order expansion in the small scattering angles. However this expansion is not unique! The form in (11.16) is obtained with the additional requirement that the equation should reproduce the stability of a full *statistical equilibrium* in phase space (Bonderup et al., 1972). This is obviously fulfilled for (11.16) since in such an equilibrium the density in transverse energy is proportional to the allowed area, $g_0(E_\perp)\pi A(E_\perp)$. Since the available area is constant at large $E_\perp$, also g_0 becomes constant. This is special for two dimensions. For planar channeling an analogous equation can be derived, with $A(E_\perp)$ replaced by the half-period of oscillation, $T(E_\perp)$ (at large angles the time between crossings of planes).

In a perfect crystal, the diffusion is due to scattering by individual electrons and to fluctuations in atomic scattering associated with thermal displacements. In an amorphous target, nuclear multiple scattering dominates. The mean square multiple scattering angle increases linearly with depth (apart from a logarithmic factor) and, as a scaling length, Lindhard introduced the depth corresponding to an rms scattering angle equal to ψ_1,

$$l_{n,\psi_1} = \frac{2}{\pi N d^2 L_n \psi_1^2}\,, \tag{11.17}$$

where the logarithmic factor, L_n, is of order 5–10. This length is roughly proportional to the energy of the particle and hence channeling can be stable over very large thicknesses at high energies. At GeV energies, the dechanneling lengths are macroscopic (centimeters) and planar channeling in bent crystals can be used for beam bending without too much loss (Baurichter et al., 2000).

An example illustrating the accuracy of the description by diffusion is shown in Fig. 11.14 (Kennedy et al., 1992). The calculations applied an accurate potential and included dechanneling by electronic and thermal scattering in the diffusion approximation. The two scattering mechanisms complement each other. The thermal fluctuations dominate at large transverse energies and, for example, cause the planar shoulder to be smeared out rapidly. On the other hand, thermal scattering is very weak for well channeled ions, and electronic scattering is therefore important for the increase of the minimum yield with depth of penetration.

11.7 Applications

11.7.1 Dechanneling by Crystal Defects

When dechanneling by defects is included, the diffusion equation may not be suitable. Alternative approaches are solution of a master equation, which can include large jumps in transverse energy (Gärtner et al., 1984), or brute force computer simulation.

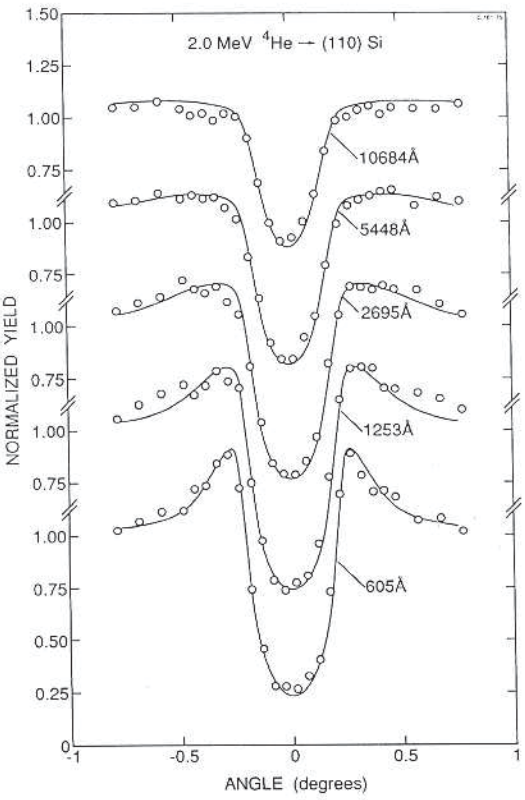

Fig. 11.14 Depth dependence of backscattering for 2 MeV He near a (110) plane in Si, compared with dechanneling calculation (Kennedy et al., 1992)

The detection of crystal defects after ion implantation has probably been the most important application of channeling. For example, it has been of decisive importance in the development of ion implantation for doping of semiconductors. With backscattering of MeV beams of protons or helium ions, the crystal perfection as a function of depth can be measured, as illustrated in Fig. 11.15 (Feldman et al., 1982). The energy scale for the backscattered particles can be converted into a depth scale, as shown at the bottom. The spectrum for a beam aligned with an axis is shown for a virgin crystal as well as for an implanted crystal, and the difference in the yield can be ascribed to a combination of direct backscattering from defects and increased backscattering from atoms in perfect parts of the crystal due to dechanneling. This latter part is indicated by the dashed line and when it is subtracted the depth distribution of the damage is obtained. Methods for analysis of such spectra are today readily available and, all in all, dechanneling is a very well developed field, except for the integration of the influence of electron capture and loss by heavy ions to be discussed later.

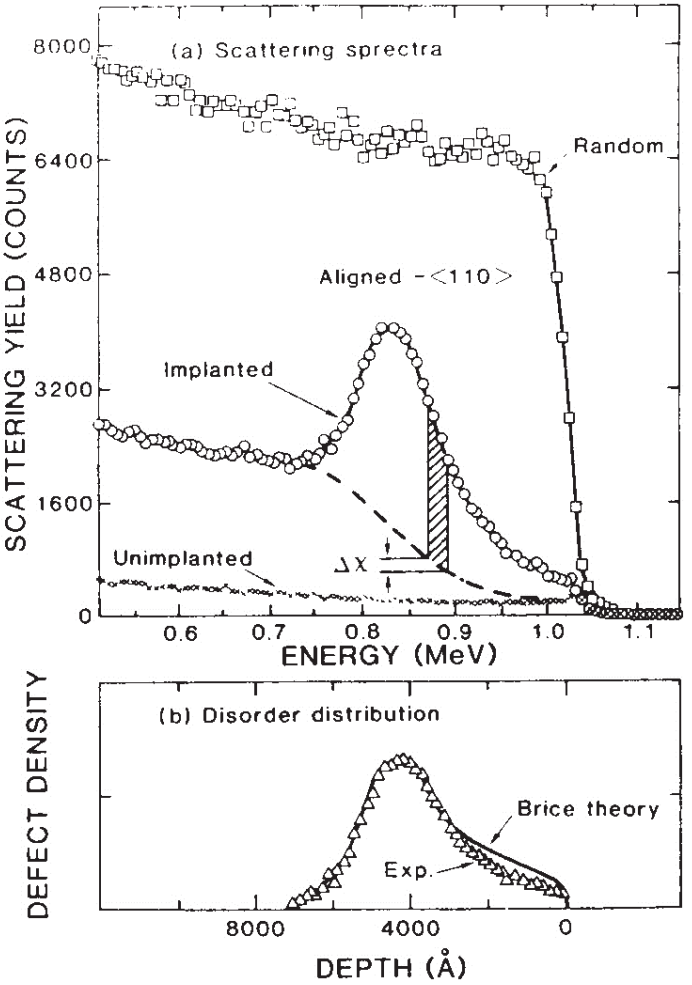

Fig. 11.15 Illustration of the extraction of a damage profile from backscattering in aligned and random directions (Feldman et al., 1982)

11.7.2 Localization of Impurities by Channeling and Blocking

Another important application of channeling has been the use of the strong dip in yield of a close-encounter reaction to determine the location of impurity atoms in a crystal lattice. An example is the determination of the lattice configuration of nitrogen implanted into silicon (Rasmussen and Nielsen, 1994). Nitrogen impurities can be detected at low concentrations by a (p, α) reaction. The observed yield of this reaction together with the backscattering yield from the Si lattice is shown in

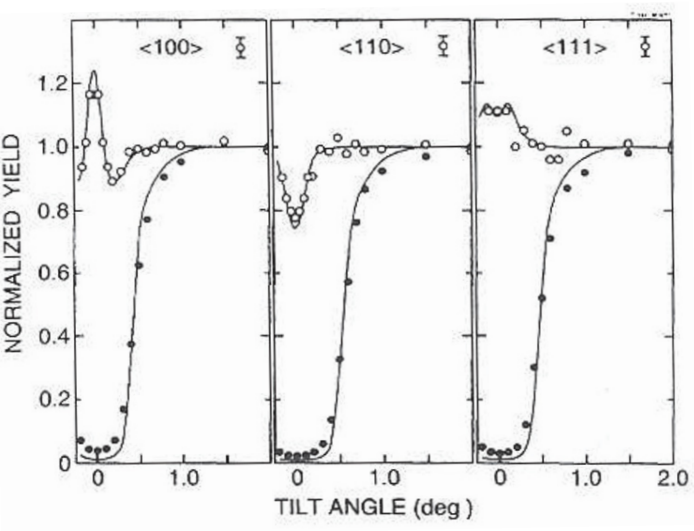

Fig. 11.16 Angular distributions in yield of (p, α) reaction and of backscattering from Si crystal implanted with nitrogen. The lines are from calculations including dechanneling (Rasmussen and Nielsen, 1994)

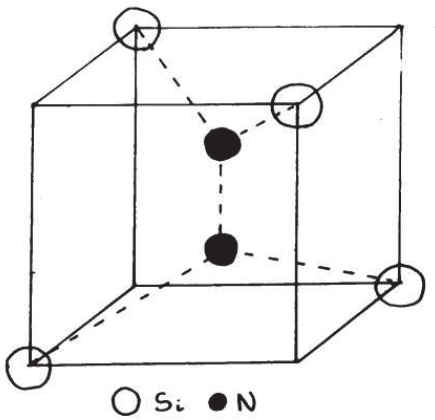

Fig. 11.17 Nitrogen dumb-bell replacing substitutional atom in Si lattice (Rasmussen and Nielsen, 1994)

Fig. 11.16 for angular scans through the three major axes. The scans are averaged over the azimuthal angle whereby perturbations by planar effects are largely eliminated.

The data are consistent with the dumb-bell configuration illustrated in Fig. 11.17. Two nitrogen atoms replace one silicon atom. The lines through the data points are from calculations for such a configuration. The dumb-bells are oriented randomly along the three equivalent ⟨100⟩ axes (edges of cube). Nitrogen is substitutional along one axis and interstitial along the other two. This gives a superposition of 1/3

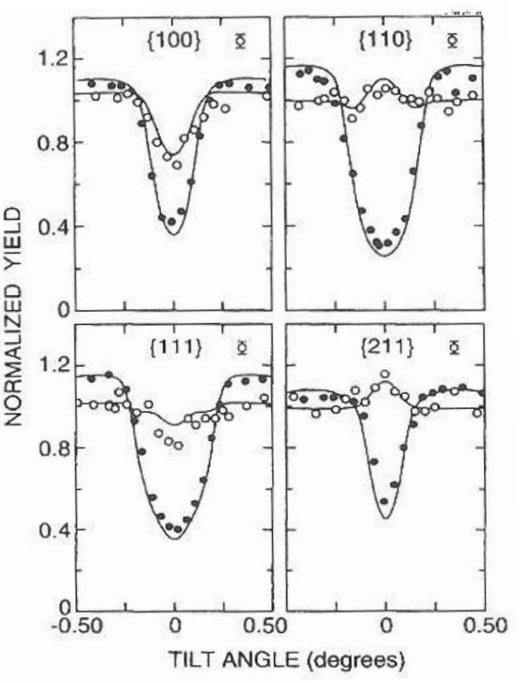

Fig. 11.18 Planar angular scans of (p, α) and backscattering yields for nitrogen implanted Si crystal, compared with calculations including dechanneling (Rasmussen and Nielsen, 1994)

dip and 2/3 narrow peak. An accurate potential (Doyle-Turner) has been used and dechanneling for a perfect lattice has been included. This is seen to give excellent agreement with the data, both for the impurity and for the host lattice. As seen in Fig. 11.18, also the observed structures for channeling along three different planes were found to be in good agreement with the simulation (planar scans sometimes give crucial information! (Nielsen et al., 1988)).

The equivalence of channeling and blocking implies that impurities can just as well be localized by observation of blocking dips for charged particles emitted from the impurity atoms. A very early example is Domeij's observation of a strong blocking dip for α-particles from ^{222}Rn implanted into a tungsten crystal (Domeij and Björkqvist, 1965). The measurements on electrons and positrons discussed above (Uggerhøj and Andersen, 1968) showed that information on lattice location can also be obtained from observation of the blocking effects for these light particles. This is very useful since beta emitting isotopes are ubiquitous in the periodic table. A pioneering effort on quantitative application of this method has been made by Hofsäss (Hofsäss, 1996).

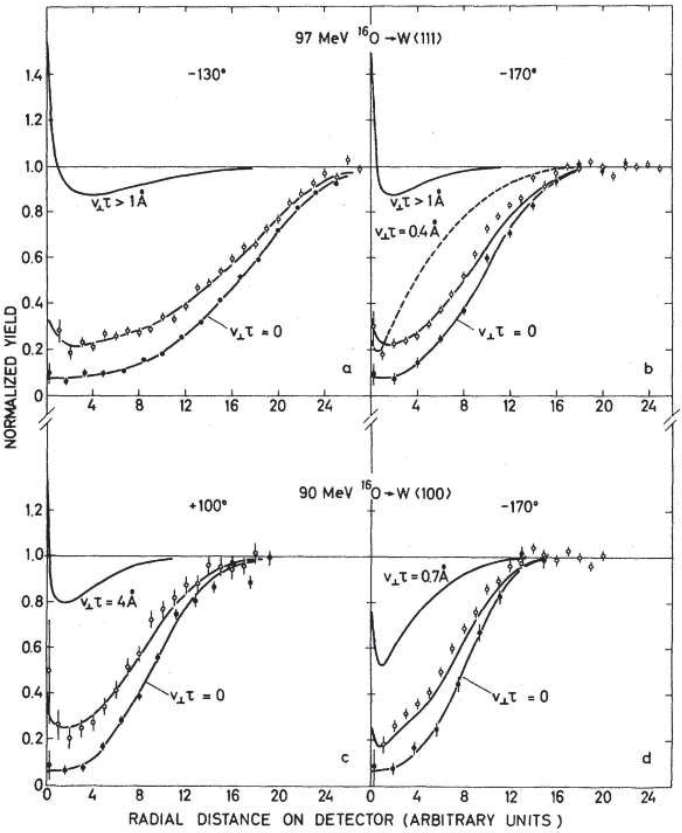

Fig. 11.19 Fission fragment blocking dips for ^{16}O→W at two bombarding energies (open circles) compared with results for prompt fission (solid circles). The latter were simulated by scaling according to (11.7) the dips obtained for elastic scattering of 40-MeV ^{16}O. The uppermost curve in each subfigure was calculated for an exponential decay with the average recoil distance indicated. The dip is nearly independent of recoil distance for average recoils longer than 1 Å. (Andersen et al., 1976)

11.7.3 Crystal Blocking for Determination of Nuclear Lifetimes

In analogy to the lattice localization of impurities the blocking effect can be used to determine how far from a lattice site the emission of charged particles takes place. For a nuclear reaction proceeding by formation of a compound nucleus, one may thereby determine the average recoil distance $v_\perp\tau$, where $v_\perp$ is the component of the compound nucleus velocity perpendicular to the axis and τ is the compound nucleus lifetime (Gibson, 1975).

Several groups have studied fission lifetimes with this technique. Since the early seventies I have been working with a group mainly from Aarhus and from the Chalk

River Nuclear Laboratories on development of this technique to study heavy ion induced fission of heavy nuclei. Because the recoil is large in these reactions very short times can be measured, down to about one attosecond. This is still very long on the nuclear time scale and times of order 10^{-21} s are expected from statistical models at the very high excitation energies just after formation of a compound nucleus. In a series of experiments with ^{12}C, ^{16}O, ^{19}F projectiles on W and Ta crystals, we found results consistent with this expectation. Very little narrowing of the dips was found but there was an increase in the minimum yield compared with dips in elastic scattering. As seen in Fig. 11.19, the results could be fitted with a superposition of mostly fast fission without lifetime effects and a contribution from slow fission after cooling down of the nucleus by emission of several neutrons (Andersen et al., 1976). As for the lattice-location experiments discussed above, the axial dips are integrated over the azimuthal angle to eliminate planar effects.

Recently we have continued the experiments with heavier projectiles. The idea is to investigate the influence of viscosity on the nuclear mass flow at high internal temperatures. Results from other types of measurements, e.g., on the number of neutrons emitted prior to fission and on emission of giant-dipole gamma rays from the compound nucleus, have indicated that the lifetime can be rather long. The first measurements with 170-180 MeV ^{32}S projectiles gave fission blocking dips which were virtually identical to dips in elastic backscattering, scaled in angle with $(Z_1/E)^{1/2}$ according to (11.7) (Karamian et al., 2003). This indicates that the lifetime of the fission is below about 1 as and there is no component larger than about 1% with much longer lifetime.

A comparison with elastic backscattering is a very useful zero-lifetime normalization. However, it is actually somewhat surprising that the agreement is so close since the fission fragments carry many electrons which should contribute to the screening of the Coulomb interaction with tungsten nuclei. Also in earlier experiments with oxygen projectiles the scaling was found to be quite accurate, as seen in Fig. 11.19.

Very recently we have continued these experiments at Oak Ridge National Labs with even heavier projectiles (Andersen et al., 2008). The analysis indicates a clear narrowing of the fission dips compared with the scaled dip in elastic scattering. This is quite exciting because the time delay must be very long on the nuclear time scale, of order 10^{-18} s, and a large fraction of the fission events must experience this delay. In Fig. 11.20 the results for bombardment of a thin W crystal with ^{58}Ni ions are compared with a calculated dip for an exponential decay with average displacements of about 8 pm. The elastic dips (lower half of figure) are seen to be in excellent agreement with the calculation for zero displacement, including a small increase in minimum yield ascribed to crystal defects and a correction for mosaic spread in the epitaxially grown crystals. The fission dips in the upper half of the figure are compared with elastic dips scaled according to (11.7). The lifetime effect is very clear. The measured dips are in excellent agreement with dips calculated for exponential decay with average recoil about 8 pm, corresponding to a lifetime of order 1 as. The lifetime cannot be explained in the Bohr-Wheeler picture of multiple-chance fission of a compound nucleus, and it is instead interpreted as a signal of

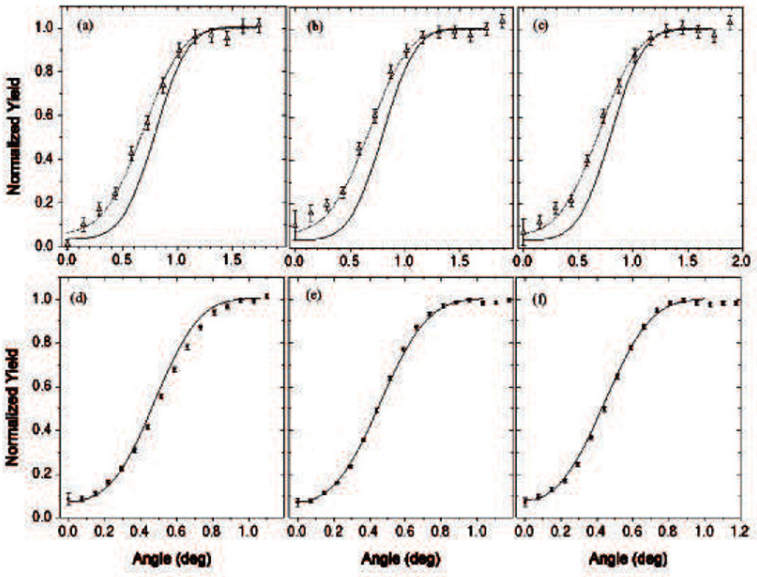

Fig. 11.20 Blocking dips in fission and elastic scattering for 330-MeV (a,d), 350-MeV (b,e), and 375-MeV (c,f) ^{58}Ni in W, compared with calculations. The dotted curves include exponential distributions of recoil displacements from a ⟨111⟩ row, with average values (a) 8 pm, (b) 9 pm, and (c) 8 pm (Andersen et al., 2008)

very high viscosity of the nuclear mass flow in the fission process. The physical picture of the united nucleus must be closer to a drop of syrup rather than of water. These results may also be important for the interpretation of recent very surprising observations of long fission lifetimes for super-heavy compound nuclei created in heavy-ion reactions (Drouart et al., 2005).

The observations shown in Figs. 11.19 and 11.20 are also interesting from a methodological point of view. They give a clear demonstration of the power of the technique to determine not only average displacements but also the distribution of displacements. The observations in Fig. 11.20 show that small displacements from a lattice site are most easily detected by the narrowing of the width of the blocking (or channeling) dip, rather than by the increase of the minimum yield. The surprising accuracy of the scaling of the elastic dips is a problem which deserves theoretical and perhaps also further experimental study.

11.8 Restricted Equilibrium in Axial Channeling

All through the history of channeling, computer simulation has played a prominent role. The earliest ideas were inspired by simulation of the penetration of low-energy

ions through crystals (Robinson and Oen, 1963), and simulation is still a very valuable tool for interpretation of experiments. Probably the most advanced code was developed by John Barrett at Oak Ridge, and he made important contributions to the theory of channeling on the basis of the simulations. An example is the observation that the minimum yield in the axial channeling dip is underestimated by a factor of two to three, the so-called Barrett factor (Barrett, 1973b). His search for an explanation of this factor led him to publish a paper with the title: "Breakdown of the Statistical-Equilibrium Hypothesis in Channeling" (Barrett, 1973a).

The basic observation is illustrated in Fig. 11.21. The lines indicate simulated (transverse) trajectories of ions incident on a crystal parallel to an axis and hitting the surface close to a string. In the transverse motion, the ions are accelerated away from this string and their transverse energy, $\epsilon \equiv E_\perp$, is given for each picture. The strings are indicated by dots, and the figure shows that the flux of ions tends to be focussed onto other strings. This focussing clearly violates the assumption of a rapid trend towards statistical equilibrium on an energy shell in the transverse phase space.

This paper appeared to be a heavy blow to Lindhard's theory of channeling, in which, as noted above, arguments based on statistical equilibrium play a key role. The problem must be rooted in a restriction in phase space hindering the establishment of a full equilibrium. Typically, such a hindrance is associated with a symmetry and a corresponding conservation law, like for instance conservation of angular momentum for a system with rotational symmetry. For axial channeling, the symmetry is the regular arrangement of the strings in a two-dimensional lattice, and the conservation law is the conservation of transverse energy with respect to planes for ions moving nearly parallel to the planes.

This is illustrated in Fig. 11.22a, showing a stereogram of a small angular region around a $\langle 100 \rangle$ direction in a cubic lattice (Uguzzoni et al., 1992). The major planes containing the axis are indicated, and the circle shows the boundary for axial channeling at the angle ψ_1. Well outside the circle, planar channeling takes place inside the full drawn lines parallel to the plane, but close to the axis planar channeling is replaced by the so-called string-of-strings channeling with a critical angle that decreases with decreasing angle to the axis. The regions of channeling with respect to the strongest planes are hatched. Very close to the axis, the concept of planar channeling loses its meaning entirely.

Planar channeling divides the transverse phase space into regions with poor communication. An ion in the hatched region remains there on a depth scale determined by planar dechanneling and, vice versa, an ion outside the hatched area is prevented from entering this area by scattering on strings. Figure 11.22b illustrates how we can understand Barrett's results from this division. An ion starting its trajectory very close to a string is blocked from the regions of phase space corresponding to planar channeling. As indicated by the two small stereograms embedded in the figure, the blocked angular region depends on the position in the transverse plane. In the accessible, restricted phase space, we may assume a rapid trend towards equilibrium. Compared with a full equilibrium, the probability for getting very close to a string

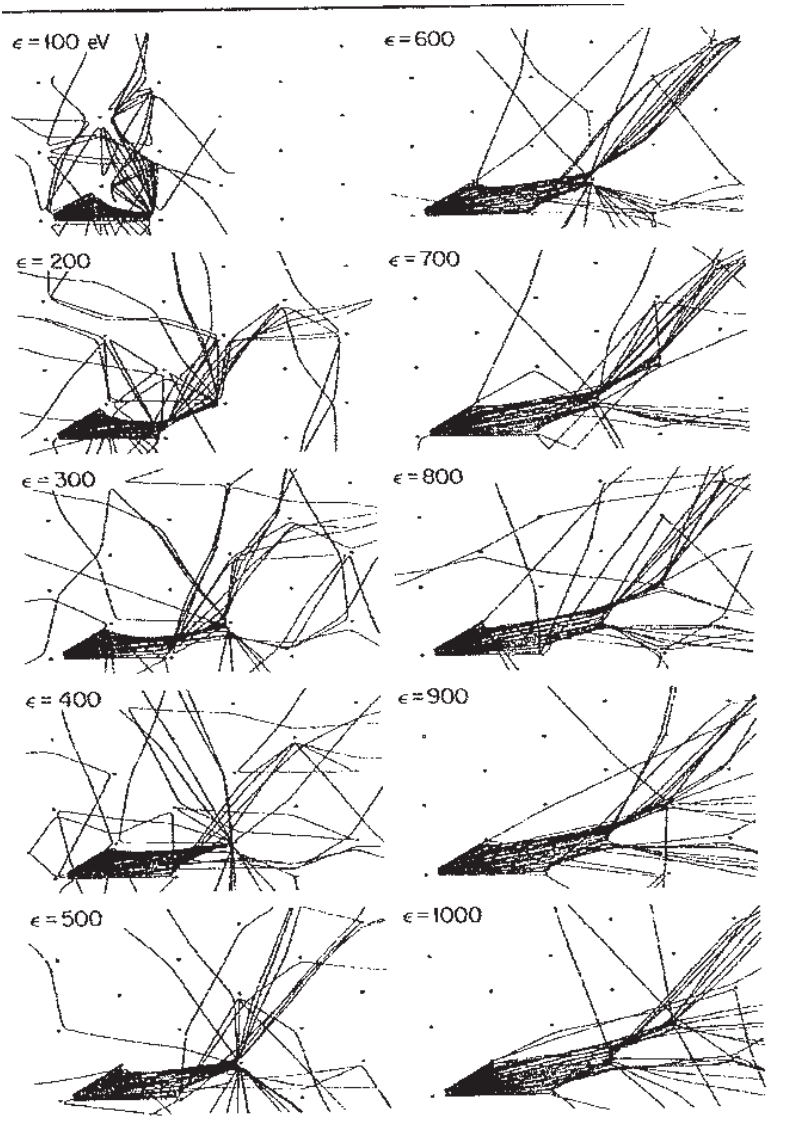

Fig. 11.21 Projection onto (111) plane of trajectories of 3-MeV protons moving nearly parallel to [111] direction in tungsten at 1200 K (Barrett, 1973a)

again is then higher by the ratio of the four dimensional volume of the full phase space to the volume of the restricted phase space.

These ideas were supported by simulations and appear to account quite well for a major part of the Barrett factor (Uguzzoni et al., 2000). There is an additional contribution from strong thermal fluctuations in the first collision with a string at

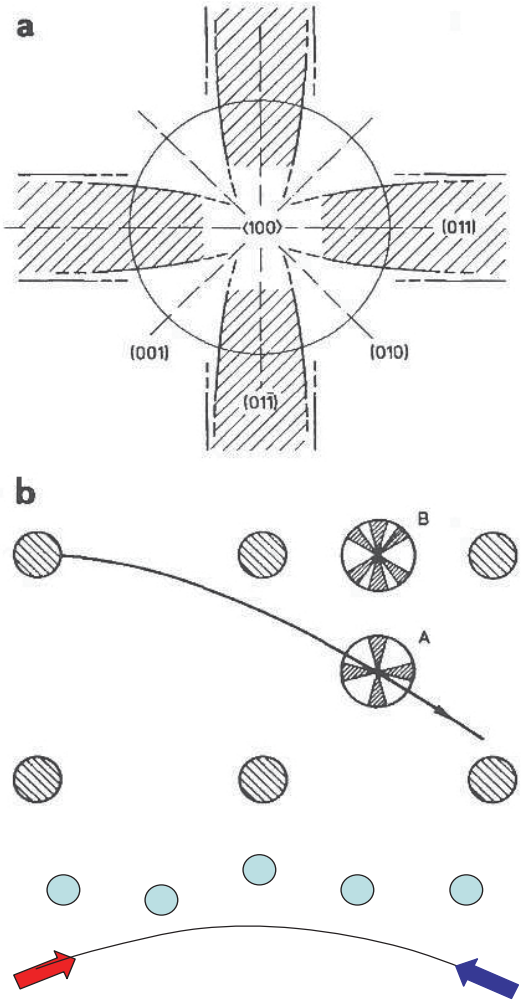

Fig. 11.22 (a)Stereogram indicating regions of planar channeling near a ⟨100⟩ axis in Si, for a particle in region A. (b) Transverse plane for Si [100]. The blocked angular regions are indicated for two regions A and B, and a trajectory for a particle moving out radially from a string is shown (Uguzzoni et al., 1992)

Fig. 11.23 Reversibility of string collision

the crystal surface, which determines the transverse energy of the ions giving the minimum yield. Thus the first attack on the concept of statistical equilibrium in channeling was repelled and in the process new insight was gained.

11.9 Cooling and Heating in Ion Transmission through Crystals

The second attack on statistical equilibrium in channeling was of an even more fundamental nature. As noted above, it is an important constraint in the derivation of the diffusion equation for dechanneling that a constant density in phase space

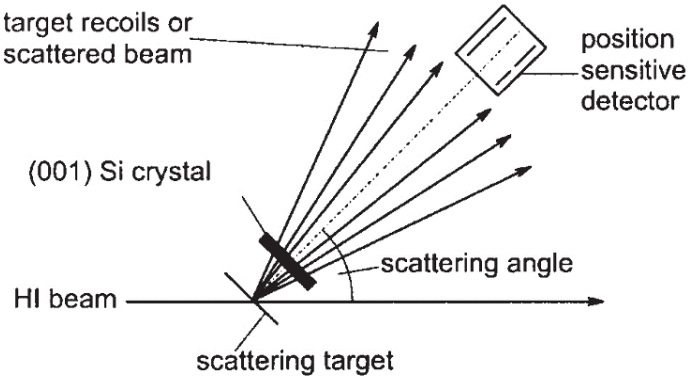

Fig. 11.24 Geometry for transmission experiment (Assmann et al., 1999)

should be an equilibrium. The phase space is now not limited to a transverse-energy shell but extends out to angles much larger than the critical angle. The requirement follows from basic symmetries of the multiple scattering.

Consider for example the thermal scattering of an ion colliding with a string, as illustrated in Fig. 11.23. If the energy loss in the collision is ignored, the trajectory is reversible, and this implies that thermal scattering leading from $E_\perp$ to $E'_\perp$ has the same probability as scattering from $E'_\perp$ to $E_\perp$. It is easy to see that the same symmetry must hold for changes in transverse energy due to electronic collisions. Until recently, it was believed that the only deviations from this general rule were due to energy loss of the projectile and that they must be small. The observations to be described in the following therefore came as a great surprise.

The set up shown in Fig. 11.24 was designed by Assmann et al. to give a sensitive test of the equilibrium hypothesis for heavy ions transmitted through a thin crystal (Assmann et al., 1999, Grüner et al., 2003). By scattering of a heavy-ion beam in a thin foil, a thin Si crystal was illuminated with a beam with large angular divergence, and behind the crystal the angular distribution of the ions was measured with a position sensitive detector. An isotropic beam with uniform intensity gives a constant distribution in transverse phase space inside the crystal, and if this distribution is stable, the beam should remain isotropic after the passage of the crystal.

The results shown in Fig. 11.25 are dramatically different. To the left are the two-dimensional intensity distributions and to the right the azimuthally averaged intensity as a function of the angle to the axis. For carbon ions there is a strong accumulation of flux near the axis and the planes, denoted cooling (reduction of transverse energy). The transmission of Cu ions is an intermediate case, with cooling along the axis and the strongest planes but a depletion of the flux ('heating') along the weaker planes. For transmission of the heavier iodine ions, there is almost exclusively heating, and for the heaviest Au ions there is strong heating along all channeling directions.

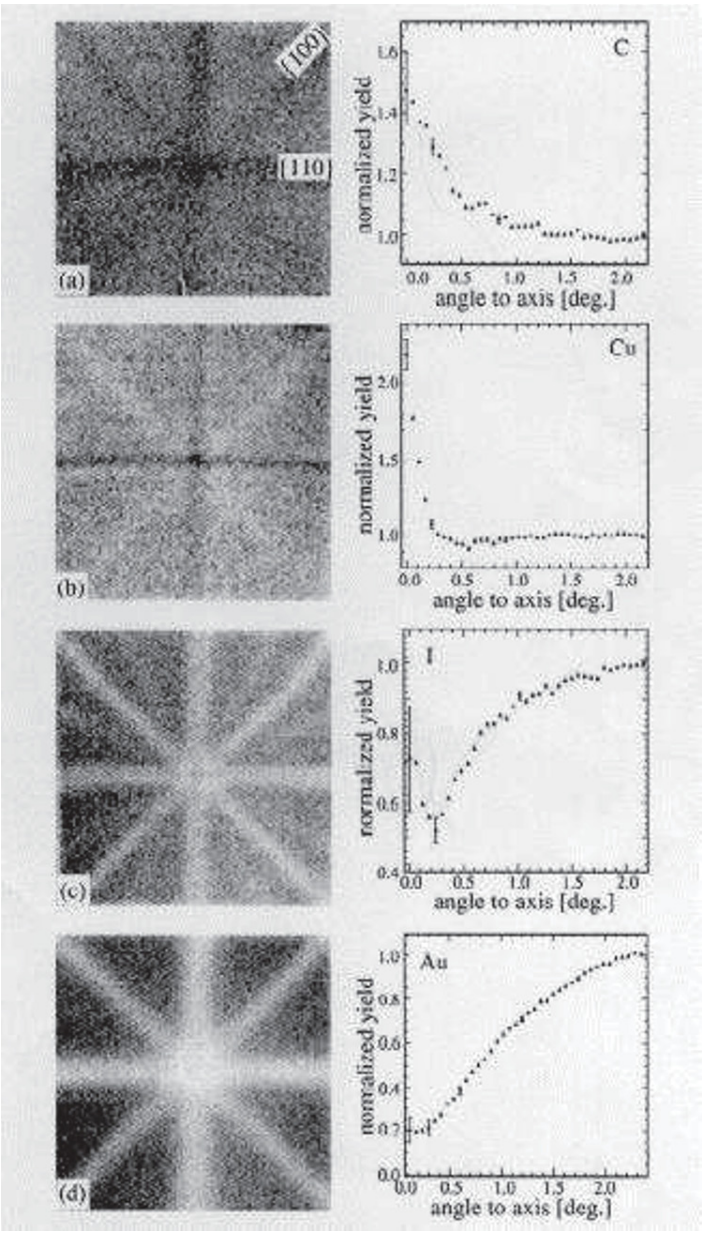

Fig. 11.25 Flux distributions of heavy ions after transmission through (001) Si crystal. To the right circularly averaged intensities; (a) C recoils at 18 MeV after 8.7 µm; (b) Cu recoils at 46 MeV after 8.7 µm; (c) scattered I ions at 121 MeV after 2.9 µm; and (d) scattered Au ions at 92 MeV after 2.9 µm. The angular range is $\pm 2.2°$ (Assmann et al., 1999)

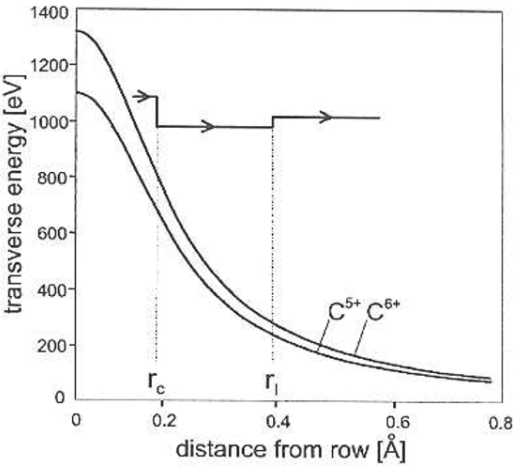

Fig. 11.26 ⟨100⟩ Si string potentials for C^{5+} and C^{6+} ions, in the point-charge approximation, see (11.6). The horizontal line indicates the transverse energy of an ion capturing an electron at r_c and losing it at r_l (Assmann et al., 1999)

The explanation must involve a phenomenon breaking the reversibility of trajectories, and the effects are far too strong to be caused by energy loss. Instead it was proposed that capture and loss of electrons by the penetrating ions may be responsible. For highly stripped ions with net charge Q the effective continuum potential is proportional to Q, (11.3) with $Z_1 e \to Q$. Electron capture then leads to a reduction of the transverse potential energy and electron loss to an increase. If, on the average, electron capture takes place at smaller distances from strings than electron loss there will be a net cooling effect, and this is indeed predicted to be the case at very high velocities, from the known impact-parameter dependencies of capture and loss in this limit.

The mechanism is illustrated in Fig. 11.26. A C^{6+} ion is moving away from a string with transverse energy close to 1100 eV. At the distance r_c it captures an electron and loses the transverse energy $U^{(1)}(r_c)$. Later at a distance r_l the electron is lost again and the transverse energy $U^{(1)}(r_l)$ is gained. The cycle has led to a net loss of transverse energy, i.e. to cooling.

These phenomena clearly offer an opportunity to study the impact parameter dependence of capture and loss processes. In particular for heavy ions carrying many electrons these processes are not well understood. However, for such ions the influence of the ion charge state on the interaction potential cannot be described in the simple manner expressed in (11.3). It is also a challenge to integrate capture and loss processes into the formalism for calculation of dechanneling, although there has been promising progress (Malyshevsky, 2005).

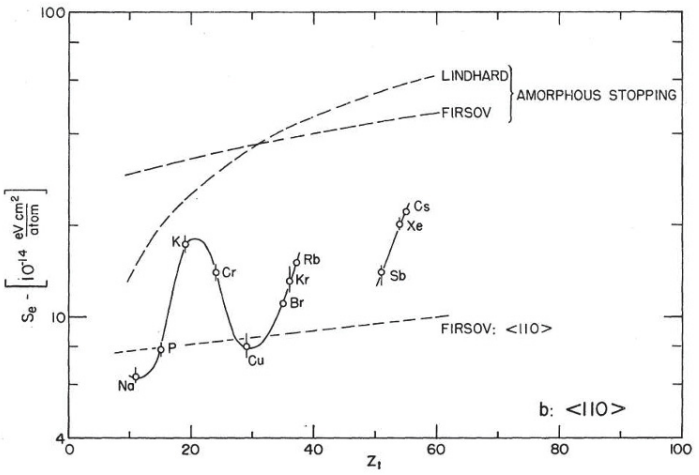

Fig. 11.27 Electronic-stopping cross section at velocity $v = 1.5 \cdot 10^8$ cm/s versus the atomic number of the projectile, derived from the range of a perfectly channeled ion along a $\langle 110 \rangle$ direction in tungsten (Eriksson et al., 1967)

11.10 Secondary Processes

We shall now turn to aspects of channeling which Lindhard denoted secondary phenomena, i.e., phenomena which are influenced by channeling but do not in turn affect the steering of the ions very much.

11.10.1 Energy Loss for Channeled Particles

The most prominent example is stopping. Studies of ion ranges, both computer simulations and range measurements, played a very important part in the discovery of channeling (see, for example, the introduction to Eriksson et al. (1967). The energy loss to atomic recoils, the so-called nuclear energy loss, is reduced most by channeling, and very long ranges of low-energy heavy ions were observed for incidence parallel to an axis in a crystal.

The selection by channeling of large impact parameters with atoms makes it possible to study the electronic energy loss at low velocities where nuclear energy loss dominates. A nice example is illustrated in Fig. 11.27 (Eriksson et al., 1967). The oscillatory dependence of the electronic stopping cross section, S_e, on Z_1 stems from the so-called Ramsauer-Townsend effect. The cross section for electron scattering on the penetrating ion may be written as a sum over angular momenta and at low velocity the s-wave cross section dominates. With increasing strength of the scattering potential, the s-wave phase shift increases, and the cross section has strong minima

when the phase shift passes through multiples of 2π (Finnemann, 1968, Briggs and Pathak, 1973). The oscillations were first seen in the stopping in amorphous foils but the elimination of atomic recoils and the confinement of electronic scattering to the thin electron gas far from atoms make the oscillations much more prominent.

At high velocities the slowing down is mainly due to electronic energy loss. For small Z_1 it may be obtained by a quantum perturbation calculation. The resulting Bethe formula may be written as an integral over impact parameters, leading to a logarithm of the ratio of an adiabatic radius divided by half the reduced wavelength of the electrons in the ion rest frame,

$$-\frac{dE}{dx} = NS_e = \frac{4\pi Z_1^2 e^4}{mv^2} N Z_2 \ln\left(\frac{v/\bar{\omega}}{\lambda\!\!\!^{-}/2}\right) \tag{11.18}$$

The observations of a reduced electronic energy loss for a substantial fraction of MeV protons penetrating several micron thick crystals demonstrated convincingly that channeling is not a simple transparency effect for low energy ions.

Asymptotically for large v the expression in (11.18) has equal contributions from large and small impact parameters (equipartition). Therefore the energy loss is at high velocities reduced by about a factor of two for the best channeled particles (Lindhard, 1965). As demonstrated by Esbensen and Golovchenko (1976), the theory simplifies in the high-velocity limit, and excellent agreement with measurements of the energy loss for relativistic channeled particles in thin Si and Ge crystals was obtained (Esbensen et al., 1978). Also the shape of the energy distribution for channeled particles could be accounted for when fluctuations of large energy transfers in single collisions with electrons were taken into account (Landau distribution).

Many other experiments and calculations on the stopping of channeled ions have been published (Cohen and Dauvergne, 2004) but still the full potential of such studies for testing the stopping power theory has in my view not been realized. An attempt at a detailed comparison with standard stopping theory for swift heavy ions is discussed in the following.

In the experiment 15.3 MeV/u Br^{33+} ions were passed through a very thin Si crystal and both the emergent charge state and the energy-loss spectrum was measured with a magnetic spectrometer (Andersen et al., 1996). As illustrated in Fig. 11.28, the 33+ ions with only the K-shell electrons remaining undergo very little capture or loss of electrons when the ions are incident along a ⟨110⟩ axis. This phenomenon of 'frozen charge state' was first observed and applied by Datz and coworkers in Oak Ridge in their pioneering experiments on channeling of high-energy, heavy ions (Krause and Datz, 1996). It is important for the analysis of the energy loss because the complication of a fluctuating charge state is removed.

The energy spectra for exiting 33+ and 32+ ions are shown in Fig. 11.29. For reference, also the energy spectrum for ions incident in a random (i.e., non-channelling) direction is shown, and the energy loss is given as a fraction of the random energy loss (4.9 MeV for 1 μm Si). Nearly all the 33+ ions have an energy loss much smaller than for random incidence, reflecting that nearly all the ions are channeled. The spectrum for the much fewer 32+ ions contains two parts, well chan-

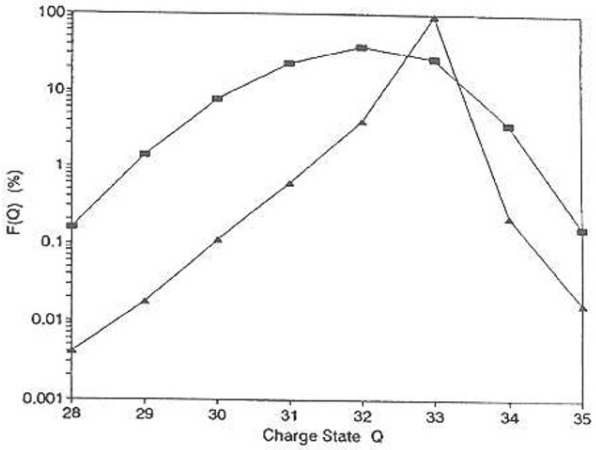

Fig. 11.28 Charge-state distributions for a random (squares) and a $\langle 110 \rangle$ aligned (triangles) beam of 15.3 MeV/u Br^{33+} ions after passage of a 1 μm Si crystal (Andersen et al., 1996)

neled ions which have captured a valence electron, with an energy spectrum similar to that for 33+ ions, and poorly channeled ions which have entered the crystal close to a string and scattered to angles of order ψ_1, with energy loss similar to or even larger than random. There is also a small component of such ions in the 33+ spectrum but it is strongly enhanced for 32+ ions because the capture probability is much higher for random than for channeled ions (Fig. 11.28).

For the analysis of the energy loss, the well channeled ions have been divided into three groups. For fixed trajectory, the straggling in energy loss is small. This can be seen from the width of the random energy loss peak which has about equal contributions from charge-exchange straggling and Bohr straggling (fluctuations in hard collisions). For channeled particles there is only the Bohr straggling and it is reduced due to the lower electron density. In contrast to the situation for relativistic particles discussed above, the width of the energy loss distribution therefore comes mainly from the distribution in transverse energy and the associated variation of the allowed area in the transverse plane. If the spatial variation of the energy loss rate is known, the energy distribution can be calculated and compared with the measurement.

The analysis was based on a simple description of the energy loss as consisting of three parts, the energy transfers to K-, L-, and M-shell electrons. The corresponding oscillator strengths and excitation frequencies could be estimated rather accurately, and the dependence of the energy loss on transverse energy was then calculated. Compared with the Bethe-Bloch formula given above there are two important corrections for heavy ions. First Bohr's kappa, see (11.12) with $Z_2 = 1$, is larger than unity and the classical counterpart, the Bohr formula, should be applied instead, with the reduced electron wavelength replaced by the classical collision diameter. Second, there may be a significant, so-called Barkas correction which is of third

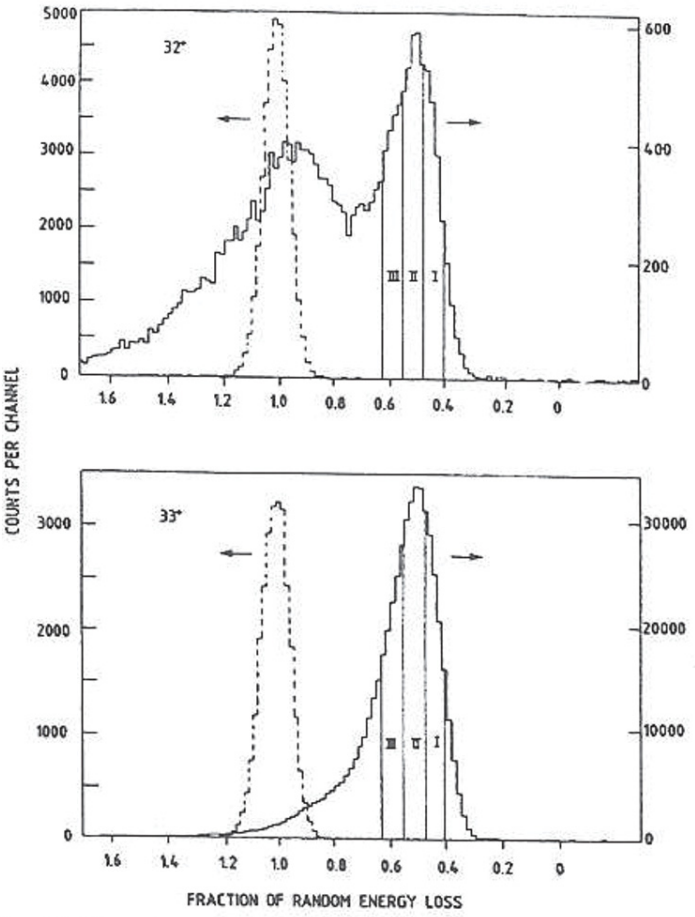

Fig. 11.29 Energy-loss of transmitted $32+$ and $33+$ ions for a beam of 15.6 MeV/u $^{79}Br^{33+}$ ions. Spectra for random (stipled lines) and $\langle 110 \rangle$ (solid lines) alignment are shown as functions of the energy loss relative to the average random loss of $\Delta E = 4.9$ MeV for the 1 μm thick Si target (Andersen et al., 1996)

order in Z_1. It is about 5%, only, for the present case. Good agreement with the measurement was obtained. The dependence of the stopping on transverse energy turns out to come partly from the spatial variation of the density of valence (M-shell) electrons, partly from the adiabatic cut-off of energy loss to the L-shell at large impact parameters with atoms.

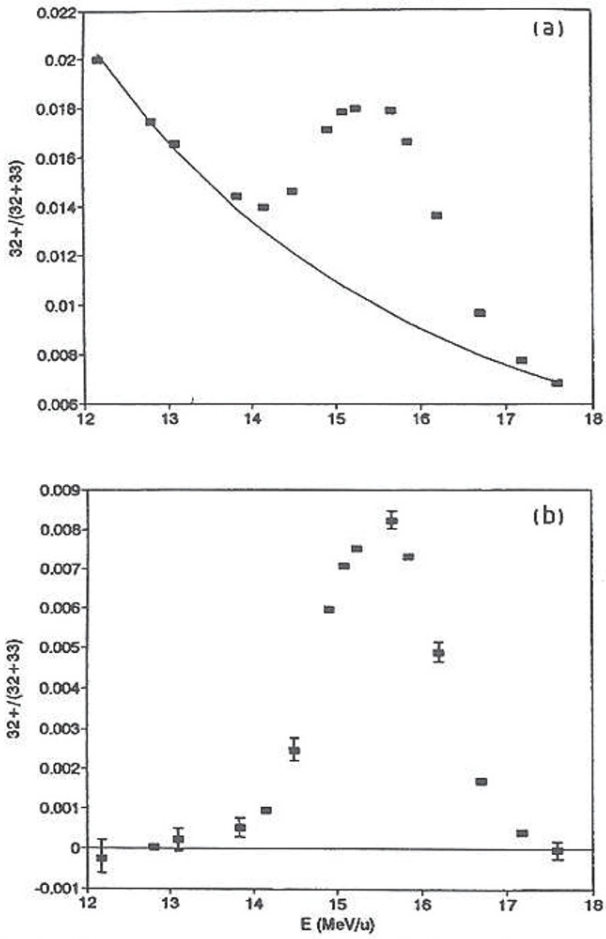

Fig. 11.30 (a) The charge state fraction $32^+/(32^+ + 33^+)$ for channeled ions with energy loss in the windows I, II, and III in Fig. 11.29, as a function of the ion energy. (b) Data in (a) after subtraction of a smooth background (Andersen et al., 1996)

11.10.2 Crystal as Special Target for Atomic Processes

Studies of energy loss are just one example of the use of crystals as special targets for measurements on atomic processes (Krause and Datz, 1996). For channeled ions, the target is essentially a gas of the valence electrons. This has been utilized to study capture processes like radiative electron capture and dielectronic electron capture.

An example from the experiment on Br^{33+} ions discussed above is illustrated in Fig. 11.30. The ratio between the numbers of 32+ and 33+ ions within the energy window I+II+III in Fig. 11.29 is here plotted as a function of the bombarding energy. The peak in Fig. 11.30b, obtained after subtraction of a smooth background from

other capture processes, occurs at a velocity where the energy of a valence electron in the ion frame of reference matches the K-shell binding energy minus twice the L-shell binding. An electron can then be captured with simultaneous excitation of a K-shell electron. The width of the resonance comes from the spread of electron velocities in the electron gas.

Another process which should be mentioned in this connection is resonant coherent excitation, sometimes called the Okorokov effect (Okorokov, 1965). Here a Fourier component of the periodic field from strings of atoms is used to excite a bound electron. Channeling is again used to avoid close collisions and thereby to maintain a well defined atomic state during the interaction. The excitation can be observed either by detection of radiative de-excitation outside the crystal or by observation of the emergent charge state distribution as a function of bombarding energy. At velocities where a multiple of the frequency of collisions with atoms on a string matches a transition frequency in the ion, the atomic excitation gives rise to an increase in the rate of electron loss and hence to an increase in the charge state. The effect was first observed unambiguously at Oak Ridge (Moak et al., 1979). Recently, mainly a Japanese group working at the high-energy accelerator laboratory RIKEN has been active in this area, extending the observations to heavier ions carrying a few electrons (Nakai et al., 2005).

11.11 Concluding Remarks

The physics of channeling is rich in interesting, sometimes quite surprising phenomena, and channeling and blocking have very many applications. I have reviewed some of the aspects of channeling which I have found it most exciting to work on, and I hope that the reader will experience some of this excitement. With the rapid development of computers, simulation has become increasingly important in the interpretation of experiments, but the analytical theory founded by Jens Lindhard remains the basis for our qualitative understanding of the phenomena.

Channeling is a mature field but there are still challenging problems to attack. The basic binary scattering is described by a screened Coulomb potential and, except for simple, limiting cases, there is considerable uncertainty in the representation of the combined screening by target and projectile electrons. I have mentioned two cases where this uncertainty is a problem. One is the application of blocking to measure nuclear lifetimes. It is important to be able to compare blocking dips for reaction products and for elastically scattered projectile ions, and this requires an accurate scaling of the critical angle for blocking with the atomic number of the blocked ions. Another example is the analysis of ‘heating’ and ‘cooling’ phenomena in the penetration of energetic heavy ions through thin crystals where a precise description of the dependence of the interaction potential on the ion charge state is needed.

Channeling of ions in crystals makes it possible to study the impact parameter dependence of atomic processes. The simplest example is energy loss, and studies of the modified stopping under channeling conditions played an important role in

the discovery of channeling. Usually the question has been what we can learn about the ion channeling from the energy loss spectrum. One may turn the question around and ask what we have learned about energy loss processes from channeling observations and what we can learn. I have argued that if experiments and calculations are planned with this question in mind there may be scope for new investigations of the energy loss of channeled ions. New opportunities are also offered by the recently discovered 'cooling' and 'heating' of ion beams transmitted through thin crystals, phenomena which are very sensitive to the impact parameter dependence of the capture and loss of electrons.

References

Alguard M.J., Swent R.L., Pantell R.H., Datz S., Barrett J.H., Berman B.L. and Bloom S.D. (1980): Radiation from channeled leptons. Nucl Instrum Methods **170**, 7–13

Andersen J.U., Andersen S.K. and Augustyniak W.M. (1977): Electron channeling. Mat Fys Medd Dan Vid Selsk **39 no. 10**, 1–58. URL `http://www.sdu.dk/Bibliotek/matfys`

Andersen J.U., Augustyniak W.M. and Uggerhøj E. (1971): Channeling of positrons. Phys Rev B **3**, 705–711

Andersen J.U., Bonderup E., Lægsgaard E., Marsh B.B. and Sørensen A.H. (1982): Axial channeling radiation from MeV electrons. Nucl Instrum Methods **194**, 209–224

Andersen J.U., Bonderup E., Lægsgaard E. and Sørensen A.H. (1983a): Incoherent scattering of electrons and linewidth of planar-channeling radiation. Physica Scripta **28**, 308–330

Andersen J.U., Bonderup E. and Pantell R.H. (1983b): Channeling radiation. Ann Rev Nucl Part Sci **33**, 453–504

Andersen J.U., Chevallier J., Ball G.C., Davies W.G., Forster J.S., Geiger J.S., Davies J.A., Geissel H. and Kanter E.P. (1996): Dielectronic recombination and energy loss for He-like ^{79}Br ions channeled in a thin single crystal of Si. Phys Rev A **54**, 624–635

Andersen J.U., Chevallier J., Forster J.S., Karamian S.A., Vane C.R., Beene J.R., Galindo-Uribarri A., del Campo J.G., Gross C.J., Krause H.F. et al. (2008): Attosecond lifetimes in heavy-ion induced fission measured by crystal blocking. Phys Rev C **78**, 064609

Andersen J.U. and Feldman L.C. (1970): Comparison of average-potential models and binary-collision models of axial channeling and blocking. Phys Rev B **1**, 2063–2069

Andersen J.U., Lægsgaard E., Nielsen K.O., Gibson W.M., Forster J.S., Mitchell I.V. and Ward D. (1976): Time evolution of heavy-ion-induced fission studied by crystal blocking. Phys Rev Lett **36**, 1539–1542

Assmann W., Huber H., Karamian S.A., Grüner F., Mieskes H.D., Andersen J.U., Posselt M. and Schmidt B. (1999): Transverse cooling or heating of channeled ions by electron capture and loss. Phys Rev Lett **83**, 1759

Barrett J.H. (1973a): Breakdown of the statistical-equilibrium hypothesis in channeling. Phys Rev Lett **31**, 1542

Barrett J.H. (1973b): Monte Carlo channeling calculations. Phys Rev B **3**, 1527–1547

Baurichter A., Biino C., Clément M., Doble N., Elsener K., Fidecaro G., Freund A., Gatignon L., Grafteröm P., Gyr M. et al. (2000): Channeling of high-energy particles in bent crystals - Experiments at the CERN SPS. Nucl Instrum Methods B **164-165**, 27–43

Bonderup E., Esbensen H., Andersen J.U. and Schiøtt H.E. (1972): Calculations on axial dechanneling. Radiat Eff **12**, 261–266

Briggs J. and Pathak A. (1973): Momentum transfer cross sections and the Z_1 oscillations in stopping power. J Phys C **6**, L153 – L157

Cohen C. and Dauvergne D. (2004): High energy ion channeling. Principles and typical applications. Nucl Instrum Methods **225**, 40–71

Datz S., Berman B.L., Dahling B.A., Hynes M.V., Park H., Kephart J.O., Klein R.K. and Pantell R.H. (1986): On the dependence of electron planar channeling radiation upon lattice vibration amplitude. Nucl Instrum Methods B **13**, 19–22

Davies J.A. (1983): The channeling phenomenon - and some of its applications. Physica Scripta **28**, 294–302

Domeij B. and Björkqvist K. (1965): Anisotropic emission of α-particles from a monocrystalline source. Phys Lett **14**, 127

Doyle P.A. and Turner P.S. (1968): Relativistic Hartree-Fock X-ray and electron scattering factors. Acta Cryst A **24**, 390–397

Drouart A., Charvet J.L., Dayras R., Nalpas L., Volant C., Chbihi A., Rodriguez C.E., Frankland J.D., Morjean M., Chevallier M. et al. (2005): Evidence of $Z = 120$ compound nucleus formation from lifetime measurements in the ^{238}U+Ni reaction at 6. 62 MeV/nucleon. In *Proc. Int. Symposium on Exotic Nuclei, Peterhof 2004*, 192–197. World Scientific

Eriksson L., Davies J.A. and Jespersgaard P. (1967): Range measurements in oriented tungsten single crystals (0. 1-1. 0 MeV). I. Electronic and nuclear stopping powers. Phys Rev **161**, 219–234

Esbensen H., Fich O., Golovchenko J.A., Madsen S., Nielsen H., Schiøtt H.E., Uggerhøj E., Vraast-Thomsen C., Charpak G., Majewski S. et al. (1978): Random and channeled energy loss in thin germanium and silicon crystals for positive and negative 2-15-GeV/c pions, kaons, and protons. Phys Rev B **18**, 1039–1054

Esbensen H. and Golovchenko J.A. (1976): Energy loss of fast channeled particles. Nucl Phys A **298**, 382–396

Feldman L.C., Mayer J.W. and Picraux S.T. (1982): *Materials Analysis by Ion Channeling*. Academic Press, New York

Finnemann J. (1968): En redegørelse for resultaterne af beregninger over spredning af elektroner med lav energi på afskærmede Coulombfelter. Master's thesis, Aarhus University

Gärtner K., Hehl K. and Schlotzhauer G. (1984): Axial dechanneling : II. Point defects. Nucl Instrum Methods B **4**, 55–62

Gemmell D.S. (1974): Channeling and related effects in motion of charged particles through crystals. Rev Mod Phys **46**, 129–227

Gibson W.M. (1975): Blocking measurements of nuclear decay times. Ann Rev Nucl Sci **25**, 465–508

Grüner F., Assmann W., Bell F., Schubert M., Andersen J.U., Karamian S., Bergmaier A., Dollinger G., Gorgens L., Günther W. et al. (2003): Transverse cooling and heating in ion channeling. Phys Rev B **68**, 174104

Guanere M., Sillou D., Spighel M., Cue N., Gaillard M.J., Kirsch R.G., Poizat J.C., Remmillieux J., Berman B.L., Cattillon P. et al. (1982): Sharp-line and broad-continuum radiation from electrons channeled in diamond. Nucl Instrum Methods **194**, 225–228

Hau L.V. and Andersen J.U. (1993a): Channeling radiation beyond the continuum model: The phonon 'Lamb shift' and higher-order corrections. Phys Rev A **47**, 4007–4032

Hau L.V. and Andersen J.U. (1993b): Line shifts of channeling raditation from MeV electrons. Radiat Eff **25**, 75–80

Hau L.V., Lægsgaard E. and Andersen J.U. (1990): Thermal vibrations in Si studied by channeling-radiation spectroscopy. Nucl Instrum Methods B **48**, 244–247

Hofsäss H. (1996): Emission channeling. Hyperfine Interactions **97-98**, 247–283

Karamian S.A., Forster J.S., Andersen J.U., Assmann W., Broude C., Chevallier J., Geiger J.S., Grüner F., Khodyrev V.A., Malaguti F. et al. (2003): Fission lifetimes of Th nuclei measured by crystal blocking. Europ Phys J A **17**, 49–56

Kennedy E.F., Nielsen B.B. and Andersen J.U. (1992): Planar channeling dips in backscattering yield. Nucl Instrum Methods B **67**, 236–240

Krause H.F. and Datz S. (1996): Channeling heavy ions through crystalline lattices. Adv At Mol Opt Phys **37**, 139–180

Kumakhov M.A. (1976): On the theory of electromagnetic radiation of charged particles in a crystal. Phys Lett A **57**, 17–18

Lervig P., Lindhard J. and Nielsen V. (1967): Quantal treatment of directional effects for energetic charged particles in crystal lattices. Nucl Phys A **96**, 481

Lindhard J. (1965): Influence of crystal lattice on motion of energetic charged particles. Mat Fys Medd Dan Vid Selsk **34 no. 14**, 1–64

Malyshevsky V.S. (2005): Transverse cooling or heating of channeled ions by electron capture and loss. Phys Rev B **72**, 094109

Moak C.D., Datz S., Crawford O.H., Krause H.F., Dittner P.F., del Campo J.G., Biggerstaff J.A., Miller P.D., Hvelplund P. and Knudsen H. (1979): Resonant coherent excitation of channeled ions. Phys Rev A **19**, 977–993

Nakai Y., Ikeda T., Kanai Y., Kambara T., Fukinishi N., Komaki K., Kondo C., Azuma T. and Yamazaki Y. (2005): Resonant coherent excitation of 2s electron of Li-like Fe ions to the $n = 3$ states. Nucl Instrum Methods B **230**, 90–95

Nielsen B.B., Andersen J.U. and Pearton S.J. (1988): Lattice location of deuterium interacting with the boron acceptor in silicon. Phys Rev Lett **60**, 321–324

Okorokov V.V. (1965): The coherent excitation of nuclei moving through a crystal. Yad Fiz **2**, 1009. Engl. Translation: Sov. J. Nucl. Phys. **2**, 719 (1966)

Pedersen M.J., Andersen J.U. and Augustyniak W.M. (1972): Channeling of positrons. Radiat Eff **12**, 47–52

Rasmussen F.B. and Nielsen B.B. (1994): Microstructure of the nitrogen pair in crystalline silicon studied by ion channeling. Phys Rev B **49**, 16353–16360

Robinson M.T. and Oen O.S. (1963): Computer studies of the slowing down of atoms in crystals. Phys Rev **132**, 2385–2398

Sørensen A.H. and Uggerhøj E. (1987): Channeling and channeling radiation. Nature **325**, 311–318

Tsyganov E.N. (1976a): Estimates of cooling and bending processes for charged particle penetration through a monocrystal. Fermilab TM **684**

Tsyganov E.N. (1976b): Some aspects of the mechanism of a charge particle penetration through a monocrystal. Fermilab TM **682**

Tulinov A.F., Kulikauskas V.S. and Malov M.M. (1965): Proton scattering from a tungsten single crystal. Phys Lett **18**, 304–307

Uggerhøj E. (1966): Orientation dependence of the emission of positrons and electrons from ^{64}Cu embedded in single crystals. Phys Lett **22**, 382–383

Uggerhøj E. and Andersen J.U. (1968): Influence of lattice structure on motion of positrons and electrons through single crystals. Can J Physics **46**, 543–550

Uggerhøj U.I. (2005): The interaction of relativistic particles with strong crystalline fields. Rev Mod Phys **77**, 1131–1171

Uguzzoni A., Andersen J.U. and Ryabov V. (1992): Thermal fluctuations in surface transmission for axial channeling. Nucl Instrum Methods B **67**, 231–235

Uguzzoni A., Gärtner K., Lulli G. and Andersen J.U. (2000): The minimum yield in channeling. Nucl Instrum Methods B **164-165**, 53–60

Author and Subject Index

P. Sigmund, *Particle Penetration and Radiation Effects Volume 2*,
Springer Series in Solid-State Sciences 179, DOI: 10.1007/978-3-319-05564-0,

Sun et al. (2007), 226, 227, 231
Surzhykov et al. (2005), 114, 146
Susuki et al. (2000), 525, 526, 545
Szymczak and Wittmaack (1994), 529, 545
Sørensen (2002), 206, 221, 230
Sørensen (2007), 166, 194
Sørensen (2010), 207, 231
Tahir et al. (1994), 528, 545
Tal and Levy (1981), 16, 42
Tawara et al. (1985), 89, 95
Tersoff (1986), 250, 280
Thomas (1926), 12, 42
Thomas (1927), 46, 48, 49, 67, 95
Thwaites (1983), 183, 195
Tilinin (1995), 377, 378, 415
Tolstikhina and Shevelko (2013), 46, 77, 95
Tomita et al. (2010), 510, 545
Tosaki et al. (2005), 399, 415
Toshima et al. (1987), 71, 96
Toyoda et al. (2003), 529, 545
Tsyganov (1976a), 558, 588
Tsyganov (1976b), 558, 588
Tulinov et al. (1965), 557, 588
Uggerhøj and Andersen (1968), 558, 559, 569, 588
Uggerhøj (1966), 558, 588
Uggerhøj (2005), 551, 564, 588
Uguzzoni et al. (1992), 573, 575, 588
Uguzzoni et al. (2000), 574, 588
Vager and Gemmell (1976), 536, 545
Vager et al. (1989), 530, 545
Valdes and Arista (1994), 298, 338
Vicanek and Urbassek (1988), 459, 476
Vockenhuber et al. (2013), 141, 146, 226, 228, 231
Vogt et al. (1986), 49, 96
Vollmer (1974), 97, 135, 146
Wang and Ho (1995), 393, 415
Wang and Nastasi (2010), 465, 476
Ward et al. (1979), 348, 415
Watt (1996), 387, 415
Wedepohl (1967), 245, 246, 280
Weick et al. (2000), 221, 231
Weng et al. (2006), 87, 96
Wentzel (1926), 81, 96
Westmoreland and Sigmund (1970), 469–471, 476
Weyl (1953), 353, 415
Wick (1949), 436, 476
Williams (1939), 304, 338
Wilson and Bisson (1971), 246, 280
Wilson et al. (1977), 246, 247, 264, 280, 462, 476
Winterbon et al. (1970), 258, 270, 280, 438, 441–443, 456, 457, 471, 477
Winterbon (1968), 382, 383, 415
Winterbon (1972), 259, 280, 457, 476
Winterbon (1975), 449, 450, 454, 457, 476
Winterbon (1977), 97, 139, 146
Winterbon (1983a), 459, 477
Winterbon (1983b), 457, 458, 477
Winterbon (1986), 450, 477
Winterbon (1987), 318, 339
Winterbon (1989), 318, 339
Winter (2002), 334, 339, 536, 545
Witte and Wölfel (1958), 246, 280
Yamamura and Takeuchi (1984), 267, 280
Yamamura and Takeuchi (1987), 462, 477
Yamamura (1988), 510, 545
Yang et al. (1991), 223, 225–228, 231, 399, 415
Yarlagadda et al. (1978), 16, 43
Zajfman et al. (1990), 519, 546
Zajfman (1990), 519, 521, 523, 524, 545
Zhang and Weber (2003), 348, 415
Zhang et al. (2002), 348, 415
Ziegler et al. (1985), 154, 177, 178, 195, 247, 269, 280, 383, 415, 516, 546
Ziegler et al. (2008), 177, 195, 469, 477
Ziegler (1980), 177, 195
Ziegler (2012), 183, 195, 350, 351, 387, 415
Ziemba and Everhart (1959), 253, 263, 280
Ziman (1972), 405, 415
Zinoviev (2011), 265, 266, 280